AVERTISSEMENT

Ce document est le fruit d'un long travail approuvé par le jury de soutenance et mis à disposition de l'ensemble de la communauté universitaire élargie.

Il est soumis à la propriété intellectuelle de l'auteur. Ceci implique une obligation de citation et de référencement lors de l'utilisation de ce document.

D'autre part, toute contrefaçon, plagiat, reproduction illicite encourt une poursuite pénale.

Contact : ddoc-theses-contact@univ-lorraine.fr

LIENS

Code de la Propriété Intellectuelle. articles L 122. 4
Code de la Propriété Intellectuelle. articles L 335.2- L 335.10
http://www.cfcopies.com/V2/leg/leg_droi.php
http://www.culture.gouv.fr/culture/infos-pratiques/droits/protection.htm

Ecole Doctorale SIReNa – Sciences et Ingénierie des Ressources Naturelles

THÈSE

présentée et soutenue publiquement pour l'obtention du titre de

Docteur de l'Université de Lorraine
Mention « Géosciences »

par **Julien PERRET**

Répartition spatio-temporelle du système métallogénique de l'or panafricain au sein du bouclier arabo-nubien : étude multi-scalaire le long de la suture de Keraf (Soudan)

18 juin 2021

Membres du jury :

Rapporteurs

M. Thomas BLENKINSOP	Professeur, School of Earth and Environmental Sciences, Cardiff University
M. Yannick BRANQUET	Maître de Conférences HDR, UMR 6118, Université de Rennes

Examinateurs

M. Alain CHAUVET	Directeur de Recherche, UMR 5243, Université de Montpellier
Mme. Blandine GOURCEROL	Ingénieure-chercheur, BRGM, Orléans
M. Patrick LEDRU	Professeur - Titulaire d'une chaire industrielle ORANO, UMR 7359, Université de Lorraine
Mme. Anne-Sylvie ANDRÉ-MAYER	Professeur, UMR 7359, Université de Lorraine Directrice de thèse
M. Aurélien EGLINGER	Maître de Conférences, UMR 7359, Université de Lorraine Co-directeur de thèse
M. Julien FENEYROL	Géologue d'exploration senior, Arethuse Geology, Aix-en-Provence Co-directeur de thèse

Invité

M. Laurent AILLÈRES	Professeur, School of Earth, Atmosphere & Environment, Monash University, Melbourne
M. David JOUSSELIN	Maître de Conférences, UMR 7358, Université de Lorraine
M. Rémi BOSC	Gérant, Arethuse Geology, Aix-en-Provence

UMR 7359 GeoRessources, Université de Lorraine – CNRS
Faculté des Sciences et Technologies, Rue Jacques Callot, BP 70239
54506 Vandoeuvre-lès-Nancy

Résumé

L'or est un élément sidérophile préférentiellement contenu dans les enveloppes internes de la Terre. La compréhension des mécanismes permettant son transfert vers l'écorce terrestre passe par l'étude de l'évolution géodynamique des segments de croûte dite juvénile, *i.e.,* dérivée de matériel extrait directement du manteau. Le système métallogénique de l'or s'intéresse donc (i) à l'environnement géodynamique favorable à la fertilisation en or de la croûte et (ii) au(x) contexte(s) tectono-métamorphique(s) ayant permis la remobilisation de ce réservoir et sa concentration sous forme d'occurrences minéralisées. Cette démarche est appliquée aux sutures de Keraf et d'Atmur-Delgo au sein du bouclier arabo-nubien, le plus grand segment au monde de croûte juvénile néoprotérozoïque et l'une des principales provinces aurifères panafricaines. Si ces structures sont considérées comme des marqueurs de la formation du supercontinent Gondwana au Soudan et hébergent de nombreux gisements aurifères, leur évolution géodynamique et métallogénique reste méconnue.

Deux pics d'activité magmatique à signatures isotopiques Hf et Nd suprachondritiques enregistrent la formation et la maturation de différents arcs insulaires le long de ces zones de suture entre 840-810 Ma et 760-655 Ma. La longue durée de vie (185 millions d'années) de l'arc insulaire décrit le long de la suture de Keraf et sa nature juvénile prédominante expliqueraient la fertilisation crustale en or à l'échelle régionale. La première phase de croissance crustale, uniquement enregistrée le long de la suture de Keraf, est associée à un événement aurifère mineur, de nature magmato-hydrothermale. La seconde période d'activité magmatique est associée au fonctionnement d'arcs insulaires le long des sutures de Keraf et d'Atmur-Delgo.

Le couplage d'observations et de mesures réalisées du terrain au laboratoire illustre la continuité spatiale du contrôle structural des minéralisations postérieures au premier événement aurifère décrit. D'une part, un épisode minéralisateur a lieu vers 755-725 Ma, lors d'un continuum de déformation exprimé par la mise en place de plis en fourreau et de structures minéralisées linéaires. Les roches encaissantes de la minéralisation sont affectées par un métamorphisme au faciès amphibolite inférieur. À l'échelle du district, cet événement aurifère est associé à l'accrétion tectonique dans le prisme sédimentaire en avant de l'arc d'Atmur-Delgo. À l'échelle microscopique, la minéralisation résulte de la remobilisation syn-métamorphique du stock d'or contenu par les sulfures préexistant. D'autre part, plusieurs gisements d'or orogénique sont exprimés sous forme de veines d'extension hébergées par des corps intrusifs, illustrant un fort contrôle rhéologique de la minéralisation. Les veines minéralisées sont formées selon le mécanisme de faille-valve, en réponse à la réactivation épisodique et localisée de décrochements crustaux jusqu'à 550 Ma au sein de la suture de Keraf. Les deux événements minéralisateurs exprimés le long des sutures d'Atmur-Delgo et de Keraf sont respectivement le plus ancien associé à des veines aurifères et le plus jeune d'or orogénique décrits à ce jour au sein du bouclier arabo-nubien.

L'application du système métallogénique permet de définir des clés d'exploration à l'échelle du district qui traduisent des processus magmatiques (*e.g.,* reliques d'arc insulaire) et contextes tectono-métamorphiques (*e.g.,* prisme d'accrétion, décrochements tardi-orogéniques) contrôlant des minéralisations aurifères aux caractéristiques structurales, géochimiques et chronologiques très variables dans la partie occidentale du bouclier arabo-nubien. Cette stratégie diffère singulièrement de l'approche typologique dont l'efficacité se limite à (i) un unique type de minéralisation et à (ii) la prospection à l'échelle du gisement.

Abstract

Gold is a siderophile element preferentially concentrated in the Earth's mantle and core. The understanding of mechanisms leading to its transfer towards the crust requires the study of the geodynamical evolution of juvenile crust portions, *i.e.,* crystallized from melt directly extracted from the mantle. The gold mineral system thus combines the deciphering of crustal fertilization geodynamical processes and subsequent transient tectono-metamorphic setting(s) favorable for remobilization of this metal-enriched reservoir and formation of mineralized occurrences. This approach is applied to the Keraf and Atmur-Delgo sutures which are part of the Arabian-Nubian shield, the world-largest track of Neoproterozoic juvenile crust and one of the main Pan-African gold provinces. Although these structures are considered as insightful windows into the assembly of Gondwana in Sudan and host major gold deposits, their coupled geodynamical-metallogenic evolution remains poorly understood.

We report the existence of two magmatic flare-ups with suprachondritic Hf and Nd signals, recording the build-up and maturation of island arcs along these suture zones between 840-810 Ma and 760-655 Ma. The ~185 Myr-long lifespan of the island arc described along the Keraf suture and its predominant juvenile nature likely accounted for crustal gold fertilization at the regional scale. The earliest crustal growth stage, only recorded along the Keraf suture, is coeval to minor magmatic-hydrothermal gold event. Both the Keraf and Atmur-Delgo sutures keep record of the second island arc flare-up.

The matching between field and laboratory data exemplifies the district- to microscopic-scale spatial continuity of structural control on later gold-bearing structures described in this study. On one hand, a gold event occurred between 755-725 Ma, during high-strain progressive deformation expressed by sheath folding and the formation of linear ore shoots under lower amphibolite facies metamorphism. It likely relates to tectonic accretion of the sedimentary wedge at the Atmur-Delgo intra-oceanic subduction site. At the microscopic scale, the ore formation involved the syn-metamorphic remobilization of the gold budget contained in earlier sulfide generations. On another hand, several orogenic gold deposits display intrusion-hosted mineralized extension veins, highlighting a strong rheological control on ore deposition. The fault-valve mechanism induced the formation of mineralized veins, triggered by episodic and localized reactivation of crustal strike-slip shears within the Keraf suture zone until 550 Ma. Gold events described along the Atmur-Delgo and Keraf sutures are the oldest vein-type gold and youngest orogenic gold episodes reported throughout the Arabian-Nubian shield to this day, respectively.

The mineral system approach therefore enables district-scale ore targeting by translating magmatic processes (*e.g.,*) and tectono-metamorphic settings into environments and geological features (*e.g.,* relics of an island arc and/or an accretionary wedge, presence of late collisional strike-slip shears) favoring the formation of gold occurrences with very distinct structural, geochemical and timing characteristics in the western Arabian-Nubian shield. This alternative view of ore deposits contrasts sharply with the typological strategy which targets a single class of ore occurrence with an effectiveness limited to the deposit scale.

REMERCIEMENTS

Vers (petit coin bucolique de Bourgogne),

le 15 avril 2021

Une quarantaine de *v0*, *v1*, *v2_bis_AE_ASAM_JF_XXmissing* plus tard, quelques longues journées (et courtes nuits) de labeur furent nécessaires à l'assemblage des ô combien inestimables *vf* composant les parties de ce manuscrit, m'enfonçant toujours plus dans les abysses de Word, puis la lumière fût. Aux lecteurs ayant fait preuve de suffisamment de courage pour continuer au-delà du résumé, j'espère que vous me pardonnerez volontiers ces quelques pages supplémentaires, qui, si elles ne sont pas nécessaires à assurer la fonction de cale-porte destinée d'ici quelques mois à cet ouvrage, me permettront d'évoquer bon nombre de personnes dont le soutien, l'intérêt porté à ces travaux et l'affection sont d'une valeur inestimable.

Je pense en premier lieu à Anne-Sylvie, Aurélien et Julien, qui m'auront accompagné dans les tréfonds du désert nubien, et dont l'encadrement de ces travaux aura été extrêmement complémentaire, compte-tenu de vos sensibilités respectives. Merci pour votre disponibilité à toute épreuve, les heures passées à discuter, débattre, et à corriger les épreuves aboutissant à ce manuscrit. Je remercie également Arethuse Geology, et plus particulièrement Rémi Bosc, d'avoir initié ce projet de R&D, ainsi que l'ensemble des acteurs m'ayant fait confiance pour le concrétiser, à la croisée des chemins entre industrie et recherche académique. Ce projet de recherche a bénéficié de l'attribution d'une bourse par établissement d'une Convention Industrielle de Formation par la Recherche (CIFRE) de la part de l'Association Nationale pour la Recherche et la Technologie. Les sociétés Orca Gold Inc. et Managem, dont les prospects aurifères sont étudiés, sont également remerciées pour leur soutien financier, logistique et humain ainsi que l'accès fourni à leurs données. Je pense plus particulièrement à Hugh Stuart, Craig Hartshrone, Ema Abanyin, Bushra Abdelsalam, Mawia Mohameday et Isam Eldin (Orca Gold Inc.) ainsi qu'à Hassan Nabil, Aomar Ennaciri, Attaiaa Hachem, Hassan Ait Benmouh, Mohamed Niyazi et El Alami Boukkari (Managem).

Les travaux présentés ont été essentiellement réalisés au sein du laboratoire GeoRessources. Je tiens à remercier très sincèrement l'ensemble des membres du laboratoire, depuis le pôle administratif jusqu'aux différentes plateformes analytiques en passant par les titulaires, post-doctorants, doctorants, stagiaires et les services d'entretien, qui font de GeoRessources un véritable espace de vie et d'émulation, aussi bien scientifique qu'humaine. Concernant les stagiaires, j'adresse un grand merci à Alix, Diego et Hugo que j'ai eu la chance de suivre avec grand plaisir sur leurs thématiques de recherche, qu'elles soient en lien avec mon sujet de thèse ou non. Bon vent à vous trois. Célestine, je te remercie pour le travail de qualité exceptionnel que tu as fourni lors de ton stage de M2 et de la confiance que tu nous/m'a accordée pour t'accompagner. Échanger avec toi est toujours un plaisir et ta contribution à ce manuscrit est significative. Je te souhaite le meilleur dans la suite de ton aventure avec GeoRessources et Arethuse !

Les données discutées dans ce manuscrit sont également le fruit d'un travail collaboratif impliquant d'autres laboratoires français et internationaux. Je remercie donc, dans le désordre,

Pierre Bouilhol, Jérôme Ganne, Fabrice Barou, Marc Poujol, Laurent Aillères, Armin Zeh et Alexandre Voinot pour leur contribution, leur disponibilité et nos échanges stimulants.

J'aimerais également exprimer ma gratitude envers les membres du jury extérieurs à l'encadrement de cette thèse qui ont accepté de l'évaluer: Thomas Blenkinsop et Yannick Branquet en qualité de rapporteurs ; Alain Chauvet, Blandine Gourcerol et Patrick Ledru en tant qu'examinateurs. Laurent Aillères et David Jousselin font partie de ce jury en tant qu'invités, du fait de leur implication dans ce projet de doctorat. Laurent a participé à la réflexion sur le contrôle structural et contexte géodynamique de mise en place des minéralisations présentées dans cette étude. Cette collaboration aurait dû aboutir sur un séjour de deux mois à *Monash University* dans son équipe de recherche afin de parfaire ces discussions, projet avorté en raison de la pandémie mondiale de Covid-19. David était quant à lui membre du comité de suivi de thèse ayant évalué l'avancé progressive des travaux au cours des trois ans passés. Merci à vous deux pour vos conseils éclairés et vos encouragements.

Il est désormais temps de remercier tous ceux qui rencontrés un peu partout en France et à l'étranger, depuis de plus ou moins longues années, dont l'influence ne se manifeste peut-être pas concrètement dans ce manuscrit, mais dont la présence et le soutien ont été prépondérants dans la réussite de cette entreprise.

À Nancy

À la Puschglinger family, votre joie de vivre et votre enthousiasme de tous les instants fait chaud au cœur et le petit Noa semble avoir hérité du gène !! Pour Elio c'est encore un peu tôt, mais comment ne pas craquer devant cette petite boule d'amour ? Ornella, merci mille fois pour ces moments passés à discuter de tout et de rien, tes encouragements répétés et ta force de volonté contagieuse. Glin, si j'admire ta rigueur scientifique (« c'est anecdotique » *vs* « c'est *key* !! »), ton goût de la sémantique et ton enthousiasme débordant, tu représentes bien plus qu'un modèle d'excellence scientifique pour moi. Et puisque les meilleures idées nous viennent autour d'un petit verre de rhum ou deux, j'espère que nous serons particulièrement inspirés sous peu !

Chez les Mayer, je demande Manu : merci de m'avoir appris à faire du vélo, à charge de revanche (ou de récidive...) ! Anne-Sylvie, ton implication totale pour tes étudiants, ton positivisme à toute épreuve et ton amour de la géochimie (☺) ne font aucun doute. Au même titre qu'Aurélien, je te considère comme étant bien plus que la directrice de thèse idéale que tu es, en témoignent les nombreux moments partagés au Québec, en Écosse, au Soudan ou encore dans le Tarn... mais également toutes ces réunions informelles, prétexte pratique pour une petite pause-café pas déméritée (il fallait bien une double négation pour clore ce paragraphe) !!!

À l'hôtel le Moal-Teitler, dont la qualité du gîte et du couvert n'est surpassée que par la sympathie, le sourire et le goût de la vie de ses gérants ! Plus sérieusement, merci infiniment à vous deux, Yo et Alizé, pour les excellents moments passés en votre compagnie, votre soutien et votre accueil si chaleureux à chacune de mes venues. J'ai hâte de trinquer avec vous, à Nancy, en Bourgogne, ou, qui sait, en Nouvelle-Cal ?...

Daf' et Raph, j'espère que nous remettrons à très vite notre escapade grimpe ! Merci pour tous ces cafés partagés en votre compagnie, en plus de tous les autres moments, agrémentés de réflexions profondes (ou pas)... Prenez soin de vous.

Dimit', le représentant en chef des crevettes grimpeuses, ex-étoile montante du basket-ball ligérien, amateur de Ricou et de Sum 41, coiffeur et danseur étoile à ses heures perdues... Ton déménagement a causé la faillite de la corporation des kinés nancéiens quand même... J'espère qu'on se fera bientôt ce trek ensemble et que de belles aventures de grimpe et de bistrots lillois se présagent dans un futur proche !

À tous les copains du labo, et les plus anciens remontent à l'époque dorée de Doc GeoRessources où je n'étais qu'un stagiaire préposé au café (10 cuillères rases !) sous la directive de Pierre, *aka* Chaton. Pierre, merci encore de tout ce que j'ai appris avec toi et Merca. Merci à toute la fine équipe de m'avoir si bien accueilli à l'époque et les bons moments passés. Comment poursuivre sans mentionner la figure tutélaire de cette bande de joyeux lurons, qui a su se fondre dans la masse et s'adapter au flux et reflux des générations successives de doctorants et post-doctorants, l'inamovible Julien ? Merci de m'avoir fait ouvrir les yeux sur les dangers de la surconsommation de salade et la nécessité de rester carré-carré. Passons désormais au père Turlin, le tyran du café (*cf* 7 lignes plus haut). Au-delà de ça, merci pour les heures passées à discuter de science, de la vie, bref, de tout ! Alors, on le fait quand ce tour des Écrins ? Audrey, merci pour les journées passées à bosser au soleil, tes histoires extravagantes qui n'ont d'égal que l'emphase que tu y mets, et l'initiation au hula hoop, malgré mon manque de prédisposition pour la discipline. La Gigue, je garde un souvenir ému de notre escapade lilloise avec le père Laurent, que l'on peut résumer par le tiercé gagnant PMU-serviette-bar à cocktails. Père Foucaud, bien que ton sourire carnassier soit un peu glaçant, ça fonctionne apparemment pas mal pour enchaîner les prix ! Prépare toi, on reprend le T-Roc dans le Tarn cette année, on va voir si mamie Anne-Sylvie suit le rythme (ce n'est pas moi qui l'ai dit !) ! Enfin, Émeline, je ne peux manquer d'évoquer notre amour commun de Lyon !!

J'ai évidemment une pensée pour mes compagnons de cordée, membres honoraires de la Gold Team dirigée par ASAM et Aurélien, les pères Combes et Dakouré. Merci pour les bons moments passés ensemble qui tournaient souvent autour de la malbouffe, j'y vois une forte influence de Vincent !

Merci à Gillou et Damien pour l'accueil chaleureux, les bons petits plats et les spécialités liquides faites maison servis à la cantine officieuse adoptée par bon nombre de membres du 5ème-6^{éme} étage du laboratoire. Les équipes B4 (sous la houlette du duo de choc Eglingero-Carpentiero) et Gold Team la recommandent vivement et attendent avec impatience sa réouverture.

Puisque Loïc ne va pas sans Chris (désolé Yasmine !), vient le moment de remercier les Vosges ~~et la Haute-Saône~~ de fournir de tels spécimens. Il y a quelques défauts de fabrication (faut pas s'attendre à quoi non plus !), mais c'est globalement du robuste et du massif (à l'exception des chevilles et des tibias). Présentation : partenaires de course (#teamorangejersey), ils se plaisent à ruiner les efforts consentis lors d'une sortie, qui surpassait comme de coutume toutes les limites du raisonnable, en se goinfrant des bons petits plats concoctés par, au choix, Chris-Yasmine-Mamou-le Voyou. Si la bonne humeur est toujours au rendez-vous et la bromance jamais très loin, quelques nuages noirs font leur apparition au détour d'une occasion croquée ou d'un

vol absolu sur Fifa (j'ai entendu « seum » ?). Vous l'aurez compris les copains, j'ai hâte de vous retrouver et merci mille fois pour tous les bons moments passés ensemble. Yasmine, *aychek* pour tout également et pour nous supporter, enfin surtout Loïc !! *Boussa kbira* !

Dark Noiram, ce n'est finalement pas un surnom qui te va si bien... Merci pour les heures passées au téléphone à se raconter nos vies, nos tracas, nos joies. Être présent quand on a besoin l'un de l'autre, c'est finalement ça qui compte !!

Bastien, merci mon vieux pour les bons moments passés à Nancy, puis plus récemment à Toulouse, les conseils de films, de bouquins, etc..., toutes nos discussions également et ta présence. J'espère qu'on arrivera à se faire une sortie grimpe sous peu !

À Aix-en-Provence

Julien, tu as finalement décidé si c'est de l'andésite ou de l'andésite basaltique à Ariab ? ☺ Ce qui est certain, aucun de nous deux n'est partisan du *Boukra inch'Allah* ! Si ton sens du détail frôle quand même la maniaquerie (☺), j'espère avoir su m'en imprégner. Merci mille fois pour ta disponibilité à mon égard et ton regard critique toujours pertinent. Merci également de ta confiance sur le terrain et de tout ce que tu m'as appris sur la gestion de projets d'exploration. J'en garde d'excellents souvenirs. Désormais, tu viens quand tu veux en Bourgogne, histoire de voir à quel point c'est mieux que l'Auvergne !!

Rémi, je te remercie de ta grande souplesse et de la liberté que tu m'as laissée au cours de ces trois années, que ce soit en termes d'objectifs scientifiques ou pour m'autoriser à réaliser des vacations en parallèle de mon travail de recherche. Merci également de m'avoir permis de participer à deux missions de terrain dans le cadre des projets d'Arethuse au Soudan. J'ai découvert une façade de l'exploration où la géologie est finalement très secondaire, faite de débrouillardise et d'adaptabilité nécessaires à parer tout contre-temps d'origine logistique, humaine et/ou climatique (*Welcome to Paradise !*). Malgré quelques sueurs froides, ces expériences ont été extrêmement enrichissantes et j'en garde d'excellents souvenirs. J'espère que les perspectives ouvertes au terme de ce projet seront à la hauteur des espérances que tu avais lorsque tu as initié cette collaboration avec Anne-Sylvie.

Chez Arethuse, merci à Naima pour ta gentillesse infinie et l'un des meilleurs couscous de ma vie !!! Merci également à Floriane et Jacques pour les bons moments passés ensemble à Aix.

Enfin, merci à Jan pour son soutien logistique très efficace et rassurant pendant les missions de terrain en outre des discussions enflammées sur le Super Rugby !

En Bourgogne

Élodie et Coline, il n'y a finalement pas grand-chose à dire... Ça fait tant d'années que l'on se connaît, et même si l'on se voit que rarement désormais, votre soutien et votre amitié me sont chères, *« Tié la famille ! »*.

Clem, « t'abuses !!! », ça te rappelle rien ?? Toujours un plaisir de te retrouver, et d'entendre tes histoires !! Merci pour tous les bons moments passés ensemble, depuis Dijon jusqu'à la Roumanie, et ta présence à tout instant mon copain !

Coco, on se sera suivi pas mal de temps depuis Dijon jusqu'à la thèse... Merci pour les bons moments passés toutes ces années et bon courage pour la fin, on en voit le bout !

« Ionion la meilleure », qu'ajouter d'autre ?? Blague à part, merci Marion pour tout et ces discussions parfois philosophiques qui nous emmènent loi !!

Déborah et Sandrine, merci pour votre soutien et votre écoute si précieuse.

Camille, merci infiniment pour tout ce que tu m'as apporté et d'avoir été le personnage principal de mes plus beaux souvenirs.

Je clôturerai cette salve de remerciements en évoquant le pilier indéfectible sur lequel je n'ai de cesse de me reposer, ma famille. Vous m'avez toujours soutenu, peu importe mes choix, les craintes et doutes que vous pouviez ressentir. Vous m'avez aidé à me relever lorsque je n'en avais pas la force. Papa, Maman, quelques mots ne suffiront pas à vous exprimer tout mon amour et la reconnaissance de tout ce que vous avez fait pour moi. Lucie, tu as toujours été là pour moi, depuis qu'on est gamin et je ne t'en remercierai jamais assez. Enfin, ma petite Mady, à l'heure où j'écris ces lignes, tu te fais encore attendre et pourtant, tu es une source de bonheur irradiant toute la famille depuis quelques mois. Si tu voyais l'agitation et les sourires que tu causes !! J'ai hâte de te rencontrer, et peut-être qu'un jour, nous relirons ces lignes ensemble, toi assise sur les genoux de ton parrain.

N'oublions pas Bella, Hélia et Paillette ; merci pour l'amour que vous nous portez au quotidien et le réconfort qu'offre votre présence à nos côtés.

à nos grands-parents et arrière-grands-parents,
et l'écho de nos rires d'enfant

TABLE DES MATIÈRES

Résumé iii

Abstract v

REMERCIEMENTS vii

TABLE DES MATIÈRES xv

LISTE DES FIGURES xxvii

LISTE DES TABLEAUX xxxv

LISTE DES ANNEXES xxxix

GLOSSAIRE xliii

INTRODUCTION GÉNÉRALE 1

Préambule – Pourquoi s'intéresser à l'or, en particulier au Soudan ? 3

1. La notion de système métallogénique (*mineral system*) 7

1.1. Émergence du concept et définition 7

1.2. Les gîtes métallifères, traceurs géodynamiques à l'échelle d'un cycle orogénique 9

2. Compréhension actuelle des systèmes métallogéniques de l'or 12

2.1. L'or, un élément chimique traceur des transferts entre le manteau et la croûte 12

2.2. L'exemple du craton ouest-africain 23

3. Contexte géodynamique du bouclier arabo-nubien 24

3.1. Du « Panafricain » (ca. 1000-542 Ma) à l'orogenèse est-africaine-antarctique (ca. 1100-550 Ma) 24

3.2. Mise en place du bouclier arabo-nubien 29

3.3. Mise en place de la suture de Keraf 42

4. Le bouclier arabo-nubien : une province aurifère de classe mondiale 44

4.1. Systèmes métallogéniques aurifères du bouclier arabo-nubien 44

4.2. Potentiel aurifère le long de la suture de Keraf 47

4.3. Lacunes de connaissances 49

5. Problématiques et approche multi-scalaire proposée 50

6. Organisation du manuscrit 52

7. Support scientifique et financier, collaborations extérieures 55

PARTIE I – ÉVOLUTION LITHOSPHÉRIQUE DE LA PARTIE CENTRALE DE LA SUTURE DE KERAF 57

Préambule 59

Chapitre I – Long-lived Neoproterozoic island-arc along the central Keraf suture, NE Sudan 61

Résumé 63

Abstract 65

1. Introduction 67

2. Geological setting 71

2.1. The East African-Antarctic orogeny and greater Gondwana assembly 71

2.2. Keraf arc-continent suture between the Arabian-Nubian shield and West Gondwana 72

2.3. Lithological-tectonic evolution of the Keraf arc-continent suture 73

3. Sampling and analytical techniques 74

3.1. Sampling philosophy and field observations 74

3.2. Analytical techniques 78

4. Results 81

4.1. Whole-rock geochemistry 81

4.2. U-Pb ages of zircon 88

4.3. Hf isotope analyses of zircon 98

4.4. Sr and Nd isotope whole-rock analyses 99

5. Lithospheric evolution of the central Keraf suture between *ca.* 840-620 Ma 104

5.1. Intra-oceanic subduction and Keraf island arc-back-arc system 104

5.2. Magmatic events recorded through the central Keraf suture 105

6. Insights into the Pan-African tectono-magmatic evolution of the northeastern flank of West Gondwana 111

6.1. Scope of the ~185 Myr-long-lived Keraf island arc at the Gondwana scale 111

6.2. Reconciliation of the geometry of the Keraf and Atmur-Delgo arc systems 112

6.3. Insights into the tectono-magmatic evolution of the northeastern flank of West Gondwana 114

7. Conclusions 118

Acknowledgements 119

Supplementary Materials 120

PARTIE II – DÉFORMATION À L'ÉCHELLE CRUSTALE ET MINÉRALISATIONS AURIFÈRES 145

Préambule 147

Chapitre II – Subvertical, linear and progressive deformation related to gold mineralization at the Galat Sufar South deposit, Nubian shield, NE Sudan 149

Résumé 151

Abstract 153

1. Introduction 155

2. Geological setting 157

2.1. Regional geology 157

2.2. Local geology 161

3. Sampling, methodology and structural glossary 165

3.1. Sampling and methodology 165

3.2. Definition of ductile and brittle deformation and scale-sensitivity 167

4. Macro- to micro-scale deformation history and related alteration/mineralization events 168

4.1. Cryptic, ductile-dominated D_{1GSS} deformation stage 176

4.2. Main ductile D_{2GSS} deformation stage 177

4.3. Weak ductile/brittle D_{3GSS} deformation stage 179

4.4. Late brittle D_{4GSS} deformation stage 181

5. Controls on deformation and progressive *vs* multiphase nature 184

5.1. Controls on deformation and impact on mineralization 185

5.2. Progressive vs multiphase deformation history 187

6. From deposit-scale to regional-scale deformation history 188

6.1. Deposit-scale subvertical, linear control on ore shoot distribution 188

6.2. Deposit- and regional-scale sheath fold formation 192

6.3. Record of the ADS tectonics 196

7. Conclusions 198

Acknowledgements 200

Chapitre III – Tectonic record and gold mineralization in the central part of the Neoproterozoic Keraf suture, Gabgaba district, NE Sudan 201

Résumé 203

Abstract 205

1. Introduction 207

2. Geological setting 209

3. Lithologies, structures and gold mineralization of the central Keraf suture 215

3.1. Lithological framework of the central Keraf suture 218

3.2. Structural framework of the central Keraf suture 220

2.2. Mineralized structures of the Gabgaba gold district 227

3. Interpretation of the tectonic and gold history of the central Keraf suture 236

3.1. Tectonic evolution of the central Keraf suture 236

3.2. Gold mineralization events of the central Keraf suture 238

4. Discussion 244

4.1. Reappraisal of the tectonic setting of the central Keraf suture 244

4.2. Polyphase gold dominated by syn-Keraf shear zone mineralization in the Gabgaba gold district 247

5. Conclusions 251

Acknowledgements 252

PARTIE III – ENREGISTREMENT DES PROCESSUS MINÉRALISATEURS À L'ÉCHELLE MICROSCOPIQUE 253

Préambule 255

Chapitre IV – Structural and geochemical ore-forming processes in deformed gold deposits: towards an integrated, multi-scale and -method approach 257

Résumé 259

Abstract 261

1. Introduction 263

2. Current insights from HRXCT, EBSD and LA-ICP-MS into geoscience 265

2.1. High-resolution X-ray computed tomography 266

2.2. Electron back-scattered diffraction 267

2.3. Laser ablation inductively-coupled plasma mass spectrometry 268

3. Case study: the Galat Sufar South gold deposit, northeastern Sudan 270

4. Sampling and analytical procedures 275

4.1. Field study 275

4.2. Sampling and petrography 276

4.3. High-resolution X-ray computed tomography 276

4.4. Electron back-scattered diffraction 277

4.5. Laser ablation inductively-coupled plasma mass spectrometry on pyrite 278

5. Results and integration to previous petrological-structural field observations 279

5.1. Petrological-structural description of the mineralised sulphide assemblages 279

5.2. High-resolution X-ray computed tomography 285

5.3. Electron back-scattered diffraction 287

5.4. LA-ICP-MS geochemical signature of pyrite generations 291

6. A holistic ore-forming model 299

6.1. Structural control on mineralisation 299

6.2. Deformation-induced geochemical ore forming processes 301

7. Conclusions 305

Acknowledgements 307

Electronic Supplementary Materials 308

Chapitre V – Textural and geochemical record of fault-valve mechanism in pyrite, Central Zone gold deposit, Gabgaba district, NE Sudan 315

Résumé 317

Abstract 319

1. Introduction 321

2. Geological setting 323

2.1. Regional geology 323

2.2. Local geology 327

2.3. Mineralized structures and pyrite generations at the deposit to macroscopic scales 328

3. Sampling and analytical methods 331

3.1. Sampling 331

3.2. Optical and scanning electron microscopy 331

3.3. Laser-ablation inductively-coupled plasma mass-spectroscopy analysis of the trace element concentrations of pyrite 332

4. Results 333

4.1. Deformation, alteration and mineralization at the microscopic scale 333

4.2. Micro-textures of pyrite 340

4.3. Trace element concentrations of pyrite 342

5. Petrological-structural model of the Central Zone gold deposit 349

6. Discussion 352

6.1. Constraints on structurally-driven mineralizing fluid flow mechanisms 353

6.2. From deposit-scale footprints to microscopic-scale fingerprints 355

6.3. Towards a fault-valve system? 359

7. Conclusions 363

Acknowledgements 364

Supplementary Materials 365

PARTIE IV – DONNÉES COMPLÉMENTAIRES ET DISCUSSION GÉNÉRALE 371

Préambule 373

Chapitre VI – Complementary data: timing of gold mineralization along the Neoproterozoic Atmur-Delgo and Keraf sutures, western Nubian shield 375

Résumé 377

Abstract 379

1. Introduction 381

2. Geological setting 384

3. Sampling and analytical techniques 384

3.1. Sampling philosophy 384

3.2. Analytical techniques 386

4. Results 392

4.1. Petrographic description of studied samples 392

4.2. Whole-rock geochemistry 402

4.3. U-Pb ages and Hf compositions of zircon 407

4.4. U-Pb ages of apatite 408

4.5. Chlorite-phengite-quartz-water multi-equilibria calculations 415

5. Discussion 421

5.1. How does the Galat Sufar South magmatic event fit into the regional lithospheric evolution? 421

5.2. Pressure-temperature-timing constraints on Galat Sufar South gold mineralization and related geodynamical setting 422

5.3. Timing of orogenic gold at the Gabgaba district recorded by the WG03 deposit ...425

5.4. Additional constraints on Keraf island arc magmatic activity 426

6. Conclusions 428

Supplementary Materials 429

Chapitre VII – General discussion..... 439

1. Deciphering of the Pan-African gold mineral system along the Keraf suture 441

1.1. Geodynamical setting favorable for crustal growth and gold fertilization.....443

1.2. Favorable lithospheric architecture and tectonic triggers for gold mineralization..448

1.3. Ore deposition mechanisms 455

1.4. Ore preservation 456

2. Downscaling of the Keraf gold mineral system at the Arabian-Nubian shield scale.....458

2.1. Gold deposits coeval to magmatic and/or tectonic accretion.....459

2.2. Syn- to late collisional orogenic gold deposits.....463

2.4. Polyphase gold mineralization: ore remobilization and/or superimposition.....463

3. Perspectives 465

3.1. Towards a better understanding of geodynamical processes… 465

3.2. Towards a better understanding of magmatic-hydrothermal gold-forming processes during island arc magmatism.....467

4. Shifting from the gold mineral system to exploration targeting.....468

RÉFÉRENCES ..... a

LISTE DES FIGURES

INTRODUCTION GÉNÉRALE

Figure 0-1 : Le front pionnier aurifère dans l'espace saharo-sahélien (Chevrillon-Guibert et al., 2019) 7
Figure 0-2: Approche multi-scalaire pour l'étude des systèmes métallogéniques (mineral systems), depuis l'échelle cristallographique jusqu'à l'échelle lithosphérique..... 8
Figure 0-3 : Distribution temporelle des occurrences des principaux types de minéralisation connus et lien avec les contextes géodynamiques à la jonction ou à la séparation entre les masses continentales (Goldfarb et al., 2010) 11
Figure 0-4 : Concentration en or de différentes roches (Pitcairn, 2011) 13
Figure 0-5 : Évolution des ressources en or cumulées des gisements d'or orogénique et du volume de croûte continentale formé au cours des temps géologiques (Goldfarb et al., 2010) 20
Figure 0-6 : Reconstruction des supercontinents **(a)** Rodinia d'après Oriolo et al. (2017) et (**b**) Gondwana, modifiée d'après Gray et al. (2008) et Feneyrol (2012).....26
Figure 0-7 : Reconstruction du contexte paléo-tectonique lors de l'orogenèse est-africaine-antarctique (EAAO) entre 600 et 550 Ma par Grenholm (2019), d'après Merdith et al. (2017)27
Figure 0-8 : Carte régionale de l'orogène est-africain-antarctique (EAAO) avant la rupture du Gondwana au Mésozoïque (Grenholm, 2019) 30
Figure 0-9 : Âge des principaux domaines crustaux formant la partie nord de l'orogène est-africain-antarctique et timing des assemblages d'arcs à l'origine du bouclier arabo-nubien (ANS), modifiée d'après Fritz et al. (2013) 34
Figure 0-10 : Structures tardi-tectoniques, granitoïdes tardi- à post-orogéniques et bassins sédimentaires dans le BAN (Fritz et al., 2013) 40
Figure 0-11 : Événements géologiques majeurs ayant abouti à la mise en place du bouclier arabo-nubien (Arabian-Nubian Shield), modifiée d'après Fritz et al. (2013) 41
Figure 0-12 : Localisation de la suture de Keraf et de la zone de suture d'Atmur-Delgo (Abdelsalam et al., 1998). 43
Figure 0-13 : Contexte structural et occurrences aurifères du bouclier nubien 49
Figure 0-14 : Échelles d'investigation du système métallogénique aurifère exprimé le long de la suture de Keraf au sein du bouclier arabo-nubien néoprotérozoïque pour chacun des chapitres composant ce manuscrit 52

PARTIE I

Chapitre I

Figure 1-1: a Plate tectonic reconstruction at 500 Ma highlighting the ca. 950-550 Ma East African-Antarctic orogen (EAAO) location between East and West Gondwana, modified after Grenholm (2019) and references therein (Johnson et al., 2011; Fritz et al., 2013; Johnson, 2014; Merdith et al., 2017). **b** Regional map of the EAAO prior to Gondwana break-up at ca. 200 Ma, simplified after Grenholm (2019) 70
Figure 1-2: Geological map of the central Keraf suture, adapted after Bailo et al. (2003), Managem (2011), and field observations (Perret et al., under review).....73

Figure 1-3: Early, **s**yn- to post-Keraf arc igneous rocks of the central Keraf suture 77
Figure 1-4: Scanning electron microscopy image representative of dated zircon grains in back-scattered electron mode (BSE-SEM).....79
Figure 1-5: Whole-rock major element composition of samples from this study (circles) and syn-Keraf arc-related samples from Bailo et al. (2003) (diamonds).....82
Figure 1-6: Whole-rock trace element composition of samples from this study (circles) and syn-Keraf arc-related samples from Bailo et al. (2003) (diamonds).....83
Figure 1-7: Weighted mean plots (2σ error) of $^{206}Pb/^{238}U$ single zircon ages from dated samples 93
Figure 1-8: Crossplots considering Hf, Nd and Sr isotopic data from this study (circles) and syn-Keraf arc-related samples from Bailo et al. (2003) (diamonds) 100
Figure 1-9: Geodynamical sketch in a lithospheric cross-section across the central Keraf suture representing the long-lived island arc activity, suturing and post-collisional magmatic events recorded in our data between ca. 840 and ca. 620 Ma 110
Figure 1-10: Map view of the possible regional-scale geodynamical scenario leading to the formation of the western Nubian shield 113

PARTIE II

Chapitre II

Figure 2-1: The Arabian-Nubian shield (ANS) location and structural framework, simplified after Johnson et al. (2011) and Fritz et al. (2013) 158
Figure 2-2: Lithostructural framework of the Block 14 area (NE Sudan), modified after Orca Gold Inc. (2017) 163
Figure 2-3: Outcrop observations nearby the GSS gold deposit 164
Figure 2-4: Example of the lithology, deformation, alteration and mineralization changes at the GSS gold deposit 166
Figure 2-5: Main deformation features of the studied samples at the sample and microscopic scales 169
Figure 2-6: Asymmetrical strain fringe evidence for micro-scale C_2 shearing 170
Figure 2-7: Oriented microphotograph of sample GS-22-10 under cross-polarized, transmitted light interpreted by adding the successive deformation microstructures and their kinematic sense (view from SSE) 171
Figure 2-8: Oriented microphotograph of sample GS-38-08 under cross-polarized, transmitted light interpreted by adding the successive deformation microstructures and their kinematic sense (view from SSE) 172
Figure 2-9: Main lithology and alteration features of the studied samples 174
Figure 2-10: Main ore features of the studied samples 175
Figure 2-11: Schematic evolution of the Z shortening direction from D_{2GSS} to D_{3GSS} (view from SSE) 180

Figure 2-12: Paragenetic sequence displayed by the ore-bearing meta-volcanosedimentary horizon at the GSS gold deposit.....182
Figure 2-13: Schematic petro-structural model for the gold mineralization at the GSS gold deposit (view from SSE).....184
Figure 2-14: Outcrop and core structural features and stereonet structural data plot.....190
Figure 2-15: Schematic 3D block diagram of the GSS gold deposit 191
Figure 2-16: GSS area satellite imagery analysis.....193

Chapitre III

Figure 3-1: The Keraf suture in the framework of the East African-Antarctic orogeny (EAAO)..
.....212
Figure 3-2: Geological map of the central Keraf suture hosting the Gabgaba gold district, adapted after Managem (2011) and relying on field observations.....216
Figure 3-3: A-B crustal cross-section through the central Keraf suture 217
Figure 3-4: Lithologies of the central Keraf suture.....219
Figure 3-5: Outcrop expression of the S_0 bedding and relationships with the D_{1a}-D_{1b} deformation stages in meta-sediments.....223
Figure 3-6: Outcrop expression of the regional D_{1a} deformation stage in the Keraf pre-tectonic assemblage rocks, relationships with the D_{1b} deformation stage and stereonet analysis.....224
Figure 3-7: Outcrop expression of the D_{1b} deformation stage in the Keraf pre-tectonic assemblage rocks and stereonet analysis 225
Figure 3-8: Outcrop expression of the D_2 deformation phase in meta-sediments.....226
Figure 3-9: Geological maps of the WG03 (**a**), Central Zone (**b**) and UTM (**c**) deposits belonging to the Gabgaba gold district, adapted after Managem internal reports.....227
Figure 3-10: Gold-mineralized structures in outcrop at the Gabgaba gold district 232
Figure 3-11: Gold-mineralized structures in drill cores and hand samples at the Gabgaba gold district.....233
Figure 3-12: Gold-mineralized structures at the microscopic scale at the WG03 and Central Zone gold deposits.....234
Figure 3-13: Stereonet analysis of the main gold-mineralized structures at the Gabgaba gold district.....241
Figure 3-14: Tectonic interpretation for the formation of the main gold-bearing structures at WG03 (**a**), Central Zone (**b**) and UTM **(c**) deposits 242
Figure 3-15: Relative timing of the Gabgaba district gold deposits (WG03, Central Zone and UTM) regarding the deformation history recorded by the central Keraf suture.....250

PARTIE III

Chapitre IV

Figure 4-1: Geological setting of the Galat Sufar South (GSS) gold deposit, adapted after Perret et al. (2020).....271

Figure 4-2: Simplified mineral paragenesis of the Galat Sufar gold deposit, modified after Perret et al. (2020).....273
Figure 4-3: Macroscopic scale features of pyrite generations identified at the Galat Sufar South gold deposit.....274
Figure 4-4: Microscopic scale features of pyrite generations identified at the Galat Sufar South gold deposit.....284
Figure 4-5: High-resolution X-ray computed tomography (HRXCT) results for the sample billet GS-34-07.....286
Figure 4-6: Electron back-scattered diffraction (EBSD) analysis of disseminated $Py_{1b/2}$ facies (sample GS-22-08).....289
Figure 4-7: Electron back-scattered diffraction (EBSD) analysis of $Py_{1b/2}$ facies in quartz-pyrite-dominated veinlet (sample GS-34-05).....291
Figure 4-8: Box and whisker plots of some trace element concentrations of the various generations of pyrite from the Galat Sufar South gold deposit, northeastern Sudan.....292
Figure 4-9: LA-ICP-MS trace element maps (Au, Ag, Te, Sb, Cu, Pb, As, Co) of a Py_{1b} altered core enclosing numerous mineral inclusions and with a Py_2 overgrowth (sample GS-22-08) ...294
Figure 4-10: LA-ICP-MS trace element maps (Au, Ag, Te, Sb, Cu, Pb, As, Co) of a composite Py_{1b}-Py_2-Ccp_2-$electrum_2$ assemblage within a gold-bearing quartz-pyrite-(carbonate) veinlet (sample GS-34-05).....295
Figure 4-11: Insights from the suggested multi-scale, multi-method approach for the understanding of the structural control defined by L_2 on gold mineralisation at the Galat Sufar South gold deposit, northeastern Sudan.....300
Figure 4-12: Insights from the suggested multi-scale, multi-method approach for the understanding of the geochemical ore-forming processes in relation with deformation at the Galat Sufar South gold deposit, northeastern Sudan.....304

Chapitre V

Figure 5-1: Geological setting of the Gabgaba gold district in the framework of the Sudanese Nubian shield, modified after Perret et al. (under review).....326
Figure 5-2: Lithological-structural framework of the Central Zone deposit (Perret et al., under review).....327
Figure 5-3: Field and macroscopic observations of the main structural and textural features of the mineralized veins at the Central Zone deposit.....329
Figure 5-4: Macroscopic observations on drill core of the different pyrite generations at the Central Zone deposit.....330
Figure 5-5: a Macroscopic and **b** microscopic (cross-polarized, transmitted light) observations of the oriented meta-sedimentary sample collected on outcrop.....335
Figure 5-6: Main petrological-structural features of the D_{1a} main deformation stage.....336
Figure 5-7: Interpretative sketch of the progressive formation of asymmetric strain fringes around a pyrite grain.....337

Figure 5-8: Main petrological-structural features of the D_{1b} deformation stage at the microscopic scale....339
Figure 5-9: Micro-textures of the main pyrite generations unraveled at the Central Zone gold deposit....341
Figure 5-10: Mineral inclusions in the Py_{1a} generation....341
Figure 5-11: Representative time-resolved LA-ICP-MS outputs for Py_{1a} grains....342
Figure 5-12: Binary diagrams discriminating the different pyrite generations from the Central Zone deposit....344
Figure 5-13: Box and whisker plots of As, Au, Ni, Co, Te, Pb, Ag and Sb concentrations in pyrite generations from the Central Zone deposit....346
Figure 5-14: Gold concentration in different pyrite grains depending on the textural position of the LA-ICP-MS 50 µm-large ablation spots....347
Figure 5-15: Mineral paragenesis recorded at the Central Zone gold deposit....349
Figure 5-16: Suggested petrological-structural model for the Central Zone gold deposit, from D_{1a} to D_{1b} deformation stages....350
Figure 5-17: Inferred fault-valve mechanism during the D_{1b} deformation stage for the formation of mineralized quartz-ankerite-(albite) veins and their alteration halos in granitoids....360

PARTIE IV

Chapitre VI

Figure 6-1: Location of the Galat Sufar South, WG03 and Central Zone deposits within the Atmur-Delgo and Keraf sutures, western Nubian shield....383
Figure 6-2: Cathodoluminescence photographs representative of dated apatite grains recovered from the Galat Sufar South, WG03 and Central Zone deposits....388
Figure 6-3: Macroscopic and microscopic features of lithologies mapped nearby the Galat Sufar South gold deposit and considered in this study....394
Figure 6-4: Syn-gold mineralization D_{2GSS}-chlorite-phengite-apatite-pyrite mineral assemblage in ash tuffs at the Galat Sufar gold deposit....395
Figure 6-5: Syn-gold mineralization hydrothermal apatite at the WG03 deposit, Gabgaba gold district (WG03-05)....397
Figure 6-6: Syn-gold mineralization hydrothermal apatite at the WG03 deposit, Gabgaba gold district (WG03-11)....398
Figure 6-7: Syn-gold mineralization hydrothermal apatite at the WG03 deposit, Gabgaba gold district (WG03-12)....399
Figure 6-8: Magmatic apatite in ore-hosting granitoid at the Central zone deposit, Gabgaba gold district (CZ11)....400
Figure 6-9: Magmatic apatite in ore-hosting granitoid at the Central zone deposit, Gabgaba gold district (CZ12)....401
Figure 6-10: Whole-rock major and trace element composition of Galat Sufar South igneous and pyroclastic rocks....403

Figure 6-11: U-Pb dating and Hf isotope composition of zircon from the syn-Atmur Delgo suture GS-OC-01 trachyandesite, Galat Sufar South gold deposit.....408
Figure 6-12: Tera-Wasserburg diagrams for U-Pb dating of apatite grains from the (**a**) Galat Sufar South, (**b** and **c**) WG03 and (**d**) Central Zone gold deposits.....412
Figure 6-13: Plot of the phyllosilicate compositions from the samples GS-55-02 and GS-55-04 in **am**esite-(**clin**ochlore + **daph**nite)-**sud**oite (**a**, chlorite, n=41) and **cel**adonite-**mus**covite-**pyr**ophyl**l**ite (**b**, phengite, n=45) end-member ternaries.....415
Figure 6-14: Pressure-temperature equilibrium conditions resulting from chlorite-phengite-quartz-water multi-equilibria calculation for the syn-gold mineralization D_{2GSS} deformation stage at the Galat Sufar South deposit.....417
Figure 6-15: Statistical processing of pressure-temperature conditions estimated from chlorite-phengite-quartz-water multi-equilbria calculations for the syn-gold mineralization D_{2GSS} deformation stage at the Galat Sufar South deposit.....418
Figure 6-16: Map view of the possible regional-scale oceanic subduction scenario recorded along the Atmur-Delgo suture (modified after **Chapter I**).....421

Chapitre VII

Figure 7-1: Gold mineral system diamond illustrating critical factors for ore genesis along the Atmur-Delgo and Keraf sutures, western Neoproterozoic Nubian shield.....442
Figure 7-2: Geodynamical sketch in a lithospheric cross-section across the central Keraf suture with representation of the successive gold events occurring during Keraf suturing, with associated schematic map views.....453
Figure 7-3: Timechart summarizing the gold mineralization, magmatic and tectonic events unraveled across the Neoproterozoic Keraf and Atmur-Delgo sutures during this study.....454
Figure 7-4: Pressure-temperature-timing constraints on gold mineralization throughout the Nubian shield.....462

LISTE DES TABLEAUX

INTRODUCTION GÉNÉRALE

Tableau 0-1 : Comparaison des données de production d'or pays par pays en 2017 selon deux sources différentes 5

PARTIE I

Chapitre I

Table 1-1: List of studied samples 75
Table 1-2: List of studied samples 87
Table 1-3: U-Pb isotopic compositions of zircon grains used in this study 98
Table 1-4: Lu-Hf isotopic compositions of zircon grains used in this study 102
Table 1-5: Rb-Sr and Sm-Nd whole-rock isotopic compositions of early, syn- and post-Keraf arc igneous rocks used in this study.....103

PARTIE II

Chapitre II

Table 2-1: Samples used in this study 165
Table 2-2: Summary of the deformation, alteration and mineralization features observed at the macro- to micro-scale at the GSS gold deposit 183

Chapitre III

Table 3-1: Summary of the D_{1a}-D_{1b} and D_2 deformation episodes unraveled across the central Keraf suture 214
Table 3-2: Geographic coordinates reported as WGS 84 and brief description of the key outcrops discussed in the text.....215

PARTIE III

Chapitre IV

Table 4-1: List of samples from this study, along with the corresponding analyses that they underwent. 277
Table 4-2: Summary of the LA-ICP-MS trace element concentrations (in ppm) of the various pyrite generations from the Galat Sufar South gold deposit 298

Chapitre V

Table 5-1: List of the studied samples 333
Table 5-2: L Summary of the LA-ICP-MS trace element concentrations (in ppm) of the various pyrite generations from the Central Zone gold deposit 348

PARTIE IV

Chapitre VI

Table 6-1: List of studied samples 385
Table 6-2: Results of major and trace elements of whole-rock analyses for samples from the Galat Sufar South gold deposit 406
Table 6-2: U-Pb isotopic compositions of zircon grains recovered from GS-OC-01 trachyandesite used in this study 410
Table 6-4: Lu-Hf isotopic compositions of zircon grains recovered from GS-OC-01 trachyandesite used in this study 411
Table 6-5: U-Pb isotopic compositions of apatite grains used in this study 414
Table 6-6: Electron microprobe analyses of white mica-phengite (n=45) and chlorite (n=41) from samples GS-55-02 and -04 collected from the Galat Sufar South gold deposit 420

LISTE DES ANNEXES

PARTIE I

Chapitre I

Supplementary Material 1-1: Scanning electron microscopy images illustrating zircon morphologies and U-Pb and Hf zircon isotope dataspot location in back-scattered electron mode (BSE-SEM) 120
Supplementary Material 1-2: U-Pb isotopic compositions of zircon standards used in this study 123
Supplementary Material 1-3: Lu-Hf isotopic compositions of zircon grains used in this study 127
Supplementary Material 1-4: U-Pb, Nd and Sr isotopic data compilation across the Keraf suture, the Atmur-Delgo suture and the Saharan meta-craton nearby 130

PARTIE III

Chapitre IV

Supplementary Material 4-1: Video file for the HRXCT-assisted 3D reconstruction of the internal structure of the oriented sample billet GS-34-07 308
Supplementary Material 4-2: Extensive dataset of LA-ICP-MS trace element concentrations (in ppm) of the various pyrite generations from the Galat Sufar South gold deposit, northeastern Sudan 309

Chapitre V

Supplementary Material 5-1: Extensive dataset of LA-ICP-MS trace element concentrations (in ppm) of the various pyrite generations from the Central Zone gold deposit, northeastern Sudan 365

PARTIE IV

Chapitre VI

Supplementary Material 6-1: Processing of micro-XRF elemental maps using the open-source MARCIA Python routine to get a quantitative mineral map: example of setting of thresholds in Si intensity in spectra for thin section WG03-05 429
Supplementary Material 6-2: Scanning electron microscopy images illustrating zircon morphologies of GS-OC-01 trachyandesite and U-Pb and Hf zircon isotope dataspot location in back-scattered electron mode (BSE-SEM) 430
Supplementary Material 6-3: Cathodoluminescence microphotographs of dated apatite grains with U-Pb dataspot location 431
Supplementary Material 6-4: Chlorite-phengite-quartz-water multi-equilibria calculated from coexisting chlorite and white mica compositions 435

GLOSSAIRE

Ce glossaire explicite la définition de termes clés utilisés dans ce manuscrit. Lorsque plusieurs définitions existent pour un même terme, ou que son emploi porte à confusion dans la littérature, les différentes significations qui lui sont attribuées sont détaillées. Nous préciserons laquelle est considérée dans ce travail de thèse. Les termes sont définis en français et traduits en anglais en italique entre parenthèses.

Accrétion magmatique (*magmatic accretion*) : accumulation de magma de composition basaltique en base de croûte (*magmatic underplating*) et ayant été extrait du manteau. Ce phénomène contribue à la formation de croûte au niveau des rides océaniques et d'arcs volcaniques insulaires ou continentaux à l'aplomb des zones de subduction océan-océan ou océan-continent.

Accrétion tectonique (*tectonic accretion*) : formation de croûte par écaillage tectonique et mise en place de nappes formées d'unités découplées d'une plaque plongeante. En effet, en contexte de subduction océanique, le découplage thermique et mécanique entre la croûte de la plaque inférieure et le manteau lithosphérique sous-jacent favorise l'accrétion tectonique au niveau du prisme d'accrétion sédimentaire en avant-arc ainsi que la fusion partielle du matériel crustal sus-jacent à plus grande profondeur (Vanderhaeghe, 2012 ; Moyen et al., 2017). Il n'existe donc pas nécessairement de déconnexion temporelle entre accrétion magmatique au niveau d'une zone de subduction intra-océanique et accrétion tectonique. Cependant, il reste discutable de limiter la notion d'accrétion tectonique au découplage d'unités de la plaque plongeante car cette définition n'inclue pas la formation et l'épaississement du prisme orogénique pendant la subduction continentale, bien que les processus de découplage impliqués soient similaires.

Arc magmatique ou **volcanique** (*magmatic, volcanic arc*) : Un arc magmatique est une chaîne de volcans de plusieurs centaines à milliers de kilomètres de long se formant à l'aplomb d'une zone de subduction. Le terme d'arc volcanique est communément employé car les roches volcaniques sont souvent prépondérantes par rapport aux roches plutoniques dans ces édifices, bien que ces dernières soient tout de même présentes. Un arc insulaire ou océanique (*island* or *oceanic magmatic arc*) se forme dans un contexte de subduction intra-océanique, lorsqu'une portion de lithosphère océanique subducte sous une autre (*e.g.,* les nombreux arcs du sud-ouest du Pacifique dont celui d'Izu-Bonin-Mariannes). Un arc continental (*continental magmatic arc*) se forme lorsque la lithosphère océanique subducte sous la lithosphère continentale (*e.g.,* les Andes). Un arc peut être complètement ou partiellement immergé, ce qui est souvent le cas des arcs immatures, *i.e.,* arcs insulaires jeunes et peu développés tels que ceux du Pacifique Sud-

Ouest. Les arcs les plus matures, *i.e.,* arcs océaniques évolués ou arc continentaux, comme l'arc andin sont complètement émergés. Les Aléoutiennes, au large de l'Alaska, forment un arc insulaire divisé en sections aériennes et sous-marines se succédant le long du front volcanique. Les arcs magmatiques se caractérisent par une signature géochimique tholéiitique à calco-alcaline. Le basalte et le basalte andésitique sont des lithologies fréquentes dans les arcs océaniques alors que l'andésite et la dacite sont préférentiellement exprimés dans les arcs continentaux, ce qui est également vrai pour l'équivalent plutonique de ces lithologies. Les magmas felsiques sont essentiellement mis en place sous forme de batholithes plutoniques bien que les roches volcaniques felsiques se retrouvent fréquemment dans les arcs continentaux. On parle de complexe d'arc magmatique (*magmatic arc complex*) lorsque l'on considère l'ensemble formé par ces roches magmatiques et les roches volcanoclastiques associées. Les complexes d'arc ayant enregistré au moins un cycle supercontinental et ayant été préservés, au moins partiellement, sont souvent déformés et métamorphisés à un degré variable (DiPietro, 2012 ; Condie, 2015). On peut citer comme exemples, du plus vieux au plus jeune, le complexe anorthositique néoarchéen de Fiskenæsset (Groenland ; Polat et al., 2009), le complexe mésoprotérozoïque de Vijayan au Sri Lanka (Kröner et al., 2013), celui néoprotérozoïque de Bougmane dans l'Anti-Atlas marocain (Triantafyllou et al., 2018) et enfin le complexe d'arc magmatique du bloc litho-tectonique cambrien de Takaka en Nouvelle-Zélande (Münker et Cooper, 1999).

Bloc crustal (*crustal block*) : l'emploi de ce terme sera limité dans ce manuscrit aux micro-continents formés de lithosphère continentale résultant du boudinage puis de la fragmentation de marge cratonique archéenne à mésoprotérozoïque. Ces fragments, parfois séparés par de la lithosphère océanique, ont migré et ont été localement piégés dans des ceintures orogéniques néoprotérozoïques ou plus récentes.

Ceinture *vs* **système orogénique** (*orogenic belt* vs *system*) : étymologiquement, un orogène est une zone où se forme les montagnes puisqu'en grec, *oros* signifie « relief » et *genes* « formation » (Gilbert, 1890). Une ceinture orogénique est donc une chaîne de montagnes formée au cours d'un cycle supercontinental passé, au niveau d'une marge active dans un système de convergence entre deux plaques tectoniques. Les chaînes de montagnes actuelles, comme les Alpes, qui se rattache à la chaîne himalayenne, ou la cordillère des Andes, sont des ceintures orogéniques en cours de formation. Les ceintures orogéniques préservées à travers les âges et observables à la surface de la Terre de nos jours font classiquement 1000 km de long pour 100 à 500 km de large et correspondent à

des zones où la succession d'épisodes de déformation compressive a occasionné la formation de reliefs et leur érosion (concomitante puis plus tardive). Selon le degré de collision atteint le long de la ceinture considérée, les événements magmatiques synchrones de sa formation peuvent enregistrer (i) la subduction océan-océan (signature tholéiitique à calco-alcaline plus ou moins alcaline, faible contamination crustale), (ii) la subduction océan-continent (signature calco-alcaline à tendance alcaline et remobilisation de la base de croûte continentale, forte contamination crustale), (iii) la subduction continentale, la collision arc-continent puis continent-continent (signature à dominance calc-alcaline et régulièrement peralumineuse du fait d'une forte remobilisation en base de croûte) et (iv) l'extension post-orogénique (changement vers des signatures potassiques fortes à extrêmes). Ces signatures géochimiques sont notamment à considérer avec précaution et ne doivent pas être considérées indépendamment de la nature des granitoïdes formés et de la signature géochimique des unités lithosphériques en présence (*e.g.,* Bonin et al., 2019). Des lambeaux de lithosphère océanique à signature chimique variable et préservés sous forme d'ophiolites dans les zones de suture peuvent témoigner d'une période de formation de croûte océanique antérieure à précoce lors de l'évolution de la ceinture orogénique (*e.g.*, ophiolites intra-océaniques formées à l'aplomb des zones de dorsale *vs* ophiolites formées en zone de supra-subduction ou en arrière-arc dans un système d'arc magmatique ; Dilek et Furnes, 2011 ; van Hinsbergen et al., 2015). Plusieurs ceintures orogéniques peuvent former un réseau anastomosé, plus ou moins connecté. Elles forment alors un seul et même système orogénique (*orogenic system*) pouvant atteindre 20000 km de long pour 100 à 1000 km de large, correspondant à une période de temps (20 à 200 millions d'années) et une évolution tectonique données. Un système orogénique exprime donc plus ou moins l'enregistrement d'un cycle supercontinental (Roeder et al., 2013). Par exemple, le système orogénique néoprotérozoïque panafricain se développe lors de la mise en place du supercontinent Gondwana et se compose principalement des ceintures orogéniques est-africaine, du Kuunga, du Damara-Zambezi-Irumide et ouest-africaine-Brasiliano (Grenholm, 2019).

Collision arc-continent (*arc-continent collision*) : épaississement de la croûte continentale par juxtaposition et empilement de nappes d'unités crustales découplées thermiquement et mécaniquement de la lithosphère sous-jacente au niveau d'un prisme orogénique pendant la subduction continentale, mettant en contact un arc magmatique et une lithosphère continentale. Cependant, la déconnexion temporelle entre accrétion tectonique lors de la subduction océanique et collision arc-continent n'est pas

systématique dans le cas où une ceinture orogénique n'atteint pas le même degré d'évolution en tout point de son extension à un instant donné.

Contrainte (*stress*) : force effective appliquée sur une roche rapportée à une unité de surface, équivalent à une pression (Fossen, 2016). La confusion entre contrainte et déformation (*strain* et *deformation*) est fréquente, notamment en termes d'interprétation structurale : si l'observation d'un marqueur de déformation donne un aperçu plus ou moins apparent de l'état de déformation finie accommodé par un objet, remonter à un état de contrainte n'est pas trivial et nécessite parfois des hypothèses lourdes de conséquence quant au régime tectonique impliqué (*e.g.,* déformation co-axiale) . Dans ce manuscrit, il sera donc essentiellement fait mention de déformation afin de prévenir toute surinterprétation des observations faites.

Craton (*craton*) : partie ancienne et stable de la lithosphère continentale comprenant un ou plusieurs noyaux archéens (4000-2500 Ma) et présentant une ou plusieurs racines lithosphériques épaisses (jusqu'à 400 km). On parle de méta-craton, comme dans le cas du méta-craton du Sahara dans ce manuscrit, concernant les cratons impliqués dans des processus de collision entre continents et ayant enregistré des processus tectono-magmato-métamorphiques syn-orogéniques le long de la(les) marge(s) impliquée(s) (Liégeois et al., 2013). Le méta-craton se différencie d'une ceinture orogénique par (i) l'absence d'événements géodynamiques précédant la phase de collision du cycle orogénique concerné, (ii) l'absence d'épaississement crustal, de métamorphisme de haute pression et de déformation intense associée à la phase de subduction, (iii) la préservation des blocs litho-tectoniques océaniques allochtones hérités, (iv) une activité magmatique post-collision intense et associée à des zones de cisaillement plutôt qu'à un amincissement crustal, occasionnant un fort métamorphisme basse pression-haute température et (v) des ceintures orogéniques intracontinentales qui ne sont pas initiées par une subduction et la fermeture d'un ou plusieurs bassins océaniques (Liégeois et al., 2013).

Croûte juvénile (*juvenile crust*) : en termes de **processus**, des magmas juvéniles sont extraits depuis le manteau peu de temps avant leur incorporation dans la croûte au niveau des rides océaniques, des point chauds et des ceintures orogéniques, contribuant à la croissance crustale. Le matériel ainsi formé présente un âge de résidence crustale proche de son âge de mise en place. La **définition isotopique** du terme juvénile correspond à une signature en traceurs isotopiques (Sr, Nd, Pb, Hf) proche du manteau appauvri (Moyen et al., 2017 ; Couzinié et al., 2020). Il est donc nécessaire de préciser

dans quel sens le terme « juvénile » est employé, la définition du processus n'impliquant pas celle isotopique et *vice versa.* En effet, la signature isotopique d'une phase d'extraction mantellique peut être dominée par une composante crustale en cas de recyclage d'une faible proportion ($< 20\%$) de matériel crustal dans la source mantellique mobilisée, du fait du caractère incompatible de Sr, Nd, Pb et Hf (*e.g.*, les vaugnérites ; Moyen et al., 2017). Au contraire, des roches provenant de la remobilisation de matériel crustal peuvent exprimer une signature isotopique juvénile si elles dérivent d'une source crustale ignée ou méta-sédimentaire ayant une composante isotopique juvénile (Moyen et al., 2017). Dans la suite de ce manuscrit, nous emploierons le terme « juvénile » pour caractériser une croûte extraite du manteau **et** possédant une signature isotopique proche de celle du manteau appauvri.

Croûte recyclée (*recycled crust*) : « part de croûte retournée dans le manteau par subduction ou délamination » (Eglinger, 2013). Cette définition est valable qu'importe la nature continentale ou océanique de la croûte.

Croûte remobilisée (*reworked crust*) : « part de croûte soumise à la déformation et au métamorphisme au cours des orogenèses. Cette remobilisation peut affecter directement les marges de cratons et/ou les sédiments issus de l'érosion des cratons » (Eglinger, 2013). Cette définition est valable qu'importe la nature continentale ou océanique de la croûte.

Cycle supercontinental ou **orogénique** ou **de Wilson** (*supercontinental cycle, orogenic cycle, Wilson cycle*) : « au cours des temps géologiques, les déplacements des masses continentales, sous l'influence des mouvements mantelliques, peuvent être décrits de manière cyclique. C'est en 1966 que J. T. Wilson propose que tout bassin océanique prenne naissance à l'intérieur d'un continent, d'un rift continental puis s'agrandit entre les marges continentales passives. Par la suite, la subduction de la lithosphère océanique, le long de l'une au moins des marges devenue active, induit la fermeture de ce domaine océanique jusqu'à la collision finale de deux masses continentales, entraînant la création de relief (orogénie ou orogenèse) à la limite de plaques. Seule une suture ophiolitique témoigne de la disparition d'ancien domaine océanique. Ainsi est né le cycle de Wilson qui se décompose donc en différents intervalles de temps reflétant différents contextes géodynamiques : (i) rifting continental ; (ii) ouverture d'un domaine océanique ; (iii) expansion de l'océan ; (iv) subduction sous une marge continentale ou océanique ; (v) collision. Chaque fin de cycle de Wilson est caractérisée par la réunification des ensembles continentaux en supercontinents. Chaque formation d'un supercontinent entraîne la disparition d'une portion de lithosphère océanique et, simultanément, permet la

formation de terrains de haut-grade métamorphique dans les zones de collision. Après quelques millions d'années, ces supercontinents vont se fragmenter sous l'influence de plumes mantelliques gigantesques, ou superplumes » (Eglinger, 2013).

Déformation (*strain* et *deformation*) : le même terme renseigne la mesure du changement de forme et de volume subie par une roche (*strain*) et le déplacement collectif des points la composant par rapport à un référentiel externe fixe, en réponse à l'action d'une force (*deformation*). La *deformation* est la résultante de plusieurs types de déplacement de points au sein de la roche, à savoir la translation, la rotation, la distorsion et la dilatation (Fossen, 2016).

Déformation, ductile *vs* **fragile** (*ductile* vs *brittle deformation*) : la nature ductile ou fragile de la déformation peut correspondre à une réalité rhéologique (opposition entre la croûte inférieure ductile et la croûte supérieure fragile) mais l'utilisation de ces termes est ambiguë (Tikoff et al., 2013). Plusieurs critères peuvent notamment conditionner le passage d'un domaine à l'autre, qu'ils soient quantitatifs (*e.g.,* limite de résistance à une déformation imposée au matériau ; Heard, 1960) ou géométriques (*e.g.,* le caractère fragile de la déformation dépend de la présence de discontinuités dans le champ de déplacement résultant ; Twiss et Moores, 2007). De plus, la nature ductile ou fragile de la déformation dépend de l'échelle d'investigation (Rutter, 1986 ; Snoke et al., 1998). Les travaux présentés dans ce manuscrit se basant en premier lieu sur des observations de terrain, la nomenclature proposée permettra de « distinguer de quelle manière se fait la déformation » (Tikoff et al., 2013) aux échelles de la structure minéralisée et du gisement. Pour faire simple, la déformation ductile s'exprime par la mise en place de fabriques planaires pénétratives et de plis alors que la déformation fragile correspond aux failles et fractures (Twiss et Moores, 2007).

Déformation, épisode *vs* **phase ou étape** (*deformation phase* vs *stage*) : les épisodes (*phases*) de déformation se succèdent de façon discrète dans le temps et correspondent à des régimes tectoniques distincts (orientation des directions principales de déformation, style tectonique et contexte géodynamique qui changent de l'une à l'autre). Si plusieurs épisodes sont reconnus, la déformation est dite **polyphasée**. Au sein d'un épisode de déformation donné, plusieurs phases ou étapes de déformation (*stages*) peuvent être considérées. Dans ce cas, les structures observées résultent d'un seul et même événement tectonique mais doivent être séparées car elles expriment par exemple un changement progressif de style tectonique (*e.g.,* de ductile à ductile-fragile) ou la rotation des directions principales de déformation au cours de cet événement. La règle de parcimonie

veut alors que l'on intègre toutes ces structures dans un unique « modèle structural et cinématique » plutôt que de multiplier les épisodes de déformation ; la déformation est dite **progressive** (Fossen et al., 2019).

Échelle (*scale*) : les différentes échelles d'observation utilisées dans cette étude sont définies latéralement mais correspondent à une profondeur d'investigation du même ordre de grandeur. Il s'agit des échelles (i) **lithosphérique** (jusqu'à plusieurs 100^{aines} de km), (ii) **crustale** (10^{aines} de km à km), (iii) **locale** (km à m), (iv) **macroscopique** (dm à cm), (v) **microscopique** (mm à µm) et (vi) **cristallographique** ($<100^{aines}$ de µm). D'un point de vue métallogénique, les échelles d'intérêt sont la **province métallogénique** (jusqu'à plusieurs 100^{aines} de km), le **district** (100 à 10 km) et le **champ** (10 à 1 km) **miniers**, le **gisement** (km à m), la **structure minéralisée** (*ore shoot* ; 10^{aines} de dm à quelques mm) puis le **porteur de la minéralisation** (*ore mineral* ; <1 mm en général) (Jébrak et Marcoux, 2008).

Magma primaire *vs* **primitif** *vs* **parent** *vs* **dérivé** (*primary* vs *primitive* vs *parental* vs *derivative melt*) : un magma primaire est un magma ayant subi pas ou peu de différenciation par cristallisation fractionnée et dérivant de la fusion partielle du manteau (Ganne et Feng, 2017). Un magma primitif est quant à lui simplement un magma pas ou peu évolué, le plus mafique d'une série, peu importe de quel type de roche il provient (communication personnelle de P. Bouilhol). Un magma parent est celui dont une série magmatique découle par évolution, à partir duquel des magmas plus différenciés sont formés par retrait de la phase solide formée par cristallisation fractionnée. Ces derniers sont nommés magmas dérivés (Ganne et Feng, 2017). Le magma parent de la fin d'une série magmatique est donc lui-même dérivé du magma primitif duquel elle découle.

Orogène d'accrétion *vs* **de collision** (*accretionary* vs *collision orogen*) : La définition suivante est complétée d'après celle proposée par Cagnard (2005). Au sens strict, un orogène d'accrétion s'apparente à une zone de subduction océanique, incluant des zones de supra-subduction en avant-arc, l'arc magmatique à proprement parler et l'arrière-arc (Cawood et al., 2009). Au sens large, mais de façon impropre, un orogène d'accrétion est considéré comme le résultat de l'amalgamation de multiples arcs insulaires et/ou de micro-continents ainsi que de prismes d'accrétion sédimentaire formés le long de multiples zones de subduction océanique. Il consiste donc en un collage d'unités litho-tectoniques d'origine variée (plateaux océaniques, morceaux de continents...) accrétées à une marge continentale plus ou moins lointaine. Les orogènes d'accrétion peuvent être en avancée (*advancing orogen* ; *i.e.*, les Andes) ou en retrait (*retreating orogen* ; *i.e.*, le Pacifique

Ouest) selon si la plaque chevauchante avance vers la plaque enfouie ou si le front de subduction de celle-ci s'éloigne de la plaque supérieure, respectivement. Les orogènes en avancée présentent une ceinture de plis et de chevauchement (*fold and thrust belt*) d'avant-pays tandis que ceux en retrait sont caractérisés par la présence de bassins d'arrière-arc développés en régime extensif (Cawood et al., 2009). Les orogènes d'accrétion contiennent peu (ou pas) de matériel crustal hérité et remobilisé mais sont caractérisés par une croissance crustale importante (Windley, 1992, 2003). Cette dernière était par exemple particulièrement forte au Précambrien, lorsque les orogènes d'accrétion étaient prédominants (*e.g.,* Taylor et McLennan, 1985, 1995 ; Condie, 1998, 2000). Ces derniers sont également des lieux privilégiés de recyclage et remobilisation de la croûte continentale par subduction et enfouissement de la plaque chevauchée dans le manteau lithosphérique et érosion concomitante de la plaque sus-jacente (Cawood et al., 2009).

La définition initiale d'un orogène d'accrétion, *i.e.*, un système d'arc magmatique en zone de subduction océanique, a donc été largement remaniée au cours du temps. Si l'on revient à cette nomenclature originelle, elle reste néanmoins très ambiguë puisqu'elle n'inclut pas nécessairement de création de relief (*e.g.,* l'arc insulaire actuel des Tonga-Kermadec n'est pas un haut topographique, loin s'en faut), comme le sous-entend pourtant le concept d'orogenèse. De plus, il n'y a pas nécessairement d'accrétion sédimentaire en avant de la plupart des arcs intra-océaniques modernes, à l'exception des zones de subduction des petites Antilles et aléoutienne (Gerya, 2011). Nous n'emploierons donc pas le terme « orogène d'accrétion » dans ce manuscrit, que nous attribuons aux systèmes d'arcs continentaux formés le long d'une marge active, où l'accumulation de matériel crustal et la formation de relief est systématique. En cas d'enregistrement d'un prisme sédimentaire en contexte de zone de subduction intra-océanique fossile ou actuelle, nous emploierons plutôt le terme de « zone de subduction de type accrétion » (*accretionary-type subduction zone* ; Guillot et al., 2009).

La cratonisation permet la préservation des ensembles formés par collage de multiples complexes d'arcs. Les plaques lithosphériques engagées dans la subduction océanique vont se coupler temporairement par localisation de la déformation le long de zones de faiblesse thermique et/ou mécanique, *i.e.,* l'arc magmatique ou la région d'arrière-arc (Cawood et al., 2009 ; Vanderhaeghe, 2012). Ce couplage est favorisé par l'accrétion de plusieurs unités litho-tectoniques, le faible pendage de la subduction et un déplacement absolu de la plaque chevauchante rapide sur la plaque en subduction (Cawood et al., 2009). Il s'agit là de processus typiques de collision, d'où une confusion

légitime autour du concept d'orogène d'accrétion, et du sens large qui lui est couramment attribué. Finalement, selon la nomenclature que nous proposons, tous les orogènes seraient de type collision, puisqu'une phase de collision arc-continent ou continent-continent est nécessaire à leur préservation suite à la subduction. Il y aurait simplement une variabilité dans la nature des terrains impliqués et l'intensité des processus de collision en jeu, conduisant à l'enregistrement d'une histoire géologique parfois complexe (Brown et al., 2020). La phase de collision constitutive d'un orogène est marqués par la localisation de la déformation le long de chevauchements d'échelle lithosphérique juxtaposant des unités lithologiques métamorphisées à un degré variable (Gapais et al., 2009). D'après Windley, (1992, 2003), ces domaines correspondent à des zones de remobilisation de croûte ancienne (par le jeu des chevauchements, de l'épaississement crustal associé et de la fusion partielle) et sont associés à peu, voire parfois pas, de croissance crustale (*e.g.,* vaugnérites décrites dans le Massif central ; Moyen et al., 2017).

Panafricain (*Pan-African*) : terme qualifiant le système orogénique auquel est associé n'importe quel événement tectonique et/ou thermique néoprotérozoïque (*ca.* 1000-542 Ma), sans autre distinction, depuis la rupture du supercontinent Rodinia et l'ouverture de l'océan Mozambique jusqu'à la formation du supercontinent Gondwana (Kröner, 1984). Le terme brasiliano-panafricain est également employé pour souligner la continuité des ceintures orogéniques formées sur le continent sud-américain actuel (Brito Neves et al., 1999), bien que la notion de panafricain n'induit plus de restriction spatiale au continent africain tel que nous le connaissons.

Ressources et **réserves** (*mineral ressources, reserves*) : ces termes sont employés dans ce manuscrit selon les définitions de Jébrak et Marcoux (2008) qui ont repris les critères de classification des normes minières internationales (NI43-101, JORC, PERC…). « Une ressource minérale est une concentration de matériel naturel, solide, inorganique ou fossilisé dans la croûte dont la forme, la quantité et la teneur, ou la qualité, pourraient permettre l'extraction économique. On distingue trois catégories de ressources : mesurées (*measured mineral resources* ; intérêt économique intrinsèque, haut degré de certitude sur la connaissance du tonnage, de la densité, la forme, la qualité, la teneur etc… du minerai), indiquées (*indicated mineral resources* ; intérêt économique intrinsèque mais moins de certitude quant à la connaissance de leurs caractéristiques) et inférées (*inferred mineral resources* ; intérêt économique intrinsèque mais faible degré de confiance, probabilité de devenir des ressources mesurées faibles). […] Les réserves minérales sont définies comme la partie économiquement exploitable des ressources mesurées et

indiquées, démontrée au moins par une étude de faisabilité préliminaire. Une telle étude doit comprendre des informations sur le cubage du minerai avec une courbe tonnage-teneur, l'exploitation, le traitement des minerais et l'économie du projet. Les réserves tiennent donc compte de possibles dilutions du minerai au cours de l'exploitation. » Les réserves sont séparées entre les réserves probables (*probable reserves* ; probabilité de récupération de 50% au moins) et celles prouvées (*proven reserves* ; probabilité de récupération estimée à plus de 90%).

-tectonique, pré-, syn- à **post-** (*pre-, syn-, post-tectonic*) : la chronologie relative de structures ou de générations de minéraux peut être discutée en considérant un épisode ou une phase de déformation de référence. En appliquant les principes fondamentaux de continuité, recoupement, inclusion et superposition, il est possible d'étudier si les objets d'intérêt sont formés avant, en même temps ou après ceux synchrones de la déformation de référence. Ils sont alors qualifiés de pré-, syn- ou post-tectoniques, respectivement. Il est important de noter que l'emploi de ces termes, s'il est très pratique, nécessite au préalable de bien définir la déformation de référence choisie. En règle générale, il s'agit de la phase de déformation contrôlant le grain structural à l'échelle de travail proposée.

Système métallogénique (*mineral system*) : concept relatif à tous les facteurs géologiques contrôlant la formation et la préservation des gîtes métalliques. Les principaux facteurs sont le contexte géodynamique, la chronologie relative et la durée des événements minéralisateurs, leur relation aux épisodes tectoniques régionaux, la source et la nature des fluides, magmas et métaux impliqués, les mécanismes de transport et dépôt des métaux formant le gîte métallifère, ainsi que les modifications post-dépôt. Cette approche implique une vision des systèmes minéralisateurs intégrant l'âge d'extraction mantellique, représentant la fertilisation de cet élément au sein de la croûte continentale, ainsi que l'âge de concentration de l'élément considéré dans un gîte (*e.g.,* Barnicoat, 2007 ; McCuaig et al., 2010 ; Hronsky et al., 2012 ; McCuaig et Hronsky, 2014 ; Champion et Huston, 2016).

Unité litho-tectonique ou **tectonostratigraphique** (*terrane*) : une *terrane* est un fragment crustal constitutif d'un orogène. Il s'agit d'un ensemble de roches, d'affinité juvénile ou non, d'extension régionale, ayant enregistré une histoire géologique qui lui est propre. Distinguer deux *terranes* revient donc à montrer que leurs enregistrements stratigraphique, pétrologique, géochimique, structural, géochronologique et géophysique respectifs diffèrent. Les *terranes* sont ensuite juxtaposées entre elles et/ou avec des blocs crustaux hérités et/ou à la marge de cratons le long de zones de suture. Les analogues

modernes des *terranes* sont les microcontinents, les arcs magmatiques, les chaînes volcaniques intraplaques etc… qui seront à terme amalgamés les uns aux autres par le jeu de la tectonique des plaques (Chetty, 2017 et références citées).

Zone de cisaillement (*shear zone*) : marqueur tectonique fréquent des ceintures orogéniques, exprimée de façon fractale depuis l'échelle lithosphérique jusqu'à l'échelle microscopique. Une zone de cisaillement correspond au volume de roches où la déformation s'accommode intensément, de façon ductile (*e.g.,* présence de mylonites, de structures C/S), ductile-fragile (*e.g.,* présence de veines en extension en échelon) ou fragile (*e.g.,* présence de cataclasites), selon les niveaux structuraux considérés (Passchier et Trouw, 2005). Traditionnellement, les accidents « froids », uniquement cassants, sont nommés **zones de faille** et se distinguent des zones de cisaillement à composante ductile. Ces dernières sont prédominantes dans les orogènes exposant des niveaux crustaux intermédiaires à profonds. Une zone de faille peut donc très bien être l'expression superficielle d'une zone de cisaillement enracinée en profondeur. Une zone de cisaillement peut accommoder du cisaillement pur également appelé aplatissement (*pure shearing*, déformation coaxiale), simple (*simple shearing*, déformation non-coaxiale) ou une combinaison de ces deux modes. Le jeu observé le long d'une zone de cisaillement peut être normal, inverse, transpressif ou transtensif et les accidents décrochants ne sont donc pas les seuls à pouvoir être qualifiés de zones de cisaillement (Fossen, 2016 ; Chetty, 2017 et références citées).

Zone de suture (*suture*) : ceinture de déformation intense le long de laquelle différentes unités litho-tectoniques séparées par un domaine océanique se juxtaposent entre elles, avec des blocs crustaux ou à la marge d'un craton. La suture est dite arc-arc ou arc-continent selon la nature des terrains qu'elle juxtapose. Au sein des ceintures orogéniques, les sutures signalent l'emplacement des paléo-bassins océaniques qui se sont refermés au niveau de zones de subduction et/ou obduction. Une zone de suture se définit par :
(i) une zone ophiolitique préservant une partie ou l'intégration de la lithosphère océanique (roches ultramafiques à mafiques type serpentinite, gabbro, basalte en coussin et roches sédimentaires recouvrant le plancher océanique type chert ou radiolarite ; Haldar, 2020) formée en contexte de ride océanique et/ou d'arc océanique ; (iii) traces de magmatisme calco-alcalin à l'aplomb de la paléo-zone de subduction d'une croûte océanique ; (iv) métamorphisme bimodal avec des unités métamorphiques présentant un faible ratio température/pression, pouvant atteindre les faciès schiste bleu-éclogite, voire granulite dans les zones de subduction et d'autres unités métamorphisées selon un ratio

température/pression élevé, comme les granulites ou les migmatites, formées en contexte d'arrière-arc ou de plateau orogénique (Brown et al., 2020) ; (v) présence d'anomalies gravimétriques, magnétiques et signatures géochronologiques et isotopiques variables illustrant la juxtaposition de portions lithosphériques distinctes (Chetty, 2017). Cependant, la présence d'ophiolites dépend du degré d'océanisation du bassin ouvert en période de rifting intracontinental, en amont de sa fermeture, ainsi que de leur degré de préservation. Le degré métamorphique atteint dépend quant à lui de l'intensité des processus de collision engagés. Afin de s'affranchir de ces paramètres, nous considèrerons la **formation d'une suture** (*suturing*) comme débutant dès l'initiation de la subduction océanique et du magmatisme d'arc précédant la collision et ce quel que soit le degré d'océanisation atteint en amont et le degré de collision atteint lors du collage des différents blocs litho-tectoniques, micro-continents et blocs crustaux entre eux.

INTRODUCTION GÉNÉRALE

Préambule – Pourquoi s'intéresser à l'or, en particulier au Soudan ?

Si la métallogénie permet une meilleure compréhension des processus à l'origine de la concentration des métaux dans l'écorce terrestre, cette science trouve une application directe dans le domaine de l'exploration minière. Elle est donc fortement corrélée à une réalité socio-économique d'utilisation des ressources métalliques au quotidien. Avant de présenter la philosophie guidant ce projet de doctorat, il convient donc de le replacer dans son contexte économique et sociétal.

L'or, objet de toutes les fascinations pour de nombreuses civilisations, a toujours eu une place privilégiée dans l'étude des ressources minérales (*e.g.,* Spooner et Barrie, 1993 ; Robert et al., 1997 ; Sillitoe, 2000, 2008 ; Hofstra et al., 2003 ; Goldfarb et al., 2005 ; Dubé et al., 2007 ; Skirrow et Davidson, 2007 ; Ayer et al., 2008 ; Bissig et Cooke, 2014 ; Dubé et Mercier-Langevin, 2015 parmi bien d'autres) pour les enjeux économiques majeurs qu'il représente. Élément de numéro atomique 79, il s'agit d'un métal jaune, caractérisé par sa forte densité (19,32), sa forte conductivité électrique et son inaltérabilité, aussi bien dans l'air que dans l'eau (Labbé, 2019a). Il est également le métal le plus malléable et ductile qui soit, ce qui en fait un matériau aux multiples applications. Aujourd'hui, les demandes en or concernent essentiellement le monde de la bijouterie (53%), de la finance (fabrication de lingots, de barres et de pièces et achats des banques centrales à hauteur de 24% et 12%, respectivement) et de l'industrie, avec des applications pour l'électronique (6%), la médecine, le développement des énergies renouvelables, les sciences aérospatiales et les nouvelles technologies (chiffres sur l'année 2018 ; World Gold Council, 2020). Les stocks d'or accumulés par les banques centrales (33 763 tonnes d'or (t Au) en juin 2018) démontrent son importance dans le monde de la finance. Ils suffiraient à couvrir plus de cent ans de la consommation de ce métal à des fins techniques et industrielles au rythme atteint en 2017 pour ces secteurs. À titre de comparaison, les stocks accumulés pour les autres métaux dans l'industrie n'excédent que rarement quelques mois de consommation. Ceci explique pourquoi l'or est un métal

précieux, mais pas considéré comme critique au regard des analyses de criticité des métaux publiées ces dernières années (BRGM, 2018 ; Labbé, 2019a et références citées).

Intéressons-nous désormais à la relation à l'or entretenue au cours du temps par les populations de notre région d'étude, le nord-est du Soudan. Historiquement, l'or est exploité depuis l'Antiquité en Afrique de l'Est, notamment en Égypte et en Nubie (nord-est du Soudan essentiellement). Au-delà de sa valeur marchande, il était considéré comme « la chair des dieux » et donc omniprésent dans les temples, palais et tombeaux (Klemm et Klemm, 2013a). Les traces d'exploitation de l'or, exclusivement extrait de veines de quartz et de dépôts alluvionnaires dans les *wadis*, remontent à 4000 ans avant JC (Klemm et Klemm, 2013e) dans le désert oriental d'Égypte et dans le désert de Nubie soudanais (Klemm et Klemm, 2013b, 2013c, 2013d). On estime qu'environ 7 t Au ont été extraites durant la période de règne des pharaons, pour un total de 18 t Au en considérant les périodes ptolémaïque et arabe s'étalant jusqu'en 1350 après JC (Klemm et al., 2001).

Aujourd'hui, de façon surprenante à la lumière de ce passé florissant, le Soudan n'est pas considéré comme une puissance minière aurifère de premier ordre (Alexander et al., 2019). Cette appréciation est en général discutée à la lumière de la production minière nationale officielle et déclarée, et met en exergue les puissances minières reconnues que sont la Chine, l'Australie, la Russie, les États-Unis ou encore le Canada (dans le cas de l'or ; Tableau 0-1). En réalité, la production minière d'un pays dépend largement du contexte économique résultant de nombreux paramètres tels que sa stabilité politique, sociale et économique, sa politique minière, les garanties qu'il offre pour l'implantation de compagnies locales et étrangères d'exploration (mesure de l'indice de la « facilité de faire des affaires » créé par la Banque mondiale et mesurant les réglementations nationales favorables aux investissements de compagnies multi-nationales), *etc*… Tous les pays ne valorisent donc pas leur potentiel minier de façon égale et ne sont pas considérés comme des puissances minières, à juste titre, sans qu'il faille pour autant minimiser l'importance de leurs richesses métalliques.

Pays	Labbé (2019b) (t Au)	Alexander et al. (2019) (t Au)
Chine	426,1	426,1
Australie	296,9	295,0
Russie	270,7	270,7
États-Unis	244,5	230,0
Canada	176,2	175,6
Pérou	151,1	162,3
Ghana	143,4	101,7
Afrique du Sud	137,1	139,9
Mexique	126,8	126,8
Soudan	**105,0**	**14,5**
Indonésie	96,4	154,3
Ouzbékistan	90,9	84,9
Kazakhstan	85,3	59,9
Brésil	80,0	80,0
Argentine	63,0	63,3
Papouasie Nouvlle-Guinée	62,5	62,5
Mali	49,3	52,2
Guinée	46,7	22,4
Burkina Faso	46,4	49,1
Tanzanie	43,5	49,1
Colombie	42,1	50,6
Europe (sans Russie)		56,9
Europe (UE à 28 pays)	31,3	
Autres pays	511,8	531,5
Total	3327,0	3259,3

Tableau 0-1 : Comparaison des données de production d'or pays par pays en 2017 selon deux sources différentes.

Un autre biais réside dans l'incertitude des chiffres d'extraction d'or publiés qui peuvent être cohérents (*e.g.,* Chine, Russie, Mexique, Brésil) ou varier très légèrement (*e.g.,* Australie, Afrique du Sud, Burkina Faso, Mali), considérablement (*e.g.,* États-Unis, Pérou, Kazakhstan, Guinée) voire du tout au tout (*e.g.,* Soudan, Indonésie) d'une source à l'autre (Tableau 0-1 ; Alexander et al., 2019 ; Labbé, 2019b). L'incertitude inhérente à ces estimations est due au fait qu'il est impossible, ou du moins très difficile, de comptabiliser l'intégralité de l'or produit (Labbé, 2019b). En effet, certaines compagnies implantées dans plusieurs pays ne distinguent pas la part de chacun dans les chiffres de production qu'ils communiquent. De manière plus critique, certains pays ne sont pas en mesure ou choisissent de ne pas tracer tous les mouvements d'or du fait de la difficulté de suivre cette production depuis l'échelle industrielle (plusieurs dizaines de

tonnes d'or produites par an) à l'échelle artisanale correspondant à l'orpaillage (jusqu'à moins d'un kilogramme d'or par an) (Labbé, 2019b). La contribution de l'orpaillage est la plus difficile à quantifier, et pourtant elle est essentielle à l'estimation du potentiel aurifère d'un pays. Alors qu'il est totalement interdit et absent de certains pays (*e.g.,* Canada), il est monnaie courante dans d'autres où, bien qu'il puisse être autorisé et contrôlé par l'État, avec un suivi de la production possible, il est souvent clandestin, illégal et donc difficilement quantifiable (Labbé, 2019b).

Le cas du Soudan illustre parfaitement ce paradoxe. Les autorités ont déclaré une production de 105 t Au en 2017, ce qui place le Soudan dans le top 10 des pays producteurs d'or cette année-là (Tableau 0-1). Pourtant, seules deux mines sont actuellement opérées à l'échelle industrielle et n'auraient pas produit plus de 14,5 t Au (Tableau 0-1), voire moins de 5 t Au selon d'autres sources, en 2017 (Labbé, 2019b). L'immense majorité de la production aurifère soudanaise provient en effet de l'orpaillage et de l'extraction artisanale qui a connu un essor sans précédent en 2009 et engendré une vague qui s'est depuis propagée dans l'espace saharo-sahélien jusqu'en Afrique de l'Ouest (Fig. 0-1 ; Chevrillon-Guibert et al., 2019 et références citées). Ce phénomène se traduit par l'affluence de dizaines de milliers de personnes dans le désert où elles s'improvisèrent orpailleurs, équipées de façon semi-artisanale par une nouvelle génération de détecteurs de métaux. La diffusion de ces engins a été largement favorisée par l'autorisation de leur importation en 2008, l'instauration d'un partenariat économique avec la Chine et l'implantation de relais économiques soudanais à Dubaï (Chevrillon-Guibert et al., 2019 et références citées). C'est une véritable toile entrepreneuriale qui s'est alors emparée du désert soudanais et profite depuis très largement des richesses aurifères méconnues de ce pays. L'or représente désormais plus de la moitié de la valeur marchande des exportations depuis le Soudan qui se serait potentiellement hissé au second rang des plus gros exportateurs d'or d'Afrique derrière le Ghana (Chevrillon-Guibert et al., 2019 et

références citées). Le potentiel aurifère du Soudan ne s'est donc pas estompé depuis sa mise en valeur antique et mérite que l'on s'y intéresse, ce que propose cette étude.

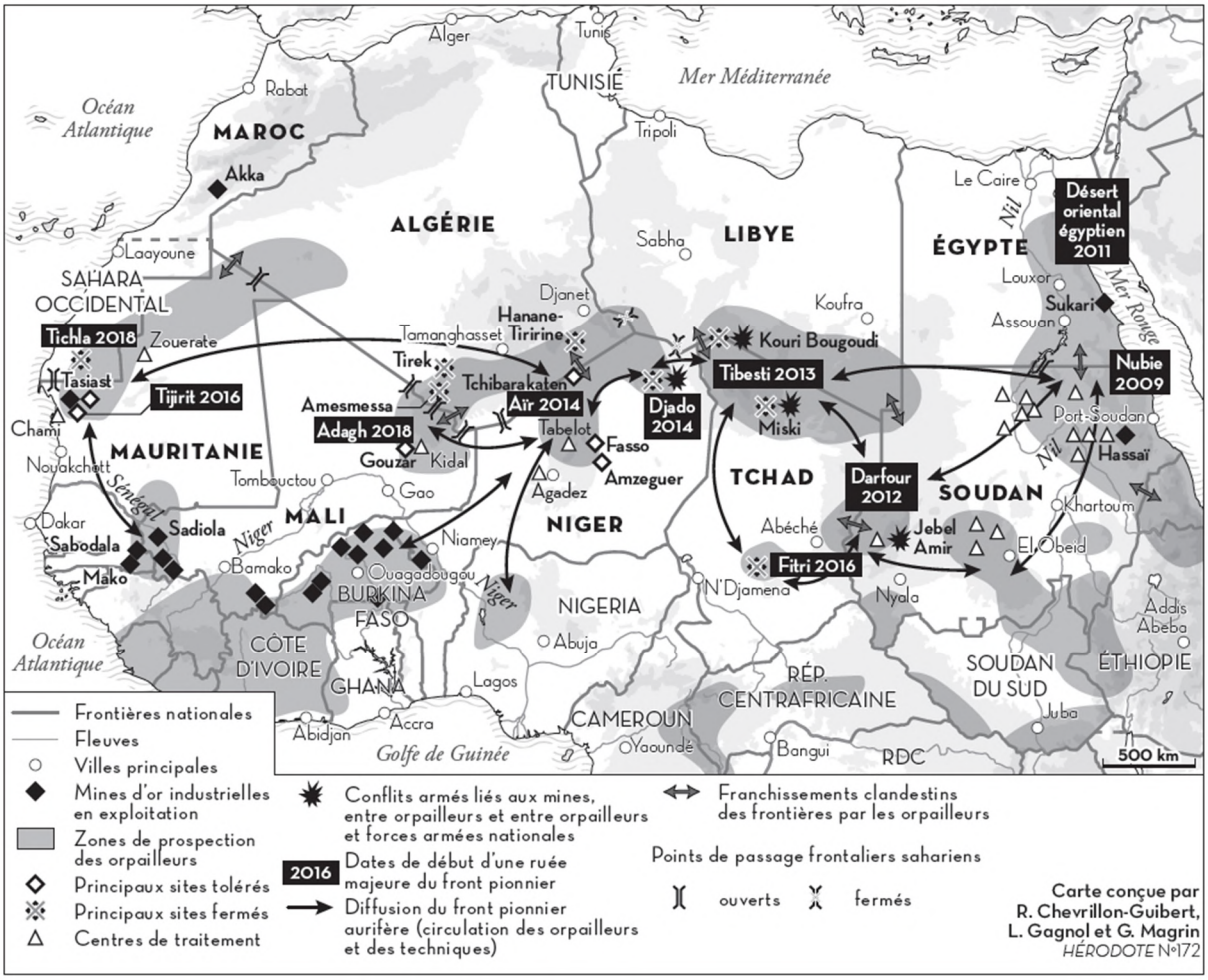


Figure 0-1 : Le front pionnier aurifère dans l'espace saharo-sahélien (Chevrillon-Guibert et al., 2019).

1. La notion de système métallogénique (*mineral system*)

1.1. Émergence du concept et définition

La demande globale en métaux précieux, telle que l'or, est toujours plus importante et requiert donc une remise en question constante de la part de l'industrie minière, notamment en termes de stratégie d'exploration minière aux échelles de la province métallogénique (jusqu'à plusieurs 100^{aines} de km) et du district et champ miniers (100 à 1 km) (Jébrak et Marcoux, 2008). Le choix de nouvelles cibles d'exploration à ces échelles passe par une **compréhension accrue des systèmes minéralisés dans leur cadre**

géodynamique s'appuyant sur le paradigme **source-transport-dépôt** (McCuaig et Hronsky, 2014). Les gisements métalliques résultent d'une variété de processus géologiques, **d'échelle lithosphérique à microscopique** (Fig. 0-2), concentrant les métaux dans un volume réduit et en quantité suffisante pour que leur exploitation soit rentable (Jenkin et al., 2015). Si la concentration en l'élément d'intérêt ne permet pas d'assurer une exploitation rentable à un instant donné, on parle d'anomalie, d'occurrence ou de gîte métallique, cette catégorisation dépendant d'une réalité économique variable dans le temps et du niveau de connaissance du site. Les gisements occupent ainsi, par définition, un petit volume et ont une faible extension par rapport à la surface et l'épaisseur de la croûte continentale, même s'ils sont le produit final de processus qui peuvent être d'échelle lithosphérique (McCuaig et al., 2010 ; Hronsky et al. 2012). Cette approche multi-scalaire (Fig. 0-2) de la compréhension des processus conduisant à la formation des gisements métalliques, et donc de ciblage des minéralisations, a été historiquement développée par les français (Launay, 1913 ; de par l'emprise coloniale leur donnant accès à des échelles de comparaison régionale à continentale), puis par l'école soviétique (Bilibin, 1955, de par l'étendue de l'ensemble du bloc soviétique).

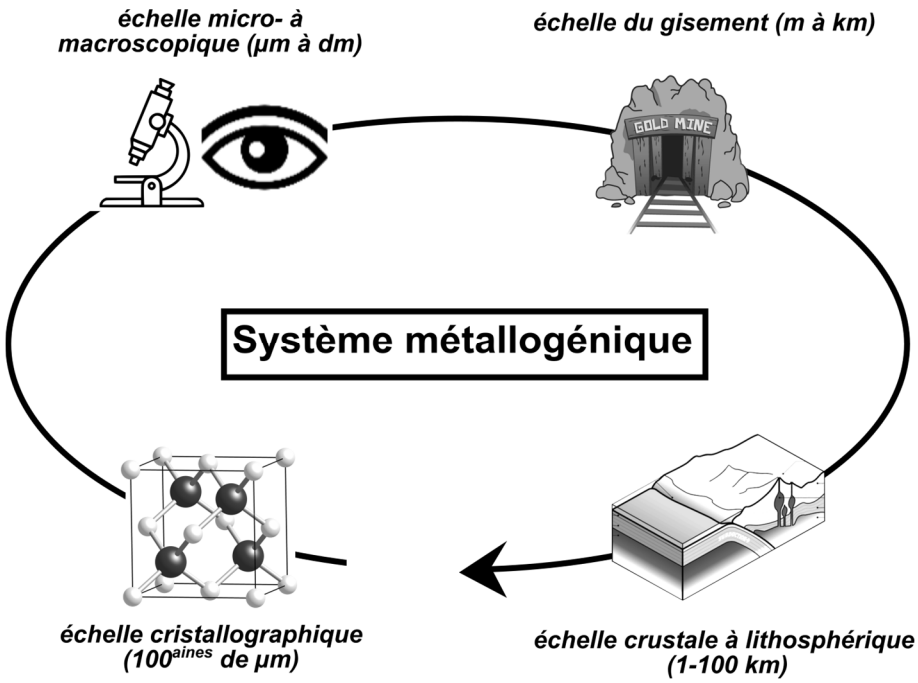


Figure 0-2 : Approche multi-scalaire pour l'étude des systèmes métallogéniques (*mineral systems*), depuis l'échelle cristallographique jusqu'à l'échelle lithosphérique.

A l'heure actuelle, le concept de **système métallogénique (*mineral system*)** est défini comme relatif à tous les facteurs géologiques contrôlant la formation et la préservation des gisements (Wyborn et al., 1994 ; McCuaig et Hronsky, 2014). Bien qu'il y ait de ce fait de nombreuses interprétations de ce qu'est un système métallogénique (*e.g.*, Wyborn et al., 1994 ; Barnicoat, 2007 ; McCuaig et al., 2010 ; Huston et al., 2012), la plupart prennent en considération **le contexte géodynamique**, **la chronologie relative et la durée des événements minéralisateurs**, **leur relation aux épisodes tectoniques régionaux**, **la source et la nature des fluides, magmas et métaux impliqués**, **les mécanismes de transport et dépôt des métaux** formant le gîte métallifère, ainsi que **les modifications post-dépôt**. Cette approche implique une vision des systèmes minéralisateurs intégrant **l'âge d'extraction mantellique**, représentant la fertilisation de cet élément au sein de la croûte continentale (*e.g.,* intégration du cycle de l'uranium à l'évolution de la ceinture panafricaine du Lufilien ; Eglinger, 2013), ainsi que l**'âge de concentration** de l'élément considéré. Un **zoom-dézoom spatial** (Fig. 0-2) **et temporel** s'avère donc nécessaire à l'étude de ces systèmes, depuis l'échelle temporelle **instantanée** à l'échelle **d'un ou plusieurs cycles orogéniques**. Cette approche, permettant la compréhension des relations entre systèmes minéralisés, magmatisme et tectonique lithosphérique, fait désormais consensus quant à son intérêt en termes de ciblage à l'échelle régionale pour l'exploration minière (*e.g.,* McCuaig et al., 2010 ; Griffin et al., 2013 ; McCuaig et Hronsky, 2014 ; Wyman et al., 2016).

1.2. Les gîtes métallifères, traceurs géodynamiques à l'échelle d'un cycle orogénique

Les gîtes métallifères sont l'expression à petite échelle de nombreux processus terrestres se déroulant à différentes échelles de temps et d'espace (Meyer, 1988 ; Barley et Groves, 1992 ; Bierlein et al., 2002 ; Groves et al., 2005a ; Kerrich et al., 2005 ; Groves

et Bierlein, 2007 ; Cawood et al., 2013). Ils sont d'ailleurs répartis de façon hétérogène aussi bien dans l'espace que dans le temps (Lindgren, 1909 ; Turneaure, 1955 ; Meyer, 1988 ; Barley et Groves, 1992 ; Titley, 1993 ; Groves et al., 2005b ; Kerrich et al., 2005 ; Groves et Bierlein, 2007 ; Bierlein et al., 2009 ; Goldfarb et al., 2010 ; Maier et Groves, 2011 ; Cawood et Hawkesworth, 2015). Barley et Groves (1992) ont proposé l'intervention de trois facteurs expliquant cette répartition inégale : (i) l'évolution de l'hydrosphère et de l'atmosphère, (ii) la modification du flux de chaleur terrestre au cours du temps et (iii) la dynamique tectonique à long terme.

La formation des gisements s'inscrit donc pleinement dans l'histoire géodynamique et il est possible de les utiliser comme traceurs de l'évolution de la Terre au cours des temps géologiques. La distribution des âges de ces gisements est ainsi actuellement utilisée afin de caractériser les cycles tectoniques majeurs associés à la jonction et à la séparation périodiques des continents lors de cycles supercontinentaux successifs (Fig. 0-3 ; Goldfarb et al., 2010). Cawood et Hawkesworth (2015) pointent néanmoins le manque d'exhaustivité de cet enregistrement temporel non seulement occasionné par (i) le recyclage crustal au niveau des zones de subduction, (ii) la remobilisation syn-tectonique et/ou syn-métamorphique des gîtes préexistants et (iii) le remaniement généré par l'érosion. Ils insistent également sur le biais systématique concernant l'interprétation de la préservation de certains objets au cours des périodes de jonction puis de séparation des masses continentales. En effet, la conservation d'un gîte métallique dépend, entre autres, de sa chronologie relative vis-à-vis d'un cycle supercontinental, du contexte tectonique auquel il est associé, ou encore de sa profondeur de mise en place, faisant intervenir des échelles de temps très différentes (Groves et al., 2005a ; Cawood et Hawkesworth, 2015). Par exemple, la plupart des gîtes porphyriques ont été formés dans les premiers kilomètres de l'écorce crustale au niveau des marges convergentes actives. Ils se sont mis en place pendant la subduction, en cours de cycle supercontinental, dont le potentiel de préservation des objets formés (*e.g.,* arcs magmatiques) est faible malgré

le grand volume de croûte formé (Cawood et Hawkesworth, 2015). Ces caractéristiques expliquent le faible enregistrement des gîtes porphyriques précambriens qui ont subi au moins un cycle supercontinental et ont été largement remobilisés et remaniés suite à leur mise à l'affleurement (Fig. 0-3 ; Groves et al., 2005a ; Kerrich et al., 2005).

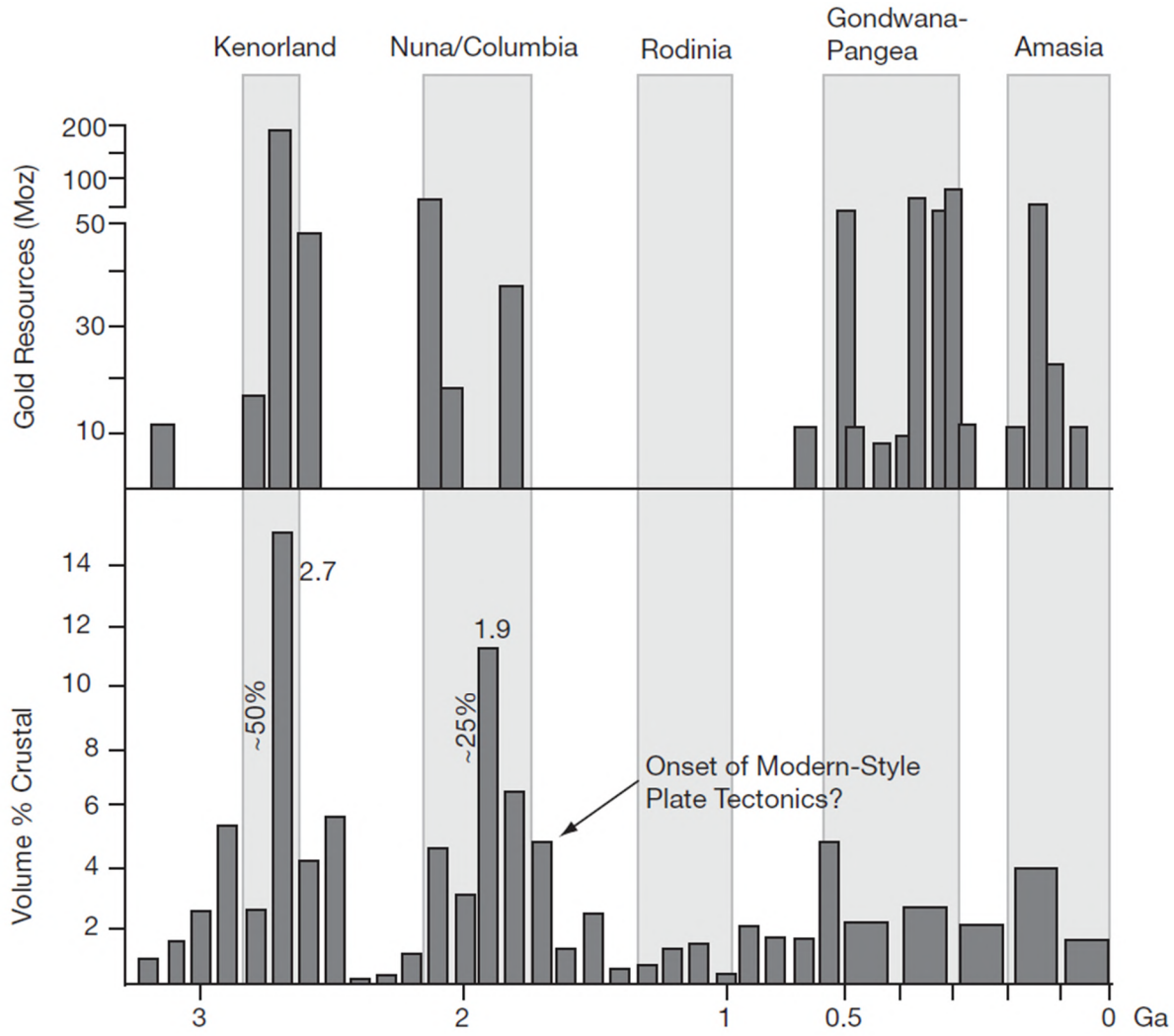


Figure 0-3 : Distribution temporelle des occurrences des principaux types de minéralisation connus et lien avec les contextes géodynamiques à la jonction ou à la séparation entre les masses continentales (Goldfarb et al., 2010).

Comme proposé par Stein (2014), il est nécessaire de tracer la mobilité des éléments (métaux) au cours du temps et à travers l'espace dans une vision tridimensionnelle du système Terre afin de mieux comprendre les processus à l'origine des gîtes métallifères, mais également de la croissance et de l'évolution crustale. (i) Les améliorations récentes en termes de précision et de robustesse des méthodes géochronologiques, (ii) les avancées des méthodes de micro-échantillonnage et/ou de séparation de minéraux et (iii) le

développement analytique des méthodes de quantification chimique *in situ* et de nouveaux instruments de mesure ont permis l'acquisition plus systématique de données géochronologiques pour les systèmes métallogéniques (Stein, 2014). La contrainte de l'évolution de la lithosphère enregistrée par les gîtes métallifères se fait donc désormais selon les composantes spatiales mais également temporelle (Champion et Huston, 2016).

2. Compréhension actuelle des systèmes métallogéniques de l'or

2.1. L'or, un élément chimique traceur des transferts entre le manteau et la croûte

2.1.1. La question de la source de l'or

L'or, en tant qu'élément chimique, se classe dans la famille des éléments sidérophiles : sa très grande affinité pour le fer fait qu'il a été préférentiellement concentré dans le noyau lors de la différenciation de la Terre primitive (Wood et al., 2006). La teneur en or du manteau primitif (*primitive mantle*), réservoir hypothétique ayant la composition globale de la croûte terrestre et du manteau, est donc très faible, sa moyenne étant de 0,88 ppb (Fig. 0-4 ; Palme et O'Neill, 2003). Le *clarke* de l'or, *i.e.,* sa concentration dans la croûte continentale supérieure, monte à 1,3 ppb (Rudnick et Gao, 2003). Pourtant, le réservoir manteau-croûte est plus hétérogène que cela dans le détail puisque la teneur en or des différents types de roche le constituant (mantelliques, magmatiques ou sédimentaires) varie sur plus de 2 ordres de grandeur (de <0,1 ppb à >20 ppb) et est affectée par le degré métamorphique enregistré (Fig. 0-4 ; compilation par Pitcairn, 2011).

- *Manteau lithosphérique*

Les teneurs en or mesurées dans des xénolithes du manteau sont comprises entre 0,1 et 6,9 ppb (*e.g.,* Mitchell et Keays, 1981 ; Barnes et al., 1985 ; Schmidt et al., 2003) mais peuvent atteindre jusqu'à 23,5 ppb dans des péridotites appartenant à des complexes ophiolitiques (*e.g.,* Barnes et al., 1985 ; Lorand et al., 1989 ; Luguet et al.,

2003), ce qui témoigne de l'hétérogénéité du manteau lithosphérique. Celle-ci serait due à des processus métasomatiques permettant l'enrichissement et/ou l'épaississement du manteau lithosphérique sous-continental (*sub-continental lithospheric mantle* ou *SCLM*) (*e.g.,* Bierlein et al., 2006a, 2009 ; Pitcairn, 2011 ; Saunders et al., 2018), notamment par recyclage (*recycling*) de fragments de croûte enrichie en or (*e.g.,* Eglinger et al., 2017 ; Frimmel, 2018).

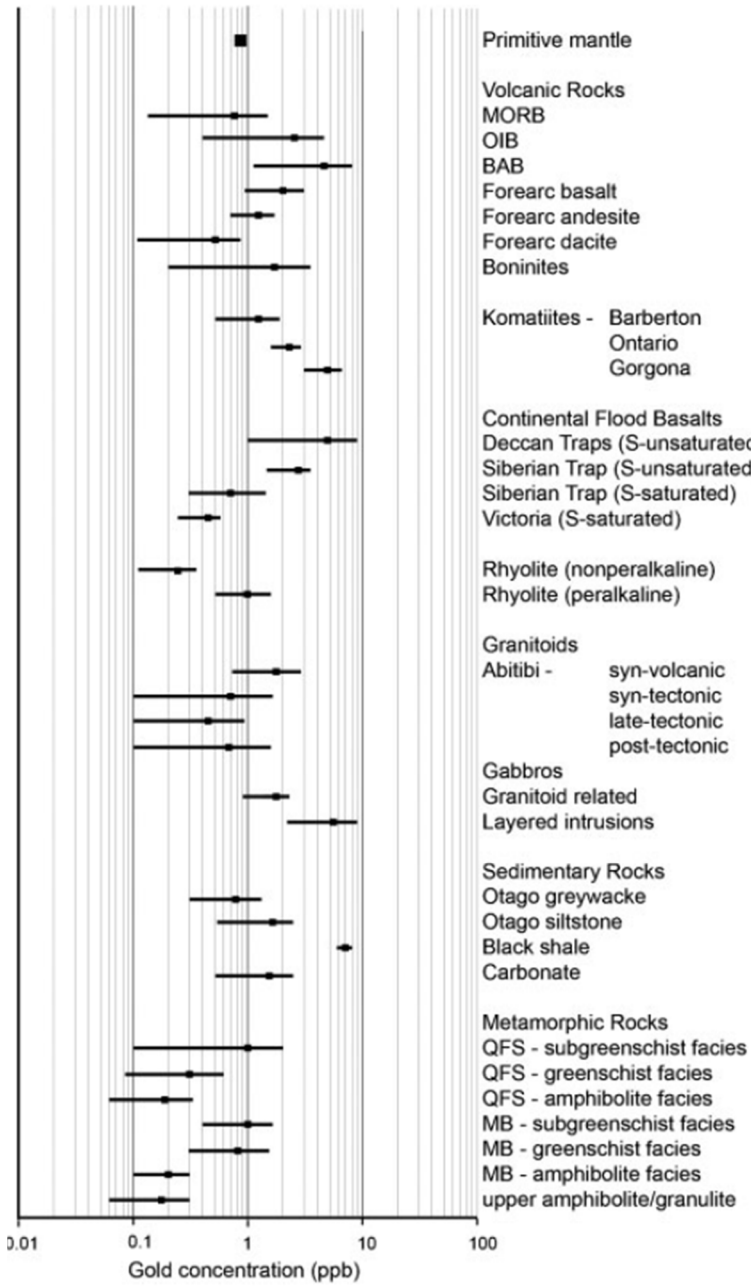


Figure 0-4 : Concentration en or de différentes roches (Pitcairn, 2011). Les valeurs moyennes sont données et la barre d'erreur correspond à ± 2σ. Les abbréviations sont : *MORB = Mid-Ocean Ridge Basalt, OIB = Oceanic Island Basalt, BAB = Back-Arc Basalt, QFS = Quartzo-Feldspathic Schist, MB=Meta-Basite.*

- *Roches magmatiques*

La concentration en or des roches magmatiques est contrôlée par (i) le comportement du soufre dans le magma, (ii) le caractère oxydé ou réduit du système magmatique, (iii) le degré de fusion partielle et (iv) le degré de cristallisation fractionnée :

(i) Le coefficient de partage de l'or entre les sulfures et les silicates est de l'ordre de 10000 et un magma saturé en soufre pourrait théoriquement former des roches préférentiellement enrichies en or. Pourtant, c'est rarement le cas puisque la phase sulfurée du magma, enrichie en or et plus dense, reste la plupart du temps dans le manteau appauvri. Cela explique notamment pourquoi les *MORB* (*Mid-Ocean Ridge Basalts*), pourtant formés à partir d'un magma saturé en soufre (*e.g.,* Mathez, 1976), sont finalement assez pauvres en or (0,75 ppb ; Keays et Scott, 1976 ; Tatsumi et al., 1999 ; Webber et al., 2010) par rapport aux trapps du Deccan (4,6 ppb), résultant de la cristallisation d'un magma sous-saturé en soufre où cette séparation entre phases sulfurée et silicatée n'a pas eu lieu (Keays et Lightfoot, 2010).

(ii) Les magmas oxydés (à forte fugacité d'oxygène) peuvent contenir jusqu'à 10 fois plus de soufre présent sous forme de sulfates que les magmas réduits (Jugo et al., 2005 ; Mungall et al., 2006 ; Jugo, 2009) : ils peuvent donc restés sous-saturés en soufre tout en transportant plus d'or, formant des roches magmatiques juvéniles plus enrichies en or (Jugo, 2009). Ceci explique pourquoi les roches magmatiques mises en place en contexte d'avant-arc (*forearc basalt* ou *FAB* : 2,0 ppb ; Terashima et al., 1994), d'arrière-arc (*back-arc basalt* ou *BAB* : 4,7 ppb ; Allan, 1992 ; Cawood et Fryer, 1994) ou de point chaud (*oceanic island basalt* ou *OIB* : 2,4 ppb ; Fryer et Greenough, 1992 ; Tatsumi et al., 1999, 2000) sont plus enrichies en or que les *MORB* mis en place à l'aplomb des dorsales océaniques à partir de magmas plus réduits (Pitcairn, 2011). Les plateaux océaniques résultant d'un magmatisme de type point chaud (ou *plume* mantellique) sont considérés comme des sources potentielles d'or pour la mise en place de minéralisations aurifères ultérieures (*e.g.,* Bierlein et Pisarevsky, 2008). L'enrichissement en or de la

croûte océanique est alors accru si les systèmes de point chaud et de dorsale océanique se superposent, comme c'est le cas actuellement en Islande où la teneur en or de la croûte est 13 fois supérieure à celle de *MORB* classiques (*e.g.,* Webber et al., 2013).

(iii) Plus le degré de fusion partielle est fort, moins le magma aura tendance à être saturé en soufre puisqu'il s'agit d'un élément incompatible, qui est donc concentré dans la phase liquide, *i.e.,* le magma, dès le début de fusion du manteau (Keays, 1995). Les boninites et komatiites, formées à partir d'un magma primaire résultant d'une forte fusion partielle, sont donc préférentiellement enrichies en or (1,25-1,95 ppb ; Anhaeusser et al., 1975 ; Hamlyn et al., 1985 ; Brügmann et al., 1987). Dans un contexte d'avant-arc, la formation de boninite peut résulter d'un magma formé par fusion partielle d'un manteau appauvri qui contient la phase sulfurée, enrichie en or, et séparée de la phase silicatée d'un premier magma saturé en soufre : l'enrichissement en or de ces roches est alors d'autant plus conséquent (Hamlyn et al., 1985).

(iv) Enfin, au cours de la cristallisation fractionnée d'un magma enrichi, l'or se concentre dans les termes les plus mafiques (en contexte d'avant-arc – basalte : 2,0 ppb et dacite : 0,48 ppb ; Terashima et al., 1994).

En somme, il existe donc un lien génétique entre l'extraction de l'or depuis le réservoir mantellique et la formation de nouveaux segments de croûte océanique juvénile par accrétion magmatique de matériel juvénile enrichi en or (i) au niveau des rides océaniques, en particulier à l'Archéen (mise en place de komatiites), ou en présence combinée d'un point chaud (*e.g.,* Webber et al., 2013). Cependant, l'environnement géodynamique le plus favorable à l'extraction d'or depuis le manteau vers la croûte reste (ii) les limites de plaques convergentes peu évoluées, avec formation de croûte océanique juvénile en arrière-arc.

- *Roches sédimentaires*

La nature des roches sédimentaires est très variable selon la diversité de réservoirs desquels elles dérivent. La roche mère d'un sédiment peut notamment être préalablement enrichie en or, voire contenir un gîte aurifère, ce qui engendre la formation de placers lors de la phase de sédimentation. Une fois la roche sédimentaire formée, un possible enrichissement en or lors d'un événement hydrothermal ultérieur peut également avoir lieu. La coexistence ou non de ces deux processus explique la variabilité de la teneur en or exprimée par les roches sédimentaires (0,1 à 30 ppb pour les argillites, siltites, grès ou conglomérats mais jusqu'à 1000 ppb dans les horizons sédimentaires riches en sulfures ou dans les formations de fer rubanées ; Crocket, 1993). Si l'on écarte un possible enrichissement hydrothermal épigénétique, le contenu en or d'une roche sédimentaire dépend de (i) l'incorporation de minéraux détritiques aurifères et (ii) de la précipitation de sulfures aurifères lors de la diagenèse (Pitcairn et al., 2006, 2010 ; Ketris et Yudovich, 2009). Les roches sédimentaires les plus enrichies en or sont alors sans surprise les schistes noirs (*black shales* ; 7 ppb ; Ketris et Yudovich, 2009), où les conditions réductrices permises par la présence de matière organique facilitent la complexation de l'or contenu dans l'eau de mer et son incorporation lors de la précipitation des sulfures diagénétiques (Pitcairn, 2011).

Pour résumer, l'or se concentre principalement (i) dans les roches magmatiques juvéniles, peu différenciées, mises en place au niveau du plancher océanique (surtout vrai pour l'Archéen où le régime thermique plus important a permis la formation de komatiites) ; (ii) au niveau de marges tectoniques convergentes peu évoluées où l'accrétion magmatique l'emporte sur l'accrétion tectonique du prisme sédimentaire ; ou (iii) dans des roches sédimentaires potentiellement riches en sulfures aurifères diagénétiques.

2.1.2. Or orogénique et traçage des grandes périodes de formation crustale

Le système métallogénique de l'or orogénique s'intéresse aux minéralisations aurifères présentant les caractéristiques suivantes, depuis l'échelle de la province métallique jusqu'à l'échelle du gisement (Kerrich et Wyman, 1990 ; Goldfarb et al., 2001, 2005 ; Groves et al., 2003, 2018, 2019 ; Weinberg et al., 2004 ; Bierlein et al., 2006 ; Dubé et Gosselin, 2007 ; Tomkins et Grundy, 2009 ; Blenkinsop et al., 2020a):

(i) d'âge archéen à tertiaire ;

(ii) associées à des ceintures orogéniques formées au niveau de marges convergentes de type subduction ;

(iii) mises en place le long d'objets structuraux d'ordre multiple au sein de méga-structures d'échelle crustale à lithosphérique, entre 5 et 10 km de profondeur ;

(iv) hébergées par des séquences métamorphisées dans le faciès schiste vert à amphibolite composées de fragments de croûte océanique, d'arcs, arrière-arcs à signature tholéiitique à calco-alcaline et comportant des intrusifs pré-, syn- à post-tectoniques. Ces ensembles sont nommés « ceintures de roches vertes » d'après la définition donnée pour l'Archéen par Anhaeusser (2014). Les gîtes d'or orogénique peuvent également être hébergés par des séquences sédimentaires à volcano-sédimentaires appartenant à des prismes d'accrétion. Ces gisements d'or sont hébergés dans la croûte et expriment des teneurs de l'ordre du ppm. Ils représentent ainsi de fortes anomalies géochimiques associées à des facteurs d'enrichissement pouvant atteindre 1000 à 10 000 fois le *clarke*. Ces concentrations anomaliques sont en relation directe avec l'évolution biogéochimique globale de la Terre et des processus géologiques de différenciation manteau-croûte puis de recyclage et/ou remobilisation de la croûte (Frimmel, 2008, 2018) ;

(v) présentant un fort contrôle structural, la minéralisation étant exprimée la plupart du temps sous forme de veines de faille laminées ou de veines d'extension à faible

pendage avec une altération proximale à quartz-ankérite-séricite-sulfures-albite et des structures héritées pouvant être réactivées.

Cependant, de nombreuses questions restent en suspens concernant les processus minéralisateurs engagés dans la formation de gîtes d'or orogénique :

(i) **Quelle est la source de l'or ?** Magmas primaires (*i.e.,* extrait directement du manteau) ou primitifs (*i.e.,* magma peu évolué dérivant de la fusion partielle d'une roche préalablement enrichie en or) à l'origine de croûte océanique (*e.g.,* Pitcairn et al., 2015 ; Augustin et Gaboury, 2017) ou sédiments (*e.g.,* Large et al., 2007, 2011 ; Gaboury, 2013) ? Les magmas issus de la fusion partielle d'un manteau métasomatisé et/ou d'une croûte continentale recyclée sont par exemple considérés comme la source principale d'or dans le cas de minéralisations aurifères associées à des intrusions (*intrusion-related deposits ; e.g.,* Bierlein et McKnight, 2005 ; Hart, 2005 ; Eglinger et al., 2017 ; Masurel et al., 2019). Une question fondamentale reste d'ailleurs de savoir s'il faut opposer or orogénique et *intrusion-related deposits* (Sillitoe et Thompson, 1998 ; Hart et Goldfarb, 2005 ; Pitcairn et al., 2006, 2015 ; Phillips et Powell, 2009 ; Tomkins, 2010, 2013 ; Kendrick et al., 2011 ; Large et al., 2011, 2012 ; Gaboury, 2013, 2019 ; Goldfarb et Groves, 2015).

(ii) **Quand se forme la minéralisation ?** Arrive-t-elle au pic de métamorphisme comme proposé par le modèle continu (*continuum model* ; Groves, 1993 ; Groves et al., 1998) ou plutôt à la transition entre les faciès schiste vert et amphibolite lors du métamorphisme prograde en accord avec le modèle métamorphique (*metamorphic model* ; Powell et al., 1991 ; Phillips et Powell, 2009, 2010) ?

(iii) **La minéralisation exprimée est-elle polyphasée on non** (Kerrich et Cassidy, 1994 ; Meffre et al., 2016 ; Goldfarb et al., 2017 ; Thébaud et al., 2020 ; Masurel et al., en presse) **?**

Quoi qu'il en soit, l'étude des gisements d'or orogénique, couplés à l'utilisation de traceurs géochimiques, permet de documenter les processus de transfert de matériel depuis le manteau jusqu'à la croûte de par (i) leur diversité d'âge (de l'Archéen au Phanérozoïque) et d'encaissants (des ceintures de roches vertes aux séquences turbiditiques), (ii) leur association spatio-temporelle à des orogènes relativement immatures, où l'accrétion magmatique et tectonique et la mise en place de croûte juvénile l'emporte sur la collision arc-continent et le recyclage crustal et (iii) leur lien génétique avec des événements magmato-tectoniques majeurs (*e.g.,* Kerrich et Wyman, 1990 ; Wyman et al., 2016). Par exemple, les grandes périodes connues d'âge précambrien de formation de minéralisations de type or orogénique sont principalement datées à *ca.* 2,80-2,55 Ga et à *ca.* 2,1-1,8 Ga et semblent être corrélées aux périodes de formation de croûte juvénile les plus importantes de l'histoire de la Terre à 2,7 et 1,9 Ga (Fig. 0-5). Or, ces périodes sont interprétées comme des maxima d'activité magmatique de type point chaud et donc de fertilisation en or de la croûte océanique aux cours des cycles orogéniques concernés (Goldfarb et al., 2001 ; Condie, 2007 ; Condie et al., 2009). Concernant le pic de formation de gisements d'or orogénique à 2,75-2,55 Ga, une autre explication est proposée par Frimmel (2018). Il suggère l'existence (i) d'une phase d'enrichissement en or de la croûte associée à l'activité photosynthétique de tapis microbiens en atmosphère anoxique à 2,9 Ga, (ii) dont le démantèlement aurait engendré la formation de paléoplacers aurifères entre 2,9 et 2,7 Ga et l'enrichissement en or de sédiments marins lors de la sédimentation. Ensuite, (iii) le recyclage de ces ensembles le long des marges actives en subduction aurait ensuite permis la métasomatose et l'enrichissement en or du *SCLM* qui est alors une source préférentielle pour la mise en place des gisements d'or orogénique. Dans les deux cas, la répartition temporelle des gisements d'or orogénique est donc bien directement corrélée à l'enrichissement en or de l'écorce terrestre et du manteau lithosphérique, lui-même associé à des transferts depuis le manteau vers la croûte, ou inversement, au cours des temps géologiques.

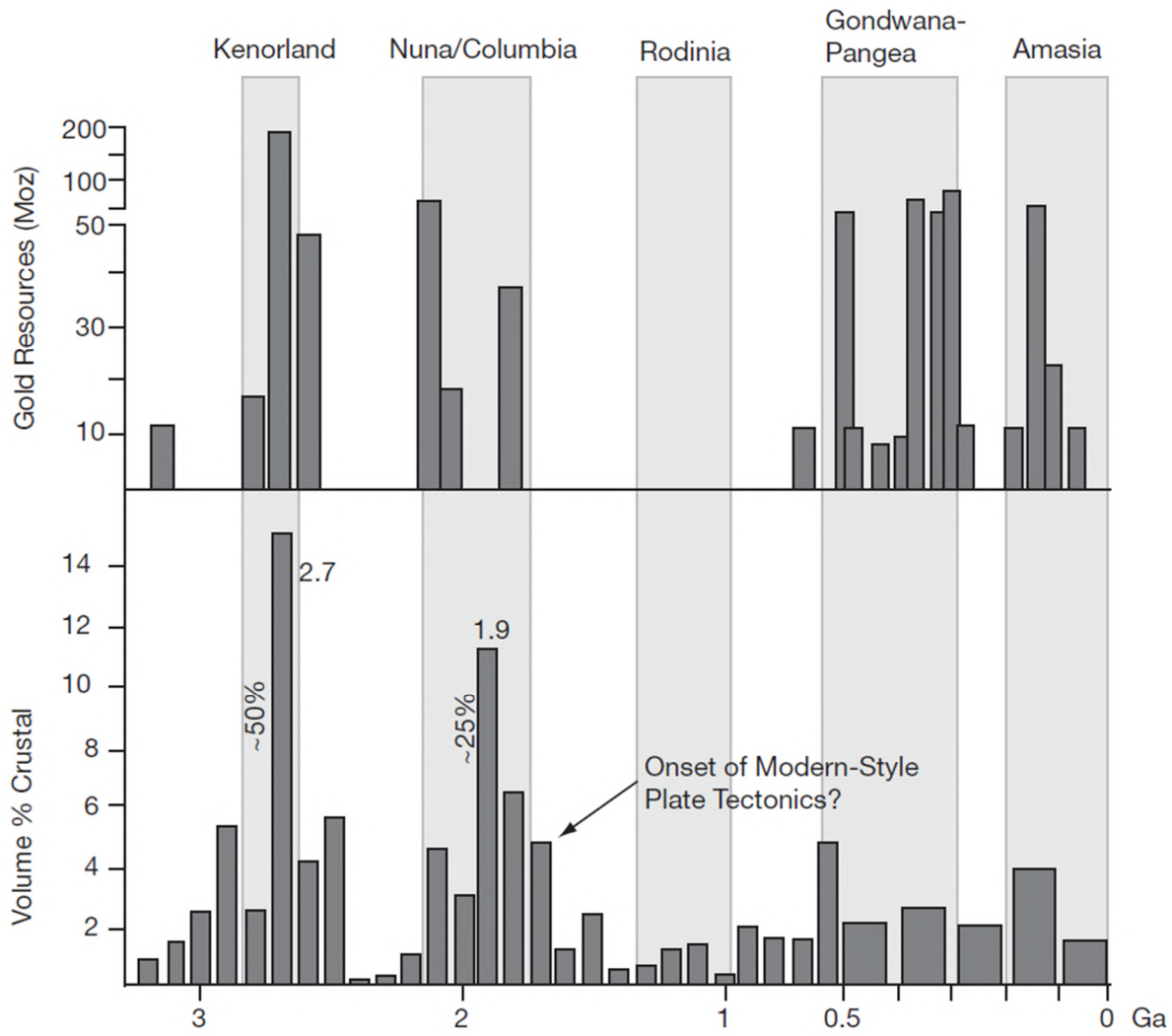


Figure 0-5 : Évolution des ressources en or cumulées des gisements d'or orogénique et du volume de croûte continentale formé au cours des temps géologiques (Goldfarb et al., 2010). L'exemple des gisements d'or orogénique montre que leur distribution au cours des temps géologiques permet de retracer les périodes de formation de croûte continentale juvénile au cours des cycles tectoniques majeurs depuis l'Archéen jusqu'au Phanérozoïque.

2.1.3. La mobilité de l'or dans les fluides hydrothermaux et métamorphiques

Aucun gisement d'or associé directement à la cristallisation d'un magma n'est connu à ce jour, et l'extraction d'or en sous-produit de gisements magmatiques représente moins de 1% de la production totale d'or. L'or transporté dans les magmas primaires et primitifs permet donc un enrichissement tout relatif de la croûte terrestre, qui n'est pas suffisant à la formation de gisements d'or. L'enrichissement ultérieur en or se fait donc principalement par circulation hydrothermale, qui transporte bien plus efficacement l'or que les magmas (Frimmel, 2008).

Comment un des métaux les plus inertes de la classification périodique des éléments peut-il alors être mobilisé depuis les réservoirs évoqués auparavant? Plus le faciès métamorphique atteint pour une roche donnée est fort, plus sa teneur en or est faible (baisse de 0,90 ppb à 0,21 ppb entre le faciès schiste vert inférieur et le faciès amphibolite pour les métabasites d'Otago, *MB* ; Fig. 0-4 ; Pitcairn, 2011 et références citées). Cette perte en or des protolithes s'accompagne d'une mobilité en arsenic et antimoine et d'une déshydratation généralisée des roches métamorphiques lors de la dévolatilisation de la croûte associée au métamorphisme prograde et au passage schiste vert-amphibolite. L'or ainsi mobilisé peut contribuer à la formation de gisements aurifères (Powell et al., 1991 ; Pitcairn et al., 2006, 2015 ; Phillips et Powell, 2010 ; Tomkins, 2010 ; Pitcairn, 2011 ; Yardley et Cleverley, 2015). D'ailleurs, des calculs de bilan de masse ont montré que la quantité d'or mobilisée par dévolatilisation lors du métamorphisme prograde subi par l'orogène alpin en Nouvelle-Zélande est largement supérieure à celle cumulée dans les gisements d'or orogénique actuellement reconnus dans la région (*e.g.,* Pitcairn et al., 2014).

Mais comment l'or est-il transporté au sein de ces fluides ? Les modèles actuels considèrent que les sulfures et chlorures représentent les ligands responsables de la mobilisation et/ou précipitation de l'or via des fluides dans la lithosphère (Krauskopf, 1951 ; Helgeson et Garrels, 1968 ; Seward, 1973 ; Hedenquist et Lowenstern, 1994 ; Barnes, 1997 ; Loucks et Mavrogenes, 1999 ; Simon et Ripley, 2011 ; Kouzmanov et Pokrovski, 2012 ; Pokrovski et al., 2014 ; Morrissey et Tomkins, 2020). Pokrovski et Dubessy (2015) ainsi que Pokrovski et al. (2015) ont notamment démontré que les anions sulfurés tels que S_3^- forment des complexes très stables avec l'ion Au^+ en solution aqueuse à haute température (>250°C) et pression (>100 bar), donc spécifiquement en conditions métamorphiques. La présence de CO_2 dans le fluide, courante dans ces mêmes conditions, permet également de tamponner le pH et de favoriser la complexation entre l'or et le soufre réduit en solution (Phillips et Evans, 2004 ; Yardley et Cleverley, 2015). Leur mise

en mouvement permet le transport d'or, possiblement sous forme colloïdale (*e.g.,* Petrella et al., 2020), et la précipitation de la minéralisation se fait souvent par chute de pression du fluide minéralisateur associée au contexte tectonique local (*e.g.,* Upton et Craw, 2014a, 2014b) et à des processus quasi instantanés à l'échelle des temps géologiques, tels que le système de valve sismique (*fault valve system* ; *e.g.*, Sibson et al., 1988 ; Weatherley et Henley, 2013 ; Peterson et Mavrogenes, 2014 ; Sibson, 2020a, 2020b ; Voisey et al., 2020). La précipitation d'or est également contrôlée par d'autres facteurs tels que la présence d'interactions fluide-roche avec l'encaissant (*e.g.,* Evans et al., 2006), le processus d'ébullition (*boiling*) du fluide hydrothermal (*e.g.,* Weatherley et Henley, 2013), le possible mélange entre plusieurs fluides (Bateman et Hagemann, 2004 ; Beaudoin et Pitre, 2005 ; Beaudoin et Chiaradia, 2016) ou encore les contrôles électrochimique et cristallographique sur la chemiosorption d'or à la surface des sulfures tels que la pyrite ou l'arsénopyrite (*e.g.,* Möller et Kersten, 1994 ; Chouinard et al., 2005 ; Gaboury et Oré Sanchez, 2020). Ces sulfures, sous le contrôle du comportement de As en solution, peuvent incorporer de l'or sous forme « invisible », *i.e.*, de nano-inclusions ou en substitution dans le réseau cristallin, à hauteur de 1,1 et 1,5 % poids Au pour une pyrite arsénifère et une arsénopyrite selon des ratio atomiques Au/As de 0,14 et 0,0071, respectivement (*e.g.,* Reich et al., 2005 ; Deditius et al., 2014 ; Merkulova et al., 2019 ; Pokrovski et al., 2019). Ces minéraux sont très largement décrits dans les gisements d'or orogénique et des processus de remobilisation d'or invisible associés à la déformation contribuent fréquemment à la libération d'or « visible », *i.e.*, sous forme de micro-inclusions dans les sulfures ou de particules libres plus imposantes (*e.g.,* Large et al., 2007 ; Sung et al., 2009 ; Velasquez et al., 2014 ; Meffre et al., 2016 ; Augustin et Gaboury, 2018 ; Gregory et al., 2019 ; Voute et al., 2019).

2.2. L'exemple du craton ouest-africain

L'application du concept de système métallogénique a notamment fait ses preuves en Afrique de l'Ouest, dans le cadre d'une recherche scientifique active sur les systèmes aurifères associés au cycle orogénique éburnéen (Paléoprotérozoïque : 2,15-2,07 Ga), notamment via le projet WAXI (West African eXploration Initiative). Ce projet revisite le concept même d'or orogénique, montrant que le système aurifère est systématiquement polyphasé et s'étale sur près de 150 millions d'années depuis les phases d'accrétion magmatique et tectonique jusqu'à la collision arc-continent (*e.g.,* Thébaud et al., 2020 ; Masurel, en presse). Le lien avec l'évolution tectono-métamorphique de cette région est également fort avec une remobilisation de l'or durant les phases prograde et rétrograde de métamorphisme et une évolution des teneurs en fonction des grandes phases de déformation (*e.g.,* Baratoux et al., 2015 ; Block et al., 2015, 2016 ; Eglinger et al., 2017 ; Fontaine et al., 2017). Ce projet démontre notamment comment l'étude des minéralisations aurifères tardi-orogéniques a permis de réviser le modèle de croissance crustale pour le craton ouest-africain lors de l'orogenèse éburnéenne (*e.g.,* Eglinger et al., 2017). La subduction éburnéenne serait associée à un épisode de métasomatisme et d'enrichissement en or du manteau lithosphérique sous-continental sous le craton ouest-africain, par assimilation et recyclage de sédiments dérivés d'arcs insulaires juvéniles éburnéens ou de fragments de croûte continentale (tonalite-trondjhemite-granodiorite ou TTG) archéenne enrichie. Plus tardivement, en contexte post-collisionnel, la délamination de la lithosphère sous le craton ouest-africain aurait été à l'origine d'un flux de chaleur intense par remontée asthénosphérique. Celui-ci aurait permis la fusion partielle du (i) *SCLM*, source mantellique métasomatisée et enrichie en or et (ii) des segments de croûte continentale juvénile paléoprotérozoïque et archéenne, avec des preuves de remobilisation (*reworking*) interne de cette dernière à proximité du domaine archéen de Kénéma-Man. Cet épisode magmatique tardif est considéré comme le moteur des circulations fluides et de la migration de l'or depuis sa source mantellique vers la

croûte continentale, à l'origine de la mise en place des minéralisations paléoprotérozoïques de type or orogénique tardives reconnues massivement dans le domaine paléoprotérozoïque de Baoulé-Mossi (Eglinger et al., 2017). Cet exemple démontre bien le lien intime reliant la formation de gîtes aurifères et les processus géodynamiques et comment l'étude des premiers permet la compréhension des seconds. Cette approche a conduit, dans le cas du craton ouest-africain, à la proposition d'un nouveau modèle d'évolution crustale impliquant un épisode de délamination de la lithosphère continentale (Eglinger et al., 2017).

3. Contexte géodynamique du bouclier arabo-nubien

Ce projet de doctorat s'intéresse à la province aurifère néoprotérozoïque du bouclier arabo-nubien (BAN ou *Arabian-Nubian shield* abrégé en *ANS* dans les figures), formant la partie occidentale de la péninsule arabique et l'extrémité nord-est du continent africain (Fig. 0-6). Nous nous intéresserons plus particulièrement à la suture de Keraf (SK) et sa zone d'interférence avec la suture d'Atmur-Delgo (SAD). Dans cette partie, l'histoire géodynamique associée à cette région est présentée. Le cycle panafricain (*ca.* 1000-542 Ma) sera présenté ainsi que le contexte régional du BAN avant de détailler l'histoire de mise en place de la SK.

3.1. Du « Panafricain » (ca. 1000-542 Ma) à l'orogenèse est-africaine-antarctique (ca. 1100-550 Ma)

À l'origine, le terme « panafricain » décrivait un événement tectono-métamorphique conclu il y a ~ 500 Ma, exprimé par des ceintures orogéniques mobiles mises en place autour de cratons mésoprotérozoïques à archéens et ayant très largement modelé le continent africain tel que nous le connaissons actuellement (Kennedy, 1964). Cependant, ce qualificatif est désormais utilisé pour décrire n'importe quel événement

tectonique et/ou thermique néoprotérozoïque (*ca.* 1000-542 Ma), sans outre distinction, depuis la rupture du supercontinent Rodinia (Fig. 0-6a) et l'ouverture de l'océan Mozambique jusqu'à la formation du supercontinent Gondwana, sans limite spatiale à l'Afrique (Fig. 0-6b ; Kröner, 1984). Le terme « brasiliano-panafricain » est également employé (Brito Neves et al., 1999).

Le scénario type du cycle supercontinental (rupture d'un supercontinent – ouverture de bassins océaniques – fermeture par subduction – collision entre des masses continentales formant un nouveau supercontinent) est cependant remis en question entre la rupture de Rodinia et la formation du Gondwana puis de la Pangée, entre le Néoprotérozoïque et le Phanérozoïque (Merdith et al., 2019). En effet, la rupture de Rodinia, débutée entre ~ 900 Ma (Stern, 1994) et ~ 825 Ma (Li et al., 2008), n'est pas complétée avant ~ 600 Ma (ouverture de l'océan Iapetus entre *ca.* 610-600 Ma ; Oriolo et al., 2017) alors que l'assemblage de certains blocs continentaux (*e.g.,* cratons de Rio de la Plata, Congo, São Fransisco, ouest-africain et amazonien ; Fig. 0-6a) a déjà débuté à *ca.* 630-600 Ma dans ce qui deviendra Gondwana de l'Ouest (*West Gondwana* sur la Fig. 0-6b ; *e.g.,* Oriolo et al., 2017).

De même, contrairement à ce qu'évoque le terme « panafricain », il est reconnu que certains blocs continentaux ne seront accrétés à Gondwana de l'Ouest qu'au milieu du Cambrien (*ca.* 480 Ma ; Schmitt et al., 2018 et références citées). Le Gondwana peut-il alors être considéré comme un supercontinent néoprotérozoïque à part entière ? Cette question est de plus en plus débattue et l'assemblage final du Gondwana ne serait possiblement qu'une étape intermédiaire au sein d'un cycle supercontinental, dominé par l'existence de larges masses continentales et ponctué de brèves périodes de dispersion et d'amalgamation des blocs continentaux, se prolongeant jusqu'à la formation de la Pangée à ~ 300 Ma (Grenholm, 2019 ; Merdith et al., 2019 et références citées).

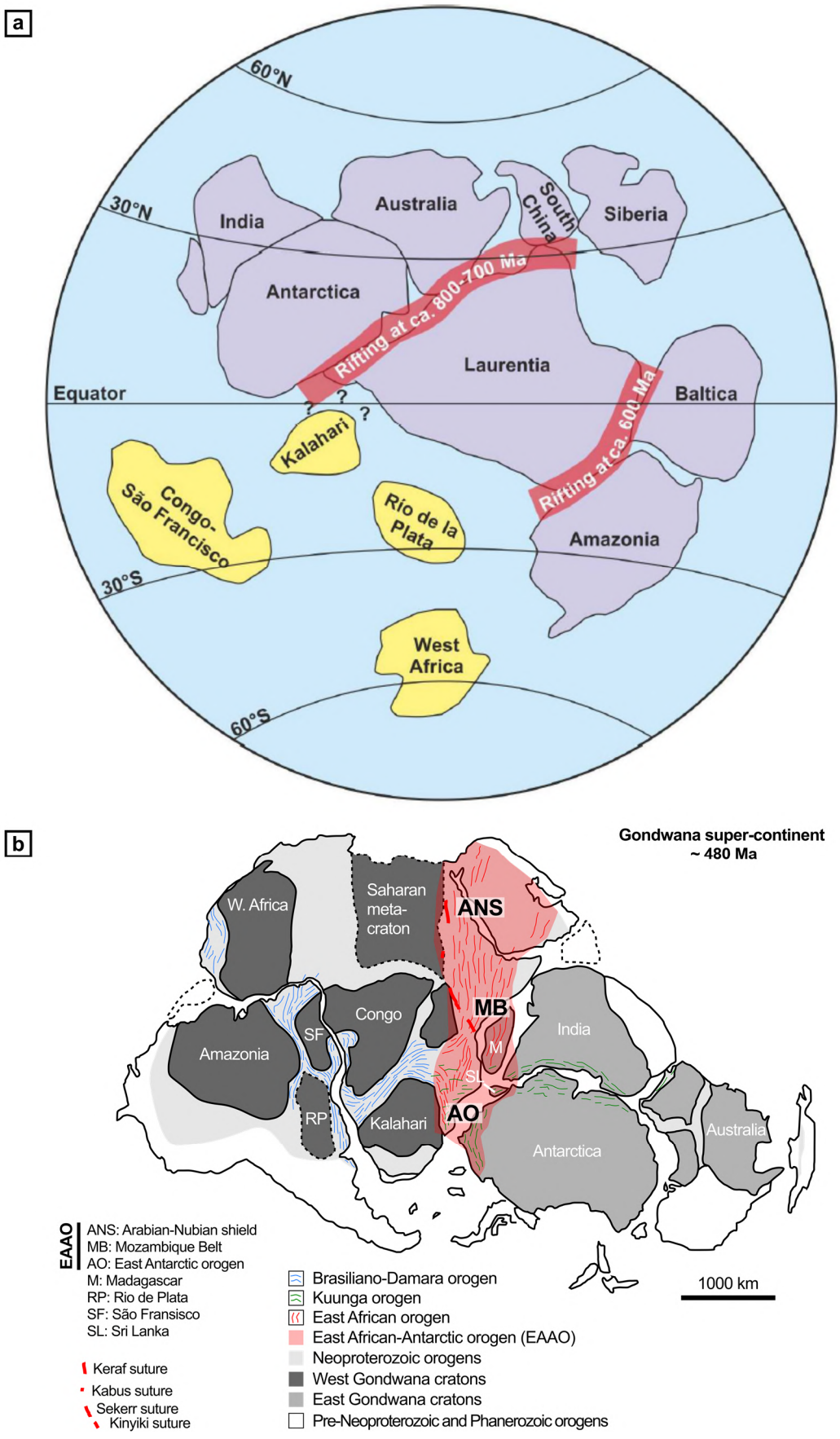


Figure 0-6 : Reconstruction des supercontinents (**a**) Rodinia d'après Oriolo et al. (2017) et (**b**) Gondwana, modifiée d'après Gray et al. (2008) et Feneyrol (2012).

L'orogenèse est-africaine est à l'origine de l'amalgamation des cratons du Sahara et du Congo à l'ouest (Figs. 0-6b, 0-7) et de l'Azanie à l'est (*Az* ; Fig. 0-7) à *ca.* 650-620 Ma. Elle est poursuivie par l'orogenèse du Kuunga (*Kuunga orogen* ; Fig. 0-6b) conduisant à l'amalgamation des cratons du Congo, de São Fransisco et indien au nord, Kalahari et Antarctique au sud à *ca.* 600-500 Ma : cet enchaînement est responsable de l'unification des continents Gondwana de l'Ouest et de l'Est (Fig. 0-6b ; Fritz et al., 2013 et références citées). Nous considèrerons dès lors l'orogenèse est-africaine-antarctique (*EAAO* ; Fig. 0-7) comme le cycle orogénique au cours duquel le Gondwana s'est globalement formé (Jacobs et al., 1998; Li et al., 2008; Seton et al., 2012; Fritz et al., 2013; Domeier et Torsvik, 2014; Merdith et al., 2017), par collision est-ouest entre Gondwana de l'Ouest et de l'Est, entre *ca.* 1100-550 Ma, d'après les bornes temporelles fixées par Grenholm (2019).

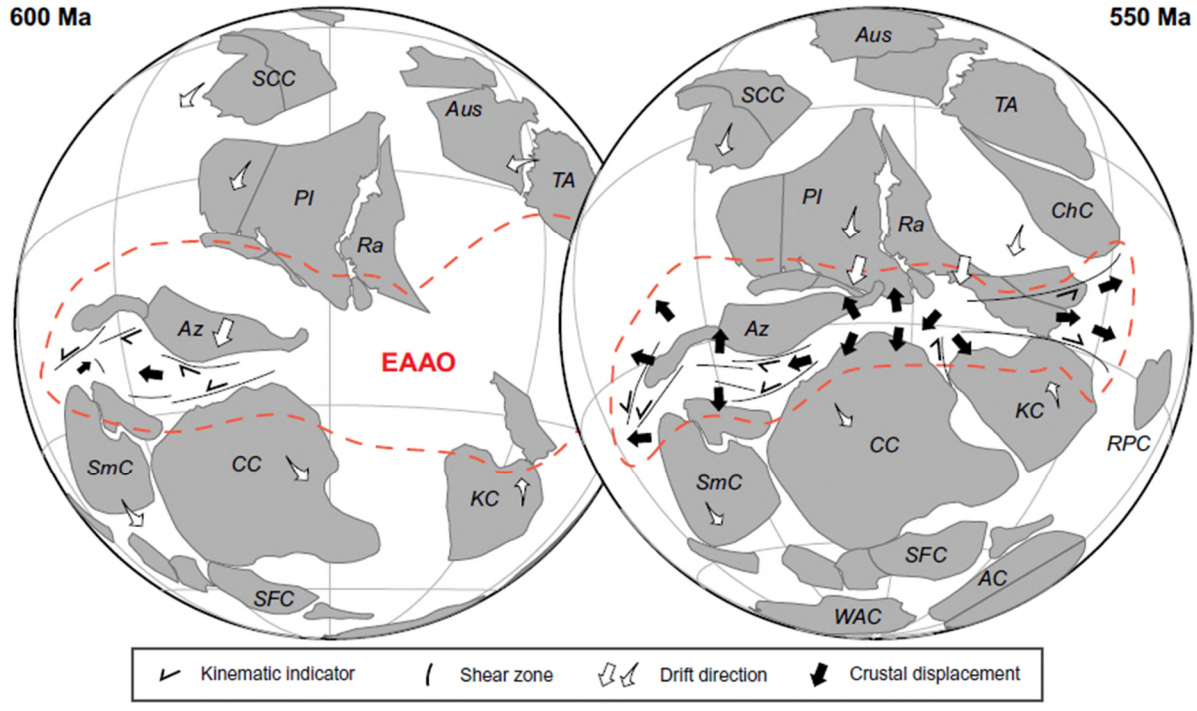


Figure 0-7 : Reconstruction du contexte paléo-tectonique lors de l'orogenèse est-africaine-antarctique (EAAO) entre 600 et 550 Ma par Grenholm (2019), d'après Merdith et al. (2017). Les abréviations sont AC = craton amazonien, Aus = cratons australiens, Az = Azanie, CC = craton du Congo, ChC = craton de Chron, KC = craton du Kalahari, MB = ceinture du Mozambique, PI = péninsule indienne, RA = province de Rayner, RPC = craton de Rio de la Plata, SFC = craton de São Francisco, SmC = méta-craton du Sahara, SCC = craton du sud de la Chine, TA = Terre Adélie, WAC = craton ouest-africain.

Avant la rupture du Gondwana au Mésozoïque, l'orogène est-africain-antarctique s'étendait sur plus de 6000 km de long pour une largeur pouvant excéder 2000 km à travers le paléo-continent (Figs. 0-7, 0-8 ; Stern, 1994 ; Johnson et al., 2011 ; Fritz et al., 2013 ; Johnson, 2014 parmi d'autres). Du nord au sud, il peut être divisé en trois segments (Fig. 0-8) : (i) le bouclier arabo-nubien (composé des boucliers arabique et nubien (*arabian* et *nubian shields*) et prolongé par les boucliers ouest- et sud-éthiopiens au sud (*W.* et *S. Ethiopian shields*) ; (ii) la ceinture du Mozambique (*Mozambique belt* ou *MB*) ; (iii) et l'orogène ouest-antarctique (*AO*). L'orogène est-africain est bordé, du nord au sud, par le méta-craton du Sahara, les cratons du Congo et du Kalahari sur sa marge occidentale, et par le bloc indien, l'Australie et leurs extensions antarctiques sur sa marge orientale (Figs. 0-7, 0-8).

La ceinture du Damara-Zambezi-Irumide (ou Damara-Lufilien-Zambezi ; Eglinger et al., 2013), orientée est-ouest, se connecte à l'orogène est-africain-antarctique au niveau de la ceinture du Mozambique en Tanzanie et au Mozambique dans le prolongement de l'orogène du Kuunga (Fig. 0-6b ; Fritz et al., 2013). Pourtant, des différences de relations géométriques et temporelles existent le long de cette intersection même (*e.g.,* Fritz et al., 2013). Il s'avère donc primordial (i) de ne plus résumer la mise en place de ces structures à un unique cycle panafricain comme évoqué précédemment et (ii) de considérer l'histoire tectonique le long de l'orogène est-africain-antarctique segment par segment, de part un style tectonique nécessairement hétérogène le long d'une structure de telle ampleur (*e.g.,* Fritz et al., 2013). Nous nous intéresserons par la suite à la formation et l'évolution du bouclier arabo-nubien au cours de l'orogenèse est-africaine-antarctique, objet de cette étude.

3.2. Mise en place du bouclier arabo-nubien

Le bouclier arabo-nubien (BAN, *ANS* sur les figures), couvrant une surface de $2{,}7.10^6$ km² (Johnson, 2014), forme la partie septentrionale de l'orogène est-africain-antarctique (Stern, 1994 ; Johnson et Woldehaimanot, 2003 ; Kusky et al., 2003 ; Fritz et al., 2013). Il s'étend de façon intermittente jusqu'au Mozambique et la partie méridionale de Madagascar, sur plus de 3500 km (Fig. 0-8a ; Stern, 1994 ; Johnson, 2014). Il a été divisé en deux parties lors de l'ouverture de la mer Rouge au Miocène, le bouclier nubien (*Nubian shield*) s'étendant du désert de Sinaï (Égypte) au Kenya à l'ouest et le bouclier arabique (*Arabian shield*) formant la partie occidentale de la péninsule arabique à l'est (Fig. 0-8a ; Vail, 1983). Le BAN résulte de la collision entre le méta-craton du Sahara (*SmC*) et le craton du Congo (*CC*) à l'ouest et l'Azanie (*Azania*) à l'est lors de l'orogenèse est-africaine (Fig. 0-8a ; Fritz et al., 2013).

L'Azanie serait formée d'un ou plusieurs blocs continentaux compris entre le craton du Congo et la péninsule indienne (*PI ;* Fig. 0-8 ; Collins et Pisarevsky, 2005) sous forme de fragments de croûte archéenne à paléoprotérozoïque rencontrés depuis l'Arabie Saoudite jusqu'à Madagascar, en passant par le Yémen (Whitehouse et al., 2001 ; Collins et Windley, 2002). Cette continuité fait donc le lien géographique entre l'assemblage du BAN et celui de la ceinture du Mozambique (Windley et al., 1996) au sein de l'orogène est-africain-antarctique (Fig. 0-8a).

L'influence de l'orogenèse du Kuunga, seconde étape du cycle orogénique est-africain-antarctique, n'est pas visible dans le BAN. Cependant, elle s'exprime probablement sous la couverture phanérozoïque dans la partie centrale de la péninsule arabique (Johnson et al., 2011 ; Cox et al., 2012).

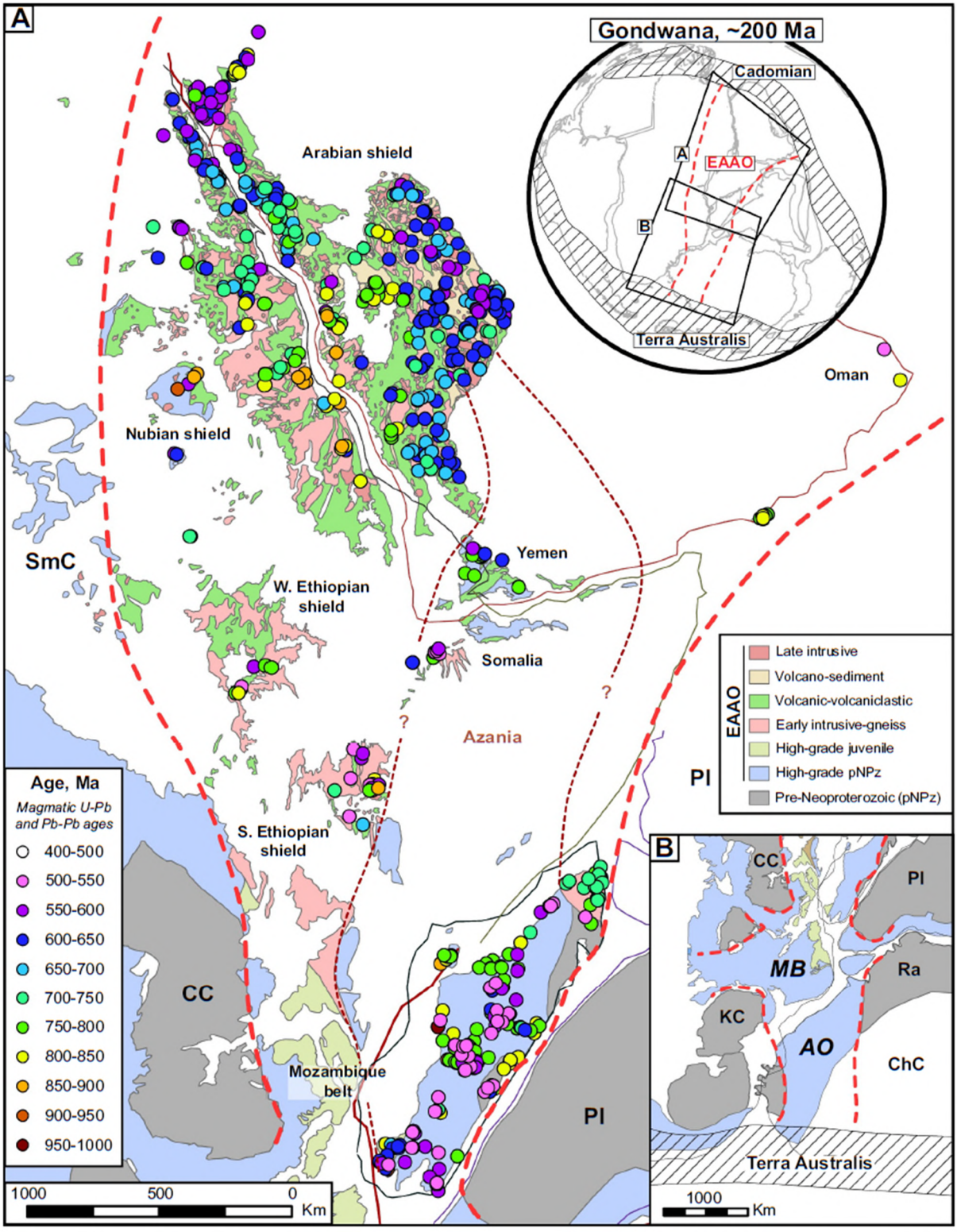


Figure 0-8 : Carte régionale de l'orogène est-africain-antarctique (EAAO) avant la rupture du Gondwana au Mésozoïque (Grenholm, 2019). **a** Zoom sur le segment nord de l'orogène est-africain-antarctique et contraintes temporelles existantes. **b** Zoom sur le segment sud de l'orogène est-africain-antarctique. Les abréviations sont AO = orogène antarctique, CC = craton du Congo, ChC = craton de Chron, KC = craton du Kalahari, MB = ceinture du Mozambique, PI = péninsule indienne, RA = province de Rayner, SmC = méta-craton du Sahara.

3.2.1. Accrétion magmatique et assemblage précoce du bouclier arabo-nubien

Le BAN est essentiellement composé de croûte néoprotérozoïque juvénile (synthèses par Johnson et al., 2011 ; Fritz et al., 2013 ; Johnson, 2014) à l'exception de l'unité litho-tectonique (*terrane*) paléoprotérozoïque de Khida (*ca.* 1800-1650 Ma). Selon la nomenclature suivie dans ce manuscrit, il convient plutôt de considérer cet ensemble comme un bloc crustal, puisqu'il s'agirait d'un fragment lithosphérique appartenant à Azanie ayant été incorporé dans le BAN (Figs. 0-8a, 0-9 ; Whitehouse et al., 2001 ; Johnson et al., 2011). La formation du BAN résulte de l'assemblage d'arcs magmatiques juvéniles formés au Néoprotérozoïque, à l'aplomb des multiples zones de subduction où l'océan mozambicain est consommé (Johnson et al., 2011 ; Fritz et al., 2013). De par leurs différences d'âge de mise en place, de stratigraphie, de style structural et, localement, de signature isotopique, les assemblages d'arcs sont divisés en unités litho-tectoniques distinctes formant des *terranes*. Ces dernières sont séparées par des zones de suture ophiolitiques parfois reprises en décrochement (Fig. 0-9 ; Johnson et al., 2011 ; Fritz et al., 2013 ; Johnson, 2014 et références associées). La présence de suture témoigne de la présence d'un paléo-domaine océanique entre deux unités litho-tectoniques ayant évolué indépendamment avant d'être regroupées. Ces fragments correspondent aux restes de la lithosphère océanique développée sous l'océan mozambicain entre *ca.* 845-675 Ma (Fig. 0-9 ; Johnson, 2014) et préservés au cours des processus de subduction puis d'exhumation-obduction.

Plusieurs phases de formation d'arcs magmatiques insulaires avec développement de bassins d'arrière-arc ont été reconnues dans le BAN entre *ca.* 870-615 Ma (Johnson, 2014). Les roches exprimées (basalte, boninite, andesite, rhyolite, roches volcanoclastiques et volcano-sédimentaires et roches plutoniques de type diorite-tonalite-trondjhemite-granodiorite) sont d'affinité tholéiitique à calco-alcaline (*e.g.,* Hargrove et al., 2006), avec une chimie parfois proche de celles des *MORB* (Johnson, 2014). Les limites temporelles de la formation de ces complexes d'arc restent cependant floues (*e.g.,*

ca. 890-580 Ma sur la Fig. 0-9 ; Fritz et al., 2013) et varient selon le sens donné au terme « accrétion » dans la littérature (accrétion magmatique et/ou tectonique, confusion avec collision arc-continent ?).

- *Étape 1 : le sud et le cœur du bouclier arabo-nubien*

La partie méridionale du BAN (du sud du Kenya à la suture de Nakasib-Bir Umq ; Fig. 0-9) s'est formée dans un premier temps (Johnson et al., 2003) : suite à la dislocation de Rodinia, les premières traces de plancher océanique sous l'océan Mozambique sont datées à *ca.* 860-830 Ma ; la subduction et la formation de bassins d'arc et d'arrière-arc ont eu lieu jusqu'à ~ 750 Ma ; enfin, la fermeture des bassins et la collision entre les arcs insulaires s'est produite entre *ca.* 750-650 Ma (exemple de la ceinture de Tuludimtu en Éthiopie ; Woldemichael et al., 2010). Les arcs au nord de cette zone se sont assemblés le long des sutures arc-arc de Nakasib-Bir Umq et de Barka (Fig. 0-9) entre *ca.* 800-700 Ma (*e.g.,* Abdelsalam et Stern, 1996a). Pour la partie centrale du BAN (située entre la suture de Nakasib-Bir Umq et la suture Yanbu-Sol Hamed-Allaqi-Heiani ; Fig. 0-9), la formation puis la collision des arcs insulaires ont eu lieu grossièrement en même temps qu'au sud, bien que des âges plus jeunes soient relevés, à *ca.* 830-710 Ma (*e.g.,* Johnson et al., 2003, 2011). La formation de ces sutures a enregistré un raccourcissement nord-sud exprimé par des chevauchements à vergence sud mis en place au niveau de zones de subduction à pendage nord (Fritz et al., 2013). Le synchronisme de ces structures, exprimant un raccourcissement nord-sud, avec les sutures de la partie sud du BAN, associées à un raccourcissement est-ouest, est à l'origine d'interférences au contact entre ces deux domaines du BAN (Fritz et al., 2013). La bordure ouest du BAN est marquée par la suture océan-continent, orientée nord-sud, de Keraf-Kabus et la suture océan-océan, orientée est-ouest, d'Atmur-Delgo (*ca.* 750-650 Ma). Alors que la seconde a été formée suite à la fermeture d'un bras aulacogène de l'océan mozambicain pénétrant le méta-craton du Sahara, la suture de Keraf-Kabus marque la limite entre le BAN et l'unité litho-tectonique de Rahaba-Absol (ou Bayuda,

selon les auteurs), qui appartient au méta-craton du Sahara (Fig. 0-9 ; Denkler et al., 1993 ; Harms et al., 1994 ; Schandelmeier et al., 1994a ; Abdelsalam et Stern, 1996a ; Küster et Liégeois, 2001 ; Bailo et al., 2003 ; Küster et al., 2008).

- *Étape 2 : le nord du bouclier arabo-nubien*

La partie septentrionale du BAN (au nord de la suture Yanbu-Sol Hamed-Allaqi-Heiani ; Fig. 0-9) correspond au bloc litho-tectonique de Midyan-désert oriental (*Eastern Desert*) formé puis accrété entre *ca.* 760-730 Ma au reste du BAN, le long de la suture Yanbu-Sol Hamed-Allaqi-Heiani (Ali et al., 2010a, 2010b ; Johnson et al., 2011). Des restes d'arcs volcaniques calco-alcalins datés à *ca.* 1030-930 Ga, et plus fréquemment entre *ca.* 870-740 Ma et 640-620 Ma témoignent cependant d'une histoire géodynamique plus complexe à l'échelle de la région du Sinaï depuis la fin du Mésoprotérozoïque (*e.g.,* Be'eri-Shlevin et al., 2012 ; Abu El-Enen et Whitehouse, 2013 ; Eyal et al., 2014).

- *Étape 3 : l'est du bouclier arabo-nubien*

L'amalgamation à *ca.* 680-640 Ma des blocs litho-tectoniques d'Afif et de Tathlith (Fig. 0-9) finalise la formation du proto-BAN (*proto-ANS* ; Johnson et al., 2011). L'unité litho-tectonique d'Afif est un ensemble composite incorporant le sous-bloc crustal paléoprotérozoïque de Khida à un ensemble d'arcs volcaniques formés à *ca.* 840-820 Ma, 750-720 Ma et 700-680 Ma (Johnson et al., 2011 ; Fritz et al., 2013 ; Johnson, 2014). Ce dernier épisode conclue la formation du proto-BAN et est associé à de nombreux événements tectoniques, métamorphiques et magmatiques regroupés en un épisode appelé « l'orogenèse de Nabitah » (*Nabitah orogeny* ; Stoeser et Stacey, 1988).

- *Étape 4 : l'extrême nord-est du bouclier arabo-nubien*

Les blocs litho-tectoniques Ad Dawadimi et Ar Rayn sont les plus orientaux et les derniers assemblés au proto-BAN (Fig. 0-9) au niveau de la zone de suture d'Al-Amar à *ca.* 620-600 Ma. Cette zone de suture héberge notamment l'ophiolite d'Halaban, reliquat de croûte océanique formée dans un bassin d'arrière-arc à *ca.* 680-670 Ma (*e.g.,* Al-Saleh et Boyle, 2001).

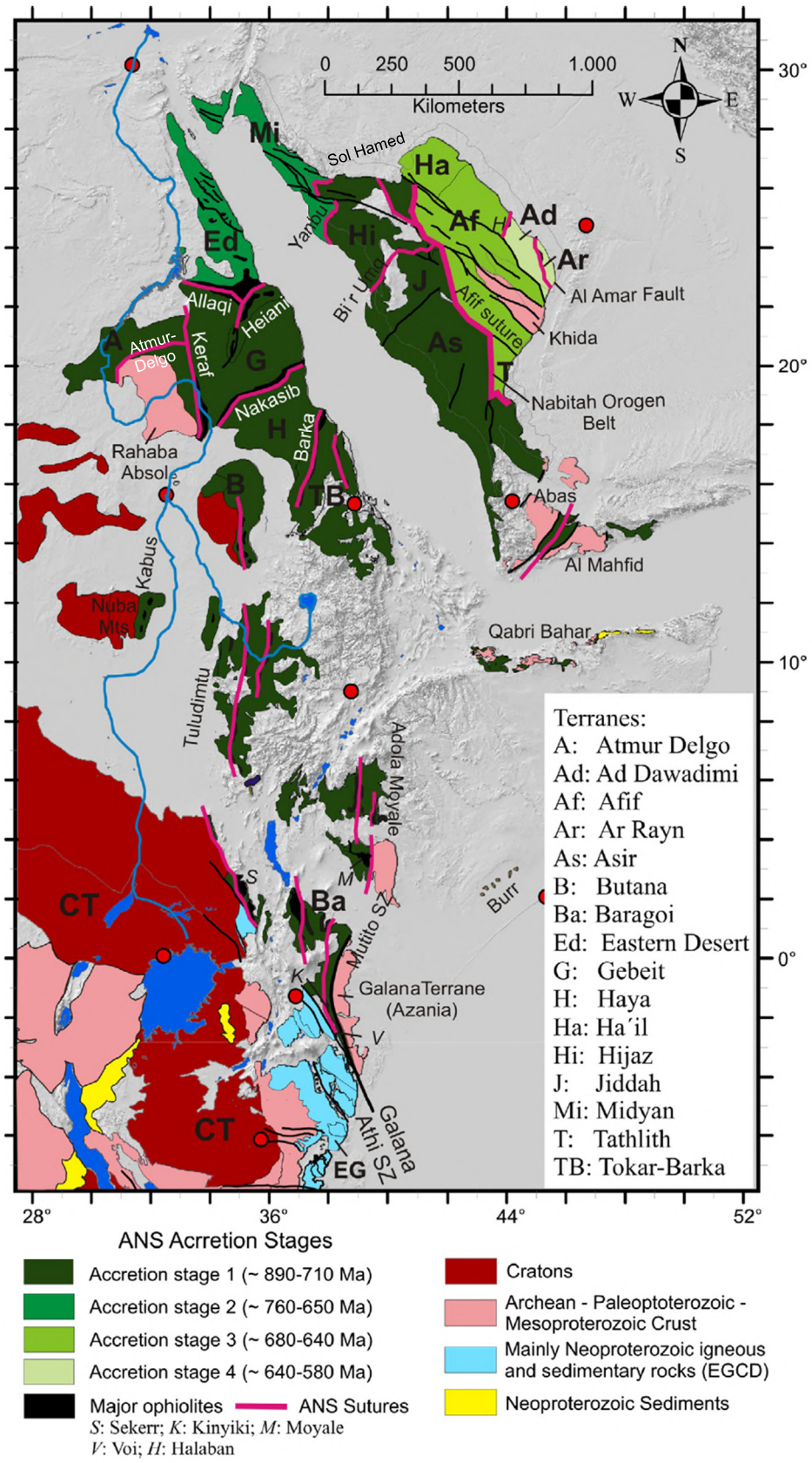


Figure 0-9 : Âge des principaux domaines crustaux formant la partie nord de l'orogène est-africain-antarctique et timing des assemblages d'arcs à l'origine du bouclier arabo-nubien (*ANS*), modifiée d'après Fritz et al. (2013).

3.2.2. Collision et consolidation du bouclier arabo-nubien

Le diachronisme des processus d'accrétion magmatique (mise en place du plancher océanique, développement de bassins d'arrière-arc lors de la subduction océanique) et de collision arc-arc (assemblage des arcs et des unités litho-tectoniques indépendantes au niveau de zones de suture) à l'échelle du BAN est évident : alors que le raccourcissement est-ouest à l'origine de l'assemblage de la partie sud du BAN était déjà initié à 750 Ma, la lithosphère océanique se développait encore dans sa partie orientale. Ainsi, la phase de juxtaposition des arcs insulaires et d'épaississement crustal du BAN a débuté plus tôt dans la partie sud que dans la partie nord du BAN, impactant directement le style tectonique et le degré métamorphique maximal enregistrés.

- *Au sud du bouclier arabo-nubien*

Dans la partie méridionale du BAN, les zones de suture ophiolitique sont métamorphisées au faciès amphibolite supérieur à *ca.* 650-620 Ma, durant un épisode de raccourcissement est-ouest (Fritz et al., 2013 et référence citées). Le faciès granulite est atteint pour les ensembles orthogneissiques néoprotérozoïques environnants, qui sont partiellement migmatisés : la nature de ces terrains reste incertaine mais il est probable qu'il s'agisse de racines d'arcs exhumées présentant des reliques du métamorphisme associé aux phases antérieures de subduction (*e.g.,* Stern et al., 2012 et références citées). L'interférence entre les directions de raccourcissement orthogonales entre les parties sud et centrale du BAN a pu être compensée par un épaississement crustal accru dans le BAN méridional, à l'origine de la généralisation de ces conditions métamorphiques extrêmes (Fritz et al., 2013). Le prolongement de la collision oblique nord-ouest - sud-est permet l'assemblage final du BAN au méta-craton du Sahara par collision arc-continent, avec le développement d'un épisode transpressif superposant la zone de cisaillement de Keraf à la suture de Keraf-Kabus (650-580 Ma ; Abdelsalam et al., 1995, 1998, 2003 ; Abdelsalam et Stern, 1996a ; Bailo et al., 2003 ; Johnson et al., 2017).

- *Au coeur du bouclier arabo-nubien*

Les sutures de Nakasib-Bir Umq et de Yanbu-Sol Hamed-Allaqi-Heiani, limitant la partie centrale du BAN, ont enregistré la collision avec les parties nord et sud du BAN, respectivement. Un métamorphisme régional ayant atteint le faciès schiste vert (avec de rares évidences de faciès amphibolite également pour la suture de Nakasib) a affecté les nappes charriées lors de cet épisode (Abdelsalam et Stern, 1993 ; Abdelsalam, 2010) à *ca.* 650-600 Ma (Fritz et al., 2013). Deux hypothèses sont d'ailleurs toujours discutées concernant la mise en place de la suture de Nakasib-Bir Umq qui pourrait résulter : (i) de la fermeture d'un domaine océanique le long d'une zone de subduction est-ouest à vergence nord, et donc d'un raccourcissement nord-sud (Abdelsalam et Stern, 1993 ; Abdelsalam, 2010) ; ou (ii) d'une fermeture le long d'une zone de subduction à vergence sud avec une même direction de raccourcissement (*e.g.,* Schandelmeier et al., 1994b ; Wipfler, 1996). La présence de nappes et chevauchements à pendage sud ou nord, selon leur positionnement le long du flanc nord ou sud de cette suture respectivement, exprime une structure en fleur suggérant l'enracinement de cette zone de suture entre le cœur et la partie sud du BAN (Schandelmeier et al., 1994a ; Wipfler, 1996 ; Johnson et al., 2003 et références citées).

- *Au nord du bouclier arabo-nubien*

Les conditions du pic de métamorphisme en pression et température ont été atteintes à *ca.* 620-607 Ma dans l'unité litho-tectonique du désert oriental (Eliwa et al., 2008 ; Fritz et al., 2013 et références citées ; Elisha et al., 2017, 2019). Le modèle actuel propose que cette unité ait été formée suite à la fermeture de plusieurs systèmes d'arrière-arc développés en arrière d'une zone de subduction à pendage nord-ouest qui correspondrait à la suture d'Hafafit Sud (El-Naby et Frisch, 2006 ; Abd El-Naby et al., 2008 ; Abdeen et Abdelghaffar, 2011). Les chevauchements à faible pendage et à vergence nord-ouest dominant le schéma structural local (*a contrario* des structures redressées visibles pour le reste du BAN) exprimeraient la mise en place d'un rétro-prisme

d'accrétion (*retro-wedge*), développé entre *ca.* 650-600 Ma. Dans cette configuration, les chevauchements ont mis au contact des nappes supra-crustales métamorphisées dans le faciès schiste vert avec des dômes gneissiques de haut grade métamorphique (0,8-1,3 GPa - 680 °C ; Neumayr et al., 1998 ; Loizenbauer, 2001 ; Abd El-Naby et al., 2008 ; Abu El-Enen et al., 2016 ; Elisha et al., 2017, 2019) où la migmatisation aurait été généralisée entre *ca.* 620-610 Ma (Elisha et al., 2019). Ce modèle de rétro-prisme est néanmoins remis en cause puisque les ophiolites, très nombreuses dans le désert oriental, seraient dérivées d'un plancher océanique formé en contexte d'avant-arc entre 835 et 720 Ma (Azer et Stern, 2007), et non en contexte d'arrière-arc comme impliqué par cette proposition.

3.2.3. Évolution tardi- à post-orogénique du bouclier arabo-nubien

L'évolution tardi- à post-orogénique est marquée par l'effondrement gravitaire de l'orogène est-africain associé à un régime extensif. En résulte la mise en place de failles décrochantes, de détachements, de bassins sédimentaires mollassiques (*marine vs terrestrial,* marins ou terrestres ; Fig. 0-10) ou encore de bassins en *pull-apart* à *ca.* 580-500 Ma (Fig. 0-10 ; Fritz et al., 2013 et références citées).

- *Au sud du bouclier arabo-nubien*

Dans la partie la plus méridionale du BAN se rattachant à la ceinture du Mozambique, les prémices des zones de cisaillement tardi-orogéniques (Fig. 0-10) sont datées entre *ca.* 595-570 Ma et l'isotherme 500 °C, correspondant à la mise en place du jeu décrochant, n'est franchi qu'aux alentours de 520 Ma (*e.g,* Kenya ; Mathu et al., 2015). Ces structures se sont donc formées à relativement haute température (association locale avec la mise en place de migmatites) et dans un régime de déformation coaxiale repris plus tardivement en décrochement (Fritz et al., 2013 et références citées).

Plus au nord de cette partie du BAN, en Érythrée, l'isotherme 500 °C est franchi lors de l'exhumation des roches de haut grade métamorphique à *ca.* 585-570 Ma (*e.g.,*

Ghebreab et al., 2005) et la mise en place de décrochements est visible dès ~ 545 Ma (*e.g.,* Tadesse et al., 1997). Certaines ceintures ophiolitiques sont également reprises en décrochement dans un continuum de déformation associé à une convergence oblique (Fig. 0-10 ; *e.g.,* Allen et Tadesse, 2003).

- *Au cœur du bouclier arabo-nubien*

Dans la partie centrale du BAN, les sutures sont recoupées par des zones de cisaillement orientées nord-sud dans la partie nubienne, qui sont mises en place rapidement après le pic de métamorphisme (Fig. 0-10) : Oko au sud (*ca.* 640-560 Ma ; Abdelsalam, 1994, 2010 ; Johnson et al., 2011) et Hamisana au nord (660-580 Ma ; Stern et al., 1989 ; Miller et Dixon, 1992 ; de Wall et al., 2001 ; Johnson et al., 2011). Ces deux structures ont accommodé une forte déformation et résultent d'une histoire tectonique polyphasée. Celle-ci a débuté par une première phase de raccourcissement coaxial, associée à un métamorphisme de faciès schiste vert (pour l'Oko) ou schiste vert supérieur-amphibolite (pour l'Hamisana), avant la mise en place des décrochements à plus faible température en période tardi-orogénique (Stern et al., 1989 ; Miller et Dixon, 1992 ; Abdelsalam, 1994, 2010). L'histoire de l'Oko s'est prolongée par la mise en place d'une structure en fleur associée à un raccourcissement est-ouest qui a duré dans le temps (Abdelsalam, 1994, 2010). Dans la partie arabique du BAN, les sutures ophiolitiques sont recoupées par le système de failles de Najd, associé à l'orogène Nabitah (Fig. 0-10 ; Fritz et al., 2013 et références citées). La zone de cisaillement d'Hamisana serait le conjugué de ce système (de Wall et al., 2001). Enfin, la collision oblique nord-ouest - sud-est entre le BAN et le méta-craton du Sahara s'est poursuivie en période tardi-orogénique puisque la zone de cisaillement de Keraf a recoupé des granitoïdes datés entre 620-580 Ma (Fig. 0-10 ; Abdelsalam et al., 2003).

- *Au nord du bouclier arabo-nubien*

Dans la partie nord du BAN, les éléments magmato-tectoniques majeurs sont associés à la période tardi-orogénique : il s'agit de zones de cisaillement ductile-fragile appartenant au système de Najd, ayant favorisé la formation de bassins sédimentaires (en contexte extensif ou transtensif, *i.e.,* en *pull-apart*), l'exhumation de dômes gneissiques (*gneiss domes*) et la mise en place de granitoïdes syn- à tardi-tectoniques entre *ca.* <650-580 Ma (Fig. 0-10 ; Fritz et al., 2013 et références citées). L'intrusion de dykes mafiques à felsiques post-tectoniques à affinité alcaline, particulièrement visibles dans le nord du bouclier arabique, datés entre *ca.* 590-545 Ma, a marqué la fin de l'activité du système décrochant de Najd et l'initiation d'une phase d'extension nord-sud lors des dernières phases de stabilisation du BAN (Johnson et al., 2011 ; Fritz et al., 2013).

La présence de dômes gneissiques dans le désert oriental égyptien n'est pas tant associée aux failles du système de Najd qu'à la présence de détachements de grande échelle et de complexes à noyau métamorphique, communément nommés *metamorphic core complexes* (*e.g.*, Fritz et al., 1996 ; Blasband et al., 1997, 2000 ; Neumayr et al., 1998 ; Bregar et al., 2002 ; Abd El-Naby et al., 2008 ; Meyer et al., 2014). La chronologie relative des zones de cisaillement les bordant est donc discutée ; sont-elles synchrones de l'exhumation de ces dômes et ont elles accommodé une déformation dans un régime transtensif (Fritz et al., 1996, 2002) ou sont-elles des reliques de chevauchements nord-ouest - sud-est ayant rejoué (Andresen et al., 2010) ? L'exhumation de ces *metamorphic core complexes* a eu lieu entre *ca.* 620-590 Ma et est associée à un gradient géothermique fort (30 à 50 °C/km) et à un métamorphisme de moyenne à haute température (jusqu'à 700 °C) et de basse pression (<0,5 GPa) (*e.g.,* Eliwa et al., 2008).

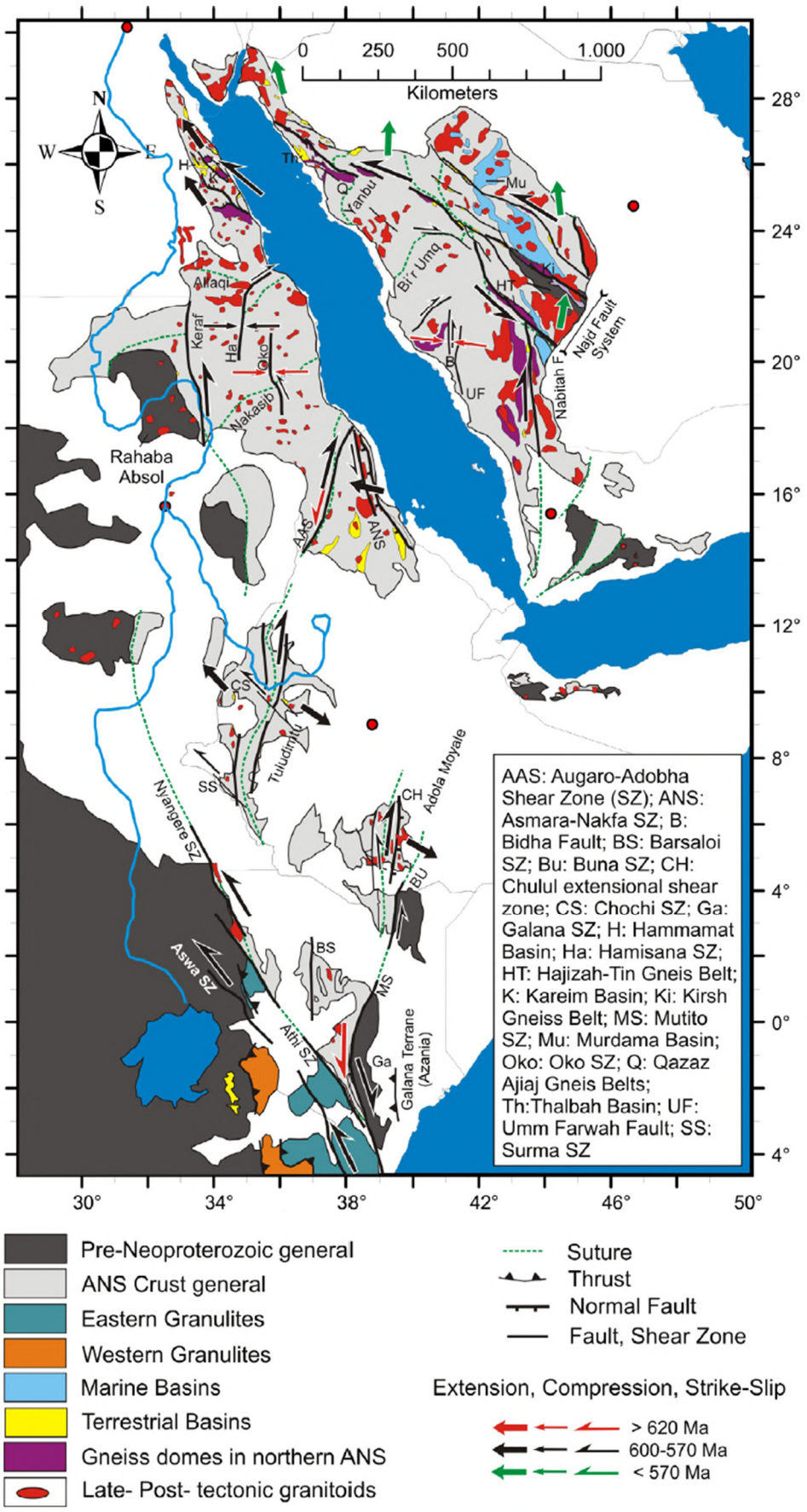


Figure 0-10 : Structures tardi-tectoniques, granitoïdes tardi- à post-orogéniques et bassins sédimentaires dans le BAN (Fritz et al., 2013).

Le magmatisme tardi-orogénique à anorogénique a également été particulièrement important dans cette partie du BAN (Fig. 0-10 ; *e.g.,* Lundmark et al., 2012 ; Eliwa et al., 2014 ; Abu El-Enen et al., 2016). Les granitoïdes formés sont essentiellement alcalins et sont potentiellement associés à un épisode magmatique déclenché par une remontée asthénosphérique et un amincissement lithosphérique provoqué par la délamination du *SCLM* sous le BAN (*e.g.,* Farahat et al., 2007 ; Be'eri-Shlevin et al., 2009a ; Johnson et al., 2011). Ce processus est également invoqué par Avigad et Gvirtzman (2009) pour expliquer l'abondance de granitoïdes tardifs dans la partie nord du bouclier arabique (Fig. 0-10) qui seraient associés à l'ultime épisode d'extension nord-sud évoqué auparavant. Cette explication est en accord avec le gradient géothermique et les conditions métamorphiques relevés dans le nord du BAN en contexte tardi- à post-collisionnel.

Les éléments de mise en place du BAN évoqués dans cette partie sont synthétisés sur la Figure 0-11. Cette synthèse illustre clairement le diachronisme nord-sud des événements magmato-tectoniques ayant permis la formation du BAN depuis la mise en place de la lithosphère océanique jusqu'au magmatisme tardi- à post-orogénique, nécessitant de bien distinguer l'évolution de ses segments sud, central et nord comme proposé ci-dessus.

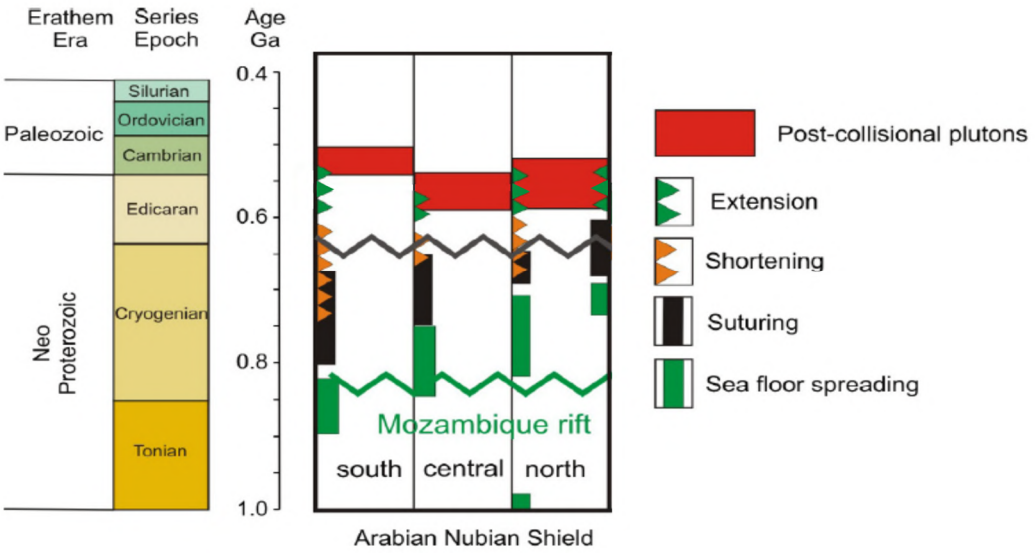


Figure 0-11 : Événements géologiques majeurs ayant abouti à la mise en place du bouclier arabo-nubien (*Arabian-Nubian Shield*), modifiée d'après Fritz et al. (2013).

3.3. Mise en place de la suture de Keraf

La suture de Keraf (SK, *Keraf suture* ; Fig. 0-12) appartient à l'ensemble de sutures de Keraf-Kabus-Sekerr-Kinyiki, plus ou moins connecté, qui s'étend depuis l'Égypte jusqu'au Kenya, sur 500 km de long pour 50 à 100 km de large (Fig. 0-6 ; Almond et Ahmed, 1987 ; Stern, 1994 ; Abdelsalam et al., 1995, 1998). La SK appartient au BAN néoprotérozoïque et sa formation résulte de la juxtaposition des unités litho-tectoniques le composant au méta-craton du Sahara paléoprotérozoïque à archéen, constituant la partie nord de Gondwana de l'Ouest. La formation de la SK a fait suite à la fermeture d'un bassin d'arrière-arc, signant la disparition de l'océan mozambicain entre le futur BAN (*i.e.,* l'orogène est-africain-antarctique) et le méta-craton du Sahara (*i.e.,* Gondwana de l'Ouest) (Fig. 0-9 ; Vearncombe, 1983 ; Burke et Sengör, 1986 ; Frisch et Pohl, 1986 ; Berhe, 1990 ; Abdelsalam et Dawoud, 1991 ; Ries et al., 1992 ; Mosley, 1993 ; Abdelsalam et al., 1998 ; Fritz et al., 2013). La présence de l'océan mozambicain est préservée sous forme d'un assemblage lithologique limité spatialement à la SK, nommé assemblage pré-tectonique de Keraf (*KPTA ;* Ahmed Suliman, 2000). Il est composé des reliques d'un bassin d'arrière-arc (*e.g.,* Schandelmeier et al., 1994b ; Stern, 1994 ; Abdelsalam et al., 1995 ; Abdelrahman et al., 2017) et d'une marge continentale passive (*e.g.,* Stern et al., 1993). Toutes les roches du *KPTA* (paragneiss, ophiolites de Keraf, séquence volcanosédimentaire, méta-sédiments silicoclastiques et marbres) sont affectées par l'histoire tectonique associée à la formation de la SK et les épisodes de déformation ultérieurs.

L'océan mozambicain occupait le bassin d'arrière-arc à l'origine de la SK depuis lequel un bras aulacogène pénétrant le méta-craton du Sahara a été initié puis a avorté (Burke et Sengör, 1986 ; Abdelrahman, 1993 ; Abdelsalam et al., 1998 ; Johnson et al., 2013). La fermeture de ce réentrant océanique à *ca.* 750-650 Ma par l'enchaînement d'une subduction à vergence nord puis d'un épisode de collision est à l'origine de la suture d'Atmur-Delgo (SAD, *Atmur-Delgo suture* ; Fig. 0-12). Celle-ci sépare désormais les

unités litho-tectoniques d'Halfa au nord, appartenant au BAN, et de Bayuda au sud, appartenant au méta-craton du Sahara (Schandelmeier et al., 1994a ; Abdelsalam et al., 2003). L'unité litho-tectonique de Bayuda a enregistré une histoire tectono-métamorphique antérieure à la formation du BAN l'ayant conduit au faciès amphibolite à ~ 920 Ma (*e.g., Bayudian event;* Küster et al., 2008 ; Evuk et al., 2014) mais des épisodes tectoniques, métamorphiques et magmatiques associés à l'orogenèse est-africaine y sont tout de même visibles (*e.g.,* Abdelsalam et al., 2003 ; Evuk et al., 2014 ; Karmakar et Schenk, 2015).

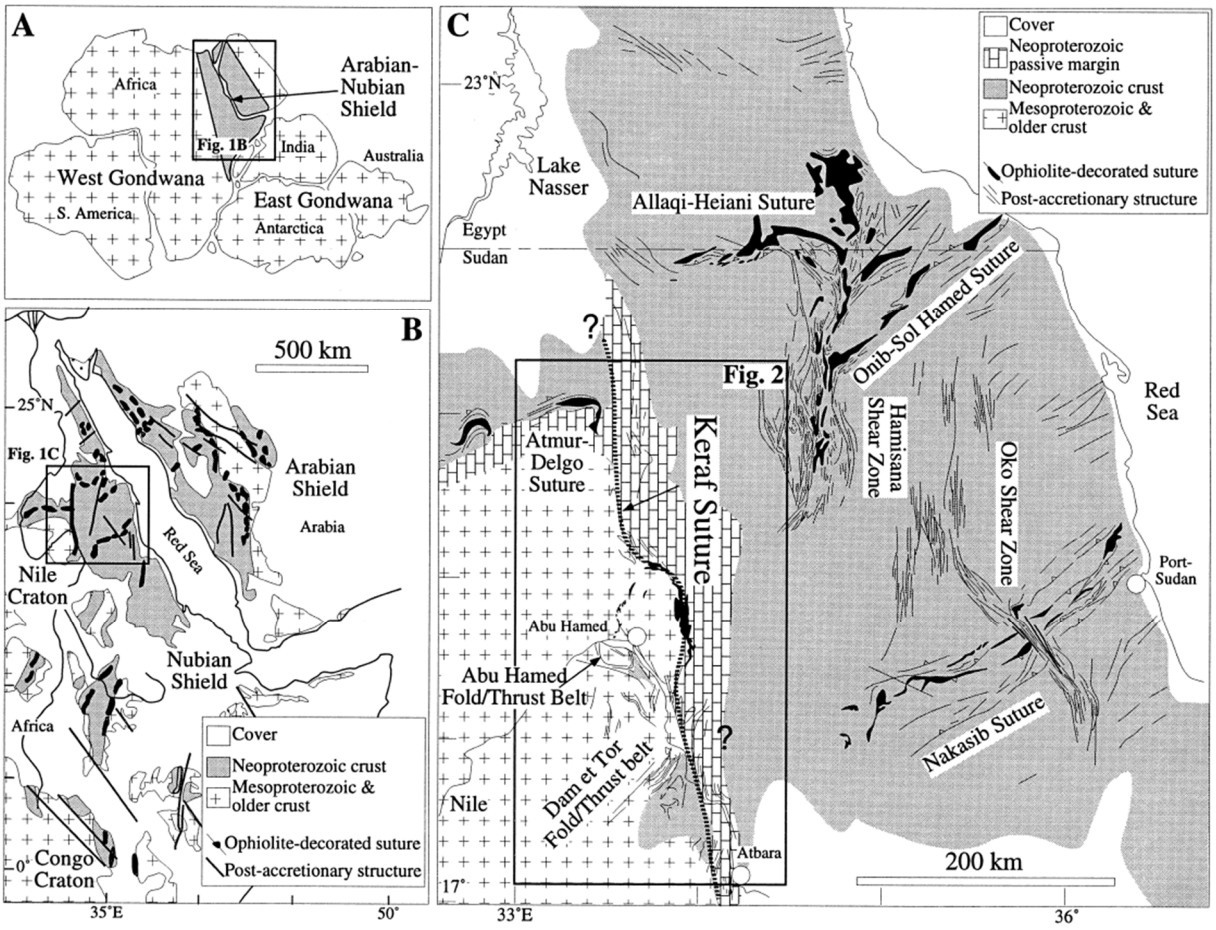


Figure 0-12 : Localisation de la suture de Keraf et de la zone de suture d'Atmur-Delgo (Abdelsalam et al., 1998). **a** Localisation du bouclier arabo-nubien entre Gondwana de l'Ouest et de l'Est. **b** Zoom sur le bouclier arabo-nubien. **c** Contexte pétro-structural du bouclier nubien et de la zone de suture de Keraf.

La formation de la SK à ~ 750-640 Ma (Abdelsalam et al., 1998) est contemporaine de la mise en place de la SAD, au cours d'un épisode compressif associé à une subduction à vergence est suivie d'une collision oblique nord-ouest - sud-est. En phase tardi-

orogénique, cette collision s'est transformée en transpression senestre , occasionnant la superposition de la zone de cisaillement de Keraf (ZCK) *sensu stricto* à la SK entre ~ 650-580 Ma (Abdelsalam et al., 1995, 1998 ; Abdelsalam et Stern, 1996a, 1996b). La zone d'interférence entre la SAD et la SK présente alors un schéma structural complexe, témoin de cette histoire tectonique polyphasée (Abdelsalam et al., 1995 ; Abdelsalam et Stern, 1996b ; Ahmed Suliman, 2000 ; Abdelsalam et al., 2003).

4. Le bouclier arabo-nubien : une province aurifère de classe mondiale

4.1. Systèmes métallogéniques aurifères du bouclier arabo-nubien

Conformément à l'histoire géodynamique détaillée dans la section précédente, le BAN peut être vu comme un assemblage d'arcs magmatiques, de séries volcanosédimentaires calco-alcalines associées et de fragments de plancher océanique préservés sous forme d'ophiolites, le tout étant déformé, accrété et associé à des ensembles de granitoïdes pré-, syn- à post-collisionnels. Par conséquent, le BAN possède toutes les caractéristiques d'une ceinture de roches vertes néoprotérozoïque, au même titre que ses semblables archéennes et paléoprotérozoïques d'Abitibi (Canada), du craton du Yilgarn (Australie) et d'Afrique de l'Ouest, d'après les éléments d'identification donnés pour les ceintures de roches vertes archéennes par Anhaeusser (2014). L'orogène est-africain-antarctique, et en particulier le BAN, est d'ailleurs considéré comme l'équivalent néoprotérozoïque du craton ouest-africain, avec lequel il partage (i) une architecture litho-tectonique globale semblable résultant d'événements géodynamiques aux durées comparables, (ii) une signature crustale juvénile prédominante, (iii) des conditions de métamorphisme similaires (si l'on excepte le métamorphisme de haut grade généralisé dans le ceinture du Mozambique) ou encore (iv) l'enregistrement d'événements magmatiques aux timing relatif et signature géochimique proches (Grenholm, 2019). Les différences majeures entre ces deux ensembles sont la présence de komatiites dans

l'orogène birrimien, à relier à un changement de régime thermique global lié au refroidissement de la Terre entre le Paléoprotérozoïque et le Néoprotérozoïque, et celle accrue de granites anorogéniques dans le BAN (Grenholm, 2019 et références citées).

Si les ceintures de roches vertes précambriennes du Yilgarn ou d'Afrique de l'Ouest sont réputées pour les nombreux gîtes aurifères qu'elles hébergent, quel est le potentiel métallogénique du BAN qui leur ressemble tant ? Le BAN est considéré comme une des provinces les plus prometteuses pour l'exploration polymétallique (or et métaux de base) dans les années à venir (Plyley et al., 2009 ; Trench et Groves, 2015 ; Barrie et al., 2016). Il constituerait d'ailleurs la principale ressource mondiale d'or néoprotérozoïque (Johnson et al., 2017). Si le bouclier nubien, qui nous intéressera plus particulièrement dans la suite de ce manuscrit, souffre d'un manque d'attention en termes d'exploration comparé au bouclier arabique voisin où de nombreux gisements sont documentés (Johnson et al., 2017), il représente à lui tout seul une province aurifère en émergence (> 45 Mozt d'or, soit plus de 1,4 t Au découverts sur les 10 dernières années). L'exploitation artisanale d'or y est largement répandue, notamment en Érythrée et au Soudan (Barrie et al. 2016, Johnson et al. 2017 parmi d'autres), avec un essor de l'activité artisanale remontant à 2009 (Chevrillon-Guibert et al., 2019 et références citées). Le BAN, et en particulier le bouclier nubien, pourrait donc suivre l'exemple du craton ouest-africain en termes de renouvellement de l'activité minière dans les années à venir, ce dernier étant marqué par un renouveau de l'exploration aurifère depuis une quinzaine d'années (première province paléoprotérozoïque aurifère mondiale ; Goldfarb et al., 2017).

La caractérisation de nouvelles ressources en or au cours des deux dernières décennies a été particulièrement forte dans la partie nord-est du Soudan. Les gîtes aurifères décrits dans le bouclier nubien sont de trois types principaux (Fig. 0-13 ; Elsamani et al., 2001 ; Botros, 2002, 2004 ; Bierlein et al., 2016 ; Johnson et al., 2017) :

(i) Une minéralisation aurifère associée aux sulfures volcanogéniques massifs (SVM) qui sont particulièrement présents dans la chaîne d'Ariab-Arbaat, dans le bloc litho-

tectonique d'Haya au sud de la suture Nakasib. Par exemple, le SVM d'Hadal Awatib, long de 3,1 km, n'a d'équivalent que les SVM de Neves Corvo (ceinture pyriteuse ibérique, Portugal) et de Kidd Creek (Ontario, Canada) (Barrie et al., 2016) en termes de dimension et présente des ressources totales estimées à 68,8 Mt at 1,22 % poids Cu, 0,74 % poids Zn et 1,1 g/t Au (Bosc et al., 2012). L'altération supergène est à l'origine de la libération de l'or au sein de chapeaux de fer (*gossans*) et de roches silico-barytiques (*SBR*) recouvrant les lentilles de sulfures massifs et peuvent contenir jusqu'à 10 ppm Au (Cottard et al., 1986 ; Plyley et al., 2009). Les districts de Bisha et d'Asmara (Barrie et al., 2016) en Érythrée sont d'autres exemples similaires au district minier d'Ariab au Soudan. Ce type de minéralisation est daté à 892-884 Ma (*e.g.,* Lescuyer et al., 2004).

(ii) Un gîte de type porphyre Cu-Au a été décrit à Jebel Ohier au Soudan et il s'agit du premier pour le bouclier arabo-nubien ; ses ressources totales en or s'élèvent à environ 0,93 Mozt (29,65 t) Au à une teneur de coupure de 0,15 % poids Cu (substance principale économiquement rentable). La minéralisation est datée à 816-812 Ma (Bierlein et al., 2016, 2020). D'autres gîtes de type porphyre Cu-(Au) ont récemment été décrits en Égypte (Um Mongul prospect ; Abd El-Rahman et al., 2017) et en Érythrée (Daero Paulos prospect ; Perelló et al., 2020). À l'échelle du BAN, de rares épithermaux aurifères sont également décrits, tels que celui de Mahd adh Dhahab, dans le bouclier arabique (Johnson, 2013). Ces gîtes ne sont pas indiqués sur la Figure 0-13.

(iii) Une minéralisation aurifère dans les veines de quartz associées aux zones de cisaillement communément qualifiée de type or orogénique. Il s'agit de la minéralisation la plus présente dans le bouclier nubien (Elsamani et al., 2001 ; Botros, 2004 ; Zoheir et al., 2019a). De nombreuses mines ont été en activité et de nombreux gîtes ont été décrits notamment en Égypte (Sukari par exemple), dans les parties centrale et méridionale du désert oriental égyptien (*e.g.,* Klemm et al., 2001 ; Botros, 2002 ; Helmy et al., 2004 ; El Kazzaz, 2012 ; Osman, 2014 ; Helmy et Zoheir, 2015 ; Khalil et al., 2016 ; Fawzy, 2017). Ces gîtes sont spatialement associés aux zones de cisaillement décrochantes de premier

ordre du bouclier nubien, telles que celles d'Oko et d'Hamisana. Les données géochronologiques disponibles dans le désert oriental d'Égypte datent ce type de minéralisation aux alentours de 600 Ma (Zoheir et al., 2019a et références citées).

4.2. Potentiel aurifère le long de la suture de Keraf

Depuis 2009, des gîtes aurifères sont explorés par Managem Soudan dans le district aurifère de Gabgaba (WG03, UTM et Central Zone au sein du bloc d'exploration 15), centré sur la SK (Fig. 0-13 ; Managem, 2011). WG03 exclu, les ressources à Gabgaba sont désormais estimées à 2,8 Mozt Au (87,1 t Au) pour des réserves s'élevant à 1,6 Mozt Au (49,8 t Au) (Managem, 2019). Orca Gold Inc. mène également un projet d'exploration au niveau de la zone d'interférence entre la SK et la SAD (Bloc d'exploration 14 ; Fig. 0-13). La compagnie a délimité deux prospects situés *a priori* dans la SK : Galat Sufar South (GSS ; Fig. 0-13) et Wadi Doum (WD). Les ressources indiquées pour GSS s'élèvent à 75,6 Mt à une teneur moyenne de 1,27 g/t Au (teneur de coupure fixée à 0,6 g/t Au) pour un total de 3,08 Mozt (95,8 t) Au (Duckworth, 2018).

L'activité de ces deux compagnies et l'ensemble des occurrences relevées (Fig. 0-13) le long de la SK et de sa zone d'interférence avec la SAD justifient donc le potentiel aurifère de ces structures. Leur position à l'interface entre le BAN et le méta-craton du Sahara en font des marqueurs tectoniques privilégiés de l'évolution tectonique associée à la mise en place du BAN. Suivant la philosophie du système métallogénique, l'étude des minéralisations aurifères de GSS et du district de Gabgaba permettra donc de mieux contraindre les processus lithosphériques ayant conduit à la formation de la zone de suture, puis de cisaillement, de Keraf, et inversement.

4.3. Lacunes de connaissances

Malgré l'intérêt évident que représentent la SK et la SAD en termes de compréhension de l'évolution crustale associée à la mise en place du BAN lors du Néoprotérozoïque (Harms et al., 1990, 1994 ; Denkler et al., 1993 ; Schandelmeier et al., 1994b ; Bailo et al., 2003), ces structures n'ont été que très peu étudiées, si ce n'est par traitement d'imagerie satellite (Abdelsalam et al., 1995 ; Abdelsalam et Stern, 1996b) et de rares études de terrain (*e.g.,* Ahmed Suliman, 2000 ; Bailo et al., 2003). Les gîtes aurifères qu'elles abritent ne sont uniquement documentées par de rapports non publiés rédigés par des consultants pour les compagnies explorant ces occurrences et une unique étude récente (Gaboury et al., 2020), alors que les minéralisations aurifères du désert oriental égyptien sont, en comparaison, très bien documentées (Zoheir et al., 2019a et références citées).

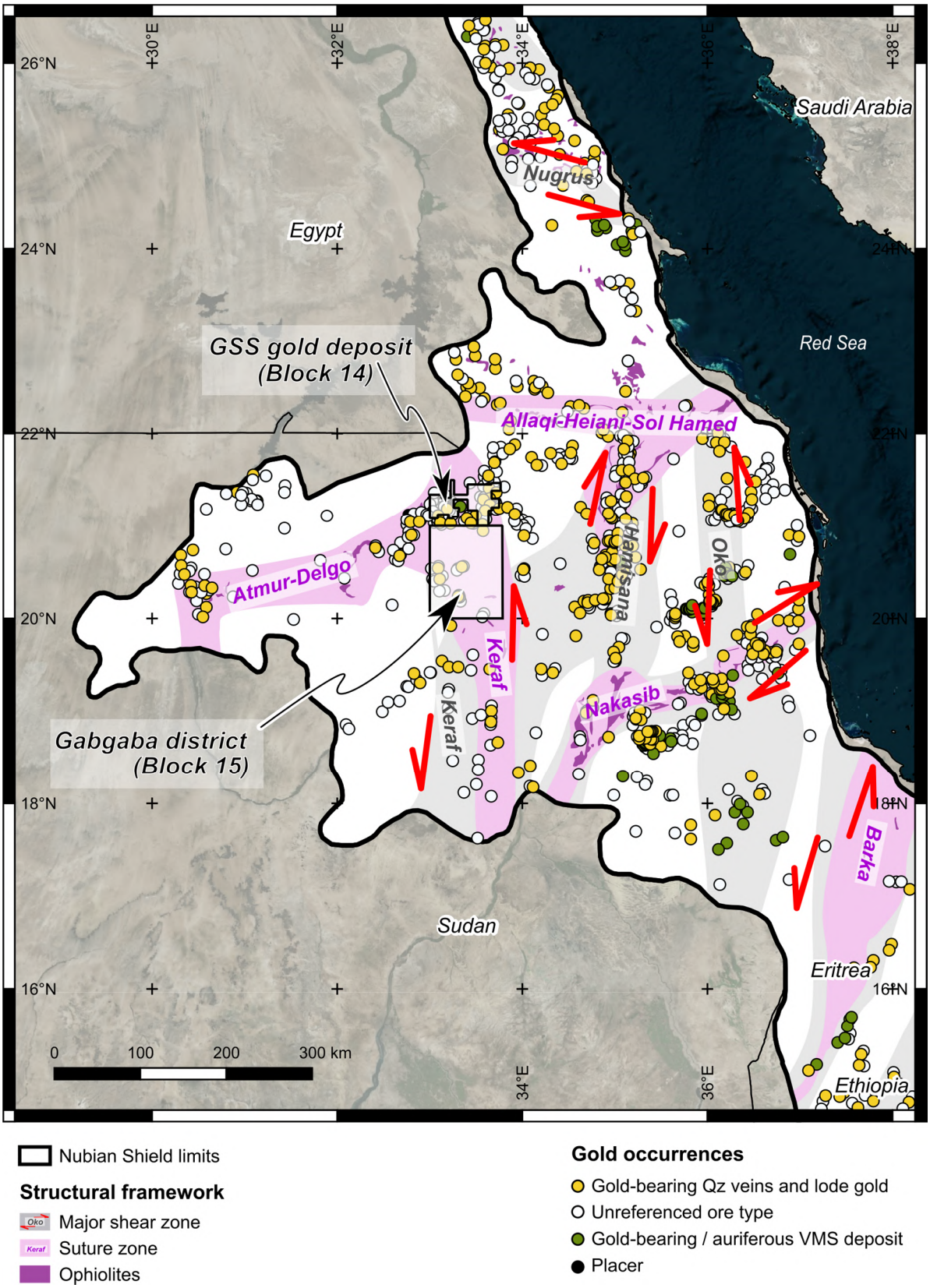


Figure 0-13 : Contexte structural et occurrences aurifères du bouclier nubien. Les ophiolites sont dessinées, et les zones de cisaillement et de sutures interprétées (nommées d'après Johnson et al., 2011), à partir des cartes géologiques nationales égyptienne, soudanaise, érythréenne et éthiopienne (Egyptian Geological Survey and Mining Authority, 1981 ; Geological Research Authority of the Sudan, 1988 ; Tadesse et al., 2000 ; AMEC, 2004). Les occurrences aurifères proviennent de la base de données SIG d'Arethuse Geology. Le fond provient de l'imagerie satellitaire ©BingAerial. Les coordonnées sont données dans le système WGS 84.

5. Problématiques et approche multi-scalaire proposée

Les sections précédentes justifient le potentiel aurifère de la partie soudanaise du BAN qui s'exprime par de nombreux gîtes de types différents, associés à des contextes géodynamiques variés au cours de l'orogenèse est-africaine-antarctique au Néoprotérozoïque. Pour autant, bien que la philosophie du système métallogénique soit désormais largement adoptée par la communauté scientifique, elle n'a jamais été appliquée dans cette région du monde qui reste finalement très peu étudiée. Des interrogations émergent alors sur le polyphasage de l'or et l'importance de l'intégration des systèmes métallogéniques à la compréhension de l'histoire géodynamique de cette région et *vice-versa*. Ce projet de doctorat a donc pour objectif de décrire le système métallogénique de l'or panafricain au sein du BAN en s'intéressant plus particulièrement à la SK et sa zone d'interférence avec la SAD (nord-est du Soudan) pour :

(i) tracer l'évolution crustale enregistrée le long de la suture néoprotérozoïque de Keraf et discuter de l'héritage éventuel de croûte archéenne à mésoprotérozoïque associée à la présence du méta-craton du Sahara à l'ouest de cette structure ;

(ii) caractériser la typologie et la chronologie relative des minéralisations aurifères décrites le long de la suture de Keraf tout en réévaluant l'histoire tectonique régionale dans laquelle elles s'inscrivent ;

(iii) contraindre les processus minéralisateurs tectoniques et géochimiques en jeu;

(iv) contraindre la chronologie absolue des événements aurifères décrits et les intégrer à l'évolution magmato-tectono-métamorphique régionale en termes de mobilisation de source(s) d'or, transport des fluides minéralisateurs et dépôt de la minéralisation.

Une **approche multi-scalaire** est requise afin de répondre à ces objectifs. Le cœur de ce travail de doctorat réside dans les études de terrain réalisées de l'échelle crustale à l'échelle macroscopique (cartographie et *logging* sur carottes de forage). Les données acquises à plus petite et grande échelles *via* l'utilisation de multiples méthodes

analytiques viennent compléter ce socle. Le couplage de données acquises du terrain au laboratoire, à des échelles spatiales s'étalant sur 11 ordres de grandeur (de la centaine de km au µm), fait l'originalité de ce travail. La stratégie proposée est la suivante :

(i) **Aux échelles géodynamique et régionale :** le canevas structural du bouclier nubien est seulement décrit à très petite échelle et est relativement peu interprété en termes de phases de déformation dans le cycle géodynamique néoprotérozoïque. Une synthèse SIG des données géochronologiques et isotopiques publiées pour le BAN a été construite. Elle a été complétée par la réalisation d'un transect géologique recoupant la partie centrale de la SK afin de tracer l'évolution crustale et tectono-magmatique de la région. Les observations réalisées sur les objets minéralisés aux échelles supérieures ont ensuite été intégrées à l'histoire géodynamique proposée.

(ii) **À l'échelle du gisement :** les gisements aurifères de Galat Sufar South (GSS) et du district de Gabgaba (WG03, Central Zone et UTM), opérés par Orca Gold Inc. et Managem, et localisés le long de la SAD et de la partie centrale de la SK, ont fait l'objet d'une étude structurale de terrain approfondie afin de mieux caractériser les phases de déformation locales. Ces données ont été comparées et intégrées à la compréhension du grain structural régional. De même, les événements minéralisateurs décrits ont été replacés au sein cette évolution spatio-temporelle.

(iii) **Aux échelles macroscopique et microscopique :** la caractérisation des événements de déformation et de minéralisation décrits à plus petite échelle a été réalisée par une étude macro- à micro-structurale et pétrographique poussée jusqu'à l'échelle cristallographique. Les événements minéralisateurs et de déformation majeurs ont ensuite été contraints en termes de conditions pression-température, de chronologie absolue et de signature géochimique. Ces contraintes s'avèrent nécessaires à la compréhension du lien entre évolution tectonique et événements minéralisateurs à l'échelle régionale.

6. Organisation du manuscrit

Les résultats de ce projet de recherche et leurs implications sont présentés en **quatre parties**, composées d'**un ou deux chapitre(s)** chacune. Leur découpage suit l'approche multi-scalaire proposée pour cette étude. Un préambule résume pour chaque partie les apports fondamentaux des chapitres qu'elle contient et permet d'assurer une continuité lors du saut d'échelle d'une partie à l'autre. La Figure 0-14 synthétise les échelles de réflexion pour chacun des chapitres composant ce manuscrit.

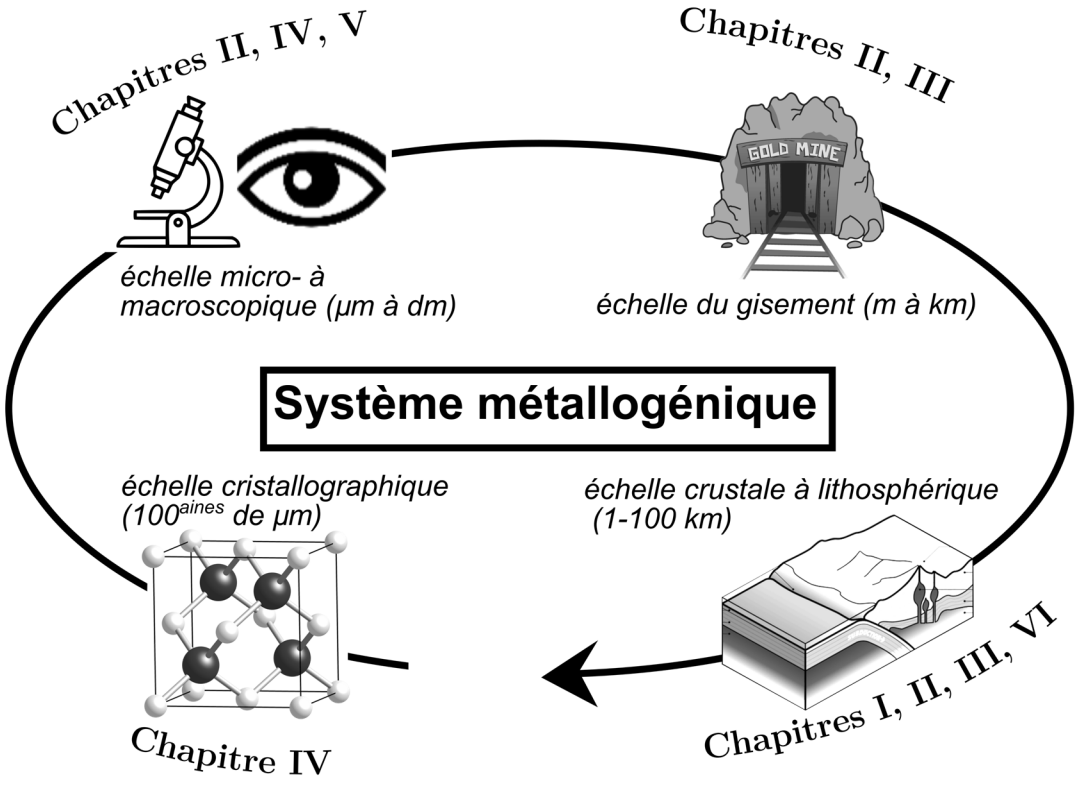


Figure 0-14 : Échelles d'investigation du système métallogénique aurifère exprimé le long de la suture de Keraf au sein du bouclier arabo-nubien néoprotérozoïque pour chacun des chapitres composant ce manuscrit.

La première partie (**Partie I**) aborde le sujet à l'échelle lithosphérique et est composée d'un unique chapitre. Le **Chapitre I** est un article en préparation pour soumission au journal *Gondwana Research.* Il présente les données géochronologiques et isotopiques U-Pb, Hf, Sr, Nd obtenues au cours de ce doctorat afin de discuter l'évolution lithosphérique de la partie centrale de la suture de Keraf, des processus tectono-magmatiques engagés et de leur signification à l'échelle de l'évolution géodynamique de Gondwana.

La seconde partie (**Partie II**) se focalise à l'échelle régionale et crustale. Le **Chapitre II** est un article publié dans le *Journal of Structural Geology* en juin 2020. À partir de l'exemple du gisement aurifère de Galat Sufar South, il détaille comment l'étude d'un gîte déformé depuis l'échelle pluri-kilométrique jusqu'à l'échelle microscopique permet de mieux contraindre l'histoire tectonique associée à la minéralisation et de l'intégrer à l'échelle régionale. Le **Chapitre III** est un article en cours de révision pour publication dans le *Journal of African Earth Sciences,* établissant une coupe crustale à travers la partie centrale de la suture de Keraf, au niveau du district aurifère de Gabgaba. Le canevas structural régional et la chronologie relative des occurrences aurifères repérées (WG03, Central Zone et UTM) dans le district vis-à-vis de l'histoire tectonique enregistrée par cette structure d'échelle lithosphérique sont discutés.

La troisième partie (**Partie III**) s'intéresse à l'échelle microscopique. Le **Chapitre IV** est un article en cours de révision pour publication dans un ouvrage de la *Geological Society of London* intitulé *Recent Advances in Understanding Gold Deposits: From Orogeny to Alluvium*. Il présente une approche multi-scalaire et multi-disciplinaire, conduite depuis le terrain jusqu'au laboratoire, qui permet de mieux contraindre les processus tectoniques et géochimiques en jeu dans la mise en place de gîtes aurifères déformés. L'originalité de cette approche réside dans le couplage (i) d'observations réalisées lors d'une étude pétro-structurale de terrain classique, (ii) avec des méthodes analytiques micro-structurales atypiques (tomographie à rayons X à haute résolution et analyse par diffraction d'électrons rétro-diffusés) et (iii) une méthode d'analyse géochimique *in situ* des sulfures associés à la minéralisation (spectrométrie de masse à plasma induit par ablation laser). Les bénéfices de l'approche proposée pour la compréhension des mécanismes couplant déformation et minéralisation et pour l'industrie minière sont illustrés pour le gisement de Galat Sufar South. Le **Chapitre V** est un article en préparation pour soumission à *Economic Geology.* Il s'appuie sur les travaux de recherche de M2 de Célestine Berthier (Université de Lorraine) réalisés entre Février

et Juillet 2020, et complétés par des données géochimiques obtenues ultérieurement. Le projet de recherche de Célestine Berthier s'intégrait dans le cadre de ce doctorat et a été encadré par Julien Perret, Aurélien Églinger et Anne-Sylvie André-Mayer au sein du laboratoire GeoRessources (Nancy). L'article proposé s'appuie sur une étude micro-texturale et structurale détaillée des veines minéralisées et des générations de pyrite exprimées au sein du gisement aurifère de Central Zone (district de Gabgaba), couplée au traçage de leur signature géochimique par spectrométrie de masse à plasma induit par ablation laser. Une discussion portant sur les processus de minéralisation aurifère en jeu à l'échelle microscopique est tenue.

La quatrième partie (**Partie IV**) clôt ce manuscrit. Elle débute par le **Chapitre VI** qui présente les contraintes obtenues par datation U-Pb sur apatite hydrothermale et magmatique des épisodes de déformation-minéralisation principaux à l'origine des gisements de Galat Sufar South et WG03 et de l'intrusion des granitoïdes hébergeant la minéralisation à Central Zone. Des données complémentaires géochimiques et isotopiques U-Pb et Hf sur zircon d'intrusifs d'arc ainsi que des calculs de multi-équilibre chlorite-phengite-quartz-eau dans les tufs minéralisés permettent de mieux comprendre le contexte géodynamique de la suture d'Atmur-Delgo au moment de la formation du gisement de Galat Sufar South, puisque cette zone n'est pas le transect géodynamique réalisé (**Partie I**). Le **Chapitre VII** fait office de discussion générale et a pour objectif d'intégrer les occurrences aurifères étudiées (Galat Sufar South et district aurifère de Gabgaba) à l'échelle de l'évolution géodynamique des sutures d'Atmur-Delgo et de Keraf. La présentation des implications de cette étude pour la compréhension globale du système métallogénique aurifère panafricain au sein du bouclier arabo-nubien et en termes d'exploration marquera le point final de ces travaux de thèse.

7. Support scientifique et financier, collaborations extérieures

Cette thèse a reçu le support scientifique et financier de plusieurs organismes : (i) la société Arethuse Geology qui a souhaité développer son pôle R&D à travers ce projet, (ii) l'Association Nationale pour la Recherche et la Technologie (ANRT) *via* l'attribution d'une bourse par établissement d'une Convention Industrielle de Formation par la Recherche (CIFRE) N°2017/1737, et (iii) les sociétés Orca Gold Inc. et Managem, partenaires de ce projet centré sur l'étude de leurs prospects aurifères.

Les travaux de terrain nécessaires à cette étude ont nécessité une étroite collaboration avec les équipes de terrain d'Orca Gold Inc. et de Managem Soudan, en particulier Craig Hartshorne, Ema Abanyin et Bushra Abdelsalam d'une part et Aomar Ennaciri d'autre part. L'ensemble des personnels de ces compagnies basés à Khartoum a également contribué au bon déroulement logistique de ces travaux, au même titre que Jan Duvenage, *project manager* expatrié au Soudan pour le compte d'Arethuse Geology. Au laboratoire, l'approche pluri-disciplinaire et multi-scalaire de ce travail implique la collaboration de plusieurs équipes de recherche dont les laboratoires GeoRessources (Nancy), Géosciences Environnement Toulouse, Géosciences Montpellier, Géosciences Rennes, du Centre de Recherches Pétrographiques et Géochimiques (Nancy), la *School of Earth, Atmosphere and Environment* (Melbourne, Australie), l'*Institut für Geowissenschaften* (Francfort, Allemagne), le *KIT-Karlsruhe Institute of Technology* (Karlsruhe, Allemagne) et le *Department of Geological Sciences and Geological Engineering* de *Queen's University* (Kingston, Canada).

PARTIE I – ÉVOLUTION LITHOSPHÉRIQUE DE LA PARTIE CENTRALE DE LA SUTURE DE KERAF

Préambule

Les gisements métalliques résultent d'une variété de processus géologiques, d'échelle lithosphérique à microscopique, concentrant les métaux dans un volume réduit et en quantité suffisante pour que leur exploitation soit rentable (Jenkin et al., 2015). À l'échelle lithosphérique, le concept de système métallogénique considère donc la nécessité d'un environnement fertile et d'une architecture lithosphérique favorable à la mise en place de gîtes métallifères (McCuaig et al., 2010 ; Hronsky et al. 2012). Cette approche implique donc d'étudier l'histoire géodynamique de la zone investiguée afin d'identifier le(s) contexte(s) géodynamique(s) favorable(s) à la fertilisation de l'élément d'intérêt au sein de la croûte continentale, correspondant à son âge d'extraction mantellique. Les orogènes formés par amalgamation de blocs lithotectoniques dérivant de complexes d'arc, sont connus pour être des zones de transfert préférentiel de matériel mantellique vers la croûte, dont l'or (*e.g.,* Sawkins, 1990 ; Saunders et Tarney, 1991 ; Bierlein et al., 2009 ; Cawood et al., 2009 ; Pitcairn, 2011 ; Hronsky et al., 2012). Le bouclier arabo-nubien, résultant du collage de nombreuses arcs insulaires néoprotérozoïque et des complexes associés, n'échappe pas à la règle et est considéré comme étant à la fois la portion de croûte juvénile la plus importante au monde et la principale ressource d'or d'âge néoprotérozoïque (Johnson, 2014 ; Johnson et al., 2017).

La **Partie I** de ce manuscrit sera donc dédiée au traçage de l'évolution lithosphérique enregistrée par les zones de suture de Keraf et d'Atmur-Delgo, sur lesquelles notre étude se focalise. On s'intéressera en particulier à la partie centrale de la zone de suture de Keraf qui héberge le district aurifère de Gabgaba (**Chapitres III** et **V**). L'intégration des observations structurales et pétrographiques réalisées sur le terrain avec les données géochimiques, géochronologiques et isotopiques obtenues pour un panel de roches magmatiques associées au fonctionnement d'un arc à l'endroit de la suture de Keraf doit permettre d'établir l'évolution spatiale et temporelle du système géodynamique en jeu et les processus tectono-magmatiques impliqués. Une fois ce cadre établi, une réflexion sur la signification de ces mécanismes à l'échelle du cycle supercontinental de Gondwana sera tenue. Les parties suivantes s'intéresseront quant à elles à la chronologie et aux mécanismes de mobilisation et accumulation d'or à partir de ce réservoir fertile depuis l'échelle du district (**Partie II**) jusqu'à l'échelle microscopique (**Partie III**).

Chapitre I – Long-lived Neoproterozoic island-arc along the central Keraf suture, NE Sudan

Julien Perret[1,2,*], Aurélien Eglinger[2], Pierre Bouilhol[3], Anne-Sylvie André-Mayer[2], Julien Feneyrol[1], Armin Zeh[4], Rémi Bosc[1]

Article en préparation pour soumission à *Gondwana Research*.

[1] Arethuse Geology EURL, BP 80017, Latitude Arbois, 1060 rue René Descartes, 13290 Les Milles, France

[2] GeoRessources, Université de Lorraine, CNRS, 54000 Nancy, France

[3] CRPG, Université de Lorraine, CNRS, UMR 7358, 54500 Vandoeuvre-lès-Nancy, France

[4] KIT-Karlsruhe Institute of Technology, Campus South, Institute for Applied Geosciences, Mineralogy and Petrology, 76131 Karlsruhe, Germany

Résumé

La suture arc-continent de Keraf sépare le bouclier arabo-nubien juvénile, d'âge néoprotéozoïque, du méta-craton du Sahara remobilisé lors du Panafricain. Cette zone est donc propice à l'étude des processus tectono-magmatiques associés à la croissance crustale en jeu lors de la formation de Gondwana de l'Ouest. Notre propos s'appuie sur des données de géochimie en roche totale, de datation U-Pb et d'isotopie Hf, Sr et Nd sur roches magmatiques échantillonnées le long d'une coupe d'environ 80 km de long à travers la partie centrale de la suture de Keraf.

L'arc insulaire de Keraf enregistre (i) une première phase de magmatisme juvénile avec des signatures isotopiques suprachondritiques ($\varepsilon Hf_{(i)}$=+9,6±1,6 ; $\varepsilon Nd_{(i)}$=+4,7±2,0) puis (ii) une période de maturation s'étalant entre 760 et 655 Ma impliquant le mélange de magmas provenant de la remobilisation de la croûte d'arc préexistante et directement extrait du manteau. Ce mélange est suggéré par le découplage des systèmes isotopiques Hf (baisse de $\varepsilon Hf_{(i)}$ de +11,6 à +6,2) et Nd (âges modèles mixtes de 0,96 à 0,84 Ma). Le développement synchrone d'un arc continental le long de la marge active du méta-craton du Sahara est probable. Un épisode de remobilisation crustale post-collision est exprimé dans la suture de Keraf, avec des signatures isotopiques restant suprachondritiques ($\varepsilon Hf_{(i)}$=+8,5±0,9 ; $\varepsilon Nd_{(i)}$=+4,1±1,0), et affecte également le méta-craton du Sahara.

L'arc insulaire de Keraf présente la durée de vie la plus longue décrite à ce jour dans le bouclier arabo-nubien. À l'échelle mondiale, les paléo-arcs dépassant les 100 millions d'années d'existence sont rares et systématiquement d'âge néoprotérozoïque. Il s'agit certainement-là d'une particularité inhérente à l'évolution géodynamique de Gondwana, connue pour différer du cycle supercontinental classique.

Mots-clés

Gondwana de l'Ouest ; bouclier arabo-nubien ; suture arc-continent de Keraf ; maturation d'un arc insulaire ; magmatisme d'arc juvénile.

Abstract

The Keraf arc-continent suture separates the juvenile Neoproterozoic Arabian-Nubian shield and the Saharan meta-craton affected by Pan-African crustal reworking. It is thus appropriate to enlighten the tectono-magmatic events and crustal growth processes involved in western Gondwana assembly. To this end, we carried out whole-rock geochemistry, U-Pb geochronology and Hf, Sr and Nd isotope analyses on igneous rocks sampled along a ~80 km-long geological transect through the central part of the Keraf suture.

The studied Keraf island arc evolved from (i) juvenile magmatism between *ca.* 840-810 Ma, with suprachondritic $\varepsilon Hf_{(i)}$ (+9.6±1.6) and $\varepsilon Nd_{(i)}$ (+4.7±2.0) values to (ii) protracted arc maturation between *ca.* 760-655 Ma. The latter flare-up involved mixing between older arc crust reworking and juvenile magmatism as inferred from the decoupling of Hf (decrease of $\varepsilon Hf_{(i)}$ from +11.6 to +6.2) and Nd (mixed crustal residence ages of *ca.* 0.96-0.84 Ga) isotopic systems. In parallel, a continental arc likely evolved along the eastern margin of the Saharan meta-craton. After Keraf arc-continent collision, post-collisional crustal reworking affected both the isotopically juvenile central Keraf suture ($\varepsilon Hf_{(i)}$ = +8.5±0.9; $\varepsilon Nd_{(i)}$= +4.1±1.0) and the reworked Saharan meta-craton margin nearby at *ca.* <620 Ma.

The Keraf island arc is the longest-lived island arc system of the Arabian-Nubian shield up to date. Paleo-island arcs with >100 Myr lifetime are rare and systematically of Neoproterozoic age. The record of extra-long-lived island arcs is therefore considered as another specificity of the geodynamical evolution of Gondwana, already known to differ from the classical supercontinent cycle scenario.

Keywords

West Gondwana; Arabian-Nubian shield; Keraf arc-continent suture; island arc maturation; juvenile arc magmatism.

1. Introduction

Suture zones are linear belt of intense deformation along which ancient cratons, continental crustal blocks and oceanic- to arc-derived litho-tectonic blocks, *i.e.,* terranes, join together in orogenic systems (Dewey, 1969). Sutures are characterized at first order by (i) the record of former oceanic basins by ophiolites, *i.e.,* spreading centers at mid-ocean ridges and/or within back-arc, intra-arc basins and fore-arcs of incipient island arcs, (ii) evidence for calc-alkaline arc magmatism at a paleo-oceanic subduction site, (iii) bimodal metamorphism with paired low and high temperature/pressure metamorphic units formed in subduction zones and in back-arcs and orogenic hinterland, respectively (Brown et al., 2020) and (iv) the collage of terranes with distinct lithological, structural, geochronological and isotopic signatures, among other features (review by Chetty, 2017). They therefore represent a precious record of the early tectono-magmato-metamorphic evolution of orogenic cycles represented by magmatic accretion at mid-ocean ridges and in island arcs. It is especially true where suturing, which ends with arc-arc or arc-continent collision, is not followed by continent-continent collision which tends to overprint this early capture during later evolution towards collisional-type orogens (Cawood et al., 2009; Vanderhaeghe, 2012; Brown et al., 2020). The arc magmatic activity is evidenced by juvenile material accretion – considered from both isotopic and melt source points of view, *i.e.,* the *"isotopic signature is no-where near the depleted mantle"* (Moyen et al., 2017) and the crust is extracted *"from the mantle not long before its incorporation into the belts*" (Couzinié et al., 2020) –, and thus subduction sites are valuable keys to understanding crustal growth processes (Windley, 1992, 2003) and plate convergence vectors and velocity (Brown et al., 2011).

The Gondwana supercontinent had formed during Pan-African (*ca.* 1000-542 Ma; Kröner, 1984) by the collage of West and East Gondwana to the East African-Antarctic orogen (EAAO) along arc-continent sutures (Fig. 1-1a; Kröner, 1993; Stern, 1994, 1994; Jacobs et al., 1998; Kusky et al., 2003; Meert, 2003; Li et al., 2008; Seton et al., 2012;

Fritz et al., 2013; Domeier and Torsvik, 2014; Merdith et al., 2017; Grenholm, 2019). The Arabian-Nubian shield (ANS) forms the northern part of the EAAO (Fig. 1-1b). It is the largest track of Neoproterozoic juvenile crust worldwide (Johnson, 2014), as illustrated by extensive U-Pb, Hf, Sr, Nd, Pb and O isotopic data (*e.g.,* Andersson et al., 2006; Hargrove et al., 2006; Be'eri-Shlevin et al., 2009b, 2009c; Stern et al., 2010a, 2020; Moghazi et al., 2012; Ali et al., 2013; Eyal et al., 2014; Johnson, 2014; Robinson et al., 2014, 2015a, 2015b; Blades et al., 2015; Saeed et al., 2020). If most ophiolites of the ANS had formed in supra-subduction zones (*e.g.,* Stern et al., 2004; Blades et al., 2019) others relate to multiple settings such as fore-arc (*e.g.,* Dilek and Ahmed, 2003; Sehsah and Eldosouky, 2020), back-arc (*e.g.,* Abdelrahman, 1993; El-Naby and Frisch, 2006), mid-ocean ridge seafloor (*e.g.,* Zimmer et al., 1995; Dilek and Ahmed, 2003) and even intracontinental rift Dilek and Ahmed (2003). The diversity in ophiolite type through the ANS illustrates well the multiple geodynamical settings favorable to oceanic crust production during the EAAO. The ANS is therefore well-suited to track magmatic and tectonic accretion processes during the Gondwana supercontinent cycle. Besides, Spencer et al. (2013) suggested that Gondwana-suturing orogens mostly involved single-sided arc-continent subduction zones, inducing a greater crustal recycling/reworking of ancient cratonic crust than during Mesoproterozoic Rodinia supercontinent cycle. The recording of Pan-African tectono-metamorphic and magmatic events in the Saharan meta-craton, west to the Nubian shield, goes in that sense (Fig. 1-1b; *e.g.,* Ries et al., 1985; Kröner et al., 1987; Rahman et al., 1990; Küster and Liégeois, 2001).

This study therefore focuses on the boundary between the Saharan meta-craton westwards and the Neoproterozoic juvenile ANS eastwards, known as the Keraf suture, where both crustal growth and crustal reworking during Gondwana assembly are likely recorded, making it the *"best window into the tectonic history of the northeastern flank of West Gondwana"* (Bailo et al., 2003). However, despite back-arc ophiolites, island arc rocks, post-collisional plutons and amphibolite to granulite facies-metamorphosed rocks

have been recognized along the Keraf suture (*e.g.,* Ahmed Suliman, 2000; Bailo et al., 2003; Abdelrahman et al., 2017), its tectono-magmato-metamorphic evolution remains uncertain at the lithospheric scale.

We propose to fill the gap in knowledge concerning the Neoproterozoic magmatic record of the central Keraf suture. To that purpose, we sampled early to syn-Keraf arc-related igneous rocks and post-Keraf arc plutons along a ~80 km-long geological transect (Fig. 1-2). Relying on the structural model previously suggested along the same transect (Perret et al., under review), we combine whole-rock geochemistry, U-Pb geochronology, Hf, Sr and Nd isotope analyses to (i) trace Keraf magmatic processes and source evolution through time and space and (ii) figure out how they relate to Pan-African reworking of the Saharan meta-craton and (iii) illustrate these processes in lithospheric-scale cross-sections and map cartoons. Besides, the study of the Neoproterozoic Keraf arc represents the opportunity to compare its evolution with that of Neoproterozoic to modern-day magmatic arc systems.

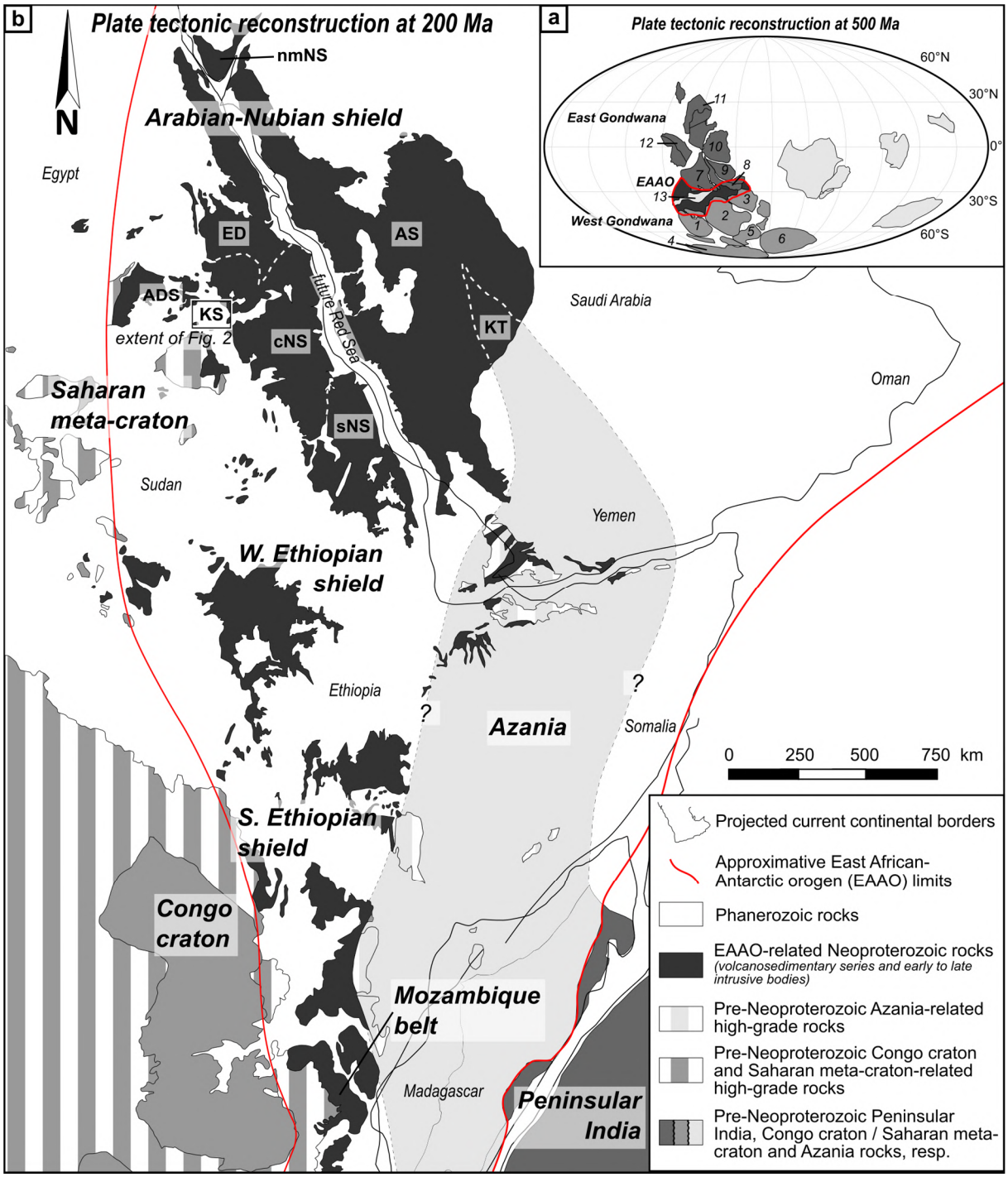


Figure 1-1: a Plate tectonic reconstruction at 500 Ma highlighting the *ca.* 950-550 Ma East African-Antarctic orogen (EAAO) location between East and West Gondwana, modified after Grenholm (2019) and references therein (Johnson et al., 2011; Fritz et al., 2013; Johnson, 2014; Merdith et al., 2017). Numbered cratons and crustal blocks which are part of East and West Gondwana are 1: Saharan meta-craton; 2: Congo craton; 3: Kalahari craton; 4: West African craton; 5: Sao Francisco craton; 6: Amazon craton; 7: Peninsular India; 8: Rayner Province; 9: Chron craton; 10: Terre Adélie; 11: Australian cratons; 12: South China craton; 13: Azania. **b** Regional map of the EAAO prior to Gondwana break-up at *ca.* 200 Ma, simplified after Grenholm (2019). The black rectangle delimits the extent of Figure 1-2 across the Keraf suture in the western Arabian-Nubian shield. The Arabian-Nubian shield subdivisions are ADS: Atmur-Delgo suture; AS: Arabian shield minor the Khida terrane; cNS: central Nubian shield; ED: Eastern Desert; KS: Keraf suture; KT: Khida terrane, isotopically distinct from the rest of the Arabian shield; nmNS: northernmost Nubian shield (Sinai Peninsula); sNS: southern Nubian shield.

2. Geological setting

2.1. The East African-Antarctic orogeny and greater Gondwana assembly

Jacobs et al. (1998) introduced the notion of East African-Antarctic orogeny, considering a temporal and spatial continuity between: (i) the East African orogeny, which led to amalgamation of arc terranes in the ANS, formation of the Mozambique belt southwards and collage of continental blocks forming modern-day parts of Madagascar, Sri Lanka, India, Seychelles and East Antarctica to the east, Saharan meta-craton, Congo and Kalahari cratons to the west; and (ii) the Kuunga orogeny, expressed by the collage of Australia and another portion of East Antarctica with previous elements (Kröner, 1993; Stern, 1994; Meert et al., 1995; J. Jacobs et al., 2003a, 2003b; Kusky et al., 2003; Fritz et al., 2013). Most authors outline the EAAO as the collage between West and East Gondwana (Fig. 1-1a; Li et al., 2008; Seton et al., 2012; Fritz et al., 2013; Domeier and Torsvik, 2014; Merdith et al., 2017). It is however worth noticing that both West and East Gondwana did not fully exist until their Cambrian final assembly in their southern parts (Meert, 2003; Gray et al., 2008; Oriolo et al., 2017; Schmitt et al., 2018; Boniface, 2019).

The final collision suture of the EAAO, related to the closure of the Mozambique ocean between East and West Gondwana, likely resulted in the Nabitah zone, the Baragoi ophiolite klippe, the Cobué and Manica belts from Saudi Arabia to Kenya, and extends down to Antarctica (Shackleton, 1996). Westwards, the contact between the EAAO and West Gondwana is defined by a line of arc-continent sutures and ophiolite-decorated belts, namely the Keraf-Kabus-Sekerr-Kinyiki stretching from Egypt to Kenya (Vearncombe, 1983; Burke and Sengör, 1986; Frisch and Pohl, 1986; Berhe, 1990; Abdelsalam and Dawoud, 1991; Ries et al., 1992; Mosley, 1993; Abdelsalam et al., 1998; Fritz et al., 2013).

2.2. Keraf arc-continent suture between the Arabian-Nubian shield and West Gondwana

We focus on the central part of the Keraf suture, interpreted as the western boundary between the ANS, *i.e.,* the northern part of the EAAO, and the Saharan meta-craton (Figs. 1-1b, 1-2; Stern, 1994; Fritz et al., 2013; Johnson, 2014). The ANS is mainly composed of juvenile magmatic arcs and ophiolites, which are remnants of the subduction and obduction processes that completely consumed the Mozambique ocean and related ensialic marginal basins (Vail, 1983, 1985; Burke and Sengör, 1986; Almond and Ahmed, 1987; Abdelsalam and Dawoud, 1991; Stern, 1994; Abdelsalam et al., 1995, 1998; Abdelsalam and Stern, 1996b; Johnson et al., 2011; Fritz et al., 2013; Abdelrahman et al., 2017). The shift from juvenile Hf, Nd, Sr, O and Pb signature of the bulk of Neoproterozoic arc terranes, except from the reworked Paleoproterozoic Khida crustal block (Fig. 1-1b; Whitehouse et al., 2001), to the more evolved isotopic compositions of surrounding Archean to Paleoproterozoic cratons is used to delimitate the position of the Keraf arc-continent suture between the ANS and West Gondwana (Ries et al., 1985; Denkler et al., 1993; Sultan et al., 1993, 1994; Harms et al., 1994; Küster and Liégeois, 2001; Bailo et al., 2003; Küster et al., 2008; Evuk, 2013; Evuk et al., 2014, 2017; Johnson, 2014). Nevertheless, Pan-African tectono-metamorphic and magmatic events are recorded west to the Keraf suture, in the Bayuda and Sabaloka terranes which are parts of the Saharan meta-craton (*e.g.,* Ries et al., 1985; Kröner et al., 1987; Rahman et al., 1990; Küster and Liégeois, 2001), making the boundaries of the Keraf suture highly uncertain (*e.g.,* Abdelsalam and Stern, 1996b; Ahmed Suliman, 2000; Küster and Liégeois, 2001; Evuk et al., 2014). Besides, the widespread influence of Pan-African tectono-magmatic events on the evolution of the flank of West Gondwana is hardly understood at the lithospheric scale.

2.3. Lithological-tectonic evolution of the Keraf arc-continent suture

The lithological framework of the central Keraf suture records different geodynamical settings such as magmatic arc and back-arc basin (volcanoclastic sequences and andesitic flows; *e.g.,* Schandelmeier et al., 1994b; Stern, 1994; Abdelsalam et al., 1995; Abdelrahman et al., 2017; Perret et al., under review[1]) and passive continental margin (carbonate-rich and siliciclastic meta-sediments; *e.g.,* Stern et al., 1993). These rocks have been affected by deformation during Keraf suturing, *i.e.,* oceanic subduction and arc-continent collision (Fig. 1-2; Ahmed Suliman, 2000; Perret et al., under review).

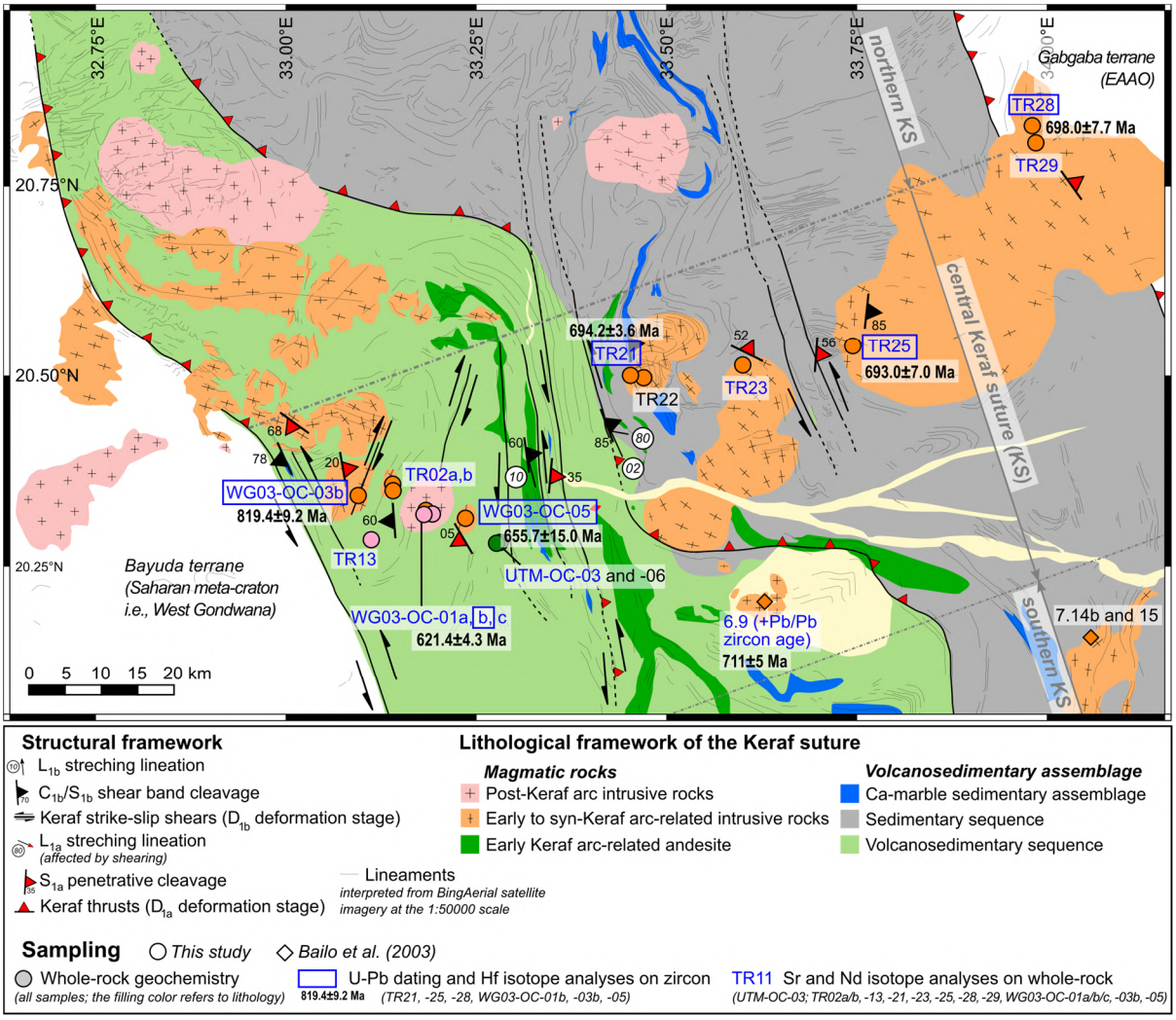


Figure 1-2: Geological map of the central Keraf suture, adapted after Bailo et al. (2003), Managem (2011), and field observations (Perret et al., under review). The location of samples used in this study is indicated as well as the analytical work carried out for each of them (Table 1-1). Samples from Bailo et al. (2003) located in the map extent and discussed in the text are shown. Geographic coordinates are reported as WGS 84.

[1] **Chapter III**

Initial convergence and ocean closure occurred along a north-trending magmatic arc system that was active at *ca.* 800-750 Ma (Abdelsalam et al., 1998; Bailo et al., 2003). Then, an oblique convergence D_{1a} resulted into arc-continent collision between *ca.* 750-640 Ma expressed by Keraf west-verging thrusting and the regional S_{1a} penetrative fabric in the central Keraf suture (Fig. 1-2; Abdelsalam et al., 1998; Perret et al., under review). Finally, progressive deformation D_{1b} translated thrusting into sinistral shearing at *ca.* 640-580 Ma, which led to the formation of C_{1b} shear zones throughout the central Keraf suture (Fig. 1-2; Abdelsalam et al., 1998; Perret et al., under review).

3. Sampling and analytical techniques

3.1. Sampling philosophy and field observations

We present geochemical and isotopic data from igneous rocks (n=16) cropping out along a southwest-trending transect through the central Keraf suture (Fig. 1-2). Sample location and the analytical work carried out for each of them are given in Table 1-1. We distinguish between early (n=5) and syn-Keraf arc-related rocks and (n=5 and 8, respectively) on one hand, and undeformed post-Keraf arc plutons (n=3) on the other hand. These groups are separated relying on the regional lithological-structural framework suggested by Perret et al. (under review). The separation between early and syn-Keraf arc-related rocks is suggested by geochemical, geochronological and isotopic evidence presented further in this study (see section 4.). For convenience, the "meta-"prefix will not precede the name of deformed and metamorphosed rocks in what follows.

Sample ID	Easting (°)	Northing (°)	Description*	Results presented in this study		
				Whole-rock geochemistry (Figs. 1-5 and 1-6; Table 1-2)	*U-Pb and Hf isotopes on zircon (Figs. 1-7 and 1-8; Tables 1-3 and 1-4)*	*Sr-Nd isotopes on whole-rock (Fig. 1-8; Table 1-5)*
Early Keraf arc-related samples						
TR02a	33.1402	20.3577	Quartz-diorite	x		x
UTM-OC-03	33.3027	20.2845	Andesite	x		x
UTM-OC-06	33.2990	20.2829	Andesite	x		
WG03-OC-01c	33.1837	20.3234	Monzodiorite	x		x
WG03-OC-03b	33.0950	20.3431	Quartz-diorite	x	x	x
Syn-Keraf arc-related samples						
TR02b	33.1405	20.3578	Granodiorite	x		x
TR21	33.4512	20.5002	Quartz-monzodiorite	x	x	x
TR22	33.4698	20.4969	Quartz-monzodiorite	x		
TR23	33.6000	20.5142	Granodiorite	x		x
TR25	33.7448	20.5399	Diorite	x	x	x
TR28	33.9806	20.8292	Quartz-monzodiorite	x	x	x
TR29	33.9851	20.8068	Granodiorite	x		x
WG03-OC-05	33.2364	20.3132	Granodiorite	x	x	x
Post-Keraf arc-related samples						
TR13	33.1125	20.2853	Monzogranite	x		x
WG03-OC-01a	33.1838	20.3233	Granodiorite	x		x
WG03-OC-01b	33.1838	20.3233	Monzogranite	x	x	x

Geographic coordinates are reported as WGS84.
**Protolith lithologies are mentioned for early to syn-Keraf arc-related ortho-derived rocks which have undergone deformation and metamorphism, relying on Streckeisen (1976) classification.*

Table 1-1: List of studied samples. Geographic coordinates are reported as WGS 84. Analytical work carried out for each sample is detailed.

3.1.1. Early to syn-Keraf arc-related igneous rocks

Early Keraf arc-related volcanic rocks are schistose low-grade andesite interlayered with volcanoclastic and sedimentary rocks (Fig. 1-3a). They form together the volcanosedimentary series which dominates the regional lithological framework (Fig. 1-2). This assemblage is strongly affected to completely transposed by the regional S_{1a} penetrative fabric related to Keraf thrusting (Figs. 1-2, 1-3a).

Early to syn-Keraf arc-related complex batholiths intrude within the volcanosedimentary series (Fig. 1-2). They range from dioritoids to granitoids according

to field observations (according to nomenclature of Le Maitre et al., 2005). The plutonic rocks variably express the S_{1a} gneissic foliation as their selvages may be intensively deformed whereas their inner part look undeformed (Fig. 1-3c and d). The dip-plunging L_{1a} stretching lineation is locally preserved where the S_{1a} gneissic foliation is the best expressed (Fig. 1-3d). C_{1b} Keraf strike-slip shear zones visible at the regional scale may cut across these batholiths as expressed by the S_{1b} penetrative fabric at the macroscopic scale (Figs. 1-2, 1-3b).

3.1.2. Post-Keraf arc-related igneous rocks

Post-Keraf arc granitoids are plutons of variable size in map view (Fig. 1-2) and typically cropping out as up to tens of m-high piles composed of up to several m-large boulders (Fig. 1-3e). The presence of feldspar phenocrysts or xenocrysts in an intermediate term (WG03-OC-01a) and diffuse contacts with the more felsic coarse-grained host granitoid (WG03-OC-01b) witness the interactions between felsic and intermediate magmas that may be interpreted as mechanical mingling between two coexisting magmas (Fig. 1-3f). Mafic xenoliths (WG03-OC-01c) are enclosed in the pluton (Fig. 1-3f). Except from a weak magmatic fabric rarely observed, the post-Keraf arc intrusive rocks show no anisotropic feature at the macroscopic scale.

Figure 1-3 (p. 77): Early, syn- to post-Keraf arc igneous rocks of the central Keraf suture. Outcrop location refers to sample ID in Figure 1-2. Indexing of structures refers to regional deformation stages (Fig. 1-2; Perret et al., under review). **a** The early Keraf arc-related andesite is schistose as affected by the regional S_{1a} penetrative fabric. **b** The early Keraf arc-related dioritoid is foliated along the S_{1b} cleavage in a C_{1b} shear zone. **c-d** Syn-Keraf arc-related plutonic rocks are dioritoids to granitoids more or less foliated along the regional S_{1a} penetrative fabric. **e-f** Post-Keraf arc granitoids crop out as undeformed intrusions cutting across the regional structures. They display a mingling texture between an intermediate and a more felsic terms (WG03-0C-01a and b, respectively) and they enclose dioritoid xenoliths (WG03-0C-01c).

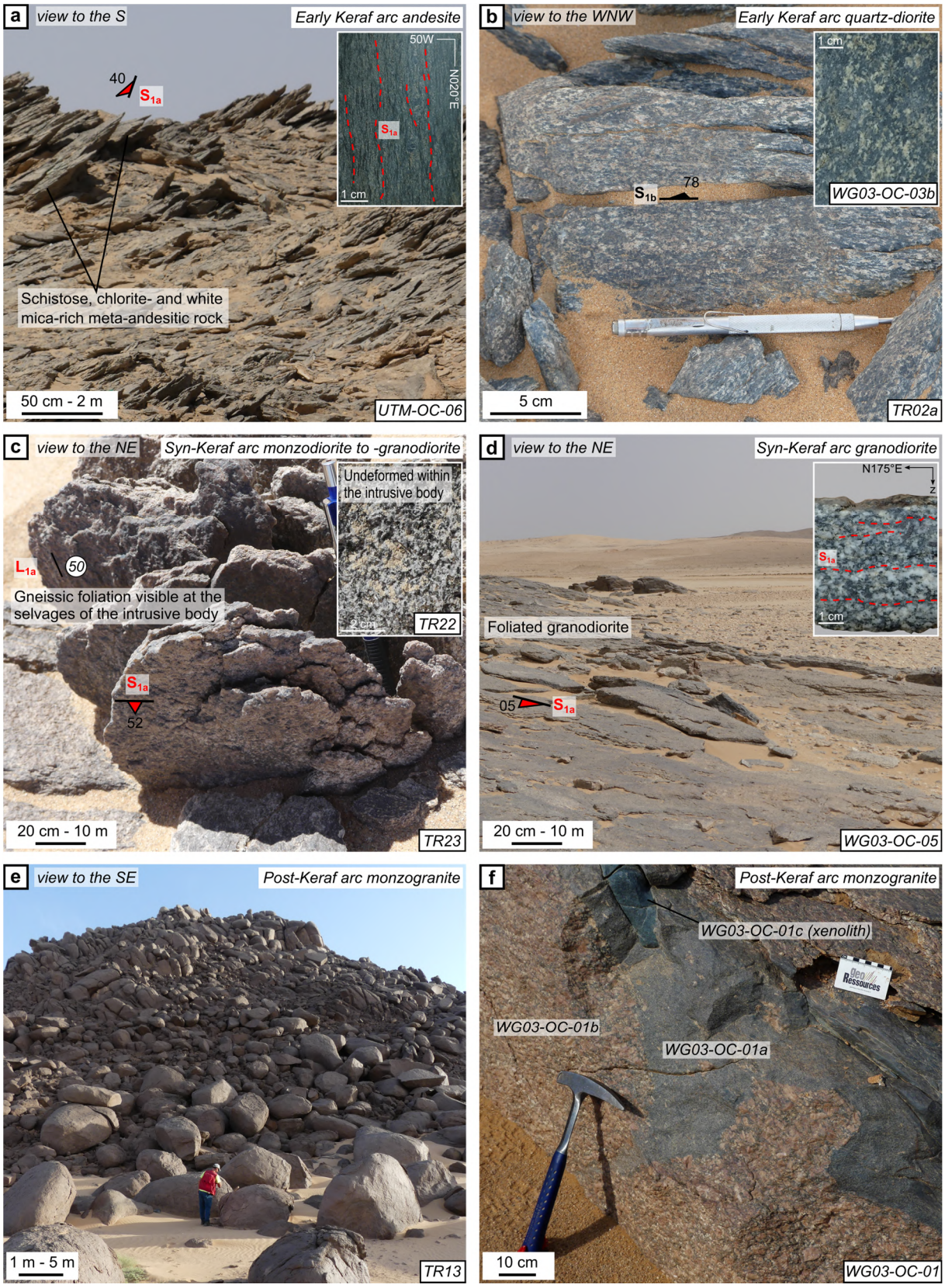


Figure 1-3: Early, syn- to post-Keraf arc igneous rocks of the central Keraf suture. See detailed caption on p. 76.

3.2. Analytical techniques

3.2.1. Whole-rock geochemistry

Whole-rock major and trace element compositions of sixteen samples were respectively determined by inductively-coupled plasma optical emission spectrometry and mass spectrometry, using a Thermo Fischer ICap 6500 and a Thermo Fischer IcapQ spectrometers, respectively, at the Service d'Analyse des Roches et des Minéraux (SARM, CRPG-CNRS, Vandœuvre-lès-Nancy, France). Sample preparation, analytical conditions and limits of detection are detailed in Carignan et al. (2001). Relative analytical uncertainties are close to 2% for major elements, and between 5% and 20% for trace elements depending on their concentration. The whole-rock S concentration of studied samples has been measured using a CS-analyzer with an approximate limit of detection of 0.01 wt. %. The whole-rock Au concentration has been measured by ALS for three samples *via* fire assay and inductively-coupled plasma atomic emission spectroscopy analysis, with a limit of detection of 1 ppb.

3.2.2. Zircon separation and imagery

Six samples were selected for U-Pb dating and Hf isotope analyses on zircon (Table 1-1). Zircon separation was performed at the Centre de Recherches Pétrographiques et Géochimiques (CRPG-CNRS, Vandœuvre-lès-Nancy, France). Samples were crushed using a jaw and then a roll crusher. Zircon grains were extracted from the 75-125 and 125-250 µm size fractions using a Frantz magnetic separator and di-iodomethane heavy liquid separation with a density of 3.32 g/cm^3. Selected zircon grains of various shape and size were handpicked in ethanol using a binocular microscope. The most representative crystals were mounted into epoxy resin blocks and then ground and polished to expose their center parts. They were imaged using back-scattered and secondary electron scanning microscopy (BSE- and SE-SEM) at the Karlsruhe Institute of Technology (Germany).

Analyzed zircon grains range from weakly to strongly prismatic grains with a pyramidal shape and show no to strong oscillatory magmatic zoning (Fig. 1-4). They all show patchy recrystallization patterns. Rounded and fractured zircon grains are recovered from syn-Keraf arc-related and post-Keraf arc samples.They are interpreted as inherited. As well as potential antecrysts and xenocrysts, inherited zircon grains may serve as substrate for later zircon autocryst overgrowing (Fig. 1-4; Miller et al., 2007). Further cathodoluminescence imagery will be carried out at the GeoRessources laboratory (Vandœuvre-lès-Nancy, France) in the weeks to come to better image internal textures and zoning patterns in zircon to classify them.

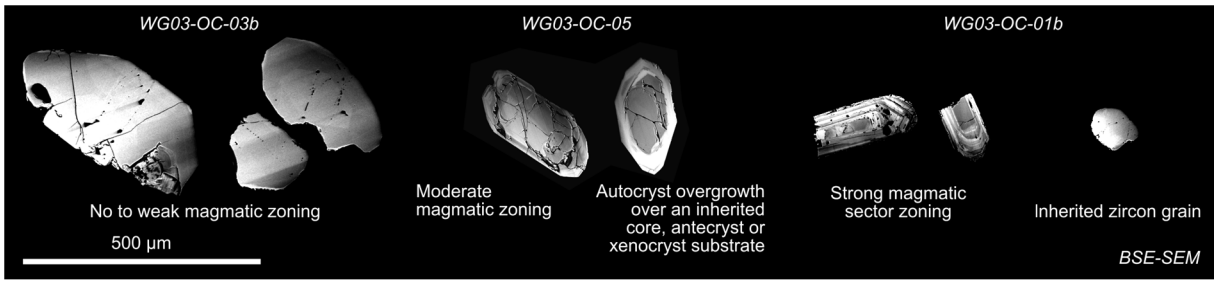


Figure 1-4: Scanning electron microscopy image representative of dated zircon grains in back-scattered electron mode (BSE-SEM).

3.2.3. U-Pb dating and Hf isotope analyses of zircon

Zircon grains were first analyzed for U-Pb and later for Hf isotopes by laser ablation-inductively coupled plasma-sector fieldmass spectrometry (LA-ICP-SF-MS). A first U-Pb analytical session was performed with a Resonetics M50 193 nm Excimer laser system coupled to a Thermo-Scientific ELEMENT 2 at Goethe University (Frankfurt, Germany) for samples WG03-OC-01a, -03b and -05. A second U-Pb analytical session was carried out at Karlsruhe Institute of Technology (Germany) for samples TR21, TR25 and TR28. Hf isotopes were analyzed with a Resonetics M50 193 nm Excimer laser system coupled to a Thermo-Scientific NEPTUNE at Goethe University (Frankfurt, Germany) for all samples. Instruments and processing parameters are described by Gerdes and Zeh (2009) with modifications in Zeh and Gerdes (2012). Laser spots of 40-50 µm diameter

for Hf isotope analyses were placed on-top of U-Pb laser spots of 25-33 µm-diameter. Zircon standards used in the bracketing procedure are: (i) GJ-1 (Jackson et al., 2004), Plešovice (Sláma et al., 2008), BB (Santos et al., 2017) and Kaap Valley (Takenaka et al., 2015) for U-Pb dating; (ii) GJ-1 (Morel et al., 2008) and Temora 1 and 2 (Woodhead et al., 2004; Xu et al., 2004; Woodhead and Hergt, 2005; Wu et al., 2006) for Hf isotopes. $\varepsilon Hf_{(i)}$ values are calculated back to $^{206}Pb/^{238}U$ single zircon concordant ages for magmatic zircon grains.

3.2.4. Sr and Nd whole-rock isotope analyses

Fourteen samples were investigated for their Sr and Nd isotope whole-rock signature. Analyses were carried out at the CRPG-CNRS (Vandœuvre-lès-Nancy, France). Between 100 and 200 mg of bulk powders are dissolved by adding 4 mL of concentrated HNO_3 and 1 mL of concentrated HF and heating for one to two days at 115°C. Samples were then dried down and heated again at 125°C for one day after the addition of HCl. Then, samples are mixed with 2 mL HNO_3 and chromatographic columns are used to separate Sr, Rb and rare earth elements (REE) following the methods of Pin et al. (1994) and Pin and Zalduegui (1997) which involve the TRU.Spec resin to extract the REE from the matrix, the Sr.Spec to separate Sr and the Eichrom LN.Spec to isolate Nd and Sm.

For Sr isotopic compositions, the resulting solutions were analyzed with a Triton Plus thermal ionization mass spectrometer. Among the five Faraday cages used, one monitors Rb. Internal normalization was applied using $^{86}Sr/^{88}Sr = 0.1194$, in order to correct for instrumental fractionation. Standard NBS987, certified by the National Institute of Standards and Technology, was analyzed after every third sample for quality assurance. Sr total chemistry blanks consistently yielded to values below 100 pg which are negligible relative to the quantities of Sr measured in the samples. For Nd isotopic compositions, the solutions were analyzed with a Neptune multi-collection ICP-MS. Internal normalization was applied using $^{146}Nd/^{144}Nd = 0.7219$, in order to correct for

instrumental fractionation (Luais et al., 1997). Standard JNdi (Tanaka et al., 2000) was analyzed after every third sample for quality assurance. Nd and Sm total chemistry blanks were highly reproducible, consistently yielding to values below 100 pg which are negligible relative to the quantities of Nd and Sm measured in the samples.

Initial $(^{87}Sr/^{86}Sr)_i$, $(^{143}Nd/^{144}Nd)_i$ and $\varepsilon Nd_{(i)}$ were subsequently obtained by back-calculation to ages of igneous crystallization determined by U–Pb dating on zircon. We approximated the crystallization age for undated samples relying on field petrographic and geochemical relationships with dated samples.

4. Results

4.1. Whole-rock geochemistry

4.1.1. Early Keraf arc-related igneous rocks

With SiO_2 contents ranging from 44.4 to 49.5 wt. %, early Keraf arc-related igneous rocks are mostly mafic rocks except for one which is intermediate (WG03-OC-03b with 55.7 wt. % SiO_2; Table 1-2). Regarding their major element composition, volcanic rocks are andesite whereas plutonic rocks are quartz-diorite to monzodiorite (Fig. 1-3a, b; Table 1-1). In the feldspar diagram, the plutonic rocks are weakly potassic as they plot along the plagioclase feldspar trend (Fig. 1-5a). Both plutonic and volcanic rocks are metaluminous (Fig. 1-5b).

Normalized to chondrite (Sun and McDonough, 1989), andesite, quartz-diorite and monzodiorite display fairly flat light to heavy rare earth element (LREE and HREE) patterns with an abundance enrichment ratio of ~10-30 relative to chondrite and slightly higher values for LREE than HREE (La_N/Nd_N in the range of ~1.0-1.3, Dy_N/Lu_N in the range of ~1.1-1.3; Fig. 1-6a, d). Sr and Eu anomalies are defined by $Eu_N/Eu^*_N = Eu_N/(Sm_N.Gd_N)^{0.5}$ and $Sr_N/Sr^*_N = Sr_N/(Pr_N.Nd_N)^{0.5}$ ratios, respectively. Andesite shows no to low negative Sr and Eu anomalies whereas plutonic rocks may present relatively

high Sr (*e.g.*, ~3) and moderate Eu positive (*e.g.*, ~1.2) anomalies, for (*e.g.*, quartz-diorite sample; Fig. 1-6e). These positive anomalies may indicate plagioclase accumulation and the cumulate nature of the dioritoids (Chappell and Wyborn, 2004). It is worth noticing that the mafic monzodiorite xenolith enclosed in the post-Keraf arc granitoid pluton (Fig. 1-3f; Table 1-1) has broadly the same major and trace element composition as early Keraf arc-related dioritoids.

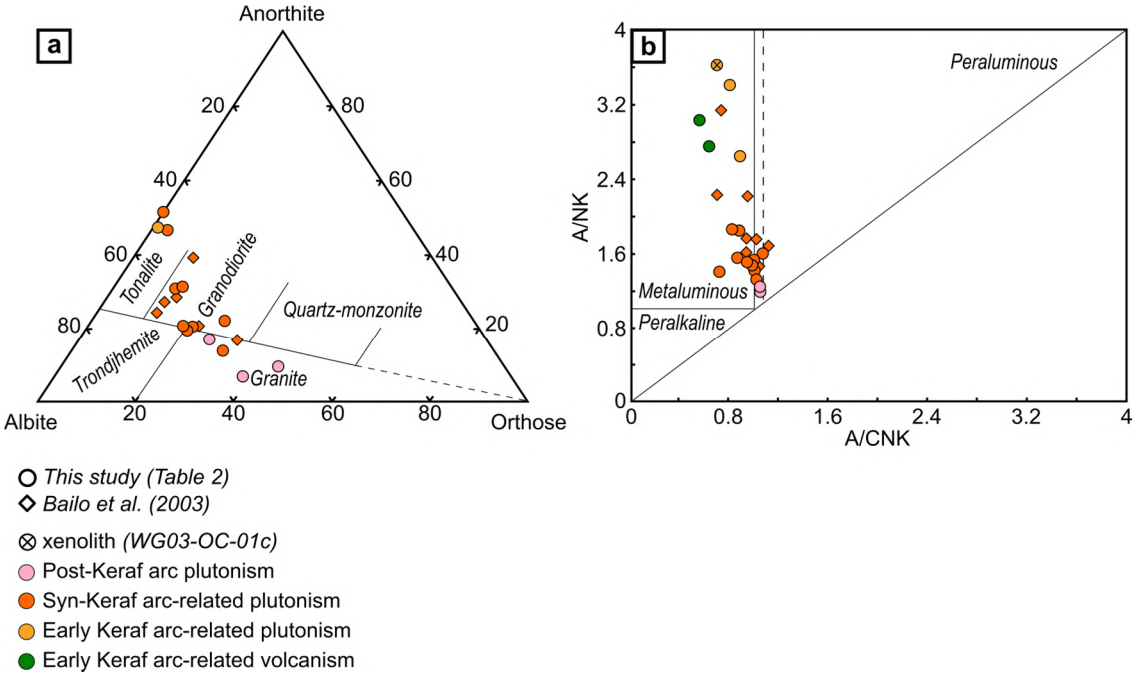


Figure 1-5: Whole-rock major element composition of samples from this study (circles) and syn-Keraf arc-related samples from Bailo et al. (2003) (diamonds). **a** Feldspar triangle for plutonic rocks with > 10% modal quartz (O'Connor, 1965). **b** A/CNK vs A/NK crossplot for all samples (Shand, 1943). The dashed line represents the incertitude field between the metaluminous and peraluminous domains. Whole-rock compositions of samples from this study are compiled in Table 1-2.

4.1.2. Syn-Keraf arc-related igneous rocks

The major element compositions classify syn-Keraf arc-related granitoids as part of an intermediate to felsic, metaluminous, I-type diorite-granodiorite-granite suite (Figs. 1-3b-d, 1-5; Table 1-1). They consistently display REE patterns with a steeper decreasing slope for LREE than for HREE (La_N/Nd_N in the range of ~1.5-3.3, Dy_N/Lu_N in the range of ~0.8-1.8; Fig. 1-6b, d). The steeper the LREE slope, the higher the LREE enrichment and the lower the HREE and Y abundances relative to chondrite are (*e.g.*, La_N/Nd_N =

3.3 / enrichment factor of 200 for La / <3 ppm ΣHREE for WG03-OC-05 granodiorite *vs* La_N/Nd_N = 1.8 / enrichment factor of 75 for La / >11 ppm ΣHREE for TR29 granodiorite; Fig. 1-6b, f). Moreover, half of the studied granitoids have a Sr anomaly between 1.5 and 2 (Fig. 1-6e), suggesting again their probable cumulate nature.

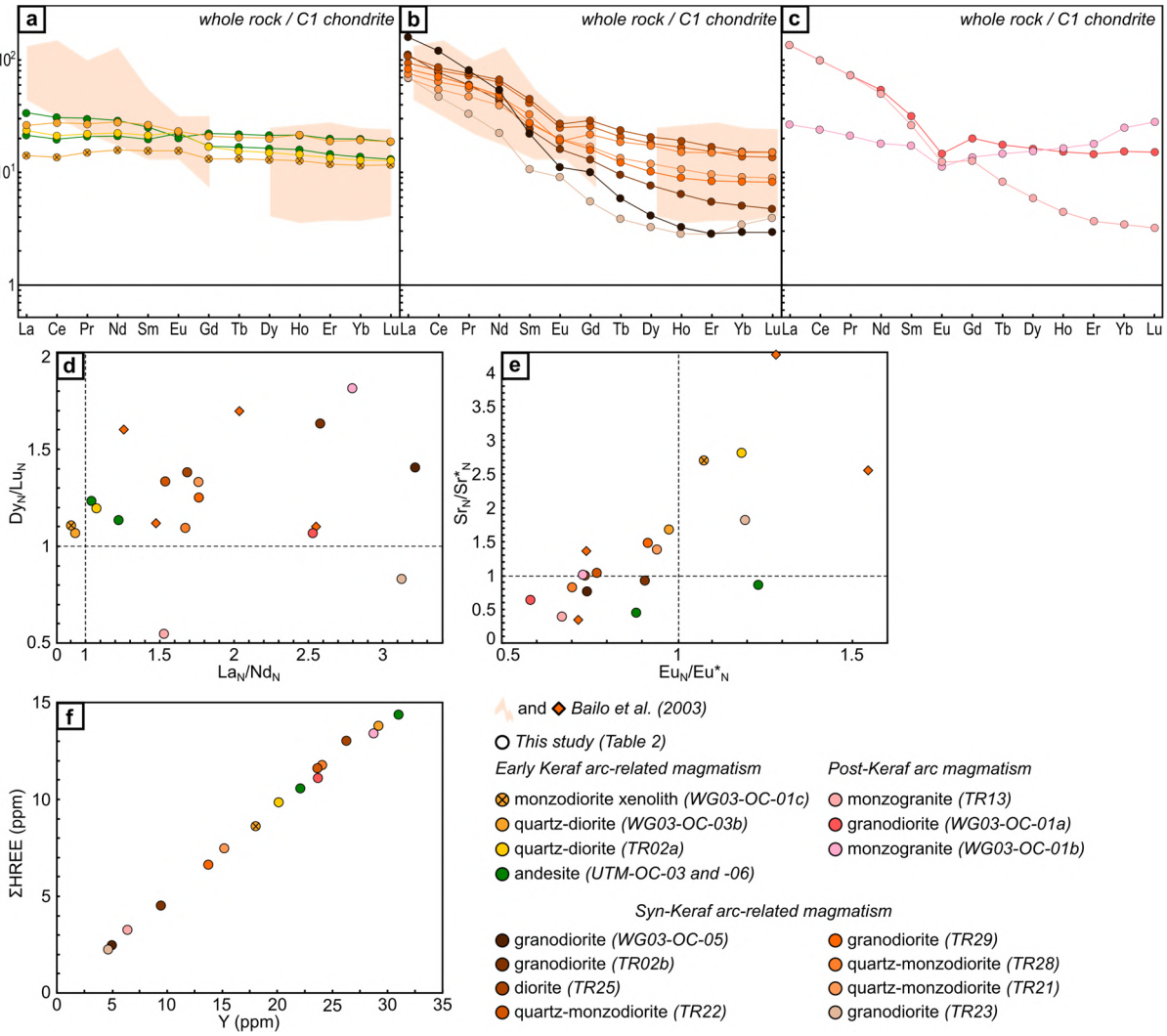


Figure 1-6: Whole-rock trace element composition of samples from this study (circles) and syn-Keraf arc-related samples from Bailo et al. (2003) (diamonds). Distinct hues are considered to separate between rocks belonging to a given generation. **a-c** C1 chondrite-normalized rare earth trace element diagrams for (**a**) early, (**b**) syn-Keraf arc-related and (**c**) post-Keraf arc igneous rocks. **d** C1 chondrite-normalized La_N/Nd_N vs Dy_N/Lu_N ratio crossplot (Sun and McDonough, 1989). The dashed lines represent flat LREE and HREE patterns. **e** Eu_N/Eu^*_N vs Sr_N/Sr^*_N anomaly crossplot. Eu and Sr anomalies are calculated as the ratio between the C1 chondrite-normalized Eu_N and Sr_N values with $Eu^*_N = (Sm_N.Gd_N)^{0.5}$ and $Sr^*_N = (Pr_N.Nd_N)^{0.5}$, respectively (Sun and McDonough, 1989). The dashed lines represent null Eu and Sr anomalies. **f** Y vs ΣHREE (from Tb to Lu) crossplot. Whole-rock compositions of samples from this study are compiled in Table 1-2.

4.1.3. Post-Keraf arc-related igneous rocks

Post-Keraf arc plutons are formed by felsic rocks (> 60 wt. % SiO_2; Table 1-2) that plot in the granite field of the feldspar diagram (Fig. 1-5a). They are mostly formed by coarse-grained monzogranite-granodiorite assemblage (WG03-OC-01b and -01a, respectively; Fig. 1-3f; Table 1-1). It is unclear whether these rocks are metaluminous or peraluminous (Fig. 1-5b). They show very distinct REE patterns, even for the granodiorite and monzogranite samples collected on the same outcrop, confirming they result from the mixing of different magmas as suggested from textural evidence (Figs. 1-3f, 1-6c). From one sample to another, there is a change in the LREE decreasing slope value although it remains consistent with the range of values observed for syn-Keraf arc-related granitoids (La_N/Nd_N in the range of ~1.5-3.1; Fig. 1-6c, d). Besides, post-Keraf arc plutons may show a bell-shaped concave-down pattern with a slight depletion in intermediate REE relative to LREE and HREE (*e.g.,* WG03-OC-01b), flat or decreasing HREE pattern with enrichment ratios relative to chondrite similar to syn-Keraf arc-related granitoids (*e.g.,* WG03-OC-01a and TR13, respectively; Fig. 1-6c, d, f). The most consistent geochemical features that help to separate post-Keraf arc plutons from earlier igneous rocks are their null to negative Sr and Eu anomalies (~0.3-1 and ~0.65-0.75, respectively; Fig. 1-6e).

ID	*Early Keraf arc-related samples*					*Syn-Keraf arc-related samples*								*Post-Keraf arc samples*		
	TR02a	UTM-OC-03	UTM-OC-06	WG03-OC-01c	WG03-OC-03b	TR02b	TR21	TR22	TR23	TR25	TR28	TR29	WG03-OC-05	TR13	WG03-OC-01a	WG03-OC-01b
Major elements (wt. %)																
SiO_2	49.5	47.4	44.4	45.3	55.7	68.2	58.7	56.8	73.2	58.9	62.3	68.2	72.8	72.6	68.6	69.8
Al_2O_3	18.0	12.1	13.3	17.7	16.9	15.0	15.8	16.3	13.4	16.4	15.3	15.2	13.6	13.7	15.4	15.0
Fe_2O_3	11.0	9.8	10.2	11.5	10.0	2.9	6.4	7.8	1.5	4.4	5.9	3.3	2.3	1.5	3.1	3.4
MnO	0.20	0.11	0.14	0.21	0.21	0.04	0.09	0.12	0.04	0.05	0.09	0.06	0.03	0.03	0.07	<0.02
MgO	5.0	4.9	7.0	6.7	2.7	1.2	2.9	3.2	0.39	3.3	2.3	1.2	0.96	0.26	0.77	0.09
CaO	9.6	9.2	9.2	11.4	7.1	2.9	5.3	6.2	1.7	6.1	4.4	3.4	2.4	1.3	2.5	0.98
Na_2O	3.0	2.4	2.9	1.9	3.7	4.5	4.3	4.3	4.1	6.8	4.0	4.7	3.9	3.5	4.6	4.6
K_2O	0.31	<0.03	0.06	1.6	0.32	2.4	1.4	1.6	3.3	0.50	3.1	2.2	1.9	4.8	3.1	4.7
TiO_2	0.97	1.3	1.4	0.83	1.2	0.41	0.76	1.0	0.17	1.5	0.83	0.51	0.35	0.20	0.40	0.19
P_2O_5	0.28	0.15	0.14	0.11	0.35	0.13	0.21	0.29	<0.10	0.34	0.22	0.19	0.14	<0.10	0.13	<0.10
S	<0.01	<0.01	<0.01	<0.01	<0.01	<0.01	<0.01	<0.01	0.02	<0.01	<0.01	<0.01	<0.01	<0.01	0.01	<0.01
L.O.I.	1.1	11.4	10.6	1.5	1.1	1.6	3.0	1.2	1.1	0.98	0.80	0.77	0.72	1.1	0.53	0.62
Minor and trace elements (ppm)																
Au*					11								5			2
As	0.53	4.5	16.4	0.98	<0.53	<0.53	2.0	4.6	1.9	2.0	6.7	0.67	<0.53	<0.53	0.54	0.73
Ba	132	15.3	21.6	171	115	665	337	360	1122	248	409	463	509	637	625	377
Be	0.60	0.42	0.53	0.60	0.61	1.4	0.99	1.1	0.94	1.1	1.3	1.1	1.4	2.0	2.9	3.0
Bi	<0.05	<0.05	<0.05	0.26	<0.05	0.06	0.05	0.08	<0.05	<0.05	0.11	0.05	<0.05	0.06	0.09	<0.05
Cd	0.39	0.03	0.10	0.14	0.11	0.19	0.07	0.12	0.05	0.07	0.09	0.07	0.05	0.07	0.10	0.07
Co	29.6	28.7	23.8	37.3	15.4	6.0	16.8	21.5	2.0	12.0	15.0	7.2	3.6	1.7	4.9	1.3
Cr	66.5	93.1	306	63.9	6.8	22.5	56.2	40.4	6.0	45.7	45.6	15.6	12.8	5.2	13.8	7.7
Cs	0.41	<0.02	0.07	3.9	0.25	1.1	0.95	1.1	1.2	0.2	2.6	0.76	2.8	2.2	2.1	1.2
Cu	106	37.1	43.7	68.5	40.9	17.2	37.4	31.2	7.9	8.4	61.6	12.4	5.6	5.0	28.6	3.8
Ga	21.2	15.3	14.5	18.1	19.6	21.0	20.4	20.7	14.2	18.9	19.0	19.4	17.5	19.6	20.8	23.1
Ge	1.4	1.2	1.3	1.5	1.4	0.92	1.1	1.3	1.1	1.2	1.3	1.0	0.81	0.99	1.2	1.3
Hf	0.45	3.0	2.2	1.0	1.7	4.5	3.6	4.7	2.4	9.5	6.7	3.7	3.7	4.7	5.1	12.3
In	0.08	0.06	0.07	0.07	0.08	<0.03	0.05	0.06	<0.03	0.04	0.05	<0.03	<0.03	<0.03	<0.03	<0.03

Table 1-2 ***(continued)***

ID	*Early Keraf suture samples*					*Syn Keraf suture samples*								*Post-Keraf suture samples*		
	TR02a	UTM-OC-03	UTM-OC-06	WG03-OC-01c	WG03-OC-03b	TR02b	TR21	TR22	TR23	TR25	TR28	TR29	WG03-OC-05	TR13	WG03-OC-01a	WG03-OC-01b
Minor and trace elements (ppm)																
Mo	<0.50	<0.50	<0.50	<0.50	<0.50	0.83	1.1	0.70	<0.50	0.82	0.59	0.51	0.58	<0.50	0.60	1.9
Nb	1.5	5.1	5.8	1.2	2.1	3.5	2.7	3.3	2.3	3.5	4.6	3.2	2.2	7.6	10.7	5.9
Ni	17.7	36.6	90.6	601	18.2	91.4	506	21.3	86.6	245	215	16.3	6.8	4.2	162	17.4
Pb	9.8	0.93	0.73	4.9	4.8	9.3	5.6	6.8	13.3	2.3	8.8	7.7	8.7	19.8	13.1	25.1
Rb	7.0	0.39	0.65	125	7.1	53.3	31.8	35.3	61.2	3.1	86.3	35.0	68.2	152	105	138
Sb	0.17	0.87	0.36	<0.06	0.07	0.12	0.27	0.48	0.48	0.23	0.61	0.16	<0.06	0.08	<0.06	<0.06
Sc	36.1	34.4	39.0	50.5	32.0	6.2	14.8	15.6	1.4	17.9	13.4	5.7	3.7	2.4	3.4	1.1
Sn	0.47	1.2	0.98	0.78	0.75	2.0	1.1	1.8	0.68	1.5	2.3	1.0	1.2	2.7	2.3	1.6
Sr	443	95.2	129	296	327	341	433	499	361	506	307	578	357	170	292	139
Ta	0.10	0.43	0.46	0.09	0.16	0.37	0.22	0.28	0.36	0.32	0.51	0.37	0.28	0.92	1.2	0.86
Th	0.09	0.96	0.37	0.20	2.0	6.5	3.0	4.5	5.7	2.8	6.2	3.1	10.9	21.6	9.5	101
U	0.05	0.28	0.14	0.46	1.8	2.5	0.83	1.0	1.5	1.6	2.4	1.3	2.8	4.9	4.3	22.9
V	265	235	223	263	133	42.9	119	146	9.7	91.7	109	48.6	23.2	10.1	30.4	22.8
W	<0.80	2.0	1.1	<0.80	<0.80	<0.80	<0.80	<0.80	<0.80	<0.80	<0.80	<0.80	<0.80	<0.80	<0.80	<0.80
Y	20.2	31.1s	22.1	18.1	29.2	9.5	15.2	23.7	4.7	26.3	24.1	13.8	5.0	6.5	23.7	28.8
Zn	138	74.3	91.0	107	125	63.1	77.4	89.0	40.8	19.7	67.6	54.6	50.1	48.5	66.7	12.3
Zr	14.8	101	80.0	24.9	48.1	179	134	165	81.5	428	244	131	142	147	189	326
La	5.6	8.1	5.1	3.3	6.0	26.8	16.5	22.5	16.6	26.1	18.5	19.9	40.6	33.0	32.1	6.4
Ce	12.7	18.7	11.9	8.2	17.1	48.6	34.0	50.2	29.2	54.1	39.3	44.5	75.5	61.6	61.4	14.9
Pr	2.0	2.8	1.9	1.4	2.5	5.6	4.5	6.8	3.1	7.1	5.3	5.7	7.5	6.7	6.9	2.0
Nd	10.3	13.1	9.6	7.2	12.7	20.4	18.5	29.0	10.5	30.5	21.9	22.2	24.8	23.2	25.0	8.2
Sm	3.1	3.8	2.9	2.3	3.8	3.6	4.0	6.2	1.6	6.7	4.9	4.2	3.3	3.9	4.8	2.6
Eu	1.3	1.2	1.3	0.87	1.3	0.91	1.1	1.4	0.52	1.5	1.1	1.1	0.63	0.70	0.83	0.64
Gd	3.4	4.4	3.4	2.6	4.2	2.6	3.4	5.2	1.1	5.9	4.4	3.2	2.0	2.5	4.0	2.7
Tb	0.56	0.79	0.60	0.47	0.75	0.35	0.49	0.76	0.14	0.87	0.68	0.45	0.22	0.30	0.64	0.54
Dy	3.7	5.3	4.0	3.1	4.9	1.9	2.9	4.5	0.81	5.2	4.3	2.6	1.0	1.5	4.0	3.8

Table 1-2 ***(continued)***

ID	*Early Keraf suture samples*					*Syn Keraf suture samples*								*Post-Keraf suture samples*		
	TR02a	UTM-OC-03	UTM-OC-06	WG03-OC-01c	WG03-OC-03b	TR02b	TR21	TR22	TR23	TR25	TR28	TR29	WG03-OC-05	TR13	WG03-OC-01a	WG03-OC-01b
Minor and trace elements (ppm)																
Ho	0.79	1.2	0.87	0.69	1.1	0.35	0.59	0.92	0.16	1.1	0.92	0.50	0.18	0.24	0.85	0.90
Er	2.1	3.1	2.3	1.9	3.0	0.89	1.6	2.5	0.45	2.7	2.5	1.4	0.46	0.60	2.4	2.9
Tm	0.32	0.48	0.35	0.29	0.47	0.13	0.23	0.35	0.07	0.38	0.38	0.20	0.07	0.08	0.37	0.53
Yb	2.0	3.1	2.2	1.9	3.0	0.82	1.5	2.3	0.56	2.5	2.6	1.4	0.48	0.55	2.5	4.1
Lu	0.31	0.46	0.32	0.28	0.46	0.12	0.22	0.34	0.10	0.38	0.39	0.20	0.07	0.08	0.38	0.69
Total	99.0	98.8	99.3	98.7	99.1	99.2	98.8	98.8	98.9	99.2	99.2	99.6	99.1	99.0	99.2	99.4

L.O.I. = loss on ignition.

Total is given in wt. %.

**Au data are from ALS fire assays carried out for WG03-OC-01b, -03b and -05 samples.*

Table 1-2: List of studied samples. Geographic coordinates are reported as WGS 84. Analytical work carried out for each sample is detailed.

4.2. U-Pb ages of zircon

U-Pb and Hf isotope laser spot emplacements on BSE-SEM images of dated zircon grains are provided in Supplementary Material 1-1. Results and raw data processing details for U-Pb data are given in Table 1-3. U-Pb isotopic compositions of zircon standards used in this study are provided in Supplementary Material 1-2. We follow the nomenclature of Miller et al. (2007) to determine the inherited, xenocrystic, antecrystic or autocrystic of dated zircon grains.

4.2.1. Early Keraf arc-related quartz-diorite

Recovered zircon grains from *WG03-OC-03b quartz-diorite* are subhedral, fractured, more or less prismatic, the coarsest ones (> 100 µm) being more rounded (Fig. 1-4). U content is low (up to 131 ppm) and Th/U ratios are typically magmatic, varying between 0.4 and 0.7. Twenty-five measurements were made on the same number of zircon grains. Two analyses (a209 and a211) have been filtered as their degree of concordance is over the 95-105 % range considered for concordant datapoints. $^{206}Pb/^{238}U$ single zircon ages span continuously over *ca.* 840-820 Ma. The spread in $^{206}Pb/^{238}U$ concordant ages must be interpreted in terms of magmatic processes. There is indeed no textural, nor geochemical and analytical evidence for the existence of any tectono-metamorphic resetting or analytical disturbance which could account for such a Concordia-parallel Pb loss. The four youngest datapoints are well clustered and yield to a $^{206}Pb/^{238}U$ weighted mean age of 819.4±9.2 Ma (MSWD = 0.031; Fig. 1-7a). We interpret this as the crystallization age of the quartz-diorite batholith and related zircon grains as autocrysts whereas *ca.* 840-820 Ma zircon grains are antecrysts recording cascading magmatic pulses over this 20 Myr-long period (Miller et al., 2007). Further cathodoluminescence imagery is however required to better investigate zircon internal zoning to confirm the latter hypothesis and the antecryst-autocryst nomenclature. The interpretation of the spread in $^{206}Pb/^{238}U$ single zircon ages detailed in this section is valid for the analysis of U-Pb zircon age datasets of syn-Keraf arc-related batholiths.

4.2.2. Syn-Keraf arc-related dioritoids and granitoids

Zircon grains from the *TR28 quartz-monzodiorite* are strongly fractured, subhedral with rare ~200 µm-long euhedral prismatic grains. They show patchy internal zoning and strong recrystallization patterns. U concentration is systematically <250 ppm and Th/U ratios indicate a magmatic origin (~0.4-0.9). Twenty-nine measurements were made on individual zircon grains and only two discordant datapoints were filtered (U142 and U170). $^{206}Pb/^{238}U$ single zircon ages range from 743±16 Ma to 694±19 Ma with consistent >35 Ma overlapping of two successive 2σ error bars. If sorted by increasing $^{206}Pb/^{238}U$ age, there is however quite an abrupt change between the fifth and the sixth datapoints with a smaller superimposition of 2σ error bars (705±19 Ma and 710±18 Ma). We therefore considered the five youngest zircon autocrysts to provide a $^{206}Pb/^{238}U$ weighted mean ultimate crystallization age of 698.0±7.7 Ma (MSWD =0.21; Fig. 1-7b) whereas older zircon antecrysts likely record earlier arc activity with several successive pulses occurring between *ca.* 745 and 700 Ma.

The *TR21 quartz-monzodiorite* contains zircon grains with similar shapes as zircon in TR28 quartz-monzodiorite, although recrystallization patterns are less frequent. U contents (<170 ppm except for three analyses at 461, 274 and 194 ppm) and Th/U ratios (~0.6-1.0) are also similar to TR28. Forty-one analyses were carried out on individual grains. Two of them were filtered as they were discordant (U186 and U202). $^{206}Pb/^{238}U$ single zircon ages spread consistently from 738±16 Ma to 686±14 Ma, the longest time gap being between 705±15 Ma and 702±18 Ma datapoints. If considering the nineteen zircon grains with $^{206}Pb/^{238}U$ ages equal or lower than 702±18 Ma, which are the most euhedral prismatic grains, we calculate a $^{206}Pb/^{238}U$ weighted mean crystallization age of 694.2±3.6 Ma (MSWD =0.35; Fig. 1-7c), preceded by an uninterrupted record of arc activity since *ca.* 740 Ma.

Recovered zircon grains from the *TR25 diorite* are subhedral, fractured, prismatic to quite rounded. Except from patchy recrystallization patterns, they do not present any

internal zoning but cathodoluminescence imagery will be mandatory to confirm so. Thirty-seven dataspots were made on as many zircon grains. One measurement (U97) is filtered because of its >105% degree of concordance as well as another one (U96) which present an anomalously low U/Th ratio of 0.06. For the other measurements, U concentration remains rather low (up to 184 ppm) and Th/U ratios are representative of magmatic zircon (0.3-0.9). Similarly to TR28 and TR21 quartz-monzodiorites, zircon from the TR25 diorite steadily records arc activity from 747±16 Ma to 682±14 Ma. The five zircon autocrysts with the youngest $^{206}Pb/^{238}U$ single ages are quite clustered and define a $^{206}Pb/^{238}U$ weighted mean crystallization age of 693.0±7.0 Ma (MSWD =0.79; Fig. 1-7d).

The *WG03-OC-05 granodiorite* displays both up to 500 µm-long euhedral prismatic grains with internal oscillatory zoning and patchy recrystallization patterns and fractured, rounded, quite altered grains with no clear zoning on BSE-SEM images (Fig. 1-4). Out of the twenty-five measurements made over twenty-one grains, nine are not considered further as they are discordant. Rounded, no to weakly zoned, zircon grains have low U contents (63, 89, 194 and 439 ppm) and magmatic U/Th ratios (0.3-0.6). $^{206}Pb/^{238}U$ single ages range from 841±17 Ma to 812±19 Ma. Besides, these rounded cores are sometimes overgrown by brighter zircon rims similar to neoformed prismatic zircon grains with oscillatory zoning (very high U concentrations mostly above 900 ppm and up to 1464 ppm, lower magmatic Th/U ratios around ~0.2). Zircon cores are therefore interpreted as inherited zircon whereas rims are ante- or autocrysts. For the nine following measurements on rims around inherited zircon or neoformed zircon grains, $^{206}Pb/^{238}U$ single ages span from 762±18 Ma to 655±15 Ma. Zoned grains have younger rims than cores: *ca.* 700 Ma cores may be interpreted as zircon antecrysts resulting from early magmatic pulses that may have form substrates, similarly as *ca.* 840-810 Ma inherited zircon grains, for new zircon growth. <700 Ma zircon would therefore result from subsequent antecryst to autocryst crystallization within the latest magmatic pulses

until the youngest one recorded at 655±15 Ma (Fig. 1-7e). This age is therefore considered to represent the ultimate crystallization age of the batholith. Finally, three zircon grains with a very fractured and recrystallized aspect have concordant $^{206}Pb/^{238}U$ single ages between *ca.* 550-500 Ma suggesting the resetting of the isotopic system and Pb loss related to later tectono-metamorphic events.

4.2.3. Post-Keraf arc monzogranite

Among the thirty-one measurements made on twenty-nine grains recovered from the *WG03-OC-01b monzogranite*, a first batch of recovered zircon grains display a rounded shape, a fractured aspect, <125 ppm U concentrations, Th/U ratios >0.8 and $^{206}Pb/^{238}U$ single ages of *ca.* 826 Ma and *ca.* 745 Ma. They are considered as inherited grains and sometimes have autocrystic overgrowths (Fig. 1-4). Newly crystallized zircon also forms as >200 µm-long, prismatic grains with a well expressed oscillatory zoning. They have 107-1103 ppm U concentration, Th/U ratio in the range of ~0.4-0.5 and $^{206}Pb/^{238}U$ single age spreading between *ca.* 628-606 Ma. Eleven concordant analyses for this zircon generation yield to a $^{206}Pb/^{238}U$ weighted mean crystallization age of 621.4±4.3 Ma (MSWD=0.41; Fig. 1-7f). Four younger concordant zircon grains with fractured aspect and recrystallization patterns likely relate to *ca.* 550-500 Ma later tectono-metamorphic events.

4.2.4. Overall U-Pb zircon dataset

Plotting concordant $^{206}Pb/^{238}U$ single zircon ages for all samples dated in this study provides an insightful overview of Keraf magmatic arc flare-ups, *i.e.,* periods "*where the volume of magmatism added to the crust is much greater than average amounts"* (Paterson and Ducea, 2015), recorded by zircon (Fig. 1-7g): (i) a first one is recorded between *ca.* 840-810 Ma by antecrysts and autocrysts in early Keraf arc-related dioritoids and inherited zircon in syn-Keraf arc-related batholiths and post-Keraf arc plutons; (ii) a second protracted arc flare-up recorded by multiple magmatic pulses between *ca.* 760-

655 Ma, with ultimate crystallization ages spanning over *ca.* 700-655 Ma for sampled batholiths; (iii) a post-Keraf arc magmatism at *ca.* 625-617 Ma, expressed by granodiorite-monzogranite plutons; and (iv) later tectono-metamorphic events at *ca.* 570-550 Ma and *ca.* 500 Ma recorded by recrystallized zircon grains affected by post-crystallization Pb loss and isotopic resetting.

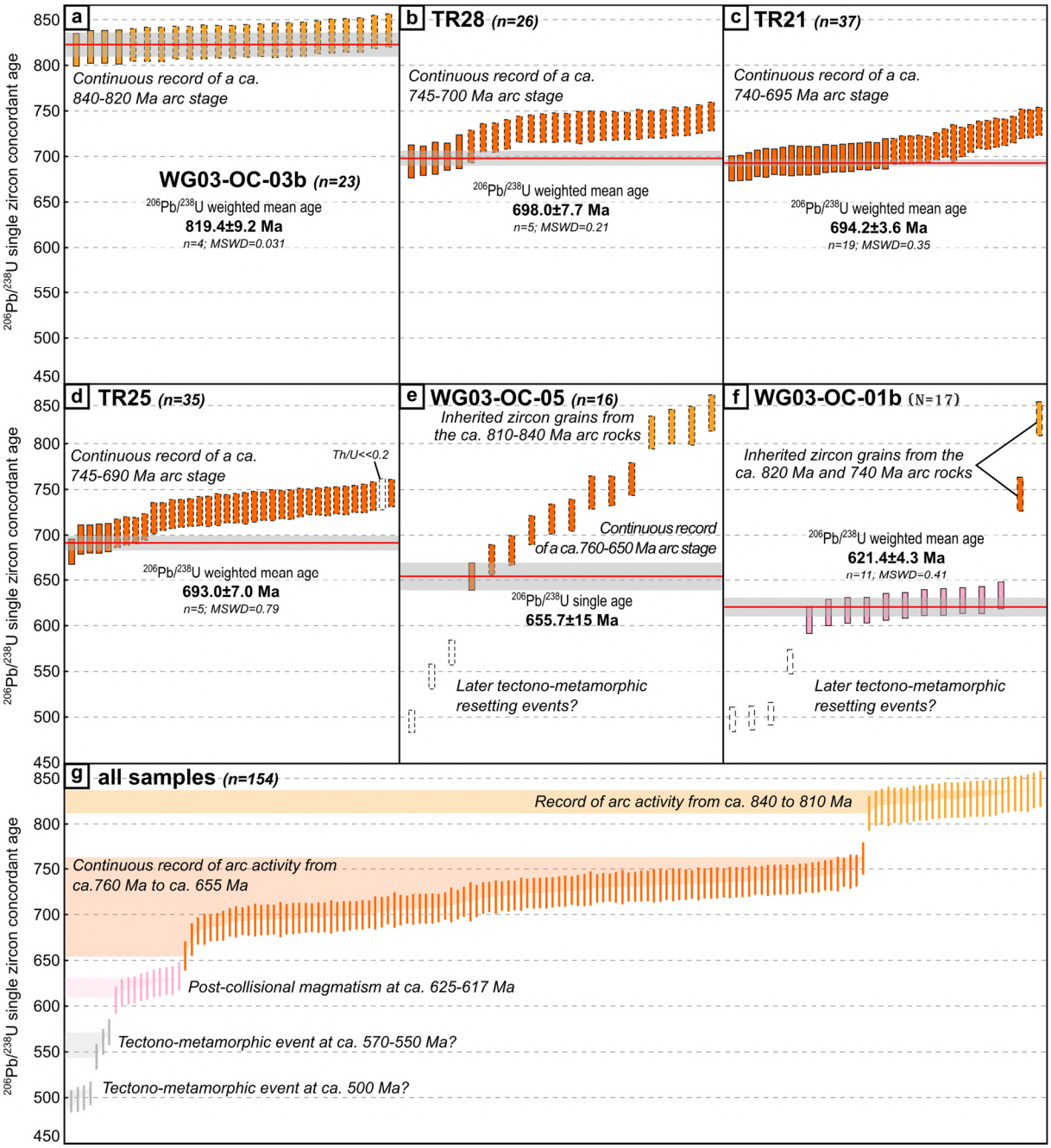


Figure 1-7: Weighted mean plots (2σ error) of $^{206}Pb/^{238}U$ single zircon ages from dated samples. Data out of the 95-105% range of degree of concordance have been filtered prior to plotting. Plots have been arranged in descending order to highlight distinct groups and generations of zircon grains, separated by filling color. Data bars with plain-line contour are considered for $^{206}Pb/^{238}U$ weighted mean crystallization age calculation. Samples have been ranged by decreasing crystallization age. **a** WG03-OC-03. **b** TR28. **c** TR21. **d** TR25. **e** WG03-OC-05. **f** WG03-OC-01b. **g** $^{206}Pb/^{238}U$ single zircon ages for all samples dated in this study. Plots are produced using Isoplot program (Ludwig, 2007). The accompanying BSE-SEM images illustrating zircon morphologies and dataspot locations are provided in Supplementary Material 1-1.

ID	$^{207}Pb^{a}$	U^{b}	Pb^{b}	$\frac{Th}{U}^{b}$	$^{206}Pbc^{c}$	$\frac{^{206}Pb^{d}}{^{238}U}$	±2σ	$\frac{^{207}Pb^{d}}{^{235}U}$	±2σ	$\frac{^{207}Pb^{d}}{^{206}Pb}$	±2σ	ρ[e]	$\frac{^{206}Pb}{^{238}U}$	±2σ	$\frac{^{207}Pb}{^{235}U}$	±2σ	$\frac{^{207}Pb}{^{206}Pb}$	±2σ	conc.[f]
U-Pb	(cps)	(ppm)	(ppm)	U	(%)		(%)		(%)		(%)			(Ma)		(Ma)		(Ma)	(%)
WG03-OC-03b *(early Keraf arc)*																			
a191	13367	67	10	0.50	0.01	0.13650	2.4	1.26	2.7	0.06697	1.209	0.90	825	19	828	16	837	25	99
a192	12530	65	9	0.52	0.02	0.13670	2.4	1.255	2.6	0.06655	1.014	0.92	826	19	825	15	824	21	100
a193	23015	115	17	0.67	0.00	0.13800	2.4	1.259	2.5	0.06619	0.7245	0.96	833	19	828	14	812	15	103
a199	11737	59	9	0.53	0.02	0.13780	2.5	1.263	2.7	0.06646	1.111	0.91	832	19	829	15	821	23	101
a200	18847	95	14	0.63	0.01	0.13800	2.5	1.257	2.6	0.06605	0.8363	0.95	833	19	826	15	808	18	103
a201	13900	71	10	0.48	0.01	0.13670	2.5	1.243	2.6	0.06595	0.7896	0.95	826	19	820	15	805	17	103
a202	16740	85	12	0.50	0.01	0.13670	2.4	1.241	2.6	0.06584	0.8209	0.95	826	19	819	15	801	17	103
a203	13970	71	10	0.42	0.00	0.13620	2.5	1.249	2.6	0.06652	0.8999	0.94	823	19	823	15	823	19	100
a204	12594	64	9	0.55	0.00	0.13650	2.4	1.251	2.7	0.0665	1.084	0.91	825	19	824	15	822	23	100
a205	21976	112	17	0.70	0.00	0.13510	2.4	1.232	2.5	0.06613	0.7434	0.96	817	19	815	14	811	16	101
a206	21539	109	17	0.73	b.d.	0.13760	2.4	1.248	2.6	0.06574	0.8006	0.95	831	19	822	15	798	17	104
a207	10230	53	8	0.51	0.02	0.13720	2.5	1.24	2.6	0.06557	0.9911	0.93	829	19	819	15	793	21	105
a208	13795	71	10	0.48	0.01	0.13570	2.5	1.237	2.6	0.06609	0.8795	0.94	820	19	817	15	809	18	101
a210	11795	60	9	0.55	0.01	0.13690	2.4	1.239	2.6	0.06563	0.9741	0.93	827	19	819	15	795	20	104
a212	17594	90	13	0.71	0.00	0.13570	2.4	1.238	2.6	0.06616	0.9266	0.93	820	19	818	15	811	19	101
a213	13050	67	10	0.55	0.00	0.13700	2.5	1.235	2.6	0.06539	0.821	0.95	828	19	817	15	787	17	105
a214	8797	45	7	0.55	0.02	0.13700	2.4	1.243	2.7	0.06584	1.201	0.90	827	19	820	15	801	25	103
a215	12369	63	9	0.45	0.02	0.13860	2.4	1.259	2.6	0.06589	0.95	0.93	837	19	827	15	803	20	104
a216	14491	73	11	0.49	0.02	0.13610	2.4	1.242	2.6	0.06621	0.8715	0.94	822	19	820	15	813	18	101
a217	14135	71	10	0.45	0.02	0.13570	2.4	1.247	2.6	0.06668	0.8483	0.94	820	19	822	15	828	18	99
a218	27704	131	20	0.66	0.24	0.13710	2.5	1.261	2.7	0.0667	1.021	0.93	828	20	828	16	829	21	100
a219	19518	99	15	0.57	0.02	0.13890	2.4	1.275	2.6	0.06655	0.8205	0.95	838	19	834	15	824	17	102
a220	13860	71	10	0.45	0.01	0.13620	2.5	1.253	2.6	0.0667	0.935	0.93	823	19	825	15	829	20	99
a209	*6922*	*36*	*5*	*0.61*	*0.05*	*0.1375*	*2.4*	*1.233*	*2.7*	*0.0650*	*1.194*	*0.90*	*831*	*19*	*816*	*15*	*775*	*25*	*107*
a211	*5399*	*28*	*4*	*0.45*	*0.06*	*0.1378*	*2.5*	*1.227*	*2.9*	*0.0646*	*1.557*	*0.85*	*832*	*19*	*813*	*17*	*761*	*33*	*109*
TR21 *(syn-Keraf arc)*																			
U172	11387	70	9	0.77	b.d.	0.11320	2.3	0.9761	2.7	0.06252	1.528	0.83	691	15	692	14	692	33	100
U173	14797	91	12	1.00	b.d.	0.11590	2.2	1.006	2.7	0.06295	1.534	0.82	707	15	707	14	707	33	100
U174	8575	53	7	0.73	b.d.	0.11730	2.5	1.023	3.0	0.06328	1.559	0.85	715	17	715	15	718	33	100
U175	43550	274	35	0.95	0.06	0.11030	2.3	0.9639	2.6	0.06339	1.201	0.89	674	15	685	13	721	25	93
U182	13303	80	11	0.88	b.d.	0.11970	2.2	1.054	2.5	0.06388	1.182	0.88	729	15	731	13	738	25	99
U183	20608	122	16	0.97	b.d.	0.11420	2.4	0.9929	2.8	0.06308	1.506	0.85	697	16	700	14	711	32	98
U184	19740	118	16	0.89	b.d.	0.11910	2.4	1.046	2.8	0.06367	1.444	0.86	725	17	727	15	731	31	99
U185	22759	139	19	1.02	b.d.	0.11410	2.3	0.987	3.0	0.06273	1.949	0.76	697	15	697	15	699	42	100
U187	25098	157	20	0.95	b.d.	0.11220	2.2	0.9656	2.6	0.06239	1.402	0.84	686	14	686	13	688	30	100
U188	16828	101	14	1.01	b.d.	0.11920	2.2	1.042	3.5	0.06339	2.786	0.62	726	15	725	19	721	59	101
U189	26520	170	22	0.93	b.d.	0.11410	2.4	0.9856	2.7	0.06265	1.391	0.86	696	16	696	14	696	30	100
U190	20513	122	16	0.98	b.d.	0.11330	2.5	0.9794	3.1	0.06269	1.825	0.81	692	17	693	16	698	39	99
U191	15811	96	12	0.72	b.d.	0.11870	2.4	1.04	3.7	0.06354	2.779	0.65	723	16	724	19	727	59	100
U192	20819	124	17	1.01	b.d.	0.12080	2.3	1.065	3.6	0.0639	2.729	0.64	735	16	736	19	738	58	100
U193	21319	126	17	0.95	b.d.	0.11650	2.3	1.027	2.6	0.0639	1.228	0.88	711	16	717	14	738	26	96
U194	12865	79	10	0.82	b.d.	0.11710	2.4	1.017	2.9	0.06299	1.731	0.81	714	16	713	15	708	37	101
U195	15930	96	13	0.90	b.d.	0.11350	2.2	0.9909	3.2	0.06335	2.273	0.70	693	15	699	16	720	48	96
U196	16355	100	13	0.70	b.d.	0.11550	2.2	0.9992	2.6	0.06275	1.282	0.87	705	15	703	13	700	27	101
U197	18546	118	15	0.91	b.d.	0.11450	2.3	0.9912	3.0	0.06278	1.871	0.78	699	16	699	15	701	40	100
U198	25354	156	20	0.96	b.d.	0.11230	2.2	0.9785	2.7	0.06318	1.487	0.83	686	15	693	14	714	32	96
U199	15048	69	9	0.95	b.d.	0.11710	3.1	1.018	5.4	0.06305	4.461	0.57	714	21	713	28	710	95	101
U200	18147	104	15	1.04	b.d.	0.12130	2.3	1.068	3.9	0.06383	3.165	0.58	738	16	738	21	736	67	100
U201	11268	66	9	0.68	b.d.	0.12080	2.4	1.066	3.5	0.06402	2.569	0.68	735	17	737	19	742	54	99
U203	31253	194	24	0.69	b.d.	0.11580	2.4	1.003	3.2	0.06283	2.192	0.73	707	16	706	17	702	47	101
U204	14632	88	12	0.84	b.d.	0.11800	2.3	1.034	3.9	0.06353	3.072	0.61	719	16	721	20	726	65	99

Table 1-3 ***(continued)***

ID	$^{207}Pb^{a}$	U^{b}	Pb^{b}	$\underline{Th}^{b}$	$^{206}Pbc^{c}$	$\underline{^{206}Pb^{d}}$	±2σ	$\underline{^{207}Pb^{d}}$	±2σ	$\underline{^{207}Pb^{d}}$	±2σ	ρ[e]	$\underline{^{206}Pb}$	±2σ	$\underline{^{207}Pb}$	±2σ	$\underline{^{207}Pb}$	±2σ	conc.[f]
U-Pb	(cps)	(ppm)	(ppm)	U	(%)	^{238}U	(%)	^{235}U	(%)	^{206}Pb	(%)		^{238}U	(Ma)	^{235}U	(Ma)	^{206}Pb	(Ma)	(%)
U211	22822	138	18	0.97	b.d.	0.11430	2.4	0.9939	4.1	0.06304	3.321	0.59	698	16	701	21	710	71	98
U212	14371	85	11	0.88	b.d.	0.11870	2.3	1.037	3.2	0.06336	2.185	0.72	723	16	723	16	720	46	100
U213	11491	67	9	0.83	b.d.	0.11500	2.6	0.9994	4.0	0.06303	3.004	0.66	702	18	703	20	709	64	99
U214	18755	115	15	0.93	b.d.	0.11370	2.5	0.9868	4.0	0.06293	3.106	0.63	694	16	697	20	706	66	98
U215	20148	127	17	0.96	b.d.	0.11370	2.5	0.9828	3.8	0.06272	2.923	0.64	694	16	695	19	699	62	99
U216	74546	461	57	0.59	b.d.	0.11590	2.4	1.008	3.3	0.06308	2.245	0.73	707	16	708	17	711	48	99
U217	7876	49	6	0.66	b.d.	0.11360	2.4	0.9902	3.6	0.06324	2.656	0.67	693	16	699	18	716	56	97
U218	13347	83	11	0.86	b.d.	0.11470	2.2	0.9973	3.4	0.06303	2.535	0.66	700	15	702	17	709	54	99
U219	12626	77	10	0.82	b.d.	0.11580	2.4	0.9972	3.6	0.06244	2.757	0.65	707	16	702	19	689	59	103
U220	15038	88	11	0.89	b.d.	0.11460	2.4	0.9923	3.7	0.06278	2.841	0.64	700	16	700	19	701	61	100
U221	14698	88	11	0.89	b.d.	0.11370	2.6	0.9936	3.7	0.0634	2.568	0.71	694	17	701	19	722	54	96
U222	27648	167	21	0.73	b.d.	0.11370	2.4	0.9809	3.4	0.06255	2.39	0.71	694	16	694	17	693	51	100
U223	17271	103	13	0.84	b.d.	0.11260	2.4	0.9784	3.6	0.06302	2.613	0.68	695	16	693	18	709	56	97
U186	*15435*	*75*	*11*	*1.00*	*0.73*	*0.1174*	*2.4*	*0.989*	*7.6*	*0.0611*	*7.194*	*0.32*	*716*	*16*	*698*	*39*	*642*	*155*	*112*
U202	*18415*	*71*	*10*	*0.81*	*1.25*	*0.1116*	*5.1*	*1.002*	*10.9*	*0.0651*	*9.6*	*0.47*	*682*	*33*	*705*	*57*	*777*	*202*	*88*
TR25	*(syn-Keraf arc)*																		
U88	10576	68	8	0.60	b.d.	0.11510	2.4	1.012	3.2	0.06374	2.027	0.77	702	16	710	16	733	43	96
U95	11781	70	9	0.69	b.d.	0.12140	2.2	1.062	2.6	0.06347	1.276	0.87	738	15	735	13	724	27	102
U96	22167	133	15	0.06	b.d.	0.12260	2.5	1.076	2.7	0.06365	0.9638	0.93	746	18	742	14	730	20	102
U98	18909	116	16	0.88	b.d.	0.11910	2.3	1.038	3.4	0.06322	2.412	0.70	725	16	723	18	715	51	101
U99	16990	111	15	0.94	b.d.	0.11800	2.6	1.036	3.6	0.06365	2.478	0.72	719	17	722	19	730	53	99
U100	11743	74	9	0.57	b.d.	0.11400	2.4	0.9903	2.8	0.063	1.35	0.88	696	16	699	14	708	29	98
U101	15962	95	13	0.76	b.d.	0.12170	2.2	1.069	2.4	0.06371	1.034	0.90	740	15	738	13	732	22	101
U102	21037	134	17	0.79	b.d.	0.11390	2.5	1	3.2	0.06368	1.869	0.81	696	17	704	16	731	40	95
U103	18249	116	15	0.63	b.d.	0.12120	2.3	1.063	2.8	0.06363	1.486	0.84	737	16	735	15	729	31	101
U104	16796	106	14	0.86	b.d.	0.11830	2.3	1.032	2.9	0.06324	1.712	0.80	721	16	720	15	716	36	101
U105	19318	117	16	0.85	b.d.	0.12280	2.2	1.082	2.9	0.06391	1.802	0.78	747	16	745	15	739	38	101
U106	14958	98	13	0.63	b.d.	0.12120	2.2	1.055	4.0	0.06315	3.324	0.55	737	15	731	21	713	71	103
U107	15200	95	12	0.63	b.d.	0.12180	2.3	1.072	3.9	0.06383	3.16	0.59	741	16	740	21	736	67	101
U109	21581	129	18	0.87	b.d.	0.12060	2.3	1.066	2.6	0.06413	1.097	0.90	734	16	737	14	746	23	98
U108	10293	66	8	0.58	b.d.	0.11560	2.4	1.014	3.7	0.06363	2.769	0.66	705	16	711	19	730	59	97
U110	30967	184	25	0.89	b.d.	0.12140	2.3	1.065	2.6	0.0636	1.211	0.89	739	16	736	14	728	26	101
U111	12889	77	10	0.74	b.d.	0.12100	2.3	1.057	2.7	0.06334	1.399	0.86	736	16	732	14	720	30	102
U112	19769	121	16	0.81	b.d.	0.11630	2.2	1.019	2.6	0.06353	1.414	0.84	709	14	713	13	726	30	98
U113	17357	107	15	0.84	b.d.	0.12220	2.3	1.07	2.8	0.06354	1.625	0.82	743	16	739	15	726	34	102
U114	29948	138	20	0.82	b.d.	0.11960	2.6	1.04	4.5	0.06302	3.648	0.58	729	18	724	24	709	78	103
U115	15264	93	12	0.76	b.d.	0.11980	2.3	1.043	2.9	0.06317	1.748	0.79	729	16	726	15	714	37	102
U116	11973	70	9	0.73	b.d.	0.11890	2.3	1.04	3.8	0.06343	3.044	0.61	724	16	724	20	723	65	100
U117	10371	66	9	0.65	b.d.	0.12110	2.1	1.06	4.6	0.06349	4.055	0.47	737	15	734	24	725	86	102
U124	29283	182	24	0.87	b.d.	0.11560	2.2	0.9951	2.6	0.06242	1.379	0.85	705	15	701	13	689	29	102
U125	17226	100	13	0.80	b.d.	0.12060	2.4	1.057	3.1	0.06356	1.962	0.77	734	16	732	16	727	42	101
U126	16574	102	14	0.82	0.51	0.11880	2.4	1.029	2.7	0.06283	1.236	0.89	724	16	718	14	703	26	103
U127	16885	107	14	0.83	b.d.	0.11990	2.6	1.046	3.1	0.0633	1.685	0.84	730	18	727	16	718	36	102
U128	13694	81	11	0.69	b.d.	0.11930	2.5	1.056	5.3	0.06416	4.689	0.47	727	17	732	28	747	99	97
U129	27759	179	23	0.90	b.d.	0.11410	2.5	0.9766	2.7	0.06206	1.189	0.90	697	16	692	14	676	25	103
U130	22125	136	18	0.67	b.d.	0.11930	2.4	1.039	2.7	0.06317	1.142	0.90	726	16	723	14	714	24	102
U131	15702	109	14	0.72	b.d.	0.12050	2.5	1.081	2.8	0.06504	1.341	0.88	733	17	744	15	776	28	95
U132	16387	101	14	0.85	b.d.	0.11990	2.4	1.041	2.9	0.063	1.605	0.83	730	16	724	15	708	34	103
U133	19705	117	16	0.84	b.d.	0.12030	2.3	1.063	3.0	0.0641	1.993	0.75	732	16	736	16	745	42	98
U134	14462	92	12	0.74	b.d.	0.11430	2.4	0.9946	2.6	0.06313	1.097	0.91	698	16	701	13	713	23	98

Table 1-3 ***(continued)***

ID	$^{207}Pb^{a}$	U^{b}	Pb^{b}	$\underline{Th}^{b}$	$^{206}Pbc^{c}$	$\underline{^{206}Pb}^{d}$	±2σ	$\underline{^{207}Pb}^{d}$	±2σ	$\underline{^{207}Pb}^{d}$	±2σ	ρ[e]	$\underline{^{206}Pb}$	±2σ	$\underline{^{207}Pb}$	±2σ	$\underline{^{207}Pb}$	±2σ	conc.[f]
U-Pb	(cps)	(ppm)	(ppm)	U	(%)	^{238}U	(%)	^{235}U	(%)	^{206}Pb	(%)		^{238}U	(Ma)	^{235}U	(Ma)	^{206}Pb	(Ma)	(%)
U135	14312	92	12	0.82	b.d.	0.11160	2.2	0.9557	2.9	0.06212	1.844	0.77	682	14	681	14	678	39	101
U136	11911	74	9	0.32	0.02	0.12020	2.5	1.051	2.8	0.06341	1.259	0.89	732	17	729	15	722	27	101
U97	*13910*	*88*	*12*	*0.79*	*b.d.*	*0.1233*	*2.6*	*1.059*	*3.1*	*0.0623*	*1.711*	*0.83*	*750*	*18*	*734*	*16*	*684*	*37*	*110*
TR28	*(syn-Keraf arc)*																		
U137	30538	190	24	0.54	b.d.	0.11820	2.3	1.029	2.7	0.06313	1.449	0.84	720	16	718	14	713	31	101
U138	15403	91	12	0.59	b.d.	0.12170	2.3	1.07	3.7	0.06376	2.892	0.62	740	16	739	20	734	61	101
U139	22202	135	18	0.79	b.d.	0.11980	2.1	1.046	2.5	0.06328	1.237	0.87	730	15	727	13	718	26	102
U140	16568	102	12	0.64	b.d.	0.11070	2.4	0.976	2.8	0.06393	1.394	0.87	677	16	692	14	739	30	92
U141	16475	95	12	0.57	b.d.	0.12130	2.3	1.066	2.6	0.06371	1.151	0.89	738	16	737	14	732	24	101
U143	23505	147	20	0.83	0.16	0.12040	2.2	1.056	2.4	0.06361	1.092	0.89	733	15	732	13	729	23	101
U144	22987	145	18	0.58	b.d.	0.11430	2.7	0.9858	3.0	0.06258	1.305	0.90	697	18	697	15	694	28	101
U145	15232	90	12	0.69	b.d.	0.12030	2.5	1.05	3.4	0.06329	2.272	0.74	732	18	729	18	718	48	102
U146	30383	180	23	0.54	b.d.	0.12010	2.4	1.05	2.6	0.06339	1.185	0.89	731	16	729	14	721	25	101
U153	25394	148	20	0.74	b.d.	0.12040	2.3	1.056	3.1	0.06363	2.056	0.75	733	16	732	16	729	44	100
U154	25394	148	20	0.74	b.d.	0.12040	2.3	1.056	3.1	0.06363	2.056	0.75	733	16	732	16	729	44	100
U155	31704	192	23	0.54	b.d.	0.11380	2.5	0.9931	2.6	0.06328	0.9571	0.93	695	16	700	13	718	20	97
U156	26130	142	20	0.89	b.d.	0.11990	2.2	1.051	2.7	0.06353	1.564	0.82	730	15	729	14	726	33	101
U157	26586	149	19	0.61	b.d.	0.12000	2.3	1.052	2.6	0.06357	1.282	0.87	730	16	730	14	727	27	100
U158	14159	84	11	0.58	b.d.	0.12080	2.3	1.069	2.9	0.06414	1.737	0.80	735	16	738	15	746	37	99
U159	17684	107	14	0.59	0.39	0.12010	2.3	1.052	2.6	0.0635	1.244	0.88	731	16	730	14	725	26	101
U160	16187	94	12	0.58	b.d.	0.12220	2.3	1.067	3.0	0.06336	2.004	0.75	743	16	737	16	721	43	103
U161	16082	99	12	0.55	b.d.	0.11820	2.4	1.032	2.7	0.06333	1.171	0.90	720	17	720	14	719	25	100
U162	13671	73	9	0.59	b.d.	0.12130	2.3	1.065	2.8	0.06368	1.646	0.81	738	16	736	15	731	35	101
U163	37791	228	28	0.49	b.d.	0.11550	2.8	1.005	3.1	0.06307	1.308	0.91	705	19	706	16	710	28	99
U164	32550	197	24	0.48	b.d.	0.11650	2.7	1.023	2.9	0.06365	0.9368	0.95	710	18	715	15	730	20	97
U165	13868	81	10	0.52	b.d.	0.12070	2.4	1.052	2.6	0.0632	1.13	0.90	735	17	730	14	715	24	103
U166	13706	80	10	0.48	b.d.	0.12070	2.2	1.059	2.4	0.06364	0.9687	0.92	735	15	733	13	730	21	101
U167	22301	130	17	0.52	b.d.	0.12010	2.6	1.057	3.1	0.06381	1.7	0.84	731	18	732	16	735	36	99
U168	18958	113	14	0.54	b.d.	0.11880	2.4	1.043	2.7	0.06368	1.255	0.88	724	16	725	14	731	27	99
U169	34826	215	26	0.48	b.d.	0.11370	2.8	0.988	3.1	0.063	1.302	0.91	694	19	698	16	708	28	98
U171	29332	171	21	0.59	b.d.	0.11460	2.3	0.9933	2.6	0.06288	1.366	0.86	699	15	700	13	704	29	99
U142	*28348*	*240*	*11*	*0.66*	*b.d.*	*0.0363*	*5.0*	*0.287*	*8.1*	*0.0574*	*6.348*	*0.62*	*230*	*11*	*256*	*18*	*508*	*140*	*45*
U170	*34657*	*227*	*25*	*0.55*	*b.d.*	*0.1004*	*3.2*	*0.931*	*4.2*	*0.0672*	*2.657*	*0.77*	*617*	*19*	*668*	*21*	*844*	*55*	*73*
WG03-OC-05	*(syn-Keraf arc)*																		
a221c*	41569	194	29	0.57	0.25	0.13810	2.6	1.277	2.7	0.06711	0.8346	0.95	834	20	836	15	841	17	99
a222r	171601	1013	118	0.23	0.05	0.11570	2.4	1.019	2.5	0.06385	0.6215	0.97	706	16	713	13	737	13	96
a223c*	13213	63	9	0.43	0.21	0.13550	2.8	1.24	3.1	0.06639	1.414	0.89	819	21	819	18	819	30	100
a225	150669	943	106	0.21	0.32	0.11190	2.5	0.9543	2.7	0.06185	0.8843	0.94	684	16	680	13	669	19	102
a228	191082	1135	127	0.22	0.34	0.11000	2.7	0.9372	2.9	0.06181	1.003	0.94	673	17	671	14	668	21	101
a237c*	16930	89	12	0.28	0.27	0.13420	2.4	1.239	2.6	0.067	0.8887	0.94	812	19	819	15	838	19	97
a248*	101067	439	63	0.44	0.02	0.13540	2.5	1.239	2.5	0.06633	0.4312	0.99	819	19	818	14	817	9	100
a224r	103105	612	73	0.24	0.20	0.11850	2.6	1.044	2.6	0.06386	0.5064	0.98	722	18	726	14	737	11	98
a227	92375	521	67	0.43	0.13	0.12310	2.4	1.084	2.5	0.06387	0.6582	0.97	748	17	746	13	737	14	102
a235c	65077	408	48	0.23	0.00	0.11780	2.5	1.023	2.5	0.06295	0.5045	0.98	718	17	715	13	707	11	102
a236r	251402	1464	181	0.23	0.12	0.12290	2.6	1.091	2.7	0.0644	0.3903	0.99	747	19	749	14	755	8	99
a246	179657	1090	125	0.48	0.39	0.10690	2.5	0.9167	2.7	0.0622	1.179	0.90	655	15	661	13	681	25	96
a249	63309	378	50	0.47	0.02	0.12540	2.5	1.102	2.5	0.06369	0.4385	0.98	762	18	754	13	731	9	104
a233	*30360*	*177*	*16*	*0.17*	*0.77*	*0.08814*	*2.6*	*0.7189*	*3.0*	*0.05915*	*1.366*	*0.89*	*545*	*14*	*550*	*13*	*573*	*30*	*95*
a244r	*46915*	*380*	*35*	*0.23*	*0.34*	*0.09270*	*2.5*	*0.761*	*2.7*	*0.05953*	*0.946*	*0.94*	*572*	*14*	*575*	*12*	*587*	*21*	*97*
a250	*33288*	*345*	*28*	*0.31*	*0.01*	*0.07997*	*2.5*	*0.6241*	*2.5*	*0.0566*	*0.695*	*0.96*	*496*	*12*	*492*	*10*	*476*	*15*	*104*
a226	*70308*	*390*	*53*	*0.74*	*0.12*	*0.12130*	*2.4*	*1.115*	*2.5*	*0.0667*	*0.6366*	*0.97*	*738*	*17*	*761*	*14*	*828*	*13*	*89*

Table 1-3 ***(continued)***

ID	$^{207}Pb^a$	U^b	Pb^b	$\underline{Th}^b$	$^{206}Pbc^c$	$\underline{^{206}Pb}^d$	±2σ	$\underline{^{207}Pb}^d$	±2σ	$\underline{^{207}Pb}^d$	±2σ	ρ[e]	$\underline{^{206}Pb}$	±2σ	$\underline{^{207}Pb}$	±2σ	$\underline{^{207}Pb}$	±2σ	conc.[f]
U-Pb	(cps)	(ppm)	(ppm)	U	(%)	^{238}U	(%)	^{235}U	(%)	^{206}Pb	(%)		^{238}U	(Ma)	^{235}U	(Ma)	^{206}Pb	(Ma)	(%)
a229	*97602*	*483*	*58*	*0.20*	*1.15*	*0.11660*	*2.6*	*0.9784*	*3.9*	*0.06087*	*2.901*	*0.67*	*711*	*18*	*693*	*20*	*635*	*62*	*112*
a230c	*477342*	*3813*	*421*	*0.26*	*1.02*	*0.10940*	*3.1*	*0.9828*	*3.8*	*0.06515*	*2.126*	*0.83*	*669*	*20*	*695*	*19*	*779*	*45*	*86*
a231r	*64784*	*498*	*29*	*0.12*	*1.78*	*0.05648*	*4.3*	*0.4341*	*6.3*	*0.05575*	*4.565*	*0.68*	*354*	*15*	*366*	*19*	*442*	*102*	*80*
a232	*12139*	*66*	*9*	*0.47*	*1.01*	*0.12450*	*2.5*	*1.183*	*3.0*	*0.06894*	*1.742*	*0.82*	*756*	*18*	*793*	*17*	*897*	*36*	*84*
a234	*199114*	*1266*	*138*	*0.41*	*0.27*	*0.10370*	*2.6*	*0.9483*	*2.6*	*0.06632*	*0.5725*	*0.98*	*636*	*16*	*677*	*13*	*816*	*12*	*78*
a243c	*92254*	*671*	*66*	*0.71*	*2.19*	*0.08755*	*2.5*	*0.6786*	*4.7*	*0.05621*	*3.909*	*0.54*	*541*	*13*	*526*	*19*	*461*	*87*	*117*
a245	*114206*	*674*	*69*	*0.26*	*0.45*	*0.09727*	*3.1*	*0.8397*	*3.6*	*0.06261*	*1.808*	*0.86*	*598*	*18*	*619*	*17*	*695*	*39*	*86*
a247	*1343103*	*9091*	*1093*	*0.22*	*0.75*	*0.11810*	*3.0*	*1.084*	*3.3*	*0.06662*	*1.478*	*0.90*	*719*	*20*	*746*	*18*	*826*	*31*	*87*
WG03-OC-01b *(post-Keraf arc)*																			
a161	92661	659	71	0.53	0.67	0.10000	2.5	0.8356	3.3	0.06058	2.179	0.75	615	14	617	15	624	47	98
a162	14624	107	11	0.42	0.22	0.10040	2.4	0.839	2.7	0.06062	1.038	0.92	617	14	619	12	626	22	99
a163*	13215	72	10	0.89	1.45	0.12240	2.7	1.072	9.4	0.06351	9.042	0.29	745	19	740	51	725	192	103
a166	18623	126	14	0.69	0.71	0.10100	2.5	0.8433	3.1	0.06053	1.872	0.79	620	15	621	14	623	40	100
a168	117921	817	86	0.43	0.00	0.10050	2.4	0.8315	2.5	0.05999	0.4468	0.98	618	14	614	12	603	10	102
a169	44637	315	37	0.86	0.08	0.10130	2.4	0.8483	2.6	0.06074	0.7601	0.96	622	15	624	12	630	16	99
a170	65129	456	49	0.42	0.33	0.10180	2.4	0.8494	2.5	0.06053	0.6885	0.96	625	15	624	12	622	15	100
a178	49154	354	40	0.67	0.34	0.10230	2.5	0.8552	4.0	0.06061	3.036	0.64	628	15	628	19	625	65	100
a180	150980	1103	116	0.40	0.00	0.10220	2.4	0.8568	2.5	0.06078	0.6058	0.97	628	15	628	12	631	13	99
a181	30524	243	25	0.47	0.02	0.09864	2.5	0.826	2.6	0.06073	0.8489	0.95	606	14	611	12	630	18	96
a188	121138	822	89	0.46	0.18	0.10200	2.5	0.8531	2.6	0.06066	0.6989	0.96	626	15	626	12	627	15	100
a190*	24320	123	25	2.56	0.01	0.13680	2.5	1.244	2.6	0.06598	0.6861	0.96	826	19	821	14	806	14	103
a159	*52429*	*343*	*39*	*0.68*	*1.19*	*0.10000*	*2.6*	*0.8094*	*6.2*	*0.05871*	*5.584*	*0.42*	*614*	*15*	*602*	*28*	*556*	*122*	*110*
a160	*106001*	*888*	*75*	*0.24*	*1.06*	*0.08144*	*2.6*	*0.6495*	*4.1*	*0.05784*	*3.211*	*0.63*	*505*	*13*	*508*	*17*	*524*	*70*	*96*
a164	*1112533*	*6824*	*842*	*0.38*	*0.06*	*0.12140*	*2.5*	*0.9632*	*2.5*	*0.05754*	*0.4175*	*0.99*	*739*	*17*	*685*	*13*	*512*	*9*	*144*
a165	*83166*	*585*	*63*	*0.41*	*0.10*	*0.10320*	*2.5*	*0.8528*	*2.5*	*0.05995*	*0.5273*	*0.98*	*633*	*15*	*626*	*12*	*602*	*11*	*105*
a167	*226007*	*1546*	*165*	*0.31*	*0.00*	*0.10560*	*2.4*	*0.8719*	*2.4*	*0.05988*	*0.3253*	*0.99*	*647*	*15*	*637*	*12*	*599*	*7*	*108*
a171c	*476519*	*1623*	*137*	*0.52*	*19.19*	*0.05167*	*3.2*	*0.3482*	*10.00*	*0.04887*	*9.445*	*0.32*	*325*	*10*	*303*	*26*	*142*	*222*	*229*
a173c	*268073*	*3144*	*104*	*0.25*	*8.19*	*0.02070*	*4.1*	*0.1628*	*8.2*	*0.05704*	*7.076*	*0.50*	*132*	*5*	*153*	*12*	*493*	*156*	*27*
a174r	*565582*	*5532*	*216*	*0.21*	*12.66*	*0.02282*	*5.4*	*0.1708*	*10.60*	*0.05429*	*9.136*	*0.51*	*145*	*8*	*160*	*16*	*383*	*205*	*38*
a175r	*431743*	*8962*	*200*	*0.27*	*11.11*	*0.01464*	*3.6*	*0.1042*	*9.4*	*0.05162*	*8.696*	*0.38*	*94*	*3*	*101*	*9*	*268*	*199*	*35*
a176	*39925*	*318*	*28*	*0.40*	*1.41*	*0.08245*	*2.5*	*0.6184*	*6.1*	*0.0544*	*5.509*	*0.42*	*511*	*12*	*489*	*24*	*388*	*124*	*132*
a177	*63655*	*289*	*32*	*0.46*	*6.27*	*0.08060*	*2.7*	*0.6357*	*10.9*	*0.0572*	*10.51*	*0.25*	*500*	*13*	*500*	*44*	*499*	*232*	*100*
a179	*194105*	*743*	*106*	*0.57*	*1.94*	*0.11720*	*2.5*	*0.9143*	*4.3*	*0.05659*	*3.511*	*0.58*	*714*	*17*	*659*	*21*	*476*	*78*	*150*
a182	*120673*	*985*	*83*	*0.30*	*0.77*	*0.08030*	*2.8*	*0.6342*	*3.1*	*0.05728*	*1.325*	*0.90*	*498*	*13*	*499*	*12*	*502*	*29*	*99*
a183	*80854*	*676*	*42*	*0.45*	*4.25*	*0.04912*	*2.5*	*0.3899*	*5.1*	*0.05758*	*4.485*	*0.49*	*309*	*8*	*334*	*15*	*514*	*99*	*60*
a184	*109682*	*741*	*69*	*0.32*	*1.15*	*0.08818*	*2.6*	*0.6959*	*3.2*	*0.05723*	*1.822*	*0.82*	*545*	*14*	*536*	*13*	*500*	*40*	*109*
a185	*114603*	*847*	*88*	*0.37*	*0.07*	*0.10140*	*2.4*	*0.8324*	*2.7*	*0.05956*	*1.183*	*0.90*	*622*	*14*	*615*	*13*	*588*	*26*	*106*
a186	*24440*	*191*	*19*	*0.54*	*0.65*	*0.09514*	*2.5*	*0.8002*	*2.8*	*0.061*	*1.223*	*0.90*	*586*	*14*	*597*	*13*	*639*	*26*	*92*
a187	*28229*	*234*	*23*	*0.46*	*0.21*	*0.09089*	*2.5*	*0.7433*	*5.0*	*0.05931*	*4.299*	*0.51*	*561*	*14*	*564*	*22*	*579*	*93*	*97*
a189	*28052*	*234*	*17*	*0.38*	*0.95*	*0.06404*	*3.0*	*0.538*	*3.5*	*0.06093*	*1.726*	*0.87*	*400*	*12*	*437*	*12*	*637*	*37*	*63*

In italics: excluded for crystallization age calculation (out of the 95-105% degree of concordance range, inherited zircon grains, later tectono-metamorphic event-related Pb-loss or Th/U<0.2).

In bold: datapoints considered for crystallization age calculation.

** Inherited zircon.*

c-core, r-rim.

Spot size = 33 µm for samples WG03-OC-01b, -03b and -05, 25 µm for samples TR21, TR25 and TR28; depth of crater ~15µm.

$^{206}Pb/^{238}U$ error is the quadratic additions of the within run precision (2 S.E.) and the external reproducibility (2 S.D.) of the reference zircon. $^{207}Pb/^{206}Pb$ error propagation (^{207}Pb signal dependent) following Gerdes and Zeh (2009). $^{207}Pb/^{235}U$ error is the quadratic addition of the $^{207}Pb/^{206}Pb$ and $^{206}Pb/^{238}U$ uncertainty.

[a] Within run background-corrected mean ^{207}Pb signal in cps (counts per second).

[b] U and Pb content and Th/U ratio were calculated relative to GJ-1 reference zircon for samples WG03-OC-01b, -03b and -05. They were calculated relative to BB1 reference zircon (itself referenced against GJ-1 zircon) for samples TR21, TR25 and TR28.

[c] Percentage of the common Pb on the ^{206}Pb. b.d. = below dectection limit.

[d] *Corrected for background, within-run Pb/U fractionation (in case of $^{206}Pb/^{238}U$) and common Pb using Stacey and Kramers (1975) model Pb composition and subsequently normalized to GJ-1 (ID-TIMS value/measured value); $^{207}Pb/^{235}U$ calculated using $^{207}Pb/^{206}Pb/(^{238}U/^{206}Pb.1/137.88)$.*

[e] *ρ is the $^{206}Pb/^{238}U$ / $^{207}Pb/^{235}U$ error correlation coefficient.*

[f] *Degree of concordance (%) = $^{206}Pb/^{238}U$ age / $^{207}Pb/^{206}Pb$ age.100.*

Table 1-3: U-Pb isotopic compositions of zircon grains used in this study. BSE- and SE-SEM images illustrating zircon morphologies and dataspots are provided in Supplementary Material 1-1.

4.3. Hf isotope analyses of zircon

The Hf isotopic compositions of concordant, magmatic zircon grains that have been dated in this study are the first Hf data reported from the overall Keraf suture (Table 1-4, Fig. 1-8a). Results and raw data processing details for Hf isotopes are given in Table 1-4. Hf isotopic compositions of zircon standards used in this study are provided in Supplementary Material 1-3.

Early Keraf arc-related zircon grains, with $^{206}Pb/^{238}U$ single ages between *ca.* 837-812 Ma, have $\varepsilon Hf_{(i)}$ values ranging from +7.4±1.0 to +10.7±0.8 (mean value of +9.5±1.6, n=14). $\varepsilon Hf_{(i)}$ for inherited zircon grains in the syn-Keraf arc-related granodiorite (WG03-OC-05) does not exceed +9.3±0.8 and reaches the lowest <+8.0 values associated with the oldest two-stage model ages up to 1.22 Ga. Otherwise, two-stage model ages T_{DM2} span from 1.12 to 1.05 Ga.

Syn-Keraf arc-related zircon grains, show a decrease in $\varepsilon Hf_{(i)}$ values from the 762-711 Ma to the 711-677 Ma and 655 Ma $^{206}Pb/^{238}U$ single age ranges. Associated $\varepsilon Hf_{(i)}$ values are +9.8±2.5 (n=25, up to +11.7±1.0), +8.7±1.6 (n=10) and +6.2±1.7 (n=1), respectively. Except the youngest zircon grain and another one formed at *ca.* 684 Ma which have rather high two-stage model ages of 1.16 and 1.14 Ga respectively, all the other grains have consistent T_{DM2} ages of 1.09-0.94 Ga.

ca. 625-617 Ma post-Keraf arc plutons host zircon autocrysts displaying among the lowest, yet still highly positive, $\varepsilon Hf_{(i)}$ values reported in this study (+8.5±0.9, n=5). Corresponding T_{DM2} ages spread from 1.02 to 0.99 Ga.

4.4. Sr and Nd isotope whole-rock analyses

Crystallization age-back calculated $\varepsilon Nd_{(i)}$ values are +4.7±2.0 (n=4), +5.2±1.4 (n=7), +4.1±1.0 (n=3) for early, syn-Keraf arc-related and post-Keraf arc igneous rocks, respectively (Table 1-5, Fig. 1-8b). Nd isotopic data look consistent for undated samples with crystallization ages estimated relying on field petrographic and geochemical relationships with dated plutonic rocks. If such consistency in Nd isotopic signature between dated and non-dated samples is no substitute for robust geochronological data on non-dated igneous rocks, it suggests at least that field and geochemical relationships are likely reliable. The lowest $\varepsilon Nd_{(i)}$ value is reached for the post-Keraf arc monzogranite (+3.3±1.6; WG03-OC-01b) and there is a cluster of >+5.1 values for *ca.* 700-690 Ma dioritoids and granitoids. Nevertheless, Nd isotopic compositions overlap from early and syn-Keraf arc-related to post-Keraf arc igneous rocks if considering 2σ error bars (Fig. 1-8c). The *ca.* 655 Ma granodiorite (WG03-OC-05) and *ca.* 620 Ma monzogranite (WG03-OC-01b) have T_{DM2} values similar to the *ca.* 820 Ma igneous rocks (1.12-1.00 Ga). The remaining <700 Ma plutonic rocks have the lowest two-stage model ages (0.96-0.84 Ga).

Most of initial $(^{87}Sr/^{86}Sr)_i$ values are low, ranging from ~0.7024 to ~0.7038. There must be an analytical error for present-day measurement of $^{87}Sr/^{86}Sr$ ratio for the monzodiorite xenolith which is unrealistically low (<0.70000; WG03-OC-01c). This data is not considered further. It seems that there is a decrease in Sr signature from early (>0.7034 except for a quartz-diorite at 0.7027) to syn-Keraf arc-related (0.7026-0.7030) and post-Keraf arc (<0.7027) igneous rocks. However, the overall range in $(^{87}Sr/^{86}Sr)_i$ values is too tight when considering 2σ error bars to consider this evolution as significant (Fig. 1-8c).

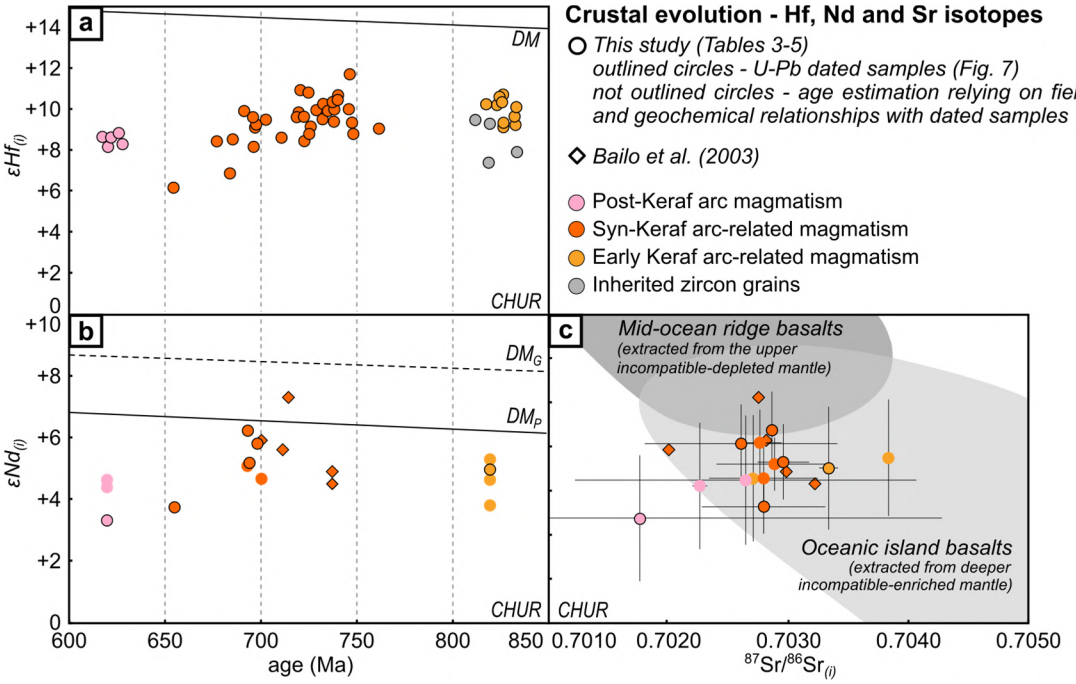


Figure 1-8: Crossplots considering Hf, Nd and Sr isotopic data from this study (circles) and syn-Keraf arc-related samples from Bailo et al. (2003) (diamonds). Outlined symbols refer to samples that have been dated in this study whereas not outlined ones correspond to undated samples with crystallization age estimated relying on field and geochemical relationships with dated dioritoids and granitoids. $^{206}Pb/^{238}U$ concordant age of single zircon (this study) or Pb/Pb zircon crystallization ages (Bailo et al., 2003) of plutonic rocks vs (**a**) their initial zircon epsilon hafnium composition $\varepsilon Hf_{(i)}$ (depleted mantle (DM) evolution from Blichert-Toft and Puchtel (2010) and (**b**) their initial whole-rock epsilon neodymium composition $\varepsilon Nd_{(i)}$ (depleted mantle DM_P and DM_G evolution from DePaolo (1981) and Goldstein et al. (1984), respectively). **c** $^{87}Sr/^{86}Sr_{(i)}$ vs $\varepsilon Nd_{(i)}$ crossplot with 2σ error bars. Mid-ocean ridge basalt and oceanic island basalt isotopic fields are from White (2015). CHUR stands for chondritic uniform reservoir for the three crossplots.

ID Lu-Hf	$^{176}Yb/^{177}Hf$ [a]	±2σ	$^{176}Lu/^{177}Hf$ [a]	±2σ	$^{178}Hf/^{177}Hf$	Sig_{Hf} [b] (V)	$^{176}Hf/^{177}Hf$	±2σ [c]	$^{176}Hf/^{177}Hf_{(i)}$ [d]	age [f] (Ma)	±2σ	conc. [g]	$\varepsilon Hf_{(i)}$ [d]	±2σ [c]	T_{DM2} (Ga)
WG03-OC-03b *(early Keraf arc)* – **1st analytical session**															
a191	0.0229	1	0.00078	0	1.46720	19	0.282567	22	0.282555	825	19	99	10.6	0.8	1.07
a192	0.0343	2	0.00114	0	1.46726	22	0.282584	22	0.282566	826	19	100	10.7	0.8	1.05
a193	0.0184	6	0.00065	2	1.46725	21	0.282541	21	0.282531	833	19	103	9.2	0.8	1.12
a199	0.0111	11	0.00038	3	1.46727	9	0.282545	27	0.282539	832	19	101	9.7	0.9	1.10
a200	0.0371	6	0.00124	2	1.46721	21	0.282579	21	0.282559	833	19	103	10.1	0.8	1.06
a201	0.0223	8	0.00079	2	1.46725	23	0.282547	23	0.282534	826	19	103	9.1	0.8	1.11
a202	0.0222	7	0.00076	3	1.46727	20	0.282553	22	0.282541	826	19	103	9.3	0.8	1.10
a203	0.0333	2	0.00112	1	1.46722	21	0.282570	22	0.282553	823	19	100	10.2	0.8	1.08
a204	0.0239	4	0.00081	2	1.46726	21	0.282569	22	0.282556	825	19	100	10.3	0.8	1.07
a205	0.0321	1	0.00110	1	1.46724	21	0.282578	22	0.282561	817	19	101	10.2	0.8	1.06
TR21 *(syn-Keraf arc)* – **2nd analytical session**															
U183	0.0248	8	0.00068	2	1.46725	11	0.282611	30	0.282601	697	16	98	9.1	1.1	1.02
U184	0.0235	1	0.00064	0	1.46729	11	0.282605	29	0.282596	725	17	99	9.5	1.0	1.03
U185	0.0222	2	0.00061	1	1.46727	12	0.282594	27	0.282585	697	15	100	8.5	1.0	1.05
U187	0.0146	6	0.00042	1	1.46730	11	0.282588	30	0.282582	686	14	100	8.2	1.1	1.06
U188	0.0231	1	0.00063	0	1.46727	11	0.282614	29	0.282606	726	15	101	9.9	1.0	1.02
U189	0.0174	10	0.00048	2	1.46729	12	0.282599	28	0.282593	696	16	100	8.8	1.0	1.04
U190	0.0193	7	0.00053	2	1.46722	12	0.282614	28	0.282606	692	17	99	9.2	1.0	1.01
U191	0.0082	2	0.00024	0	1.46732	12	0.282569	29	0.282566	723	16	100	8.4	1.0	1.09
U192	0.0238	4	0.00065	1	1.46726	10	0.282610	31	0.282601	735	16	100	9.9	1.1	1.02
U193	0.0230	8	0.00065	2	1.46724	7	0.282589	31	0.282580	711	16	96	8.6	1.1	1.06
TR25 *(syn-Keraf arc)* – **2nd analytical session**															
U88	0.0204	8	0.00058	2	1.46729	10	0.282617	31	0.282609	702	16	96	9.5	1.1	1.01
U95	0.0121	9	0.00036	2	1.46729	11	0.282605	29	0.282600	738	15	102	10.0	1.0	1.02
U96	0.0129	14	0.00039	4	1.46730	11	0.282601	29	0.282596	746	18	102	10.0	1.0	1.03
U98	0.0290	8	0.00079	2	1.46726	10	0.282643	29	0.282632	725	16	101	10.8	1.0	0.96
U99	0.0263	11	0.00074	3	1.46728	9	0.282614	28	0.282603	719	17	99	9.7	1.0	1.02
U100	0.0192	6	0.00055	2	1.46731	10	0.282624	29	0.282616	696	16	98	9.6	1.0	0.99
U101	0.0265	3	0.00074	1	1.46730	10	0.282629	27	0.282619	740	15	101	10.7	1.0	0.99
U103	0.0198	0	0.00056	0	1.46727	11	0.282619	29	0.282611	737	16	101	10.3	1.0	1.00
U104	0.0327	6	0.00091	2	1.46729	10	0.282651	29	0.282639	721	16	101	10.9	1.0	0.95
U105	0.0348	14	0.00097	4	1.46729	9	0.282657	29	0.282644	747	16	101	11.7	1.0	0.94
TR28 *(syn-Keraf arc)* – **2nd analytical session**															
U137	0.0187	4	0.00057	1	1.46725	11	0.282614	28	0.282606	720	16	101	9.8	1.0	1.01
U138	0.0193	8	0.00058	3	1.46729	10	0.282621	33	0.282613	740	16	101	10.5	1.2	1.00
U139	0.0208	7	0.00063	2	1.46725	11	0.282614	28	0.282605	730	15	102	9.9	1.0	1.01
U140	0.0189	2	0.00057	1	1.46732	11	0.282603	28	0.282595	677	16	92	8.4	1.0	1.03
U141	0.0207	2	0.00058	0	1.46729	10	0.282593	29	0.282585	738	16	101	9.4	1.0	1.05
U143	0.0224	7	0.00067	2	1.46730	12	0.282616	28	0.282607	733	15	101	10.1	1.0	1.01
U144	0.0229	5	0.00068	2	1.46733	11	0.282614	29	0.282605	697	18	101	9.2	1.0	1.01
U145	0.0214	2	0.00063	0	1.46724	16	0.282607	27	0.282598	732	18	102	9.8	1.0	1.03
U153	0.0213	9	0.00063	2	1.46726	10	0.282620	29	0.282612	733	16	100	10.2	1.0	1.00
U154	0.0174	1	0.00053	0	1.46727	12	0.282598	28	0.282591	733	16	100	9.5	1.0	1.04
WG03-OC-05 *(syn-Keraf arc)* – **1st analytical session**															
a221c	0.0263	3	0.00083	1	1.46724	19	0.282495	22	0.282482	834	20	99	7.9	0.8	1.21
a223c	0.0034	0	0.00008	0	1.46725	43	0.282531	21	0.282529	819	21	100	9.3	0.7	1.12
a224r	0.0420	10	0.00121	3	1.46721	20	0.282616	23	0.282600	722	18	98	9.6	0.8	1.03
a225	0.0179	2	0.00060	1	1.46734	17	0.282555	26	0.282547	684	16	102	6.9	0.9	1.14
a226	*0.0156*	*2*	*0.00050*	*1*	*1.46726*	*15*	*0.282576*	*22*	*0.282569*	*738*	*17*	*89*	*8.9*	*0.8*	*1.08*
a233	*0.0246*	*4*	*0.00082*	*1*	*1.46726*	*36*	*0.282591*	*22*	*0.282582*	*545*	*14*	*95*	*5.0*	*0.8*	*1.13*
a236r	0.0207	1	0.00062	1	1.46724	22	0.282585	22	0.282576	747	19	99	9.3	0.8	1.06

Table 1-4 ***(continued)***

ID Lu-Hf	$^{176}Yb/^{177}Hf$ [a]	±2σ	$^{176}Lu/^{177}Hf$ [a]	±2σ	$^{178}Hf/^{177}Hf$	Sig_{Hf} [b] (V)	$^{176}Hf/^{177}Hf$	±2σ[c]	$^{176}Hf/^{177}Hf_{(i)}$[d]	age [f] (Ma)	±2σ	conc.[g]	$\varepsilon Hf_{(i)}$ [d]	±2σ [c]	T_{DM2} (Ga)
a246	0.0413	7	0.00143	3	1.46724	32	0.282564	47	0.282547	655	15	96	6.2	1.7	1.16
WG03-OC-05 *(syn-Keraf arc)* – **2nd analytical session**															
a227	0.0109	2	0.00026	0	1.46728	11	0.282563	27	0.282559	748	17	102	8.7	0.9	1.09
a228	0.2107	40	0.00630	13	1.46728	14	0.282658	31	0.282578	673	17	101	7.7	1.1	1.09
a229	*0.0290*	*9*	*0.00085*	*3*	*1.46731*	*14*	*0.282561*	*26*	*0.282549*	*711*	*18*	*112*	*7.6*	*0.9*	*1.13*
a230c	*0.0300*	*17*	*0.00092*	*7*	*1.46741*	*12*	*0.282564*	*31*	*0.282552*	*669*	*20*	*86*	*6.7*	*1.1*	*1.14*
a231r	*0.0436*	*55*	*0.00116*	*14*	*1.46730*	*12*	*0.282604*	*33*	*0.282597*	*354*	*15*	*80*	*1.2*	*1.2*	*1.18*
a232	*0.0394*	*44*	*0.00107*	*11*	*1.46731*	*11*	*0.282586*	*29*	*0.282570*	*756*	*18*	*84*	*9.3*	*1.0*	*1.07*
a234	*0.0269*	*13*	*0.00076*	*4*	*1.46734*	*11*	*0.282567*	*28*	*0.282558*	*636*	*16*	*78*	*6.2*	*1.0*	*1.14*
a235c	0.0251	13	0.00064	3	1.46730	13	0.282572	29	0.282563	718	17	102	8.2	1.0	1.10
a237c*	0.0268	31	0.00090	10	1.46733	11	0.282554	27	0.282540	812	19	97	9.5	1.0	1.10
a245	*0.0464*	*15*	*0.00128*	*3*	*1.46731*	*12*	*0.282596*	*29*	*0.282581*	*598*	*18*	*86*	*6.2*	*1.0*	*1.11*
a247	*0.0364*	*27*	*0.00090*	*7*	*1.46739*	*11*	*0.282584*	*55*	*0.282571*	*719*	*20*	*87*	*8.5*	*1.9*	*1.08*
a248*	0.0143	14	0.00044	4	1.46735	13	0.282482	28	0.282475	819	19	100	7.4	1.0	1.22
a249	0.0399	23	0.00123	8	1.46732	11	0.282577	28	0.282559	762	18	104	9.0	1.0	1.09
WG03-OC-01b *(post-Keraf arc)* – **1st analytical session**															
a188	0.0478	14	0.00155	4	1.46724	18	0.282658	23	0.282639	626	15	100	8.8	0.8	0.99
a178	0.0291	4	0.00101	1	1.46723	19	0.282635	23	0.282623	628	15	100	8.3	0.8	1.02
a177	*0.0513*	*7*	*0.00164*	*2*	*1.46736*	*14*	*0.282676*	*47*	*0.282661*	*500*	*13*	*100*	*6.7*	*1.7*	*1.00*
a169	0.0314	7	0.00108	2	1.46728	20	0.282649	21	0.282636	622	15	99	8.6	0.8	1.00
a168	0.0373	8	0.00130	2	1.46728	20	0.282655	22	0.282640	618	14	102	8.7	0.8	0.99
a166	0.0424	17	0.00138	5	1.46722	19	0.282640	24	0.282624	620	15	100	8.2	0.9	1.02
a160	*0.0629*	*29*	*0.00192*	*9*	*1.46725*	*15*	*0.282667*	*27*	*0.282648*	*505*	*13*	*96*	*6.4*	*1.0*	*1.02*

Corresponding U-Pb dataspot IDs are indicated.

In italics: out of 95-105% degree of concordance and post-crystallization tectono-metamorphic event-related Pb loss dataspots.

** Inherited zircon grains.*

[a] $^{176}Yb/^{177}Hf=(^{176}Yb/^{173}Yb)_{true}.(^{173}Yb/^{177}Hf)_{measured}.(M^{173}(Yb)/M^{177}(Hf))b(Hf)$, $b(Hf)=ln(^{179}Hf/^{177}Hf_{true} / {}^{179}Hf/^{177}Hf_{measured})/ln(M^{179}(Hf)/M^{177}(Hf))$, M=mass of respective isotope. The Lu/Hf were calculated in a similar way by using the Lu/Hf and b(Yb). Quoted uncertainties (absolute) relate to the last quoted figure. The effect of the inter-element fractionation on the Lu/Hf was estimated to be about 6% or less based on analyses of the GJ-1 and Temora zircons.

[b] Mean Hf signal in volt.

[c] Uncertainties are quadratic additions of the within-run precision and the daily reproducibility of the zircon GJ-1. Uncertainties for GJ-1 is 2 S.D. (2 standard deviation).

[d] Initial $^{176}Hf/^{177}Hf$ and $\varepsilon Hf_{(i)}$ calculated using the age (Ma), and the CHUR parameters:
$^{176}Lu/^{177}Hf = 0.0336$, and $^{176}Hf/^{177}Hf = 0.282785$ (Bouvier et al., 2008).

[e] Two-stage model age in billion years using the measured $^{176}Lu/^{177}Lu$, the estimated age (Ma), a value of 0.01113 for the average continental crust (second stage), and a depleted mantle $^{176}Lu/^{177}Hf$ and $^{176}Hf/^{177}Hf$ of 0.03933 and 0.283294 (Blichert-Toft and Puchtel, 2010).

[f] $^{206}Pb/^{238}U$ age.

[g] Degree of concordance (%) = $^{206}Pb/^{238}U$ age / $^{207}Pb/^{206}Pb$ age.100.

Table 1-4: Lu-Hf isotopic compositions of zircon grains used in this study. BSE- and SE-SEM images illustrating zircon morphologies and dataspots are provided in Supplementary Material 1-1.

Sample ID	age (Ma)	Rb* (ppm)	Sr* (ppm)	$^{87}Sr/^{86}Sr$	±2σ	$(^{87}Sr/^{86}Sr)_i$	±2σ	Sm* (ppm)	Nd* (ppm)	$^{143}Nd/^{144}Nd$	±2σ	$Nd_{(i)}$	±2σ	$\varepsilon Nd_{(i)}$	±2σ	T_{DM2} (Ga)
Early Keraf arc-related samples																
WG03-OC-01c	***819***	125	296	0.709648	0.000004	**0.695614****	0.001407	2.3	7.2	0.512809	0.000003	2.29700	7.22700	**3.8**	2.1	**1.12**
TR02a	***819***	7.0	443	0.703245	0.000009	**0.702723**	0.000061	3.1	10.3	0.512805	0.000005	3.11400	10.25470	**4.7**	2.0	**1.06**
UTM-OC-03	***819***	0.39	95.2	0.703982	0.000006	**0.703845**	0.000020	3.8	13.1	0.512780	0.000003	3.75410	13.13770	**5.3**	1.9	**1.01**
UTM-OC-03	***819***	0.39	95.2	0.703982	0.000006	**0.703845**	0.000020	3.8	13.1	0.512780	0.000003	3.75410	13.13770	**5.3**	1.9	**1.01**
WG03-OC-03b	**819**	7.1	327	0.704077	0.000005	**0.703353**	0.000077	3.8	12.7	0.512804	0.000004	3.78740	12.69910	**5.0**	2.0	**1.03**
Syn-Keraf arc-related samples																
TR02b	***700***	53.3	341	0.707252	0.000008	**0.702803**	0.000453	3.6	20.4	0.512465	0.000003	3.61630	20.43370	**4.7**	1.0	**0.96**
TR21	**694**	31.8	433	0.705037	0.000008	**0.702967**	0.000215	4.0	18.5	0.512605	0.000003	4.01620	18.52220	**5.2**	1.2	**0.92**
TR23	***693***	61.2	361	0.707672	0.000006	**0.702896**	0.000484	1.6	10.5	0.512424	0.000003	1.59040	10.46240	**5.1**	0.9	**0.92**
TR25	**693**	3.1	506	0.703044	0.000008	**0.702874**	0.000025	6.7	30.5	0.512668	0.000003	6.71840	30.50470	**6.2**	1.2	**0.84**
TR28	**698**	86.3	307	0.710581	0.000006	**0.702618**	0.000802	4.9	21.9	0.512653	0.000004	4.89990	21.88100	**5.8**	1.3	**0.87**
TR29	***698***	35.0	578	0.704491	0.000010	**0.702773**	0.000182	4.2	22.2	0.512554	0.000003	4.16530	22.20890	**5.8**	1.1	**0.87**
Post-Keraf arc-related samples																
TR13	***620***	152	170	0.724818	0.000007	**0.702273**	0.002261	3.9	23.2	0.512481	0.000003	3.93920	23.24070	**4.4**	0.9	**0.92**
WG03-OC-01a	***620***	106	292	0.711759	0.000007	**0.702657**	0.000917	4.8	25.0	0.512542	0.000003	4.75810	25.00360	**4.6**	1.0	**0.91**
WG03-OC-01b	**620**	138	139	0.726846	0.000010	**0.701772**	0.002517	2.6	8.2	0.512773	0.000006	2.56000	8.22460	**3.3**	1.6	**1.01**
WG03-OC-05	**655**	68.2	357	0.707890	0.000007	**0.702805**	0.000516	3.3	24.8	0.512333	0.000003	3.32290	24.78760	**3.7**	0.7	**1.00**

**The relative error associated with whole-rock Rb, Sr, Sm and Nd concentrations is 5%.*

*** The $(^{87}Sr/^{86}Sr)_i$ value calculated for sample WG03-OC-01c are unrealistic, leading to wonder about the significance of the measured $^{87}Sr/^{86}Sr$ ratio.*

Considered crystallization ages are $^{206}Pb/^{238}U$ weighted mean or single zircon ages from this study (Fig. 1-7). The crystallization age for samples that have not been dated is written in italics and approximated from field petrographic and geochemical relationships.

The Rb-Sr and Sm-Nd decay constants are $1.42.10^{-11}$ y^{-1} and $6.54.10^{-21}$ y^{-1}, respectively (Steiger and Jäger, 1977; Lugmair and Marti, 1978).

$\varepsilon Nd_{(i)}$ values are calculated after the present-day CHUR Sm-Nd isotopic composition from Jacobsen and Wasserburg (1980).

T_{DM2} is the two-stage model age for extraction from the depleted mantle calculated after the present-day depleted mantle and continental crust Sm-Nd isotopic composition from Liew and Hofmann (1988).

Table 1-5: Rb-Sr and Sm-Nd whole-rock isotopic compositions of early, syn- and post-Keraf arc igneous rocks used in this study.

5. Lithospheric evolution of the central Keraf suture between *ca.* 840-620 Ma

The geochemical, geochronological and isotopic data collected on arc-related batholiths, arc volcanic flows and late undeformed plutons are combined to structural data (Perret et al., under review) to propose a lithospheric evolution model for the central Keraf suture between *ca.* 840-620 Ma (Fig. 1-9). For each of the geodynamical stages described below, we outline the associated geodynamical system illustrated by the magmatic record. Please note that the geodynamical evolution of the island arc-related Gabgaba-Gebeit terrane to the east of the cross-section is not addressed by this study.

5.1. Intra-oceanic subduction and Keraf island arc-back-arc system

5.1.1. Intra-oceanic subduction and early to syn-Keraf island arc magmatism

Nd and Sr isotopic compositions of early to syn-Keraf arc igneous rocks plot into mid-ocean ridge basalt and oceanic island basalt fields (Fig. 1-8c). It proves they crystallized in an oceanic setting as they would have otherwise record crustal contamination at some extent, as demonstrated by the large Sr-Nd isotopic domain for continental basalts (White, 2015). Besides, they are metaluminous I-type andesite, dioritoids and granitoids with juvenile Hf ($\varepsilon Hf_{(i)} \sim +9.1 - +10.7$) , Sr ($(^{87}Sr/^{86}Sr)_i \sim 0.7034$-0.7038 and one lower value at 0.7027) and Nd ($\varepsilon Nd_{(i)} \sim +3.8 - +5.3$) isotopic compositions (Figs. 1-3e-d, 1-5, 1-6a, b, d and e, 1-8). It supports the fact that the Keraf arc system is an island arc, thus developed in an intra-oceanic subduction setting.

5.1.2. Geodynamical setting associated with Keraf ophiolites

Ophiolites have been widely documented in the Atmur-Delgo, Keraf and Bayuda areas (Barth and Meinhold, 1979; Meinhold, 1979; Ahmed et al., 1980; Dawoud, 1980; Almond and Ahmed, 1987; Abdelrahman, 1993; Denkler et al., 1993; Schandelmeier et al., 1994b; Abdelsalam et al., 1995). More specifically, the Keraf and Atmur-Delgo

ophiolites are interpreted to be oceanic seafloor remnants of connected ensialic back-arc basins related to the Mozambique ocean (Abdelrahman, 1993; Schandelmeier et al., 1994b; Stern, 1994; Abdelsalam et al., 1995; Abdelrahman et al., 2017). Despite we did not collect oceanic basement rock such as typical tholeiitic MORBs, Keraf basalts display N-MORB-like flat patterns and LREE enrichment which are typical features of back-arc basin igneous rocks (Saunders and Tarney, 1984, 1991; Abdelrahman et al., 2017). It confirms that the Keraf basin likely relates to an island arc-back-arc system similar to others recognized throughout the ANS (*e.g.,* Al-Saleh and Boyle, 2001; El-Naby and Frisch, 2006; Teklay, 2006). We will therefore consider the geodynamical evolution of the Keraf island arc-back-arc system in what follows (Fig. 1-9).

5.2. Magmatic events recorded through the central Keraf suture

5.2.1. Juvenile island arc magmatism between *ca.* 840-810 Ma

The oldest island arc dioritoids were emplaced at *ca.* 840-810 Ma at an intra-oceanic subbduction site within the Keraf back-arc basin (Fig. 1-9). Their whole-rock geochemical compositions indicate that the earliest Keraf arc-related magmas documented in this study are already evolved. Our sampling did not recorded the boninitic magmatism typical of the initiation of the proto-island arc described in modern days (Ribeiro et al., 2020). The Keraf island arc magmatic activity may therefore have initiated earlier than *ca.* 840 Ma.

Early Keraf island arc magmas represent juvenile components, with consistent supra-chondritic Hf and Nd isotopic compositions and two-stage model ages of *ca.* 1.12-1.00 Ga, for both isotopic systems. They formed mid-crustal dioritoid cumulates, as indicated by the record of plagioclase accumulation through Sr and Eu positive anomalies, which is widely recognized in paleo-island arcs (Chappell and Wyborn, 2004; DeBari and Greene, 2011). Coeval andesitic flows and volcanosediments that are interbedded with immature arc-derived sediments and detrital continental material

eroded from the Saharan meta-craton, relying on field observations (Fig. 1-9; Perret et al., under review). Such an architecture is also well-known in both modern-day and paleo-island arcs (*e.g.,* Calvert, 2011). The geometry of the system likely led to high rate of sedimentation and diversity in the nature of sediment influx, as suggested by previous studies (Abdelrahman, 1993; Stern et al., 1993; Bailo et al., 2003).

5.2.2. Mixed juvenile island arc magmatism and crustal arc reworking between *ca.* 760-655 Ma

There is a large span of magmatic pulses recorded between *ca.* 760-655 Ma by zircon antecrysts and xenocrysts of dated granitoids (Fig. 1-7g). Considering our data only, syn-Keraf arc-related igneous rocks are metaluminous I-type dioritoid to granitoid cumulates, which suggests that the Keraf island arc magmatic activity is protracted at least until *ca.* 655 Ma (Fig. 1-9). These rocks are geochemically and isotopically similar to *ca.* 740-710 Ma granitoids studied by Bailo et al. (2003) in the central and northern Keraf suture (Figs. 1-2, 1-5, 1-6, 1-8). It supports the fact that island arc magmatic activity is not limited to the central portion of the Keraf suture but rather widespread along-strike.

Ultimate crystallization ages calculated in our study spread from *ca* 700 Ma to *ca.* 655 Ma suggesting that island arc magmatic activity probably reached its climax at *ca.* 700 Ma. There is an overall LREE-enrichment from *ca.* 840-810 Ma to *ca.* 760-655 Ma Keraf arc igneous rocks. The youngest granitoids are the most evolved, with the steepest chondrite-normalized LREE patterns and lowest $\varepsilon Hf_{(i)}$ and $\varepsilon Nd_{(i)}$ values (*e.g.,* WG03-OC-05 graniodiorite with $\varepsilon Hf_{(i)} \sim +7.7 - +9.0$ and $\varepsilon Nd_{(i)} = 3.7 \pm 1.0$; Figs. 1-6a, b and d, 1-8a, b). It illustrates that the Keraf island arc has become more and more mature between *ca.* 810-655 Ma.

Yet, the lack of arc magmatic activity record between *ca.* 810-760 Ma in our data (Fig. 1-7g) could suggest to rather consider two distinct island arcs, but this proposal is supported by no key evidence. Furthermore, a ~50 Myr-long lull, *i.e., "period where the volume of magmatism added to the crust is much less than average"*, is consistent with

flare-up and lull cycle wavelength reported for Phanerozoic to modern-day magmatic arcs (Paterson and Ducea, 2015). In this sense, the lack of zircon record between *ca.* 810-760 Ma does not mean there was no arc magmatic activity at all during this period. Our sampling and zircon handpicking may indeed not be entirely representative of every magmatic events expressed throughout the studied area. It is also worth noticing that the effects of subduction-related crustal erosion and recycling on arc crustal recording are not estimated.

There is no isotopic evidence for reworking of pre-Neoproterozoic continental crust during the *ca.* 760-655 Ma Keraf arc magmatic activity. However, the texture, geochemical characteristics and $^{206}Pb/^{238}U$ single ages between *ca.* 840-810 Ma of inherited zircon grains in these rocks remind of ante- and autocrysts from early Keraf island arc dioritoids (Figs. 1-4, 1-7e, g). Besides, *ca.* 840-810 Ma and *ca.* 760-655 Ma arc rocks have similar two-stage model ages (>90% of T_{DM2} ages ranging between *ca.* 0.94-1.10 Ga). Crustal reworking of the early Keraf arc crust, or rocks with a similar model-age, therefore occurred at *ca.* 760-655 Ma (Fig. 1-9).

Whereas the Hf isotopic system suggest crustal reworking, the Nd whole-rock isotopic compositions are decoupled and rather reflect extraction of mantellic material at *ca.* 0.96-0.84 Ga. We suggest that the Nd isotopic signature of *ca.* 760-655 Ma island arc-related rocks ($\varepsilon Nd_{(i)}$ +5.2±1.4) represents a mixed whole-rock model age between two melt sources extracted from the mantle at *ca.* 1.2-1.0 Ga, *i.e.,* older Keraf island arc rocks, and *ca.* 0.76-0.65 Ga, *i.e.*, the age of magmatic pulses recorded by these samples. Such mixed Nd model ages in bulk rock are widely reported in literature where several sources with distinct isotopic signatures contribute to melt formation, including sediment assimilation, in both ancient and current orogens (*e.g.,* Carr et al., 1990; Vroon et al., 1993; Janoušek et al., 1995; Keay et al., 1997; Maier et al., 2000). In addition to arc crust reworking, there is therefore an additional juvenile mantellic component contributing to Keraf island arc magmatism between *ca.* 760-655 Ma, as the second melt source invoked

has a crustal residence age in the range of these intrusion dates (Fig. 1-9). Another island arc system involving several sources has been described in the Eastern Desert of Egypt at *ca.* 690 Ma, suggesting that such process is widespread at that time throughout the Nubian shield (*e.g.,* Stern et al., 2020).

The record of the *ca.* 760-655 Ma Keraf island arc flare-up brings insights into magmatic processes involved during this period. Firstly, we notice that the youngest, *ca.* 655 Ma granodiorite displays the lowest HREE and Y abundances relative to chondrite and a rather flat chondrite-normalized HREE pattern (WG03-OC-05). The same trend applies at a lesser extent to the older, *ca.* 700-690 Ma granitoids (Fig. 1-6b, f). It is known that the composition of the parental melt, and thus rocks which crystallize from it, depends on both its source composition and mineral phases coexisting during melting and induced fractionation. Such a decrease in HREE abundances is typical of garnet presence during petrogenesis of the parental magmas (*e.g.,* van Westrenen et al., 2001; Alonso-Perez et al., 2009; Kendrick and Yakymchuk, 2020). Melt production and fractionation occurred at pressure conditions high enough to ensure garnet stability. Similarly, the bell-shaped concave-down pattern centered on Ho for TR23 granodiorite is rather characteristic of the presence of amphibole during magma petrogenesis. We may therefore infer that juvenile melt production occurred at pressure conditions >1.2 GPa, *i.e.,* >40 km-depth approximately, to ensure garnet-amphibole fractionation in the root of the Keraf island arc (Fig. 1-9; Alonso-Perez et al., 2009).

5.2.3. Post-collisional magmatism at *ca.* 620 Ma

Post-Keraf arc granodiorite to monzogranite plutons formed at *ca.* 621.4±4.3 Ma and cuts across every inherited fabric and lithologies through the central Keraf suture (Figs. 1-2, 1-9; Table 1-1). According to their metaluminous to peraluminous nature, their consistent negative Eu anomaly but various chondrite-normalized REE patterns, they are interpreted as I-type to A-type post-collisional granitoids (Figs. 1-5b, 1-6c, e).

The best-studied granodiorite-monzogranite pluton (WG03-OC-01a and b, respectively) displays mingling textures that witness interactions between two coexisting magmas (Fig. 1-3f). These two rocks have distinct geochemical signatures. The granodiorite is I-type and very similar to the *ca.* 700-655 Ma Keraf island arc plutonic rocks whereas monzogranite has a fairly flat to steeply decreasing chondrite-normalized REE pattern, but both show similar LREE relative abundances (Fig. 1-6c). Moreover, this pluton encloses a monzodiorite xenolith with geochemical characteristics comparable to the *ca.* 840-810 Ma dioritoids (Figs. 1-3f, 1-5, 1-6a, d, e). The monzodiorite xenolith is therefore considered as a fragment of the *ca.* 840-810 Ma Keraf arc lower crust. Moreover, *ca.* 826 Ma and *ca.* 745 Ma inherited zircon grains have similar ages and internal textures as zircon ante- and autocrysts of Keraf arc-related plutonic rocks. It is in agreement with Hf and Nd isotopic compositions which are juvenile ($\varepsilon Hf_{(i)} \sim +8.2$ – $+8.8$ and $\varepsilon Nd_{(i)} = +4.1 \pm 1.0$) and lead to consistent model ages of *ca.* 1.12-0.99 Ma, comparable to the Keraf arc cumulates. All these observations point out towards reworking of the Keraf island arc crust which partially melted due to decompression in a post-collisional context (Fig. 1-9). Mixing with evolved magma extracted from the mantle cannot be excluded from our data and is also represented in Figure 9. Such a hybrid granite magmatism has notably been documented in the Eastern Desert of Egypt in an orogenic collapse setting where mantle upwelling occurred (Zoheir et al., 2021).

Other processes advocated for triggering post-collisional magmatism and asthenospheric upwelling throughout the Nubian shield are slab roll-back (*e.g.,* Farahat et al., 2011; Flowerdew et al., 2013; Abd El-Rahman et al., 2017) and lithospheric mantle delamination (Avigad and Gvirtzman, 2009; Eliwa et al., 2014; Khalil et al., 2015; Eyal et al., 2018; Megerssa et al., 2020). Lithospheric delamination should result in surface uplift and subsequent orogenic collapse in an extensive regime. Such post-collisional extensive deformation is not to weakly recorded within the central Keraf suture (Perret

et al., under review), which tends to discredit this hypothesis. Both options are nevertheless proposed in Figure 9 as our data do not allow to conclude further.

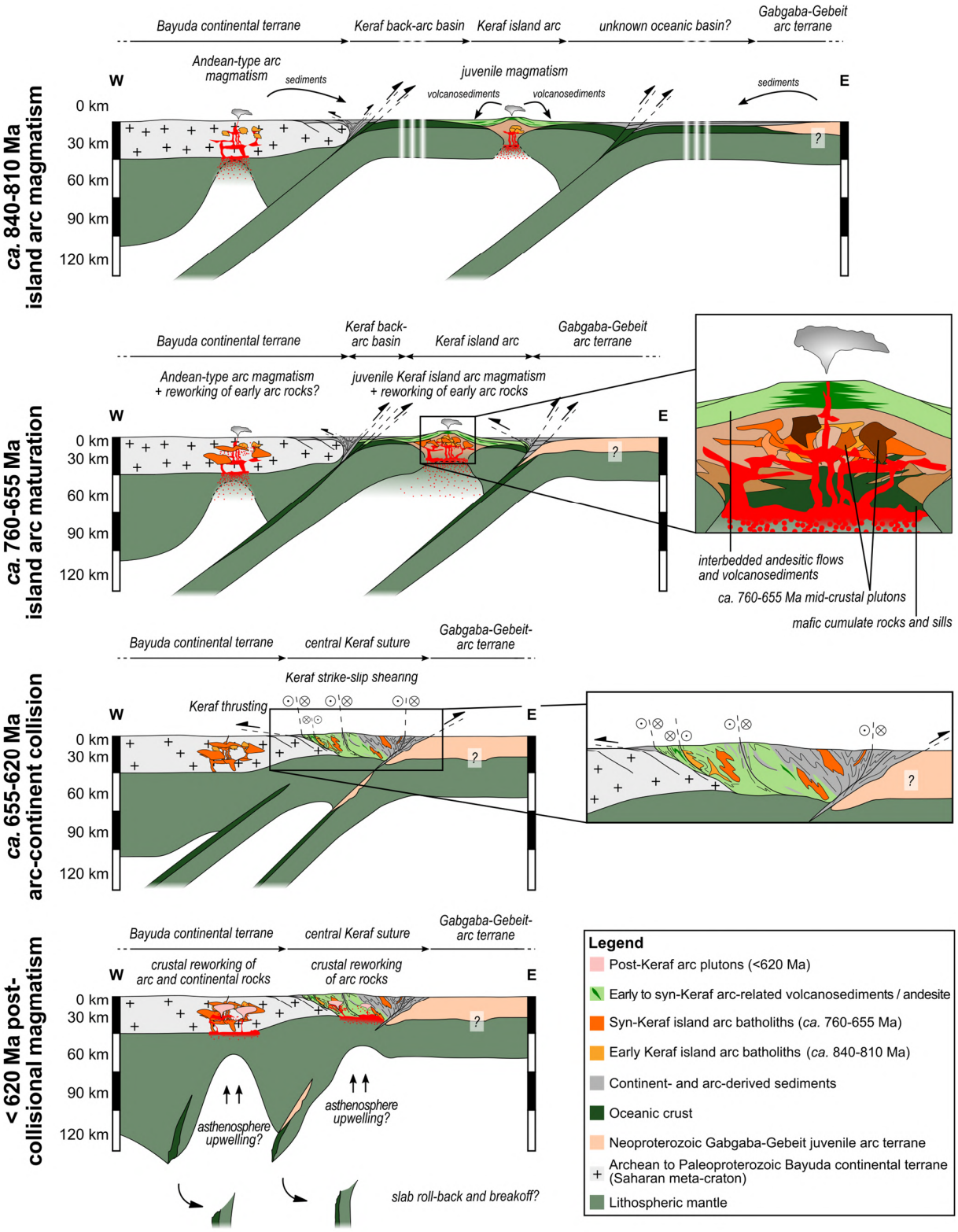


Figure 1-9: Geodynamical sketch in a lithospheric cross-section across the central Keraf suture representing the long-lived island arc activity, suturing and post-collisional magmatic events recorded in our data between *ca.* 840 and *ca.* 620 Ma. The geodynamical evolution of the island arc-related Gabgaba-Gebeit terrane to the east of the cross-section is not addressed by this study.

6. Insights into the Pan-African tectono-magmatic evolution of the northeastern flank of West Gondwana

6.1. Scope of the ~185 Myr-long-lived Keraf island arc at the Gondwana scale

We identified several depth-specific petrogenetic processes involved into the Keraf island arc maturation, *e.g.,* cumulate formation, garnet influence on melt composition and earlier arc crust reworking during, which applied to most Archean (*e.g.,* Laurent et al., 2020) to Phanerozoic (*e.g.,* Alonso-Perez et al., 2009; Jagoutz et al., 2009; DeBari and Greene, 2011; Bouilhol et al., 2015) island arcs documented in literature and even to modern-day arcs (*e.g.,* Kelemen et al., 2003; Jicha and Kay, 2018). If the magmatic processes recorded by the Keraf island arc are thus common, its lifespan is not.

Despite the absence of magmatic record between *ca.* 810-760 Ma in our data, the proposed lithospheric evolution of the central Keraf suture points towards a more or less steady island arc magmatic activity ranging between *ca.* 840-655 Ma (Fig. 1-9). The ~185 Myr lifespan of the Keraf island arc is second to none throughout the Neoproterozoic ANS. Most of ANS island arc records do not exceed 50 Myr and very few reach ~50-80 Myr lifetime (*e.g.,* data compilation of Johnson, 2014). Similar life durations are reported for other Neoproterozoic (*ca.* 820-775 Ma Shishkhid island arc, Russia; Kuzmichev and Larionov, 2013), Phanerozoic (*e.g., ca.* 130-95 Ma Kohistan-Ladakh island arc, Pakistan; Jagoutz et al., 2009; Bosch et al., 2011; Bouilhol et al., 2011) and modern-day island arc systems (*e.g.,* 46 Myr-old Aleutian and 35 Myr-old Izu-Bonin island arcs; Jicha et al., 2006; Barth et al., 2017), although the latter are still active.

Nevertheless, it is worth noticing that Eyal et al. (2014) documented the existence of *ca.* 1030-930 Ma and *ca.* 870-740 Ma island arcs in Sinai. Triantafyllou et al. (2018) also documented the existence of a 100-120 Myr-long arc activity for the Neoproterozoic Bougmane island arc complex, Anti-Atlas, Morocco. Santosh et al. (2009) even suggested the existence of a *ca.* 750-560 Ma long-lived magmatic arc associated to Palghat-Cauvery

suturing during late Neoproterozoic-Cambrian Gondwana assembly in southern India. These examples support the fact that >100 Myr-lifespan is realistic for Neoproterozoic island arcs. Our interpretation towards a prolonged maturation of the Keraf island arc therefore makes sense (Fig. 1-9). We could then wonder what degree of maturation is reached by the Keraf island arc after such a prolonged lifetime. Unfortunately, we cannot tell from the data presented in this study, as modern-day island arcs exemplify that arc maturation processes involve parameters difficult to trace in fossil island arcs such as arc migration and syn-magmatic growth of serpentinized fore-arc mantle (Ribeiro et al., 2020).

Finally, the record of extra-long-lived island arc systems during Neoproterozoic is likely another specificity of the atypical geodynamical evolution of Gondwana. The geodynamical scenario leading to its assembly indeed differs from the conventional supercontinent cycle model, with overlapping between (i) Rodinia break-up and early island arc subduction and (ii) final Gondwana collision and onset of the opening of the Iapetus ocean (Oriolo et al., 2017). Some authors even suggest that Gondwana should not be considered as a supercontinent *stricto sensu* and interpreted its assembly an intermediate stage towards the formation of Pangea at *ca.* 300 Ma (Merdith et al., 2017; Grenholm, 2019 and references therein). These perspectives raises critical questions about the dimension of oceanic and/or back-arc basins closed along such long-lived accretionary-type subduction zones during the formation Arabian-Nubian shield. Unfortunately, paleomagnetic data are lacking to bring additional knowledge about it.

6.2. Reconciliation of the geometry of the Keraf and Atmur-Delgo arc systems

We propose a schematic regional-scale reconstruction in map view of the possible geodynamical scenario leading to the formation of the western Nubian shield (Fig. 1-10). These cartoons aim at integrating data from this study with the global understanding of the geometry of the Keraf and Atmur-Delgo intra-oceanic subduction and arc-collision

systems. Previous geochronological and isotopic data published in the Atmur-Delgo, northern and southern Keraf suture, and Bayuda and Sabaloka continental terranes, which are part of the nearby Saharan meta-craton, are discussed in this section and are compiled in Supplementary Material 1-4.

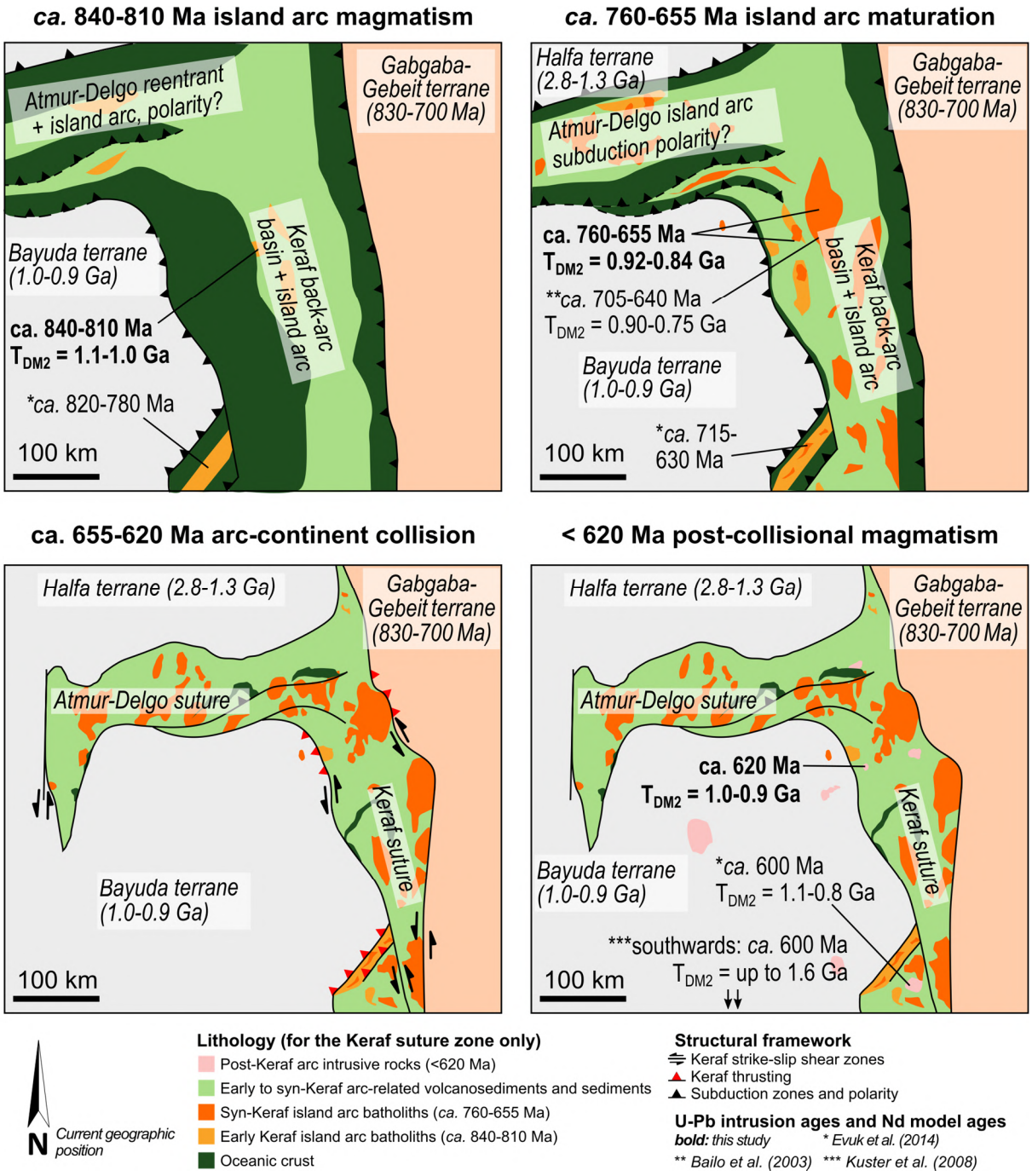


Figure 1-10: Map view of the possible regional-scale geodynamical scenario leading to the formation of the western Nubian shield. Isotopic data from literature summarized in this figure and discussed in the text are compiled in Supplementary Material 1-4.

On first hand, we considered a west-dipping polarity for Gabgaba-Gebeit-Keraf and Keraf-Saharan meta-craton subduction sites, as suggested for other north-trending subduction zones from prograding metamorphism polarity and geochemical trends across-arc (Teklay, 2006; Gamal El Dien et al., 2014). On second hand, the east-striking Atmur-Delgo suture contains an ophiolitic belt derived from an oceanic re-entrant of the Keraf back-arc basin into the Saharan meta-craton, and is contemporaneous with the Keraf suture (Burke and Sengör, 1986; Abdelrahman, 1993; Denkler et al., 1993; Harms et al., 1994; Schandelmeier et al., 1994b; Abdelsalam et al., 1998; Abdelrahman et al., 2017). North-dipping subduction is widely accepted to interpret the formation of the Atmur-Delgo suture (Denkler et al., 1993, 1994; Schandelmeier et al., 1994b).

However the proposed polarities for coexisting Keraf and Atmur-Delgo oceanic subductions suggest an unrealistic 3D slab geometry at depth in the swinging zone between the Atmur-Delgo and Keraf sutures (Fig. 1-10). A similar geometrical incoherence has been addressed in the present-day southern New Hebrides volcanic arc-back arc system, Pacific Ocean (Patriat et al., 2015). The latter authors unraveled the initiation of an incipient north-dipping subduction zone and death of the early south-dipping one as a result from the progressive retreat of the New Hebrides trench and migration of the upper plate southwards. There is no evidence from our study that similar tectonic processes could apply to the Neoproterozoic Atmur-Delgo-Keraf suture system, but it is worth noticing that realistic models accounting for coeval north-dipping and west-dipping intra-oceanic subduction could be suggested.

6.3. Insights into the tectono-magmatic evolution of the northeastern flank of West Gondwana

6.3.1. Between *ca.* 840-655 Ma

Firstly, volcanic rocks similar to andesite from this study have been recognized along the Keraf suture and even in the Saharan meta-craton (Meinhold, 1979; Dawoud,

1980; Ries et al., 1985; Abdelrahman, 1993; Stern et al., 1994). They bring consistent temporal constraints for island arc volcanism at *ca.* 880-720 Ma (whole-rock Rb-Sr dating; Ries et al., 1985). Our geochronological data and the latter ages collectively suggest that intra-oceanic subduction and related island arc magmatism initiated earlier than *ca.* 800-750 Ma as currently considered for the western Nubian shield (Abdelsalam et al., 1998; Bailo et al., 2003).

It also demonstrates that a magmatic activity coeval with early Keraf island arc magmatism is recorded in the northeastern flank of West Gondwana. For this reason, we suggest the evolution of an Andean-type continental arc at ocean-continent subduction site between the Keraf arc-related micro-terrane and the Bayuda terrane (Fig. 1-9). *ca.* 820-780 Ma dioritoids have been documented southwest to the Keraf suture (Fig. 1-10). They could either relate to the latter continental arc magmatic activity or result from another oceanic reentrant of the Keraf back-arc basin within the Saharan meta-craton, according to their juvenile nature (Supplementary Material 1-4; Evuk et al., 2014).

Secondly, Atmur-Delgo island arc igneous rocks were dated at the same period as the *ca.* 760-655 Ma Keraf arc-related batholiths (Fig. 1-10; Supplementary Material 1-4). If the concomitance of island arc magmatism along the Atmur-Delgo and the Keraf intra-oceanic subduction sites was already admitted, this study is the first to bring geochronological data suggesting that the maturation of these island arcs likely extended until *ca.* 655 Ma, far beyond the *ca.* 750 Ma limit considered so far (*e.g.,* Abdelsalam et al., 1998). In addition, *ca.* 715-630 Ma arc-related batholiths were described in the southwestern part of the Keraf suture (Fig. 1-10; Supplementary Material 1-4; Evuk et al., 2014). These data suggest either (i) the prolonged magmatic activity of the Bayuda terrane-hosted continental arc (Fig. 1-9) or (ii) the maturation of another island arc penetrating into the Saharan meta-craton south to the central Keraf suture, with a geometry likely similar to the Atmur-Delgo island arc northwards.

6.3.2. Between *ca.* 655-620 Ma

In agreement with proposed timing constraints for arc magmatism (*ca.* > 655 Ma) and post-collisional *(ca.* < 620 Ma) magmatism, arc-continent collision between the Keraf island arc and the Bayuda terrane, *i.e.,* West Gondwana, has occurred between *ca.* 655-620 Ma. At the regional scale, this tectonic event is expressed by progressive Keraf thrusting and strike-slip shearing (D_{1a} and D_{1b} in Fig. 1-2; Figs. 1-9, 1-10; Perret et al., under review). Geochronological data reappraise the *ca.* 750-640 Ma and *ca.* 640-580 Ma periods previously admitted for these deformation events (Abdelsalam et al., 1998).

The *ca.* 650-600 Ma period likely represents the climax of collision and amalgamation between juvenile terranes across the ANS. It corresponds to terminal suturing of major structures such as the Nakasib-Bir Umq (*e.g.,* Küster et al., 1993; Schandelmeier et al., 1994a; Johnson et al., 2003; Abdelsalam and Stern, 2017) and Yanbu-Sol Hamed-Allaqi-Heiani (*e.g.,* El-Sayed et al., 2004; Ali et al., 2010a; Abdeen and Abdelghaffar, 2011) ocean-ocean sutures. This period also refers to peak pressure-temperature high-grade metamorphism during suturing and thrusting of high-grade gneissic units over greenschist facies-metamorphosed supra-crustal nappes in the Eastern Desert of Egypt (*e.g.,* Neumayr et al., 1998; Loizenbauer et al., 2001; El-Naby and Frisch, 2006; Abd El-Naby et al., 2008; Eliwa et al., 2008; Abu El-Enen et al., 2016; Elisha et al., 2017, 2019). The record of the *ca.* 655-620 Ma Keraf arc-continent collision extends to the West Gondwana scale as the collision between the Congo and Kalahari cratons occurred during this time range (Kröner, 1982), although more recent studies suggest it happened between *ca.* 550-530 Ma (*e.g.,* John et al., 2004; Eglinger et al., 2016). We can conclude that the timing of Keraf arc-continent collision is representative of the final break-up of Rodinia and amalgamation of the northern part of West Gondwana, prior to its final assembly during Cambrian (Gray et al., 2008; Oriolo et al., 2017; Schmitt et al., 2018; Boniface, 2019).

6.3.3. Between *ca.* 620-530 Ma

In addition to the *ca.* 620 Ma post-collisional pluton dated in this study, several others were dated between *ca.* 600-530 Ma along the Keraf suture and within the Bayuda terrane (Figs. 1-9, 1-10; Ries et al., 1985; Kröner et al., 1987; Stern et al., 1994; Abdelsalam et al., 1998; Küster et al., 2008; Evuk et al., 2014). We could therefore imagine that the post-collisional magmatism event lasted until *ca.* 530 Ma at least. Tectono-metamorphic events recorded at *ca.* 550 Ma by zircon isotopic resetting along the central Keraf suture may relate to such magmato-thermal activity, despite no pluton as young as 500 Ma has been described in this study (Fig. 1-7g). However, it is unclear if temperature conditions reached during this period are high enough for enabling zircon isotopic resetting in the area.

Evidence for post-collisional magmatism in the pre-Neoproterozoic Saharan meta-craton implies that crustal melting evidenced in the central Keraf suture significantly affected the northeastern flank of West Gondwana as well. Model ages range from *ca.* 1.6 Ga to *ca.* 0.8 Ga for post-collisional plutons intruding the Bayuda and Sabaloka terranes (Fig. 1-9; Supplementary Material 1-4). These model ages indicate that the Pre-Neoproterozoic continental crust of West Gondwana is well affected by Pan-African tectono-magmatic events, as already described in literature (*e.g.,* Ries et al., 1985; Kröner et al., 1987; Rahman et al., 1990; Küster and Liégeois, 2001), justifying the designation "Saharan *meta*-craton" (Liégeois et al., 2013 and references therein). If these data do not confirm irrevocably the development of a former continental arc at the Keraf arc-related micro-terrane-Saharan meta-craton subduction site (Fig. 1-9), they do not discard our interpretation at least.

7. Conclusions

Geochemical, geochronological and isotopic data collectively discriminate the geodynamical evolution of the central Keraf suture between *ca.* 840-620 Ma, with strong insights into the succession of tectono-magmatic events, crustal growth and reworking processes involved in the assembly of western Gondwana. Firstly, the central Keraf suture records the existence of a ~185 Myr long-lived Neoproterozoic island arc-back system between the northeastern flank of West Gondwana and juvenile arc terranes related to the Arabian-Nubian shield. The Keraf island-arc maturation is illustrated by the shift from (i) juvenile magmatism between *ca.* 840-810 Ma to (ii) protracted mixing between juvenile magmatism and older arc crust reworking between *ca.* 760-655 Ma. In parallel to the Keraf island arc, a continental arc likely evolved along the West Gondwana-Arabian-Nubian shield active margin, as suggested by the magmatic and isotopic record of syn-Keraf arc magmatic activity within the Saharan meta-craton. Final Keraf suturing relates to subsequent arc-continent collision and stacking of the Keraf arc system over the Saharan meta-craton westwards between *ca.* 655-620 Ma. Finally, post-collisional reworking of arc-derived and continental crusts is widespread after *ca.* 620 Ma in the central Keraf suture and the Saharan meta-craton nearby, respectively.

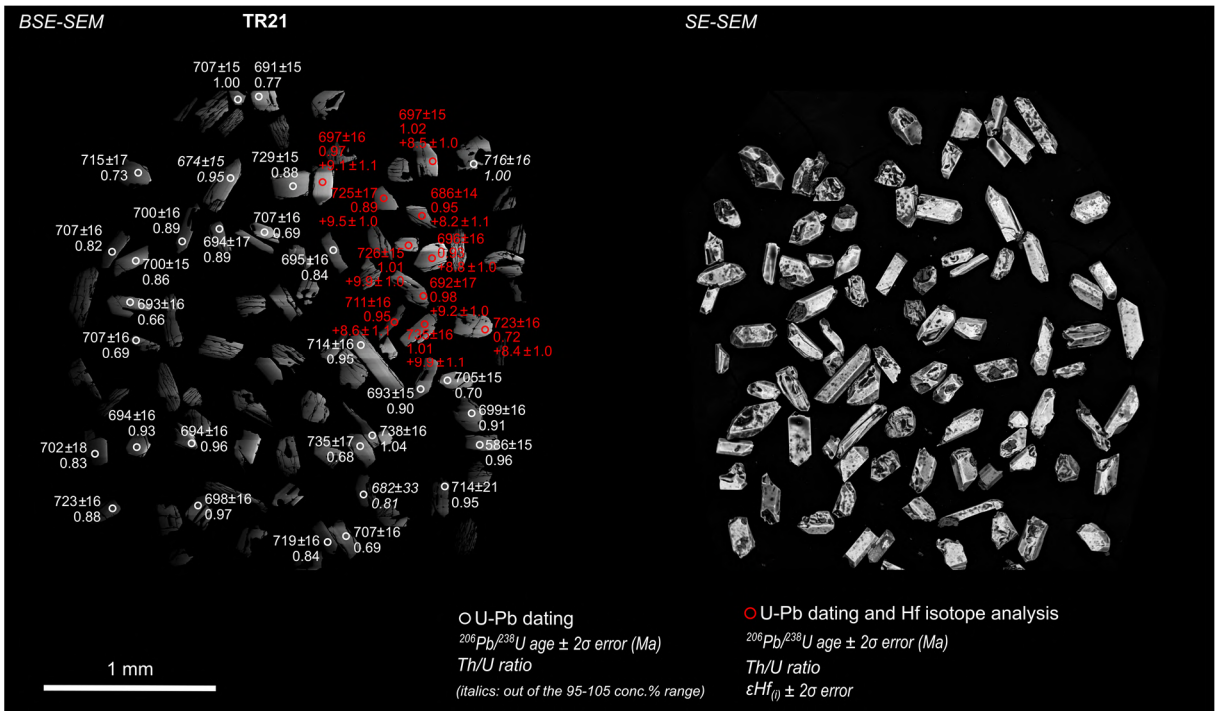
The extra-long lifespan of the Keraf island arc makes it the longest-lived island arc system of the Arabian-Nubian shield documented up to date. Island arcs with >100 Myr lifetime are rare but sometimes documented for Gondwana assembly. Conversely, there is no equivalent in Phanerozoic and modern-day island arc systems. The record of extra-long-lived Neoproterozoic island arcs is likely another specificity of the atypical Gondwana geodynamical evolution, which differs from the conventional supercontinent cycle scenario.

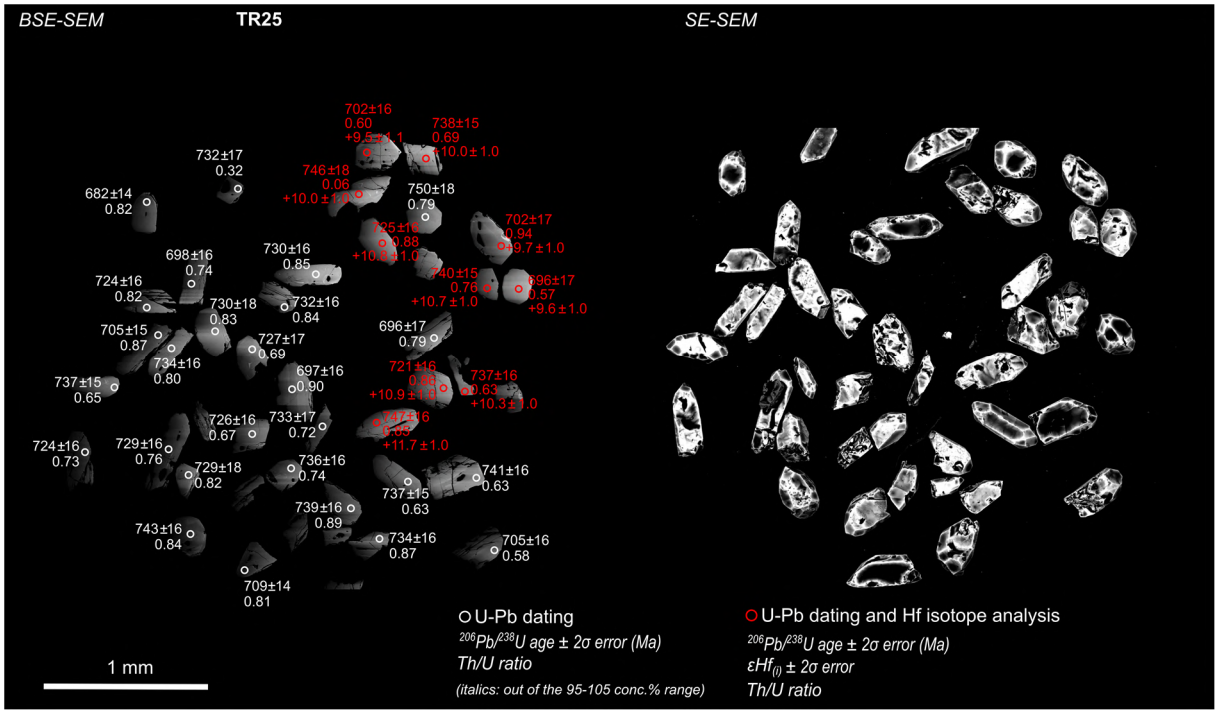
Acknowledgements

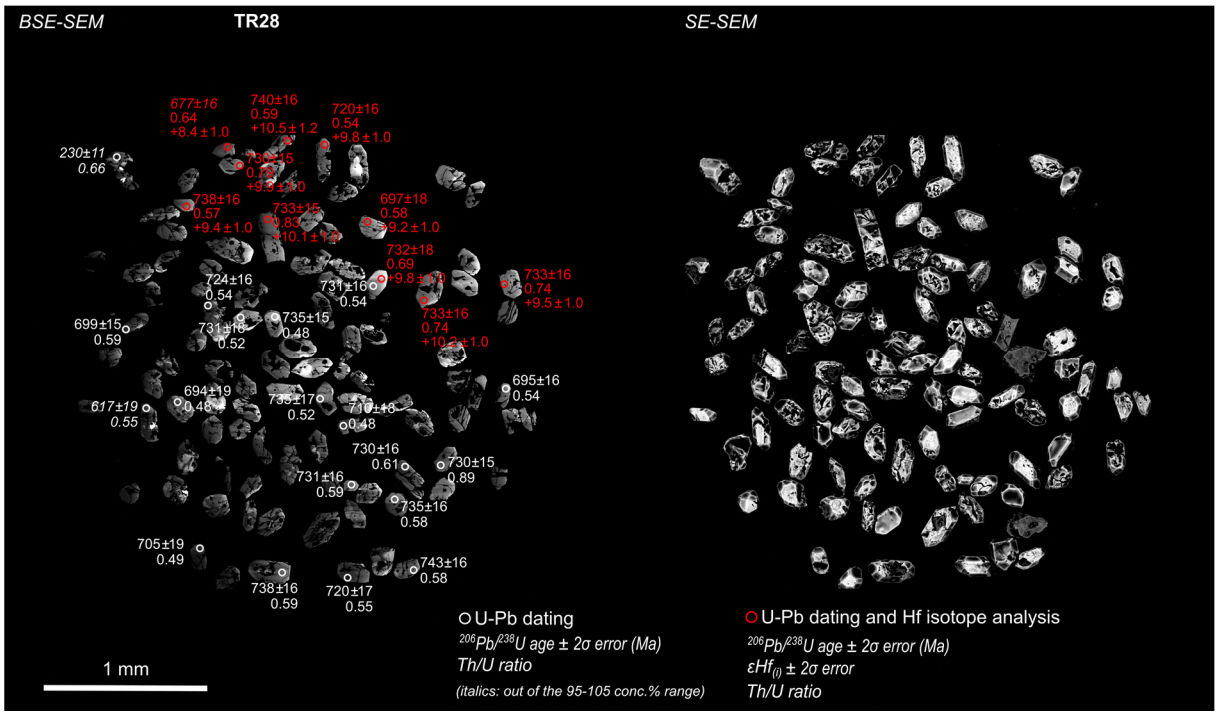
The authors are grateful to Manub-Managem team for providing access to the field, and especially to Aomar Ennaciri and El Alami Boukkari for their substantial logistical support during field work. Emmanuel Davy (CRPG-CNRS, Vandoeuvre-lès-Nancy, France) is warmly thanked for his help with sample preparation from crushing to zircon separation. This work is part of Julien Perret's PhD project which benefited of a CIFRE funding, reference CIFRE N°2017/1737, attributed by the French National Research and Technology Agency (ANRT).

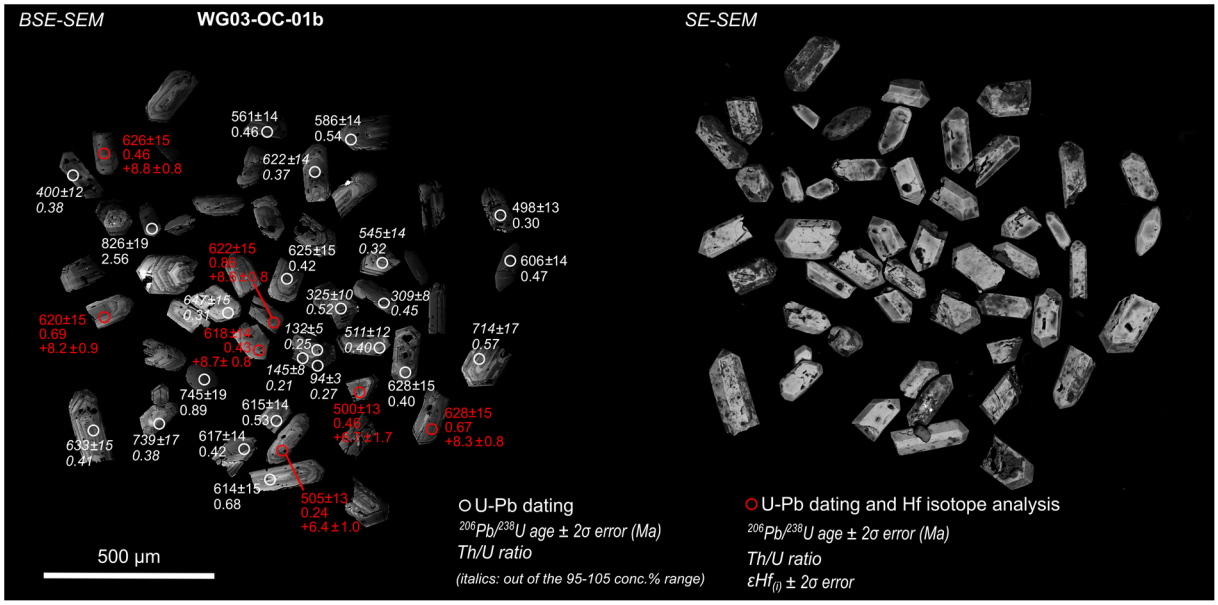
Supplementary Materials

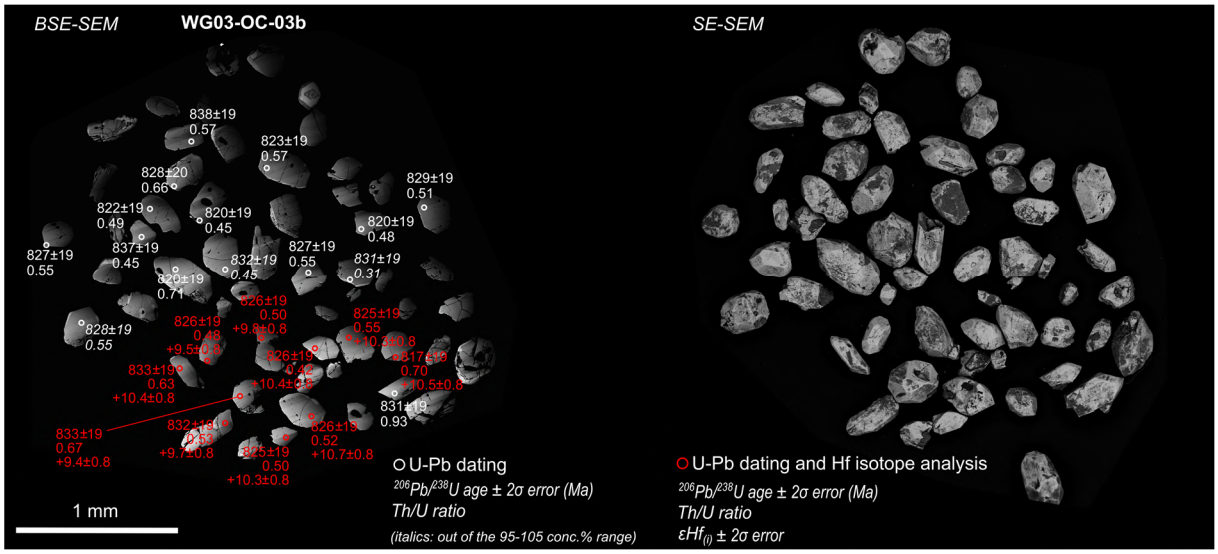
Supplementary Material 1-1: Scanning electron microscopy images illustrating zircon morphologies and U-Pb and Hf zircon isotope dataspot location in back-scattered electron mode (BSE-SEM).

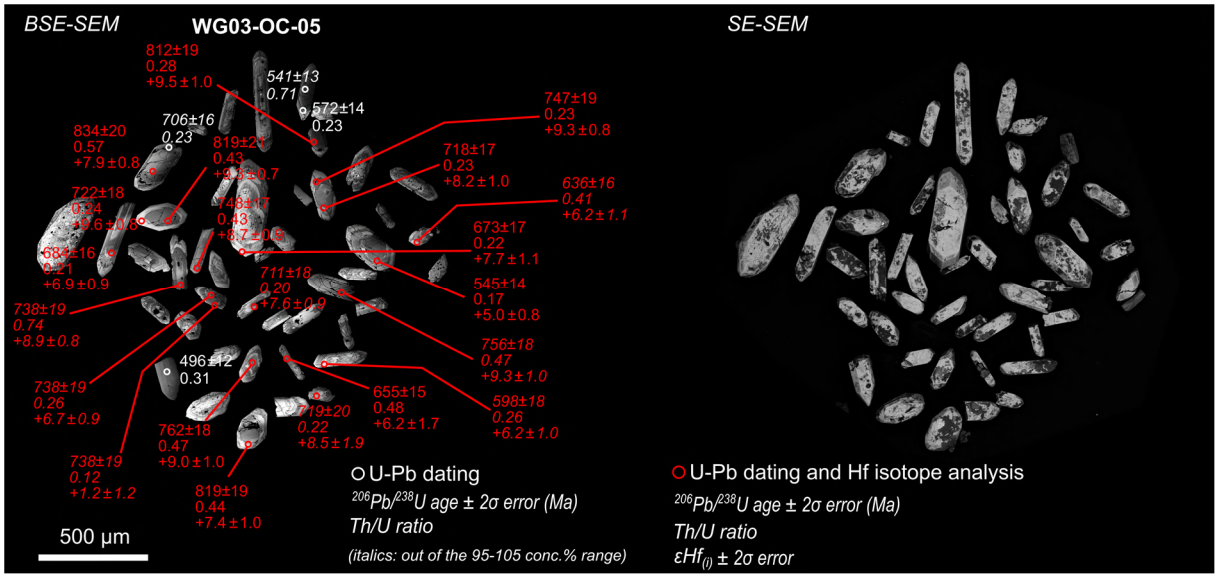





BSE-SEM
TR28
SE-SEM
677±16
0.64
+8.4±1.0
740±16
0.59
+10.5±1.2
720±16
0.54
+9.8±1.0
230±11
0.66
738±16
0.57
+9.4±1.0
733±15
0.83
+10.1±1.2
697±18
0.58
+9.2±1.0
732±18
0.69
+9.8±1.0
733±16
0.74
+9.5±1.0
724±16
0.54
731±16
0.54
699±15
0.59
731±16
0.52
735±15
0.48
733±16
0.74
+10.2±1.0
695±16
0.54
694±19
0.48
617±19
0.55
735±17
0.52
710±18
0.48
730±16
0.61
730±15
0.89
731±16
0.59
735±16
0.58
705±19
0.49
743±16
0.58
738±16
0.59
720±17
0.55
1 mm
U-Pb dating
206Pb/238U age ± 2σ error (Ma)
Th/U ratio
(italics: out of the 95-105 conc.% range)
U-Pb dating and Hf isotope analysis
206Pb/238U age ± 2σ error (Ma)
εHf(i) ± 2σ error
Th/U ratio


BSE-SEM
WG03-OC-01b
SE-SEM
561±14
0.46
586±14
0.54
626±15
0.46
+8.8±0.8
622±14
0.37
400±12
0.38
498±13
0.30
826±19
2.56
545±14
0.32
622±15
0.86
+8.6±0.8
625±15
0.42
606±14
0.47
325±10
0.52
309±8
0.45
620±15
0.69
+8.2±0.9
132±5
0.25
511±12
0.40
714±17
0.57
145±8
0.21
94±3
0.27
628±15
0.40
745±19
0.89
615±14
0.53
500±13
0.46
+6.1±1.7
628±15
0.67
+8.3±0.8
633±15
0.41
739±17
0.38
617±14
0.42
614±15
0.68
505±13
0.24
+6.4±1.0
500 µm
U-Pb dating
206Pb/238U age ± 2σ error (Ma)
Th/U ratio
(italics: out of the 95-105 conc.% range)
U-Pb dating and Hf isotope analysis
206Pb/238U age ± 2σ error (Ma)
Th/U ratio
εHf(i) ± 2σ error


BSE-SEM
WG03-OC-03b
838±19
0.57
823±19
0.57
828±20
0.66
829±19
0.51
822±19
0.49
820±19
0.45
820±19
0.48
827±19
0.55
837±19
0.45
832±19
0.45
827±19
0.55
831±19
0.31
820±19
0.71
826±19
0.50
+9.8±0.8
825±19
0.55
828±19
0.55
826±19
0.48
+9.5±0.8
833±19
0.63
+10.4±0.8
831±19
0.93
833±19
0.67
+9.4±0.8
826±19
0.52
+10.7±0.8
825±19
0.50
+10.3±0.8
1 mm
U-Pb dating
206Pb/238U age ± 2σ error (Ma)
Th/U ratio
(italics: out of the 95-105 conc.% range)
SE-SEM
U-Pb dating and Hf isotope analysis
206Pb/238U age ± 2σ error (Ma)
Th/U ratio
εHf(i) ± 2σ error


BSE-SEM
WG03-OC-05
812±19
0.28
+9.5±1.0
541±13
0.71
572±14
0.23
706±16
0.23
747±19
0.23
+9.3±0.8
834±20
0.57
+7.9±0.8
819±2
0.43
718±17
0.23
+8.2±1.0
636±16
0.41
+6.2±1.1
722±18
0.24
748±17
0.43
673±17
0.22
+7.7±1.1
684±16
0.21
+6.9±0.9
711±18
0.20
545±14
0.17
+5.0±0.8
738±19
0.74
+8.9±0.8
496±12
0.31
756±18
0.47
+9.3±1.0
738±19
0.26
+6.7±0.9
655±15
0.48
+6.2±1.7
719±20
0.22
+8.5±1.9
598±18
0.26
+6.2±1.0
762±18
0.47
+9.0±1.0
738±19
0.12
+1.2±1.2
819±19
0.44
+7.4±1.0
500 µm
U-Pb dating
206Pb/238U age ± 2σ error (Ma)
Th/U ratio
(italics: out of the 95-105 conc.% range)
SE-SEM
U-Pb dating and Hf isotope analysis
206Pb/238U age ± 2σ error (Ma)
Th/U ratio
εHf(i) ± 2σ error

Supplementary Material 1-2: U-Pb isotopic compositions of zircon standards used in this study.

ID	$^{207}Pb^a$	U^b	Pb^b	$\frac{Th}{U}^b$	$^{206}Pbc^c$	$\frac{^{206}Pb}{^{238}U}^d$	±2σ	$\frac{^{207}Pb}{^{235}U}^d$	±2σ	$\frac{^{207}Pb}{^{206}Pb}^d$	±2σ	ρ[e]	$\frac{^{206}Pb}{^{238}U}$	±2σ	$\frac{^{207}Pb}{^{235}U}$	±2σ	$\frac{^{207}Pb}{^{206}Pb}$	±2σ	conc.[f]
U-Pb	(cps)	(ppm)	(ppm)	U	(%)		(%)		(%)		(%)		(Ma)		(Ma)		(Ma)		(%)
1st analytical session																			
standard GJ-1																			
GJ1-1	657828	294	28	0.03	0.00	0.09804	2.4	0.8103	2.5	0.05995	0.61	0.97	603	14	603	11	602	13	100
GJ1-2	657449	276	26	0.03	b.d.	0.09812	2.4	0.8127	2.5	0.06007	0.53	0.98	603	14	604	11	606	11	100
GJ1-3	673090	287	27	0.03	0.00	0.09894	2.4	0.817	2.5	0.05989	0.59	0.97	608	14	606	11	600	13	101
GJ1-4	661413	288	27	0.03	b.d.	0.09892	2.4	0.8179	2.5	0.05996	0.56	0.97	608	14	607	11	602	12	101
GJ1-5	660135	296	27	0.03	b.d.	0.09675	2.4	0.803	2.5	0.0602	0.54	0.98	595	14	599	11	611	12	97
GJ1-6	630560	283	26	0.03	0.00	0.09768	2.4	0.8079	2.5	0.05999	0.61	0.97	601	14	601	11	603	13	100
GJ1-7	589258	266	25	0.03	0.00	0.09725	2.4	0.8106	2.6	0.06045	1.04	0.92	598	14	603	12	620	22	97
GJ1-8	578701	265	25	0.03	0.00	0.09777	2.4	0.8101	2.5	0.0601	0.71	0.96	601	14	603	12	607	15	99
GJ1-9	587656	262	25	0.03	0.00	0.10110	2.4	0.846	2.5	0.06068	0.65	0.97	621	14	622	12	628	14	99
GJ1-10	588463	262	25	0.03	0.00	0.10040	2.4	0.8332	2.5	0.06021	0.69	0.96	617	14	615	12	611	15	101
GJ1-11	605342	282	26	0.03	0.00	0.09604	2.4	0.7877	2.5	0.05948	0.62	0.97	591	14	590	11	585	14	101
GJ1-12	618857	289	27	0.03	0.00	0.09646	2.4	0.8004	2.5	0.06018	0.6	0.97	594	14	597	11	610	13	97
GJ1-13	640561	294	28	0.03	0.00	0.09896	2.4	0.8154	2.5	0.05976	0.61	0.97	608	14	605	12	595	13	102
GJ1-14	639201	292	28	0.03	b.d.	0.09930	2.4	0.8219	2.5	0.06003	0.62	0.97	610	14	609	12	605	13	101
GJ1-15	636101	301	28	0.03	b.d.	0.09681	2.4	0.8079	2.5	0.06053	0.57	0.97	596	14	601	11	623	12	96
GJ1-16	641833	305	28	0.03	0.00	0.09651	2.4	0.7916	2.5	0.05949	0.64	0.97	594	14	592	11	585	14	102
GJ1-17	615813	286	27	0.03	0.00	0.09974	2.4	0.8292	2.5	0.0603	0.67	0.96	613	14	613	12	614	15	100
GJ1-18	559830	262	25	0.03	0.00	0.09911	2.4	0.825	2.6	0.06037	0.79	0.95	609	14	611	12	617	17	99
GJ1-19	539056	261	25	0.03	0.00	0.09844	2.4	0.8033	2.5	0.05918	0.69	0.96	605	14	599	11	574	15	105
GJ1-20	549177	264	25	0.03	0.00	0.09831	2.4	0.8179	2.6	0.06033	0.86	0.94	605	14	607	12	616	19	98
GJ1-21	546973	270	25	0.03	0.00	0.09819	2.4	0.8162	2.5	0.06029	0.66	0.97	604	14	606	12	614	14	98
GJ1-22	550303	271	25	0.03	0.00	0.09799	2.4	0.8135	2.5	0.06021	0.72	0.96	603	14	604	12	611	15	99
GJ1-23	554197	280	26	0.03	0.00	0.09800	2.4	0.8085	2.5	0.05983	0.65	0.97	603	14	602	12	598	14	101
GJ1-24	583094	299	28	0.03	0.00	0.09712	2.4	0.8	2.5	0.05974	0.61	0.97	598	14	597	11	594	13	101
GJ1-25	568590	286	27	0.03	0.00	0.09883	2.4	0.8161	2.5	0.05989	0.57	0.97	608	14	606	11	600	12	101
GJ1-26	578961	292	28	0.03	0.00	0.09883	2.4	0.8169	2.5	0.05995	0.64	0.97	608	14	606	12	602	14	101
GJ1-27	546638	285	27	0.03	0.00	0.09758	2.4	0.8074	2.5	0.06001	0.67	0.96	600	14	601	12	604	15	99
GJ1-28	498668	261	25	0.03	0.00	0.09843	2.4	0.8121	2.5	0.05983	0.78	0.95	605	14	604	12	598	17	101
mean (n=28)						0.0982		0.8128		0.0600			604		604		605		
2 S.D.						0.0024		0.0238		0.0007			14		13		24		
standard Plešovice																			
Pleso3	2339413	1658	88	0.19	b.d.	0.05365	2.7	0.3958	2.7	0.0535	0.35	0.99	337	9	339	8	350	8	96
Pleso35	2405214	1732	92	0.19	1.15	0.05379	2.5	0.3952	2.6	0.05329	0.37	0.99	338	8	338	7	341	8	99
Pleso69	2485734	1790	95	0.19	0.45	0.05415	2.5	0.3972	2.6	0.0532	0.38	0.99	340	8	340	7	337	9	101
Pleso104	2572424	1851	98	0.19	3.40	0.05385	2.6	0.3954	2.6	0.05325	0.4	0.99	338	9	338	8	340	9	100
Pleso148	2604722	1923	103	0.19	0.69	0.05427	2.5	0.3984	2.6	0.05325	0.33	0.99	341	8	340	7	339	7	100
Pleso196	2615418	1940	104	0.19	b.d.	0.05446	2.5	0.4012	2.6	0.05343	0.36	0.99	342	8	343	7	347	8	98
Pleso240	2347350	1719	92	0.19	b.d.	0.05446	2.6	0.399	2.6	0.05314	0.38	0.99	342	9	341	8	335	8	102
Pleso285	2329236	1826	96	0.19	b.d.	0.05347	2.6	0.3929	2.6	0.0533	0.3	0.99	336	9	337	8	341	7	98
Pleso330*	1203056	930	49	0.19	0.00	0.05331	2.5	0.4062	2.7	0.05527	0.96	0.93	335	8	346	8	423	21	79
Pleso441	2564858	2053	110	0.20	b.d.	0.05442	2.4	0.4003	2.5	0.05335	0.36	0.99	342	8	342	7	344	8	99
Pleso496	2444755	2051	109	0.19	0.00	0.05405	2.6	0.3967	2.7	0.05323	0.34	0.99	339	9	339	8	339	8	100

Supplementary Material 1-2 ***(continued)***

ID U-Pb	$^{207}Pb^{a}$ (cps)	U^{b} (ppm)	Pb^{b} (ppm)	$\frac{Th^{b}}{U}$	$^{206}Pbc^{c}$ (%)	$\frac{^{206}Pb^{d}}{^{238}U}$	±2σ (%)	$\frac{^{207}Pb^{d}}{^{235}U}$	±2σ (%)	$\frac{^{207}Pb^{d}}{^{206}Pb}$	±2σ (%)	ρ[e]	$\frac{^{206}Pb}{^{238}U}$ (Ma)	±2σ	$\frac{^{207}Pb}{^{235}U}$ (Ma)	±2σ	$\frac{^{207}Pb}{^{206}Pb}$ (Ma)	±2σ	conc.[f] (%)
mean (n=11)						0.0540		0.3980		0.0535			339		340		349		
2 S.D.						0.0008		0.0073		0.0012			5		5		51		
standard BB																			
BB5	619190	291	27	0.33	b.d.	0.08984	2.6	0.7286	2.6	0.05881	0.61	0.97	555	14	556	11	560	13	99
BB36	623277	292	27	0.32	0.00	0.09098	2.5	0.7353	2.6	0.05862	0.6	0.97	561	13	560	11	553	13	102
BB37	610044	286	26	0.31	b.d.	0.09097	2.5	0.7339	2.5	0.05851	0.58	0.97	561	13	559	11	549	13	102
BB70	596382	280	26	0.31	0.00	0.09152	2.5	0.7405	2.5	0.05868	0.58	0.97	564	13	563	11	555	13	102
BB71	557184	257	24	0.31	0.00	0.09153	2.5	0.7447	2.6	0.05901	0.75	0.96	565	14	565	11	568	16	99
BB105	589551	276	26	0.34	0.00	0.09099	2.6	0.7383	2.6	0.05885	0.58	0.98	561	14	561	11	562	13	100
BB106	574936	274	25	0.31	b.d.	0.09100	2.5	0.7376	2.6	0.05879	0.54	0.98	561	13	561	11	559	12	100
BB149	570162	267	25	0.32	0.00	0.09117	2.5	0.738	2.6	0.05871	0.74	0.96	562	14	561	11	556	16	101
BB150	553369	260	24	0.32	0.00	0.09191	2.5	0.7452	2.6	0.0588	0.69	0.96	567	14	565	11	560	15	101
BB197	538414	257	24	0.33	0.00	0.09163	2.5	0.744	2.7	0.05889	0.94	0.94	565	14	565	12	563	21	100
BB198	496620	237	22	0.32	b.d.	0.09002	2.6	0.7298	2.7	0.0588	0.72	0.97	556	14	556	12	560	16	99
BB241	511064	238	22	0.33	1.45	0.09086	2.6	0.7361	2.7	0.05876	0.76	0.96	561	14	560	12	558	17	100
BB242	541947	251	24	0.33	0.00	0.09226	2.5	0.7473	2.6	0.05875	0.71	0.96	569	14	567	11	558	15	102
BB286	610690	317	29	0.32	0.26	0.08904	2.5	0.7219	2.6	0.05881	0.62	0.97	550	13	552	11	560	13	98
BB287	645906	333	31	0.33	0.48	0.09052	2.5	0.7377	2.6	0.05911	0.57	0.98	559	13	561	11	571	12	98
BB331	614335	326	29	0.30	0.06	0.08896	2.4	0.7224	2.5	0.0589	0.65	0.97	549	13	552	11	563	14	98
BB332	601320	310	28	0.31	0.22	0.08987	2.4	0.7275	2.5	0.05871	0.57	0.97	555	13	555	11	556	13	100
BB386	584229	302	28	0.33	0.37	0.08929	2.5	0.727	2.5	0.05905	0.7	0.96	551	13	555	11	569	15	97
BB387	682018	356	33	0.34	b.d.	0.08949	2.5	0.7269	2.5	0.05891	0.56	0.98	553	13	555	11	564	12	98
BB443	601777	318	29	0.32	0.40	0.09127	2.4	0.7398	2.5	0.05879	0.58	0.97	563	13	562	11	559	13	101
BB497	557489	302	28	0.31	2.39	0.09035	2.4	0.7361	2.5	0.05909	0.58	0.97	558	13	560	11	570	13	98
BB498	561184	304	28	0.31	1.15	0.09095	2.4	0.7392	2.6	0.05895	0.89	0.94	561	13	562	11	565	19	99
BB552	543634	301	28	0.33	0.33	0.09143	2.4	0.746	2.5	0.05918	0.58	0.97	564	13	566	11	574	13	98
BB553	558921	313	29	0.32	0.53	0.09166	2.5	0.7393	2.6	0.0585	0.64	0.97	565	14	562	11	549	14	103
BB597	539641	293	27	0.33	6.21	0.09179	2.5	0.7472	2.5	0.05904	0.65	0.97	566	13	567	11	569	14	100
mean (n=25)						0.0908		0.7364		0.0588			560		560		561		
2 S.D.						0.0019		0.0151		0.0004			11		9		13		
2nd analytical session																			
standard BB																			
BB1-1	648503	388	35	0.26	0.32	0.09197	2.1	0.7415	2.5	0.05847	1.32	0.85	567	11	563	11	548	29	104
BB1-2	607467	382	34	0.24	b.d.	0.09052	2.1	0.7415	2.6	0.05941	1.54	0.80	559	11	563	11	582	33	96
BB1-3	619062	379	34	0.25	b.d.	0.09014	2.2	0.7237	2.6	0.05823	1.41	0.84	556	12	553	11	538	31	103
BB1-4	414117	241	21	0.20	b.d.	0.09151	2.2	0.7294	2.6	0.05781	1.5	0.82	564	12	556	11	522	33	108
BB1-5	681855	394	35	0.26	b.d.	0.09039	2.7	0.7324	3.1	0.05876	1.47	0.88	558	14	558	13	558	32	100
BB1-6	695412	407	36	0.25	b.d.	0.09031	2.5	0.7347	3.0	0.059	1.68	0.83	557	13	559	13	567	37	98
BB1-7	700581	420	38	0.24	b.d.	0.09118	2.6	0.7355	2.9	0.0585	1.38	0.88	563	14	560	13	549	30	103
BB1-8	718280	420	38	0.25	b.d.	0.09180	3.1	0.7433	3.4	0.05872	1.4	0.91	566	17	564	15	557	30	102
BB1-9	724768	428	38	0.25	b.d.	0.09032	2.5	0.7289	2.8	0.05853	1.35	0.88	557	13	556	12	550	30	101
BB1-10	722757	403	36	0.26	b.d.	0.09091	2.7	0.7416	3.0	0.05917	1.36	0.89	561	14	563	13	573	30	98
BB1-11	684181	382	35	0.25	b.d.	0.09150	2.1	0.7366	2.5	0.05838	1.35	0.85	564	12	560	11	544	30	104
BB1-12	670140	362	32	0.26	0.05	0.09017	2.5	0.7316	3.0	0.05885	1.5	0.86	557	14	558	13	562	33	99
BB1-13	704755	402	36	0.25	b.d.	0.09030	2.2	0.7298	2.7	0.05862	1.49	0.83	557	12	556	12	553	32	101
BB1-14	446516	259	23	0.18	b.d.	0.08995	2.6	0.7278	3.0	0.05869	1.51	0.87	555	14	555	13	555	33	100

Supplementary Material 1-2 ***(continued)***

ID	$^{207}Pb^{a}$	U^{b}	Pb^{b}	$\underline{Th}^{b}$	$^{206}Pbc^{c}$	$\underline{^{206}Pb}^{d}$	±2σ	$\underline{^{207}Pb}^{d}$	±2σ	$\underline{^{207}Pb}^{d}$	±2σ	ρ[e]	$\underline{^{206}Pb}$	±2σ	$\underline{^{207}Pb}$	±2σ	$\underline{^{207}Pb}$	±2σ	conc.[f]
U-Pb	(cps)	(ppm)	(ppm)	U	(%)	^{238}U	(%)	^{235}U	(%)	^{206}Pb	(%)		^{238}U	(Ma)	^{235}U	(Ma)	^{206}Pb	(Ma)	(%)
BB1-15	717386	371	34	0.27	b.d.	0.09295	2.3	0.7506	2.7	0.05857	1.45	0.85	573	13	569	12	551	32	104
BB1-16	704173	365	33	0.27	0.07	0.09115	2.1	0.7374	2.5	0.05867	1.36	0.84	562	11	561	11	555	30	101
BB1-17	705922	407	36	0.24	b.d.	0.08942	2.2	0.7236	2.6	0.05869	1.39	0.85	552	12	553	11	556	30	99
BB1-18	736798	394	36	0.26	b.d.	0.09235	2.3	0.7458	2.7	0.05857	1.45	0.85	569	13	566	12	551	32	103
BB1-19	731230	405	36	0.26	b.d.	0.09110	2.1	0.737	2.5	0.05867	1.36	0.84	562	11	561	11	555	30	101
BB1-20	733274	380	34	0.26	0.21	0.09002	2.2	0.7285	2.6	0.05869	1.39	0.85	556	12	556	11	556	30	100
BB1-21	691650	379	34	0.24	b.d.	0.09036	2.9	0.734	3.2	0.05891	1.33	0.91	558	15	559	14	564	29	99
BB1-22	695189	356	32	0.26	b.d.	0.09105	2.4	0.7433	2.8	0.05921	1.47	0.85	562	13	564	12	575	32	98
BB1-23	693369	360	33	0.26	b.d.	0.09131	2.5	0.735	2.8	0.05838	1.32	0.88	563	13	559	12	544	29	104
mean (n=23)						0.0907		0.7321		0.0585			560		558		549		
2 S.D.						0.0017		0.0142		0.0007			10		8		23		
standard Plešovice																			
Pleso4	541545	517	26	0.13	b.d.	0.05408	2.3	0.3972	2.6	0.05327	1.15	0.90	339	8	340	8	340	26	100
Pleso5	490970	459	23	0.13	b.d.	0.05374	2.3	0.3908	2.4	0.05274	0.8	0.94	337	8	335	7	317	18	106
Pleso33	518409	495	25	0.12	b.d.	0.05319	2.2	0.3891	2.4	0.05305	0.95	0.91	334	7	334	7	331	22	101
Pleso34	519528	483	24	0.13	b.d.	0.05314	2.3	0.3949	2.5	0.0539	1.09	0.90	334	7	338	7	367	25	91
Pleso62	508173	470	24	0.13	b.d.	0.05413	2.2	0.3946	2.6	0.05287	1.26	0.87	340	7	338	7	323	29	105
Pleso63	514914	470	24	0.13	b.d.	0.05442	2.3	0.3944	2.5	0.05257	1	0.92	342	8	338	7	310	23	110
Pleso91	506990	464	24	0.13	b.d.	0.05407	2.4	0.3937	2.5	0.0528	0.76	0.95	339	8	337	7	320	17	106
Pleso92	558128	512	26	0.13	b.d.	0.05310	2.1	0.3928	2.4	0.05365	1.08	0.89	334	7	336	7	356	24	94
Pleso120	568024	528	27	0.13	b.d.	0.05473	2.2	0.4014	2.4	0.05319	1.09	0.89	343	7	343	7	337	25	102
Pleso121	604344	561	28	0.13	b.d.	0.05365	2.3	0.394	2.5	0.05327	1.07	0.90	337	7	337	7	340	24	99
Pleso149	568024	518	26	0.13	b.d.	0.05408	2.2	0.3966	2.5	0.05319	1.09	0.90	340	7	339	7	337	25	101
Pleso150	626238	583	30	0.21	b.d.	0.05334	2.3	0.3839	2.5	0.0522	0.86	0.94	335	8	330	7	294	20	114
Pleso178	632679	557	28	0.15	b.d.	0.05364	2.4	0.3924	2.7	0.05305	1.11	0.91	337	8	336	8	331	25	102
Pleso179	634507	555	28	0.13	b.d.	0.05339	2.2	0.3901	2.4	0.05299	0.87	0.93	335	7	334	7	328	20	102
Pleso207	618335	548	27	0.13	b.d.	0.05282	2.2	0.385	2.4	0.05287	0.96	0.92	332	7	331	7	323	22	103
Pleso208	605213	522	26	0.13	b.d.	0.05337	2.1	0.3917	2.3	0.05323	0.94	0.91	335	7	336	7	339	21	99
Pleso236	600611	502	25	0.13	b.d.	0.05364	2.2	0.3955	2.3	0.05348	0.68	0.95	337	7	338	7	349	15	96
Pleso237	582003	499	25	0.13	b.d.	0.05191	2.2	0.3816	2.4	0.05332	0.93	0.92	326	7	328	7	342	21	95
Pleso265	574189	489	25	0.13	b.d.	0.05317	2.2	0.3867	2.4	0.05275	0.9	0.93	334	7	332	7	318	21	105
Pleso266	572596	477	24	0.13	b.d.	0.05363	2.1	0.3904	2.2	0.0528	0.81	0.93	337	7	335	6	320	18	105
Pleso282	557068	446	23	0.13	b.d.	0.05481	2.1	0.4007	2.4	0.05303	1.05	0.90	344	7	342	7	330	24	104
Pleso283	534712	442	23	0.13	b.d.	0.05427	2.5	0.3987	2.6	0.05328	0.85	0.95	341	8	341	8	341	19	100
mean (n=22)						0.0537		0.3926		0.0531			337		336		332		
2 S.D.						0.0013		0.0103		0.0007			8		8		32		
standard Kaap Valley																			
KA1-6	245546	19	17	1.20	b.d.	0.65240	2.5	23.17	2.7	0.2575	1.02	0.92	3237	64	3234	27	3232	16	100
KA1-7	532521	44	39	1.49	b.d.	0.64670	2.7	22.73	2.8	0.2549	0.91	0.95	3215	68	3216	28	3216	14	100
KA1-35	484152	39	34	1.39	b.d.	0.61770	2.6	21.82	2.8	0.2561	0.98	0.93	3101	64	3176	27	3223	16	96
KA1-36	485929	39	35	1.46	b.d.	0.64590	2.6	22.86	2.8	0.2567	0.94	0.94	3212	67	3221	28	3226	15	100
KA1-64	448171	35	31	1.34	b.d.	0.65260	2.6	23.18	2.8	0.2576	1	0.93	3238	67	3235	28	3232	16	100
KA1-65	339934	26	23	1.25	b.d.	0.65160	2.2	22.98	2.3	0.2558	0.88	0.93	3234	55	3226	23	3221	14	100
KA1-93	545959	41	34	0.77	b.d.	0.65740	2.5	23.14	2.7	0.2553	0.89	0.94	3257	65	3233	27	3218	14	101
KA1-94	282681	21	18	0.88	b.d.	0.64750	2.4	22.88	2.5	0.2563	0.69	0.96	3218	62	3222	25	3224	11	100
KA1-122	301420	22	18	0.86	b.d.	0.65130	2.4	22.76	2.6	0.2535	0.79	0.95	3233	62	3217	25	3206	13	101

Supplementary Material 1-2 ***(continued)***

ID	$^{207}Pb^{a}$	U^{b}	Pb^{b}	$\frac{Th^{b}}{U}$	$^{206}Pbc^{c}$	$\frac{^{206}Pb^{d}}{^{238}U}$	±2σ	$\frac{^{207}Pb^{d}}{^{235}U}$	±2σ	$\frac{^{207}Pb^{d}}{^{206}Pb}$	±2σ	ρ[e]	$\frac{^{206}Pb}{^{238}U}$	±2σ	$\frac{^{207}Pb}{^{235}U}$	±2σ	$\frac{^{207}Pb}{^{206}Pb}$	±2σ	conc.[f]
U-Pb	(cps)	(ppm)	(ppm)		(%)		(%)		(%)		(%)		(Ma)		(Ma)		(Ma)		(%)
KA1-123	357381	26	21	1.22	b.d.	0.59960	2.5	21.12	2.7	0.25551	1.03	0.923	3028	60	3144	26	3219	16	94
KA1-151	366003	27	22	0.81	b.d.	0.64800	2.3	22.79	2.4	0.25510	0.91	0.933	3221	57	3218	24	3217	14	100
KA1-152	392239	30	23	0.73	b.d.	0.63430	2.3	22.3	2.6	0.255	1.18	0.893	3166	59	3197	26	3216	19	98
KA1-180	411310	31	26	1.09	b.d.	0.64100	2.2	22.65	2.3	0.25630	0.84	0.933	3193	55	3212	23	3224	13	99
KA1-181	394672	28	25	1.52	b.d.	0.65240	2.6	23.1	2.7	0.25680	0.85	0.953	3238	66	3231	27	3227	13	100
KA1-209	349002	27	23	0.98	0.06	0.64320	2.5	22.8	2.7	0.25711	0.05	0.923	3202	63	3218	27	3229	17	99
KA1-210	312747	24	21	1.16	b.d.	0.64520	2.2	22.8	2.5	0.25621	1.11	0.903	3210	56	3218	24	3224	17	100
KA1-238	339358	24	19	0.79	b.d.	0.61370	2.3	21.52	2.5	0.25430	0.99	0.923	3085	56	3162	24	3212	16	96
KA1-239	323976	24	19	1.14	b.d.	0.61330	2.2	21.62	2.5	0.25560	0.98	0.923	3083	55	3167	24	3220	16	96
KA1-267	493771	35	29	0.88	b.d.	0.65090	2.2	22.96	2.3	0.25580	0.56	0.973	3232	57	3225	23	3221	9	100
KA1-268	289532	21	18	1.22	b.d.	0.64870	2.3	22.88	2.5	0.25580	0.82	0.943	3223	59	3222	24	3221	13	100
mean (n=20)						0.6407		22.6030		0.2559			3191		3210		3221		
2 S.D.						0.0325		1.2033		0.0021			129		53		13		

$^{206}Pb/^{238}U$ error is the quadratic additions of the within run precision (2 S.E.) and the external reproducibility (2 S.D.) of the reference zircon. $^{207}Pb/^{206}Pb$ error propagation (^{207}Pb signal dependent) following Gerdes and Zeh (2009). $^{207}Pb/^{235}U$ error is the quadratic addition of the $^{207}Pb/^{206}Pb$ and $^{206}Pb/^{238}U$ uncertainty.

[a] *Within run background-corrected mean ^{207}Pb signal in cps (counts per second).*

[b] *U and Pb content and Th/U ratio were calculated relative to GJ-1 reference zircon for analytical session 1. They were calculated relative to BB1 reference zircon (itself referenced against GJ-1 zircon) for analytical session 2.*

[c] *Percentage of the common Pb on the ^{206}Pb. b.d. = below detection limit.*

[d] *Corrected for background, within-run Pb/U fractionation (in case of $^{206}Pb/^{238}U$) and common Pb using Stacey and Kramers (1975) model Pb composition and subsequently normalized to GJ-1 (ID-TIMS value/measured value); $^{207}Pb/^{235}U$ calculated using $^{207}Pb/^{206}Pb/(^{238}U/^{206}Pb.1/137.88)$.*

[e] *ρ is the $^{206}Pb/^{238}U$ / $^{207}Pb/^{235}U$ error correlation coefficient.*

[f] *Degree of concordance = $^{206}Pb/^{238}U$ age / $^{207}Pb/^{206}Pb$ age.100.*

Supplementary Material 1-3: Lu-Hf isotopic compositions of zircon standards used in this study.

ID Lu-Hf	$^{176}Yb/^{177}Hf$ [a]	±2σ	$^{176}Lu/^{177}Hf$ [a]	±2σ	$^{178}Hf/^{177}Hf$	Sig_{Hf} [b] (V)	$^{176}Hf/^{177}Hf$	±2σ [c]	$^{176}Hf/^{177}Hf_{(i)}$ [d]	age [f] (Ma)	±2σ	conc. [g]	$\varepsilon Hf_{(i)}$ [d]	±2σ [c]	T_{DM2} (Ga)
1st analytical session															
Standard GJ-1															
GJ1-01	0.0075	0.3	0.00026	0.02	1.46724	15	0.281993	23	0.281990	604	2	100	-14.7	0.8	2.22
GJ1-02	0.0075	0.3	0.00026	0.02	1.46725	15	0.282001	22	0.281998	604	2	100	-14.4	0.8	2.20
GJ1-03	0.0076	0.4	0.00026	0.02	1.46727	15	0.282002	22	0.281999	604	2	100	-14.3	0.8	2.20
GJ1-04	0.0076	0.5	0.00026	0.02	1.46724	15	0.281995	22	0.281992	604	2	100	-14.6	0.8	2.22
GJ1-05	0.0075	0.5	0.00026	0.03	1.46723	15	0.282011	23	0.282008	604	2	100	-14.0	0.8	2.19
GJ1-06	0.0076	0.5	0.00026	0.02	1.46724	15	0.282004	24	0.282001	604	2	100	-14.3	0.9	2.20
GJ1-07	0.0075	0.5	0.00026	0.02	1.46723	15	0.281990	22	0.281987	604	2	100	-14.8	0.8	2.22
GJ1-08	0.0075	0.4	0.00026	0.02	1.46725	15	0.282006	23	0.282004	604	2	100	-14.2	0.8	2.19
GJ1-09	0.0075	0.5	0.00026	0.02	1.46729	15	0.281988	24	0.281985	604	2	100	-14.8	0.8	2.23
GJ1-10	0.0075	0.5	0.00026	0.02	1.46723	15	0.282003	22	0.282000	604	2	100	-14.3	0.8	2.20
GJ1-11	0.0075	0.5	0.00026	0.02	1.46729	15	0.282029	24	0.282026	604	2	100	-13.4	0.9	2.15
GJ1-12	0.0075	0.5	0.00026	0.02	1.46725	14	0.281989	23	0.281986	604	2	100	-14.8	0.8	2.23
GJ1-13	0.0075	0.5	0.00026	0.02	1.46725	14	0.281987	23	0.281984	604	2	100	-14.9	0.8	2.23
GJ1-14	0.0075	0.4	0.00026	0.02	1.46722	14	0.282002	24	0.281999	604	2	100	-14.3	0.8	2.20
GJ1-15	0.0074	0.4	0.00026	0.02	1.46722	14	0.282009	24	0.282006	604	2	100	-14.1	0.9	2.19
GJ1-16	0.0075	0.4	0.00026	0.02	1.46724	14	0.281999	25	0.281996	604	2	100	-14.4	0.9	2.21
GJ1-17	0.0075	0.5	0.00026	0.02	1.46726	14	0.281994	23	0.281991	604	2	100	-14.6	0.8	2.22
GJ1-18	0.0074	0.4	0.00026	0.01	1.46727	14	0.281997	24	0.281994	604	2	100	-14.5	0.8	2.21
GJ1-19	0.0074	0.4	0.00026	0.02	1.46725	14	0.281997	22	0.281995	604	2	100	-14.5	0.8	2.21
GJ1-20	0.0075	0.6	0.00026	0.01	1.46722	14	0.281993	25	0.281990	604	2	100	-14.6	0.9	2.22
GJ1-21	0.0075	0.6	0.00026	0.02	1.46726	14	0.282004	24	0.282001	604	2	100	-14.3	0.9	2.20
GJ1-22	0.0074	0.4	0.00026	0.02	1.46724	14	0.282006	25	0.282003	604	2	100	-14.2	0.9	2.19
mean (n=22)	0.0075		0.00026		1.46725		0.282000		0.281997				-14.4		2.21
2 S.D.	0.0001		0.00000		0.00004		0.000019		0.000019				0.7		0.02
Standard Temora 2															
TM-01	0.0306	2	0.00119	0	1.46724	11	0.282666	24	0.282657	419	1	100	4.8	0.9	1.04
TM-02	0.0395	6	0.00125	1	1.46724	10	0.282698	26	0.282688	419	1	100	5.9	0.9	0.98
TM-03	0.0281	10	0.00095	3	1.46725	10	0.282659	25	0.282652	419	1	100	4.6	0.9	1.05
TM-04	0.0584	18	0.00186	5	1.46726	9	0.282726	24	0.282711	419	1	100	6.7	0.9	0.94
TM-05	0.0258	4	0.00099	1	1.46724	11	0.282661	26	0.282653	419	1	100	4.7	0.9	1.05
TM-07	0.0473	6	0.00162	3	1.46727	9	0.282704	27	0.282691	419	1	100	6.0	1.0	0.98
TM-08	0.0193	9	0.00067	3	1.46727	10	0.282640	26	0.282635	419	1	100	4.0	0.9	1.08
TM-09	0.0354	14	0.00124	5	1.46729	9	0.282685	30	0.282675	419	1	100	5.5	1.1	1.01
TM-10	0.0330	9	0.00125	3	1.46724	11	0.282671	25	0.282661	419	1	100	5.0	0.9	1.03
TM-11	0.0225	3	0.00081	1	1.46721	9	0.282682	26	0.282676	419	1	100	5.5	0.9	1.01
TM-12	0.0181	2	0.00064	0	1.46725	10	0.282664	27	0.282659	419	1	100	4.9	1.0	1.04
TM-13	0.0267	4	0.00099	2	1.46729	10	0.282665	28	0.282658	419	1	100	4.8	1.0	1.04
TM-14	0.0193	2	0.00068	1	1.46723	9	0.282647	24	0.282642	419	1	100	4.3	0.9	1.07
TM-15	0.0436	4	0.00148	1	1.46729	8	0.282687	36	0.282675	419	1	100	5.5	1.3	1.01
TM-16	0.0256	2	0.00083	0	1.46724	10	0.282673	25	0.282666	419	1	100	5.1	0.9	1.03
TM-17	0.0268	2	0.00087	0	1.46727	10	0.282670	28	0.282663	419	1	100	5.0	1.0	1.03
TM-18	0.0474	4	0.00161	1	1.46725	7	0.282708	27	0.282696	419	1	100	6.2	0.9	0.97
TM-19	0.0377	5	0.00126	1	1.46724	9	0.282668	27	0.282658	419	1	100	4.9	0.9	1.04

Supplementary Material 1-3 ***(continued)***

ID	$^{176}Yb/$	±2σ	$^{176}Lu/$	±2σ	$^{178}Hf/$	SigHf [b]	$^{176}Hf/$	±2σ[c]	$^{176}Hf/$	age [f]	±2σ	conc.[g]	$\varepsilon Hf_{(i)}$ [d]	±2σ [c]	T^{DM2}
Lu-Hf	^{177}Hf [a]		^{177}Hf [a]		^{177}Hf	(V)	^{177}Hf		$^{177}Hf_{(i)}$[d]	(Ma)					(Ga)
TM-20	0.0266	6	0.00096	2	1.46727	9	0.282681	25	0.282673	419	1	100	5.4	0.9	1.01
TM-21	0.0218	3	0.00076	1	1.46728	10	0.282651	26	0.282645	419	1	100	4.4	0.9	1.06
TM-22	0.0157	5	0.00054	2	1.46721	10	0.282645	27	0.282641	419	1	100	4.3	1.0	1.07
mean (n=22)	0.0309		0.00107		1.46725		0.282674		0.282666				5.1		1.03
2 S.D.	0.0225		0.00072		0.00005		0.000044		0.000039				1.4		0.04
2nd analytical session															
Standard GJ-1															
GJ1-01	0.0079	0.2	0.00025	0.05	1.46725	8	0.282007	31	0.282004	604	2	100	-14.2	1.1	2.19
GJ1-02	0.0079	0.2	0.00025	0.05	1.46723	8	0.282000	30	0.281997	604	2	100	-14.4	1.0	2.21
GJ1-03	0.0079	0.2	0.00025	0.04	1.46726	9	0.281986	30	0.281983	604	2	100	-14.9	1.1	2.23
GJ1-04	0.0080	0.2	0.00025	0.05	1.46728	8	0.282001	30	0.281998	604	2	100	-14.4	1.1	2.20
GJ1-05	0.0080	0.2	0.00025	0.04	1.46730	9	0.281984	31	0.281981	604	2	100	-15.0	1.1	2.24
GJ1-06	0.0079	0.2	0.00025	0.04	1.46730	9	0.282007	30	0.282004	604	2	100	-14.2	1.1	2.19
GJ1-07	0.0080	0.2	0.00025	0.04	1.46728	9	0.281985	29	0.281983	604	2	100	-14.9	1.0	2.23
GJ1-08	0.0079	0.2	0.00025	0.05	1.46735	8	0.282000	29	0.281997	604	2	100	-14.4	1.0	2.21
GJ1-09	0.0079	0.2	0.00025	0.04	1.46729	9	0.281990	30	0.281987	604	2	100	-14.8	1.0	2.22
GJ1-10	0.0079	0.2	0.00025	0.04	1.46727	9	0.282004	30	0.282001	604	2	100	-14.3	1.1	2.20
GJ1-11	0.0079	0.2	0.00025	0.03	1.46727	9	0.282005	30	0.282002	604	2	100	-14.2	1.1	2.20
GJ1-12	0.0079	0.2	0.00025	0.04	1.46724	9	0.282001	31	0.281998	604	2	100	-14.4	1.1	2.20
GJ1-13	0.0079	0.2	0.00025	0.04	1.46726	9	0.282019	32	0.282016	604	2	100	-13.7	1.1	2.17
GJ1-14	0.0079	0.2	0.00025	0.04	1.46725	8	0.282004	30	0.282001	604	2	100	-14.3	1.1	2.20
GJ1-15	0.0079	0.3	0.00025	0.04	1.46724	9	0.282027	28	0.282024	604	2	100	-13.5	1.0	2.16
GJ1-16	0.0079	0.3	0.00025	0.04	1.46727	8	0.282014	28	0.282011	604	2	100	-13.9	1.0	2.18
GJ1-17	0.0079	0.2	0.00025	0.04	1.46726	9	0.281996	29	0.281993	604	2	100	-14.5	1.0	2.21
GJ1-18	0.0078	0.2	0.00025	0.04	1.46724	9	0.281995	32	0.281992	604	2	100	-14.6	1.1	2.21
GJ1-19	0.0079	0.3	0.00025	0.04	1.46740	9	0.281991	29	0.281988	604	2	100	-14.7	1.0	2.22
GJ1-20	0.0078	0.2	0.00025	0.03	1.46739	9	0.281979	29	0.281976	604	2	100	-15.2	1.0	2.25
mean (n=20)	0.0079		0.000250		1.46728		0.282000		0.282669				-14.4		2.21
2 S.D.	0.0001		0.000003		0.00009		0.000024		0.000036				0.9		0.04
Standard Temora 1															
TM-01	0.0373	6	0.00108	2.1	1.46730	9	0.282675	32	0.282662	619	1	100	9.5	1.1	0.95
TM-02	0.0431	2	0.00127	0.1	1.46723	10	0.282681	29	0.282666	619	1	100	9.6	1.0	0.94
TM-03	0.0329	1	0.00098	0.3	1.46728	11	0.282687	28	0.282676	619	1	100	10.0	1.0	0.93
TM-04	0.0435	2	0.00129	0.04	1.46730	10	0.282696	28	0.282681	619	1	100	10.2	1.0	0.92
TM-05	0.0395	3	0.00114	0.5	1.46728	10	0.282663	29	0.282650	619	1	100	9.1	1.0	0.97
TM-06	0.0443	2	0.00131	0.1	1.46728	11	0.282658	29	0.282643	619	1	100	8.8	1.0	0.99
TM-07	0.0299	20	0.00090	5.3	1.46731	10	0.282658	29	0.282648	619	1	100	9.0	1.0	0.98
TM-08	0.0471	2	0.00137	0.1	1.46729	10	0.282674	30	0.282659	619	1	100	9.4	1.1	0.96
TM-09	0.0420	26	0.00126	7.4	1.46733	10	0.282673	32	0.282658	619	1	100	9.3	1.1	0.96
TM-10	0.0523	2	0.00152	0.9	1.46731	10	0.282683	29	0.282666	619	1	100	9.6	1.0	0.95
TM-11	0.0426	26	0.00127	7.3	1.46724	10	0.282704	28	0.282689	619	1	100	10.4	1.0	0.90
TM-12	0.0529	18	0.00155	5.2	1.46729	10	0.282705	30	0.282687	619	1	100	10.3	1.1	0.91
TM-13	0.0373	2	0.00106	1.0	1.46730	10	0.282683	36	0.282671	619	1	100	9.8	1.3	0.94
TM-14	0.0497	10	0.00145	3.0	1.46727	10	0.282695	30	0.282678	619	1	100	10.0	1.0	0.92
TM-15	0.0331	8	0.00103	2.6	1.46727	10	0.282699	30	0.282687	619	1	100	10.4	1.0	0.90
TM-16	0.0386	4	0.00119	0.6	1.46724	10	0.282720	29	0.282706	619	1	100	11.0	1.0	0.87
TM-17	0.0372	3	0.00125	1.5	1.46724	9	0.282706	29	0.282691	619	1	100	10.5	1.0	0.90

Supplementary Material 1-3 ***(continued)***

ID Lu-Hf	$^{176}Yb/^{177}Hf$ [a]	±2σ	$^{176}Lu/^{177}Hf$ [a]	±2σ	$^{178}Hf/^{177}Hf$	SigHf [b] (V)	$^{176}Hf/^{177}Hf$	±2σ[c]	$^{176}Hf/^{177}Hf_{(i)}$[d]	age [f] (Ma)	±2σ	conc.[g]	$\varepsilon Hf_{(i)}$ [d]	±2σ [c]	T^{DM2} (Ga)
TM-18	0.0335	22	0.00110	5.9	1.46727	11	0.282666	30	0.282654	619	1	100	9.2	1.1	0.97
TM-19	0.0339	3	0.00115	0.6	1.46732	10	0.282656	29	0.282642	619	1	100	8.8	1.0	0.99
mean (n=19)	0.0406		0.001219		1.46728		0.282683		0.282669				9.7		0.49
2 S.D.	0.0134		0.000354		0.00006		0.000037		0.000036				1.3		0.07

[a] *$^{176}Yb/^{177}Hf=(^{176}Yb/^{173}Yb)_{true}.(^{173}Yb/^{177}Hf)_{measured}.(M^{173}(Yb)/M^{177}(Hf))b(Hf)$, $b(Hf)=ln(^{179}Hf/^{177}Hf_{true} / {}^{179}Hf/^{177}Hf_{measured})/ln(M^{179}(Hf)/M^{177}(Hf))$, M=mass of respective isotope. The Lu/Hf were calculated in a similar way by using the Lu/Hf and b(Yb). Quoted uncertainties (absolute) relate to the last quoted figure. The effect of the inter-element fractionation on the Lu/Hf was estimated to be about 6% or less based on analyses of the GJ-1 and Temora zircons.*

[b] *Mean Hf signal in volt.*

[c] *Uncertainties are quadratic additions of the within-run precision and the daily reproducibility of the zircon GJ-1. Uncertainties for GJ-1 is 2 S.D. (2 standard deviation).*

[d] *Initial $^{176}Hf/^{177}Hf$ and $\varepsilon Hf_{(i)}$ calculated using the age (Ma), and the CHUR parameters:*
$^{176}Lu/^{177}Hf$ = 0.0336, and $^{176}Hf/^{177}Hf$ = 0.282785 (Bouvier et al., 2008).

[e] *Two-stage model age in billion years using the measured $^{176}Lu/^{177}Lu$, the estimated age (Ma), a value of 0.01113 for the average continental crust (second stage), and a depleted mantle $^{176}Lu/^{177}Hf$ and $^{176}Hf/^{177}Hf$ of 0.03933 and 0.283294 (Blichert-Toft and Puchtel, 2010).*

[f] *$^{206}Pb/^{238}U$ age.*

[g] *Degree of concordance (%) = $^{206}Pb/^{238}U$ age / $^{207}Pb/^{206}Pb$ age.100.*

Supplementary Material 1-4: U-Pb, Nd and Sr isotopic data compilation across the Keraf suture, the Atmur-Delgo suture and the Saharan meta-craton nearby. Geographic coordinates are reported as WGS 84.

U-Pb isotopic data on zircon

U-Pb isotopic data of zircon

°E WGS84	°N WGS84	ANS location	Sample ID	Dating method	**Age (Ma)**	**2σ (Ma)**	n (if >1)	MSWD	**Age interpretation**	**Reference**
32.85	16.15	Saharan meta-craton	?	$^{207}Pb/^{206}Pb$	**2650-1000**				**Detrital income**	
32.85	16.15	Saharan meta-craton	?	$^{207}Pb/^{206}Pb$	**719.0**	**81.0**			**Detrital income**	
32.85	16.15	Saharan meta-craton	SAB 5 1-3	$^{207}Pb/^{206}Pb$	**2521.0**	**13.0**			**Detrital income**	
32.85	16.15	Saharan meta-craton	SAB 5 1-4	$^{207}Pb/^{206}Pb$	**2624.0**	**10.0**			**Detrital income**	
32.85	16.15	Saharan meta-craton	SAB 5 2-1	$^{207}Pb/^{206}Pb$	**959.0**	**170.0**			**Detrital income**	
32.85	16.15	Saharan meta-craton	SAB 5 2-2	$^{207}Pb/^{206}Pb$	**1024.0**	**165.0**			**Detrital income**	
32.85	16.15	Saharan meta-craton	SAB 5 3-1	$^{207}Pb/^{206}Pb$	**1978.0**	**23.0**			**Detrital income**	
32.85	16.15	Saharan meta-craton	SAB 5 3-2	$^{207}Pb/^{206}Pb$	**1939.0**	**21.0**			**Detrital income**	
32.85	16.15	Saharan meta-craton	SAB 5 4-1	$^{207}Pb/^{206}Pb$	**1776.0**	**62.0**			**Detrital income**	
32.85	16.15	Saharan meta-craton	SAB 5 5-1	$^{207}Pb/^{206}Pb$	**1953.0**	**22.0**			**Detrital income**	
32.85	16.15	Saharan meta-craton	SAB 5 5-2	$^{207}Pb/^{206}Pb$	**1442.0**	**59.0**			**Detrital income**	
32.85	16.15	Saharan meta-craton	SAB 5 6-1	$^{207}Pb/^{206}Pb$	**1724.0**	**98.0**			**Detrital income**	**Kröner et al. (1987)**
32.85	16.15	Saharan meta-craton	SAB 5 7-1	$^{207}Pb/^{206}Pb$	**1065.0**	**118.0**			**Detrital income**	
32.85	16.15	Saharan meta-craton	SAB 5 8-1	$^{207}Pb/^{206}Pb$	**1015.0**	**190.0**			**Detrital income**	
32.85	16.15	Saharan meta-craton	SAB 5 9-1	$^{207}Pb/^{206}Pb$	**792.0**	**195.0**			**Detrital income**	
32.85	16.15	Saharan meta-craton	SAB 5 10-1	$^{207}Pb/^{206}Pb$	**663.0**	**13.0**			**Detrital income**	
32.85	16.15	Saharan meta-craton	SAB 5 11-1	$^{207}Pb/^{206}Pb$	**937.0**	**105.0**			**Detrital income**	
32.85	16.15	Saharan meta-craton	SAB 5 11-2	$^{207}Pb/^{206}Pb$	**976.0**	**25.0**			**Detrital income**	
32.72	16.35	Saharan meta-craton	SAB 13 12-1	$^{207}Pb/^{206}Pb$	**901.0**	**78.0**			**Detrital income**	
32.72	16.35	Saharan meta-craton	SAB 13 12-2	$^{207}Pb/^{206}Pb$	**963.0**	**69.0**			**Detrital income**	
32.85	16.15	Saharan meta-craton	SAB 5B	$^{207}Pb/^{206}Pb$	**673.0**	**45.0**			**Detrital income**	
32.85	16.15	Saharan meta-craton	SAB 5B 13-1	$^{207}Pb/^{206}Pb$	**673.0**	**45.0**			**Detrital income**	
32.85	16.15	Saharan meta-craton	SAB 5B 14-1	$^{207}Pb/^{206}Pb$	**1998.0**	**17.0**			**Detrital income**	
32.85	16.15	Saharan meta-craton	SAB 5B 14-2	$^{207}Pb/^{206}Pb$	**1194.0**	**67.0**			**Detrital income**	
32.85	16.15	Saharan meta-craton	SAB 5B 15-1	$^{207}Pb/^{206}Pb$	**1063.0**	**159.0**			**Detrital income**	

U-Pb isotopic data of zircon *(continued)*

°E WGS84	°N WGS84	ANS location	Sample ID	Dating method	**Age (Ma)**	**2σ (Ma)**	*n* (if >1)	MSWD	**Age interpretation**	**Reference**
32.85	16.15	Saharan meta-craton	SAB 5B 16-1	$^{207}Pb/^{206}Pb$	**971.0**	**54.0**			**Detrital income**	
32.85	16.15	Saharan meta-craton	SAB 5B 17-1	$^{207}Pb/^{206}Pb$	**884.0**	**315.0**			**Detrital income**	**Kröner et al. (1987)**
32.85	16.15	Saharan meta-craton	SAB 5B 18-1	$^{207}Pb/^{206}Pb$	**745.0**	**23.0**			**Detrital income**	
32.85	16.15	Saharan meta-craton	SAB 5B 19-1	$^{207}Pb/^{206}Pb$	**2106.0**	**12.0**			**Detrital income**	
29.60298236	19.61997957	Atmur-Delgo suture	NGD	$^{207}Pb/^{206}Pb$	**718.0**	**11**	5		**Arc-related magmatism**	
30.6750954	19.80979061	Atmur-Delgo suture	ITGS	$^{207}Pb/^{206}Pb$	**749.0**	**12**	2		**Arc-related magmatism**	**Harms et al. (1994)**
30.78729912	20.23289215	Atmur-Delgo suture	NEDG	$^{207}Pb/^{206}Pb$	**680.0**	**12**	2		**Arc-related magmatism**	
30.89950284	20.80793623	Atmur-Delgo suture	Gst2	$^{207}Pb/^{206}Pb$	**661.0**	**12**	2		**Syn-collisional magmatism**	
30.95	21.38	Atmur-Delgo suture	WH-7	$^{207}Pb/^{206}Pb$	**1232.0**	**13.0**	2		**Inheritance**	
30.95	21.38	Atmur-Delgo suture	WH-8	$^{207}Pb/^{206}Pb$	**2428.0**	**7.0**	5		**Inheritance**	**Stern et al. (1994)**
30.95	21.38	Atmur-Delgo suture	WH-9	$^{207}Pb/^{206}Pb$	**719.0**	**14.0**	3		**Arc-related magmatism**	
30.95	21.38	Atmur-Delgo suture	WH-11	$^{207}Pb/^{206}Pb$	**2406.0**	**10.0**	2		**Inheritance**	
30.95	21.38	Atmur-Delgo suture	WH-12	$^{207}Pb/^{206}Pb$	**1744.0**	**11.0**	2		**Inheritance**	
33.6209127	20.21188635	Keraf suture	6.9	$^{207}Pb/^{206}Pb$	**711.0**	**5**	4		**Arc-related magmatism**	
33.18263134	21.05839548	Keraf suture	1.1	$^{207}Pb/^{206}Pb$	**714.0**	**7**	4		**Arc-related magmatism**	**Bailo et al. (2003)**
33.49568945	19.51564511	Keraf suture	11.13	$^{207}Pb/^{206}Pb$	**737.0**	**5**	4		**Arc-related magmatism**	
33.56205777	19.39292633	Keraf suture	11.14	$^{207}Pb/^{206}Pb$	**737.0**	**18**	4		**Arc-related magmatism**	
33.53075168	18.69490677	Saharan meta-craton	11-2A	U-Pb	**858.0**	**7.0**	9	0.65	**Arc-related magmatism**	
32.83668064	18.71995745	Saharan meta-craton	12-2	U-Pb	**921.0**	**10.0**	3	0.02	**Bayudian event**	
33.42292475	18.90133653	Saharan meta-craton	10-8A	U-Pb	**900.0**	**9.0**	3	0.02	**Bayudian event**	**Küster et al. (2008)**
33.25594332	18.66508907	Saharan meta-craton	14-3	U-Pb	**597.0**	**4.0**	7	0.04	**Post-collisional magmatism**	
32.86888254	17.05076038	Saharan meta-craton	18-8	U-Pb	**605.0**	**4.0**	5	3.90	**Post-collisional magmatism**	
32.8407069	17.14251349	Saharan meta-craton	18-5A	U-Pb	**591.0**	**5.0**	0	0.28	**Post-collisional magmatism**	
31.2267	21.4753	Saharan meta-craton	70S, 72S, 7215, 167S	$^{207}Pb/^{206}Pb$	**717.0**	**10.0**			**Post-collisional magmatism**	
31.2245	21.5031	Saharan meta-craton	70S	$^{207}Pb/^{206}Pb$	**718.8**	**18.7**			**Post-collisional magmatism**	**Shang et al. (2010a)**
31.2265	21.4751	Saharan meta-craton	72S	$^{207}Pb/^{206}Pb$	**717.8**	**19.8**	0		**Post-collisional magmatism**	
31.2197	21.4296	Saharan meta-craton	167S	$^{207}Pb/^{206}Pb$	**716.4**	**15.2**	5		**Post-collisional magmatism**	
31.2197	21.4296	Saharan meta-craton	168S	U-Pb	**717.0**	**46.0**	6	2.20	**Post-collisional magmatism**	

U-Pb isotopic data of zircon *(continued)*

°E WGS84	°N WGS84	ANS location	Sample ID	Dating method	**Age (Ma)**	**2σ (Ma)**	*n* (if >1)	MSWD	**Age interpretation**	**Reference**
31.2382	21.5088	Saharan meta-craton	74S	U-Pb	**716.0**	**61.0**	6	2.90	**Post-collisional magmatism**	**Shang et al. (2010a)**
31.2382	21.5088	Saharan meta-craton	73S	U-Pb	**720.0**	**25.0**	6	0.22	**Post-collisional magmatism**	
31.223	21.471	Saharan meta-craton	166S	U-Pb	**708.1**	**8.9**	6	0.29	**Post-collisional magmatism**	
31.2265	21.4751	Saharan meta-craton	72S	U-Pb	**745.0**	**36.0**	6	1.60	**Post-collisional magmatism**	
31.2197	21.4296	Saharan meta-craton	167S	U-Pb	**684.0**	**37.0**	2	0.45	**Post-collisional magmatism**	
31.1533	21.4117	Saharan meta-craton	169S	$^{207}Pb/^{206}Pb$	**706.8**	**17.8**	2		**Post-collisional magmatism**	
31.1054	21.4016	Saharan meta-craton	171S	$^{207}Pb/^{206}Pb$	**707.1**	**16.0**	2		**Post-collisional magmatism**	
31.1086	21.3888	Saharan meta-craton	172S	$^{207}Pb/^{206}Pb$	**707.8**	**21.7**			**Post-collisional magmatism**	
31.1086	21.3888	Saharan meta-craton	172S	U-Pb	**716.0**	**59.0**	6	0.38	**Post-collisional magmatism**	
31.1054	21.4016	Saharan meta-craton	171S	U-Pb	**775.0**	**80.0**	5	0.36	**Post-collisional magmatism**	
31.1533	21.4117	Saharan meta-craton	169S	U-Pb	**679.0**	**11.0**	4	0.94	**Post-collisional magmatism**	
31.1533	21.4117	Saharan meta-craton	169S	U-Pb	**617.1**	**5.0**	2	0.94	**Post-collisional magmatism**	
31.1533	21.4117	Saharan meta-craton	169S	U-Pb	**686.0**	**36.0**	5	0.94	**Post-collisional magmatism**	
31.1253	21.4106	Saharan meta-craton	169S, 171S, 172S, 169st, 171st, 172st, 214st	$^{207}Pb/^{206}Pb$		**702.0**	18		**Post-collisional magmatism**	
30.473	19.655	Saharan meta-craton	01S	$^{207}Pb/^{206}Pb$	**597.1**	**8.6**	3		**Post-collisional magmatism**	**Shang et al. (2010b)**
30.251	19.94	Saharan meta-craton	116S	$^{207}Pb/^{206}Pb$	**603.5**	**3.7**	5		**Post-collisional magmatism**	
30.473	19.655	Saharan meta-craton	198S	$^{207}Pb/^{206}Pb$	**603.8**	**2.1**	6		**Post-collisional magmatism**	
30.473	19.655	Saharan meta-craton	01S-1	$^{207}Pb/^{206}Pb$	**627**	**3.1**			**Inheritance**	
30.473	19.655	Saharan meta-craton	01S-2	$^{207}Pb/^{206}Pb$	**643.3**	**5.8**			**Inheritance**	
30.473	19.655	Saharan meta-craton	01S-3	$^{207}Pb/^{206}Pb$	**720.9**	**4.1**			**Inheritance**	
30.473	19.655	Saharan meta-craton	01S-4	$^{207}Pb/^{206}Pb$	**692.4**	**3.5**			**Inheritance**	
30.473	19.655	Saharan meta-craton	01S-5	$^{207}Pb/^{206}Pb$	**697.4**	**3.2**			**Inheritance**	
30.473	19.655	Saharan meta-craton	01S-6	$^{207}Pb/^{206}Pb$	**631.2**	**3.5**			**Inheritance**	
30.473	19.655	Saharan meta-craton	01S-7	$^{207}Pb/^{206}Pb$	**675.4**	**4.2**			**Inheritance**	
30.251	19.94	Saharan meta-craton	116S-1	$^{207}Pb/^{206}Pb$	**626.1**	**2.6**			**Inheritance**	
30.251	19.94	Saharan meta-craton	116S-2	$^{207}Pb/^{206}Pb$	**628.2**	**4**			**Inheritance**	
30.251	19.94	Saharan meta-craton	116S-3	$^{207}Pb/^{206}Pb$	**661.9**	**3.2**			**Inheritance**	

U-Pb isotopic data of zircon *(continued)*

°E WGS84	°N WGS84	ANS location	Sample ID	Dating method	**Age (Ma)**	**2σ (Ma)**	n (if >1)	MSWD	**Age interpretation**	**Reference**
30.251	19.94	Saharan meta-craton	116S-4	$^{207}Pb/^{206}Pb$	**637.2**	**16.9**			**Inheritance**	
30.251	19.94	Saharan meta-craton	116S-5	$^{207}Pb/^{206}Pb$	**614.7**	**3.1**			**Inheritance**	
30.251	19.94	Saharan meta-craton	116S-6	$^{207}Pb/^{206}Pb$	**628.3**	**3.3**			**Inheritance**	
30.251	19.94	Saharan meta-craton	116S-7	$^{207}Pb/^{206}Pb$	**610.6**	**3.5**			**Inheritance**	
30.251	19.94	Saharan meta-craton	116S-8	$^{207}Pb/^{206}Pb$	**613.4**	**3.3**			**Inheritance**	
30.473	19.655	Saharan meta-craton	198S-1	$^{207}Pb/^{206}Pb$	**616**	**4.1**			**Inheritance**	
30.473	19.655	Saharan meta-craton	198S-2	$^{207}Pb/^{206}Pb$	**622.5**	**2.7**			**Inheritance**	
30.473	19.655	Saharan meta-craton	198S-3	$^{207}Pb/^{206}Pb$	**621.2**	**4**			**Inheritance**	
30.473	19.655	Saharan meta-craton	198S-4	$^{207}Pb/^{206}Pb$	**645.5**	**5.2**			**Inheritance**	
30.473	19.655	Saharan meta-craton	198S-5	$^{207}Pb/^{206}Pb$	**656.5**	**7.4**			**Inheritance**	
30.473	19.655	Saharan meta-craton	198S-6	$^{207}Pb/^{206}Pb$	**715.1**	**9.9**			**Inheritance**	
30.473	19.655	Saharan meta-craton	198S-7	$^{207}Pb/^{206}Pb$	**608.7**	**4.4**			**Inheritance**	**Shang et al. (2010b)**
30.473	19.655	Saharan meta-craton	198S-8	$^{207}Pb/^{206}Pb$	**617.5**	**3.1**			**Inheritance**	
30.386	19.797	Saharan meta-craton	20S	$^{207}Pb/^{206}Pb$	**598.8**	**3.8**	5		**Post-collisional magmatism**	
30.501	19.76	Saharan meta-craton	200S	$^{207}Pb/^{206}Pb$	**602**	**3.5**	3		**Post-collisional magmatism**	
30.501	19.76	Saharan meta-craton	06S-1	$^{207}Pb/^{206}Pb$	**731.4**	**3.5**			**Inheritance**	
30.501	19.76	Saharan meta-craton	06S-2	$^{207}Pb/^{206}Pb$	**736.2**	**3.2**			**Inheritance**	
30.501	19.76	Saharan meta-craton	06S-3	$^{207}Pb/^{206}Pb$	**731.1**	**2.8**			**Inheritance**	
30.501	19.76	Saharan meta-craton	06S-5	$^{207}Pb/^{206}Pb$	**724.3**	**2.8**			**Inheritance**	
30.501	19.76	Saharan meta-craton	06S-6	$^{207}Pb/^{206}Pb$	**731.3**	**2.8**			**Inheritance**	
30.501	19.76	Saharan meta-craton	06S-7	$^{207}Pb/^{206}Pb$	**744.7**	**8.4**			**Inheritance**	
30.501	19.76	Saharan meta-craton	06S-8	$^{207}Pb/^{206}Pb$	**737.5**	**3.4**			**Inheritance**	
30.501	19.76	Saharan meta-craton	06S-9	$^{207}Pb/^{206}Pb$	**616.8**	**4**			**Inheritance**	
30.501	19.76	Saharan meta-craton	06S-10	$^{207}Pb/^{206}Pb$	**723.1**	**2.9**			**Inheritance**	
30.501	19.76	Saharan meta-craton	06S-11	$^{207}Pb/^{206}Pb$	**740**	**3.2**			**Inheritance**	

U-Pb isotopic data of zircon *(continued)*

°E WGS84	°N WGS84	ANS location	Sample ID	Dating method	**Age (Ma)**	**2σ (Ma)**	n (if >1)	MSWD	**Age interpretation**	**Reference**
30.501	19.76	Saharan meta-craton	06S-12	$^{207}Pb/^{206}Pb$	**716.3**	**3.6**			**Inheritance**	
30.501	19.76	Saharan meta-craton	06S-13	$^{207}Pb/^{206}Pb$	**722.2**	**9.9**			**Inheritance**	
30.386	19.797	Saharan meta-craton	20S-1	$^{207}Pb/^{206}Pb$	**692**	**5.1**			**Inheritance**	
30.386	19.797	Saharan meta-craton	20S-2	$^{207}Pb/^{206}Pb$	**615.3**	**7.4**			**Inheritance**	
30.386	19.797	Saharan meta-craton	20S-3	$^{207}Pb/^{206}Pb$	**628.7**	**4.1**			**Inheritance**	
30.386	19.797	Saharan meta-craton	20S-4	$^{207}Pb/^{206}Pb$	**623.3**	**4**			**Inheritance**	
30.501	19.76	Saharan meta-craton	200S-1	$^{207}Pb/^{206}Pb$	**701.4**	**3.7**			**Inheritance**	
30.501	19.76	Saharan meta-craton	200S-2	$^{207}Pb/^{206}Pb$	**635**	**5.7**			**Inheritance**	
30.501	19.76	Saharan meta-craton	200S-3	$^{207}Pb/^{206}Pb$	**639.6**	**4.5**			**Inheritance**	
30.501	19.76	Saharan meta-craton	200S-4	$^{207}Pb/^{206}Pb$	**613.8**	**8.9**			**Inheritance**	
30.501	19.76	Saharan meta-craton	200S-5	$^{207}Pb/^{206}Pb$	**622.9**	**4.5**			**Inheritance**	
30.501	19.76	Saharan meta-craton	200S-6	$^{207}Pb/^{206}Pb$	**623.9**	**4.5**			**Inheritance**	**Shang et al. (2010b)**
30.501	19.76	Saharan meta-craton	200S-7	$^{207}Pb/^{206}Pb$	**620.5**	**2.7**			**Inheritance**	
30.501	19.76	Saharan meta-craton	200S-8	$^{207}Pb/^{206}Pb$	**625.3**	**3.2**			**Inheritance**	
30.501	19.76	Saharan meta-craton	200S-9	$^{207}Pb/^{206}Pb$	**621.9**	**8.2**			**Inheritance**	
30.501	19.76	Saharan meta-craton	200S-10	$^{207}Pb/^{206}Pb$	**611.7**	**2.7**			**Inheritance**	
30.501	19.76	Saharan meta-craton	200S-11	$^{207}Pb/^{206}Pb$	**622**	**4.3**			**Inheritance**	
30.501	19.76	Saharan meta-craton	200S-12	$^{207}Pb/^{206}Pb$	**617.6**	**2.8**			**Inheritance**	
30.501	19.76	Saharan meta-craton	200S-13	$^{207}Pb/^{206}Pb$	**609.2**	**3.2**			**Inheritance**	
		Saharan meta-craton	115S	U-Pb	**600.0**	**18.0**	6	0.50	**Post-collisional magmatism**	
30.251	19.94	Saharan meta-craton	116S	U-Pb	**603.5**	**2.3**	7	0.59	**Post-collisional magmatism**	
		Saharan meta-craton	151S	U-Pb	**601.7**	**4.6**	4	6.60	**Post-collisional magmatism**	
30.473	19.655	Saharan meta-craton	198S	U-Pb	**600.6**	**1.3**	3	0.56	**Post-collisional magmatism**	
30.559	19.916	Saharan meta-craton	201S	U-Pb	**602.1**	**8.6**	3	0.05	**Post-collisional magmatism**	
33.15048973	18.53159927	Saharan meta-craton	059/1	U-Pb	**2281-1617**				**Inheritance**	
33.15048973	18.53159927	Saharan meta-craton	059/1	U-Pb	**1434-1007**				**Inheritance**	
33.39251767	18.64516622	Saharan meta-craton	015/1	U-Pb	**914.1**	**5.5**	37		**Bayudian event**	**Evuk et al.**
33.39251767	18.64516622	Saharan meta-craton	015/1	U-Pb	**1928-1656**				**Inheritance**	**(2014)**
33.49770673	18.72056724	Saharan meta-craton	193/1	U-Pb	**969.0**	**5**	26		**Bayudian event**	
33.49770673	18.72056724	Saharan meta-craton	193/1	U-Pb	**1001.0**				**Arc-related magmatism**	

U-Pb isotopic data of zircon *(continued)*

°E WGS84	°N WGS84	ANS location	Sample ID	Dating method	**Age (Ma)**	**2σ (Ma)**	*n* (if >1)	MSWD	**Age interpretation**	**Reference**
33.49770673	18.72056724	Saharan meta-craton	193/1	U-Pb	**974.0**				**Bayudian event**	**Evuk et al. (2014)**
33.55391737	18.73755011	southern Keraf shear zone	135/1	U-Pb	**813.0**	**4**	31		**Arc-related magmatism**	
33.55391737	18.73755011	southern Keraf shear zone	135/1	U-Pb	**877-840**				**Inheritance**	
33.58973213	18.74443757	southern Keraf shear zone	324/1	U-Pb	**700.0**	**7**	27		**Syn-collisional magmatism**	
33.38999595	18.44621079	southern Keraf shear zone	073/3	U-Pb	**810.0**	**10**	15		**Arc-related magmatism**	
33.57251349	18.71757649	southern Keraf shear zone	150/1	U-Pb	**794.0**	**15**	35		**Arc-related magmatism**	
33.57251349	18.71757649	southern Keraf shear zone	150/1	U-Pb	**999-895**				**Inheritance**	
33.63518933	18.63699328	southern Keraf shear zone	313/1	U-Pb	**799.0**	**16**	19		**Arc-related magmatism**	
33.40445961	18.60875471	southern Keraf shear zone	371/2	U-Pb	**2080-1726**				**Inheritance**	
33.40445961	18.60875471	Saharan meta-craton	371/2	U-Pb	**1169-1054**				**Inheritance**	
33.48848655	18.55985379	southern Keraf shear zone	376/1	U-Pb	**783.0**	**13**	24		**Arc-related magmatism**	
33.66618288	18.73272889	southern Keraf shear zone	397/1	U-Pb	**630.0**	**4**	28		**Late collisional magmatism**	
33.51534762	18.32912406	southern Keraf shear zone	293/1	U-Pb	**645.0**	**5**	32		**Late collisional magmatism**	
33.66136166	18.29606428	southern Keraf shear zone	068/1	U-Pb	**808.0**	**5**			**Arc-related magmatism**	
33.66136166	18.29606428	southern Keraf shear zone	068/1	U-Pb	**873-840**				**Inheritance**	

Nd whole-rock isotopic compositions

Nd whole-rock isotopic compositions

°E WGS84	°N WGS84	ANS location	Sample ID	age (Ma)	$\varepsilon Nd_{(i)}$	T_{DM} (Ma)	Age interpretation	Reference
28.85844555	17.68284819	Saharan meta-craton	WH-TG1	700	**-7.7**	**1700**	**Arc-related magmatism**	
28.9246221	17.50880588	Saharan meta-craton	WH-M3	690	**-6.7**	**1600**	**Syn-collisional magmatism**	
29.60136336	17.77432159	Saharan meta-craton	WHEG4	562	**-7.4**	**1800**	**Post-collisional magmatism**	
29.46536751	17.64156373	Saharan meta-craton	WHMG6	590	**-7.9**	**1800**	**Late collisional magmatism**	
26.83125738	17.67880069	Saharan meta-craton	GR-G2	700	**-15.7**	**2600**	**Arc-related magmatism**	
29.60298236	19.61997957	Saharan meta-craton	ND-G6	918	**-15.8**	**2200**	**Arc-related magmatism**	
30.33476956	20.02634813	Saharan meta-craton	NGD3	700	**-6.3**	**1600**	**Arc-related magmatism**	**Stern and Hedge (1985);**
30.24086766	19.67502551	Saharan meta-craton	NDRG4	565	**-5.3**	**1200**	**Post-collisional magmatism**	**Harms et al. (1990)**
29.93002	19.70740548	Saharan meta-craton	NDMG3	623	**-6.6**	**1500**	**Syn-collisional magmatism**	
26.7276415	22.10190387	Saharan meta-craton	GK-M3	673	**-18.9**	**2100**	**Syn-collisional magmatism**	
31.34259596	22.93447371	Saharan meta-craton	GEA-MG4	700	**-14.5**	**2500**	**Arc-related magmatism**	
31.34259596	22.93447371	Saharan meta-craton	GEA-MG8	700	**-13.1**	**1900**	**Arc-related magmatism**	
29.29861069	23.03970859	Saharan meta-craton	BSSGD4	581	**-7.0**	**1500**	**Post-collisional magmatism**	
29.3370619	22.93042621	Saharan meta-craton	BSSOG6a	700	**-6.1**	**1500**	**Arc-related magmatism**	
32.85	16.15	Saharan meta-craton	SAB 5	870	**-3.7**	**1700**	**Detrital income**	**Kröner et al. (1987)**
30.25199386	20.41288562	Atmur Delgo suture	NGD	718	**-5.7**	**1620**	**Arc-related magmatism**	
30.6750954	19.80979061	Atmur Delgo suture	ITGS	748	**-0.3**	**1280**	**Arc-related magmatism**	
30.78729912	20.23289215	Atmur Delgo suture	NEDG	680	**4.9**	**800**	**Arc-related magmatism**	
30.89950284	20.80793623	Atmur Delgo suture	Gst2	661	**4.2**	**870**	**Syn-collisional magmatism**	
31.04209507	20.28899401	Atmur Delgo suture	ASMI	546	**3.0**	**830**	**Post-collisional magmatism**	
30.93924166	20.28198128	Atmur Delgo suture	ASM2	700	**4.4**	**870**	**Arc-related magmatism**	
31.39974444	20.44327413	Atmur Delgo suture	SMG2gt	592	**-11.5**	**1940**	**Post-collisional magmatism**	
30.9556047	20.67235673	Atmur Delgo suture	ASS27b	752	**-8.5**	**1270**	**?**	**Harms et al. (1994)**
30.9556047	20.67235673	Atmur Delgo suture	ASS27c	752	**-9.1**	**1810**	**?**	
30.9556047	20.67235673	Atmur Delgo suture	ASS27d	752	**-8.3**	**950**	**?**	
32.10136349	20.93493507	Atmur Delgo suture	Gst6	700	**4.3**	**810**	**Arc-related magmatism**	
?	?	Atmur Delgo suture	93	702	**-2.9**	**1520**	**Arc-related magmatism**	
?	?	Atmur Delgo suture	552at	707	**-4.3**	**2650**	**Arc-related magmatism**	
30.24086766	19.67502551	Saharan meta-craton	NDRG	565	**-5.3**	**1230**	**Post-collisional magmatism**	
29.93002	19.70740548	Saharan meta-craton	NDMG	623	**-6.6**	**1500**	**Syn-collisional magmatism**	
29.60298236	19.61997957	Saharan meta-craton	NDG	918	**-15.8**	**2160**	**Arc-related magmatism**	

Nd whole-rock isotopic compositions *(continued)*

°E WGS84	°N WGS84	ANS location	Sample ID	age (Ma)	$\varepsilon Nd_{(i)}$	T_{DM} (Ma)	Age interpretation	Reference
31.3934	21.6589	Atmur Delgo suture	WH-3	650	**6.6**	**660**	**Post-collisional magmatism**	
30.95	21.38	Atmur Delgo suture	WH-7	700	**-19.0**	**2420**	**Syn-collisional magmatism**	
30.95	21.38	Atmur Delgo suture	WH-8	700	**-27.0**	**2810**	**Syn-collisional magmatism**	
30.95	21.38	Atmur Delgo suture	WH-9	700	**-6.1**	**1900**	**Syn-collisional magmatism**	
30.95	21.38	Atmur Delgo suture	WH-10	700	**-1.3**	**1260**	**Syn-collisional magmatism**	**Stern et al. (1994)**
30.95	21.38	Atmur Delgo suture	WH-11	700	**-21.0**	**2820**	**Syn-collisional magmatism**	
30.95	21.38	Atmur Delgo suture	WH-12	700	**-20.0**	**2400**	**Syn-collisional magmatism**	
30.95	21.38	Atmur Delgo suture	WH-14	700	**-10.0**	**2030**	**Syn-collisional magmatism**	
31.3762	21.5837	Atmur Delgo suture	WH-22	530	**4.9**	**720**	**Post-collisional magmatism**	
33.60647233	18.85947663	Saharan meta-craton	all metavolcanics	806	**5.2**		**Arc-related magmatism**	
32.88110662	18.61323723	Saharan meta-craton	all amphibolites	810	**5.2**		**Arc-related magmatism**	
32.88110662	18.61323723	Saharan meta-craton	12-4a	806	**5.5**		**Arc-related magmatism**	
32.88110662	18.61323723	Saharan meta-craton	12-6	806	**5.3**		**Arc-related magmatism**	
33.93325285	18.14123956	southern Keraf shear zone	6-2a	806	**5.2**		**Arc-related magmatism**	
33.48908036	19.13858015	Saharan meta-craton	10-5a	806	**5.0**		**Arc-related magmatism**	
33.48908036	19.13858015	Saharan meta-craton	10-1a	806	**5.0**		**Arc-related magmatism**	
33.60647233	18.85947663	southern Keraf shear zone	9-5	806	**5.2**		**Arc-related magmatism**	
33.60647233	18.85947663	southern Keraf shear zone	9-2a	806	**5.0**		**Arc-related magmatism**	
33.60647233	18.85947663	southern Keraf shear zone	9-1	806	**5.6**	**858**	**Arc-related magmatism**	
33.60647233	18.85947663	southern Keraf shear zone	11-2a	806	**5.3**	**899**	**Arc-related magmatism**	
33.93325285	18.14123956	Saharan meta-craton	6-3	806	**5.0**	**888**	**Arc-related magmatism**	**Küster and Liégeois (2001)**
32.88110662	18.61323723	Saharan meta-craton	12-3	806	**-8.7**	**2427**	**Arc-related magmatism**	
32.88110662	18.61323723	Saharan meta-craton	12-2	806	**-8.0**	**2229**	**Arc-related magmatism**	
32.88110662	18.61323723	Saharan meta-craton	12-5b	806	**-8.4**	**2041**	**Arc-related magmatism**	
33.50087922	18.46483337	Saharan meta-craton	14-9	806	**-6.0**	**2084**	**Arc-related magmatism**	
33.60647233	18.85947663	southern Keraf shear zone	11-2b	806	**3.6**		**Arc-related magmatism**	
33.93325285	18.14123956	southern Keraf shear zone	6-5	806	**4.0**		**Arc-related magmatism**	
33.93325285	18.14123956	southern Keraf shear zone	6-8b	806	**6.5**		**Arc-related magmatism**	
33.93325285	18.14123956	Saharan meta-craton	7-1	806	**5.5**	**893**	**Arc-related magmatism**	
33.50087922	18.46483337	Saharan meta-craton	14-11	806	**-12.9**	**2244**	**Arc-related magmatism**	
32.88110662	15.92329413	Saharan meta-craton	17-6	806	**-4.3**	**1695**	**Arc-related magmatism**	

Nd whole-rock isotopic compositions *(continued)*

°E WGS84	°N WGS84	ANS location	Sample ID	age (Ma)	$\varepsilon Nd_{(i)}$	T_{DM} (Ma)	Age interpretation	Reference
33.26223905	20.94973459	Keraf suture	K39B-1	700	**5.9**	**750**	**Arc-related magmatism**	
33.6209127	20.21188635	Keraf suture	6.9	711	**5.6**	**770**	**Arc-related magmatism**	
33.49568945	19.51564511	Keraf suture	11.13	737	**4.5**	**900**	**Arc-related magmatism**	**Bailo et al. (2003)**
33.56205777	19.39292633	Keraf suture	11.14	737	**4.9**	**830**	**Arc-related magmatism**	
33.18263134	21.05839548	Keraf suture	1.1	714	**7.3**	**620**	**Arc-related magmatism**	
33.53075168	18.69490677	Saharan meta-craton	9-1	860	**6.1**	**860**	**Arc-related magmatism**	
33.53075168	18.69490677	Saharan meta-craton	11-2A	860	**5.7**	**900**	**Arc-related magmatism**	
33.53075168	18.69490677	Saharan meta-craton	6-3	860	**5.6**	**890**	**Arc-related magmatism**	
32.83668064	18.71995745	Saharan meta-craton	12-3	920	**−7.9**	**2430**	**Bayudian event**	
32.83668064	18.71995745	Saharan meta-craton	12-2	920	**−7.1**	**2230**	**Bayudian event**	
32.83668064	18.71995745	Saharan meta-craton	12-5b	920	**−7.3**	**2040**	**Bayudian event**	
33.42292475	18.90133653	Saharan meta-craton	10-8A	900	**−3.3**	**1550**	**Bayudian event**	
33.42292475	18.90133653	Saharan meta-craton	10-7E	900	**−4.3**	**1830**	**Bayudian event**	
33.42292475	18.90133653	Saharan meta-craton	10-6	900	**−5.1**	**1820**	**Bayudian event**	
33.42292475	18.90133653	Saharan meta-craton	10-8B	900	**−0.3**	**1300**	**Bayudian event**	
33.6914	18.3751	Saharan meta-craton	15-2	600	**4.1**	**750**	**Post-collisional magmatism**	
33.6914	18.3751	Saharan meta-craton	15-1	600	**0.1**	**1050**	**Post-collisional magmatism**	**Küster et al. (2008)**
33.25594332	18.66508907	Saharan meta-craton	14-5	600	**2.4**	**910**	**Post-collisional magmatism**	
33.25594332	18.66508907	Saharan meta-craton	14-7	600	**1.1**	**1140**	**Post-collisional magmatism**	
33.25594332	18.66508907	Saharan meta-craton	14-3	600	**−1.5**	**1190**	**Post-collisional magmatism**	
32.86888254	17.05076038	Saharan meta-craton	18-8	600	**−2.1**	**1180**	**Post-collisional magmatism**	
32.86888254	17.05076038	Saharan meta-craton	17-4b	600	**−4.7**	**1160**	**Post-collisional magmatism**	
32.86888254	17.05076038	Saharan meta-craton	17-4f	600	**−6.1**	**1430**	**Post-collisional magmatism**	
32.86888254	17.05076038	Saharan meta-craton	18-1b	600	**−8.3**	**1440**	**Post-collisional magmatism**	
32.86888254	17.05076038	Saharan meta-craton	18-1c	600	**−6.0**	**1290**	**Post-collisional magmatism**	
32.8407069	17.14251349	Saharan meta-craton	18-5A	600	**−7.1**	**1560**	**Post-collisional magmatism**	
32.0364	18.3288	Saharan meta-craton	18-7	600	**−4.6**	**1320**	**Post-collisional magmatism**	
32.0364	18.3288	Saharan meta-craton	18-6b	600	**−5.4**	**1240**	**Post-collisional magmatism**	
31.2245	21.5031	Saharan meta-craton	70S	718	**5.4**	**804**	**Post-collisional magmatism**	
31.2265	21.4751	Saharan meta-craton	72S	718	**5.5**	**801**	**Post-collisional magmatism**	**Shang et al. (2010a)**
31.2197	21.4296	Saharan meta-craton	167S	718	**5.6**	**792**	**Post-collisional magmatism**	
31.1533	21.4117	Saharan meta-craton	169S	707	**6.3**	**860**	**Post-collisional magmatism**	

Nd whole-rock isotopic compositions *(continued)*

°E WGS84	°N WGS84	ANS location	Sample ID	age (Ma)	$\varepsilon Nd_{(i)}$	T_{DM} (Ma)	Age interpretation	Reference
31.1054	21.4016	Saharan meta-craton	171S	707	**6.5**	**830**	**Post-collisional magmatism**	**Shang et al. (2010a)**
31.1086	21.3888	Saharan meta-craton	172S	707	**6.8**	**810**	**Post-collisional magmatism**	
30.473	19.655	Saharan meta-craton	01S	600	**4.5**	**1650**	**Post-collisional magmatism**	**Shang et al. (2010b)**
30.251	19.94	Saharan meta-craton	116S	600	**3.4**	**1560**	**Post-collisional magmatism**	
30.473	19.655	Saharan meta-craton	198S	600	**4.7**	**1660**	**Post-collisional magmatism**	
30.501	19.76	Saharan meta-craton	06S	600	**8.8**	**1990**	**Post-collisional magmatism**	
30.386	19.797	Saharan meta-craton	20S	600	**7.0**	**1850**	**Post-collisional magmatism**	
30.501	19.76	Saharan meta-craton	200S	600	**2.3**	**1460**	**Post-collisional magmatism**	

Sr whole-rock isotopic compositions

Sr whole-rock isotopic compositions

°E WGS84	°N WGS84	ANS location	Sample ID	*age* (Ma)	$(^{87}Sr/^{86}Sr)_i$	**Isochron age (Ma)**	2σ (Ma)	**Age interpretation**	**Reference**
28.9246221	17.50880588	Saharan meta-craton	WH-M	*	**0.7064**	**686**	26	**Syn-collisional magmatism**	
29.46536751	17.64156373	Saharan meta-craton	WH-MG	*	**0.7086**	**585**	19	**Post-collisional magmatism**	
29.60136336	17.77432159	Saharan meta-craton	WHEG	*	**0.7080**	**562**	7	**Post-collisional magmatism**	
30.24086766	19.67502551	Saharan meta-craton	NDRG	*	**0.7064**	**565**	8	**Post-collisional magmatism**	**Stern and Hedge (1985);**
29.93002	19.70740548	Saharan meta-craton	NDMG	*	**0.7055**	**623**	37	**Syn-collisional magmatism**	**Harms et al. (1990)**
29.60298236	19.61997957	Saharan meta-craton	NDG	*	**0.7160**	**918**	40	**Arc-related magmatism**	
26.7276415	22.10190387	Saharan meta-craton	GK-M	*	**0.7050**	**673**	56	**Syn-collisional magmatism**	
29.3370619	22.93042621	Saharan meta-craton	BSSOG/BSSGD	*	**0.7054**	**592**	46	**Late collisional magmatism**	
29.29861069	23.03970859	Saharan meta-craton	BSSGD	*	**0.7055**	**581**	75	**Post-collisional magmatism**	**Bernau et al. (1987)**
32.85	16.15	Saharan meta-craton	SAB 5, SAB 5B, SAB 13	*	**0.7249**	**721**	12	**Syn-collisional magmatism**	**Kröner et al. (1987)**
30.25199386	20.41288562	Atmur Delgo suture	NGD	718	**0.7077**			**Arc-related magmatism**	
30.6750954	19.80979061	Atmur Delgo suture	ITGS	748	**0.7087**			**Arc-related magmatism**	
30.78729912	20.23289215	Atmur Delgo suture	NEDG	680	**0.7037**			**Arc-related magmatism**	
30.89950284	20.80793623	Atmur Delgo suture	Gst2	661	**0.7160**			**Syn-collisional magmatism**	
31.04209507	20.28899401	Atmur Delgo suture	ASMI	*	**0.7096**	**546**	19	**Post-collisional magmatism**	
30.93924166	20.28198128	Atmur Delgo suture	ASM2	700	**0.7095**			**Arc-related magmatism**	
31.39974444	20.44327413	Atmur Delgo suture	SMG2	592	**0.7194**			**Post-collisional magmatism**	
30.9556047	20.67235673	Atmur Delgo suture	ASS27a	752	**0.7023**			**Oceanic, seafloor magmatism**	**Harms et al. (1994)**
30.9556047	20.67235673	Atmur Delgo suture	ASS27b	752	**0.7024**			**Oceanic, seafloor magmatism**	
30.9556047	20.67235673	Atmur Delgo suture	ASS27c	752	**0.7024**			**Oceanic, seafloor magmatism**	
30.9556047	20.67235673	Atmur Delgo suture	ASS27d	752	**0.7025**			**Oceanic, seafloor magmatism**	
30.26666667	20.3166667	Atmur Delgo suture	G385	702	**0.7068**			**Arc-related magmatism**	
32.10136349	20.93493507	Atmur Delgo suture	Gst6	700	**0.7052**			**Arc-related magmatism**	
?	?	Atmur Delgo suture	93	702	**0.7057**			**Arc-related magmatism**	
?	?	Atmur Delgo suture	552at	707	**0.7049**			**Arc-related magmatism**	
31.3934	21.6589	Atmur Delgo suture	WH-1, WH-2, WH-3, WH-4, WH-6	*		**653**	20	**Post-collisional magmatism**	**Stern et al. (1994)**

Sr whole-rock isotopic compositions *(continued)*

°E WGS84	°N WGS84	ANS location	Sample ID	*age* (Ma)	$(^{87}Sr/^{86}Sr)_i$	**Isochron age (Ma)**	2σ (Ma)	**Age interpretation**	**Reference**
31.3762	21.5837	Atmur Delgo suture	WH-20, WH-21, WH-22, WH-25, WH-27, WH-28	*		**530**	10	**Post-collisional magmatism**	**Stern et al. (1994)**
32.88110662	18.61323723	Saharan meta-craton	12-4a	806	**0.7080**			**Arc-related magmatism**	
32.88110662	18.61323723	Saharan meta-craton	12-6	806	**0.7080**			**Arc-related magmatism**	
33.93325285	18.14123956	southern Keraf shear zone	6-2a	806	**0.7030**			**Arc-related magmatism**	
33.48908036	19.13858015	Saharan meta-craton	10-5a	806	**0.7030**			**Arc-related magmatism**	
33.48908036	19.13858015	Saharan meta-craton	10-1a	806	**0.7040**			**Arc-related magmatism**	
33.60647233	18.85947663	southern Keraf shear zone	9-5	806	**0.7030**			**Arc-related magmatism**	
33.60647233	18.85947663	southern Keraf shear zone	9-2a	806	**0.7030**			**Arc-related magmatism**	
33.60647233	18.85947663	southern Keraf shear zone	11-1	806	**0.7030**			**Arc-related magmatism**	
33.60647233	18.85947663	southern Keraf shear zone	9-1	806	**0.7020**			**Arc-related magmatism**	**Küster and Liégeois (2001)**
33.60647233	18.85947663	southern Keraf shear zone	11-2a	806	**0.7020**			**Arc-related magmatism**	
33.93325285	18.14123956	southern Keraf shear zone	6-3	806	**0.7010**			**Arc-related magmatism**	
32.88110662	18.61323723	Saharan meta-craton	12-3	806	**0.7160**			**Arc-related magmatism**	
32.88110662	18.61323723	Saharan meta-craton	12-2	806	**0.7160**			**Arc-related magmatism**	
32.88110662	18.61323723	Saharan meta-craton	12-5b	806	**0.7040**			**Arc-related magmatism**	
33.93325285	18.14123956	southern Keraf shear zone	6-5	806	**0.7030**			**Arc-related magmatism**	
33.93325285	18.14123956	Saharan meta-craton	7-1	806	**0.7030**			**Arc-related magmatism**	
33.50087922	18.46483337	Saharan meta-craton	14-11	806	**0.7120**			**Arc-related magmatism**	
32.88110662	15.92329413	Saharan meta-craton	17-6	806	**0.7170**			**Arc-related magmatism**	
33.18263134	21.05839548	Keraf suture	1.1	700	**0.7028**			**Arc-related magmatism**	
33.26223905	20.94973459	Keraf suture	K39B-1	711.0	**0.7028**			**Arc-related magmatism**	
33.6209127	20.21188635	Keraf suture	6.9	737	**0.7046**			**Arc-related magmatism**	**Bailo et al. (2003)**
33.49568945	19.51564511	Keraf suture	11.13	737	**0.7032**			**Arc-related magmatism**	
33.56205777	19.39292633	Keraf suture	11.14	714	**0.7030**			**Arc-related magmatism**	
33.53075168	18.69490677	Saharan meta-craton	9-1	860	**0.7028**			**Arc-related magmatism**	
33.53075168	18.69490677	Saharan meta-craton	11-2A	860	**0.7026**			**Arc-related magmatism**	
33.53075168	18.69490677	Saharan meta-craton	6-3	860	**0.7007**			**Arc-related magmatism**	**Küster et al. (2008)**
33.42292475	18.90133653	Saharan meta-craton	10-8A	900	**0.7053**			**Bayudian event**	
33.42292475	18.90133653	Saharan meta-craton	10-7E	900	**0.7055**			**Bayudian event**	

Sr whole-rock isotopic compositions *(continued)*

°E WGS84	°N WGS84	ANS location	Sample ID	*age* (Ma)	$(^{87}Sr/^{86}Sr)_i$	**Isochron age (Ma)**	2σ (Ma)	**Age interpretation**	**Reference**
33.42292475	18.90133653	Saharan meta-craton	10-6	900	**0.7028**			**Bayudian event**	
33.42292475	18.90133653	Saharan meta-craton	10-8B	900	**0.7045**			**Bayudian event**	
33.6914	18.3751	Saharan meta-craton	15-2	600	**0.7032**			**Post-collisional magmatism**	
33.6914	18.3751	Saharan meta-craton	15-1	600	**0.7036**			**Post-collisional magmatism**	
33.25594332	18.66508907	Saharan meta-craton	14-5	600	**0.7031**			**Post-collisional magmatism**	
33.25594332	18.66508907	Saharan meta-craton	14-7	600	**0.7011**			**Post-collisional magmatism**	
33.25594332	18.66508907	Saharan meta-craton	14-3	600	**0.7038**			**Post-collisional magmatism**	
32.86888254	17.05076038	Saharan meta-craton	18-8	600	**0.7042**			**Post-collisional magmatism**	**Küster et al. (2008)**
32.86888254	17.05076038	Saharan meta-craton	17-4b	600	**0.7029**			**Post-collisional magmatism**	
32.86888254	17.05076038	Saharan meta-craton	17-4f	600	**0.7038**			**Post-collisional magmatism**	
32.86888254	17.05076038	Saharan meta-craton	18-1b	600	**0.7069**			**Post-collisional magmatism**	
32.86888254	17.05076038	Saharan meta-craton	18-1c	600	**0.7061**			**Post-collisional magmatism**	
32.8407069	17.14251349	Saharan meta-craton	18-5A	600	**0.7055**			**Post-collisional magmatism**	
32.0364	18.3288	Saharan meta-craton	18-7	600	**0.7068**			**Post-collisional magmatism**	
32.0364	18.3288	Saharan meta-craton	18-6b	600	**0.7054**			**Post-collisional magmatism**	
31.2245	21.5031	Saharan meta-craton	70S	718	**0.7020**			**Post-collisional magmatism**	
31.2265	21.4751	Saharan meta-craton	72S	718	**0.7010**			**Post-collisional magmatism**	
31.2197	21.4296	Saharan meta-craton	167S	718	**0.7000**			**Post-collisional magmatism**	
31.1533	21.4117	Saharan meta-craton	169S	707	**0.7009**			**Post-collisional magmatism**	
31.1054	21.4016	Saharan meta-craton	171S	707	**0.7005**			**Post-collisional magmatism**	
31.1253	21.4106	Saharan meta-craton	169S, 171S, 172S, 169st, 171st, 172st, 214st	*	**0.7032**	**692**	35	**Post-collisional magmatism**	**Shang et al. (2010a)**
31.2245	21.5031	Saharan meta-craton	70S, 72S, 167S, 70st, 71st, 72st, 74st, 166st, 167st	*	**0.7036**	**683**	13	**Post-collisional magmatism**	
30.473	19.655	Saharan meta-craton	01S	600	**0.7004**			**Post-collisional magmatism**	
30.251	19.94	Saharan meta-craton	116S	600	**0.7026**			**Post-collisional magmatism**	
30.473	19.655	Saharan meta-craton	198S	600	**0.7050**			**Post-collisional magmatism**	**Shang et al. (2010b)**
30.501	19.76	Saharan meta-craton	04S	600	**0.7071**			**Post-collisional magmatism**	
30.473	19.655	Saharan meta-craton	117S	600	**0.7056**			**Post-collisional magmatism**	
30.473	19.655	Saharan meta-craton	119S	600	**0.7055**			**Post-collisional magmatism**	

Sr whole-rock isotopic compositions *(continued)*

°E WGS84	°N WGS84	ANS location	Sample ID	*age* (Ma)	$(^{87}Sr/^{86}Sr)_i$	**Isochron age (Ma)**	2σ (Ma)	**Age interpretation**	**Reference**
30.559	19.916	Saharan meta-craton	201S	600	**0.7051**			**Post-collisional magmatism**	**Shang et al. (2010b)**
30.386	19.797	Saharan meta-craton	19S	600	**0.7071**			**Post-collisional magmatism**	
30.39	19.896	Saharan meta-craton	48S	600	**0.7053**			**Post-collisional magmatism**	
30.501	19.76	Saharan meta-craton	06S	600	**0.7070**			**Post-collisional magmatism**	
30.386	19.797	Saharan meta-craton	20S	600	**0.7057**			**Post-collisional magmatism**	
30.501	19.76	Saharan meta-craton	200S	600	**0.7210**			**Post-collisional magmatism**	
30.501	19.76	Saharan meta-craton	05S	600	**0.7070**			**Post-collisional magmatism**	
30.501	19.76	Saharan meta-craton	43S	600	**0.7074**			**Post-collisional magmatism**	
33.1905	18.6613	Saharan meta-craton	022/4	912	**0.7066**			**Bayudian event**	**Evuk et al. (2014)**
33.27577	18.73421	Saharan meta-craton	030/1	912	**0.7095**			**Bayudian event**	
33.15048973	18.53159927	Saharan meta-craton	059/1	912	**0.7105**			**Bayudian event**	
33.5162	18.7268	southern Keraf shear zone	071/1	645	**0.7027**			**Late collisional magmatism**	
33.38999595	18.44621079	southern Keraf shear zone	073/3	810	**0.7022**			**Arc-related magmatism**	
33.5159	18.6972	southern Keraf shear zone	080/1	700	**0.7023**			**Syn-collisional magmatism**	
33.5162	18.7268	southern Keraf shear zone	097/2	700	**0.7023**			**Syn-collisional magmatism**	
33.56115	18.72431	Saharan meta-craton	145/1	969	**0.7079**			**Bayudian event**	
33.5049	18.6801	southern Keraf shear zone	177/1	700	**0.7023**			**Syn-collisional magmatism**	
33.4526	18.7328	Saharan meta-craton	195/1	969	**0.7099**			**Bayudian event**	
33.51496	18.36466	southern Keraf shear zone	291/1	645	**0.7025**			**Late collisional magmatism**	
33.51534762	18.32912406	southern Keraf shear zone	293/1	645	**0.7101**			**Late collisional magmatism**	
33.58973213	18.74443757	southern Keraf shear zone	324/1	700	**0.7027**			**Syn-collisional magmatism**	
?	?	southern Keraf shear zone	332/2	630	**0.7050**			**Late collisional magmatism**	
33.53527	18.4907	southern Keraf shear zone	352/1	803	**0.7022**			**Arc-related magmatism**	
33.4325	18.4877	southern Keraf shear zone	355/1	700	**0.7025**			**Syn-collisional magmatism**	
33.40445961	18.60875471	Saharan meta-craton	371/2	909	**0.7020**			**Bayudian event**	
33.70513	18.6848	southern Keraf shear zone	498/1	630	**0.7028**			**Late collisional magmatism**	

** Isochron age calculation.*

PARTIE II – Déformation à l'échelle crustale et minéralisations aurifères

Préambule

L'évolution lithosphérique enregistrée le long de la partie centrale de la suture de Keraf est désormais contrainte, ainsi que les processus de croissance crustale et de fertilisation en or de la croûte mis en jeu (**Partie I**). Il est désormais nécessaire de recaler les minéralisations aurifères ciblées par ce projet dans l'histoire géodynamique régionale. En effet, la connaissance de l'environnement tectonique associé à la mise en place des gisements d'or hydrothermaux déformés est fondamentale à la compréhension des processus métallogéniques associés et à l'exploration (Blenkinsop et al., 2020a). D'ailleurs, de nombreux ouvrages et publications traitent de l'importance du contrôle structural de la minéralisation (*e.g.,* McCaffrey et al., 1999 ; Cox et al., 2001; Richards et Tosdal, 2001 ; Chauvet, 2019a ; Blenkinsop et al., 2020a, 2020b ; Rowland et Rhys, 2020). Le modèle conceptuel de valve sismique associe par exemple les circulations fluides et la mise en place d'or orogénique aux cycles de charge-décharge sismique syn-déformation (synthèses par Sibson, 2020a, 2020b). Pourtant, l'étude du contrôle structural des gisements d'or hydrothermaux n'est pas chose aisée. Les événements minéralisateurs peuvent être multiples et s'étaler sur une période de plus de 100 millions d'années (*e.g.,* Augustin et al., 2017 ; Le Mignot et al., 2017 ; Thébaud et al., 2020 ; Masurel et al., sous presse). Cette histoire minéralisatrice complexe peut être liée à la réactivation de structures héritées (*e.g.,* Chauvet, 2019b ; Blenkinsop et al., 2020b), elles même associées à différents contextes tectoniques se succédant dans le temps et s'exprimant de façon variable dans l'espace. Il est donc illusoire d'envisager contraindre l'histoire tectonique régionale associée à la minéralisation à partir d'observations faites uniquement à l'échelle du gisement, et *vice versa* (Blenkinsop et al., 2020a).

Cette **Partie II** aborde donc l'histoire tectonique et les événements aurifères enregistrés le long des sutures d'Atmur-Delgo et Keraf par les gisements de Galat Sufar South (**Chapitre II**) et de WG03, Central Zone et UTM (district de Gabgaba, **Chapitre III**). Un travail pétro-structural de terrain réalisé à l'échelle du gisement, suivant une approche courante (*e.g.,* Combes et al., sous presse; Allibone et al., 2002, 2018 ; Ashley et Craw, 2004 ; Blenkinsop et Doyle, 2014 ; Masurel et al., 2017 ; Yang et al., 2018 ; Hronsky, 2020), est couplé à des observations réalisées depuis l'échelle du district (analyse d'images satellite, levé d'une coupe régionale) jusqu'aux échelles macroscopique (analyse d'affleurements et description de carottes de forage) et microscopique (analyse pétro-micro-structurale sur lame mince). Cette intégration multi-scalaire fait l'originalité de notre démarche, qui dépasse le cadre classique de l'étude structurale d'un gisement et ses limites évoquées dans le paragraphe précédent.

Chapitre II – Subvertical, linear and progressive deformation related to gold mineralization at the Galat Sufar South deposit, Nubian shield, NE Sudan

Julien Perret[1,2,*], Aurélien Eglinger[2], Anne-Sylvie André-Mayer[2], Laurent Aillères[3], Julien Feneyrol[1], Craig Hartshorne[4], Emmanuel Abanyin[4], Rémi Bosc[1]

Article publié en juin 2020 dans *Journal of Structural Geology* 135, 1-24.

https://doi.org/10.1016/j.jsg.2020.104032

[1] Arethuse Geology EURL, BP 80017, Latitude Arbois, 1060 rue René Descartes, 13290 Les Milles, France

[2] GeoRessources, Université de Lorraine, CNRS, 54000 Nancy, France

[3] School of Earth, Atmosphere and Environment, Monash University, 9 Rainforest Walk, Clayton, VIC 3800, Australia

[4] Orca Gold Inc., 885 West Georgia Street, Suite 2000, Vancouver, V6C 3E8, Canada

Résumé

Le gisement aurifère de Galat Sufar South (bloc d'exploration 14, Soudan) se situe dans une zone déformée de façon intense, à l'intersection entre la suture d'Atmur-Delgo et la zone de cisaillement de Keraf, au sein du bouclier arabo-nubien. L'étude pétro-structurale de la minéralisation aurifère exprimée depuis l'échelle micrométique jusqu'à l'échelle pluri-kilométrique permet une meilleure compréhension de l'histoire tectonique enregistrée dans cette région, peu contrainte jusqu'alors. Cette approche propose également des éléments de réflexion quant au contexte géodynamique favorable à la mise en place de ce type de minéralisations aurifères dans la partie nord-ouest du bouclier nubien.

Notre étude illustre que le gisement aurifère de Galat Sufar South a enregistré une histoire tectonique polyphasée, dominée par un premier épisode de déformation progressive et ductile. Ce dernier est associé à la mise en place de la minéralisation en or économique, contrainte géométriquement par des structures linéaires subverticales (*e.g.,* linéation d'étirement, possibles plis en fourreau). L'approche multi-scalaire suivie permet d'associer la mise en place locale de ces structures et de la minéralisation aurifère exprimée à Galat Sufar South à la fermeture de la suture d'Atmur-Delgo.

Mots-clés

Déformation progressive *vs* polyphasée ; déformation multi-scalaire ; gisement aurifère de Galat Sufar South ; bouclier arabo-nubien.

Abstract

The Galat Sufar South gold deposit, Block 14, NE Sudan, is located within a complexly deformed zone at the junction between the Keraf shear zone and the Atmur-Delgo suture, within the western portion of the Arabian-Nubian shield. The combination of a petrographic and structural study of the gold mineralization at the Galat Sufar South deposit, carried out at the µm- to tens of km-scale, allows the deciphering of the deformation history of this poorly documented area and provides insights on the geodynamical context favorable for gold mineralization in the northwesternmost Nubian shield.

Our study highlights that the Galat Sufar South gold deposit recorded a polyphase deformation history dominated by an early, ductile-dominated, progressive deformation episode associated with the economic gold mineralization. It displays an atypical structural control by subvertical simple shearing evidenced by subvertical linear features (stretching lineation and potential sheath folding). The proposed multi-scale approach helps to correlate this subvertical, linear, progressive deformation event and the coeval economic gold mineralization with the early north-northwest-orientated compressive tectonics related to the Atmur-Delgo suturing.

Keywords

Progressive *vs* multiphase deformation; Multi-scale deformation; Galat Sufar South gold deposit; Arabian-Nubian shield.

1. Introduction

In exploration geology, the structural control on ore deposits is critical (Blenkinsop et al., 2014; Chauvet, 2019a). The classical approach relying on constraining the mineralization timing within the unraveled deformation history has been widely applied, especially to gold-bearing vein deposits (*e.g.,* Blenkinsop and Doyle, 2014; Augustin et al., 2017) as they express a strong structural control (Sawkins, 1990; Groves et al., 1998, 2019; Goldfarb et al., 2001; Robb, 2005; Bierlein et al., 2006a; Richards, 2011, 2013; Gaboury, 2019). So far, the structural study of these deposits mostly focuses on deciphering the successive local states of strain responsible for mineralization-controlling structure formation (*e.g.,* Hodgson, 1989; Gaboury et al., 2001; Allibone et al., 2002; Miller and Wilson, 2004; Tunks et al., 2004; Wang et al., 2019). From the structural geology side, studying such kind of gold mineralization is therefore also a way to unravel the local deformation history.

However, such structural studies often lead to descriptions of gold-bearing vein deposits from a purely geometric point of view, which provides critical targeting keys for gold exploration at the regional scale (Groves et al., 2018), but may be inappropriate to answer the fundamental structural problem: what is the tectonic meaning of the deformation features associated with gold mineralization? The geometric approach may unnecessarily complicate the local deformation history by considering multiple, discrete deformation stages that cannot be transferred into the regional tectonic framework: this is due to a lack of consideration for progressive deformation resulting in different structural patterns that can be explained by a single "structural-kinematic model" (Fossen et al., 2019). To do so, it is critical to firstly couple structural and petrographic studies from the deposit to the mineral scale (outcrop, drillcore and thin sections) and unravel the spatial and temporal relationships between lithology, deformation, alteration and mineralization. Then, such multi-scale, petro-structural characterization of the deposit strongly helps to discuss the multiphase *vs* progressive nature of the deformation

history and better understand the regional tectonic framework associated with gold mineralization.

We propose to follow this approach considering the Galat Sufar South (GSS, Block 14 exploration license operated by Orca Gold Inc.) gold deposit, located in the northwestern part of the Nubian shield which represents the western half of the Arabian-Nubian shield (Fig. 2-1a). The GSS deposit offers the particularity of being located at the junction between two main lithospheric structures, the Keraf Shear Zone (KSZ) and the Atmur-Delgo suture (ADS) (Fig. 2-1b). It displays a strong gold endowment with probable reserves of 79.9Mt @ 1.11g/t Au for a total of 2.853 Mozt Au across the GSS deposit and combined with the nearby Wadi Doum deposit (Fig. 2-2a; Orca Gold Inc. 2019). The GSS area is known to be complexly deformed with evidence for interference folding and a complex deformation history from several GIS, radar imagery and large-scale structural studies (Abdelsalam et al., 1995; Abdelsalam and Stern, 1996a; Abdelsalam et al., 1998; Ahmed Suliman, 2000). The GSS gold deposit is part of the numerous so-called "orogenic", epigenetic gold occurrences that are structurally controlled by major shear and suture zones (Botros, 2002; Hassaan and El-Sawy, 2009; Zoheir et al., 2018a, 2019a) throughout the Nubian shield (Fig. 2-1b; Johnson et al., 2017). Yet, the GSS area is not documented to date, apart from internal reports for Orca Gold Inc.

In this study, we will therefore track the deformation evolution of the GSS area through the study of the gold mineralization and its structural control at every scale. A large exploration drillcore sample set together with field observations and satellite imagery analysis facilitated (1) the deciphering of the deposit-scale deformation history and the relationships between lithology, deformation, alteration and mineralization, from the macro- to the microscopic scale and (2) the integration of the GSS gold deposit structural history in the framework of the ADS and KSZ tectonic evolution.

2. Geological setting

2.1. Regional geology

The GSS gold deposit is located within the western portion of the Neoproterozoic Arabian-Nubian shield (ANS; Fig. 2-1a). The ANS represents the northern part of the East African-Antarctic orogeny (EAAO) (Stern, 1994; Johnson and Woldehaimanot, 2003; Kusky et al., 2003). The EAAO extends intermittently to the South down to Mozambique, southern Madagascar (Stern, 1994) and Antarctic (Grenholm, 2019 and references therein) and results from the collision of oceanic and continental fragments, *i.e.* terranes, between the Archean Sahara-Congo-Kalahari cratons westwards and the Neoproterozoic India eastwards (Fritz et al., 2013). The northernmost EAAO formed earlier than its southern extension (pressure peak metamorphism at ~ 620 Ma *vs* ~ 550 Ma, respectively) and is associated with lower temperature and pressure conditions (below the blueschist facies metamorphism *vs* high temperature, high pressure granulite to eclogite metamorphism associated with a significant crustal thickening, respectively; Fritz et al., 2013). Obduction is thought to have been more significant than subduction in the northern portion of the EAAO explaining such increase in pressure and temperature southwards (Fritz et al., 2013). The ~ 850-550 Ma formation of the ANS resulted from the collision of these Neoproterozoic terranes onto the Saharan meta-craton (Johnson and Woldehaimanot, 2003; Johnson et al., 2011 and references therein) in the framework of a "Supercontinent Cycle" described by Stern and Johnson (2010) and Johnson et al. (2011). The final set-up of the ANS is mostly composed of intra-oceanic island arc, back-arc and ophiolite assemblages preserved from the Mozambique Ocean (Fig. 2-1; Burke and Sengör, 1986).

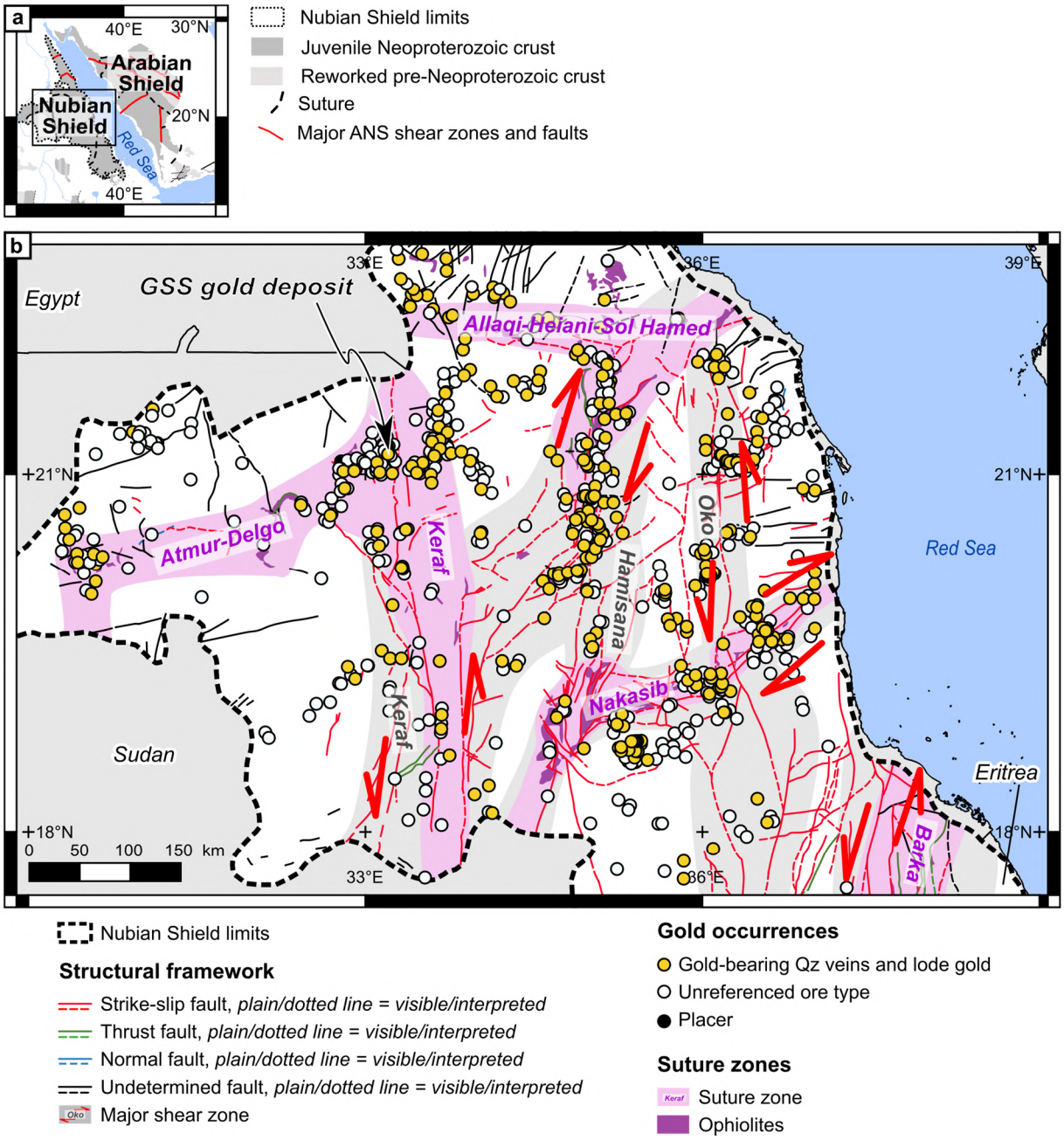


Figure 2-1: a The Arabian-Nubian shield (ANS) location, simplified after Johnson et al. (2011) and Fritz et al. (2013). The black rectangle delimits the extent of Figure 2-1b. Geographic coordinates are reported as WGS 84 / Pseudo Mercator. **b** Structural framework and gold occurrences of the Nubian shield. Ophiolites and visible faults are drawn from Sudanese, Egyptian and Eritrean geological maps while suture zones, fault prolongations and shear zones are interpreted from these features. Major Nubian shield suture and shear zones are named after Johnson et al. (2011) and references therein. Gold occurrences are from the Arethuse Geology GIS compilation database. Geographic coordinates are reported as WGS 84.

At the regional scale, the GSS gold deposit is located at the junction between the Keraf Shear Zone (KSZ) and the Atmur-Delgo suture (ADS) (Fig. 2-1b). The E-trending ADS is composed of an ophiolitic belt thought to result from an aulacogenic oceanic re-entrant within the Saharan meta-craton (Burke and Sengör, 1986; Abdelrahman, 1993;

Denkler et al., 1993; Harms et al., 1994; Schandelmeier et al., 1994b; Abdelsalam et al., 1998). The ADS formed by the closure of a small oceanic basin and further collision between the Bayuda terrane southwards and the Halfa terrane northwards at ~ 750-650 Ma, relying on metagabbro Sm-Nd whole-rock isochron ages and syn-tectonic granitoid Pb-Pb zircon ages (Harms et al., 1994). Within the GSS area, the deformation history related to the ADS development is marked by two ductile stages (Schandelmeier et al., 1994b; Abdelsalam et al., 1998, 2003), with D_1 corresponding to SSE-verging, tight, isoclinal folds and thrusts, probably associated with early thrust movement during subduction, and D_2 characterized by the refolding of D_1 structures into ENE-trending, upright folds assumed to result from collision between terranes.

Following the ADS formation, the final collision of the ANS onto the Saharan meta-craton at 650-580 Ma, relying on Rb-Sr whole-rock isochrons and "errorchrons", Sm-Nd whole rock isochrons, Sm-Nd calc-silicate, Ar-Ar hornblende and biotite plateau ages (ages compilation by Abdelsalam et al., 1998; Bailo et al., 2003), resulted in the formation of the ~ 500 km-long, ~ 50 to 100 km-wide, N-striking Keraf arc-continent suture (Almond and Ahmed, 1987; Stern, 1994; Abdelsalam et al., 1995, 1998; Bailo et al., 2003). It is thought to be the suture between the EAAO and the Saharan meta-craton and extends from southern Egypt to southern Kenya (Vail, 1988; Abdelsalam and Dawoud, 1991; Stern, 1994). As this suture zone is overprinted by a sinistral shear zone (Abdelsalam et al., 1995, 1998; Abdelsalam and Stern, 1996b, 1996a), it is called the Keraf Shear Zone (KSZ) thereafter (Fig. 2-1b). The lithologies reported in the KSZ, and therefore at the GSS gold deposit, are particular to this zone and belong to the Keraf Petro-Tectonic Assemblage (KPTA; Ahmed Sulliman, 2000). The KPTA gathers all the rocks (high- to medium-grade gneisses, Keraf ophiolitic mélange, volcanosedimentary sequences, carbonate-rich and siliciclastic meta-sediments) affected by the Keraf tectonic processes and easily distinguishable by their nature and their deformation features from surrounding rocks eastwards and westwards as defined by Ahmed Suliman (2000). The

KSZ recorded a very complex deformation history, which remains poorly understood except from rare remote sensing and large-scale structural studies; the currently described regional deformation phases along the KSZ express several ductile to brittle phases (Abdelsalam et al., 1995, 2003; Abdelsalam and Stern, 1996a; Ahmed Suliman, 2000), following the ADS formation-related D_1 and D_2 episodes previously described. The D_3 deformation stage controls the structural framework of the KSZ. The main D_3-related structures are folds visible at any scale (*e.g.,* the Abu Hamed antiform and the Atmur synform) with fold axis lineation steeply (up to 90°) or gently (down to 10°) plunging towards the NNE or the NNW due to their relative position to subsequent folding and shearing events. The primary bedding is almost transposed along the penetrative axial plane cleavage ($< 15°$ intersection angle) which is the main planar fabric observed throughout the area. D_3-related structures are largely reoriented by subsequent deformation. Also, D_3 thrusts are associated to D_3 folds and are interpreted to be responsible for (1) the emplacement of the ophiolitic mélange over the Keraf clastic meta-sediments, (2) the emplacement of the KPTA over the western flank of the Saharan meta-craton and (3) the juxtaposition of the Gabgaba-Gebeit terrane with the KPTA eastwards. N-trending, asymmetrical, upright D_4 folds are mostly visible at the meso-scale within low-grade meta-sediments and ophiolites. They show a vergence eastwards and are thought to be formed as the result of the collision of the Gabgaba-Gebeit and Bayuda terranes. E-trending symmetric open D_5 folds are visible at both the regional and outcrop scales. They plunge steeply eastwards and are superimposed over D_3 and D_4-related folds resulting in Type 1 fold interference patterns (Ramsay, 1962). A last brittle D_6 deformation phase related to the KSZ evolution is expressed by conjugate sinistral, NW- and dextral, NE-trending strike slip faults affecting all previous structures. They result from sinistral transpression that accompanied the NW-trending collision between East and West Gondwana. It is worth noticing that D_6 dominates the structural

framework of the southern part of the KSZ while D_3 and D_4 structures are mostly recognized in the northern KSZ domain.

2.2. Local geology

The Block 14 area belongs to the KPTA (Ahmed-Sulliman, 2000) and its western part, where the GSS gold deposit is located, is dominated by meta-sediments (Fig. 2-2a). At the deposit scale, the GSS gold deposit is hosted by a strongly deformed, interleaved andesitic meta-volcanosedimentary horizon, enclosed within a thick andesitic meta-volcanic sequence composed of lava flows, pyroclastic horizons and primary volcanic breccia (Fig. 2-2b). The ore-bearing horizon was altered to a variable extent and multiple times by addition of albite, sericite, silica and carbonate, in association with the mineralization, while the surrounding andesitic meta-volcanics are largely unaltered and barren. Pre-tectonic, subvolcanic calc-alkaline intrusive lenses enclosed within this sequence are more or less abundant but they do not outcrop on the extent of Figure 2-2b. The andesitic part of the GSS area is surrounded by meta-sediments (presence of interlayed marbles and muscovite-rich meta-pelites) but the exact nature of the contact between these two units remains unclear. At the deposit scale, the northwards extension of the GSS gold deposit extension is limited by a marble horizon derived from a former marine carbonate platform. The local metamorphic grade is low and does not exceed the lower amphibolite facies.

Due to its location at the junction between the ADS and the KSZ (Fig. 2-1b), the Block 14 area displays a very complex structural framework, mostly highlighted by low-grade metamorphosed interlayered meta-sediment and marble ridge contours (Fig. 2-2a). The deposit-scale structural framework is dominated by subvertical, NW-steeply plunging stretching lineations expressed in both meta-volcanosedimentary and meta-andesitic horizons (Fig. 2-2b). However, planar fabrics are weakly recognizable, mostly subvertical and displaying a very variable strike orientation (Fig. 2-2b) which is also

expressed by the meta-sediment and marble ridge contours at the Block 14 extent (Fig. 2-2a).

Southeast of the GSS deposit, at the southern edge of Block 14, interlayered marble and muscovite-rich meta-sediments outcrop, forming a kilometric closed feature visible on satellite imagery (Fig. 2-3a). It contains smaller closed contours itself, suggesting its fractal nature. At the outcrop scale, stretched, closed marble bodies are embedded in meta-sediments (Fig. 2-3b and c). The marble bodies are subvertically stretched along the same linear trend controlling the GSS structural framework (Figs. 2-2b, 2-3c and d). It is unclear if their termination only results from erosion or if it represents a fold nose with a curved subhorizontal fold axis that is parallel to the marble body stretching direction within limbs. Marble closed bodies show innermost closed contours on transverse sections (Fig. 2-3d and e). Similar outermost closed contours are seen in surrounding meta-sediments (Fig. 2-3b and c) at the dm-scale. Beyond, the well expressed cleavage in meta-sediments is affected by bending and flows between marble bodies. These outcrop observations suggest that the overall western part of Block 14 is dominated by subvertical linear features as observed at the GSS deposit.

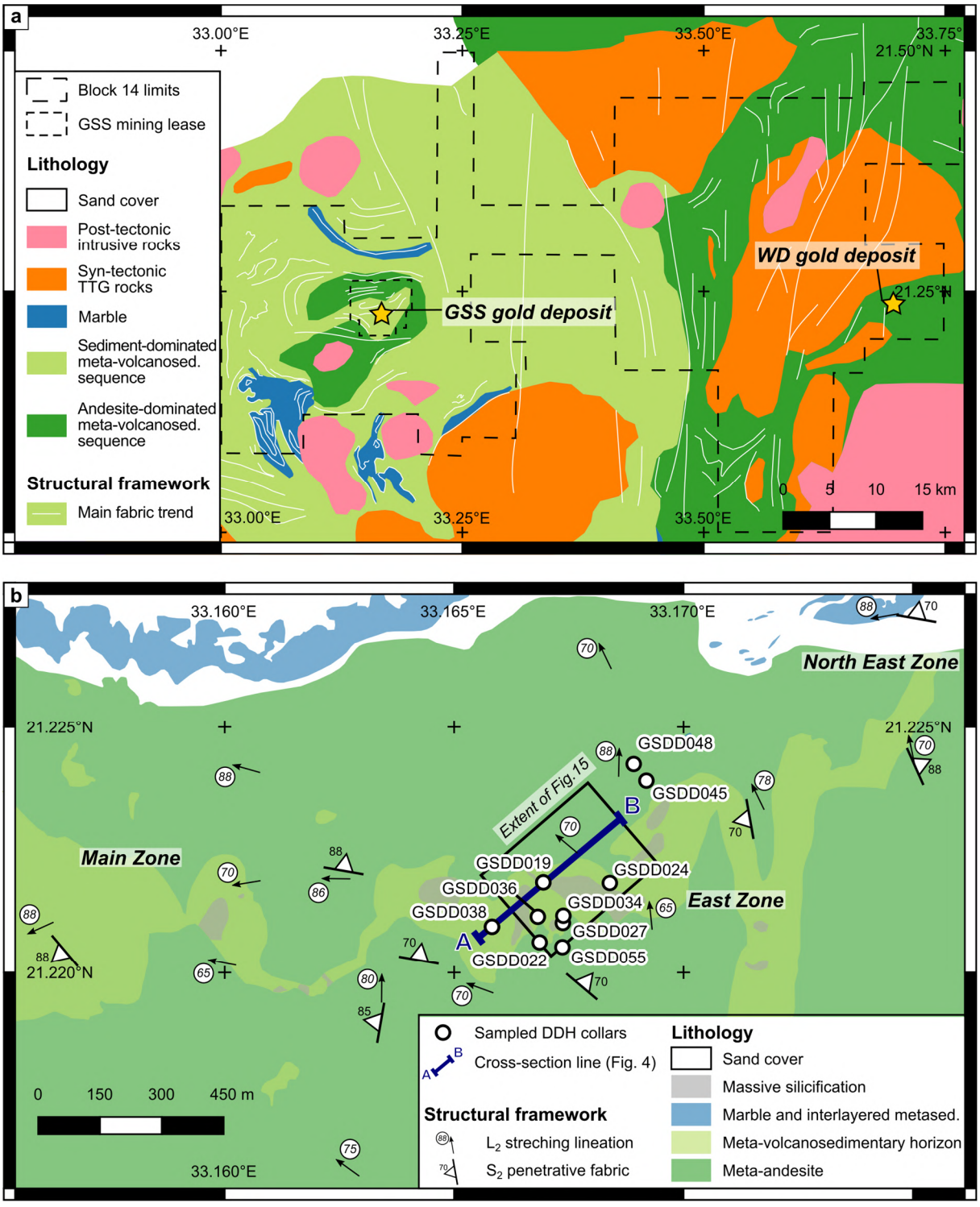


Figure 2-2: a Lithostructural framework of the Block 14 area (NE Sudan), modified after Orca Gold Inc. (2017). The Block 14 limits and the Galat Sufar South (GSS) and Wadi Doum (WD) gold deposits location are indicated. **b** Petro-structural framework of the GSS gold deposit area based on the lithological map by Orca Gold Inc. (2017) and structural measurements carried out on field. The map extent is indicated on satellite imagery in Figure 2-16a. The GSS gold deposit is hosted by a strongly deformed, interleaved meta-volcanosedimentary horizon within a thick meta-volcanic sequence. Its extension is limited by a marine carbonate platform northwards. The collar location of the logged and/or sampled diamond drill holes (DDHs) is indicated as well as the A-B cross-section line (Fig. 2-4) and the extension of the schematic block diagram drawn for GSS gold deposit (Fig. 2-15). Geographic coordinates are reported as WGS 84.

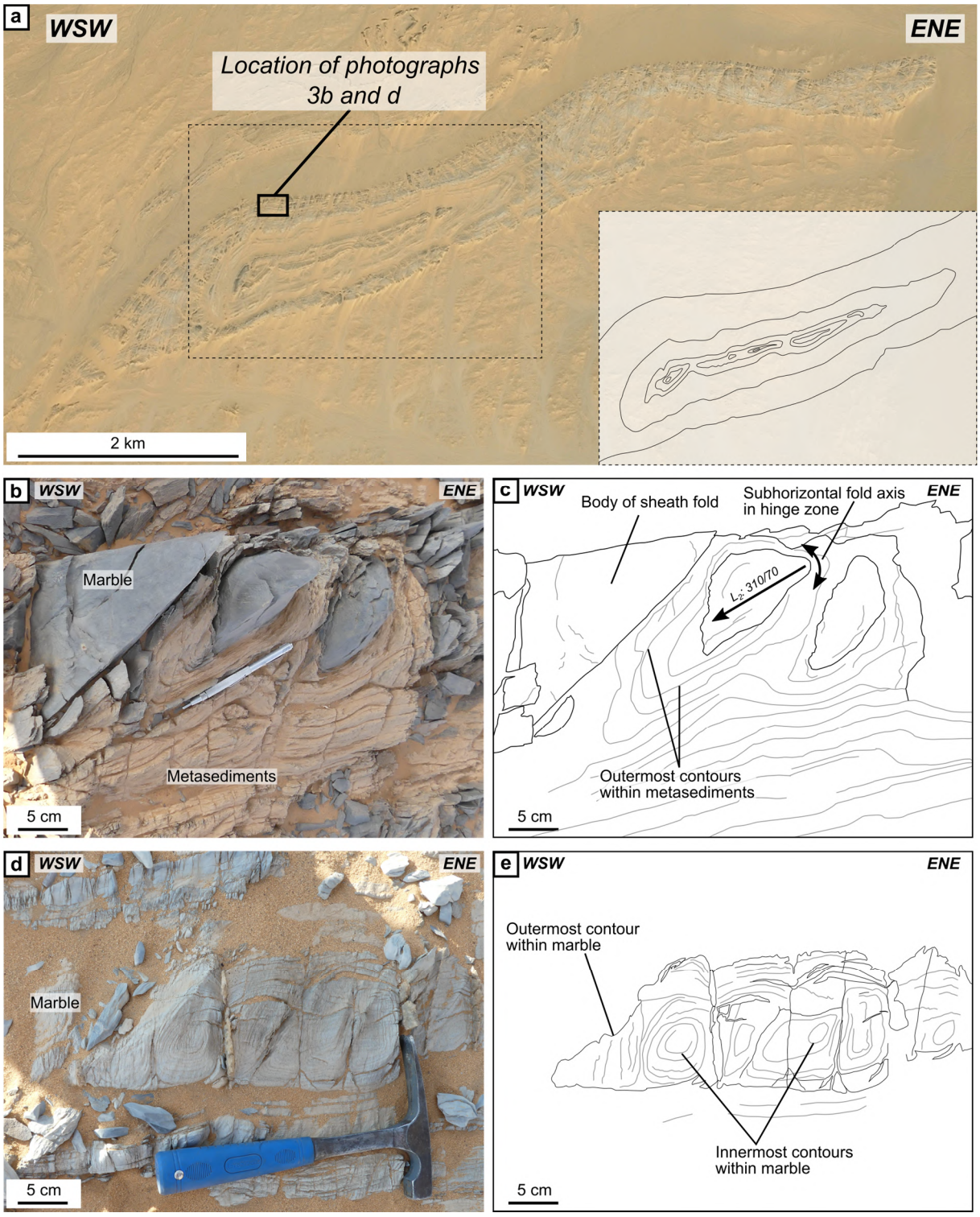


Figure 2-3: Outcrop observations nearby the GSS gold deposit. **a** Closed contours, displayed by alternating marble and meta-sediments are visible from satellite imagery (©BingAerial) southeast to the GSS area, within Block 14 (see location on Figure 2-16a). Closed contours are visible at several scales as expressed by the bottom-right sketch showing the presence of such patterns at the core of the pluri-kilometric feature of interest. Figure 2-3b and d field observation emplacement is indicated. **b** and **c** Field photograph and interpretation sketch enhancing the presence of subvertically strectched, closed marble bodies with subhorizontal top hinge fold axis embedded in meta-sediments displaying closed contours. **d** and **e** Field photograph and interpretation sketch of a transversal section across a marble body. Besides outermost closed contours also visible in Figure 2-3b, the alteration and erosion helped to display closed inner contours within marble.

3. Sampling, methodology and structural glossary

3.1. Sampling and methodology

Sample ID	Grade (g/t Au)	Results presented in this study		
		Deformation (Figs. 2-5 to 2-8)	*Lithology-alteration (Fig. 2-9)*	*Mineralization (Fig. 2-10)*
GS-22-03	0.03		x	
GS-22-06	0.08	x		x
GS-22-08	0.28	x		x
GS-22-10	0.19	x		
GS-22-13	2.40	x		
GS-22-14	3.46		x	
GS-22-16	2.07		x	
GS-22-17	0.50	x		
GS-34-05	6.45			x
GS-34-08	1.07	x		
GS-34-11	0.01	x		
GS-36-01	3.98	x	x	
GS-36-04	0.08		x	
GS-38-05	15.2			x
GS-38-08	1.06	x		
GS-38-12	7.70			x
GS-38-18	0.20		x	
GS-38-19	0.01		x	
GS-55-02	0.02	x		
GS-55-04	0.48		x	

Table 2-1: Samples used in this study. Samples are named after the DDH they have been sampled from and are ordered by increasing depth downhole. The figure number where each sample is used is indicated. The core intervals in Figure 2-4a, c and f have not been sampled. The corresponding DDH ID and their approximate depth are indicated on the photograph.

Among all exploration diamond and reverse circulation drill holes (DDHs and RCDHs, respectively) performed by Orca Gold Inc., ten oriented diamond drill cores have been logged and sampled (GS-DD-019, -022, -024, -027, -034, -036, -038, -045, -048 and -055 DDHs) to characterize lithologies, macro-structures and alteration/mineralization features within the East Zone of the GSS gold deposit (Fig. 2-2b). Figure 2-4 illustrates this logging and sampling work for the GS-DD-019 and GS-DD-038 DDHs. The most representative samples illustrated in Figs. 2-5 to 2-10 are listed in Table 2-1. Oriented thin sections have been prepared, when possible, from slabs cut on half core. As the main penetrative fabric strike orientation is variable (Fig. 2-2b) and studied DDHs form two families with orthogonal NE- and NW-trending azimuth

directions, the crosscutting angle between the slab plane and the main fabric can be quite variable which can be problematic for microstructural investigation. Then, it was checked that all presented sections approximately lie in the (X, Z) deformation plane, parallel to the stretching lineation and orthogonal to the main fabric to characterize micro-structures at best. Additional analyses were carried out using a scanning electron microscope in back-scattered electron mode (BSE-SEM) at the GeoRessources laboratory (Vandoeuvre-lès-Nancy, France) to investigate sulfide mineral internal zoning and textures.

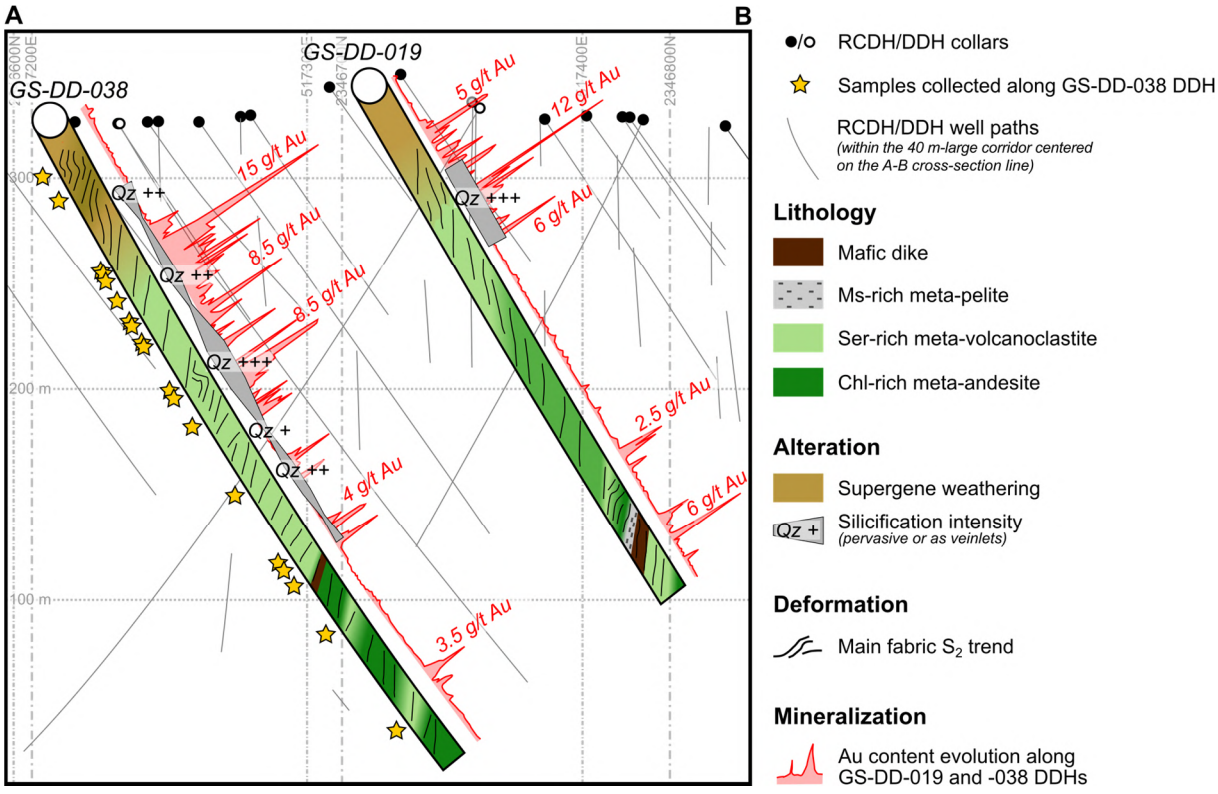


Figure 2-4: Example of the lithology, deformation, alteration and mineralization changes at the GSS gold deposit. The cross-section has been drawn considering a 40 m-large corridor centered on the A-B section line (Fig. 2-2b). Both reverse circulation (RCDH) and diamond (DDH) drill hole collars and well paths are drawn. Lithology, alteration and deformation features drawn along GS-DD-019 and -038 DDHs rely on logging carried out on site. The Au content evolution along these two DDHs refers to Au fire assay analyses from Orca Gold Inc. database. Macro and micro-scale samples collected along the GS-DD-038 DDH are indicated by yellow stars. Geographic coordinates are reported as WGS 84 / UTM zone 36N.

The main penetrative fabric affects every lithology at every scale, although its orientation is variable down to the m-scale. When possible, its orientation has been systematically measured along the studied drillcores using a core reorientation device or

"rocket launcher" and the downhole survey data from Orca Gold Inc. The stretching lineation orientation lying in the main penetrative fabric plane has been measured. Similar feature orientations have also been measured on outcrop to complete the drillcore dataset.

3.2. Definition of ductile and brittle deformation and scale-sensitivity

The deciphering of deformation stages at the GSS gold deposit and their characterization mostly relies on their *brittle vs ductile* nature. This distinction often helps to separate the upper *brittle* crust from the lower *ductile* crust when dealing with gold-bearing vein type deposits (*e.g.,* Groves et al., 1998, 2003, 2018). Such classification relies on a rheological approach, but the meaning of these terms can be ambiguous as they can be used in several different ways as detailed by Tikoff et al. (2013). For instance, the limit criteria considered to shift from one domain to another can be either quantitative (*e.g.,* experimentally, a material is said to be *ductile* when it is able to withstand more than 5% permanent strain before failure; Heard, 1960) or geometric (*e.g., brittle* deformation is characterized by discontinuities in the displacement field; Twiss and Moores, 2007). It is therefore critical to clearly state what is meant by the *brittle vs ductile* distinction in the present study.

As this study results rely on field investigation at the first order, the followed nomenclature helps "to distinguish the manner by which deformation occurs" (Tikoff et al., 2013): *brittle deformation* corresponds to faulting and fracturing, local spatial discontinuity formation in a word, while *ductile deformation* refers to "smoothly varying displacements" expressed by folding and penetrative fabrics as defined by Twiss and Moores (2007). However, these descriptors are scale-sensitive (Rutter, 1986; Snoke et al., 1998). To simplify matters, the distinct deformation stages that are presented below are qualified according to their expression at the macro-scale as they have been firstly unraveled at this scale.

4. Macro- to micro-scale deformation history and related alteration/mineralization events

The macro- to micro-structures, lithology/alteration and ore features observed at the GSS gold deposit are illustrated in Figs. 2-5 to 2-8, 2-9 and 2-10, respectively. The deformation stages deciphered at the deposit scale are described from D_{1GSS}, D_{2GSS} (ductile deformation stages), D_{3GSS} (ductile/brittle transition) to D_{4GSS} (late veining). This is done considering that D_{2GSS} is the main deformation stage, related to the S_2 penetrative foliation, controlling the GSS gold deposit structural framework as described in section 2.2. Most of the deformation and alteration features occurring prior to the D_{2GSS} main deformation stage are weakly preserved and some may have been completely overprinted. The correlation between deformation recorded at the GSS deposit and those documented regionally is discussed in section 6. Mineralogical changes due to the supergene weathering, visible up to 70 m along the studied DDHs (Fig. 2-4), are not detailed here although "sup" index refers to mineral phases formed during this alteration event.

The primary mineral assemblage of the ore-bearing meta-volcanosedimentary horizon is weakly preserved due to intense and multiple subsequent alteration events. However, the less altered meta-volcanoclastic samples display a more or less preserved lapilli tuff texture highlighted by quartz-dominated, rounded clasts stretched along the S_2 penetrative fabric (Fig. 2-9a). Besides, the presence of euhedral hornblende and magnetite phenocrysts (Fig. 2-9b and c) supports the volcanic affinity of this meta-volcanosedimentary horizon enclosed within an andesitic meta-volcanic pile (Fig. 2-2b). Muscovite-rich meta-sediments are interlayered with this horizon (Fig. 2-4).

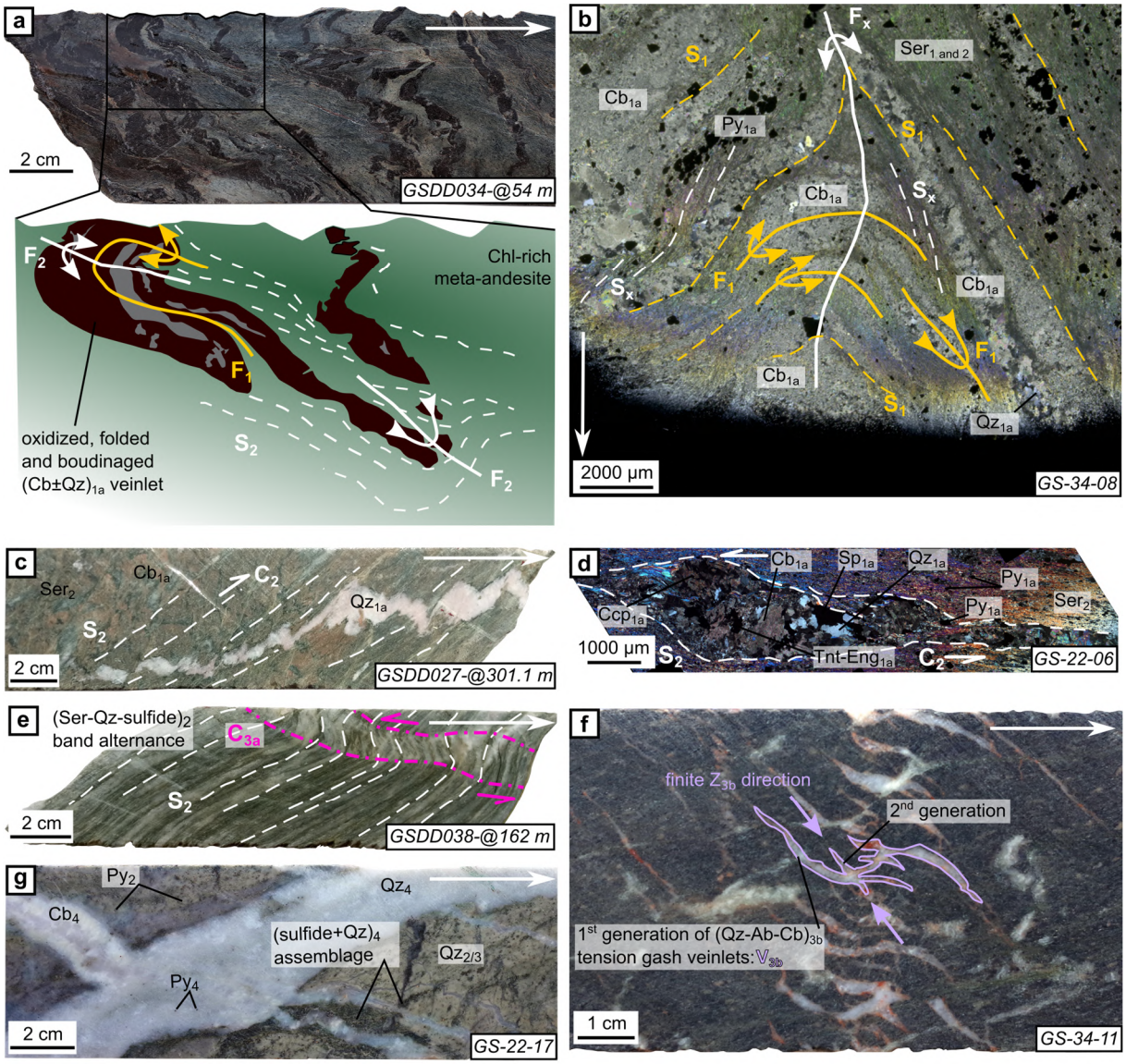


Figure 2-5: Main deformation features of the studied samples at the sample and microscopic scales. White arrows indicate the roughly 60°-plunging bottom-to-core line for oriented samples. For Figs. 2-5 to 2-10, 2-12 and 2-13 and Table 2-2, mineral abbreviations are Qz = quartz; Cb = carbonate; Ser = sericite; Ms = muscovite; Chl = chlorite; Ab = albite; Hbl = hornblende; Fe-Ti ox. = Fe-Ti oxides; Py = pyrite; Sp = sphalerite; Ccp = chalcopyrite; Gn = galena; Tnt-Eng = sulfosalt; Apy = arsenopyrite; Gers = gersdorfitte; Mag = magnetite; Hem = hematite; Cv-Dg = covellite-digenite; Bn = bornite; Sid = siderite; Brt = barite. Index refers to the mineral generation from the primary formation of the meta-volcanosedimentary horizon (index "0") to subsequent D_{1GSS} to D_{4GSS} deformation events (index "1" to "4") while "sup" refers to the late supergene weathering. **a** At the macro-scale, early D_{1GSS}-related F_1 folds affect D_{1aGSS} carbonate-(quartz) veinlets that are transposed into the S_2 penetrative fabric and refolded by the F_2 fold system (view from NNW). **b** At the micro-scale, dismembered D_{1aGSS}-related carbonate-(quartz) veinlet hinges are refolded by the F_2 fold system. S_2 is a F_2 axial plane cleavage (cross-polarized, transmitted light). **c** At the macro-scale, the S_2 penetrative fabric, highlighted by the Ser_2-rich gangue, is associated with C_2 shearing affecting a D_{1aGSS}-related Qz veinlet that is partially transposed into S_2 (view from NNW). **d** The D_{2GSS}-related C_2 shearing and S_2 shear band cleavage development is responsible for D_{1aGSS}-related carbonate-(quartz-polymetallic sulfide) veinlet boudinage and asymmetrical dismembering into S_2 (cross-polarized, transmitted light). **e** At the macro-scale, rare D_{3GSS}-related, NW-gently dipping (apparent dip), top-to-the NW C_{3a} shear bands affect the S_2-dominated gangue (view from NNW). **f** At the macro-scale, multiple generations of quartz-albite-carbonate V_{3b} *en échelon* tension gashes highlight the apparent, finite Z_{3b} orientation (view from ENE). **g** At the macro-scale, the D_{4GSS} stage occurs as quartz-carbonate hydraulic veins mostly affecting silicified intervals and containing a variable pyrite-sphalerite-chalcopyrite-galena-sulfosalt amount (view from NNW).

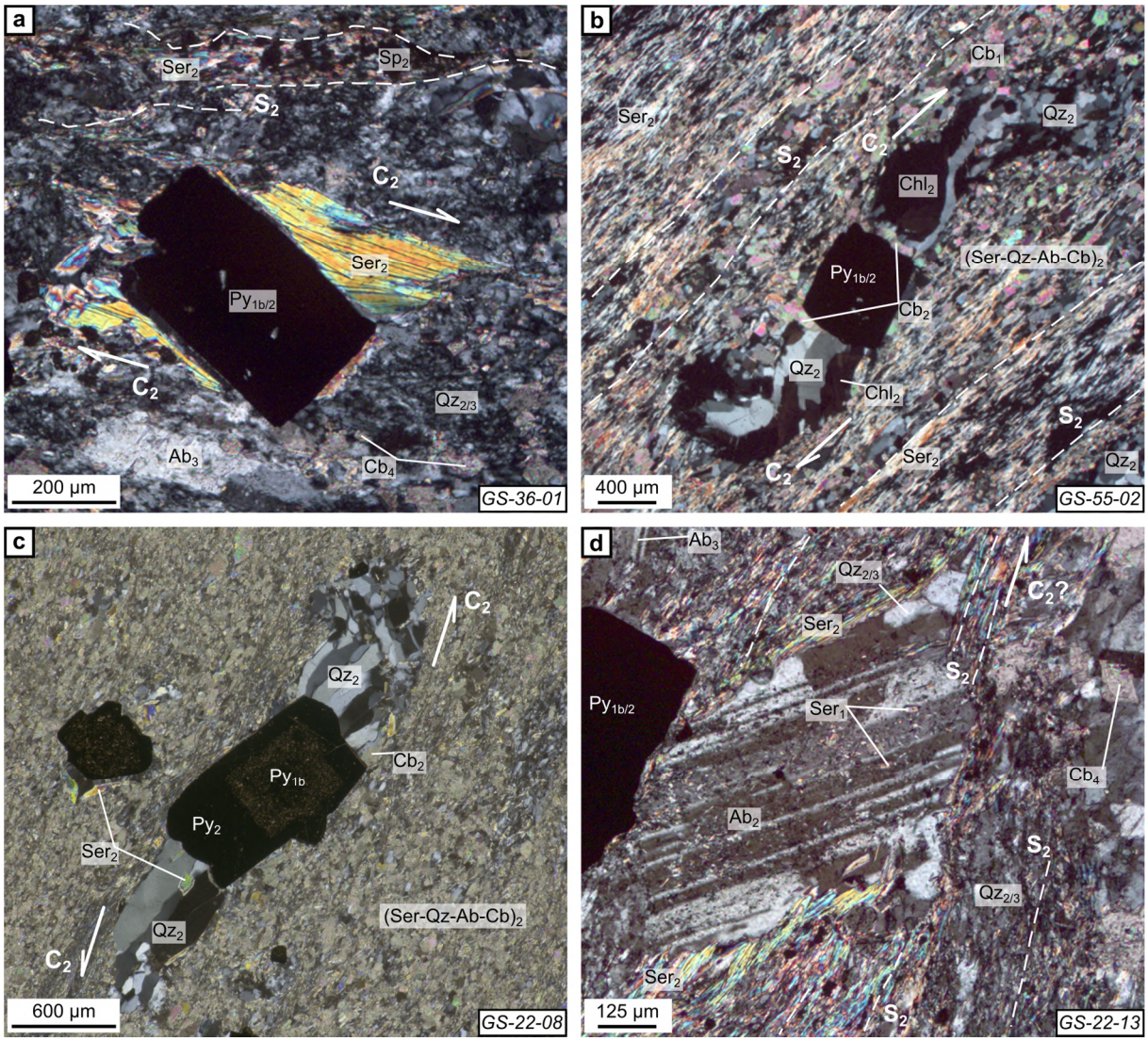


Figure 2-6: Asymmetrical strain fringe evidence for micro-scale C_2 shearing. Mineral abbreviations as in Figure 2-5. **a** Sericite-rich, asymmetrical strain fringes are developed around disseminated pyrite grains displaying the non-coaxial D_2 shearing stage kinematics (cross-polarized, transmitted light). **b** A coarse, euhedral, disseminated pyrite grain is enclosed within a sericite-quartz-carbonate-rich gangue displaying the S_2 penetrative fabric. Asymmetrical quartz-chlorite-carbonate strain fringes expressing the C_2 shearing orientation are developed around this grain (cross-polarized, transmitted light). **c** An asymmetric quartz-dominated strain fringe with minor sericite and carbonate is developed around a coarse, euhedral, zoned pyrite grain (cross-polarized, transmitted light; see pyrite description and BSE-SEM photograph in Figure 2-10b). **d** The sericite-dominated gangue is locally overprinted by a massive, pervasive, very fine-grained silicification with rare sericite and S_2 remnants. This assemblage is moderately overprinted by coarse, euhedral D_{2GSS}- to D_{3GSS}-related albite porphyroblasts. Rare D_{2GSS}-related albite porphyroblasts grains are associated with sericite-quartz asymmetrical strain fringes expressing the late D_{2GSS}-related shearing while D_{3GSS}-related albite porphyroblasts are statically grown on the silicified host rock. The overall assemblage is weakly overprinted by disseminated, fine- to medium-grained, euhedral carbonate grains (cross-polarized, transmitted light).

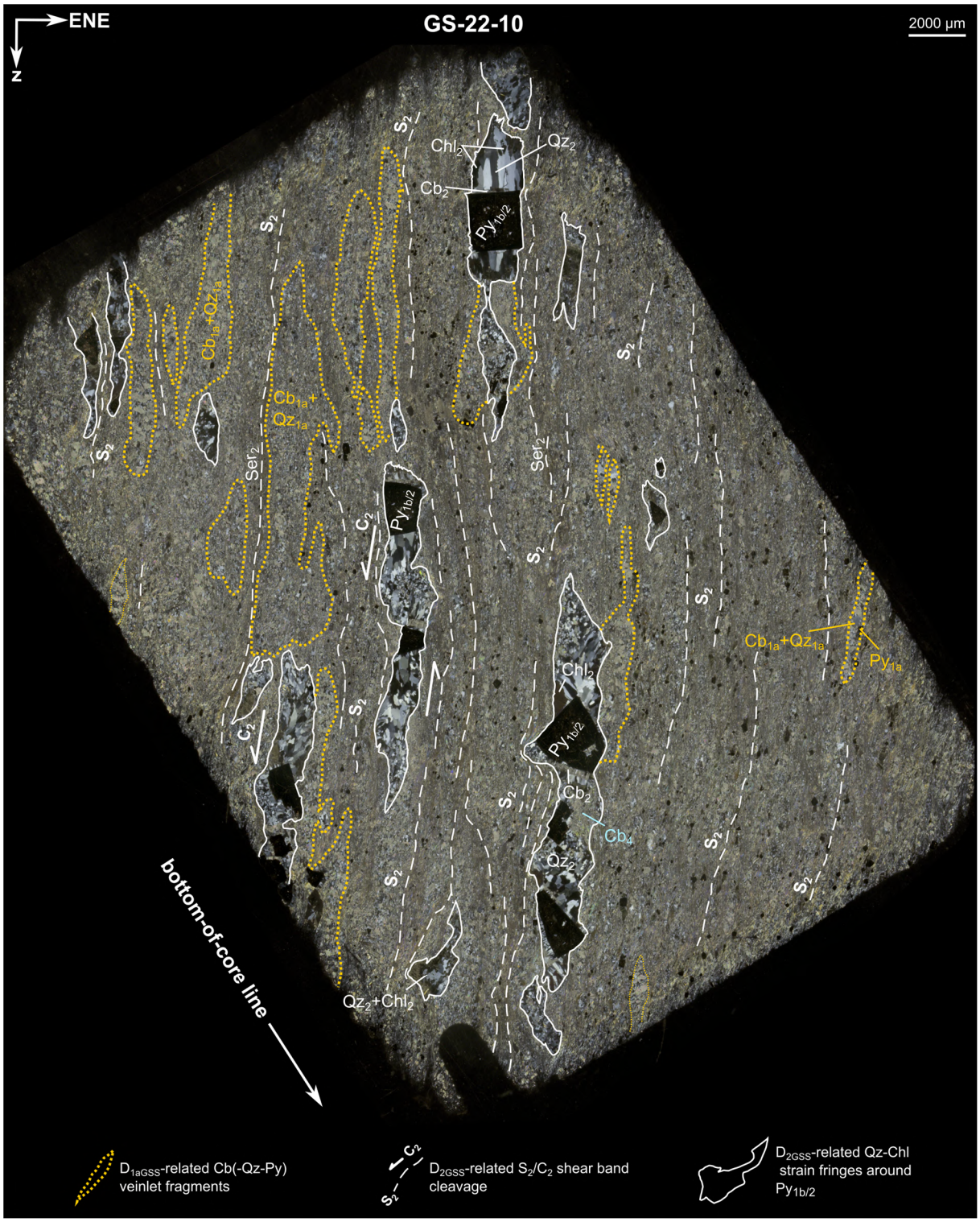


Figure 2-7: Oriented microphotograph of sample GS-22-10 under cross-polarized, transmitted light interpreted by adding the successive deformation microstructures and their kinematic sense (view from SSE). Mineral abbreviations as in Figure 2-5.

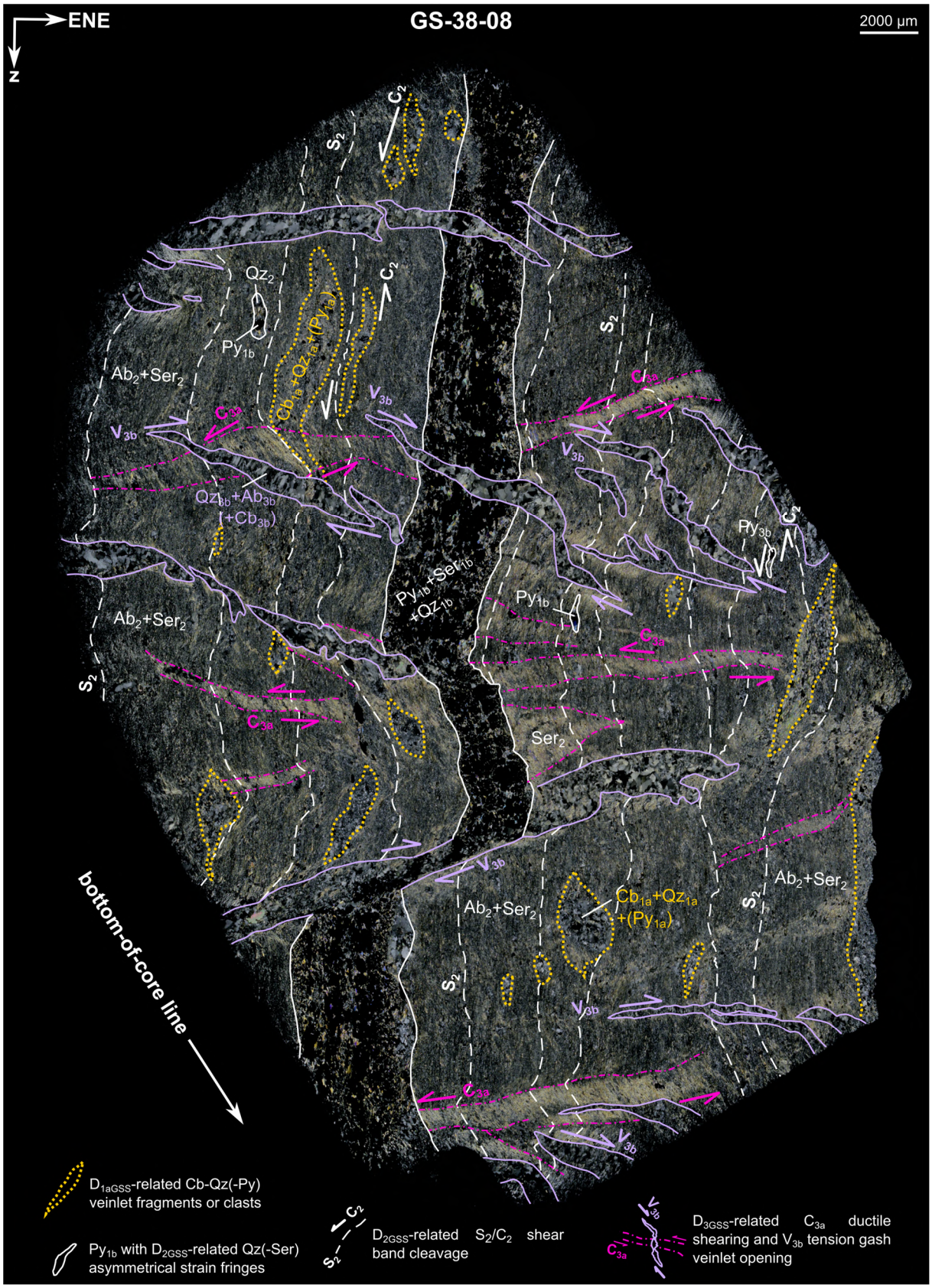


Figure 2-8: Oriented microphotograph of sample GS-38-08 under cross-polarized, transmitted light interpreted by adding the successive deformation microstructures and their kinematic sense (view from SSE). Mineral abbreviations as in Figure 2-5.

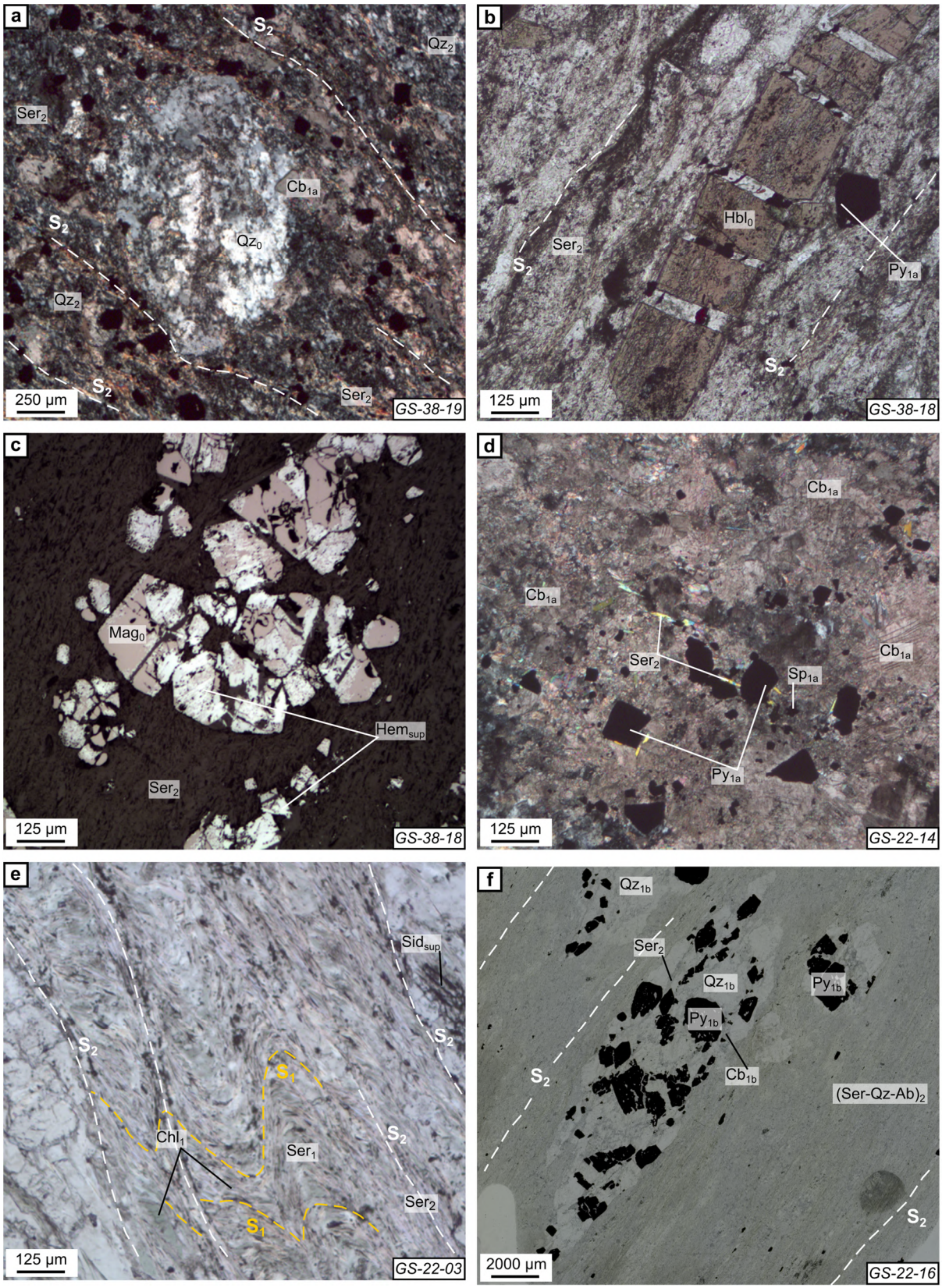


Figure 2-9: Main lithology and alteration features of the studied samples. See caption on next page.

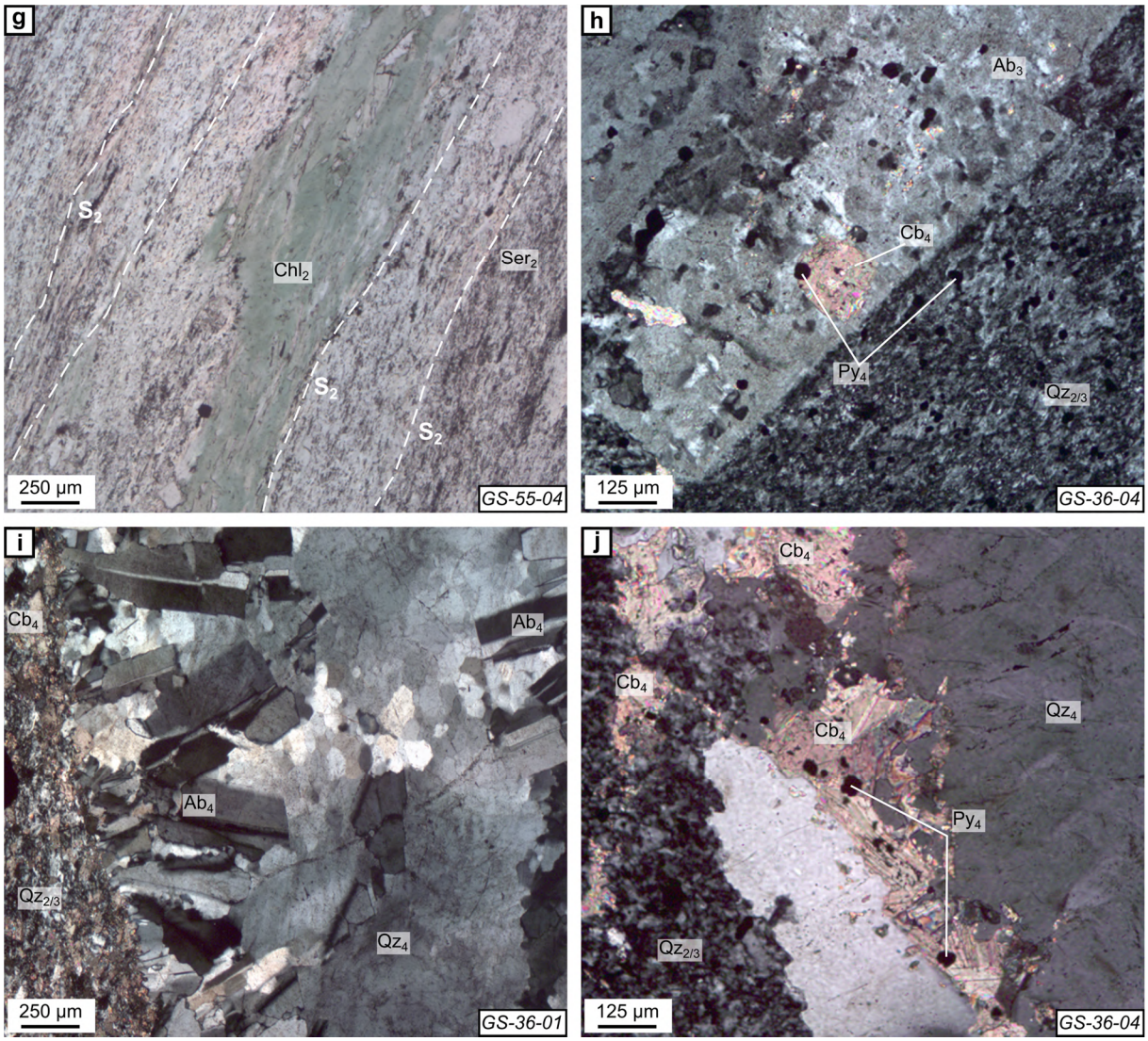


Figure 2-9 (continued): Main lithology and alteration features of the studied samples. Mineral abbreviations as in Figure 2-5. **a** mm- to pluri-millimetric-large quartz-dominated clasts are enclosed within a sericite-rich gangue and wrapped by the S_2 penetrative fabric. They display a locally well preserved lapilli tuff texture for the meta-volcanoclastic part of the meta-volcanosedimentary horizon (cross-polarized, transmitted light). **b** Up to mm-large, longitudinal sections of coarse, syn-volcanic hornblende crystals are transposed and dismembered into the S_2 penetrative fabric (plane-polarized, transmitted light). **c** Up to 200 µm-large, coarse, euhedral primary magnetite grains forming aggregates are stretched along the penetrative fabric and more or less oxidized into hematite (reflected light). **d** A massive Cb_{1a} band encloses rare D_{1aGSS}-related pyrite and sphalerite grains with evidence for rare S_2-oriented sericite grains penetrating through the band (cross-polarized, transmitted light). **e** At the micro-scale, the S_2 penetrative fabric is a crenulation cleavage expressed by sericite and affecting the previous S_1 fabric expressed by D_{1GSS}-related sericite-(chlorite) generation (plane-polarized, transmitted light). **f** A D_{1bGSS}-related pyrite-quartz-(sericite-carbonate) veinlet is dismembered into the S_2 penetrative fabric and encloses coarse, euhedral, pyrite grains (plane-polarized, transmitted light). **g** The S_2 penetrative fabric is expressed by the alternance of D_{2GSS}-related sericite and chlorite bands within the meta-volcanosedimentary horizon. **h** D_{3GSS} albite porphyroblasts overprint the $Qz_{2/3}$ silicified host rock. Fine-grained, $D_{4\ GSS}$-related pyrite grains, similar to the facies described in photograph **j**, are disseminated and weakly overprint (1) the silicified host rock, (2) albite porphyroblasts and (3) late, disseminated, euhedral carbonate grains (cross-polarized, transmitted light). **i** The D_{4GSS} veining phase is expressed by quartz-albite veins and veinlets mostly crosscutting the quartz-rich, silicified intervals. Coarse, euhedral albite grains are crystallized perpendicularly to the vein margins resulting in a comb texture (cross-polarized, transmitted light). **j** Within some quartz-dominated veinlets, quartz crystallization is followed by a veinlet reopening event and anhedral carbonate crystallization at the core of the veinlet. This D_{4GSS}-related carbonate generation is associated with very fine-grained, anhedral pyrite (cross-polarized, transmitted light).

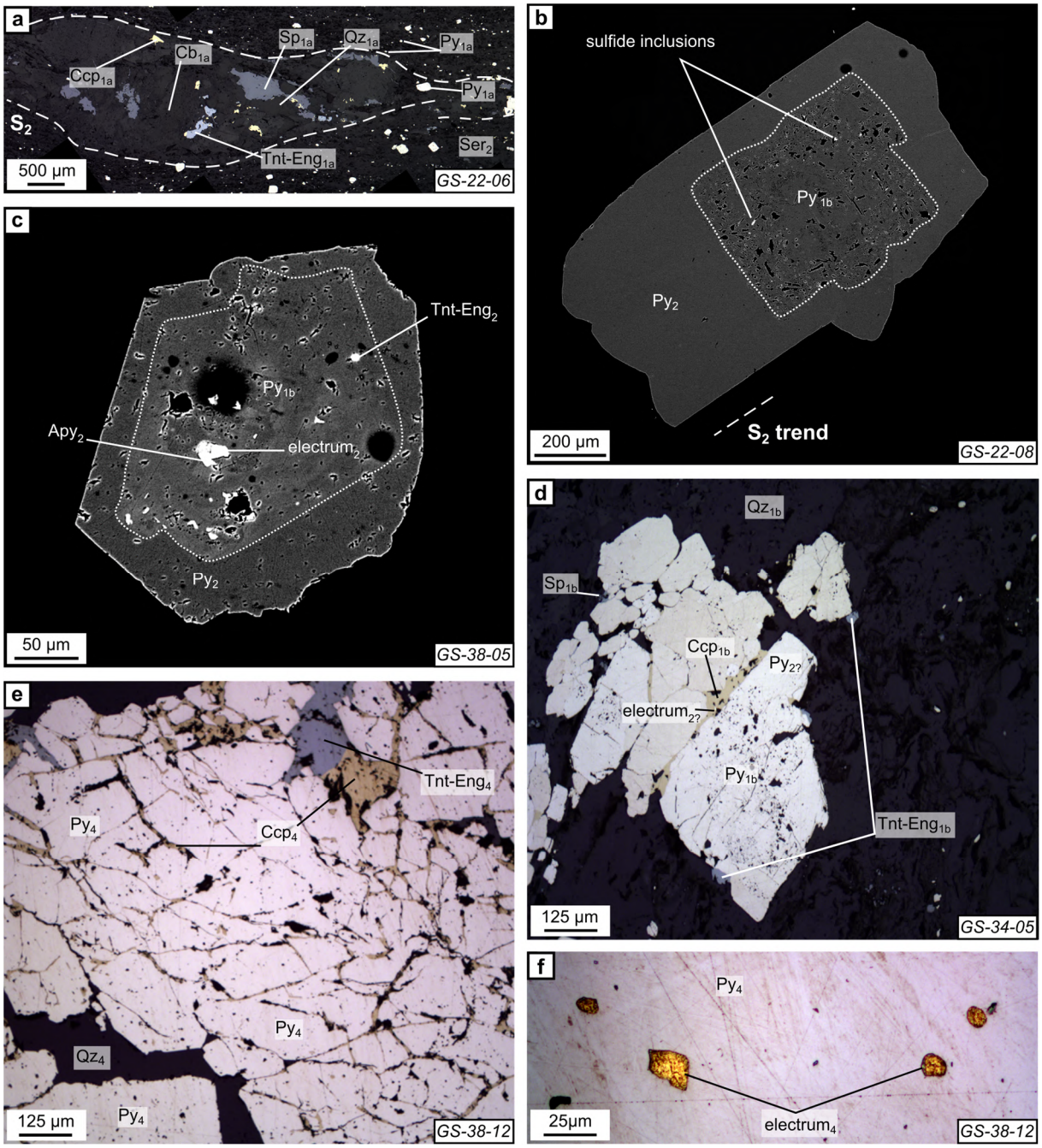


Figure 2-10: Main ore features of the studied samples. Mineral abbreviations as in Figure 2-5. **a** An early, boudinaged, D_{1aGSS}-related carbonate-(quartz) veinlet (see Figure 2-5d for cross-polarized, transmitted light photograph and description) contains minor sulfide content composed of anhedral, more or less coarse chalcopyrite, sphalerite and sulfosalt patches and rare, anhedral, coarse pyrite grains. Fine-grained, anhedral pyrite is disseminated in the sericite-rich host rock and stretched along the S_2 penetrative fabric (reflected light). **b** A coarse, subhedral, D_{1bGSS}-related pyrite disseminated in the host rock encloses numerous gangue and sulfide mineral inclusions and shows a corroded aspect. It is rimmed by an euhedral, mineral inclusion-free D_{2GSS}-related pyrite overgrowth that is preferentially developed along the S_2 penetrative fabric. No chemical zonation between the pyrite core (Py_{1b}) and the overgrowth (Py_2) is visible (back-scattered electron mode, scanning electron microscopy, BSE-SEM; see Figure 2-6c for cross-polarized, transmitted light photograph and description). **c** D_{1bGSS}-related veinlet-hosted pyrite shows internal chemical zonation and is wrapped by a subhedral, mineral inclusion-free, D_2-related pyrite overgrowth with no chemical zonation. Similarly to what is observed for disseminated pyrite in photograph **b**, the quartz veinlet-hosted pyrite core

looks corroded and hosts gangue and sulfide (arsenopyrite and sulfosalt) mineral inclusions as well as an electrum inclusion (BSE-SEM). **d** Medium-grained subhedral pyrite mass with interstitial chalcopyrite and intergrown sphalerite and sulfosalt is displayed in a D_{1bGSS}-related quartz-dominated veinlet. Pyrite grains and subgrains show a corroded aspect and Py_2 overgrowth may be present. An electrum grain is visible at the contact between the interstitial chalcopyrite and the corroded pyrite grain (reflected light). **e** Pyrite aggregates locally form a massive pyrite assemblage within D_{4GSS}-related veins. The pyrite assemblage is fractured whith interstitial chalcopyrite and sulfosalt infilling (reflected light). **f** Late veining-related pyrite grains locally enclose up to 20 µm-large electrum grains (reflected light).

4.1. Cryptic, ductile-dominated D_{1GSS} deformation stage

The D_{1GSS} deformation stage is expressed by the progressive change from D_{1aGSS} carbonate-dominated to D_{1bGSS} quartz-dominated veinlet formation. Petrographic and structural evidence to distinguish these two veinlet families are detailed below.

4.1.1. D_{1aGSS} carbonate-(quartz-pyrite) veinlets

Evidence of the D_{1GSS} deformation event is weakly preserved at the GSS gold deposit due to strong overprinting by the D_{2GSS} stage. Nevertheless, evidence for this ductile deformation prior to D_{2GSS} is given by the presence of D_{1aGSS}-related, twice folded carbonate-(quartz-pyrite) veinlets that locally highlight the S_1 fabric without evidence for subsequent deformation by this cleavage development (Fig. 2-5a and b). These veinlets are however commonly boudinaged to dismembered, transposed into and sheared by the C_2/S_2 shear band cleavage (simplified into S_2 fabric thereafter; Figs. 2-5c and d, 2-7). This deformation stage is coeval with a moderate to locally strong pervasive carbonation (Fig. 2-9d). The S_1 fabric is mostly expressed by the early Ser_1 generation which is strongly crenulated and recrystallized along the S_2 penetrative fabric (Fig. 2-9e). The sulfide income related to this deformation stage is limited with rare, fine-grained, disseminated pyrite grains and minor pyrite-sphalerite-(chalcopyrite-sulfosalt) associated within veinlets (Fig. 2-10a).

4.1.2. D_{1bGSS} quartz-pyrite-(carbonate) veinlets

Similarly to D_{1aGSS}-related veinlets, D_{1bGSS}-related quartz-pyrite-(carbonate) veinlets are more or less boudinaged to dismembered and also transposed into the S_2 penetrative

fabric (Figs. 2-7, 2-9f). Some of them are even folded by the F_2 fold system. However, they are not folded twice like D_{1aGSS}-related carbonate-quartz-(pyrite) veinlets may be. Their formation occurs therefore late during D_{1GSS} and precedes the D_{2GSS} stage.

The two veining events described are not separated from the overall ductile D_{1GSS} stage as suggested by the progressive change in vein composition, their intimate relationships to the ductile S_1 penetrative fabric development (D_{1aGSS}-related veining and ductile S_1 penetrative fabric look quite coeval) and their strong overprinting by the S_2 penetrative fabric. Veining looks to occur episodically, most probably when supra-lithostatic conditions are reached due to fluid pressure increase during deformation. Such changes in deformation expression are compatible with pressure variations that can occur in a single deformation phase. The progressive change from D_{1aGSS}-related, sometimes F_1 and F_2-folded, carbonate-dominated veinlets to D_{1bGSS}-related, sometimes F_2-folded, quartz-pyrite-dominated veinlets therefore suggests a ductile-dominated deformation continuum with episodic veining during D_{1GSS} stage.

The D_{1GSS}-related sulfide stock income increases from D_{1aGSS} to D_{1bGSS} stages. It is illustrated by (1) the presence of coarse, euhedral, Py_{1b} or zoned $Py_{1b/2}$ grains disseminated in the sericite-rich gangue, preferentially oriented along the S_2 penetrative fabric and displaying quartz-(sericite-chlorite-carbonate) asymmetrical strain fringes (Figs. 2-6a, b and c, 2-10b) and (2) moderate to major Py_{1b} presence within quartz-pyrite-(carbonate) veinlets (Figs. 2-7, 2-9f, 2-10c). The Py_{1b} pyrite generation is associated with a minor sulfide association similar to the one described for the Py_{1a} pyrite generation.

4.2. Main ductile D_{2GSS} deformation stage

A very intense alteration of the ore-bearing, meta-volcanosedimentary horizon occurred during the D_{2GSS} stage at the GSS gold deposit. Intense sericitization, together

with a strong albitization and a weak to moderate chloritization occurred, resulting in a sericite-dominated gangue expressing the S_2 penetrative fabric (Figs. 2-7, 2-8, 2-9a, b, e, f and g) alternating with chlorite-rich bands (Fig. 2-9g). F_2 folds are visible at the macro- and micro-scales and affect D_{1GSS}-related microstructures (Fig. 2-5a and b). Ser_2 flakes look to result from Ser_1 recrystallization along S_2 crenulation cleavage expressed along F_2 axial plane (Fig. 2-9e). Moreover, shearing is associated with the D_{2GSS} stage as illustrated by steep S_2 shear band cleavage (Fig. 2-5c). The non-coaxial progressive D_{2GSS} deformation is also displayed by the formation of asymmetrical, displacement-controlled quartz-(sericite-chlorite-carbonate) strain fringes around coarse pyrite grains disseminated in the gangue (Fig. 2-6a, b and c; Passchier and Trouw, 2005). The D_{2GSS} stage is associated with a moderate albitization of the host unit, as confirmed by the presence of fine-grained albite in the sericite-rich gangue (Figs. 2-6b, 2-8, 2-9f). It is also expressed by rare coarse euhedral albite porphyroblasts enclosing Ser_1 remnants and displaying sericite-quartz strain fringes with the same kinematic sense as quartz-(sericite-chlorite-carbonate) asymmetrical strain fringes around pyrite grains (Fig. 2-6d). The strain fringe geometry suggests that its late quartz infilling could be coeval with the pervasive, very fine-grained $Qz_{2/3}$ gangue that strongly overprints the S_2 penetrative fabric (Figs. 2-6d, 2-9h, i and j). This leads to the inference that a local, weak albitization and strong silicification event occurred at the very end of the D_{2GSS} shearing stage, in continuity with the increasing silicification described from D_{1aGSS}-related carbonate-(quartz-pyrite) to D_{1bGSS}-related quartz-pyrite-(carbonate) veinlets. This suggests that the transition from D_{1GSS} to D_{2GSS} episodes can be considered as a deformation continuum. This assumption is also supported by the formation of chlorite during both of these deformation stages, as Chl_1 (resp. Chl_2) is intergrown with Ser_1 (resp. Ser_2) along S_1 (resp. S_2) fabric (Fig. 2-9e and g, respectively) and Chl_2 and Ser_2 are present in D_{2GSS}-related strain fringes (Fig. 2-6a, b and c).

The D_{2GSS}-related sulfide stock income is illustrated by Py_2 overgrowth around disseminated and quartz-pyrite-(carbonate) veinlet-hosted Py_{1b} grains (Fig. 2-10b and c, respectively). These overgrowths are euhedral, oriented along the S_2 penetrative fabric and coeval with quartz-(sericite-chlorite-carbonate) strain fringe development (Figs. 2-6a, b and c, 2-10b). Py_2 overgrowths are mineral inclusion-free and chemically homogenous, relying on BSE-SEM imagery (Fig. 2-10b and c). They are systematically associated with Py_{1b} cores displaying a corroded aspect and abundant silicate and sulfide mineral inclusions (Fig. 2-10b and c). Some electrum (Au-Ag) inclusions have been observed within Py_{1b} cores when Py_2 overgrowth is present (Fig. 2-10c). Electrum grains are also visible at the contact between Py_{1b} grains and interstitial Ccp_{1b} within quartz-pyrite-(carbonate) boudinaged veinlets where Py_2 overgrowth presence is suspected (Fig. 2-10d).

4.3. Weak ductile/brittle D_{3GSS} deformation stage

The D_{3GSS} stage records the ductile/brittle transition at the GSS gold deposit. The last ductile deformation markers are conjugate C_{3a} kink to shear bands affecting the sericite-rich gangue. The first family is ENE-gently dipping with top-to-the-ENE kinematics (Fig. 2-5e) and the second one is subhorizontal with top-to-the-WSW kinematics (Fig. 2-8). The latter are crosscut by quartz-albite-carbonate veinlets with a curved geometry interpreted as V_{3b} *en échelon* tension gashes (Figs. 2-5f, 2-8). This stage is associated with a weak albitization of the host unit, as confirmed by the presence of coarse, euhedral albite porphyroblasts statically crystallized upon the $Qz_{2/3}$ silicified host rock (Figs. 2-6d, 2-9h). This alteration stage is in continuity with the D_{2GSS}-related albitization described in the previous subsection, suggesting that the D_{3GSS} stage immediately follows D_{2GSS}. Also, V_{3b} veinlets either completely crosscut D_2-related pyrite-(sericite-quartz) veinlets, or slightly deform and penetrate them (Fig. 2-8). Such transitional to sharp crosscutting relationship tends to confirm the latter hypothesis. V_{3b}

en échelon tension gashes result from brittle deformation. They are subhorizontal and well developed on both NNE- and ENE-trending core sections (Figs. 2-5f and 2-8, respectively), suggesting that they result from subhorizontal, SW-dipping, top-to-the-NE reverse faulting or subhorizontal, NE vergent shortening. Figure 2-11 schematically illustrates the change in the strain ellipsoid orientation from a ductile, subvertical shortening (Z direction) to a brittle, subhorizontal, NE-trending shortening at the GSS gold deposit during the D_{3GSS} stage. The proposed change in shortening orientation is apparent, because it may not exactly lie in the studied thin section planes, but it is likely to be close to the true shortening orientation as suggested by the very good development of V_{3b} en échelon tension gashes. The orthogonal shortening direction accounting for D_{3aGSS} regarding the previous and following deformation stages remains however unclear.

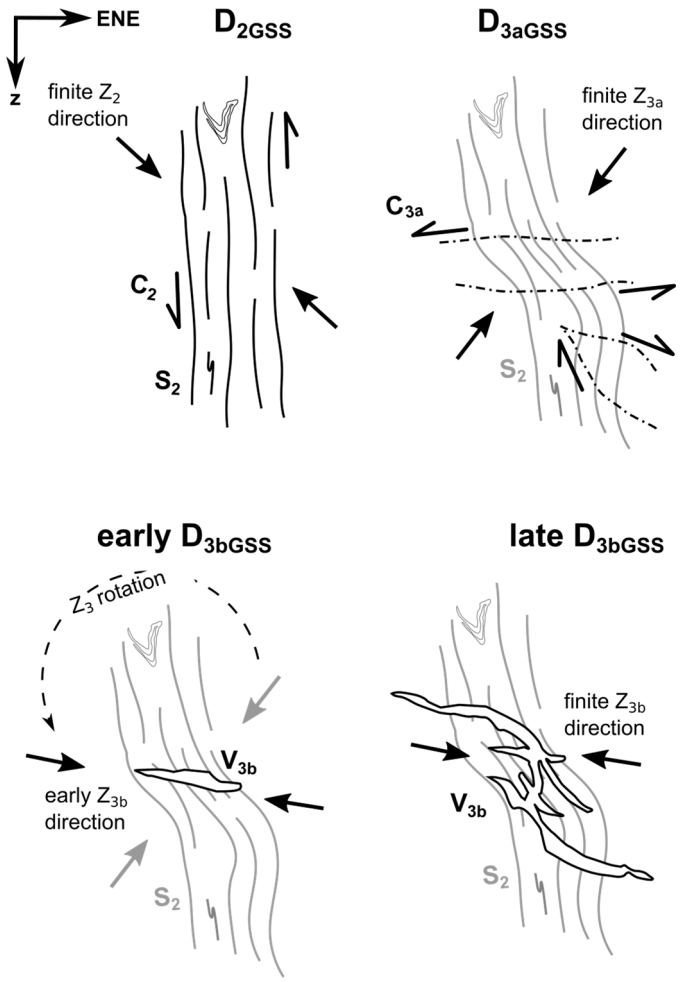


Figure 2-11: Schematic evolution of the Z shortening direction from D_{2GSS} to D_{3GSS} (view from SSE). The structure orientation and the apparent Z direction are approximately deduced from macro- to micro-scale observations (Figs. 3-5 to 3-8).

4.4. Late brittle D_{4GSS} deformation stage

Finally, a late, brittle D_{4GSS} veining stage occurred at the GSS gold deposit. The related veins only occur within the silicified meta-volcanosedimentary intervals (Figs. 2-5g, 2-9h and i). No particular vein orientation has been noticed.

The D_{4GSS} veins show a complete compositional spectrum from sulfide-free quartz-carbonate-albite (Fig. 2-9i and j; Table 2-1) to polymetallic sulfide-dominated assemblage (Fig. 2-10e; Table 2-1). This sulfide assemblage is composed of variable amount of pyrite, chalcopyrite, sulfosalt (Fig. 2-10d), sphalerite and galena. Py_4 generation shows a fractured aspect while the other sulfide minerals are interstitial to pyrite grains or infill fractures (Fig. 2-10e). Py_4 grains locally enclose electrum inclusions (Fig. 2-10f).

A carbonate infilling at the late veinlet core is due to a late reopening episode of the veinlet (Fig. 2-9j) and is associated with a weak, pervasive carbonation expressed by fine-grained, euhedral carbonate grains to anhedral patches overprinting the former alteration features (Fig. 2-9h and j). A late pyritization event, associated with the last veining stage, occurs as fine-grained Py_4 statically overgrowing on Cb_4 grains and the former mineral assemblage (Fig. 2-9h and j).

All macro- to micro-scale deformation, alteration and mineralization features described above are summarized in Table 2-2. Based on the previous observations, the relative chronology of both gangue and ore minerals within the ore-hosting meta-volcanosedimentary horizon at the GSS gold deposit is established with respect to the deformation stages deciphered at the deposit scale (Fig. 2-12). The overprinting and overlapping of alteration patterns, vein mineral assemblages (Fig. 2-12) and kinematic evidence (Fig. 2-11) described at the micro- to macro-scale from D_{1GSS} to D_{3GSS} deformation stages suggest that a single, ductile to ductile/brittle, progressive simple shear deformation stage should be considered at the GSS gold deposit. Veining during D_{1GSS} most probably resulted from episodic fluid supra-lithostatic pressure release

episodes but the vein geometry (complex folding patterns, parallel relationship with the shear band cleavage) suggests it should be considered as part of the overall, single progressive deformation stage itself. The change in deformation style from the mostly ductile D_{1GSS} stage to the ductile D_{2GSS} stage and the D_{3GSS} ductile/brittle transition should depend on several parameters such as the pore fluid pressure, the strain rate or the temperature. These factors can thus vary through time and lead to several transitions from ductile to brittle or brittle to ductile behavior in a single progressive deformation phase.

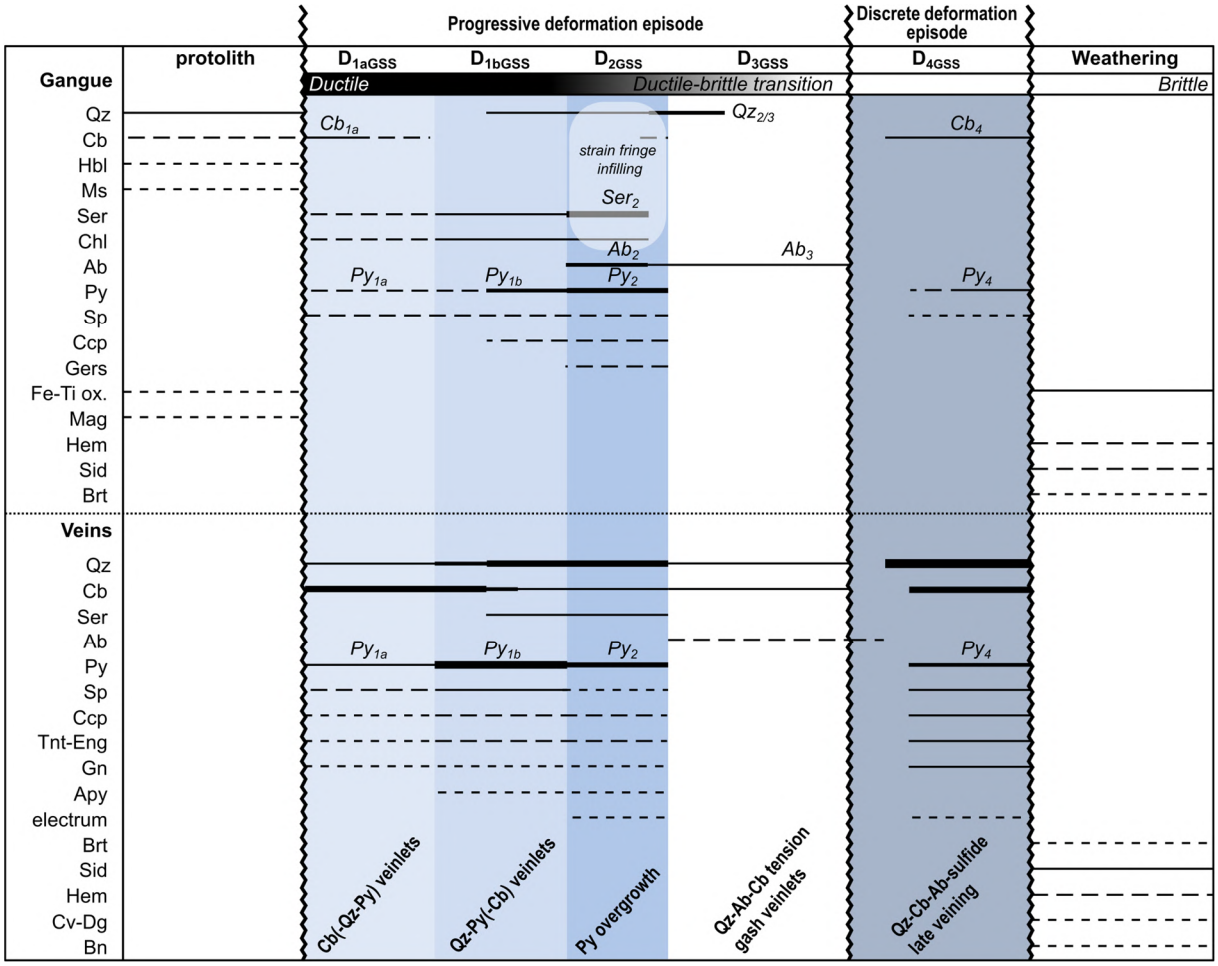


Figure 2-12: Paragenetic sequence displayed by the ore-bearing meta-volcanosedimentary horizon at the GSS gold deposit. Mineral abbreviations as in Figure 2-5. The D_{1GSS} to D_{3GSS} stages can be considered as a single, ductile to ductile/fragile deformation continuum while D_{4GSS} is likely chronologically disconnected from this phase. D_{1aGSS}-related carbonate-(quartz-pyrite) veinlets, D_{1bGSS}-related quartz-pyrite-(carbonate) veinlets, D_{2GSS}-related pyrite overgrowth and strain fringe formation, D_{3GSS}-related quartz-albite-carbonate *en échelon* tension gashes and D_{4GSS}-related quartz-carbonate-albite-polymetallic sulfide late veining episode are highlighted.

	Deformation	*Alteration*	*Mineralization*
D_{4GSS}	Brittle deformation, late veining. Limited to silicified intervals (rheological contrast). No preferential vein orientation deciphered.	Barren Qz-Cb-Ab late veining with comb texture. Weak pervasive carbonation.	Up to > 10 g/t Au along 1m but very localized high grades. Pyrite and polymetallic sulfide assemblage in ore-bearing late veinlets, presence of electrum inclusions in pyrite grains.
D_{3GSS}	Ductile/brittle transition expressed by shear kink bands crosscut by Qz-Ab-Cb *en échelon* tension gashes. Change in main strain orientation from subvertical to subhorizontal and NE-trending during the transition. Sharp to transitional crosscutting relationship with D_{1GSS}- and D_{2GSS}-related features.	Weak albitization.	None.
D_{2GSS}	Ductile deformation stage controlling the local structural framework from the micro- to deposit scales. S_2 main penetrative, subvertical shear band cleavage, subvertical, top-to-the-WSW, asymmetrical Qz-Chl-(Ser-Cb) strain fringe development around pyrite grains. Transposition, dismembering and folding of D_{1GSS}-related veinlets along the S_2 fabric. Progressive change in deformation style following D_{1GSS} stage.	Intense pervasive sericitization and chloritization expressing the S_2 fabric. Strong albitization followed by an intense, localized silicification at the very end of D_{2GSS} stage (Ab porphyroblasts with Qz-dominated asymmetrical strain fringes), in the continuity of the increasing Qz/Cb ratio during D_{1GSS} stage.	Pyrite overgrowth developed along the S_2 main fabric around corroded D_{1GSS}-related pyrite cores, coeval with sulfide and electrum inclusion formation. Correlation with the highest gold grades obtained (> 15 g/t Au) and overall > 1 g/t Au grades.
D_{1GSS}	Cryptic, ductile deformation stage strongly overprinted by the D_{2GSS} stage, separated in D_{1aGSS} and D_{1bGSS} substages. Development of a S_1 penetrative fabric weakly preserved. *D_{1aGSS}:* Cb-dominated veinlets, folded twice by the F_1 and F_2 fold systems. *D_{1bGSS}:* Qz-dominated veinlets, folded once by the F_2 fold system.	Progressive change from moderate to strong carbonation (D_{1aGSS}) to a weak carbonation and moderate to strong silicification (D_{1bGSS}). Weakly preserved pervasive sericitization and chloritization expressing the S_1 penetrative fabric.	Increase in the pyritization associated with D_{1aGSS}- to D_{1bGSS}-related veinlets. D_{1aGSS}-related veinlets correspond to very low grades (<0.1 g/t Au) while D_{1bGSS}-related veinlets are associated with higher grades (close to 1 g/t Au).

Table 2-2: Summary of the deformation, alteration and mineralization features observed at the macro- to micro-scale at the GSS gold deposit. Mineral abbreviations as in Figure 2-5.

The presence of albite and sulfide minerals in D_{2GSS}- to D_{4GSS}-related mineral assemblage (Fig. 2-12) could suggest an extended deformation continuum history up to its brittle-only expression. However, the D_{4GSS}-related veins do not display any preferential orientation or transitional crosscutting relationships with D_{1GSS}-related veinlets, contrary to what is observed with V_{3b} *en échelon* tension gashes (Fig. 2-8). The D_{4GSS} phase can therefore not be included in the progressive strain rotation history proposed in Figure 2-11. Such lack of evidence for deformation continuity with respect to the D_{1GSS} to D_{3GSS} deformation continuum leads to consider D_{4GSS} as an independent, disconnected deformation episode (Fig. 2-12). The deformation history recorded by the GSS gold deposit is therefore multiphase, although it is dominated by a first progressive deformation event.

5. Controls on deformation and progressive *vs* multiphase nature

Relying on these considerations, a schematic petro-structural model for the gold mineralization at the GSS gold deposit is provided in Figure 2-13 and highlights controls on deformation and related ore setup.

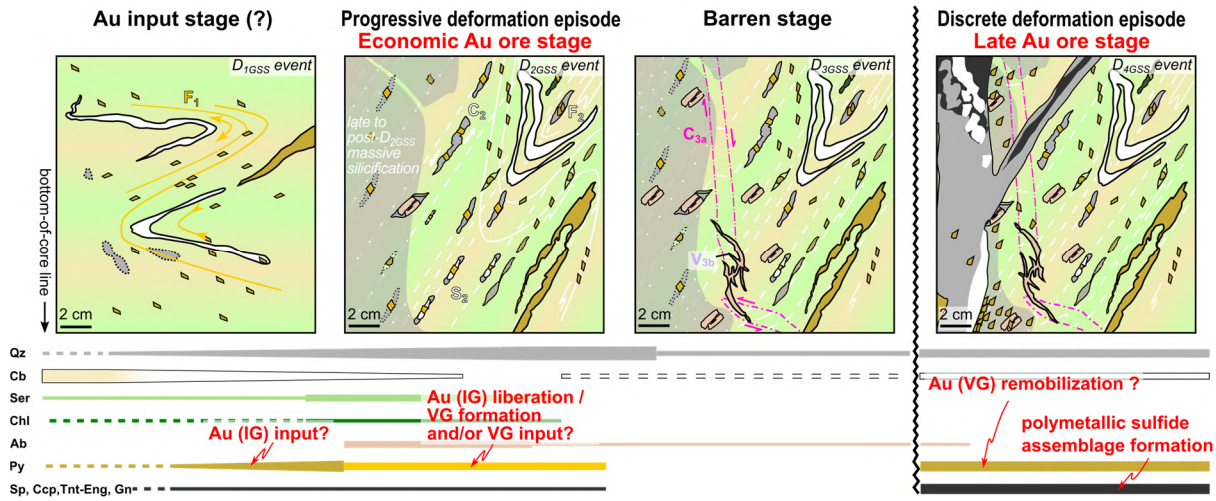


Figure 2-13: Schematic petro-structural model for the gold mineralization at the GSS gold deposit (view from SSE). Mineral abbreviations as in Figure 2-5. Supplementary abbreviations are IG = invisible gold and VG = visible gold. All the deformation features, alteration variation in nature and intensity and mineralization expressions illustrated by Figs. 2-5 to 2-10 are summarized here. In red, the supposed influence of every deformation stage on the gold endowment at the GSS gold deposit is specified.

5.1. Controls on deformation and impact on mineralization

D_{1bGSS}-related quartz-pyrite-(carbonate) veinlets and disseminated pyrite are widespread along the studied drill cores and associated with relatively low to intermediate gold grades (from 0.20 to 1 g/t Au roughly; Table 2-1). When Py_2 overgrowth is present, the highest gold grade is reached (15.2 g/t Au top grade for sample GS-38-05; Table 2-1) and the mineralization occurs mostly as electrum inclusions (visible gold or VG, Fig. 2-13) in pyrite core (Fig. 2-10c). The crystallization of Py_2 overgrowth is also associated with the corrosion of Py_{1b} core and infilling of voids by sulfide and silicate mineral inclusions (Fig. 2-10b and c). Therefore, the D_{2GSS} stage is thought to be responsible for destabilization of gold (invisible gold or IG, Fig. 2-13)-bearing Py_{1b} pyrite, liberation and recrystallization of free gold and/or new gold input accounting for the economic gold stock at the GSS gold deposit. This interpretation however relies on purely textural evidence and remains to be clearly established through an *in situ* geochemical study on pyrite.

The ore-bearing unit shows an enhanced permeability regarding the surrounding andesitic volcanics which are less altered and barren (Figs. 2-2b, 2-4, 2-12, 2-13): it preferentially drives ore- and alteration-related fluid flows. Within this unit, the deformation style is thus likely to change together with fluid pressure. High-pressure pore fluids are well documented to influence the rheology and deformation mechanisms that may affect rocks (*e.g.,* Etheridge et al., 1984) and fluid pressure may vary suddenly in such systems (*e.g.,* Cox, 1999, 2016; Cox et al., 2001). Core/rim relationships in pyrite, similar to the ones described above but with a rhythmic aspect, are notably observed at the El Callao gold district, Guiana shield, Venezuela (Velásquez et al., 2018) and at the Porgera gold deposit, Papua New Guinea (Peterson and Mavrogenes, 2014). In both case studies, the authors attribute this textural zoning to lithostatic to near-hydrostatic fluid pressure loops occurring during the deposit-hosting shear zone development according to the fault-valve model (*e.g.,* Sibson et al., 1988; Sibson, 1990; Sibson and Scott, 1998).

Such episodic, sudden pressure drops from lithostatic to near-hydrostatic regime induce boiling, phase separation (Velásquez et al., 2018) and high-grade ore deposition (Peterson and Mavrogenes, 2014). It is however worth noticing that such fluid pressure changes can also be included within a progressive deformation history, similarly to what is proposed here for the GSS deposit.

The GSS gold ore history is also associated with multiphase deformation as a minor, second gold stage is coeval with the D_{4GSS}-related late veining (Figs. 2-12, 2-13). Although the gold-bearing polymetallic assemblage (presence of electrum inclusions in Py_4; Fig. 2-10f) is locally dominant within D_{4GSS} veins and veinlets (Fig. 2-10e; Table 2-1), they may also be completely barren (Fig. 2-9h; Table 2-1). Besides, the late veining is limited to silicified intervals within the meta-volcanosedimentary horizon. This could be explained by the rheological contrast induced by the massive $Qz_{2/3}$ silicification event (Fig. 2-12) resulting in more competent, silicified intervals regarding the sericitized meta-volcanosedimentary unit. Similar inherited pervasive silicification is the main control on fracturing, pressure release and gold-bearing quartz vein precipitation at the Wona deposit, Burkina Faso, where most of the deformation and alteration was recorded before gold introduction (Augustin et al., 2016). The GSS gold deposit therefore displays evidence for a rheological control on late brittle deformation and related mineralization by an alteration feature inherited from a former fluid flow event (Chauvet, 2019b). As a result of the limited spatial extent of the D_{4GSS}-related late veining, the associated gold mineralization forms only local high-grade ore shoots (Table 2-1). Its contribution to the overall GSS gold endowment is probably low regarding the economic gold mineralization associated with the D_{1GSS} and D_{2GSS} deformation phases even though their respective contribution has not been evaluated.

Finally, the GSS gold deposit deformation history and related mineralization is probably controlled by sudden changes in host rock rheology and fluid pressure. These are included in a progressive deformation scheme, even though they may impact

subsequent, disconnected deformation/mineralization events such as the late D_{2GSS} to D_{3GSS} deformation-related pervasive silicification controlling the D_{4GSS}-related late veining. Such pre-existing alteration patterns or structures are therefore critical when it comes to ore structural control, as already largely documented (*e.g.,* Chauvet, 2019a).

5.2. Progressive vs multiphase deformation history

Recent studies in the West African Craton provided key evidence for a polyphase formation of "orogenic gold" deposits, where gold endowment is associated with one or several discrete deformation stages which are part of a multiphase deformation history (*e.g.,* Perrouty et al., 2015; Augustin and Gaboury, 2017, 2018; Augustin et al., 2017; Fontaine et al., 2017; Fougerouse et al., 2017). For instance, the two successive deformation-related ore stages deciphered at the Wassa gold deposit, Ghana, West African Craton, occurred at 2164 ± 14 Ma and 2055 ± 18 Ma based on Re-Os ages on sulfide minerals (Le Mignot et al., 2017). The ~100 Ma time lapse between these two ages suggests that they can be attributed to two separated, discrete deformation-related ore stages. Still considering the West African Craton, Augustin et al. (2017) attributed the formation of the Mana world-class gold deposit, Burkina Faso, to several mineralizing pulses associated with 3 or 4 shortening tectonic phases over a 150 Ma time lapse.

In this predominant multiphase ore model for gold-bearing vein deposits, ore-related deformation phases are therefore largely considered to be discrete. Although well demonstrated in the previous examples, discrete deformation is however easier to demonstrate by direct dating than progressive deformation as the latter is hardly constrained by a single date. The deciphering of the strain evolution and relationships between deformation and paragenetic history is thus required to make the case. This is true for instance considering the gold-bearing vein Saddle Reef deposit, Hill End Gold Field, Australia, where gold transport and deposition in veins are attributed to the middle to latest stages of regional folding following the early bedding-parallel vein formation

(*e.g.,* Windh, 1995). Petrographical and structural evidence collected for the GSS gold deposit also suggest that the economic gold mineralization (input and liberation?) is associated to the ductile progressive D_{1GSS}-D_{2GSS} deformation episode, prolonged by the barren D_{3GSS} ductile/brittle transition (Fig. 2-13). The GSS gold ore history is however also associated with multiphase deformation as it ends with a minor, second gold stage coeval with the late brittle D_{4GSS} phase (Fig. 2-13). It is therefore a unique deposit that allow to investigate both progressive and discrete ore-related deformation histories.

The lack of literature supporting a progressive deformation history related to gold mineralization such as proposed for the GSS deposit or the Saddle Reef deposit (Windh, 1995) may be explained by the possibility of methodological bias, beside the direct dating difficulty. Former studies addressing the structural framework of a given "orogenic gold" deposit mostly follow a geometric-only approach (*e.g.,* Hodgson, 1989; Allibone et al., 2002; Miller and Wilson, 2004; Tunks et al., 2004; Wang et al., 2019). They therefore invoke polyphase deformation to interpret complexly deformed areas hosting "orogenic gold" deposits, by attributing every distinct structural pattern to a new deformation stage. Prior to inferring polyphase deformation, such approach however requires to check if several tectonic phases could be explained by a single tectonic regime and if there is geochronological evidence to separate them (Fossen et al., 2019). Therefore, the importance of progressive deformation regarding gold-bearing vein type mineralization may be under-addressed.

6. From deposit-scale to regional-scale deformation history

6.1. Deposit-scale subvertical, linear control on ore shoot distribution

Systematic structural orientation measurement on core and outcrop widely spread throughout the GSS area (Fig. 2-2b) helps to integrate micro- to macro-scale deformation features at the deposit scale. The D_{2GSS}-related structures control the GSS structural

framework at every scale. At the deposit scale, subvertical linear fabrics are widespread (Fig. 2-2b). The S_2 penetrative shear band cleavage, not clearly visible in the field (Fig. 2-14a) is steeply dipping but its strike orientation is very variable (Fig. 2-2b). On drill core, cleavage planes are sometimes corrugated confirming the predominance of linear fabrics (Fig. 2-14b) and the presence of L-tectonites. They are expressed by a steeply plunging, NW-trending L_2 stretching lineation (Fig. 2-14c). A similar stretching direction is expressed by marble bodies in interlayers of marble and meta-sediments within Block 14 (Fig. 2-3b and c).

At the deposit scale, S_2 distribution is controlled by a fold system which axis is parallel to L_2 (Fig. 2-14c). Thus, the variability in S_2 strike orientation can be explained by L_2 stretching lineation predominance and S_2 rotation around this fabric. However, no clear fold hinge has been observed at the outcrop to deposit scale, suggesting that the parallel relationship between the stretching lineation and the fold axis is only valid within the limb part of the proposed fold system.

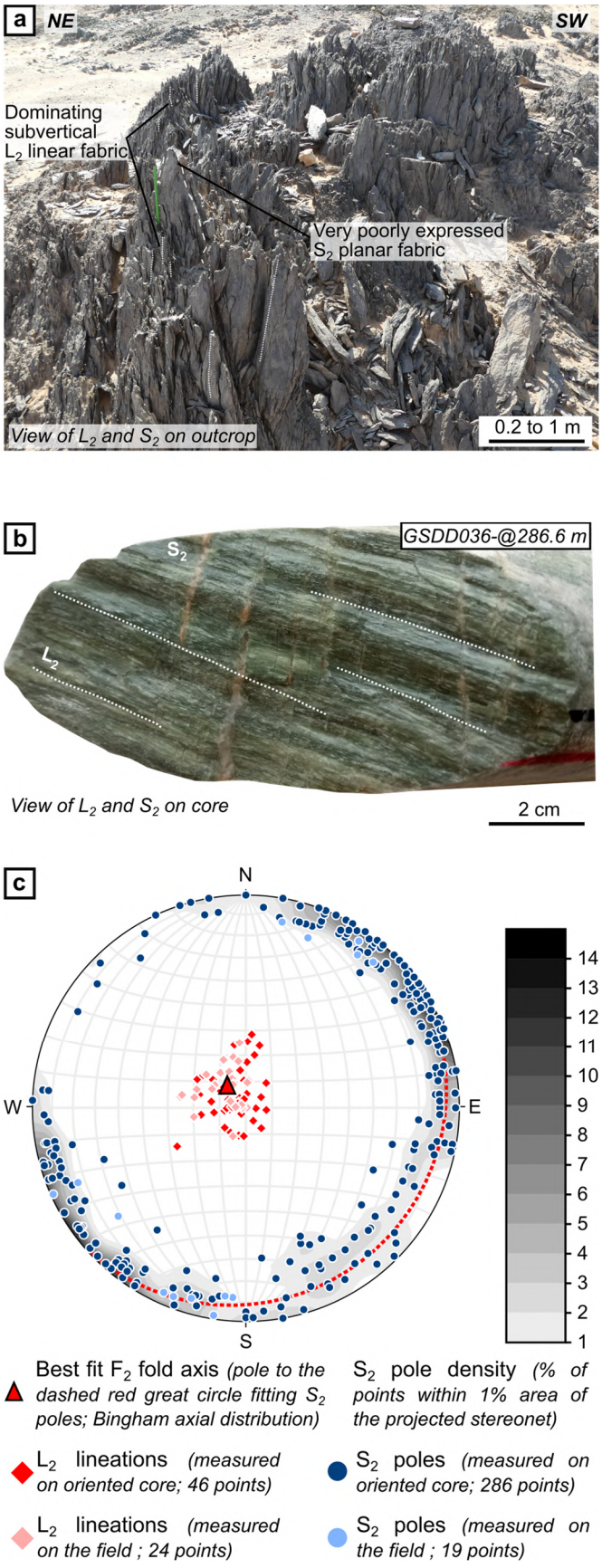


Figure 2-14: **a** On outcrop, S_2 planar fabric is hardly recognizable while linear L_2 fabric dominates. **b** L_2 stretching lineation lying in the corrugated S_2 plane visible on diamond drill core. **c** S_2 and L_2 distribution at the GSS gold deposit, adapted after Perret et al. (2019). Structural data are plotted in an equal area stereonet, lower hemisphere projection. The S_2 penetrative fabric orientation (286 measurements on core, 19 measurements in the field) displays a variable strike orientation and is subvertical. The NW-trending stretching lineation L_2 lying in S_2 planes plunges steeply westwards (46 measurements on core, 24 measurements in the field). S_2 poles plot along a subhorizontal great circle which pole falls into the L_2 main orientation area: S_2 orientation is therefore likely controlled by L_2 fabric dominating the GSS structural framework.

The Figure 2-15 proposes a schematic 3D block diagram for the GSS gold deposit, based on the lithology, alteration and deformation features described along the logged DDHs (Fig. 2-4 to 2-10) and the structural dataset acquired. Drawing of Figure 2-15 was performed after importing the structural data in Geoscience Analyst (2.60) and SKUA-GOCAD ™ - Paradigm® 15 softwares.

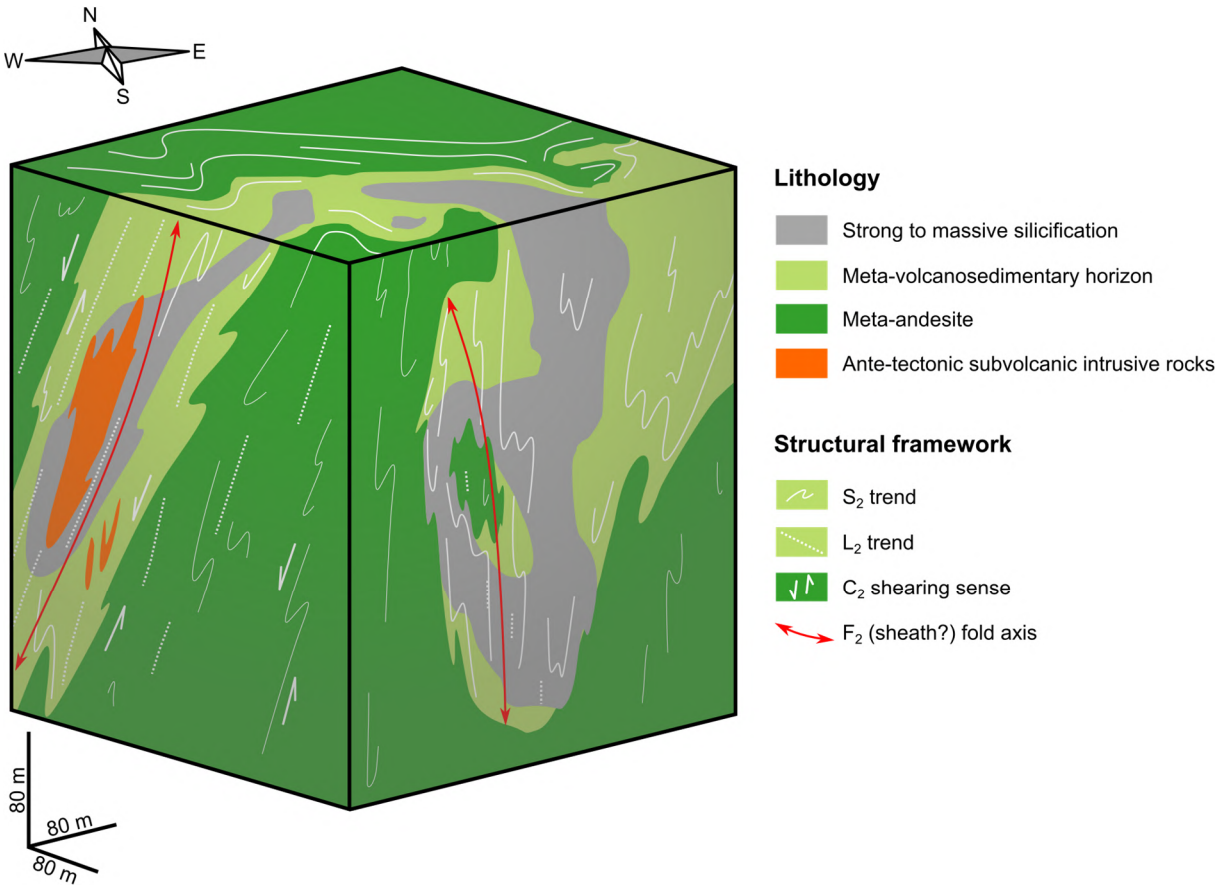


Figure 2-15: Schematic 3D block diagram of the GSS gold deposit. The block model is drawn after the lithology, alteration and deformation description from studied DDH logging and systematic structural measurement. Lithologies are the same as in Figure 2-2b. The block limits are indicated in Figure 2-2b as well. Strong to massive silicification refers to the strong presence of D_{1bGSS}-related, quartz-dominated veinlets transposed into the S_2 shear band cleavage and associated with the main ore shoots or to the late D_{2GSS} pervasive silicified intervals where D_{4GSS} veining preferentially occurs. D_{2GSS}-related structural features are highlighted.

It illustrates again the strong contribution of the L_2 linear fabric to the deposit-scale structural framework with the ore-bearing meta-volcanosedimentary horizon being subvertically stretched along it. Besides, ore shoots steeply plunge northwestwards, along with L_2 stretching lineation at the GSS gold deposit (Fig. 2-15). The ore plunge orientation is displayed by fold and boudin axes in mineralized D_{1GSS}-related veinlets. As

these veinlets are microfolded by the F_1 and the F_2 systems (Fig. 2-5a and b) and have been dismembered and transposed along the S_2 cleavage, it is very unlikely that they were emplaced parallel to S_2: their current geometry must result from the subsequent deformation history. The low angle to parallel relationship between the ore shoots and the L_2 stretching fabric shows that D_{1GSS}-related fold and boudin axes have rotated parallel to L_2 during D_{2GSS}-related subvertical simple shearing stage. This demonstrates that D_{2GSS} is a high strain, ductile deformation stage (Robert and Poulsen, 2001; Siddorn, 2011) responsible for the overall subvertical and linear orientation of ore shoots at the deposit scale.

6.2. Deposit- and regional-scale sheath fold formation

The very variable orientation of S_2 penetrative fabric is also visible at the regional scale on satellite imagery and is mostly expressed by marble and meta-sediment layer trends in the western part of Block 14 (Fig. 2-16a). ~ 100 m-scale sub-circular to stretched, closed main fabric patterns are identified (Fig. 2-16b). They are similar to the km-scale closed feature visible southeast to GSS deposit (Fig. 2-3a) and they both contain smaller closed contours suggesting the fractal nature of this pattern. Closed, subvertically stretched marble bodies embedded in meta-sediments are also visible within these large-scale structures (Fig. 2-3b, c, d and e) and the deposit-scale block diagram (Fig. 2-15) displays that the ore-bearing horizon geometry is controlled by the L_2 subvertical linear fabric around which it forms closed contours deepwards.

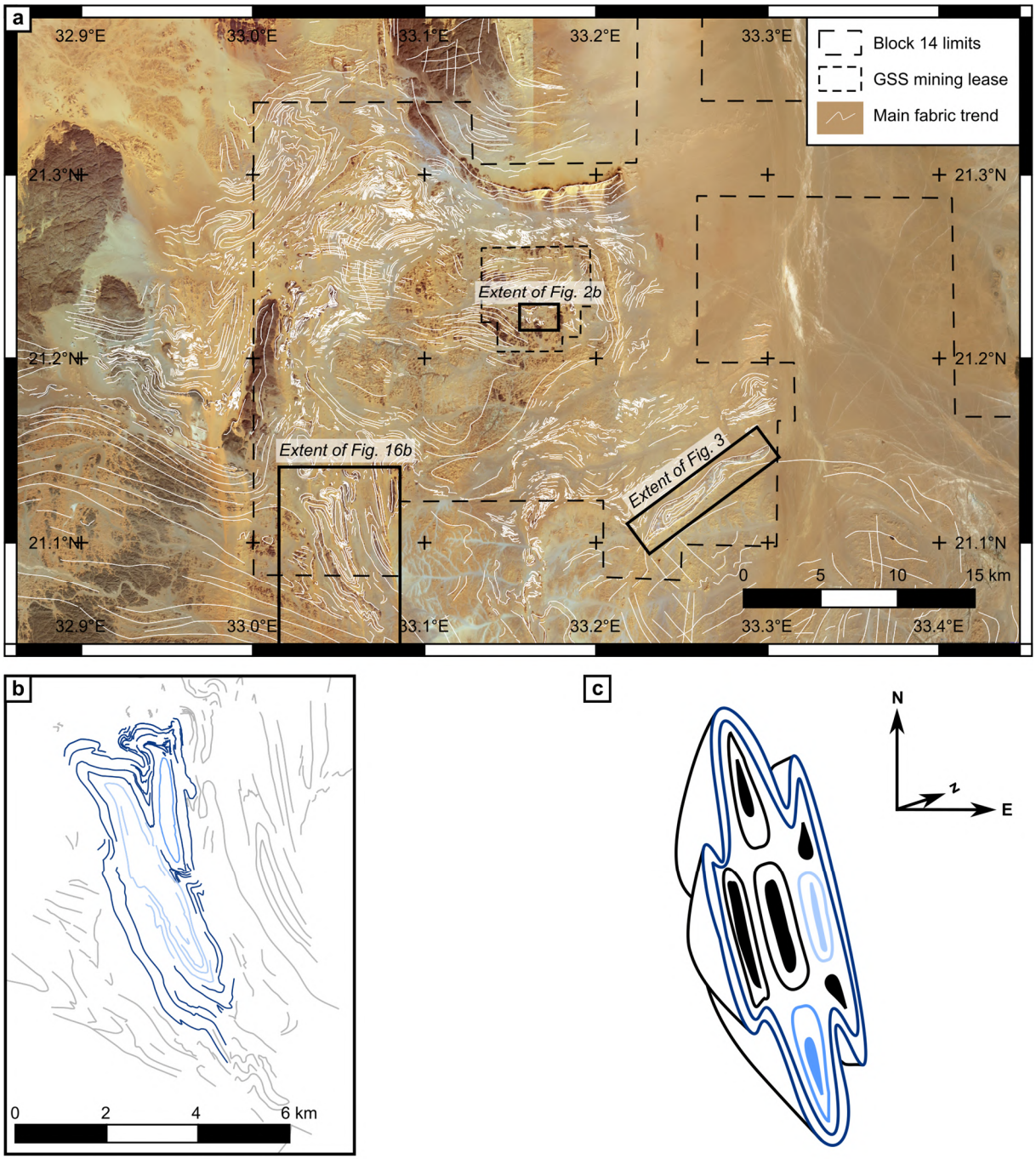


Figure 2-16: a The main fabric orientation, visible from satellite imagery (©Bing Aerial), is strongly variable at the Block 14 scale. The black rectangle delimits the extent of Figure 2-16b. Figure 2-2b and 2-3 extents are also drawn. Geographic coordinates are reported as WGS 84. **b** Zoom on a closed contour pattern in the southwest part of Block 14. **c** Comparison of the fractal closed contours with the schematic transversal section of a sheath fold from Alsop and Holdsworth (2004). The change in blue color line is relative to the innermost and outermost closed contours visible in Figure 2-16b.

There are several options to explain the presence of such closed structural patterns and the dominance of L-tectonites:

(i) *Asymmetrical boudinage*

The rheological contrast between marble and surrounding meta-sediments may account for subvertical boudinage of marble within a less competent meta-sedimentary layer which would form similar patterns as observed in Figure 2-3b, c, d and e. However, the subvertical marble body orientation would suggest a subhorizontal stretching direction in case of boudinage, which has not been observed at any scale. Such orientation does not fit with the subvertical stretching direction visible at the deposit scale on the proposed block diagram (Figs. 2-14c, 2-15). Moreover, meta-sediments do not only flow in boudin necks with bend folding and wrapping around marble bodies, but they form closed contours around them (Fig. 2-3b and c). Such patterns are also incompatible with boudinage leading to rule out this possibility.

(ii) *Interference folding*

the km-scale closed contours visible on satellite imagery (Fig. 2-16a) could likely result from Type 1 interference folding (orthogonal folding directions; Ramsay, 1962) between E-trending folds related to the ADS and N-trending folds related to the KSZ. The L_2 lineation would therefore results from intersection between these two structural trends. However, despite the strong variability in the main fabric orientation throughout the western Block 14, a single foliation generation has been observed and no superimposition between orthogonal foliation families has been observed at the outcrop and deposit scales. The main structural features observed from the outcrop to the deposit scale are therefore related to a single deformation stage.

(iii) *Sheath folding*

Without scale consideration, the closed patterns visible on satellite imagery are similar to sheath fold sections transverse to a subvertical transport direction (Fig. 2-16b

and c; models by Cobbold and Quinquis, 1980; Alsop and Holdsworth, 2004, 2006; Alsop et al., 2007; Reber et al., 2013). Their subcircular to stretched geometry is reminiscent of Type B or Type C sections, according to the classification by Alsop et al. (2007). Such sheath folds are known to form in simple or general shear deformation regime (Alsop and Holdsworth, 2006; Alsop et al., 2007), which is compatible with asymmetrical structures displayed at the micro-scale (Fig. 2-6). The latter microstructures might not be as developed as expected to invoke high strain simple shearing. The D_{2GSS} deformation is therefore rather related to general shearing with the stretching lineation being parallel to the vorticity vector. This point cannot be checked however, as no thin section has been prepared orthogonally to the lineation. Besides, it is worth noticing that such large-scale sheath folds are rarely documented. Even though the related strain is known to be high in the area (see subsection 6.1), the formation of such structures would likely represent high strain, suggesting to keep caution about the possibility of sheath folding at this scale. Considering only the deposit and outcrop scales, invoking sheath folding provides an explanation for the variability in the single main foliation strike orientation (Figs. 2-2b, 14c). In the case of sheath folding, the foliation strike orientation can rotate 360° as long as the foliation plane contains the main stretching direction. This is confirmed at the GSS deposit scale as the L_2 stretching lineation always lies in S_2 whatever its strike orientation (Fig. 2-14c). Besides, the L_2 stretching lineation is parallel to the fold axis interpreted from S_2 measurement at the GSS deposit extent. Considering sheath folding, this is true in the limb zone of sheath folds while the fold axis rotates more than 90° and becomes orthogonal to the stretching direction in the hinge zone. Unfortunately, no clear sheath fold hinge zone has been observed at the deposit scale, which prevent us from measuring clear fold axis orientations in different parts of the system. However, at the outcrop scale, marble body terminations look like fold noses (Fig. 2-3b and c). Despite that they are likely strongly affected by erosion, their noses display curved fold axis-like lines which are almost subhorizontal while the marble body

stretching direction is subvertical and parallel to the deposit-scale L_2 stretching lineation. The presence of closed contours in marble bodies and meta-sediments in proximity (Fig. 2-3b, c, d and e) is reminescent of sheath fold innermost and outermost contours, respectively (Alsop et al., 2007). Subvertical, NW-steeply plunging sheath folding could also account for the curved, L_2-stretched geometry of the ore-bearing horizon deepwards (Fig. 2-15).

Despite the lack of key evidence to irrevocably prove its existence at the deposit and outcrop scales and the need for caution when upscaling at the regional scale, sheath folding is the only proposed option that is not ruled out to interpret our multi-scale structural observations. Besides, Fossen et al. (2019) demonstrated that sheath folds (as well as refolded folds) result from progressive deformation, as long as the strain is high enough, and that their formation could often be simplified into a single, progressive deformation episode. This is confirmed by Carreras and Druguet (2019) who show that sheath folds could result from the rotation of folds towards parallelism with the extension direction in simple shear progressive deformation. Considering deposit-scale (maybe regional-scale?), D_{2GSS}-related sheath folding at the GSS gold deposit would therefore not be incompatible with the D_{1GSS} to D_{3GSS} progressive simple shear deformation deciphered at the micro- to macro-scale throughout the GSS area.

6.3. Record of the ADS tectonics

The GSS-scale ore-bearing meta-volcanosedimentary horizon is ENE-trending (Figs. 2-2, 2-15) which corresponds to the orientation of E-trending nappes resulting from the tectonics leading to the formation of the ADS between the Bayuda and Halfa terranes (Schandelmeier et al., 1994b; Abdelsalam et al., 1998). The overall orientation of the deposit-scale D_{2GSS}-related steeply plunging, NW-trending linear features is rather consistent with the early regional D_1, subduction-related thrusting and the regional D_2, collision-related upright folding. This is in agreement with the tectonic model from

Abdelsalam et al. (1998) who suggested that a NW-SE oblique convergence between East and West Gondwana resulted in the closure of the Mozambique Ocean aulacogen and the subsequent ADS formation. The transfer of the local D_{1GSS}-D_{2GSS}-(D_{3GSS}) to the regional D_1-D_2 progressive deformation is in agreement with the approach proposed by Fossen et al. (2019) and presents the advantage to (1) simplify the local deformation history associated with the GSS gold deposit formation and (2) upscale it at the regional scale.

The GSS gold deposit is therefore likely a structural marker of the ADS suturing in the northwesternmost Nubian shield. It was however described as an "orogenic gold deposit" spatially related to the transcurrent KSZ (Johnson et al., 2017) despite it was not documented to date. Yet, no shear zone with subhorizontal stretching direction has been observed in the Block 14 area. It rules out the possibility to consider that the GSS deposit formation is related to the KSZ transpressive tectonics which are mostly expressed in its southern extent (Abdelsalam et al., 1995, 2003; Ahmed Suliman, 2000; Bailo et al., 2003).

7. Conclusions

The combination of µm- to tens of km-scale petrographic and structural studies of the gold mineralization at the GSS gold deposit (NE Sudan) suggests that:

(i) The GSS gold deposit is atypical for a so-called "orogenic gold deposit" and expresses a complex polyphase deformation history with an early subvertical, linear, progressive deformation event associated with the economic gold ore. The deformation history started by a mostly ductile, high strain, simple shearing D_{1GSS}-D_{2GSS}-(D_{3GSS}) progressive deformation controlling the local structural framework. D_{1GSS}-related quartz-carbonate-pyrite veinlets are dismembered and boudinaged along the L_2 subvertical lineation in the S_2 penetrative shear band cleavage and form ore shoots parallel to L_2 fabric. This deformation continuum is prolonged by the weakly expressed D_{3GSS} ductile/brittle transition. The multiphase deformation history displayed at the GSS gold deposit ends with the late D_{4GSS} veining phase.

(ii) Pore fluid pressure variations are likely to be responsible for veining during the ductile D_{1GSS} stage and pyrite corrosion and overgrowing during D_{2GSS} stage, leading to the formation of the economic gold mineralization. The GSS gold deposit exemplifies well the change in deformation style due to fluid pore pressure variations during a ductile, progressive deformation episode. Besides, the D_4 veining phase is limited to the intensively silicified intervals of the meta-volcanosedimentary unit and results in very local high-grade ore shoots. Its contribution to the overall gold endowment at the GSS deposit is thought to be very limited when compared to the D_{1GSS}- and D_{2GSS}-related one although the exact contribution of each mineralizing event is not estimated. This last change in deformation style and its extent are therefore mostly controlled by a change in host rock rheology due to intense silicification at the end of the ductile-dominated progressive deformation.

(iii) From the outcrop to the regional scale, the D_{1GSS}-D_{2GSS}-(D_{3GSS}) progressive deformation is expressed by subvertical linear features (including potential dm- to pluri-km-scale sheath folds, which remains uncertain) dominating the structural framework. The inherited overall orientation of the ore-bearing horizon and main L-tectonites throughout the area are in agreement with the compressive tectonics between the Bayuda and Halfa terranes during the formation of the Atmur-Delgo suture.

This study therefore highlights that the multi-scale, petro-structural characterization of a gold-bearing vein deposit is a way to investigate the structural evolution of an area of interest, in this case the northwesternmost Nubian shield.

Acknowledgements

The authors are grateful to the Orca Gold Inc. team for their welcome on GSS camp and their substantial logistical support. We gratefully acknowledge T.G. Blenkinsop and D. Gaboury for their constructive comments that helped to greatly improve the manuscript and C.W. Passchier for the editorial handling. This work is part of Julien Perret's PhD project which benefited of a CIFRE funding, reference CIFRE N°2017/1737, attributed by the French National Research and Technology Agency (ANRT).

Chapitre III – Tectonic record and gold mineralization in the central part of the Neoproterozoic Keraf suture, Gabgaba district, NE Sudan

Julien Perret[1,2,*], Julien Feneyrol[1], Aurélien Eglinger[2], Anne-Sylvie André-Mayer[2], Célestine Berthier[2], Aomar Ennaciri[3], Rémi Bosc[1]

Article en révision pour publication dans *Journal of African Earth Sciences*.

[1] Arethuse Geology EURL, BP 80017, Latitude Arbois, 1060 rue René Descartes, 13290 Les Milles, France

[2] GeoRessources, Université de Lorraine, CNRS, 54000 Nancy, France

[3] Managem, BP5199, Twin Center, Tour A, Boulevard Zerktouni, Casablanca, Maroc

Résumé

La partie centrale de la suture de Keraf a enregistré une histoire tectonique complexe, relative à la formation du bouclier arabo-nubien au cours du Néoprotérozoïque, et héberge les gisements aurifères de WG03, Central Zone et UTM (district de Gabgaba, Soudan). Cette étude vise à (i) caractériser les phases de déformation ayant affecté la partie centrale de la suture de Keraf et (ii) interpréter les relations spatiales et génétiques entre structures et minéralisation aurifère. Pour ce faire, les observations pétrographiques et mesures structurales réalisées le long d'un transect géologique levé à travers le district de Gabgaba sont couplées avec une description macroscopique et microscopique des structures minéralisées.

Le canevas structural de la zone d'étude est dominé par un épisode de déformation progressive depuis la phase de chevauchement ductile D_{1a} à la phase de décrochement ductile-fragile senestre D_{1b}, en réponse à un régime de déformation convergent nord-ouest – sud-est. Un premier épisode minéralisateur mineur est associé à la phase d'accrétion magmatique précédant la suture de Keraf. L'épisode aurifère majeur, de type or orogénique, est exprimé par des veines de quartz minéralisées est synchrone de la zone de cisaillement de Keraf tardi-orogénique.

En somme, la partie centrale de la zone de suture de Keraf met en exergue le caractère polyphasé de la minéralisation aurifère localisée le long des accidents lithosphériques du bouclier arabo-nubien. Cet exemple démontre que ces structures peuvent enregistrer une histoire tectonique complexe, depuis les phases d'accrétion magmatique jusqu'à la collision tardi-orogénique, avec un contrôle structural fort des minéralisations aurifères.

Mots-clés

Bouclier arabo-nubien ; suture de Keraf ; district de Gabgaba ; tectonique chevauchante et décrochante ; minéralisation polyphasée ; or orogénique.

Abstract

The central Keraf suture recorded complex lithospheric-scale deformation associated with the formation of the Neoproterozoic Arabian-Nubian shield and hosts the WG03, Central Zone and UTM gold deposits, Gabgaba district, northeastern Sudan. This study aims at (i) unravelling the tectonic history recorded by the central Keraf suture and (ii) interpreting the spatial and genetic relationships between structural setting and gold mineralization. To this end, we coupled field petrographic observations and structural measurements made along a 50 km-long geological cross-section through the Gabgaba district with macroscopic and microscopic description of mineralized structures.

The structural setting of the central Keraf suture is dominated by progressive deformation, from ductile D_{1a} Keraf thrusting to ductile-brittle D_{1b} sinistral shearing in a prolonged northwest-orientated convergence regime. A first mineralization event, leading to a minor gold endowment, relates to magmatic accretion pre-dating D_{1a} Keraf suturing. The second gold episode is characterized by ore veining as a response to progressive late collisional D_{1b} Keraf strike-slip shearing and may be classified as orogenic gold. Most of the gold budget of the Gabgaba district formed at this stage.

In summary, the central Keraf suture exemplifies that the Arabian-Nubian shield contains significant polyphase gold mineralization along lithospheric-scale structures. These structures may record a complex tectonic evolution from magmatic accretion to collision, with a strong structural control on gold endowment.

Keywords

Arabian-Nubian shield; Keraf suture; Gabgaba district; thrust and strike-slip tectonics; polyphase mineralization; orogenic gold.

1. Introduction

Archean to Phanerozoic orogenic gold deposits are systematically associated with crustal to lithospheric-scale structures along accretionary- and collision-type convergent margins (*e.g.,* Kerrich and Wyman, 1990; Goldfarb et al., 2001, 2005; Groves et al., 2003, 2018, 2019; Weinberg et al., 2004; Bierlein et al., 2006; Eglinger et al., 2017). Lithospheric-scale transcurrent shear zones may develop at the boundary between litho-tectonic blocks or terranes and play a critical role as fluid and magma pathways (*e.g.,* Kerrich and Wyman, 1990; Sawkins, 1990; Weinberg et al., 2004, 2005; Blewett et al., 2010; Mole et al., 2019). Although these transcurrent shear zones mostly result from the syn- to late convergent stage, some record a much more complex polyphase deformation history starting earlier in the orogenic cycle with the formation of suture zones (*e.g.,* Daigneault et al., 2002; Weinberg et al., 2004; Feybesse et al., 2006). These complex, transcurrent, lithospheric-scale structures are known to host orogenic gold deposits in world-class gold provinces, such as the Boulder-Lefroy fault system in the Archean Yilgarn craton (*e.g.,* Weinberg et al., 2005; Mueller et al., 2020; Mueller, 2020), the Cadillac-Larder Lake fault zone in the Archean Abitibi subprovince (*e.g.,* Rabeau et al., 2013; Simard et al., 2013; Bedeaux et al., 2017) or the Markoye shear zone in the Paleoproterozoic West African craton (*e.g.,* Fontaine et al., 2017; Goldfarb et al., 2017). Several gold events may then occur from the magmatic arc accretion to the late orogenic periods (*e.g.,* Simard et al., 2013; Augustin et al., 2017; Eglinger et al., 2017, 2020; Le Mignot et al., 2017; Thébaud et al., 2020; Masurel et al., under review). These gold-mineralized shear zones therefore have the potential to provide important relationships between tectonic processes and gold endowment through time.

The Arabian-Nubian shield (ANS; Fig. 3-1a, b) constitutes the main Neoproterozoic gold province worldwide (Johnson et al., 2017). ANS deposits are mostly classified as orogenic gold occurrences preferentially hosted by major shear zones (*e.g.,* Elsamani et al., 2001; Botros, 2002, 2004; Helmy et al., 2004; El Kazzaz, 2012; Osman, 2014; Helmy

and Zoheir, 2015; Khalil et al., 2016; Fawzy, 2017; Zoheir et al., 2019a, 2019b, 2019c), including the Keraf shear zone (KSZ) (Johnson et al., 2017). The KSZ is mapped in northeastern Sudan and southeastern Egypt, and overprints the ~500 km-long, ~70 km-wide, north-striking ophiolite-decorated Keraf suture (KS) which is rooted deep into the lithosphere (Almond and Ahmed, 1987; Abdelrahman, 1993; Abdelsalam et al., 1995; Abdelsalam and Stern, 1996a; Ahmed Suliman, 2000). The KS is divided in the northern, central and southern sections with distinct structural settings, despite it remains a poorly studied area with uncertain shape and boundaries (Fig. 3-1c). Second-order structures are known to host gold occurrences and deposits in the central KS, forming the Gabgaba gold district explored and exploited since 2009 by Manub, a subsidiary of the Moroccan mining group Managem Ltd. (Block 15 exploration license in Fig. 3-1c; Managem, 2011). Yet, the temporal and spatial relationships between the Gabgaba gold district deposits, *i.e.,* WG03, Central Zone and UTM -indicated and measured resources up to 1.659 Mozt Au, 438 kozt Au and 308 kozt Au in May 2013, respectively (Managem, 2014)- and the wider structural framework are scarcely documented (*e.g.,* Gaboury et al., 2020):

(i) Central Zone and UTM deposits are located along a second-order structure, known as the *"West Corridor"* (Figs. 3-2, 3-3; Gaboury et al., 2020) but the interpretation of this structure as the western boundary of the central KS remains under debate (Fig. 3-2; Ahmed Suliman, 2000; Bailo et al., 2003; Abdelsalam et al., 1998; Gaboury et al., 2020).

(ii) The WG03 deposit is located along another lower-order shear zone west of the "*West Corridor"* (Fig. 3-2), it remains thus unclear if the deposit is located within the KS and if WG03 gold endowment relates in any way to KS tectonics.

Much work therefore remains to be done to understand the gold endowment history related to the central KS tectonics and the Gabgaba district is well-suited to do so. Our study serves two purposes: (i) collecting field observations and structural measurements along the central section of the KS (Figs. 3-1c, 3-2, 3-3) to propose a revised tectonic

history, unifying previous models from the literature (*e.g.,* Abdelsalam et al., 1995, 1998; Ahmed Suliman, 2000); and (ii) linking the textural and structural characteristics of the known Gabgaba deposits with the wider tectonic framework, to interpret the spatial and genetic relationships between structural setting and gold mineralization. In order to address these two points, we realized a 50 km-long geological cross-section through the Gabgaba gold district and conducted a petrological-structural study of the WG03, Central Zone and UTM gold deposits.

2. Geological setting

The ANS is the northernmost part of the East African-Antarctic orogen (EAAO; Fig. 3-1a, b; Kröner, 1993; Stern, 1994; Kusky et al., 2003; Li et al., 2008; Seton et al., 2012; Fritz et al., 2013; Domeier and Torsvik, 2014; Merdith et al., 2017; Grenholm, 2019). Its formation resulted from the amalgamation and collision between terranes, formed by juvenile magmatic arc and ophiolite assemblages which are remnants of the subduction and obduction processes that completely consumed the Mozambique ocean in the northern EAAO (Fig. 3-1a; *e.g.,* Burke and Sengör, 1986; Johnson et al., 2011; Fritz et al., 2013 and references therein). It led to the formation of suture zones that are linear belt of intense deformation along which terranes join together and sometimes superimposed by crustal-scale shear zones (Chetty, 2017). The Keraf suture and shear zone is an example of such a composite orogenic belt (KS-KSZ; Fig. 3-1b).

The extent of the KS is limited to Egypt and Sudan as it represents the northern part of the Keraf-Kabus-Sekerr-Kinyiki suture (Fig. 3-1a) that stretches to Kenya southwards (Fig. 3-1a; Vearncombe, 1983; Burke and Sengör, 1986; Frisch and Pohl, 1986; Berhe, 1990; Abdelsalam and Dawoud, 1991; Ries et al., 1992; Mosley, 1993; Abdelsalam et al., 1998; Fritz et al., 2013). Keraf suturing consisted in arc-continent collision between Neoproterozoic juvenile magmatic arcs, and the Saharan meta-craton

with consumption of the Mozambique ocean lithosphere (Vail, 1983, 1985; Almond and Ahmed, 1987; Abdelsalam and Dawoud, 1991; Stern, 1994; Abdelsalam et al., 1995, 1998; Abdelsalam and Stern, 1996b; Abdelrahman et al., 2017).

The former presence of the Mozambique ocean in place of the current KS is underlined by the Keraf Pre-Tectonic Assemblage (KPTA; Fig. 3-1c). The KPTA gathers all the rocks exposed only in the KS zone and that are affected by Keraf thrusting and strike-slipe shearing processes (Ahmed Suliman, 2000). It comprises pre-Neoproterozoic high- to medium-grade gneisses (Meinhold, 1979; Vail, 1979; Dawoud, 1980; Abdelrahman, 1993) and rock remnants related to different geodynamical settings such as magmatic arc and back-arc basin (Keraf ophiolitic mélange, volcanosedimentary sequences; *e.g.,* Schandelmeier et al., 1994; Stern, 1994; Abdelsalam et al., 1995; Abdelrahman et al., 2017) and passive continental margin (carbonate-rich and siliciclastic meta-sediments; *e.g.,* Stern et al., 1993). Following the Mozambique ocean expansion, the formation of the KS-KSZ recorded its closure and subsequent convergence:

(i) Initial convergence and ocean closure occurred along a north-trending magmatic arc system that was active at *ca.* 800-750 Ma east to the Saharan meta-craton (Abdelsalam et al., 1998; Bailo et al., 2003). At the same time, west-trending aulacogen-like oceanic reentrants started to close along magmatic arcs as well, such as the one marked by the Atmur-Delgo suture, located west of the northern KS (Fig. 3-1c; Denkler et al., 1993, 1994; Harms et al., 1994; Schandelmeier et al., 1994; Stern et al., 1994).

(ii) Then, an oblique convergence resulted into arc-continent collision and the final closure of the oceanic reentrants and the Mozambique oceanic basin between the ANS-related terranes and the Saharan meta-craton, leading to Atmur-Delgo and Keraf suturing between *ca.* 750-640 Ma (Abdelsalam et al., 1998).

(iii) Finally, oblique convergence was translated into sinistral shearing along the KS which led to its superimposition by the KSZ at *ca.* 640-580 Ma (Abdelsalam et al., 1998).

The late to post-collisional lateral displacement occurred between *ca.* 630-590 Ma and is mostly recognized along the southern part of the KSZ (Evuk et al., 2014).

(iv) The orogenic activity ended along the KS-KSZ at ~565 Ma (Bailo et al., 2003) and a post-orogenic gravitational collapse locally reactivated structures at ~550 Ma (Stern, 1994; Abdelsalam et al., 1995, 2003; Abdelsalam and Stern, 1996a, 1996b; Ahmed Suliman, 2000).

In the westernmost ANS, six deformation phases have been interpreted from satellite imagery by Abdelsalam et al. (1995). The first two ($D_{1/2ADS}$) relate to Atmur-Delgo suturing and their field expression is limited to the northwestern KS (Fig. 3-1c; Schandelmeier et al., 1994; Abdelsalam et al., 1995, 1998, 2003; Perret et al., 2020). They are not considered further as not identified in our study area. Field data more or less robustly confirmed the existence of the four last $D_{1\text{-}AS}$ to $D_{4\text{-}AS}$ deformation events, that are attributed to the formation of KS-KSZ (Fig. 3-1c; Ahmed Suliman, 2000). Details about the related structures and previous tectonic interpretations are provided in Table 3-1. However, one can doubt that up to six deformation phases can be robustly resolved at first by remote sensing in such a complexly deformed area. This is the reason why we decided not to match the $D_{1\text{-}AS}$ to $D_{4\text{-}AS}$ deformation history and rather propose our own structural interpretation below.

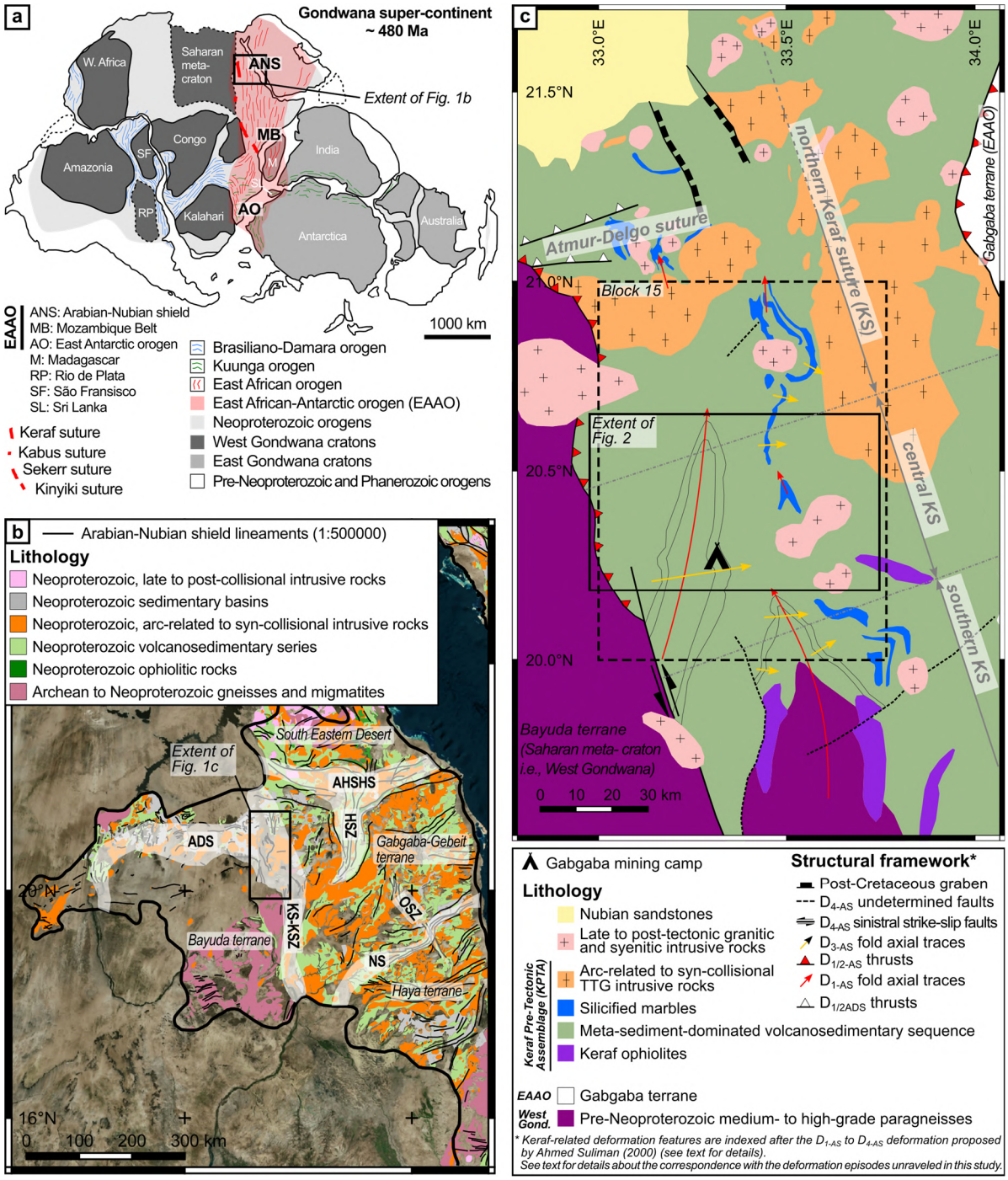


Figure 3-1: The Keraf suture in the framework of the East African-Antarctic orogeny (EAAO). **a** Gondwana super-continent reconstruction, modified after Gray et al. (2008). The location of the Keraf-Kabus-Sekerr-Kinyiki suture along the EAAO comes from Fritz et al. (2013). **b** Geological map of the Nubian part of the Arabian-Nubian shield (ANS).Lithological units are drawn from Egypt, Sudan and Eritrea national geological maps (Egyptian Geological Survey and Mining Authority, 1981; Geological Research Authority of the Sudan, 1988; Tadesse et al., 2000) after legend homogenization. The main suture and shear zones as well as terrane names are indicated after Johnson et al. (2011). Abbreviations are ADS = Atmur-Delgo suture; KS-KSZ = Keraf suture-shear zone; AHSHS = Allaqi-Heiani Sol Hamed suture; HSZ = Hamisana shear zone; NS = Nakasib suture; OSZ = Oko shear zone. Background is Google Satellite imagery from which lineaments have been drawn at 1:500000 scale. The extent of Figure 3-1c is indicated. Geographic coordinates are reported as WGS 84. **c** Geological map of the central Keraf suture (KS), from Ahmed Suliman (2000) and Bailo et al. (2003). The northern, central and southern KS limits are provided. "KPTA" stands for the Keraf Pre-Tectonic Assemblage described by Ahmed Suliman (2000) gathering all lithologies within the KS. The Block 15 exploration license hosts the Gabgaba gold district which this study focuses on. The extent of Figure 3-2 is indicated. Geographic coordinates are reported as WGS 84.

D_x	D_x-related structures	Deformation events (Ahmed Suliman, 2000)*
D_2 (< 580 Ma) **Minor gold event?**	**Any consistent significance at regional scale?** Rare north-striking east-dipping brittle F_2 fault planes reactivating C_{1b} shear zones. L_2 slickenlines plunging along the dip direction and stepped slip planes indicating top east-to-the-east normal-slip kinematics.	*None.* It is however worth noticing that north-striking normal faults are visible in the northeasternmost Saharan meta-craton, resulting from the tectonic collapse at the very end of the convergence between the ANS and the Saharan meta-craton (Denkler et al., 1994; Harms et al., 1994; Abdelsalam et al., 2003).
D_{1b} (*ca.* 640-580 Ma) **Major gold event**	**Northwest-orientated oblique convergence, Keraf strike-slip shearing** Ductile-brittle coaxial-dominated general shear accommodating weak, non-coaxial, sinistral lateral displacement. From discrete, m-scale, brittle C_{1b} strike-slip faults to several km-scale C_{1b} shear zones and emplacement of a subvertical C_{1b}/S_{1b} penetrative shear band cleavage. Evidence for a dominant sinistral (block west-to-the-south) strike-slip shearing.	*$D_{4\text{-}AS}$:* brittle, northwest-orientated, sinistral Keraf transpression resulting from the translation of the northwest-orientated oblique collision between the future ANS and the Saharan meta-craton. Presence of conjugate sinistral northwest- and dextral northeast-striking strike-slip faults affecting all previous structures. **$D_{4\text{-}AS}$ dominates the structural setting of the southern KS.**
	No corresponding structure observed in our study.	*$D_{3\text{-}AS}$:* roughly east-trending, symmetric, open folds superimposed over inherited fold patterns and are mostly visible from satellite imagery (Abdelsalam et al., 1995).
D_{1a} (*ca.* 700-640 Ma)	**Northwest-orientated oblique convergence, Keraf suturing** Main ductile deformation stage controlling the regional structural framework. Formation of a roughly north-striking gently east-dipping S_{1a} penetrative cleavage and gneissic foliation affecting pre- to syn-tectonic meta-volcanosediments and intrusive bodies, respectively. The lithological contacts of these units also tends to get parallel to S_{1a} planes.	*$D_{2\text{-}AS}$:* ongoing Keraf suturing expressed by outcrop to regional-scale north-striking west-verging axial plane folds affecting the main penetrative cleavage in low-grade meta-sediments and ophiolites, fold interference and crenulation. *$D_{1\text{-}AS}$:* ductile deformation controlling the northern KS regional structural framework related to west-verging thrusting of the ANS upon the Saharan meta-craton. The main related structures are thrusts and folds visible at any scale and more or less affected by subsequent folding and strike-slip shearing at variable scales.

Table 3-1 ***(continued)***

D_x	D_x-related structures	Deformation events (Ahmed Suliman, 2000)*
D_{1a} (*ca.* 700-640 Ma)	Rare evidence for a southeast-gently plunging L_{1a} stretching lineation along S_{1a} planes (kinematics?).	The related penetrative axial plane cleavage is the main planar fabric observed throughout the area and transposes the primary bedding in meta-sediments. The gently east-dipping main penetrative cleavage is thought to result from axial plan cleavage development together with a north-striking axial plane folding episode with a subvertical fold axis. Such folds, despite their several km wavelength according to Ahmed Suliman (2000), have not been observed during this study. **$D_{1\text{-}AS}$ and $D_{2\text{-}AS}$ dominate the structural setting of the northern KS.**

** Deformation episodes in the literature are indexed from $D_{1\text{-}AS}$ to $D_{4\text{-}AS}$ instead of D_1 to D_4 from the original work by Ahmed Suliman (2000), to avoid confusion with deformation indexing in this study. Rough age bracketing for each deformation stage is provided and discussed in the text. Deformation stages that relate to gold mineralization are indicated. Dashed lines indicate that D_{1a} and D_{1b} deformation stages are part of a single, prolonged, progressive deformation event whereas plain line indicates that D_2 is an independent deformation episode.*

Table 3-1: Summary of the D_{1a}-D_{1b} and D_2 deformation episodes unraveled across the central Keraf suture.

3. Lithologies, structures and gold mineralization of the central Keraf suture

The geological map of the investigated area is available in Figure 3-2a. Outcrops discussed in this section and illustrated by Figs. 3-4 to 3-8, 3-10 and 3-11 are located in Figure 3-2b. Their geographic coordinates and description are reported in Table 3-2. A west-southwest-trending cross-section (extent in Fig. 3-2a) has been constructed across the studied area and illustrates the relationships between lithology and the main structures (Fig. 3-3).

Outcrop ID	Easting (°)	Northing (°)	Description
#1	33.298957	20.282872	Meta-andesite
#2	33.407881	20.434828	Meta-ash to lapilli tuff
#3	33.342592	20.299510	Layered meta-sediments
#4	33.003234	20.381444	Marble ridge
#5	33.236408	20.313202	Meta-igneous rock
#6	33.112477	20.285337	Granitic pluton
#7	33.183825	20.323270	Granitic pluton with mafic xenoliths and mingling texture
#8	33.297473	20.295830	Meta-sediments
#9	33.302725	20.284508	Meta-andesite and meta-diorite
#10	33.417345	20.474591	Meta-sediments
#11	33.412464	20.467093	Meta-volcanosediments
#12	33.139907	20.358596	Meta-diorite
#13	33.095032	20.343142	Meta-diorite hosting mineralized *en échelon* quartz veins (WG03 deposit)
#14	33.292320	20.280512	Meta-sediments and mineralized quartz veins (UTM deposit)
#15	33.339023	20.304732	Granitoid-hosted mineralized quartz vein network (Central Zone deposit)
#16	33.292368	20.283458	Mineralized quartz veins and their proximal off-shoots (UTM deposit)
#17	33.236408	20.313202	Distal off-shoot of vertical mineralized veins (UTM deposit)

Table 3-2: Geographic coordinates reported as WGS 84 and brief description of the key outcrops discussed in the text.

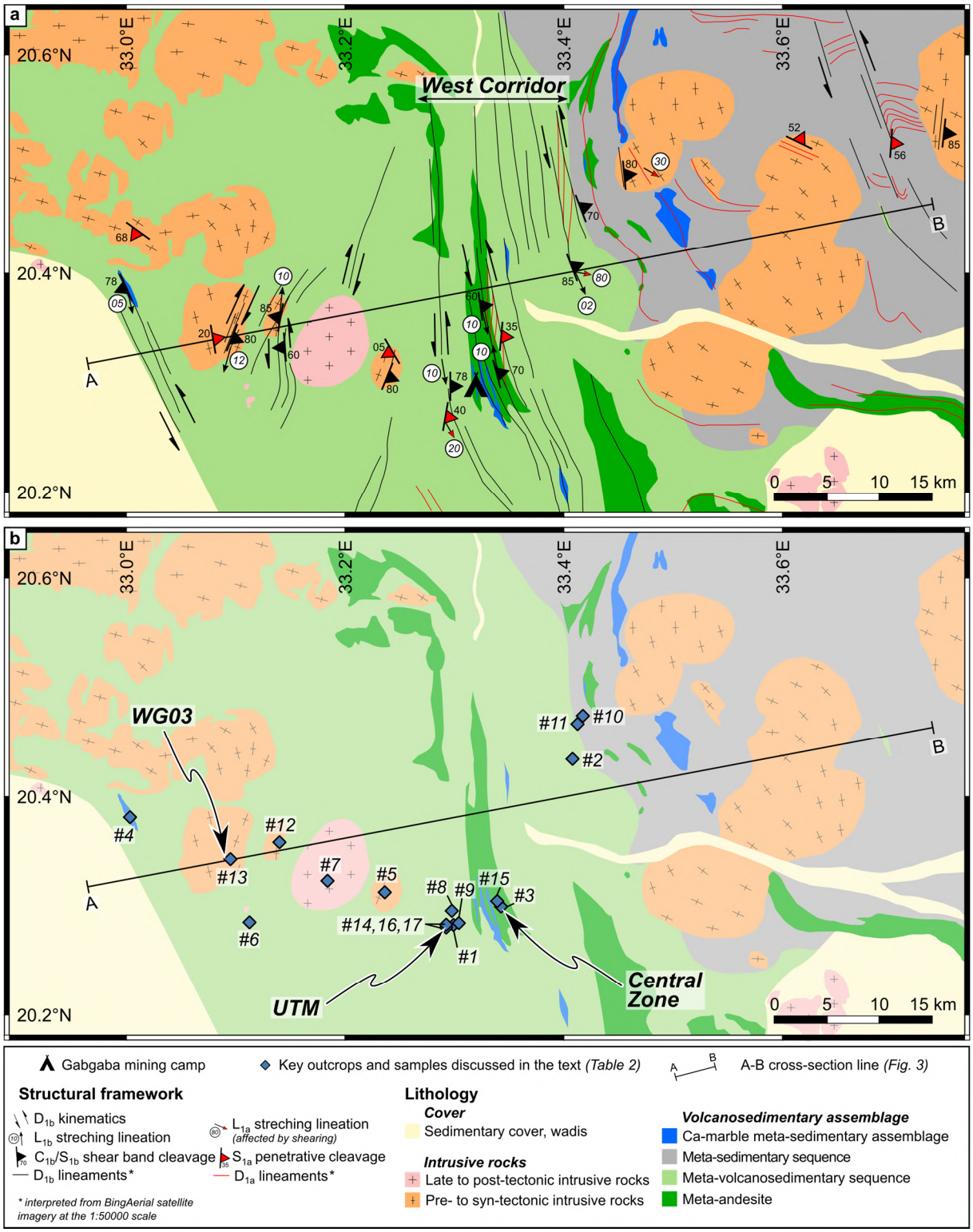


Figure 3-2: Geological map of the central Keraf suture hosting the Gabgaba gold district, adapted after Managem (2011) and relying on field observations. **a** Field structural observations and A-B cross-section line (Fig. 3-3). **b** Gabgaba gold deposits (UTM, WG03 and Central Zone) and locations of key outcrops and samples discussed in this study. Geographic coordinates are reported as WGS 84.

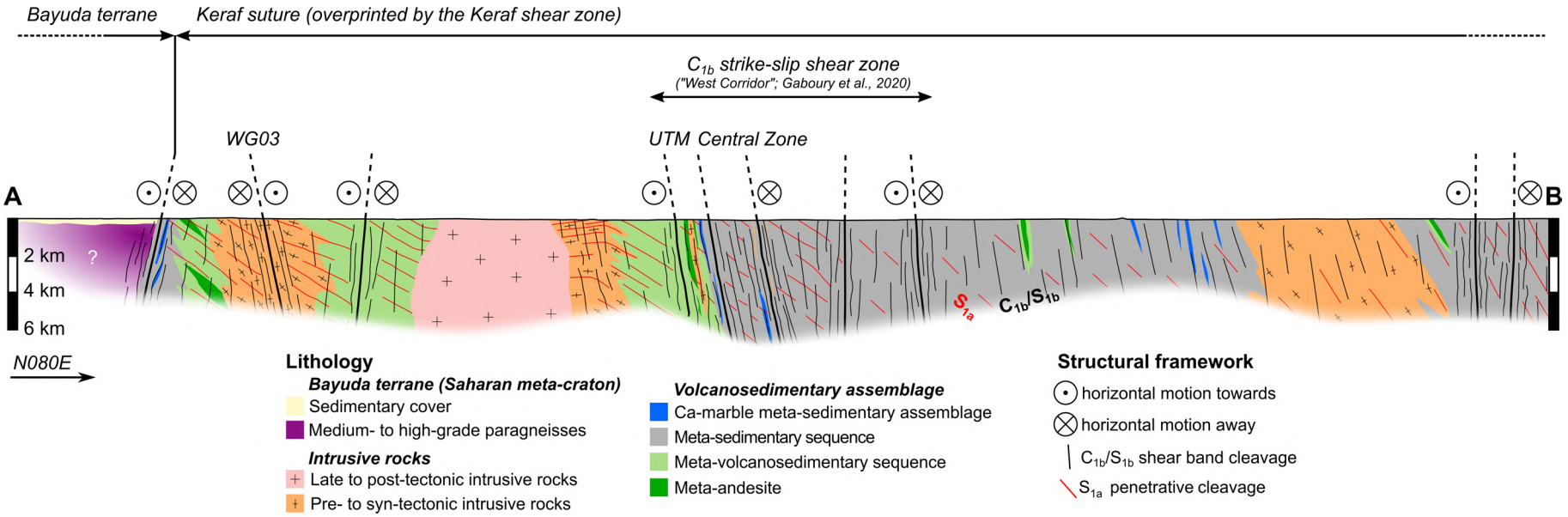


Figure 3-3: A-B crustal cross-section through the central Keraf suture. See Figure 3-2 for location.

3.1. Lithological framework of the central Keraf suture

The pre-, syn- and post-tectonic nature of lithologies observed in the central KS is relative to suturing tectonics. The pre- to syn-tectonic meta-volcanosedimentary assemblage is predominant (Figs. 3-1c, 3-2a) and is composed of:

(i) A meta-volcanoclastic sequence characterized by low-grade schistose meta-andesite and ash to lapilli tuffs (Fig. 3-4a, b). Andesite crops out well and its contact with the volcanoclastics is gradual to sharp, parallel to the main penetrative fabric (Fig. 3-3).

(ii) Meta-sediments which are mostly composed of schistose turbidites. The bedding is visible where silty layers alternate with silty to sandy layers and it is transposed (*i.e.*, its original orientation is completely or nearly completely rotated to the plane of the deformation affecting it) along the main penetrative fabric in most places (Figs. 3-3, 3-4c). Meta-sediments are interlayered with meta-volcanoclastic rocks and do not necessarily crop out well. The transition from one unit to another is gradual and difficult to map from regional to outcrop scales (Figs. 3-1c, 3-2a, 3-3). Meta-turbidites alternate with Ca-marble ridges that form outcrop- to regional-scale reliefs with sharp contacts parallel to the main penetrative cleavage (Figs. 3-1c, 3-2a, 3-3, 3-4d).

Pre- to syn-tectonic meta-diorite to tonalite-trondhjemite-granodiorite (TTG) intrusive bodies are enclosed within this extensive meta-volcanosedimentary sequence (Figs. 3-1c, 3-2a, 3-4e). Outcropping pre- to syn-tectonic intrusives are affected by a gneissic foliation that is representative of the regional penetrative fabric (Fig. 3-3). Their contacts with the surrounding meta-volcanosedimentary rocks are sharp but sheared along the regional penetrative fabric (Figs. 3-2a, 3-3, 3-4e). Post-tectonic coarse granitic intrusive bodies typically crop out as up to tens of m-high piles composed of up to 10 m-large boulders (Fig. 3-4f). These rocks show no anisotropy at macroscopic scale. Granite plutons display local heterogeneities with the presence of mafic xenoliths and micro-granular enclaves with feldspar pheno- or xenocrysts (inset in Fig. 3-4f). Their contacts with surrounding rocks are sharp and cut across every inherited fabric (Fig. 3-3).

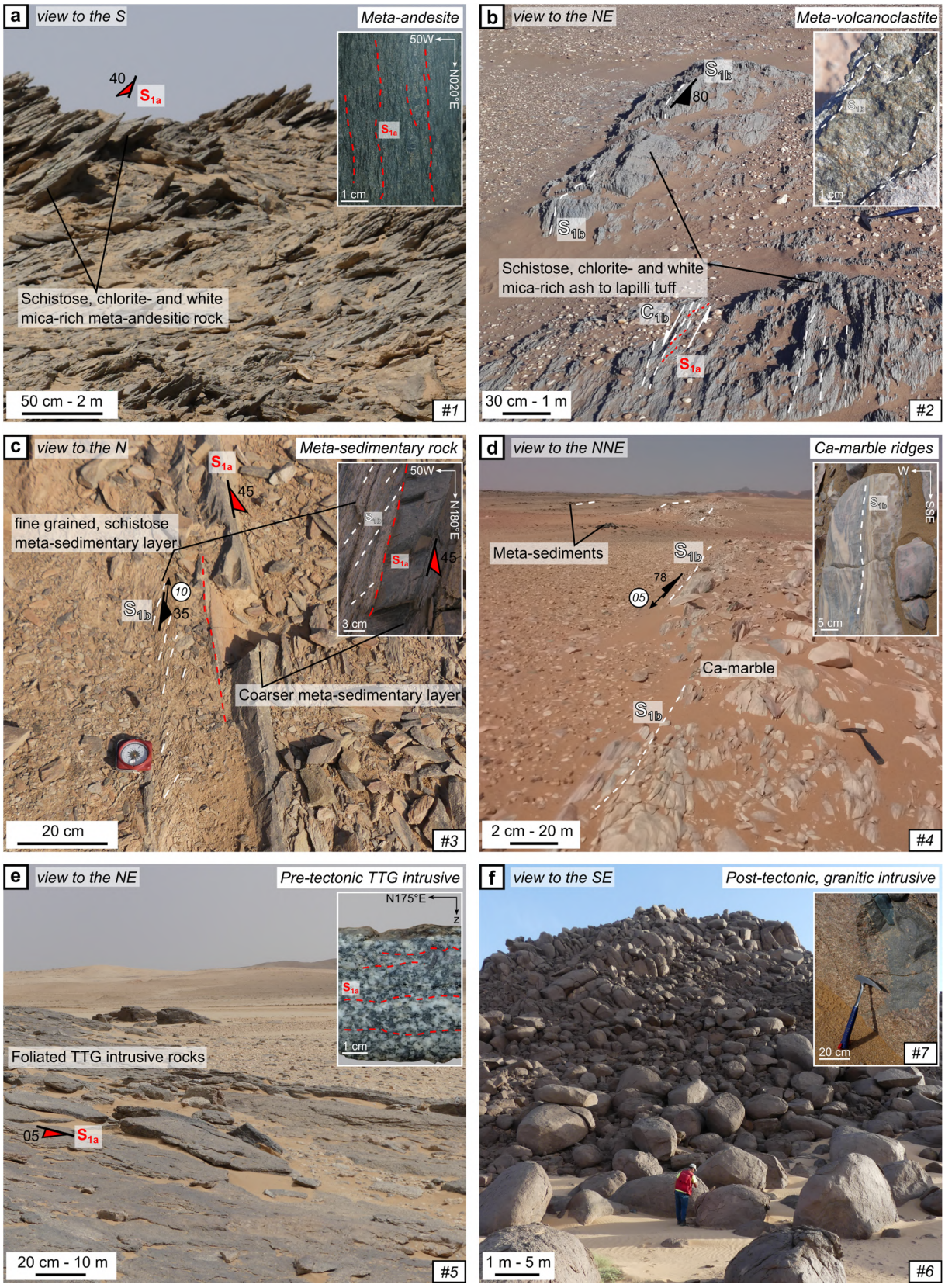


Figure 3-4: Lithologies of the central Keraf suture. Outcrop locations and structural legend as in Figure 3-2. **a** Meta-andesite. **b** Meta-volcanoclastites. **c** Meta-sediments. **d** Ca-marble ridges. **e** Pre-tectonic intrusive rocks. **f** Post-tectonic intrusive bodies.

3.2. Structural framework of the central Keraf suture

Three deformation stages and phases (D_{1a}, D_{1b} and D_2) have been defined. The *"stage" vs "phase"* nomenclature and indexing of deformation events relies on the distinction between progressive and discrete deformation (Fossen et al., 2019), which is discussed in subsection 4.1. The brittle *vs* ductile nature of the associated structures, which is a scale-sensitive description (Rutter, 1986; Snoke et al., 1998), is distinguished on field-scale observation. Similar to the approach followed by Perret et al. (2020), such nomenclature is used *"to distinguish the dominant manner by which deformation occurs"* (Tikoff et al., 2013): brittle deformation for faulting and fracturing and ductile deformation for penetrative fabric development and folding (Twiss and Moores, 2007). Table 3-1 summarizes D_{1a}-, D_{1b}- to D_2-related structures, as well as their correlation with the $D_{1\text{-}AS}$ to $D_{4\text{-}AS}$ tectonic history from literature.

3.2.1. Ductile D_{1a} deformation stage

A rare S_0 bedding is observed in meta-turbidites, highlighted by compositional layering between coarser-grained meta-greywackes alternating with finer-grained phyllitic beds (Figs. 3-4c, 3-5a and b). Considering rare outcrops, S_0 is the dominant planar fabric although it can be weakly to moderately crenulated along the northwest-striking S_{1a} crenulation cleavage (Fig. 3-5a, b).

At the studied area scale, the S_{1a} fabric is the dominant planar fabric and affects every pre- to syn-tectonic lithological units (Fig. 3-2a). In most places where meta-sediments crop out, the S_0 bedding is hardly visible because its orientation rotates to get parallel, *i.e.,* transposed, to the S_{1a} crenulation cleavage, resulting in a $S_{0/1a}$ composite fabric (Figs. 3-4c, 3-5a and b). S_{1a} is also the gneissic foliation affecting igneous intrusive bodies and the penetrative cleavage affecting andesitic rocks (Figs. 3-2a, 3-4a, 3-6a and b) and volcanosediments (Figs. 3-2a, 3-6c and d). Where not affected by subsequent deformation, the S_{1a} penetrative fabric is north-northwest- to north-northeast-striking

and gently dips eastwards whereas it is subvertical and strikes north-northwestwards where rotated by later C_{1b} shear zones (Fig. 3-6e). A stretching lineation L_{1a} is hardly visible along S_{1a} planes and weakly highlighted by stretched clasts in meta-lapilli tuffs (Fig. 3-6d). Along planes not affected by subsequent deformation, L_{1a} gently plunges southeastwards whereas it steepens where S_{1a} orientation gets closer to subsequent C_{1b}/S_{1b} shear band cleavage (Fig. 3-6f). No shear sense indicator is visible.

3.2.2. Ductile-brittle D_{1b} strike-slip shearing stage

D_{1b} structures range from regional- to outcrop-scale ductile shear zones (Figs. 3-2a, 3-3, 3-6d, 3-7a, b, and c) to local, discrete brittle faults (Figs. 3-5c, d, e and f, 3-6c). Depending on the D_{1b} strain intensity and the deformed rock rheology, the C_{1b}/S_{1b} shear band cleavage (or C_{1b}-type shear band; Passchier and Trouw, 2005) penetrates only the less competent meta-sedimentary rocks. With increasing strain: (i) the regional penetrative fabric S_{1a} is preserved (Fig. 3-4c) and locally cut across by discrete, subvertical, weakly expressed C_{1b} strike-slip faults (Figs. 3-5c, d, e and f, 3-6c); (ii) ductile-brittle C_{1b}-type shear bands are characterized from outcrop to regional scales (Figs. 3-2a, 3-3, 3-4b, 3-6d); and (iii) S_{1b} locally becomes the main penetrative fabric in C_{1b} shear zones where there is a very low obliquity between S_{1b} and C_{1b} planes (Figs. 3-3, 3-7c and d). In the latter configuration, lithological contacts and the S_{1a} cleavage have rotated along C_{1b} planes (Figs. 3-2a, 3-3, 3-5d).

There is evidence for a very limited lateral displacement along C_{1b} shear zones which does not exceed a few centimeters at the outcrop scale, even in marbles which easily flow under low strain conditions yet (Figs. 3-2a, 3-4b, 3-5e and f, 3-7a). No discrete individual shear accommodating relatively important lateral offsets has been noticed neither, suggesting that C_{1b} shear zones are homogeneous. Nevertheless, C_{1b} shear zones likely accommodate a weak, non-coaxial, strike-slip component (Figs. 3-2a, 3) as suggested by (i) the relatively short left-lateral offset along C_{1b} strike-slip shears (Fig. 3-5c, d, e, f), (ii) C_{1b}-type shear band asymmetry (Figs. 3-2a, 3-6c), (iii) the subtle presence of

subhorizontal stepped slip markers along C_{1b} planes (Figs. 3-6d, 3-7c), (iv) drag fold asymmetry in flowing marble layers (Fig. 3-7a, b) and (v) the subhorizontal orientation of the L_{1b} stretching or biotite-amphibole mineral lineation along the C_{1b} planes (Figs. 3-2a, 3-7b, c and d). The C_{1b} shear zones are mostly subvertical and display two conjugate sets (Fig. 3-7e, f). The main C_{1b} strike-slip shears are north-northwest- to north-striking and accommodate sinistral strike-slip shearing (Figs. 3-2a, 3-3, 3-6c, 3-7d). North-northeast- to northeast-striking conjugate structures are less visible and display dextral kinematics (Figs. 3-2a, 3, 3-7e and f), relying on outcrop-scale shear sense indicators described above and deflection of D_{1a}-related lineaments visible in satellite imagery within C_{1b} shear zones (Fig. 3-2a).

3.2.3. Late brittle D_2 normal faulting phase

A late, weakly expressed, brittle D_2 deformation episode has been identified in the UTM area. It is characterized by the local reactivation of the C_{1b} shear zones as normal faults (Fig. 3-8). Shear zones reactivated as normal faults that have been spotted in this study preferentially separate rock units with a strong rheological contrast, *e.g.,* between meta-diorite or granitoid intrusion and meta-volcanosediments (Fig. 3-8a). F_2 faults are north-striking and steeply east-dipping, similarly to the C_{1b} shear zone orientation in the UTM area (Figs. 3-2, 3-8a). Weakly expressed L_2 slickenlines plunging along the dip direction and stepped slip features are visible on fault planes and indicate top-to-the-east normal faulting kinematics (Fig. 3-8b).

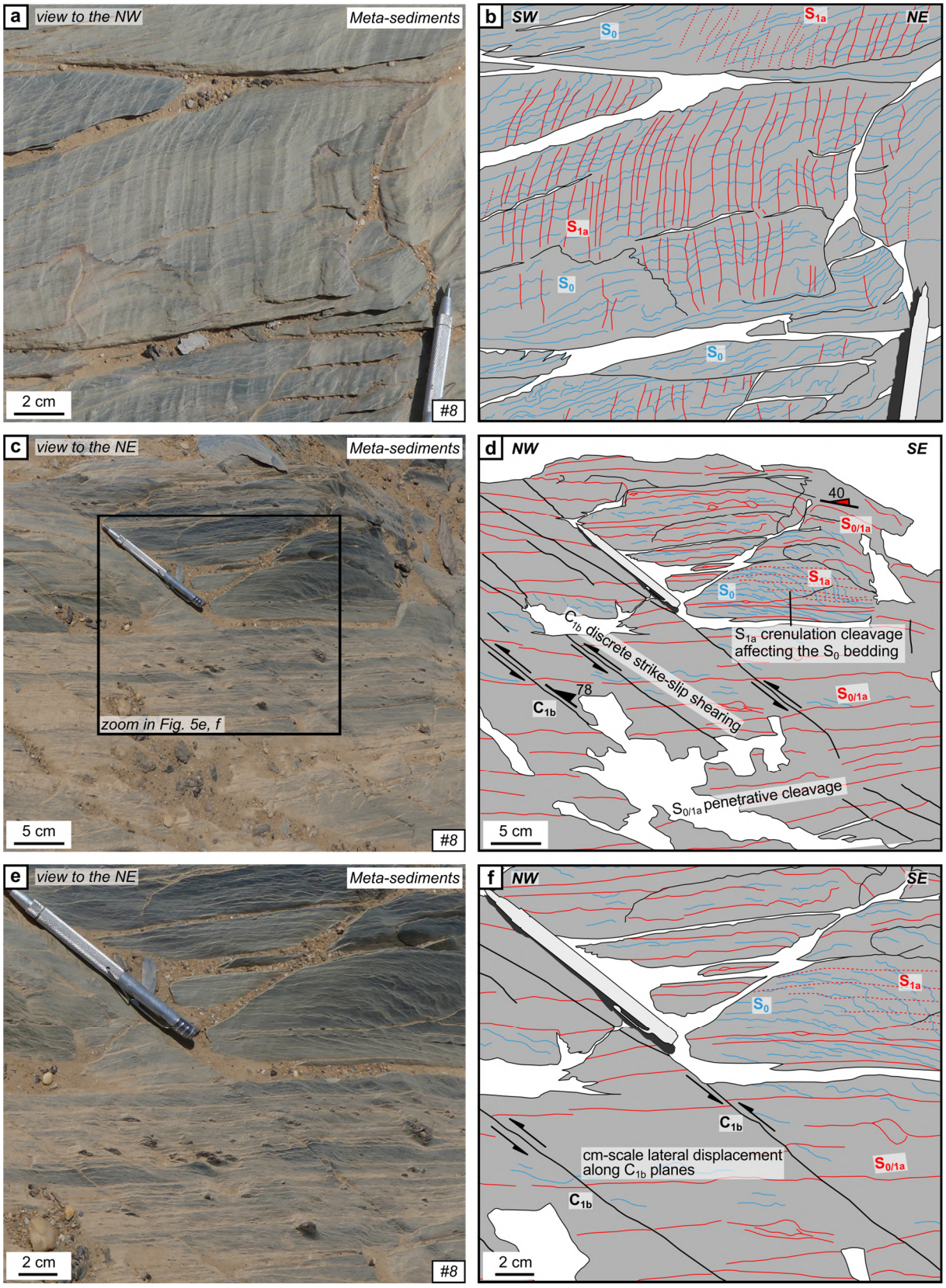


Figure 3-5: Outcrop expression of the S_0 bedding and relationships with the D_{1a}-D_{1b} deformation stages in meta-sediments. See detailed caption on p. 226.

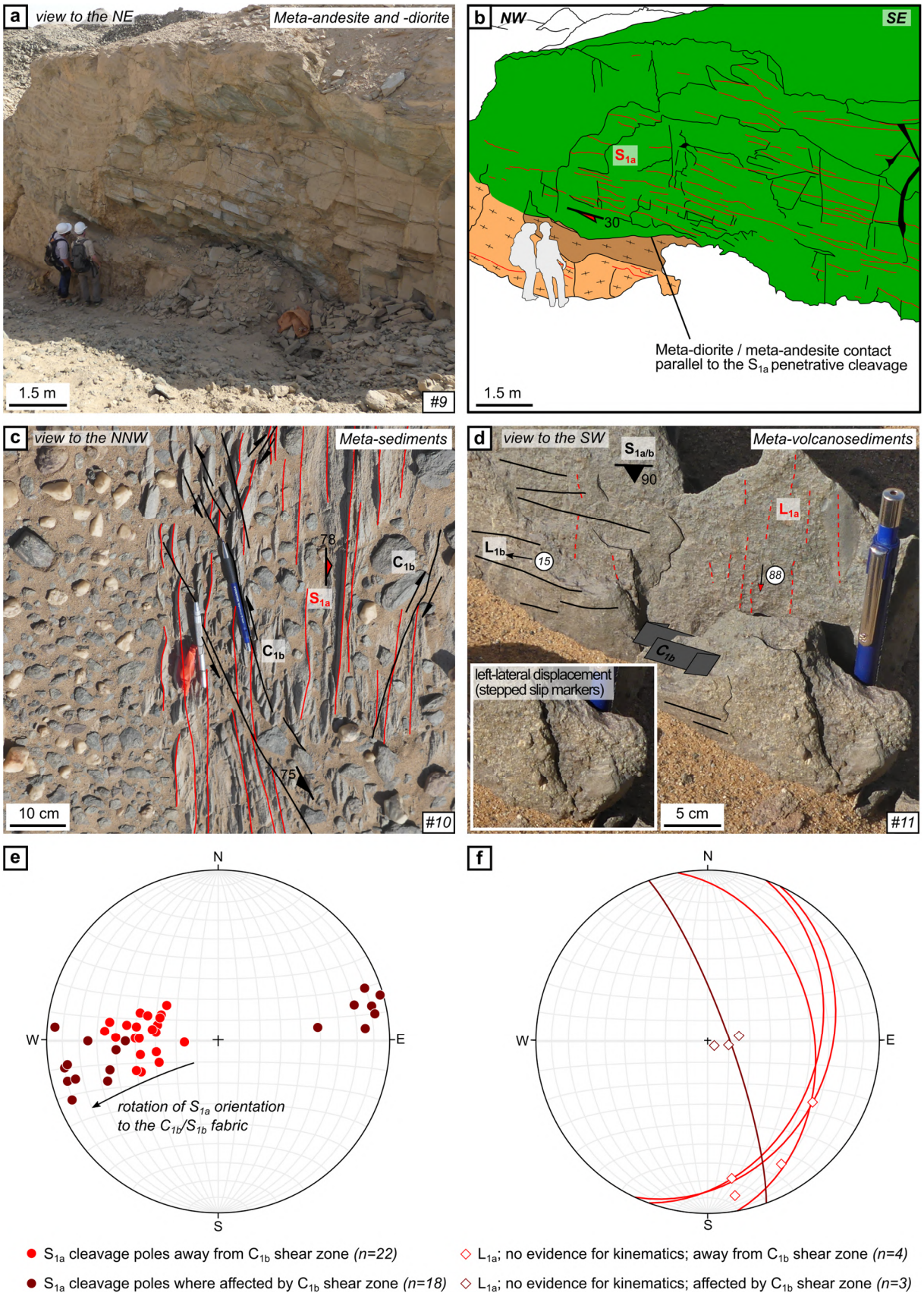


Figure 3-6: Outcrop expression of the regional D_{1a} deformation stage in the Keraf pre-tectonic assemblage rocks, relationships with the D_{1b} deformation stage and stereonet analysis. See detailed caption on p. 226.

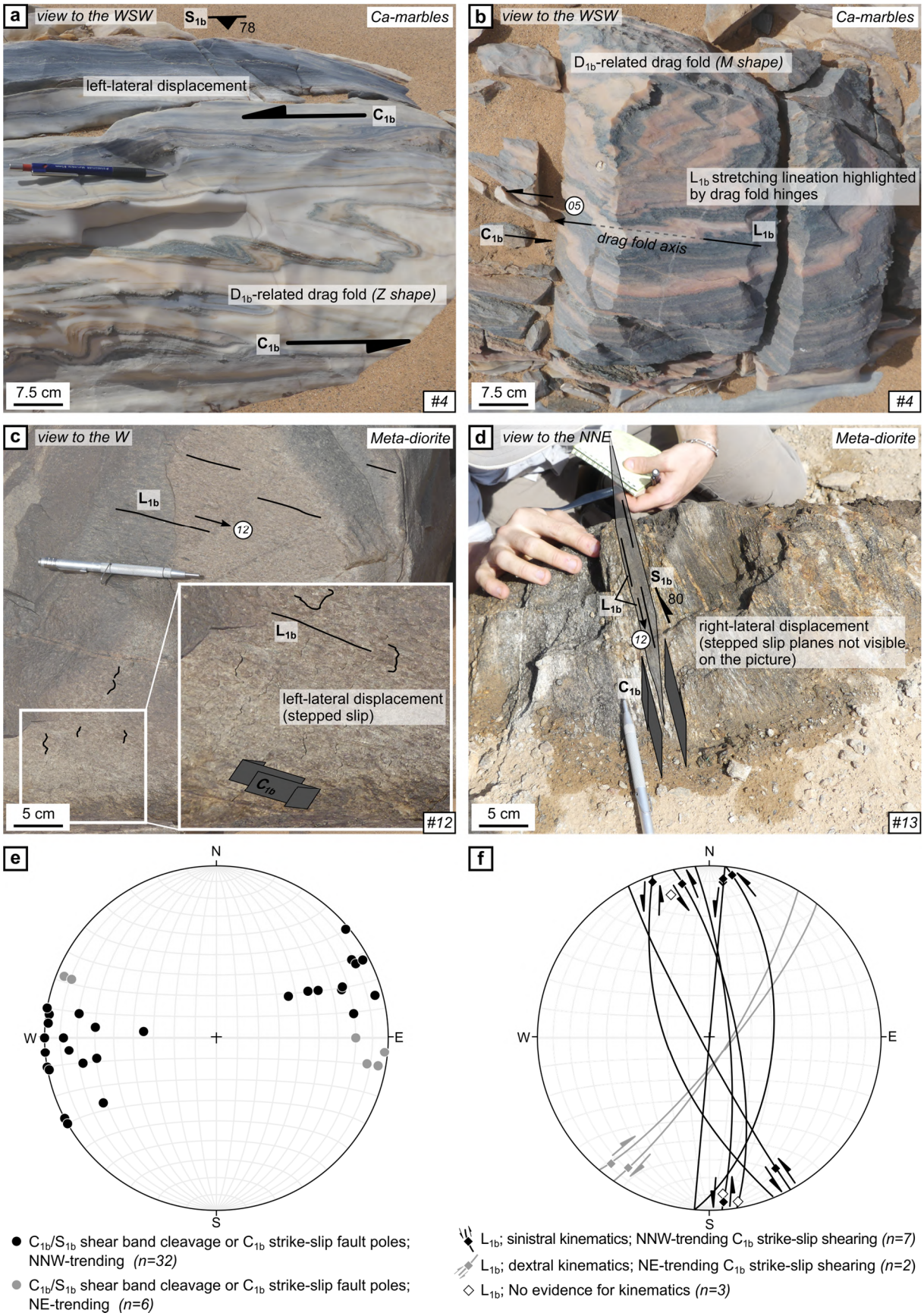


Figure 3-7: Outcrop expression of the D_{1b} deformation stage in the Keraf pre-tectonic assemblage rocks and stereonet analysis. See detailed caption on p. 226.

Figure 3-5 (p. 223): Outcrop expression of the S_0 bedding and relationships with the D_{1a}-D_{1b} deformation stages in meta-sediments. Outcrop locations and geological legend as in Figure 3-2. **a** and **b** Outcrop photograph and interpretation. The S_0 bedding is the dominant fabric and is weakly to moderately crenulated along the S_{1a} crenulation cleavage. **c** and d Outcrop photograph and interpretation. The S_0 bedding is strongly rotated to transposed along S_{1a} crenulation planes, resulting into a $S_{0/1a}$ penetrative cleavage. This fabric is cut across by discrete, C_{1b} strike-slip faults displaying sinistral kinematics, although lateral displacement is almost invisible at this scale. Rarer north- to north-northeast-striking dextral C_{1b} strike-slip faults are also visible. **e** and **f** Outcrop photograph and interpretation, zoom of the central part of photograph c. This zoom better illustrates the < cm to cm-scale left-lateral displacement along north-northwest-striking C_{1b} strike-slip faults.

Figure 3-6 (p. 224): Outcrop expression of the regional D_{1a} deformation stage in the Keraf pre-tectonic assemblage rocks, relationships with the D_{1b} deformation stage and stereonet analysis. Outcrop locations and geological legend as in Figure 3-2. **a** and **b** Outcrop photograph and interpretation. The schistose meta-andesite and foliated meta-diorite are affected by the S_{1a} regional penetrative fabric. Their contact is also parallel to this gently east-dipping fabric. **c** The S_{1a} penetrative fabric is cut across by subvertical C_{1b}-type shear bands. The weak S_{1a} orientation deflection close to C_{1b} planes indicates a cm-long left-lateral displacement. **d** The L_{1a} stretching lineation is weakly highlighted by stretched clasts in steepened S_{1a} planes within a C_{1b} shear zone. The S_{1a} fabric is transposed along the C_{1b}/S_{1b} shear band cleavage. Subhorizontal L_{1b} slickenlines associated with sinistral C_{1b} strike-slip shearing are visible. **e** S_{1a} distribution in the central Keraf suture. **f** L_{1a} distribution in the central Keraf suture.

Figure 3-7 (p. 225): Outcrop expression of the D_{1b} deformation stage in the Keraf pre-tectonic assemblage rocks and stereonet analysis. Outcrop locations and structural legend as in Figure 3-2. **a** and **b** Marble ridges flow in a ductile way along the steeply east-northeast-dipping C_{1b}/S_{1b} shear band cleavage. Internal drag folds highlight sinistral kinematics for the C_{1b} strike-slip shearing but the lateral displacement is very low, i.e., <50 cm. **c** The presence of a subhorizontal L_{1b} stretching lineation and stepped slip markers in C_{1b} planes highlights a left-lateral displacement. **d** The main penetrative cleavage is S_{1b} which is here parallel to C_{1b} orientation. A subhorizontal L_{1b} stretching lineation and stepped slip markers in C_{1b} planes highlight a right-lateral displacement, not visible on the photograph. **e** S_{1b} and C_{1b} distribution in the central Keraf suture. **f** L_{1b} distribution in the central Keraf suture.

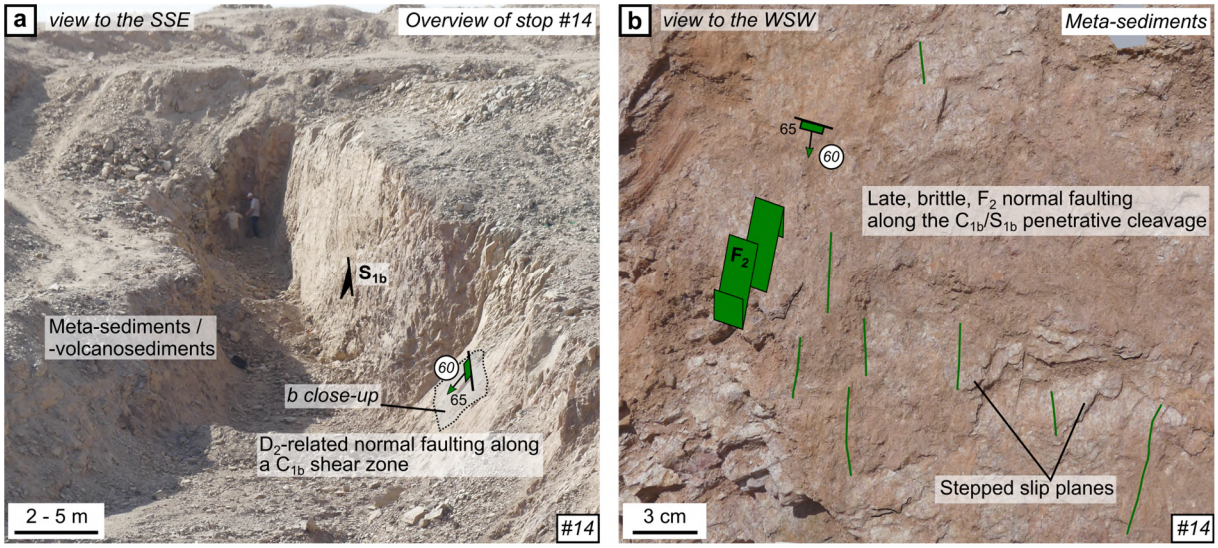


Figure 3-8: Outcrop expression of the D_2 deformation phase in meta-sediments. Outcrop location as in Figure 3-2. **a** Overview of the area investigated in Figure 3-8b. **b** C_{1b}/S_{1b} shear band cleavage is locally reactivated by brittle top-to-the-east F_2 normal faulting characterized by dip-plunging L_2 slickenline.

3.3. Mineralized structures of the Gabgaba gold district

Deposit-scale geological maps of the WG03, Central Zone and UTM deposits are given in Figure 3-9a, b and c, respectively. Gold mineralized structures are illustrated from observations on outcrop, drill core and hand samples and thin section (Figs. 3-10 to 3-12, respectively). Stereonet structural analyses for the main gold-bearing structures at WG03 and Central Zone deposits are provided in Figure 3-13.

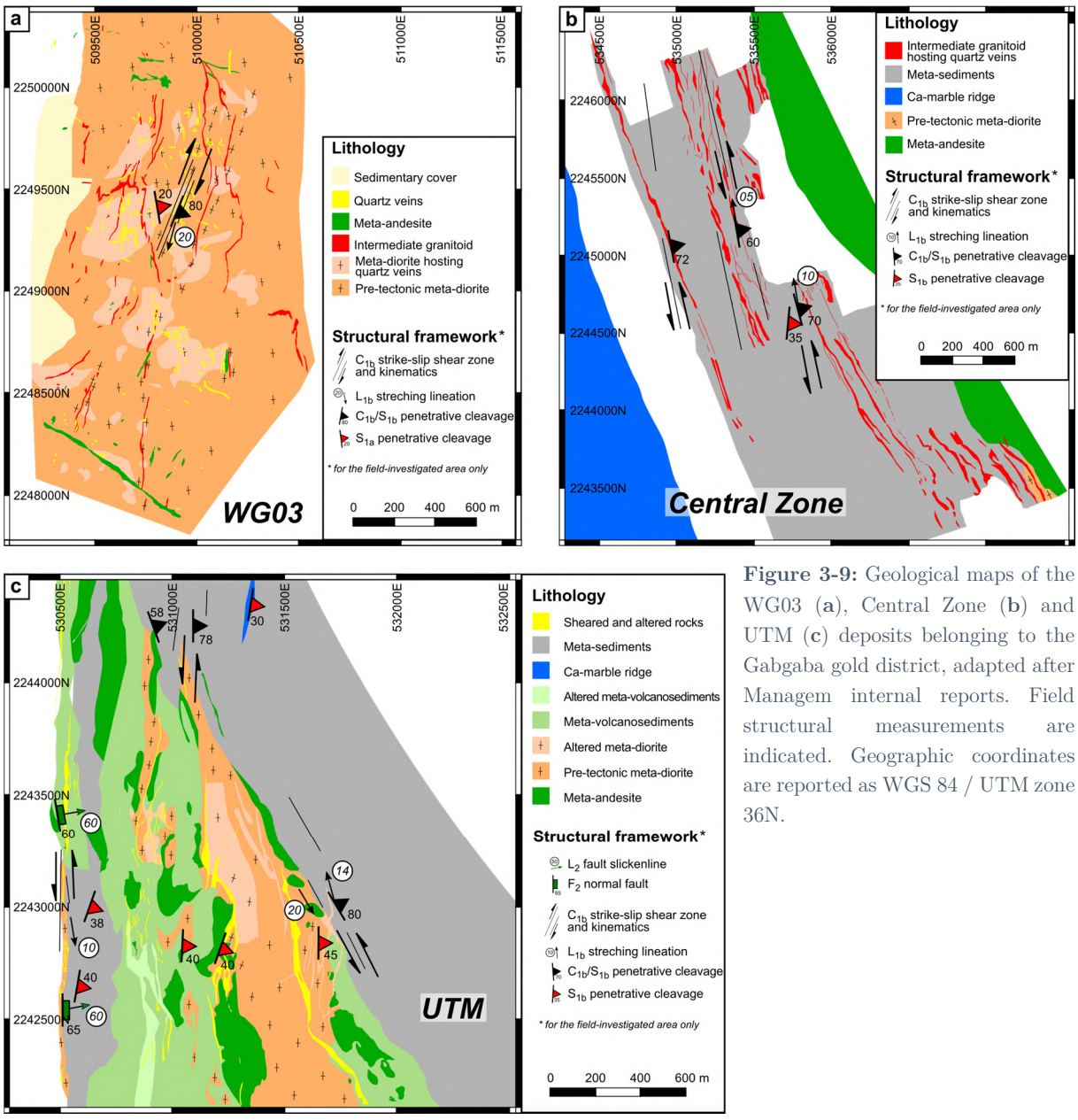


Figure 3-9: Geological maps of the WG03 (**a**), Central Zone (**b**) and UTM (**c**) deposits belonging to the Gabgaba gold district, adapted after Managem internal reports. Field structural measurements are indicated. Geographic coordinates are reported as WGS 84 / UTM zone 36N.

3.3.1. WG03 gold deposit

The WG03 deposit is located ~15 km west to the Gabgaba mining camp (Fig. 3-2b). It is hosted by a foliated pre-tectonic meta-diorite body affected by the north-northwest-striking gently east-dipping S_{1a} regional penetrative fabric (Figs. 3-9a, 3-10a). The meta-diorite intrusion is also cut across by numerous m-wide, northeast-striking, dextral C_{1b} shear zones (Figs. 3-9a, 3-10a) forming a km-wide shear zone at regional scale (Figs. 3-2a, 3, 3-10a). The host rock mineral assemblage mostly consists of amphibole, plagioclase and biotite, with minor quartz, titanite, magnetite and ilmenite (Figs. 3-11a, 3-12a and b).

Two gold mineralization events are observed at the WG03 gold deposit. The earliest mineralized features are not visible at outcrop scale. They consist of up to several cm-wide plagioclase-rich mineral assemblage segregated from the meta-diorite host rock (Fig. 3-11a). It is worth noticing that the use of the term "segregation" is used in a descriptive way below and does not imply anything about magmatic-anatexis petrological processes. The contact between these features and the gangue mineral assemblage is progressive and no sharp limit from one domain to another can be drawn at macroscopic and microscopic scales (Figs. 3-11a, 3-12a). The presence of these segregation features is associated with crystallization of plagioclase feldspar phenocrysts up to 10 cm away within the finer-grained amphibole-plagioclase-biotite mineral gangue (Fig. 3-11a, right). Pyrrhotite also forms at the transition between segregation features and host rock, associated with biotite and plagioclase (Fig. 3-12b). Where later gold-bearing structures are not visible, the presence of such plagioclase-rich patches correlates with gold grades ranging from 0.10 up to 1 g/t Au (Figs. 3-11a, 3-12a and b). However, no free gold grain nor micro-particle has been observed for such samples in thin section.

The subsequent gold-bearing structures are the most frequent at the WG03 deposit and characterized at outcrop scale. They are hydrothermal quartz-rich vein arrays cutting across the S_{1a} gneissic foliation and shaped like Type II *en échelon* veins (Fig. 3-

10a, b; Bons et al., 2012). This hydrothermal vein set sharply cuts across the meta-diorite gangue mineral assemblage and segregation features described above (Figs. 3-11b, 3-12c). Free gold grains are coeval with minor carbonation and moderate silicification spreading out from the vein margins (Fig. 3-12c, d). Gold grades range from <1 up to 30 g/t Au where the veins are observed, suggesting that the crosscutting quartz veining is the main gold mineralization event at the WG03 deposit (Figs. 3-11b, 3-12c and d). Despite the quartz internal crystal morphology is unclear in veins, the presence of coarse-grained quartz and the *en échelon* geometry of the vein array suggest that these veins are dilational (Figs. 3-10b, 3-11b, 3-12c). It means that they likely result from precipitation of minerals from fluids circulating in mode I-extensional fractures (Bons et al., 2012). The vein orientation progressively rotates from (i) subhorizontal to (ii) gently northeast-dipping and (iii) subvertical, north-northeast-striking with increasing deformation in lenses between C_{1b} shear zones, *i.e.,* veins progressively rotate parallel to C_{1b} planes and get transposed along them (Fig. 3-13a).

3.3.2. Central Zone gold deposit

The Central Zone deposit is located just east to the Gabgaba mining camp, within the several km-wide C_{1b} shear zone known as the *"West Corridor"* (Figs. 3-2a, 3-3, 3-9b). There, a subhorizontal stretching lineation L_{1b} plunges 10-12° northwards and shear sense indicators characterized the weak, left-lateral strike-slip component of the ductile-brittle shear zone (see above; Fig. 3-9b).

The gold mineralization corresponds to a well-developed vein system hosted by a network of granitoid intrusions in the Central Zone area (Fig. 3-9b). Shearing affects their contacts with surrounding meta-sediments (not illustrated in figures) but their inner part is not sheared and no penetrative fabric is visible at any scale (Figs. 3-10c, 3-11c and d, 3-12e). It is unclear whether these intrusions were injected along C_{1b} planes or are boudinaged and dismembered during D_{1b} deformation. The exact lithological nature of these granitoids remains unknown due to strong, pervasive sericitization-albitization

spreading from vein margins (Fig. 3-12e). Yet, as the major element composition of the altered granitoid is known (59 wt.% SiO_2, 19 wt.% Al_2O_3, 8 wt.% Fe_2O_3, 1 wt.% CaO, 5 wt.% Na_2O, 1 wt.% K_2O and 4 wt.% loss of ignition; unpublished data), we can approximate an intermediate to felsic nature for the unaltered protolith. The mineralized veins are a few cm up to 1 m-wide (Figs. 3-10c, 3-11c). Two sets of conjugate, connected veins are separated: the first ones are flat to gently west-northwest- or west-southwest-dipping whereas the second ones are gently east-northeast-dipping (Figs. 3-10c, 3-13b). They are composed of a quartz-ankerite-albite assemblage with a zoning from ankerite-albite-rich margins and quartz-rich core (Figs. 3-11c, 3-12e). Ankerite and albite crystals in vein display an elongate-blocky morphology perpendicular to vein walls and blocky quartz crystallization occurs as a final sealing stage (Figs. 3-11c right, 3-12e; Bons et al., 2012). It suggests that these syntaxial veins are purely dilational. Proximal pyritization of the host granitoids is associated with gold grades of about 0.1-1 g/t Au whereas up to 30 g/t Au concentration is reached where free gold is associated with quartz in veins (Figs. 3-11c and d, 3-12 e and f).

3.3.3. UTM gold deposit

The UTM deposit is located just west to the Gabgaba mining camp, within the *"West Corridor"* (Figs. 3-2a, 3-3, 3-9c). It is hosted by sheared and strongly chloritized meta-volcanosediments and foliated pre-tectonic meta-diorite intrusions (Fig. 3-9c). Granitoid intrusions similar to the ones described in the Central Zone area are visible along C_{1b} shear zones in the UTM area (Fig. 3-10d). There, late, F_2 normal faults reactivated C_{1b} shear zones along lithological-rheological contacts (Figs. 3-8a, 3-9c).

Gold-bearing quartz veins are currently being exploited at the UTM deposit. In the field, we were therefore able to approximate the gold potential of veins from how intensively they had been mined. The most important mineralized veins are subvertical, m-wide and formed along lithological-rheological contacts where F_2 normal faults are observed (Fig. 3-10d, e). These veins have never been characterized where C_{1b} shear zones

occur with no evidence for late, normal faulting reactivation. However, the genetic association between normal faulting and gold-mineralized veining remains uncertain as no kinematic evidence has been observed directly from the vein walls. Subvertical veins have off-shoots into the gently east-dipping S_{1a} cleavage affecting the surrounding meta-volcanosediments, outside from the F_2-reactivated C_{1b} shear zone (Fig. 3-10f). Off-shoots decrease in width down to a few cm at several tens of m away from the main gold-bearing, subvertical vein they spread from (Fig. 3-11e). At first sight, the mineral assemblage in mineralized veins and alteration halo at the UTM deposit is quite similar to what is observed for the Central Zone gold-bearing structures. UTM mineralized veins are quartz-ankerite-rich and somehow zoned with quartz-rich core and ankerite-rich margins (Fig. 3-11e). Veins are associated with proximal pervasive carbonation and pyritization of host rocks, whatever their lithology (Figs. 3-10e and f, 3-11e).

Unfortunately, we cannot go further with the observation of mineralization-deformation relationships at the UTM deposit. The area is indeed intensively exploited and only comprises very limited outcrops. Very few mineralized vein orientations have been measured and no reliable stereonet analysis is therefore possible. Besides, no observation on drill core and thin section has been made to better characterize relationships between macroscopic to microscopic gold-bearing structures, the related mineral assemblages and associated gold grades at the UTM deposit.

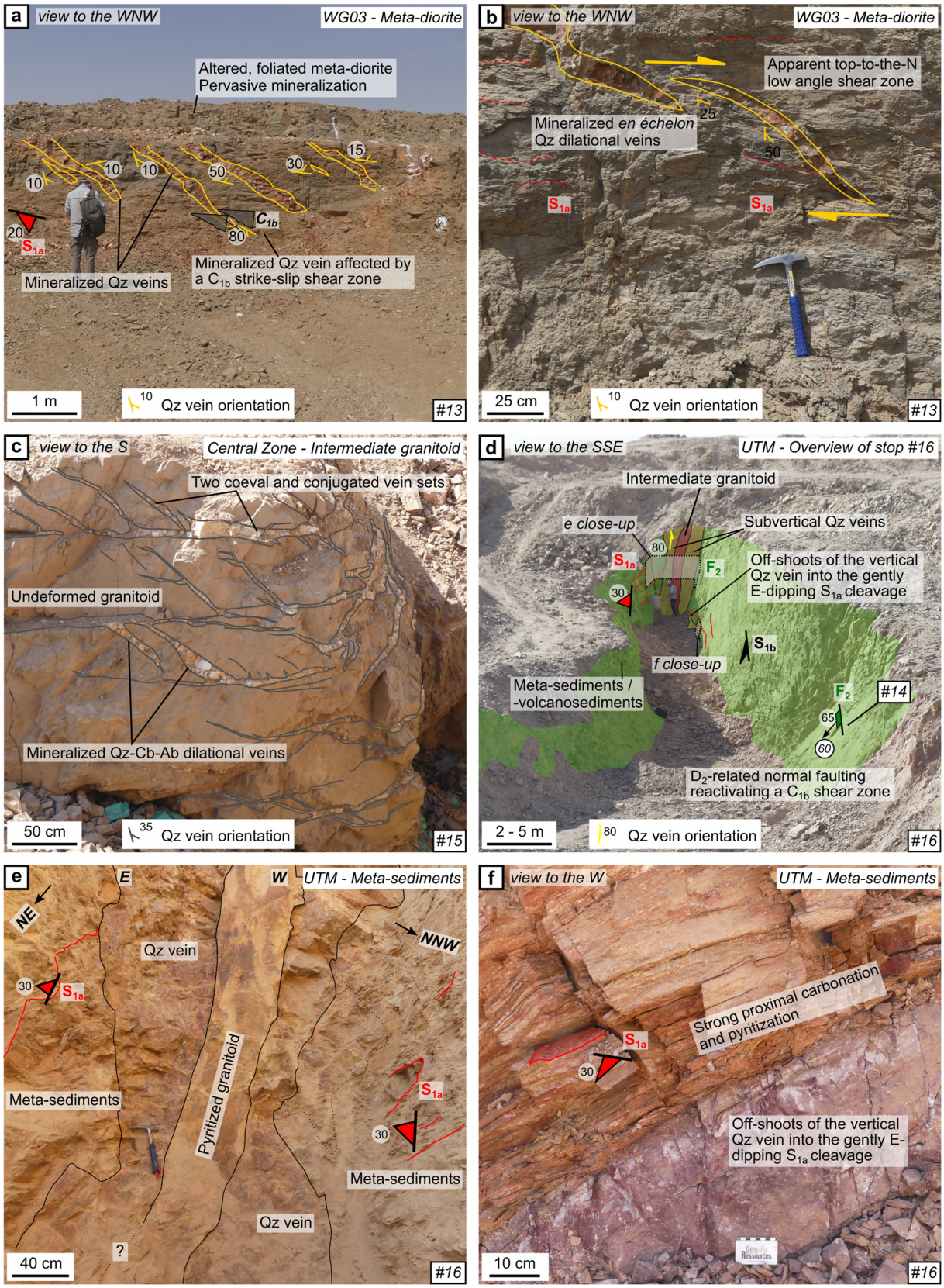


Figure 3-10: Gold-mineralized structures in outcrop at the Gabgaba gold district. See detailed caption on p. 235.

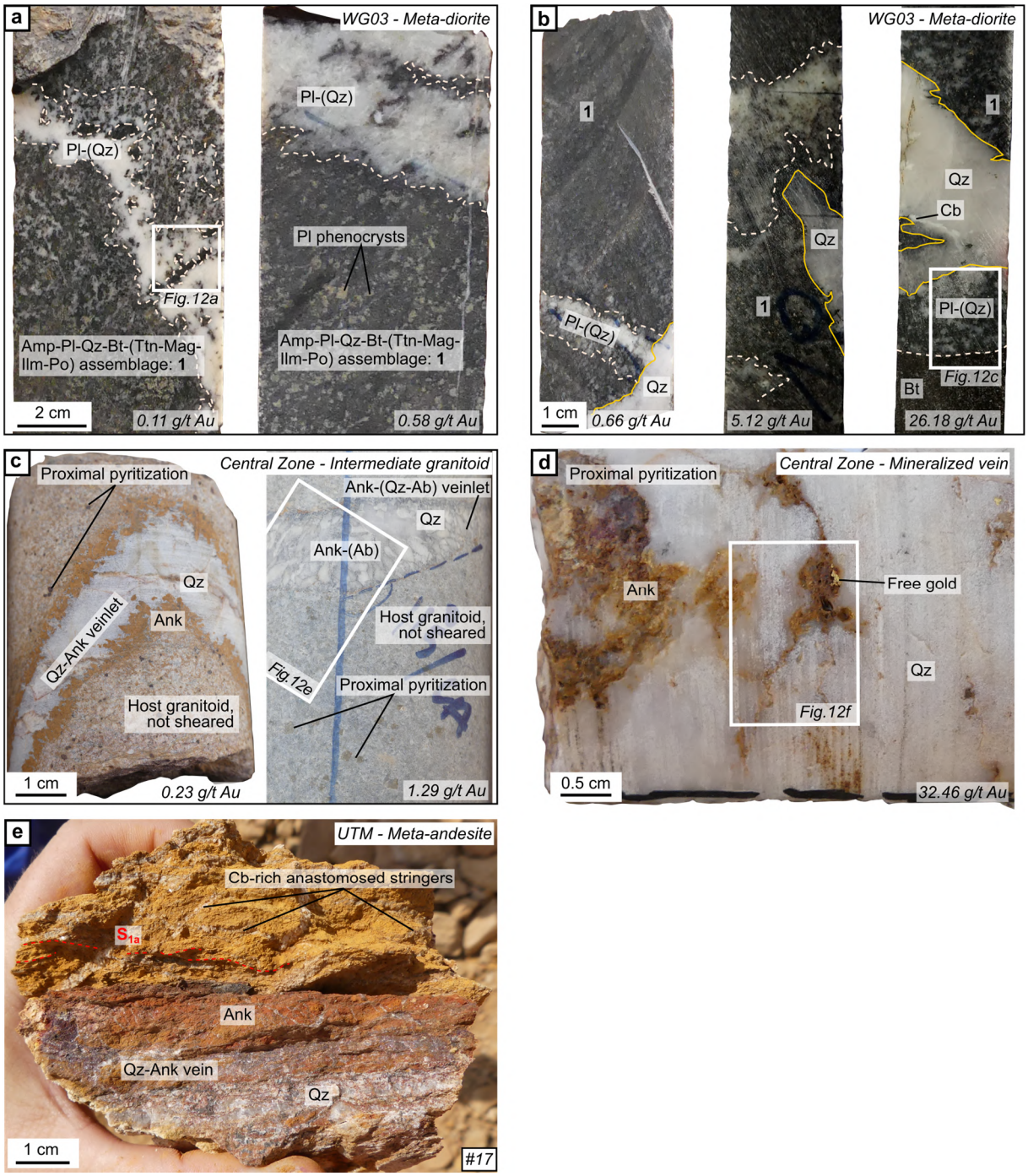


Figure 3-11: Gold-mineralized structures in drill cores and hand samples at the Gabgaba gold district. See detailed caption on p. 235.

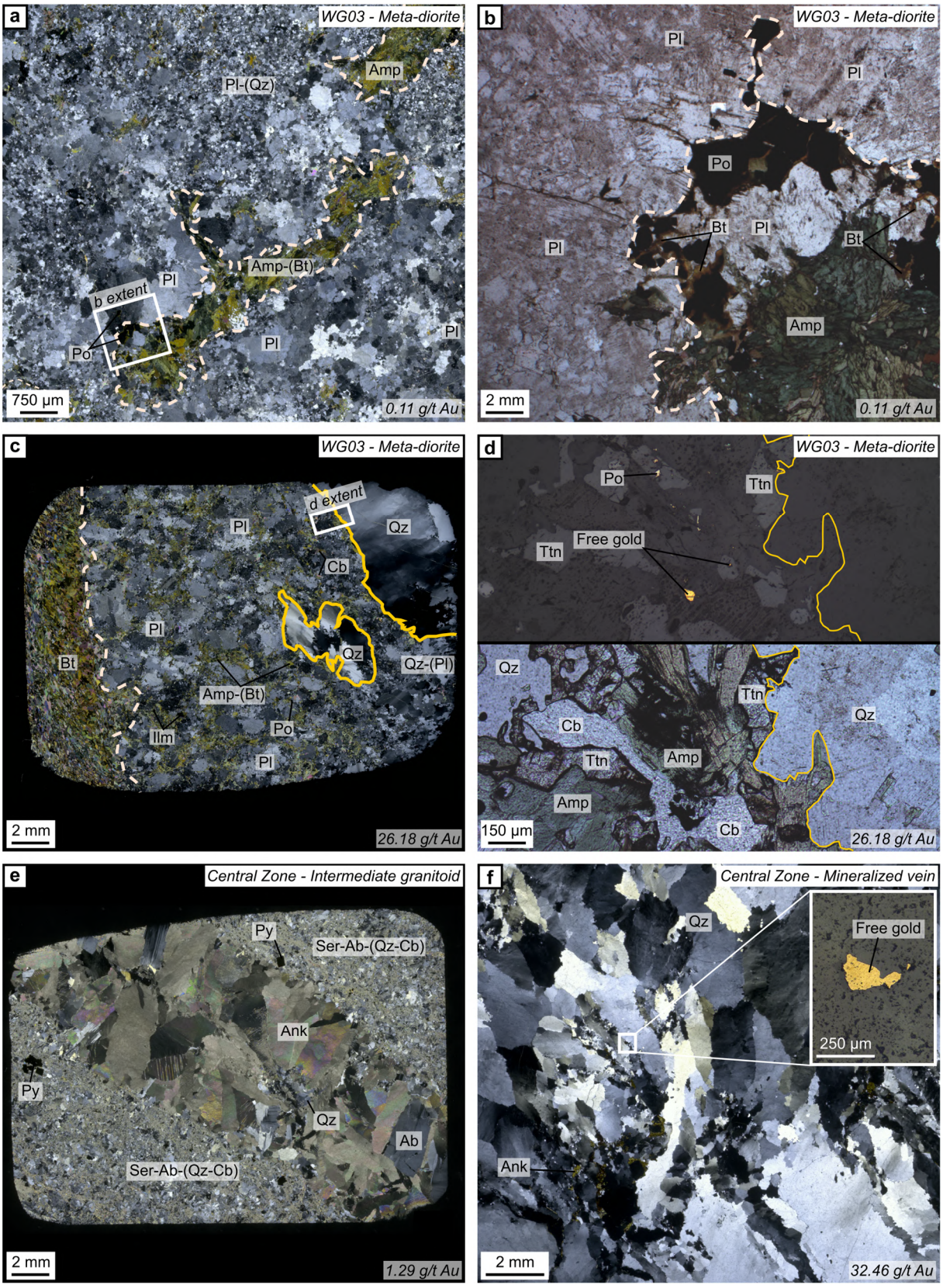


Figure 3-12: Gold-mineralized structures at the microscopic scale at the WG03 and Central Zone gold deposits. See detailed caption on p. 235.

Figure 3-10 (p. 232): Gold-mineralized structures in outcrop at the Gabgaba gold district. Outcrop locations and structural legend are the same as in Figure 3-2 and mineral abbreviations are Ab = albite; Cb = carbonate; Qz = quartz. **WG03 deposit: a** Mineralized quartz vein arrays are formed within the pre- to syn-tectonic meta-diorite hosting the WG03 deposit and cut across the penetrative S_{1a} gneissic foliation. The S_{1a} fabric and veins are locally rotated along several m-scale C_{1b} strike-slip shear zones affecting the meta-diorite. **b** Where undeformed away from any C_{1b} strike-slip shear zone, the mineralized quartz veins are en échelon dilational veins. **Central Zone deposit: c** The Central Zone ore is characterized by conjugate quartz-ankerite-albite vein sets cutting across intermediate granitoids, with rare to no lateral extension within the surrounding meta-sediments. **UTM deposit: d** Overview of the area investigated in Figure 3-10e and f. An intermediate granitoid intrusion either formed or is deformed along a C_{1b} strike-slip shear zone affecting meta-volcanosediments. Later, the shear zone has been reactivated as a F_2 normal fault at the contact between the two rock units. The mineralization is hosted in veins along F_2 planes. **e** The main ore-bearing veins are subvertical. They form where the C_{1b} shear zone has been reactivated as a F_2 normal fault. **f** Subvertical ore veins have off-shoots into the gently east-dipping S_{1a} fabric, associated with a proximal carbonation and pyritization halo.

Figure 3-11 (p. 233): Gold-mineralized structures in drill cores and hand samples at the Gabgaba gold district. Outcrop locations are the same as in Figure 3-2b and mineral abbreviations are Ab = albite; Amp = amphibole; Ank = ankerite; Bt = biotite; Cb = carbonate; Ilm = ilmenite; Mag = magnetite; Pl = plagioclase; Po = pyrrhotite; Qz = quartz; Ttn = titanite. Gold grades for WG03 and Central Zone drill core samples are from Managem fire assay analysis database. **WG03 deposit: a** An early plagioclase-(quartz) segregation assemblage has fuzzy boundaries and no sharp limit with the meta-diorite mineral gangue, mostly composed of amphibole and plagioclase feldspar (simplified into "1" in Figure 3-11a and b). Plagioclase feldspar phenocrysts are locally visible up to a few centimeters away from the vein wall. The presence of such features in the bulk mineral assemblage is associated with relatively low gold grades between 0.10 and 1.0 g/t Au. The extent of Figure 3-12a is indicated. **b** Quartz-dominated mineralized veins with sharp contacts cut across the meta-diorite mineral gangue and early segregation features. Their presence is associated with low to higher gold grades (from <1.0 up to 30 g/t Au). The extent of Figure 3-12c is indicated. **Central Zone deposit: c** Gold-bearing quartz-ankerite-albite veins show a comb texture characterized by albite syntaxial growth perpendicular to vein wall. They are zoned with ankerite-albite crystallization at the vein margins and quartz at the core. A proximal pyritization is widespread through the host granitoid which is not sheared. The approximate extent of Figure 3-12e is indicated. **d** Where free gold is visible at macroscopic scale in dm-wide quartz-(ankerite) mineralized vein, gold grade can reach up to 30 g/t Au. The approximate extent of Figure 3-12f is indicated. **UTM deposit: e** Up to several tens of meters away from m-scale, subvertical mineralized veins (Fig. 3-10f), the width of quartz-ankerite-rich off-shoots into the S_{1a} fabric drastically decreases down to a few centimeters. These mineralized veinlets are zoned, with a quartz-rich core and ankerite-dominated margins. Anastomosed carbonate-rich stringers are formed in the proximal alteration halo associated with these veinlets.

Figure 3-12 (p. 234): Gold-mineralized structures at the microscopic scale at the WG03 and Central Zone gold deposits. Mineral abbreviations are Ab = albite; Amp = amphibole; Ank = ankerite; Bt = biotite; Cb = carbonate; Ilm = ilmenite; Pl = plagioclase; Po = pyrrhotite; Py = pyrite; Qz = quartz; Ttn = titanite; Ser = sericite. Gold grades for corresponding drill core samples are from Managem fire assay analysis database. **WG03 deposit: a** (cross-polarized, transmitted light) and **b** (plane-polarized, transmitted light) The transition from the amphibole-rich meta-diorite inclusion to the plagioclase-rich segregation zone is diffuse and there is no sharp contact between them where the bulk assemblage is mineralized. Pyrrhotite is associated with biotite in the contact area between these two domains. **c** (cross-polarized, transmitted light) and **d** (above: reflected light; below: plane-polarized, transmitted light) A quartz-dominated mineralized vein sharply cuts across the meta-diorite host rock and early plagioclase-rich features. Pervasive silicification spreads from the vein margins. Free gold mineralization is associated with pervasive silicification and carbonation. **Central Zone: e** (cross-polarized, transmitted light) and **f** (cross-polarized, transmitted light; inset: reflected light) A mineralized quartz-ankerite-albite vein sharply cuts across the ore-hosting granitoid intrusion strongly sericitized. Pyritization occurred at the vein selvages. Free gold grains are visible within quartz-dominated mineralized veins.

4. Interpretation of the tectonic and gold history of the central Keraf suture

4.1. Tectonic evolution of the central Keraf suture

4.1.1. Progressive ductile to ductile-brittle D_{1a}-D_{1b} Keraf thrusting and strike-slip shearing

The ductile D_{1a} and ductile-brittle D_{1b} deformation stages control the structural setting of the central Keraf suture. Below, we interpret them regarding the formation of the KS-KSZ.

The ductile S_{1a} penetrative fabric gently dips eastwards between the C_{1b} strike-slip shear zones (Figs. 3-3, 3-6e). The rare observation of southeast-plunging L_{1a} lineation and absence of convincing passive markers that would allow assessing the amount and sense of displacement along S_{1a} planes suggest that D_{1a} deformation is coaxial-dominated general shear and that its non-coaxial component is weak. The regional penetrative fabric in the central KS is consistently attributed to Keraf suturing convergence in literature ($D_{1/2\text{-AS}}$ deformation in Fig. 3-1c and Table 3-1; Abdelsalam et al., 1998; Ahmed Suliman, 2000; Gaboury et al., 2020). At ANS scale, the significant stretching lineations are southeast-trending and were interpreted as associated with nappe emplacement with a tectonic transport from the southeast or the northwest (Shackleton et al., 1980; Ries et al., 1983; Sturchio et al., 1984; Shackleton, 1986; Bennett and Mosley, 1987; Greiling et al., 1988, 1994). We therefore propose that the ductile D_{1a} deformation stage expresses west- to northwest-verging thrusting during Keraf suturing, given the orientation of L_{1a} lineation in the studied area, despite the lack of kinematics evidence.

Ductile C_{1b} shear zones are subvertical and mostly strike north-northwestwards with left-lateral displacement, although rare north-northeast-striking, dextral shear zones have been observed (Figs. 3-2a, 3, 3-7f). These structures are attributed to the KSZ superimposition to the KS in literature, although they have previously been described as brittle structures ($D_{4\text{-AS}}$ deformation in Fig. 3-1c and Table 3-1; Abdelsalam et al., 1998;

Ahmed Suliman, 2000; Gaboury et al., 2020). We therefore suggest that D_{1b} deformation expresses the late convergent, Keraf sinistral shearing. The formation of rarer conjugate C_{1b} shear zones may therefore fit with a roughly west-orientated compression. Besides, D_{1b} deformation is thought to be coaxial-dominated general shear, similarly to what is suggested for the previous D_{1a} stage, as left-lateral displacement along C_{1b} shear planes does not exceed tens of cm at the outcrop scale. Despite a presumed change from Keraf thrusting to strike-slip shearing, the formation of the KS-KSZ likely relates to a coaxial-dominated D_{1a}-D_{1b} deformation history thus.

Ductile structures dominate for both D_{1a} and D_{1b} deformation stages and the orientation of the S_{1a} fabric progressively rotated along ductile C_{1b}-shear planes in shear lenses at every scale (Figs. 3-2a, 3-3 and 3-6e). There is therefore no field evidence for a temporal break in convergence between the penetrative D_{1a} deformation stage and the formation of C_{1b} shear zones. Despite there is a change in the expression of the deformation style from thrusting into lateral strike-slip, this may be irrelevant to mention as the magnitude of the non-coaxial component remains unknown for D_{1a} and is thought to be weak for D_{1b}. Besides, there is apparently no drastic change in stress field from D_{1a} to D_{1b} deformation, both being consistent with roughly west- to northwest-orientated compression. We therefore consider that the D_{1a} to D_{1b} deformation stages form a single, progressive, ductile to ductile-brittle deformation episode in a compressional regime (Fossen et al., 2019). Further stress field analysis and geochronological data would be required to confirm the latter hypothesis or prove otherwise.

4.1.2. Late, brittle, local D_2 extension regime and normal faulting

The tectonic history recorded in the central KS ends with a late, brittle, extensional D_2 deformation episode characterized by discrete, north-striking, east-dipping normal faults (Fig. 3-8). They have only been observed in the UTM area and their spatial extent is limited to less than a hundred meters (Fig. 3-9c). Normal faults reactivate C_{1b} shear zones, especially where rheological contrast is enhanced (*e.g.,* between intermediate

granitoid or meta-diorite intrusions and meta-volcanosediments). If these normal faults are certainly post-KSZ, their significance at regional scale is likely limited.

4.2. Gold mineralization events of the central Keraf suture

The mineralization-deformation relationships observed at the WG03, Central Zone and UTM deposits suggest that several mineralization events contributed to the overall gold endowment of the Gabgaba district. They are interpreted in terms of relative timing regarding the central KS tectonic evolution below.

4.2.1. Minor, low-grade, pre-D_{1a} gold event (WG03 deposit)

The first gold event characterized is limited to the WG03 deposit. It consists in plagioclase-rich segregation zones within the amphibole-dominated mineral gangue of the ore-hosting meta-diorite (Figs. 3-11a, 3-12a and b). There is no sharp boundary between these two domains and plagioclase feldspar is more or less abundant in both of them (Figs. 3-11a, 3-12a and b). These observations suggest that the segregation features may derive from magmatic-hydrothermal processes during the crystallization of the host meta-diorite rather than later hydrothermal processes. Similar textures were indeed observed for late magmatic *"pegmatitic veins"* at the magmatic-hydrothermal Cheechoo gold deposit, Canada (Fontaine et al., 2018; Turlin et al., 2019). However, additional work on fluid nature, composition of plagioclase feldspar and textural description must be carried out to better interpret the magmatic, magmatic-hydrothermal or hydrothermal nature of this mineralizing event. In this study, we only suggest that the first gold event recorded at the Gabgaba gold district is synchronous with pre-tectonic magmatism and therefore predates the regional D_{1a} deformation stage.

Gold grades associated with these segregation features range between 0.1-1 g/t Au and it has been checked in microscopy that gold mineralization is not related to subsequent micro-fractures bringing some gold later in the deformation history. The

absence of free gold associated with these features therefore suggests that gold is likely structurally bound in the lattice or occurs as nano-inclusions in other minerals, such as sulfides inclusions (*e.g.,* Combes et al., in press; Cook and Chryssoulis, 1990; Reich et al., 2005; Hough et al., 2011; Deditius et al., 2014; Pokrovski et al., 2019). The only sulfide mineral observed is pyrrhotite which crystallizes at the transition between plagioclase- and amphibole-rich domains (Fig. 3-12a, b). Further analytical work such as LA-ICP-MS on sulfide should be carried out to test if invisible gold is trapped in pyrrhotite or not.

4.2.2. Major, high-grade, early to syn-D_{1b} gold event (WG03 and Central Zone deposits)

The main gold-bearing structures at the WG03 deposit are quartz-rich, *en échelon* veins crosscutting the S_{1a} gneissic foliation and associated with free gold mineralization and up to 30 g/t Au grades (Figs. 3-10a and b, 3-11b, 3-12d). The sigmoidal shape of the veins in cross section view, their probable dilational nature and the flat to gently north-dipping orientation of these veins in the least deformed parts of meta-diorite lenses between C_{1b} shear zones suggest that mineralized veins formed initially along top-to-the-north low angle shear zones (Figs. 3-10b, 3-12c, 3-13a, 3-14a). This interpretation relies on assuming that the vein opening is controlled by a north-orientated subhorizontal principal stress as indicated by the direction where *en échelon* vein tips point (Fig. 3-10b). However, there is no way to be certain that the vein geometry indicates the principal stress directions at the time when they formed as they must have been subsequently rotated at some extent in C_{1b} shear lenses. Where veins are more affected by D_{1b} strike-shearing, their orientation rotates counter-clockwise within the shear lenses, resulting in sigmoidal shapes in the horizontal plane (Figs. 3-13a, 3-14a). Veins are even transposed along north-northeast-striking subvertical C_{1b} shear veins where rotation has been the most intense (Figs. 3-13a, 3-14a). We therefore suggest that gold-bearing veining at WG03 postdates the D_{1a} stage and occurred early during the D_{1b} stage. The vein

geometry model illustrated in Figure 3-14a could indeed fit with the presence of gently dipping extensional zones in an overall strike-slip regime if an extensional jog between C_{1b} shear zones happens to be characterized. However, the C_{1b} shear zone traces are not well constrained at deposit-scale and step-over sites have not been recognized in the field (Fig. 3-9a). If further work is required to answer these questions, the main gold event at WG03 is likely part of the progressive deformation leading to the formation of the KSZ anyway.

Regarding the Central Zone deposit, given the granitoid array geometry and the fact that their contacts with surrounding meta-sediments are sheared, their intrusion likely predated their boudinage and dismembering along C_{1b} planes during the early D_{1b} deformation, *i.e.,* ductile formation of the KSZ, under a northwest-orientated compressional regime (Fig. 3-14b). Free gold-bearing veins (up to 30 g/t Au) preferentially cut across the granitoid intrusions because of their enhanced competency regarding the surrounding meta-sediments (Figs. 3-10c, 3-11c and d). The characterization of two sets of conjugate, connected, purely dilational veins which are flat to gently dipping eastwards or westwards indicates their formation occurred in a compressional regime. As the veins show no shear component, it is possible to reconstruct the finite main strain directions associated with their formation, provided that deformation is coaxial (Fig. 3-14b). The latter assumption is reliable as the D_{1a}-D_{1b} deformation controlling the structural setting of the central KS is interpreted to be coaxial-dominated general shear, despite a weak non-coaxial, strike-slip component must be considered for D_{1b}. In the proposed stereonet analysis, veining at Central Zone results from a south-southeast-orientated, subhorizontal shortening direction (Fig. 3-13b). It fits with the northwest-orientated compressional regime related to the KSZ strike-slip shearing: assuming that veins were formed in response to the latter compressional regime, they may look like the principal shortening direction is south-southeast-orientated due to clockwise rotation with sinistral shearing. We therefore suggest that Central Zone

gold-mineralized veining occurred during D_{1b} sinistral shearing and formation of the KSZ second-order *"West Corridor"* (Fig. 3-14b).

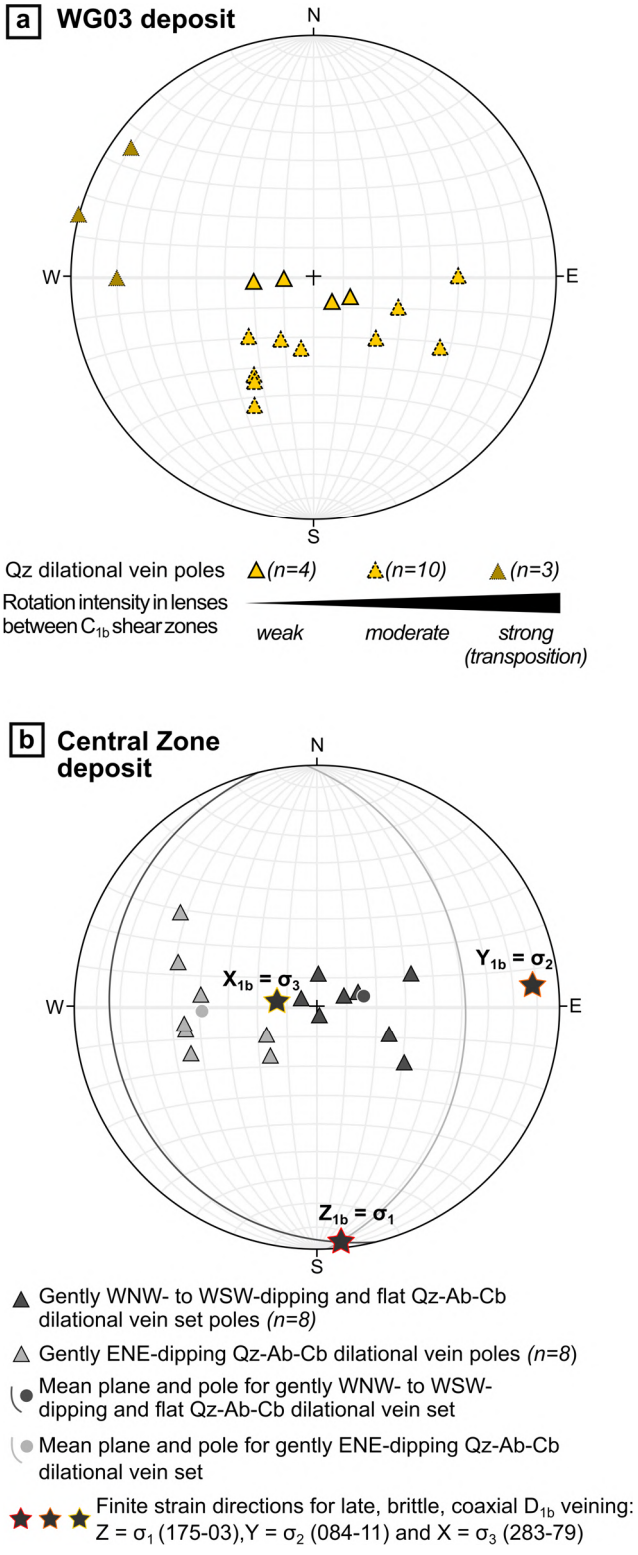


Figure 3-13: Stereonet analysis of the main gold-mineralized structures at the Gabgaba gold district. Mineral abbreviations are Ab = albite; Cb = carbonate; Qz = quartz. **a** Crosscutting quartz-dominated mineralized veins at the WG03 deposit. **b** Gold-bearing quartz-ankerite-albite veins hosted in granitoids at the Central Zone deposit.

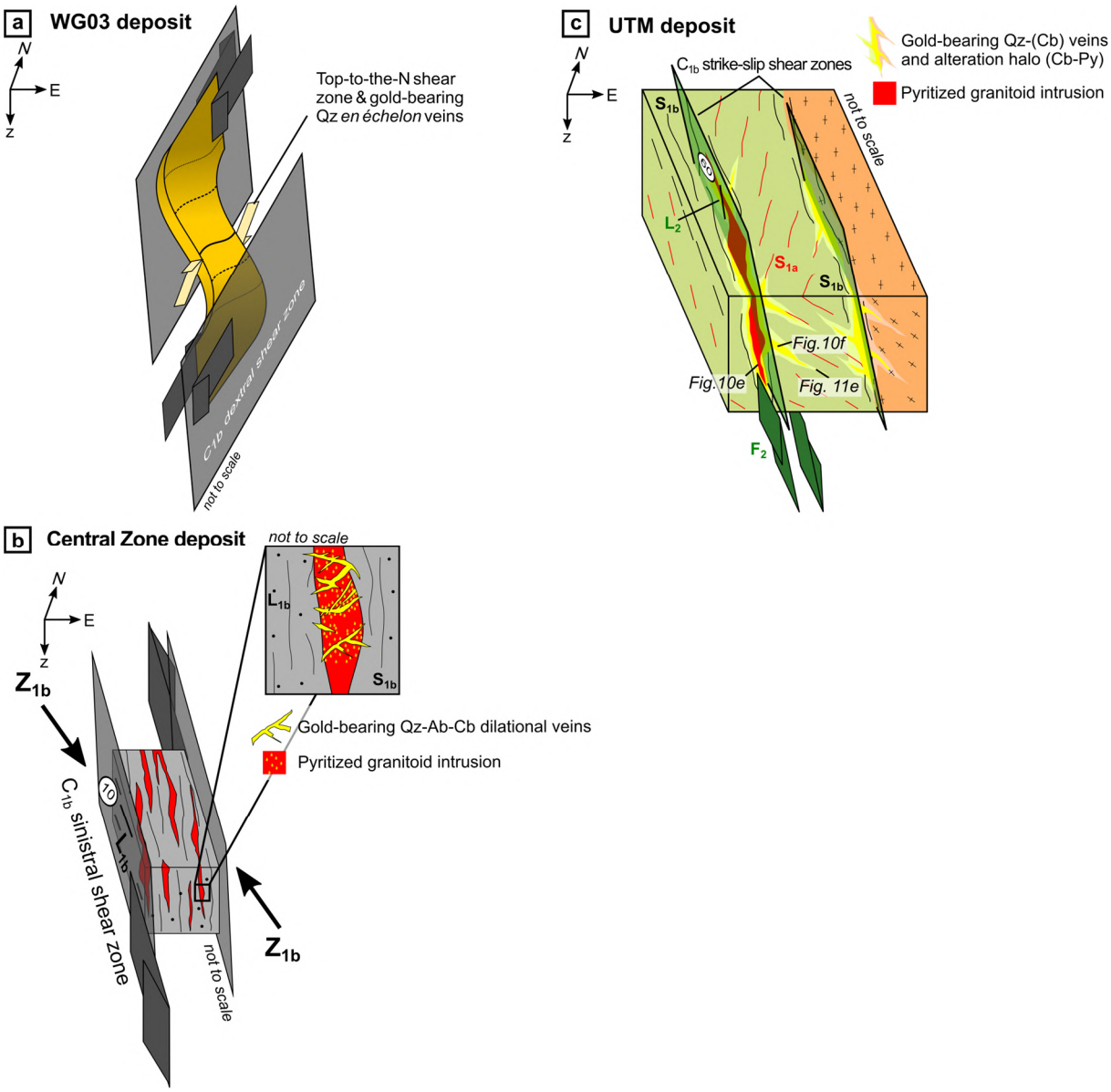


Figure 3-14: Tectonic interpretation for the formation of the main gold-bearing structures at WG03 (**a**), Central Zone (**b**) and UTM (**c**) deposits. The interpreted location of mineralized structures illustrated in Figs. 3-10e and f and 3-11e is indicated in **c**.

The WG03 and Central Zone deposits therefore highlight that a major gold event relates to progressive, ductile-brittle Keraf shearing in the central KS. According to gold grades, structure dimensions and density throughout deposit areas, the gold fertilization associated with this event is likely way higher than the gold budget represented by the early, pre-D_{1a} gold event defined at the WG03 deposit. However, we cannot conclude whether if D_{1a}-related gold results from (i) a new gold input in the system, (ii) the strong remobilization and local re-concentration of former gold, (iii) or a combination of both.

4.2.3. A late, syn-D_2 gold event (UTM deposit)?

Despite limited observations of deformation-mineralization relationships for the UTM deposit, we attempted to suggest a mineralization model for this deposit (Fig. 3-14c). The major gold-bearing veins currently exploited there are subvertical and formed along C_{1b} shear zones, only where they are reactivated as normal faults during the late brittle D_2 extensional deformation event characterized in the UTM area (Figs. 3-9c, 3-10d). The formation of these faults is favored where rheological contrast is strong, especially at contacts between rock units of variable competency, *e.g.,* granitoids and meta-sediments (Figs. 3-9c, 3-10d). We assume that fluid flow circulation and veining occurred along normal fault plane reactivation in an extensional regime. Besides, we propose that the inherited S_{1a} cleavage affecting surrounding meta-sediments is a very permeable fabric along which mineralizing fluid flow easily spread away from the fault. This mechanism would account for the presence of vein off-shoots and alteration halo into the S_{1a} fabric up to tens of m away from the main, subvertical veins (Figs. 3-10d and f, 3-11e, 3-14c). However, we lack key evidence to justify the genetic relationship between F_2 normal faults and subvertical veining as no normal-slip kinematic indicator is visible on vein walls. In addition, the very local extent and discrete manifestation of the D_2 deformation episode, limited to the UTM area, contrast with the strong gold endowment of the UTM deposit (see section 3).

Besides, it is worth noticing that the vein mineral assemblage dominated by quartz and carbonate, together with proximal pyritization, is quite similar to what is observed at the Central Zone deposit. Host lithologies are somehow the same as well, despite meta-diorite and schistose andesite are more abundant in the UTM area (Fig. 3-9b, c). We could thus legitimately wonder whether if these two deposits relate to the same mineralization event or not. We decided to separate them as the rheological control on mineralization is not expressed in the same way. At Central Zone, mineralized veins preferentially formed within granitoid intrusions deformed along C_{1b} shear zones whereas

veins never cut across the most competent plutonic units at UTM. Post-D_{1b} deformation should therefore be considered prior to or syn-veining at the UTM deposit to justify such a change in structural-rheological control on mineralization. Nevertheless, similarities between UTM and Central Zone deposits raise the possibility that the gold event characterized at the UTM deposit may overprint and/or result from remobilization of the major, syn-D_{1b} mineralized structures.

5. Discussion

Relying on our interpretation of the tectonic and gold history of the central Keraf suture (section 4), we now discuss similarities and differences with previous models and how the described deformation-mineralization events fit into the geodynamical evolution of the western Nubian shield.

5.1. Reappraisal of the tectonic setting of the central Keraf suture

5.1.1. Towards a simplified and unified regional-scale tectonic history

Our study proposes that the central KS structural framework is dominated by progressive deformation with the succession of D_{1a} and D_{1b} stages, expressing the formation of the KS and KSZ, respectively, in a roughly west- to northwest-orientated compressional regime. Despite a change in plunge value, L_{1a} and L_{1b} lineations are mostly north-northwest- to northwest-striking (Figs. 3-6f, 3-7f). These lineations have already been identified in the ANS and Mozambique belt southwards (Abdelsalam and Stern, 1996b and references therein) and were further considered as indicating the direction of plate motion during Gondwana assembly (Shackleton and Ries, 1984). Our D_{1a}-D_{1b} model is therefore in agreement with previous studies suggesting that the formation of the KS and KSZ occurred in a prolonged, northwest-orientated, oblique convergence tectonic setting (Abdelsalam et al., 1995 , 1998; Ahmed Suliman, 2000). Rotation of the regional S_{1a} penetrative cleavage and early-D_{1b} ore *en échelon* veins of the WG03 deposit in shear

lenses between C_{1b} shear zones, whatever their scale, fits with this progressive deformation model. D_{1a} Keraf suturing is constrained between *ca.* 700-640 Ma (various age compilations; Stern, 1994; Abdelsalam and Stern, 1996b) and subsequent sinistral transpression is dated at *ca.* 640-580 Ma (lower age limit from Ar/Ar dating on hornblende and biotite in deformed granitoids (*e.g.,* Abdelsalam et al., 1995, 1998; Abdelsalam and Stern, 1996a, 1996b). We can therefore consider that the syn- to late convergence D_{1a}-D_{1b} deformation and formation of the KS-KSZ occurred between *ca.* 700-580 Ma (Table 3-1).

Later, brittle D_2 deformation is characterized by discrete, top-to-the-east normal faults in meta-volcanosediments, especially formed along rheological contacts within weakened C_{1b} shear zones. These normal faults have previously been observed in the Gabgaba gold district and interpreted as post-KSZ by Gaboury et al. (2020). However, very few orientation measurements have been made and these structures are very local in meta-volcanosediments. The regional significance of the extensional D_2 deformation episode therefore remains in abeyance. We can only consider that D_2 deformation occurred <580 Ma (Table 3-1). It is however worth noticing that significant north-striking normal faults have been characterized in the northeasternmost Saharan meta-craton, south to the Atmur-Delgo suture, a few hundred km away from the studied area. These extensional structures were attributed to a post-orogenic gravitational collapse that occurred at ~550 Ma (Denkler et al., 1994; Harms et al., 1994; Abdelsalam et al., 2003).

Basically, the tectonic history unraveled within the central KS can be simplified into a single protracted deformation episode with a progressive change from thrusting to sinistral shearing, which is similar to the deformation episodes defined by Gaboury et al. (2020). Correspondence with deformation episodes of reference of the studied area, defined by remote sensing (Abdelsalam et al., 1995) and field work (Abdelsalam et al., 1998; Ahmed Suliman, 2000), is addressed in Table 3-1. The main S_{1a} penetrative fabric

and sinistral C_{1b} strike-slip shear zones are well identified in both cases. However, most of the complex structural interferences defined in literature, such as fold interference patterns associated with multiple regional- to outcrop-scale fold stages (Fig. 3-1c; Abdelsalam et al., 1995 , 1998; Ahmed Suliman, 2000), have not been characterized during this study. The regional-scale significance of these structures is therefore questionable.

5.1.2. Defining the central Keraf suture extent and deformation style

The Keraf suture is a poorly studied area with uncertain shape and boundaries (Gaboury et al., 2020 and references therein). For instance, Gaboury et al. (2020), in agreement with Abdelsalam et al. (1998), suggested that the central KS is relatively narrow. They consider that the western limit of the KS, *i.e.,* the contact between the Saharan meta-craton related Bayuda terrane to the west and the KPTA and Gabgaba terrane to the east (Fig. 3-1), is the several km-wide north-northwest-striking *"West Corridor"* hosting the Central Zone and UTM gold deposits (Figs. 3-2a, 3). If that was true, lithological units and deformation should be drastically different east and west of the *"West Corridor"*, expressing the transition from the Bayuda terrane westwards and the ANS eastwards. Yet, we observe the same lithological units and structures (S_{1a} and C_{1b}) east and west of the *"West Corridor"* (Figs. 3-2a, 3). Therefore, we would rather consider that the central KS is wider than suggested by Abdelsalam et al. (1998) and Gaboury et al. (2020), in line with the KS extent delimited by Ahmed Suliman (2000) (Figs. 3-1c, 3-2a, 3). The exact emplacement of the central KS western boundary could not be confirmed by field observations due to the presence of a Phanerozoic sedimentary cover overlying the Precambrian rocks of interest west of the limit from Ahmed Suliman (2000). The western extent of the central KS may thus remain underestimated.

Previously, the description of KSZ-related, second-order strike-slip structures was limited to the southern KS, where left-lateral displacement, if not estimated, is suggested

to be more significant than for KSZ-related structures northwards (*e.g.,* Abu Dis and Abu Hamed shear zones; Abdelsalam et al., 1998). However, although the structural framework of the central KS is dominated by Keraf suturing (D_{1a} deformation), C_{1b} shear zones are frequent within the central KS (Figs. 3-2a, 3). A C_{1b} shear zone notably overprints the interpreted Bayuda terrane-KPTA limit (Figs. 3-2a, 3). It contradicts Ahmed Suliman (2000) who suggested that this boundary was a D_{1a}-related thrust within the central KS (Fig. 3-1c). The central KS is therefore a complex area where the deformation style shifts between the thrusting- and strike-slip shearing-dominated northern and southern KS, respectively (Table 3-1; Abdelsalam and Stern, 1996b).

5.2. Polyphase gold dominated by syn-Keraf shear zone mineralization in the Gabgaba gold district

From field, macroscopic and microscopic observations, we suggest the existence of several gold events forming the Gabgaba gold district with distinct timing regarding the formation of the KS-KSZ (Fig. 3-15): (i) a first minor, pre-tectonic, (ii) a second major, late tectonic and (iii) a third potential, post-tectonic.

The first gold event we unraveled is low grade, *i.e.,* <1 g/t Au, and limited to the WG03 deposit. Disseminated pyrrhotite and the presence of feldspar-rich segregation-like features within meta-diorite characterize mineralization. Despite the magmatic or magmatic-hydrothermal nature of this ore event remains hypothetical at this point, we suggest it occurred with the pre-D_{1a} diorite intrusion (Fig. 3-15). We therefore suggest the existence of a first gold generation coeval with magmatic accretion, probably during oceanic subduction and Keraf arc-back-arc basin development, prior to ~750 Ma (Ries et al., 1985; Abdelsalam et al., 1998). Gaboury et al. (2020) did not distinguish this gold event at the WG03 deposit. Its contribution to the overall gold endowment is anyway thought to be very limited, regarding associated grades, dimensions and density of these mineralized features.

The major gold event forming most of the WG03 deposit and the entire Central Zone deposit broadly relates to *en échelon* ore veining as a response to the late collisional ductile-brittle D_{1b} shearing stage leading to the formation of the KSZ. The WG03 and Central Zone ore veins are associated with free gold mineralization and gold grades up to 30 g/t Au. Gaboury et al. (2020) observed the same major ore-bearing structures at Central Zone and WG03, with similar metamorphic, carbon-rich aqueous fluid signature for both deposits. They also attributed the mineralization event to the KSZ-related late oblique convergence, at the retrograde amphibolite-greenschist facies transition. The main difference is that Gaboury et al. (2020) attributed ore veining at Central Zone to reverse faulting at the contacts between granitoids and surrounding meta-sediments, rather than strike-slip shearing. These two options are however not mutually exclusive as (i) they both fit with a roughly northwest-orientated compressional regime and (ii) the non-coaxial component of D_{1b} deformation is thought to be very limited as discussed above. Besides, alteration is expressed by distal sericitization-(pyritization), proximal pyritization-carbonation and quartz-ankerite-albite-gold veining hosted in granitoids. The Central Zone deposit can therefore be considered as the perfect example for intrusion-hosted orogenic gold formed in a syn- to late compressional regime along second-order shear zones with typical structural, fluid, alteration and metamorphic footprints.

We attributed the formation of the UTM gold deposit to ore veining during late, brittle D_2 extension and normal faulting along reactivated shear zones. However, (i) the D_2 deformation is hardly interpretable as spatially limited to the UTM area, (ii) the genetic link between ore veins and normal faults is not clearly established and (iii) the UTM deposit displays numerous similarities with the Central Zone deposit. All these reasons make the interpretation of the UTM gold event highly uncertain. Vertical veins where not characterized by Gaboury et al. (2020) who only defined the gently east-dipping vein off-shoots into the regional S_{1a} fabric. They proposed that these veins formed

along reverse faults activated during the KSZ formation, within the second-order *"West Corridor"* hosting both the Central Zone and UTM deposits. Their interpretation is supported by a fluid signature in gold-bearing veins at UTM similar to the one reported at Central Zone and WG03. Besides, this option has the merit to simplify the gold history of the Gabgaba gold district, considering a single, syn-D_{1b} orogenic-like gold event accounting for most of the gold endowment in the central KS. The debate is still open.

Most of the gold mineralization in the central KS is therefore coeval with the late tectonic formation of the KSZ overprinting the KS. At Nubian shield-scale, ~600 My-old gold mineralization hosted by quartz veins and related to ductile-brittle transcurrent structures is mostly characterized as orogenic gold (*e.g.,* Elsamani et al., 2001; Klemm et al., 2001; Botros, 2002, 2004; Helmy et al., 2004; El Kazzaz, 2012; Osman, 2014; Helmy and Zoheir, 2015; Khalil et al., 2016; Fawzy, 2017; Zoheir et al., 2019a, 2019b, 2019c). However, there is also some evidence for gold mineralization during the magmatic accretion stage and early amalgamation of the ANS (*ca.* 830-640 Ma; age compilation by Abdelsalam and Stern, 1996b), such as the first gold event portrayed at the WG03 deposit or the syn-Atmur-Delgo suturing Galat Sufar South gold deposit (Perret et al., 2020). In the latter study, the authors indeed demonstrated that the regional Atmur-Delgo deformation shapes the local structural setting and controls the formation and geometry of ore-shoots from the deposit to the macroscopic scales. Even if less documented, the existence of pre- to early-suturing gold events across the ANS should therefore not be underestimated. To go further and better constraint the gold mineral system expressed along the central KS, it appears now critical to (i) track the regional lithospheric evolution, (ii) put geochronological constraints on the deformation and gold events and (iii) study their gold input or remobilization nature and the potential genetic links between these gold episodes.

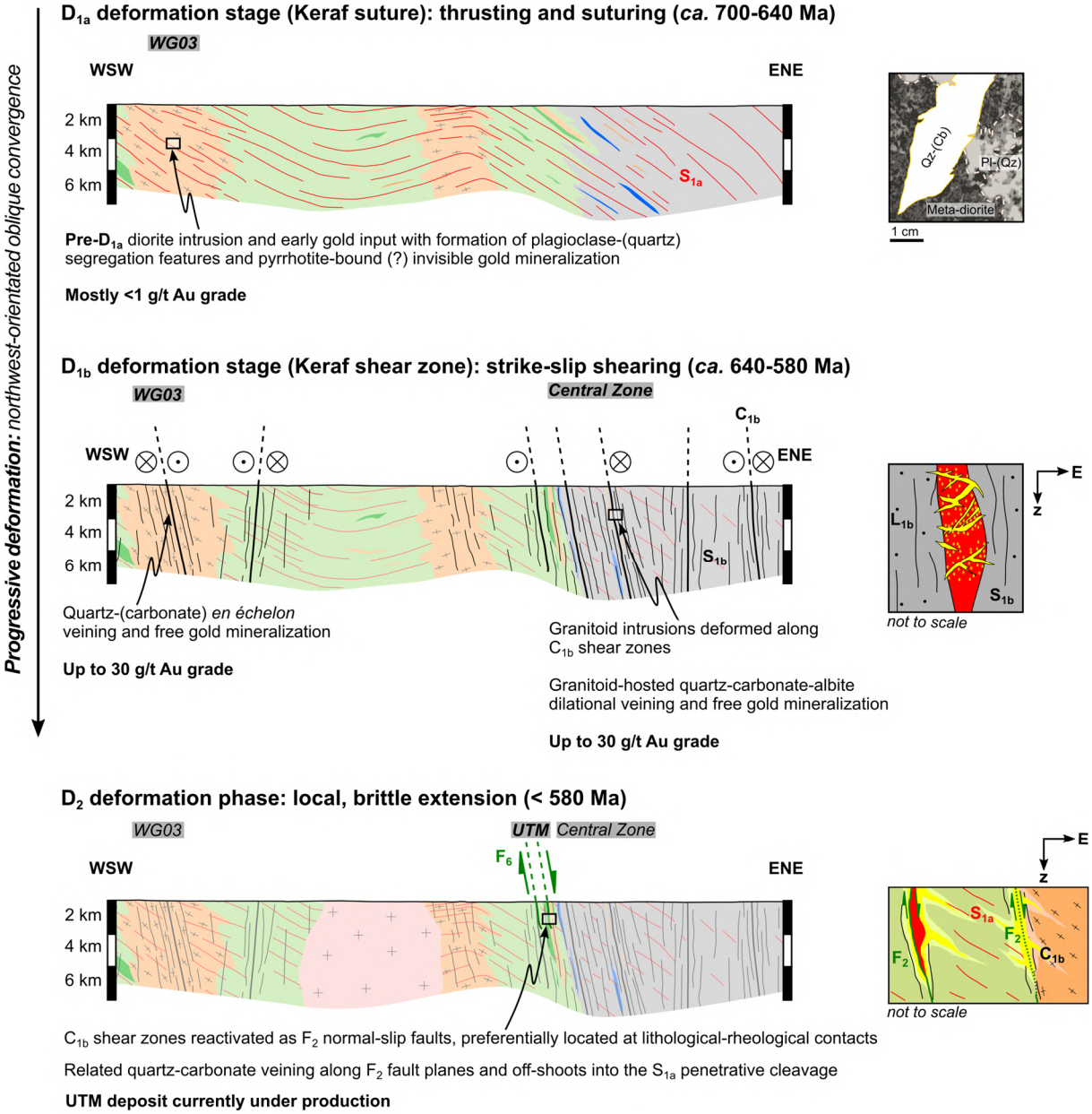


Figure 3-15: Relative timing of the Gabgaba district gold deposits (WG03, Central Zone and UTM) regarding the deformation history recorded by the central Keraf suture. Litho-structural legend is the same as in Figure 3-3 and mineral abbreviations are Cb = carbonate; Pl = plagioclase; Qz = quartz. See text for chronological constraint explanation and related references. Insets on the right correspond to schematic zooms of the black rectangle for each cross-section.

6. Conclusions

Field observations suggest that the structural framework of the central Keraf suture is dominated by a progressive, ductile to ductile-brittle D_{1a}-D_{1b} deformation characterized by the regional S_{1a} penetrative fabric and C_{1b} sinistral shear zones. This deformation relates to Keraf suturing and subsequent left-lateral shearing in a prolonged northwest-orientated compressional regime between *ca.* 700-580 Ma. However, the D_{1a}-D_{1b} deformation is thought to be coaxial-dominated shear and the non-coaxial deformation component, *i.e.,* vertical and lateral displacement along structure planes, is weak. A C_{1b} shear zone overprints the boundary between the central Keraf suture and the Saharan meta-craton westwards which was not documented by previous studies. The central Keraf suture can therefore be seen as a transition zone between the northern Keraf suture, dominated by D_{1a} deformation, and the southern Keraf suture where C_{1b} shear zones are more frequent. A late, brittle D_2 normal faulting event reactivated inherited C_{1b} shear zones. However, the significance of this deformation episode at regional scale remains uncertain as it is very local.

Relying on field and drill core relationships between structures and mineralization, we clearly define a polyphase gold history with two mineralizing events occurring in the ~30 km-wide Gabgaba gold district. The first one is pre-D_{1a} and related to magmatic accretion in the WG03 area but its contribution to the overall gold endowment is likely limited. The major gold event formed the WG03 and Central Zone deposits and is characterized by ore veining during late tectonic ductile-brittle Keraf strike-slip shearing. This mineralizing event can relate to orogenic gold, which is widespread at ANS-scale. The occurrence of a post-tectonic brittle gold event coeval with the D_2 deformation episode is suggested at the UTM deposit, but its existence remains highly uncertain.

Acknowledgements

The authors are grateful to the Manub and Managem team and especially to Attaiaa Hachem, Hassan Ait Benmouh, Mohamed Niyazi and El Alami Boukkari for their welcome on Gabgaba mining camp and their substantial logistical support. This work is part of Julien Perret's PhD project which benefited of a CIFRE funding, reference CIFRE N°2017/1737, attributed by the French National Research and Technology Agency (ANRT). This manuscript was firstly submitted for publication to Ore Geology Reviews and benefited from the insightful review comments of Daniel Müller and two anonymous reviewers. Then, careful and discerning reviews by Taija Torvela and an anonymous reviewer on the second version of the manuscript greatly helped to reconsider our interpretations and suggest more realistic conclusions. Damien Delvaux is thanked for editorial handling.

PARTIE III – Enregistrement des processus minéralisateurs à l'échelle microscopique

Préambule

Les études pétro-structurales de terrain, couplées à des observations microscopiques sur lame mince et à une analyse de linéaments sur images satellite, ont permis de contraindre la chronologie relative des événements aurifères à l'origine du gisement de Galat Sufar South et du district de Gabgaba vis-à-vis de l'histoire tectonique régionale (**Partie II**). Néanmoins, l'intégration du contrôle structural de la minéralisation à l'échelle microscopique n'en demeure pas moins complexe. Le principal écueil réside dans la perte inévitable d'information lors du passage d'objets 3D visibles sur affleurement, carottes de forage ou échantillons macroscopiques, à l'étude d'objets en 2D sur lame mince par exemple. Même un échantillonnage orienté ne permet pas de prévenir totalement cette perte d'information. Pourtant, c'est à cette échelle microscopique que les processus géochimiques minéralisateurs sont généralement établis, en couplant notamment les caractéristiques micro-texturales des assemblages minéralisés à l'évolution de leur signature géochimique (*e.g.,* Reich et al., 2017 ; Román et al., 2019). Si cette approche est largement suivie dans la littérature (*e.g.,* Combes et al., sous presse ; Large et al., 2007, 2009 ; Cook et al., 2013 ; Hazarika et al., 2013 ; Velasquez et al., 2014 ; Augustin et Gaboury, 2018 ; Gourcerol et al., 2018a, 2018b ; Li et al., 2019 ; Wu et al., 2019a ; Gourcerol et al., 2020 ; Kadel-Harder et al., 2020), le lien entre micro-structures et –textures, signature géochimique de la minéralisation et réalité tectonique à plus petite échelle n'est pas systématiquement explicité.

Dans cette **Partie III**, nous commencerons donc par proposer une approche couplant étude pétro-structurale de terrain, techniques micro-structurales 3D (micro-tomographie à rayons X et diffraction d'électrons rétro-diffusés) et géochimique *in situ* en contexte (spectrométrie de masse à plasma à couplage inductif par ablation laser sur sulfures) intégrant à toutes les échelles les contrôles structural et géochimique des gisements d'or hydrothermaux déformés (**Chapitre IV**). Nous l'appliquerons au gisement aurifère de Galat Sufar South et les bénéfices pour la recherche et l'industrie minière seront présentés. Enfin, suite à l'ancrage de l'épisode aurifère exprimé par le gisement de Central Zone dans l'évolution tectonique de la zone de suture de Keraf (**Chapitre III**), le **Chapitre V** présente une étude intégrée micro-structurale, -texturale et géochimique *in situ* des différentes générations de pyrite identifiées à Central Zone afin de mieux contraindre les processus minéralisateurs impliqués au cours de cette histoire tectonique.

Chapitre IV – Structural and geochemical ore-forming processes in deformed gold deposits: towards a multi-scale and -method approach

Julien Perret[1,2,*], Anne-Sylvie André-Mayer[2], Aurélien Eglinger[2], Julien Feneyrol[1], Alexandre Voinot[3,4], Christophe Morlot[2], Fabrice Barou[3], Yoram Teitler[2], Diego Seira[2], Rémi Bosc[1]

Article soumis pour publication dans le volume special intitulé "*Recent Advances in Understanding Gold Deposits: From Orogeny to Alluvium*" de *Geological Society of London Special Publication*.

[1] Arethuse Geology EURL, BP 80017, Latitude Arbois, 1060 rue René Descartes, 13290 Les Milles, France

[2] GeoRessources, Université de Lorraine, CNRS, 54000 Nancy, France

[3] Department of Geological Sciences and Geological Engineering, Queen's University, K7L 3N6 Kingston, Canada

[4] MacDonald Institute, Canadian Particle Astrophysics Research Centre, Stirling Hall, Department of Physics, Engineering Physics & Astronomy, Queen's University, 64 Bader lane, Kingston, ON, Canada

[5] Géosciences Montpellier, Université de Montpellier, CNRS, 34000 Montpellier, France

Résumé

Le couplage entre contrôle structural et processus géochimiques minéralisateurs est primordial pour l'étude des gisements métalliques déformés, malgré une échelle d'investigation différente : alors que le contrôle structural est habituellement contraint depuis l'échelle du district à celles du gisement et macroscopique, les processus géochimiques minéralisateurs sont décrits à l'échelle microscopique. Proposer une histoire couplant déformation et processus hydrothermaux minéralisateurs à toutes les échelles reste donc un enjeu majeur.

Cette étude propose une approche multi-scalaire innovante permettant la réconciliation d'informations structurales et géochimiques concernant les gisements hydrothermaux d'or déformés. L'originalité de notre approche, conduite du terrain au laboratoire, tient dans le couplage d'une étude pétro-structurale classique à l'apport de la micro-tomographie à rayons X de haute résolution, de la diffraction d'électrons rétro-diffusés et de la spectrométrie de masse à plasma à couplage inductif couplée à une ablation laser sur sulfures paragénétiquement associés à la minéralisation aurifère.

Appliquée à l'exemple du gisement aurifère de Galat Sufar South (bouclier nubien, Soudan), cette approche illustre les relations entre (i) la mise en place de la suture d'Atmur-Delgo avec (ii) les micro-structures affectant les sulfures et (iii) la libération d'or et la remobilisation des métaux synchrones de la recristallisation métamorphique de la pyrite. Notre étude ouvre donc la porte à la discrimination des relations déformation-minéralisation de n'importe quel autre gîte métallique déformé contenant des sulfures, moyennant l'intégration de données multiples collectées sur le terrain et au laboratoire.

Mots-clés

Gîtes aurifères hydrothermaux ; contrôle structural ; processus géochimiques minéralisateurs ; approche multi-scalaire ; micro-tomographie aux rayons X ; EBSD ; LA-ICP-MS ; gisement aurifère de Galat Sufar South.

Abstract

Integrating structural control on mineralisation and geochemical ore-forming processes is crucial in ore geology, especially when focusing on deformed ore deposits. Yet, structural and geochemical data are rarely acquired at the same scale: structural control on mineralisation is typically investigated from the district to the deposit and macroscopic scales whereas geochemical ore processes are described at the microscopic scale. The deciphering of a deformation-mineralisation history valid at every scale thus remains challenging.

This study proposes an innovative multi-scale approach that enables the reconciliation of structural and geochemical information collected at every scale, focusing on deformed gold deposits. It gathers field and laboratory information and its originality lies in coupling a classical petrological-structural study with high-resolution X-ray computed tomography, electron back-scattered diffraction and laser ablation inductively-coupled plasma mass spectrometry on mineralised sulphide mineral assemblages.

Applied to the example of the Galat Sufar South gold deposit, Nubian shield, northeastern Sudan, this approach enables to demonstrate the relationships between Atmur-Delgo suturing tectonics, micro-deformation of sulphide minerals, syn-pyrite recrystallisation metal remobilisation and gold liberation. Our contribution therefore represents a step forward a holistic field-to-laboratory approach for the study of any other sulphide-bearing, structurally-controlled ore deposit.

Keywords

Hydrothermal gold deposits; structural control; geochemical processes; multi-scalar approach; X-ray micro-tomography; EBSD; LA-ICP-MS; Galat Sufar South gold deposit.

1. Introduction

There is extensive literature on the role of deformation in the onset on hydrothermal mineralising fluid systems (McCaffrey et al., 1999; Cox et al., 2001; Richards and Tosdal, 2001; Chauvet, 2019; Blenkinsop et al., 2020a, 2020b; Rowland and Rhys, 2020), which is particularly well characterised for deformed lode gold or gold-bearing vein deposits such as orogenic gold (*e.g.,* Sibson, 1990, 2001, 2020a, 2020b; Ridley, 1993; Robert and Poulsen, 2001; Faleiros et al., 2007; Weatherley and Henley, 2013; Peterson and Mavrogenes, 2014; Cox, 2016). In addition, numerous micro-structural, geochemical and thermodynamic studies provide information on deformation-assisted geochemical processes leading to gold mineralisation in structurally-controlled gold deposits at the microscopic scale (*e.g.,* Tomkins and Mavrogenes, 2001; Weatherley and Henley, 2013; Fougerouse et al., 2016; Finch and Tomkins, 2017; Petrella et al., 2019, 2020; Gaboury and Oré Sanchez, 2020; Voisey et al., 2020). Sulphide minerals, most commonly pyrite and arsenopyrite, can host a variable amount of the gold stock in such deposits, either as free gold inclusions, structurally-bound refractory gold in the sulphide lattice, or as nano-inclusions (*e.g.,* Cook and Chryssoulis, 1990; Reich et al., 2005; Hough et al., 2011; Deditius et al., 2014; Pokrovski et al., 2019). In a given deposit, sulphide mineral texture and geochemical signature may thus indicate gold input and crystallisation-remobilisation stages (*e.g.,* Combes et al., in press; Velasquez et al., 2014; Fougerouse et al., 2017; Gourcerol et al., 2018a, 2018b, 2020; Kontak et al., 2018; Large and Maslennikov, 2020) and could be used as pathfinders for high-grade gold ore (*e.g.,* Kadel-Harder et al., 2020).

However, structural control on mineralisation and geochemical mineralisation processes are rarely documented together, as the required scale of investigation typically differs. This leads us to the conjoined study of structural and geochemical multi-scale data to show how we could reconciliate them.

Structural control on mineralisation is documented from the district to the deposit, outcrop and hand sample scales, *i.e.,* tens of to a hundred km, <1 km, up to tens of m and up to tens of cm, respectively, relying on field observations, structural measurements and conventional petrological-structural description of mineralised structures (*e.g.,* Combes et al., in press; Allibone et al., 2002, 2018; Ashley and Craw, 2004; Blenkinsop and Doyle, 2014; Masurel et al., 2017; Yang et al., 2018; Hronsky, 2020). These field-based data can be further processed by geostatistical and modelling techniques (*e.g.,* Monteiro et al., 2004; Upton and Craw, 2014b; Cowan, 2020). Structural data upscaling at the microscopic scale remains however difficult, as loss of information can occur when switching from 3D view of outcrops and drill cores to 2D view of sample slabs and thin sections, even in oriented samples.

At the deposit to macroscopic scales, the statistical analysis of extensive whole rock geochemical and lithological datasets, *e.g.,* mass-balance calculation or compositional data analysis by principal component analysis for instance, provide knowledge about elemental mobility induced by alteration and mineralisation processes which is of strong interest for ore targeting (*e.g.,* Gaillard et al., 2020; Meng et al., 2020). When zooming at the microscopic scale, unravelling geochemical ore processes requires the study of the micro-textural evolution of ore-bearing mineral assemblages together with their *in situ* geochemical signature (*e.g.,* Reich et al., 2017; Román et al., 2019). Analytical techniques such as laser ablation inductively-coupled plasma mass spectrometry (LA-ICP-MS) enable the *in situ* measurement down to a few µm-scale of minor and trace element concentrations in ore-related minerals, in relationship with micro-textural observations (*e.g.,* Román et al., 2019). This approach has been widely used to study sulphide trace element geochemistry within individual deposits (*e.g.,* Combes et al., in press; Large et al., 2007, 2009; Cook et al., 2013; Hazarika et al., 2013; Velasquez et al., 2014; Augustin and Gaboury, 2018; Gourcerol et al., 2018b, 2018a; Li et al., 2019; Wu et al., 2019a; Gourcerol et al., 2020; Kadel-Harder et al., 2020). Yet, most studies ado not address the

micro-structural and -textural characterisation of ore-bearing mineral assemblages, although such approach could bring knowledge about the relation between the deposit- and district-scale deformation history and micro-deformation-induced geochemical ore-forming processes. For instance, coupling 2D LA-ICP-MS trace element mapping on pyrite with micro-deformation analysis *via* electron back-scattered diffraction (EBSD) at the Detour Lake deposit, Canada, revealed that pyrite micro-structures are favorable for gold entrapment during syn-metamorphic fluid-assisted deformation (Dubosq et al., 2018).

In this study, we propose a multi-scale and -method approach that helps to (i) downscale structural control on mineralisation from the district and deposit-scales to the microscopic scale and (ii) bring knowledge about deformation-induced geochemical gold mineralisation processes. We coupled a classical field- and microscopy-based petrological-structural approach to laboratory 3D micro-imagery (high-resolution X-ray computed tomography, HRXCT), micro-structural analysis (electron back-scattered diffraction, EBSD) and *in situ* geochemical investigation of the gold-bearing sulphide assemblage (laser ablation inductively-couple plasma mass spectrometry on pyrite, LA-ICP-MS).

2. Current insights from HRXCT, EBSD and LA-ICP-MS into geoscience

Although the analysis of micro-structures and/or mineral geochemistry is often considered as a second rank method for the understanding of orebodies, it offers, when conducted on oriented samples, additional information on structural-mineralisation relationships. Nevertheless, such laboratory-based, microscopic scale investigations must come in support of conventional field and microscopy work. We will first present HRXCT, EBSD and LA-ICP-MS technique principles and what geoscience questions they can help answering.

2.1. High-resolution X-ray computed tomography

HRXCT is a 3D imaging technique relying on X-ray attenuation contrasts as a function of density and atomic number. It allows to reconstruct the 3D distribution of the local attenuation coefficient, *i.e.*, variation in the material density and composition, from stacking of 2D virtual slices through the studied object (Ketcham and Carlson, 2001; Cnudde and Boone, 2013; Kyle and Ketcham, 2015 and references therein). The main advantage of this technique is that it allows the investigation of the internal structures of a given material in a non-invasive and non-destructive way (Ketcham and Carlson, 2001; Cnudde and Boone, 2013; Kyle and Ketcham, 2015 and references therein).

The use of computed tomography in geoscience has increased in the last two decades, notably thanks to the possibility of multi-scale imaging, providing macroscopic information from large-sample imaging at low resolution and small-subsample imaging at higher resolution, down to a few hundreds of nanometers (Ketcham and Carlson, 2001; Mees et al., 2003; Cnudde and Boone, 2013). HRXCT uses volume reconstruction and further geometrical analysis to provide information useful for (i) petrophysical characterisation of rocks (*e.g.,* Galkin et al., 2015 and references therein), (ii) magmatic or metamorphic petrofabric studies (*e.g.,* Sayab et al., 2015; Kahl et al., 2017), (iii) fluid and melt inclusion petrography, volumetric and thermodynamic conditions reconstruction (*e.g.,* Richard et al., 2019), (iv) morphological characterisation of fossils (*e.g.,* Vasseur et al., 2019), (vi) gemology (*e.g.,* Morlot et al., 2016), and (vii) planetary science (*e.g.,* Hanna and Ketcham, 2017).

Regarding ore geology, HRXCT and other tomography methods, such as 3D neutron tomography or integrated absorption, diffraction and fluorescence tomography, are mostly used for (i) ore processing optimisation (*e.g.,* Miller et al., 2003; Dhawan et al., 2012), (ii) qualitative and quantitative investigation of ore texture and grain distribution (*e.g.,* Kyle and Ketcham, 2003; Godel et al., 2010; Godel, 2013), (iii) ore

mineral grain shape and texture characterisation (*e.g.,* Sayab et al., 2016; Prichard et al., 2018; Suuronen and Sayab, 2018), (iv) understanding the mechanisms of mineral growth (*e.g.,* Prichard et al., 2018). More importantly, these techniques have been used more recently to unravel the mechanisms of ore formation (*e.g.,* Godel et al., 2013; Kyle and Ketcham, 2015; Voisey et al., 2020). HRXCT is thus a very promising method to reconciliate macroscopic to microscopic scale 3D structural data in structurally-controlled deposits (*e.g.,* Sayab et al., 2020). At the microscopic scale (< hundreds of µm), HRXCT may be coupled with other techniques, such as electron back-scattered diffraction analyses (EBSD), to combine valuable morphological and micro-structural information that can be related to geomaterial macro-structures (*e.g.,* Vukmanovic et al., 2013; Kahl et al., 2017).

2.2. Electron back-scattered diffraction

EBSD is a scanning electron microscope-based technique that provides crystallographic and microstructural information. In short, an electron beam interacts at an angle with a sample. The electrons are diffracted following a pattern that is specific to the crystal structure and orientation of the investigated area. This method also allows to locate and characterise grain and subgrain boundaries (Schwartz et al., 2009 and references therein).

Over the past two decades, and with the advances in automation technology, EBSD has been widely employed for grain-scale orientation, phase identification, textural description, strain and micro-structural analysis in metallurgy and materials science (*e.g.,* Nowell et al., 2005; Barou et al., 2009; Schwarzer et al., 2009; Wright et al., 2011; Wilkinson et al., 2014) but also in Earth sciences (Prior et al., 2009 and references therein). The lattice-preferred orientation of minerals characterised through EBSD provides *"information about creep deformation mechanisms, conditions and kinematics"* occurring in the crust and mantle (Prior et al., 2009). Up to now, EBSD has mostly been

used for (i) rock deformation and kinematics characterisation (*e.g.,* Goswami et al., 2018), (ii) seismic implications (Vonlanthen et al., 2006), (iii) magmatic (*e.g.,* Žák et al., 2008) or metamorphic (*e.g.,* Rehman et al., 2016) process unravelling, (iv) experimental micro-structural studies (*e.g.,* Piazolo et al., 2004) and also for (v) synthetic or natural mineral grain-scale deformation mechanism characterisation (*e.g.,* Rosière et al., 2001; Barrie et al., 2010a; Halfpenny et al., 2013; Wallis et al., 2019).

When it comes to ore geology, EBSD is mostly used for the textural investigation of the ore and integration to the regional metamorphism-deformation history (*e.g.,* Boyle et al., 2004; Barrie et al., 2010b; Sayab et al., 2020) as well as the study of mineralisation processes related to micro-deformation (*e.g.,* Kolb et al., 2003; Mateen et al., 2013; Reddy and Hough, 2013; Rosière et al., 2013; Vukmanovic et al., 2013; Fougerouse et al., 2016; Dubosq et al., 2018; Cugerone et al., 2020). Except from Kolb et al. (2003) and Mateen et al. (2013), who focused on gold-related quartz alteration and veins, the latter studies focused on sulphide or oxide-dominated ore mineral assemblages (chromite, pyrite, arsenopyrite, sphalerite or hematite). Recent analytical advances also allow to simultaneously couple EBSD mapping with electron-dispersive spectrometry (EDS), which is of high interest for the visualisation of grain-scale element distribution (Schwarzer et al., 2009). EBSD mapping may also be combined with 3D or 2D imagery techniques such as HRXCT (*e.g.,* Vukmanovic et al., 2013), cathodoluminescence and Raman-in-SEM imagery (*e.g.,* Wille et al., 2018).

2.3. Laser ablation inductively-coupled plasma mass spectrometry

In situ analytical methods, such as EMPA, SIMS and nanoSIMS or LA-ICP-MS, allow to couple major, minor and trace element geochemistry of sulphide minerals with their textural evolution at the µm-scale (Reich et al., 2017; Román et al., 2019). Recent advances in atom probe tomography even enable the study of mineral geochemistry at

the sub-nanometric, atomic scale (*e.g.,* Fougerouse et al., 2016b; Gamal El Dien et al., 2019; Wu et al., 2019b; Reddy et al., 2020).

The study of trace element signatures in sulphide minerals (*e.g.,* pyrite, sphalerite and chalcopyrite) is widely used to (i) distinguish between sulphide-bearing deposit types that can be overprinted through time (*e.g.,* Ye et al., 2011; Winderbaum et al., 2012; Belissont et al., 2014; Belousov et al., 2016; Frenzel et al., 2016), (ii) track temporal changes in ore hydrothermal systems (*e.g.,* Huston et al., 1995; Maslennikov et al., 2009; Wohlgemuth-Ueberwasser et al., 2015; Bonnet et al., 2016; Gill et al., 2016; Soltani Dehnavi et al., 2017; Wang et al., 2017) and (iii) better constrain element precipitation models leading to ore formation (*e.g.,* Butler and Nesbitt, 1999; George et al., 2018). The geochemical signature of pyrite in gold deposits is commonly used to track its thermodynamic stability, characterise boiling associated with fault rupture events, as well as the partitioning of gold and other metals and metalloids in evolving, sulfur-rich, hydrothermal systems (*e.g.,* Reich et al., 2005; Deditius et al., 2009, 2014; Keith et al., 2016, 2018; Finch and Tomkins, 2017; Tardani et al., 2017; Pokrovski et al., 2019; Román et al., 2019; Wu et al., 2019b; Xing et al., 2019). The microscopic scale investigation of trace elements in pyrite also documents the crystal growth mechanisms, *e.g.,* kinetics, the source(s) of ore-forming fluids (*e.g.,* Augustin and Gaboury, 2018; Voute et al., 2019; Adam et al., 2020), and its potential contribution as a gold source (*e.g.,* Large et al., 2007, 2011). The trace element signature of sulphide minerals is also highly dependent on metamorphic conditions and may vary with sulphide recrystallisation, leading to metal remobilisation and segregation along syn- to late metamorphic structures within a deposit (*e.g.,* Morey et al., 2008; Dakota Conn et al., 2019). The coupling between deposit-scale petrological-structural study, textural characterisation of pyrite and LA-ICP-MS geochemical analyses helps tracking potential pre-tectonic gold pre-enrichment and the contribution of subsequent deformation-related hydrothermal event(s) to the overall gold endowment (*e.g.,* Sung et al., 2009; Zhao et al., 2011; Peterson and

Mavrogenes, 2014; Velasquez et al., 2014; Genna and Gaboury, 2015; Belousov et al., 2016; Salvi et al., 2016; Augustin and Gaboury, 2018; Kerr et al., 2018; Gao et al., 2019; Wu et al., 2019a).

3. Case study: the Galat Sufar South gold deposit, northeastern Sudan

Our study focuses on the Galat Sufar South (GSS) gold deposit, northeastern Sudan, owned by Orca Gold Inc. (indicated resources of 75.6 Mt @ 1.27 g/t Au for a total of 3.08 Mozt Au with a 0.6 g/t Au cut-off; Duckworth, 2018). GSS is a polyphase, sulphide-dominated, vein-type gold deposit. Mineralisation expression and relationships with deformation events have already been well-constrained from the tens of km-scale to the µm-scale by satellite imagery analysis, field and conventional microscopy work (Perret et al., 2020).

The GSS deposit is located within the western portion of the Arabian-Nubian shield (ANS; Fig. 4-1a) which represents the northern part of the East African-Antarctic Orogeny (EAAO, Stern, 1994; Johnson and Woldehaimanot, 2003; Kusky et al., 2003; Fritz et al., 2013; Grenholm, 2019). The Arabian-Nubian shield formed during a ~ 850-550 Ma "Supercontinent Cycle" (Stern and Johnson, 2010; Johnson et al., 2011) and results from the amalgamation and collision between terranes that accreted onto the Saharan meta-craton (Fig. 4-1a; Johnson and Woldehaimanot, 2003; Johnson et al., 2011 and references therein). The terranes are formed by juvenile magmatic arc and ophiolite assemblages remnants of the subduction and obduction processes that completely consumed the Mozambique ocean in the northern part of the East African-Antarctic Orogen (*e.g.,* Burke and Sengör, 1986; Johnson et al., 2011; Fritz et al., 2013 and references therein).

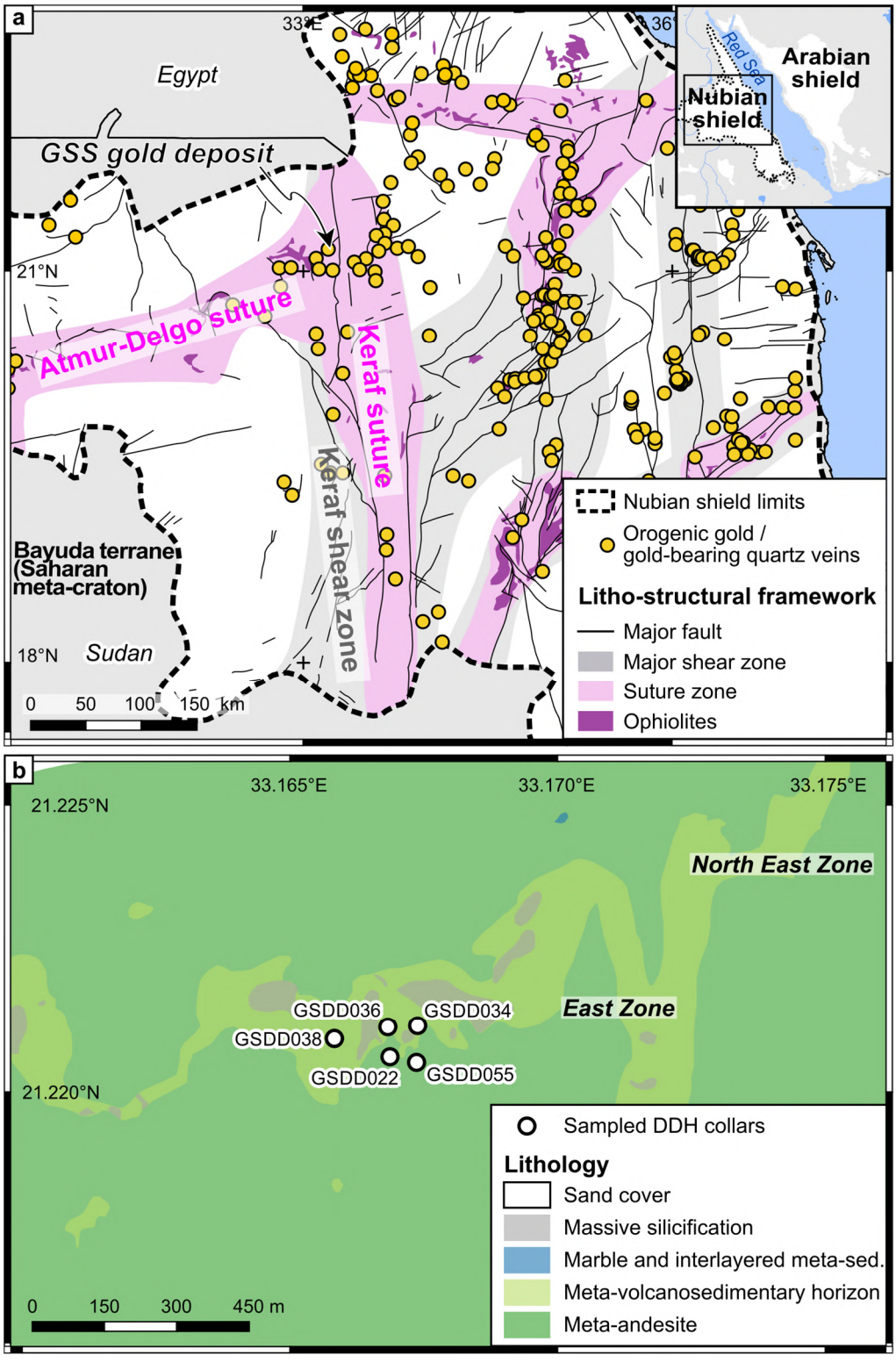


Figure 4-1: Geological setting of the Galat Sufar South (GSS) gold deposit, adapted after Perret et al. (2020). **a** Structural framework of the Nubian shield, simplified after Johnson et al. (2011) and references therein. Gold occurrences are from the Arethuse Geology GIS compilation database. **b** Lithological framework of the GSS gold deposit, modified after the lithological map provided by Orca Gold Inc. (2017). The collar location of sampled diamond drill holes (DDHs) for this study is indicated. Geographic coordinates are reported according to the WGS 84 coordinate system.

The east-striking Atmur-Delgo and north-striking Keraf sutures (ADS and KS, respectively) record the collision of the Arabian-Nubian shield with the Saharan meta-craton (Fig. 4-1a; Almond and Ahmed, 1987; Stern, 1994; Abdelsalam et al., 1995, 1998; Bailo et al., 2003). The Atmur-Delgo suture results from the closure of an aulacogenic oceanic re-entrant associated with the Mozambique ocean into the Saharan meta-craton (Burke and Sengör, 1986; Abdelrahman, 1993; Denkler et al., 1993; Harms et al., 1994; Schandelmeier et al., 1994b; Abdelsalam et al., 1998), while the Keraf suture results from the arc-continent collision of terranes forming the Arabian-Nubian shield over the Saharan meta-craton (Fig. 4-1a; Vearncombe, 1983; Burke and Sengör, 1986; Frisch and Pohl, 1986; Berhe, 1990; Abdelsalam and Dawoud, 1991; Ries et al., 1992; Mosley, 1993; Abdelsalam et al., 1998; Fritz et al., 2013). During the late collision period, the Keraf suture has been overprinted by a sinistral transpression resulting in the Keraf shear zone (KSZ) (Fig. 4-1a; Abdelsalam et al., 1995, 1998; Abdelsalam and Stern, 1996a, 1996b).

The GSS gold deposit is encompassed within a complexly deformed zone at the junction between the Atmur-Delgo and Keraf sutures (Fig. 4-1a). It is hosted by a strongly deformed, interleaved andesitic meta-volcanosedimentary horizon enclosed within a thick andesitic meta-volcanic sequence composed of lava flows, pyroclastic horizons and primary volcanic breccia (Fig. 4-1b; Perret et al., 2020). This assemblage is surrounded by meta-pelites interlayered with marbles. The deposit-scale structural framework is complex and dominated by subvertical linear fabrics, including several km- to dm-scale sheath folds inferred from satellite imagery and outcrop structural analysis (Perret et al., 2020). The GSS gold deposit recorded a complex deformation history related to several veining and alteration events. The simplified mineral paragenesis related to the deformation events is summarised in Figure 4-2 (for more details, see Perret et al., 2020). It started with an early, ductile-dominated, progressive D_{1GSS}-D_{2GSS}-(D_{3GSS}) deformation episode associated with the main gold event. It ended with a minor, late, brittle D_{4GSS} veining episode related to a minor mineralisation event (Figs. 4-2 and 4-3).

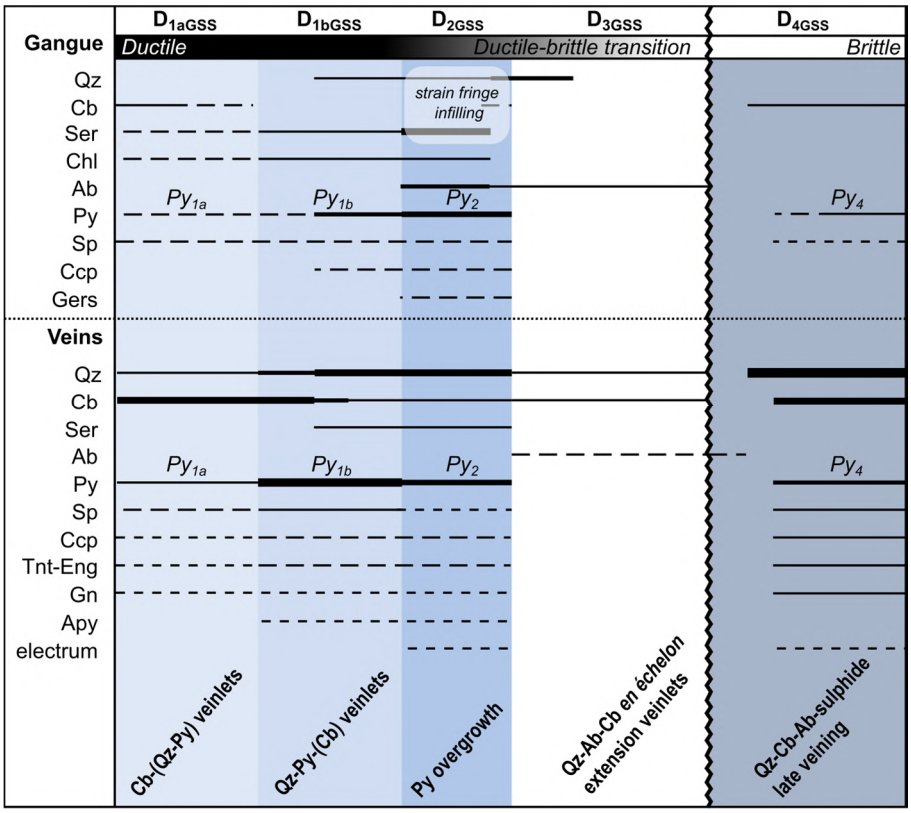


Figure 4-2: Simplified mineral paragenesis of the Galat Sufar gold deposit, modified after Perret et al. (2020). The broken line separates the D_{1GSS}-D_{2GSS}-(D_{3GSS}) progressive deformation stages from the late D_{4GSS} deformation event. Mineral abbreviations for Figs. 4-2 to 4-7, 4-9, 4-10 and 4-12 and Table 4-1 are Qz, quartz; Cb, carbonate; Ser, sericite; Chl, chlorite; Ab, albite; Py, pyrite; Sp, sphalerite; Ccp, chalcopyrite; Tnt-Eng, sulfosalt (tennantite-enargite); Gn, galena; Apy, arsenopyrite; Gers, gersdorffite. Pyrite generations are indexed regarding the deformation stage they relate to (see details in Perret et al., 2020).

The ductile D_{1GSS} deformation stage is characterised by the D_{1aGSS}-related S_1 foliation, F_1 folding and a change from carbonate-dominant with minor quartz and pyrite to D_{1bGSS}-related quartz-pyrite-dominant with minor carbonate veining and disseminated pyrite grains (Fig. 4-3a to d). The increase in pyritisation from D_{1aGSS} to D_{1bGSS} veining is correlated with an increase in gold grades (from < 0.1 g/t to ~ 1 g/t Au; fire assays data from Orca Gold Inc.'s database are given for studied samples in Table 4-1) and is thought to represent the first gold input into the system (Perret et al., 2020).

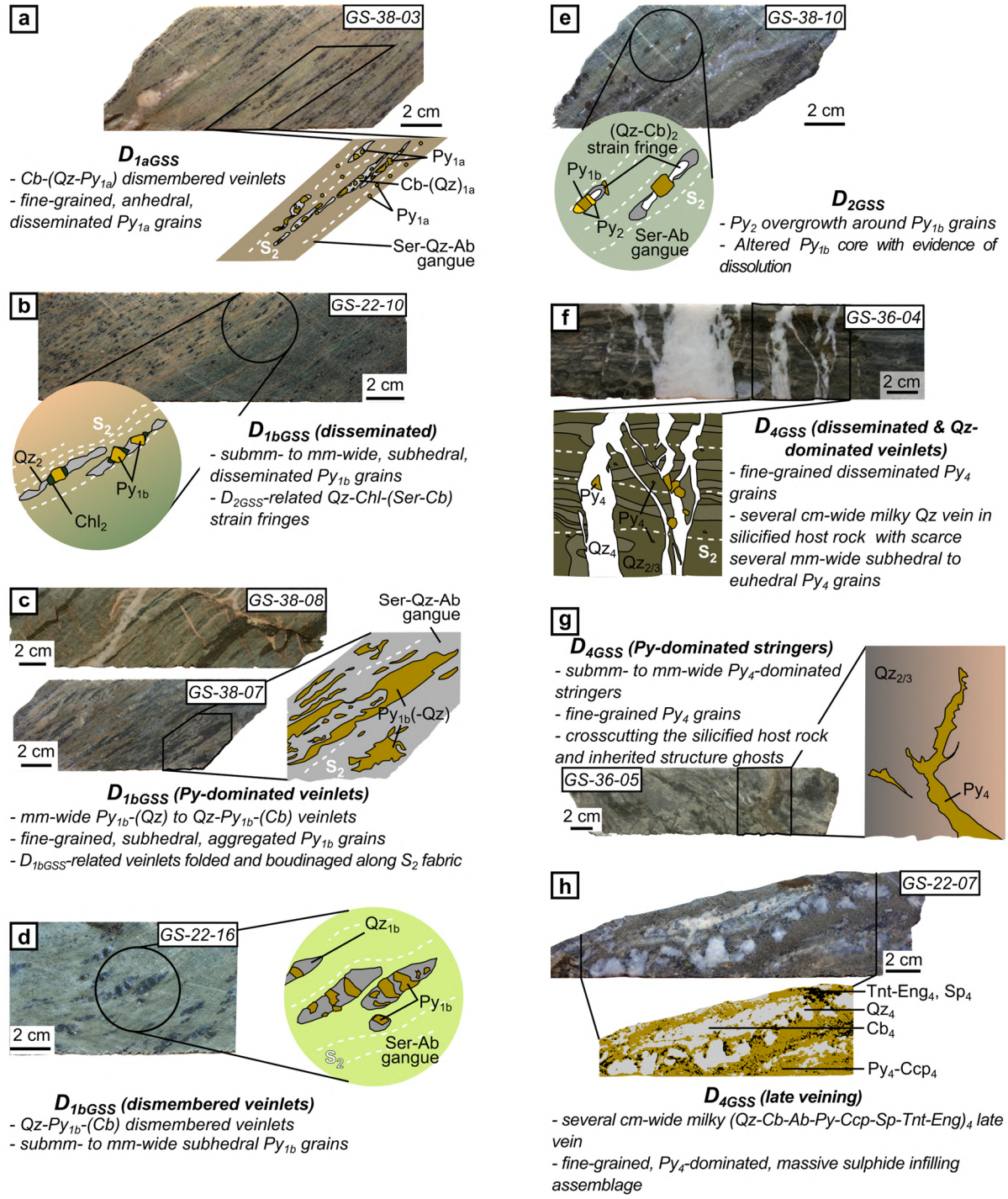


Figure 4-3: Macroscopic scale features of pyrite generations identified at the Galat Sufar South gold deposit. Mineral abbreviations are similar to Figure 4-2. Mineral generations are indexed based on the deformation stage they relate to (see details in Perret et al., 2020). **a** D_{1aGSS}-related pyrite. **b** D_{1bGSS}-related, disseminated pyrite with asymmetrical D_{2GSS}-related quartz-chlorite-(sericite-carbonate) strain fringes. **c** D_{1bGSS}-related pyrite in folded pyrite-dominated veinlets. **d** D_{1bGSS}-related pyrite in quartz-pyrite-(carbonate) veinlets. **e** D_{2GSS}-related pyrite as overgrowth around Py_{1b} grains. **f** D_{4GSS}-related pyrite disseminated in silicified intervals and enclosed in a crosscutting milky quartz veinlet. **g** D_{4GSS}-related pyrite-dominated stringers crosscutting highly silicified host rock intervals. **h** D_{4GSS}-pyrite in quartz-carbonate-albite-polymetallic sulfide assemblage late veins.

The ductile D_{2GSS} deformation stage controls the GSS structural framework from the tens of km- to the µm-scales. It is mostly characterised by subvertical, linear, ductile structures such as a L_2 stretching lineation. L_2 controls the C/S_2 (simplified into S_2 in illustrations and below) penetrative shear band cleavage orientation, which is the main planar fabric. D_{1GSS}-related veins are boudinaged, folded and dismembered along the S_2 fabric (Fig. 4-3a, c and d) and pyrite overgrowth and strain fringes are developed around D_{1GSS}-related pyrite grains (Fig. 4-3e). These micro-structures form ore shoots (>1 g/t Au, up to >15 g/t Au; Table 4-1) contributing to the main gold mineralisation at the GSS gold deposit.

The ductile-brittle D_{3GSS} transition is portrayed by kink bands affecting the sericite-rich gangue, quartz-albite-carbonate *en échelon* extension veins. No mineralisation formed during this deformation stage.

The late, brittle D_{4GSS} veining event occurred with no preferential orientation. The vein mineral assemblage ranges from barren quartz-carbonate-albite to highly mineralised (up to >10 g/t Au; Table 4-1) polymetallic sulphide assemblage (Fig. 4-3f, g and h). D_{4GSS} veining extent is limited to previously silicified host rock intervals. This episode formed very local high-grade ore shoots with a minor contribution to the overall GSS gold endowment.

The gold input or remobilisation nature of each mineralisation event remains uncertain from the petrological-structural data available up to now (Perret et al., 2020).

4. Sampling and analytical procedures

4.1. Field study

A field study has been carried out within the East Zone of the GSS gold deposit (Fig. 4-1b). Relying on observations and structural measurements on outcrops and

oriented drill cores, relationships between lithology, deformation, alteration and mineralisation have been unraveled at the deposit- to macroscopic scales (Perret et al., 2020). These findings are briefly summarised hereafter.

4.2. Sampling and petrography

Samples of interest illustrate the successive deformation stages and related mineralisation events forming the GSS gold deposit. They have been collected along several diamond drill cores within the East Zone of the GSS gold deposit (Fig. 4-1b). Samples illustrated in Figs. 4-3 to 4-10 are listed in Table 4-1. Thin sections and one-inch epoxy laser mounts have been prepared for these samples. Optical microscopy and additional analyses using a scanning electron microscope in back-scattered electron mode (BSE-SEM) were carried out for petrography work at the GeoRessources laboratory (Université de Lorraine-CNRS, Nancy, France).

4.3. High-resolution X-ray computed tomography

HRXCT analyses were performed to reconstruct the 3D geometry of sulphide-rich mineralised micro-structures which orientation cannot be measured using conventional methods. HRXCT scans of billet GS-34-07 (Table 4-1) were acquired at the GeoRessources laboratory (University of Lorraine, Nancy, France) with a Phoenix Nanotom S scanner, using a CCD Hamamatsu detector, with 2300×2300 pixels resolution. Analytical conditions were set to 75 mA current and 112 kV acceleration voltage with a 85-mm source-sample distance. Fifteen hundred projections were carried out, leading to a total scan time of 120 min. The spatial resolution was 17 µm/pixel (*i.e.,* 4913 μm^3/voxel). Data processing was carried out using the Avizo® 9.2.0. software.

Sample ID*	Grade (g/t Au)	Results presented in this study			
		Petrography (*Figs. 4-3, 4-4*)	*HRXCT* (*Fig. 4-5, Sup. Mat. 4-1*)	*EBSD* (*Figs. 4-6, 4-7*)	*LA-ICP-MS* (*Figs. 4-8 to 4-10, Table 4-2, Sup. Mat. 4-2*)
GS-22-06	0.08	x			x
GS-22-07	3.56	x			x
GS-22-08	0.28	x		x	x
GS-22-10	0.19	x			x
GS-22-16	2.07	x			
GS-34-05	6.45	x		x	x
GS-34-07	3.89	x	x		
GS-36-04	0.08	x			x
GS-36-05	0.12	x			x
GS-38-03	0.51	x			
GS-38-05	15.2	x			x
GS-38-07	3.14	x			
GS-38-08	1.06	x			x
GS-38-09	1.79	x			
GS-38-10	8.64	x			
GS-38-12	7.70	x			x
GS-55-02	0.02	x			x

** Samples are named after the ID of the diamond drill hole they have been sampled from and are organised by increasing depth. Fire assay results of the corresponding 1 m-large drill core interval have been communicated by Orca Gold Inc. All samples have been described at the macroscopic and microscopic scales, but samples GS-34-05 and GS-34-07 are not illustrated in Figs. 4-3 and 4-4.*

Table 4-1: List of samples from this study, along with the corresponding analyses that they underwent.

4.4. Electron back-scattered diffraction

EBSD analyses were performed to characterise the micro-structures of mineralised sulphide assemblage. Samples GS-22-08 and GS-34-05 were selected (Table 4-1). Simultaneous energy-dispersive spectrometry (EDS) and EBSD mapping were carried out at the University of Montpellier (France) using a Camscan Crystal Probe X500FE

scanning microscope. Probe current, acceleration voltage and chamber pressure were set to 5 nA approximately, 20 kV and 2 Pa in low-vacuum mode, respectively, with a 25-mm working distance. Step size was set to 1.2 µm (GS-22-08) and 1 µm (GS-34-05). Data collection monitoring and data processing were carried out using the AZtecHKL and HKLChannel5 Project Manager softwares, respectively.

4.5. Laser ablation inductively-coupled plasma mass spectrometry on pyrite

LA-ICP-MS data on the different pyrite generations separated at the GSS gold deposit were collected at the Queen's Facility for Isotope Research (Queen's University, Ontario, Canada) using a ThermoScientific X Series 2® quadrupole ICP-MS coupled to a NewWave/ESI 193-nm ArF Excimer laser system. Samples for which laser ablation analyses were carried out are listed in Table 4-1. The isotopes measured were ^{29}Si, ^{34}S, ^{51}V, ^{52}Cr, ^{55}Mn, ^{57}Fe, ^{59}Co, ^{60}Ni, ^{65}Cu, ^{66}Zn, ^{71}Ga, ^{75}As, ^{77}Se, ^{95}Mo, ^{107}Ag, ^{111}Cd, ^{115}In, ^{118}Sn, ^{121}Sb, ^{125}Te, ^{182}W, ^{197}Au, ^{205}Tl, ^{208}Pb and ^{209}Bi, with a dwell time of 10 ms.

Spot analyses were performed to closely match the observed micro-textures in pyrite grains with their specific trace element signatures. Care was taken in selecting spot positions, especially in Py_{1b} altered cores (see subsection 5.1.), to minimise the ablation of any visible mineral inclusion. Prior to each analysis, the background signal, or gas blank, was measured for a duration of 25 s. The beam diameter was set to 50 µm for all samples and reference materials, with a pulse frequency of 10 Hz.

Elemental maps were also produced to (i) better understand the spatial distribution of the trace elements present in the different types of pyrite, (ii) complement the data derived from spot analyses and (iii) match areas that were mapped through EBSD to better constraint micro-deformation influence on elemental mobility in sulphide mineral assemblages. The set up used for laser mapping was the same as above. Similarly to spot analyses, a 25 s gas blank was measured prior to each ablation line. Beam size was set

to 15 µm, to allow for a minimum of 40 horizontal lines per map for better image resolution. The laser scan speed was set to 8 µm/s and the pulse frequency to 10 Hz. The fluence for both spot and map analyses was about 8.0 J/cm².

The LA-ICP-MS data were reduced with Iolite 3.65 (Paton et al., 2011). Spot analyses comprise blocks of 30 spots on samples bracketed by a series of 3 spots on each of the 6 certified reference materials. Similarly, for map analyses, three standard lines were analysed for each standard at the beginning and end of the analytical run to account for analytical drift and allow semi-quantification.

The reference standards were USGS GSE-1G (Jochum et al., 2005), MASS-1 (Wilson et al., 2002), as well as FeS-4, FeS-5, PTC-1b and CCU-1e sulphide reference materials from Université du Québec à Chicoutimi, Canada (CCRM, CANMET). FeS-5 was used for trace element quantification in pyrite spot analyses and correction for variations in ablation efficiency. Limits of detection (LOD) were calculated following the Howell's method (see references in Howell and Blakey, 2013). LA-ICP-MS elemental maps were edited using the Monocle add-on to determine trace element compositions of specific areas and textures of the grains of interest (Petrus et al., 2017).

5. Results and integration to previous petrological-structural field observations

5.1. Petrological-structural description of the mineralised sulphide assemblages

From the mineral paragenesis established for the GSS gold deposit by Perret et al. (2020) (Fig. 4-2), four pyrite generations have been described and are labelled from Py_{1a} to Py_4, each referring to the deformation stage they relate to (D_{1aGSS} to D_{4GSS}). The same labelling scheme is used for the other mineral phases illustrated in the figures below. The macro- and micro-textural and -structural characteristics of each pyrite generation are documented below and illustrated in Figs. 4-3 and 4-4, respectively.

5.1.1. Py_{1a} generation

Py_{1a} generation occurs as disseminated grains in the sericite-rich gangue. They highlight the S_2 penetrative cleavage (Figs. 4-3a, 4-4a).

There are also rare, fine-grained (<100 µm), anhedral Py_{1a} grains in D_{1aGSS}-related carbonate-dominated veinlets dismembered along the S_2 fabric (Figs. 4-3a, 4-4a). Within these veinlets, Py_{1a} is associated with scarce chalcopyrite, sphalerite and sulfosalt (Fig. 4-4a).

5.1.2. Py_{1b} generation

Py_{1b} generation is characterised by disseminated grains, preferentially oriented along the S_2 penetrative cleavage. These grains are coarser than disseminated Py_{1a} grains (up to 500 µm), subhedral and display subvertical C_2 simple shearing-related asymmetrical quartz-chlorite-(sericite-carbonate) strain fringes (Figs. 4-3b, 4-4b).

Py_{1b} is also visible in D_{1bGSS}-related veinlets. The increase in pyrite modal proportion from about 30 to >50 vol% from D_{1aGSS} to D_{2bGSS} veining stages is correlated with the switch from carbonate-dominated to quartz- and/or pyrite-dominated veinlets. Pyrite-dominated veinlets may be F_2-folded, transposed and dismembered along the S_2 penetrative cleavage (Fig. 4-3c). In these veinlets, Py_{1b} is fine-grained and displays 120°-triple junction grain boundaries, *i.e.,* annealing during recrystallisation, and interstitial polymetallic sulphide minerals (sphalerite, sulfosalt in Fig. 4-4c). Dismembered quartz-dominated veinlets (Fig. 4-3d) host coarser (up to about 300 µm), subhedral Py_{1b} grains intergrown with the same sulphide mineral phases (Fig. 4-4d).

5.1.3. Py_2 generation

Py_2 grains are sometimes visible at the macroscopic scale and preferentially grow along the S_2 fabric around disseminated Py_{1b} grains displaying strain fringes (Fig. 4-3e). At the macroscopic and microscopic scales, the Py_{1b} core shows an altered aspect with evidence of dissolution (Figs. 4-3e, 4-4e). Py_2 overgrowth is also visible around altered

Py_{1b} grains in dismembered quartz-dominated veinlets (Fig. 4-4f). The development of Py_2 is coeval with the formation of mineral inclusions, within Py_{1b} core, of silicate, phosphate (apatite in Fig. 4-4e), sulphide minerals (chalcopyrite in Fig. 4-4e, arsenopyrite and sulfosalt in Fig. 4-4f) and electrum (Fig. 4-4f). Rare cogenetic gersdorffite occurs as a thin coating around the rim of Py_2 (Fig. 4-4e). This generation of pyrite is interpreted to be coeval with the S_2 main penetrative cleavage and L_2 stretching lineation which control the ore shoot distribution at the deposit scale (Perret et al., 2020).

5.1.4. Py_4 generation

The late, brittle D_{4GSS} veining encompasses all veins from non-mineralised quartz-carbonate-albite ones to polymetallic sulphide assemblage-dominated ones. Several Py_4 facies can be distinguished depending on pyrite relative abundance and textural association with other sulphide mineral phases.

Firstly, rare, coarse, subhedral Py_4 grains (Fig. 4-3f) occur with traces of intergrown sphalerite (Fig. 4-4g) in almost pyrite-free milky quartz-dominated veins. Very fine-grained disseminated Py_4 grains overprint the silicified mineral gangue at the selvages of these veins (Fig. 4-4g). These veins are non-mineralised (<0.1 g/t Au; Table 4-1).

Secondly, Py_4-dominated stringers also cut across the silicified host rock intervals (Fig. 4-3g) and are formed by aggregated subhedral to anhedral Py_4 grains of variable size with minor interstitial sphalerite (Fig. 4-4h). Disseminated Py_4 is still visible at the selvages of the pyrite stringers and seems to expand from its margins (Fig. 4-4h). These stringers are weakly mineralised (about 0.1 g/t Au; Table 4-1).

Thirdly, wider polymetallic sulphide-dominated late veins locally cut across the silicified host rock (Fig. 4-3h). Where the soft sulphide minerals, such as chalcopyrite and minor sulfosalts (Fig. 4-4i), are more abundant than pyrite, Py_4 occurs as coarse, rounded, grains embedded in the soft sulphide mineral matrix (Fig. 4-4i). Conversely, where pyrite is dominant, Py_4 aggregates are largely fractured and soft sulphide minerals

infill fractures (Fig. 4-4j). Such Py_4 grains may host electrum micro-inclusions (Fig. 4-4k). These veins are mineralised (7.7 g/t Au; Table 4-1).

While all pyrite generations were investigated for trace element signature through LA-ICP-MS analyses, HRXCT and EBSD analyses were only applied to $Py_{1a/b}$ and Py_2 generations. Indeed, $Py_{1a/b}$ and Py_2 generations relate to the regional progressive D_{1GSS}-D_{2GSS} deformation event coeval to the main gold mineralisation event defined at the GSS deposit, whereas the regional interpretation of D_{4GSS} remains unknown and associated gold mineralisation is limited (Perret et al., 2020).

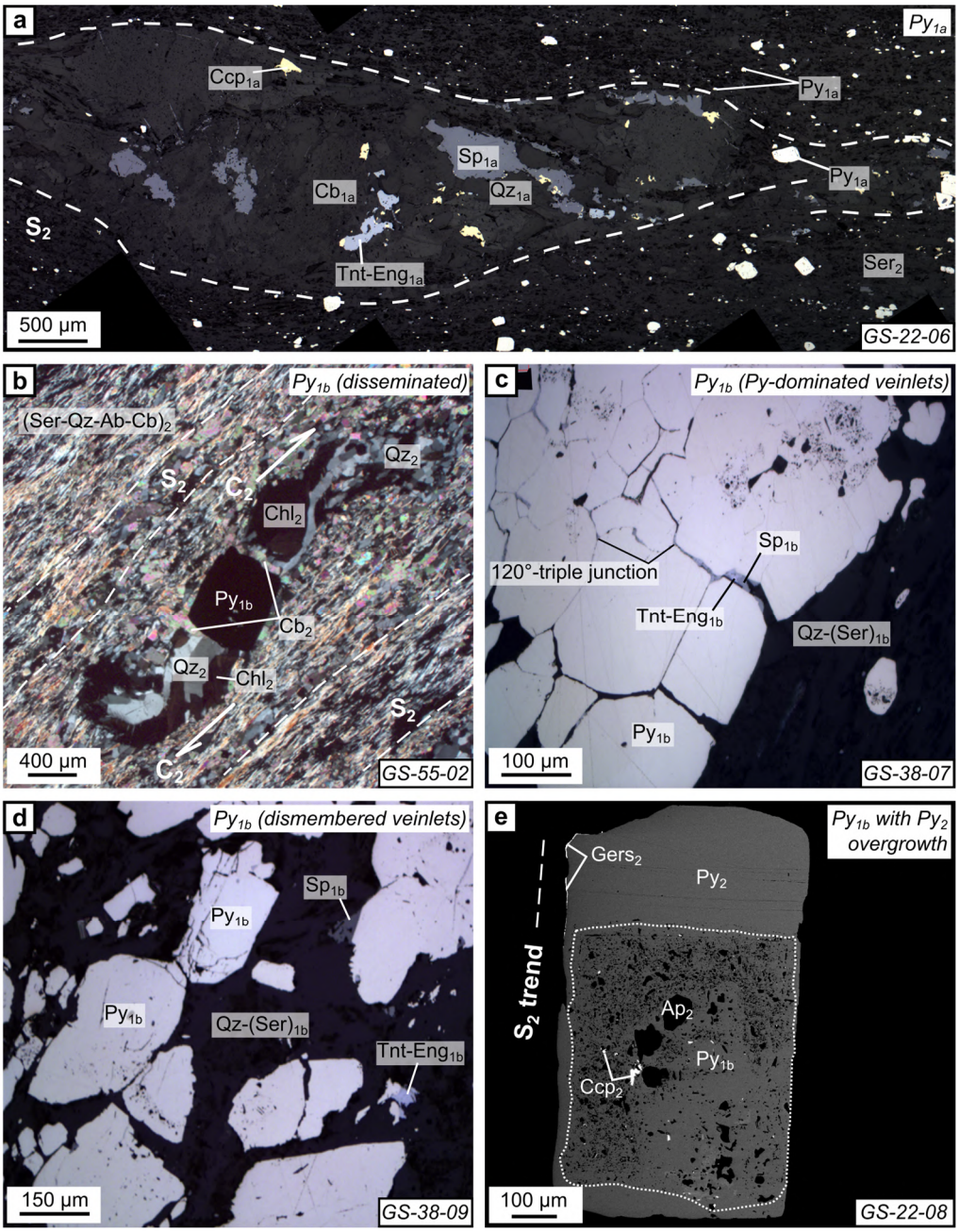


Figure 4-4: Microscopic scale features of pyrite generations identified at the Galat Sufar South gold deposit. Mineral abbreviations are similar to Figure 4-2. **a**, **b**, **e, f**, **j** and **k** photographs are from Perret et al. (2020). **a** D_{1a}-related pyrite associated with scarce chalcopyrite, sphalerite and sulfosalt in carbonate-dominated veinlets (reflected light). **b** Disseminated Py_{1b} grains are associated with quartz-chlorite-carbonate asymmetrical strain fringes related to E block-to-the-top C_2 shearing (cross-polarised, transmitted light). **c** Interstitial sulfosalt-sphalerite assemblage infilling 120°-triple junction grain boundaries in Py_{1b}-dominated veinlets (reflected light). **d** Rare sphalerite and sulfosalt associated with coarse Py_{1b} grains in quartz-pyrite-dominated dismembered veinlets (reflected light). **e** Py_2 overgrowth occurs around disseminated Py_{1b} grain with evidence of dissolution and enclosing a lot of mineral inclusions (back-scattered electron mode in scanning electron microscopy, BSE-SEM).

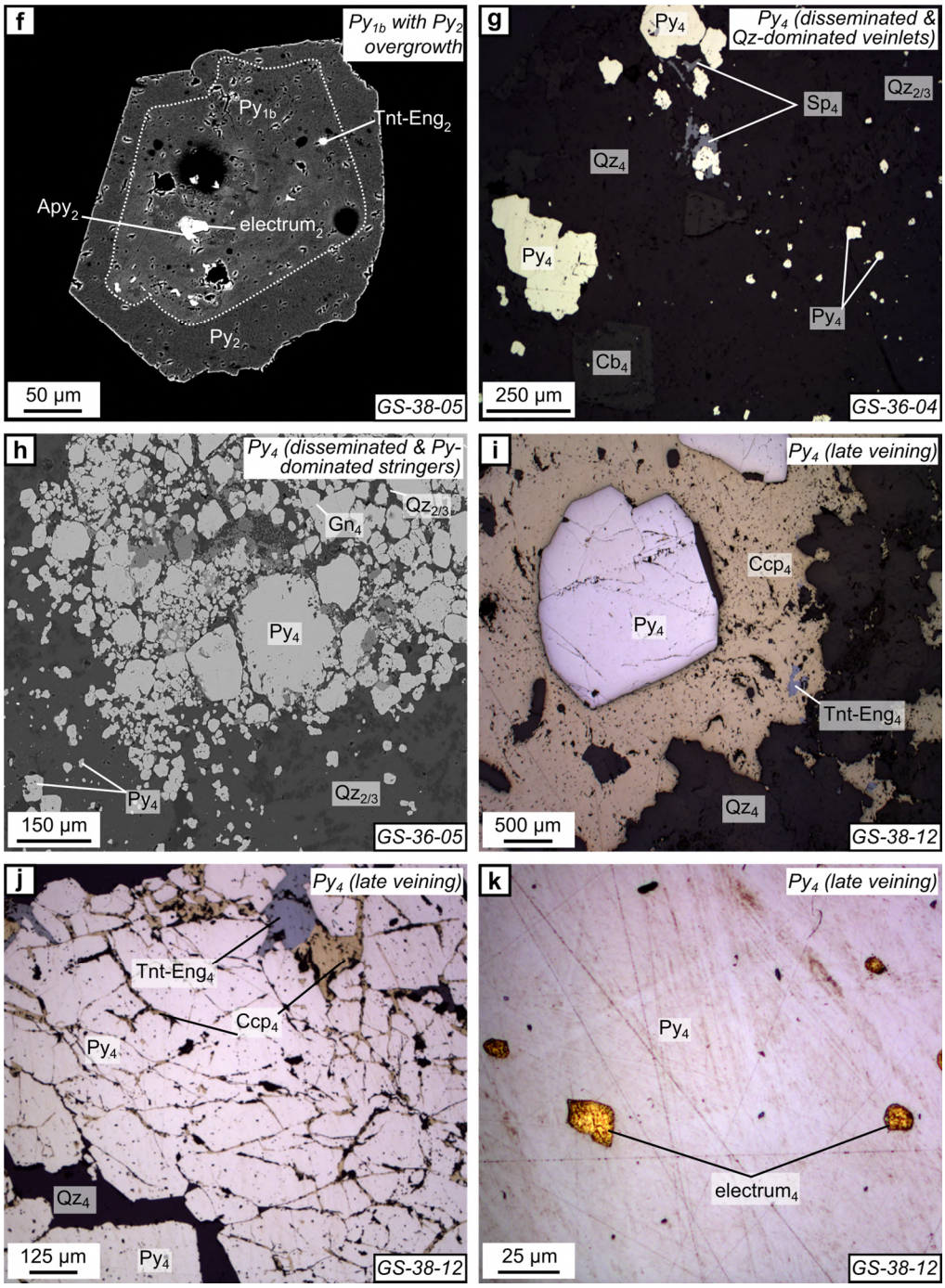


Figure 4-4 (continued): Microscopic scale features of pyrite generations identified at the Galat Sufar South gold deposit. Mineral abbreviations are similar to Figure 4-2. **a**, **b**, **e, f**, **j** and **k** photographs are from Perret et al. (2020). **f** Py_2 overgrowth around Py_{1b} grains in quartz-pyrite-dominated dismembered veinlets, presence of silicate, sulfide and electrum inclusions in the pyrite core (BSE-SEM). **g** Disseminated Py_4 spatially associated with crosscutting quartz-carbonate veinlet hosting rare, coarser Py_4 grains (reflected light). **h** Rare sphalerite is interstitial to aggregated pyrite grains in a Py_4-dominated stringer. Fine-grained, disseminated Py_4 facies expands from the margins of the stringer (BSE-SEM). **i** Coarse, rounded Py_4 grains embedded in a chalcopyrite-(sulfosalt) assemblage in quartz-carbonate-albite-sulfide late veins (reflected light). **j** Py_4 with sulfosalt-chalcopyrite assemblage infilling in pyrite grain joints and cracks in a Py_4-dominated late vein (reflected light). **k** Fine-grained electrum inclusions in Py_4 grains (reflected light).

5.2. High-resolution X-ray computed tomography

Sample GS-34-07 is a 5 cm-long slab that has been cut along a half core sample. It displays a schistose texture dominated by the subvertical S_2 cleavage along which carbonate- and sericite-rich bands alternate (Fig. 4-5a). The S_2 orientation is N080°E-84°N (Fig. 4-5a). A F_2-folded D_{1GSS}-related veinlet transposed along the S_2 cleavage is visible on this sample (Fig. 4-5a).

The fold axis orientation could not be measured directly on the drill core due to the small size of the micro-structure. An oriented billet has been cut to prepare an oriented thin section centered on this micro-fold (Fig. 4-5a and b). At the microscopic scale, the folding and individually-fragmented boudinaged structure of the D_{1aGSS}-related carbonate-dominated veinlet are clearly visible (Fig. 4-5b). However, switching from the macroscopic 3D sample and drill core observations to the microscopic 2D thin section-scale only provides a partial view of the folded veinlet. We do not have further information about the orientation of the fold axis.

The oriented billet remaining from the preparation of this thin section was scanned by HRXCT. The 3D reconstruction shows that D_{1aGSS}-related sulphide-rich veinlets are transposed and folded along the S_2 planar fabric, well characterised in the sericite-rich gangue (Fig. 4-5c). A subhorizontal section shows that F_2 folding is similar and tight, with S_2 being the related axial planar cleavage (Fig. 4-5c and d). Sulphide-rich fold hinges are more or less dismembered, which leads to the formation of linear sulphide micro-ore shoots (Fig. 4-5c and d). These linear mineralised micro-structures are parallel to the F_2 fold axis and steeply plunge westwards, which is consistent with the deposit-scale L_2 stretching lineation orientation (Perret et al., 2020). HRXCT thus illustrates that F_2 micro-hinges form L_2-parallel micro-ore shoots consistent with (i) the deposit-scale F_2 fold axis orientation and (ii) the deposit-scale ore shoot orientation that is controlled by the regional L_2 stretching lineation (Perret et al., 2020). This demonstrates the 3D continuity of the structural control on GSS gold mineralisation from the district to the

microscopic scales and strengthen conclusions suggested from conventional field and microscopy work. The complete 3D data are available in Supplementary Material 1.

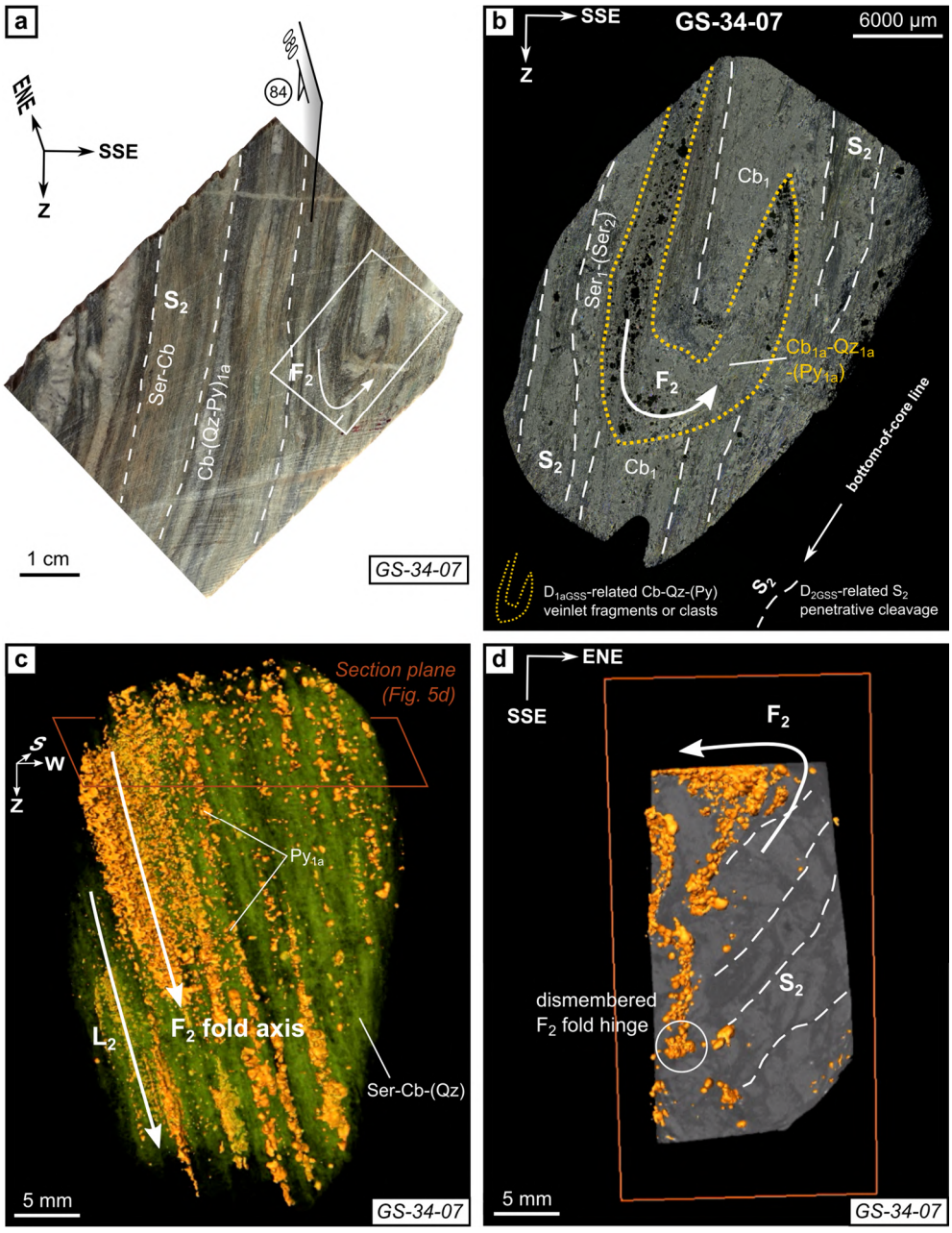


Figure 4-5: High-resolution X-ray computed tomography (HRXCT) results for the sample billet GS-34-07. Mineral abbreviations are similar to Figure 4-2. **a** View of the half core slab of sample GS-34-07. The white rectangle corresponds to the oriented billet cut for thin section preparation, centered on a F_2-folded carbonate-(quartz-pyrite) veinlet. **b** Scan of the GS-34-07 thin section (cross-polarised, transmitted light). **c** CT scan of the billet GS-34-07. Green color corresponds to gangue minerals affected by the S_2 fabric whereas orange color refers to sulfide minerals. The CT scan has been reoriented according to the orientation of the sample block. **d** Subhorizontal section across the billet GS-34-07. Gangue and sulfide minerals are in grey and orange colors, respectively.

5.3. Electron back-scattered diffraction

5.3.1. $Py_{1b/2}$ grain (GS-22-08)

We investigated a disseminated pyrite grain composed of a Py_{1b} core and a Py_2 rim (referred to as $Py_{1b/2}$ grain hereafter) in the low-grade sample GS-22-08 (0.28 g/t Au; Table 4-1; Fig. 4-6). The Py_{1b} core encloses numerous silicate, phosphate and sulphide inclusions where the Py_2 rim is observed (Fig. 4-6a). The latter preferentially grows along S_2 main fabric trend and displays a very thin gersdorffite fringe (Fig. 4-6b). Both pyrite and gersdorffite crystallise in the quadratic system, with close unit cell parameters (Bayliss, 1968, 1977). One electron back-scattered pattern (EBSP) was acquired for each mineral phase (datapoint 1 for gersdorffite and 2 for pyrite, respectively, in Fig. 4-6b close-up) to compare their respective crystallographic orientation. The 3D reconstruction of the unit cell corresponding to the EBSPs highlights the similar crystallographic orientations of the pyrite overgrowth and the gersdorffite coating. Such similarities in unit cell parameters suggest that these two mineral phases formed as a continuous crystallographic unit.

Besides, the entire pyrite grain was mapped with EBSD. Data processing allowed to isolate the coarse, disseminated pyrite grain of interest, as well as quartz grains, mostly occurring in subvertical C_2-related asymmetrical strain fringes (Fig. 4-6c). The crystallographic orientation deviation angle is mostly $<1°$ and does not exceed 5° within the $Py_{1b/2}$ core-rim grain. The textural core-rim limit is not showing any deviation in the crystallographic orientation (Fig. 4-6d). However, the crystallographic orientation of the top-western half of the composite pyrite grain differs from the one in the other half, which matches the subvertical C_2 simple shearing kinematics locally inferred from strain fringes asymmetry (Fig. 4-6d). We also observe the presence of a $>30°$ misorientation grain boundary corresponding to a single anhedral pyrite subgrain. This grain may have recrystallised after the D_{2GSS} deformation stage as the grain boundary cuts across the boundary between the Py_{1b} core and the Py_2 rim.

The pyrite {100} crystallographic axis orientation is roughly consistent across the whole $Py_{1b/2}$ grain, with the exception of the previously discussed potentially recrystallised subgrain (Fig. 4-6d). The Py_2 rim seems to have preferentially grown or recrystallised along the z axis (Fig. 4-6c). It is confirmed by the steeply north-northwest-plunging preferential orientation of the {100} axis for the $Py_{1b/2}$ grain in the pole figure (Fig. 4-6d).

In summary, the absence of subgrain boundary misorientation between the Py_{1b} core and the Py_2 rim (Fig. 4-6c) suggests that either (i) the Py_{1b} grain has been transposed along the L_2 fabric before the Py_2 overgrowth formed, through recrystallisation or a new fluid event, or (ii) the formation of Py_{1b} core is immediately followed by its destabilisation concomitant with *in situ* recrystallisation of the Py_2 rim. The preferential growth of Py_2 rim around Py_{1b} core along the L_2 stretching lineation confirms that its formation is coeval with the progressive D_{2GSS} deformation stage (Fig. 4-6d). The cristallographic continuity between the Py_2 overgrowth and the gersdorffite coating (Fig. 4-6b) supports their cogenetic precipitation. The EBSD analysis of sample GS-22-08 therefore confirms (i) the progressive nature of the D_{2GSS} deformation stage, (ii) the mineral paragenesis previously established from macroscopic and thin section observations and (iii) that the structural control on the GSS gold deposit by the L_2 fabric is visible up to the microscopic scale (Perret et al., 2020).

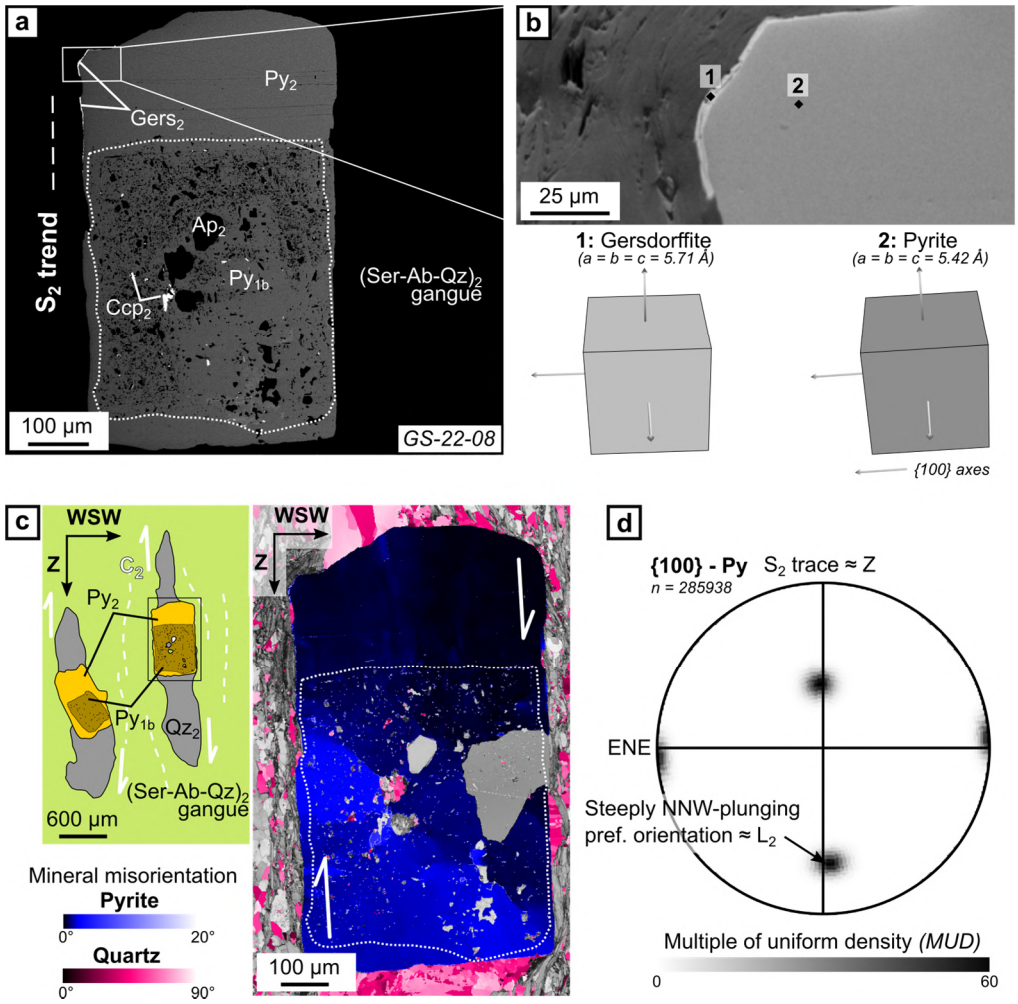


Figure 4-6: Electron back-scattered diffraction (EBSD) analysis of disseminated $Py_{1b/2}$ facies (sample GS-22-08). Mineral abbreviations are similar to Figure 4-2. **a** BSE-SEM photograph of the investigated pyrite grain. **b** Zoom on the Py_2 overgrowth and intergrown gersdorffite coating and electron back-scattered patterns (EBSPs) of gersdorffite (1) and pyrite (2). **c** Orientation deviation angle map for pyrite and quartz considering a disseminated $Py_{1b/2}$ grain with E block-to-the-top, C_2-related asymmetrical quartz strain fringes (background: orientation contrast image considering all mineral phases). **d** EBSD pole figure representing the {100} axes of the coarse $Py_{1b/2}$ grain. *n* refers to the number of individual electron EBSPs used to construct the pole figure.

5.3.2. Mineralised quartz-pyrite veinlet (GS-34-05)

EBSD maps were produced for a Py_{1b}-Py_2-Ccp_2 assemblage in a D_{1bGSS}-related quartz-pyrite-dominated veinlet within the high-grade sample GS-34-05 (@6.45 g/t Au; Table 4-1; Fig. 4-7). The mineralised micro-structure is completely dismembered along the S_2 main penetrative cleavage, making its margins hardly visible within the albite-sericite-quartz host rock. A zoom on the investigated area shows the textural relationship between Py_{1b} grain aggregates with associated Py_2 overgrowths and Ccp_2 infilling between 120°-triple junction annealed pyrite grains (Fig. 4-7a and b). Rare electrum associated

with Py_2 is visible in interstitial chalcopyrite (Fig. 4-7a and b). The orientation contrast background in Figure 4-7c shows a blurred aspect with lateral drift: this might result from a charging effect during EBSD data collection (*e.g.,* Wright et al., 2015). Individual EBSPs indexing was nevertheless sufficient and the obtained EBSD map is considered to be reliable. The crystallographic orientation deviation angle between EBSPs measured in all pyrite grains ranges from 0 to 90°. Pyrite grain and subgrain boundaries are visible (Fig. 4-7c). As observed for sample GS-22-08 (subsection 4.3.1.; Fig. 4-6), the presence of Py_2 overgrowths around Py_{1b} cores is not associated with subgrain or grain boundaries (Fig. 4-7a, b and c).

Chalcopyrite crystallises in the tetragonal system in which the {001} crystallographic axis represents the *c* long axis. Although the interstitial chalcopyrite does not show any apparent preferential orientation at the microscopic scale (Fig. 4-7a, b and c), its {001} axis is mostly subvertical and oriented along the deposit-scale L_2 stretching lineation (Fig. 4-7d). This suggests that interstitial chalcopyrite either (i) formed during the D_{2GSS} deformation stage as well or (ii) is inherited and underwent a complete recrystallisation during the D_{2GSS} stage. The first option is privileged as there is no significant evidence for chalcopyrite formation during the D_{1GSS} stage (Fig. 4-2; Perret et al., 2020). Therefore, the presence of electrum inclusions in the interstitial chalcopyrite (Fig. 4-7a, b) and intergrown with sulphide inclusions in altered Py_{1b} cores (Fig. 4-4e and f) confirms that the D_{2GSS} event relates to the main visible gold mineralisation formed at the GSS gold deposit. Although these timing relationships between ore mineral generations and deformation stages were suggested from a conventional petrological-structural study (see Fig. 4-2; Perret et al., 2020), EBSD now provides robust evidence that confirms the mineral paragenesis.

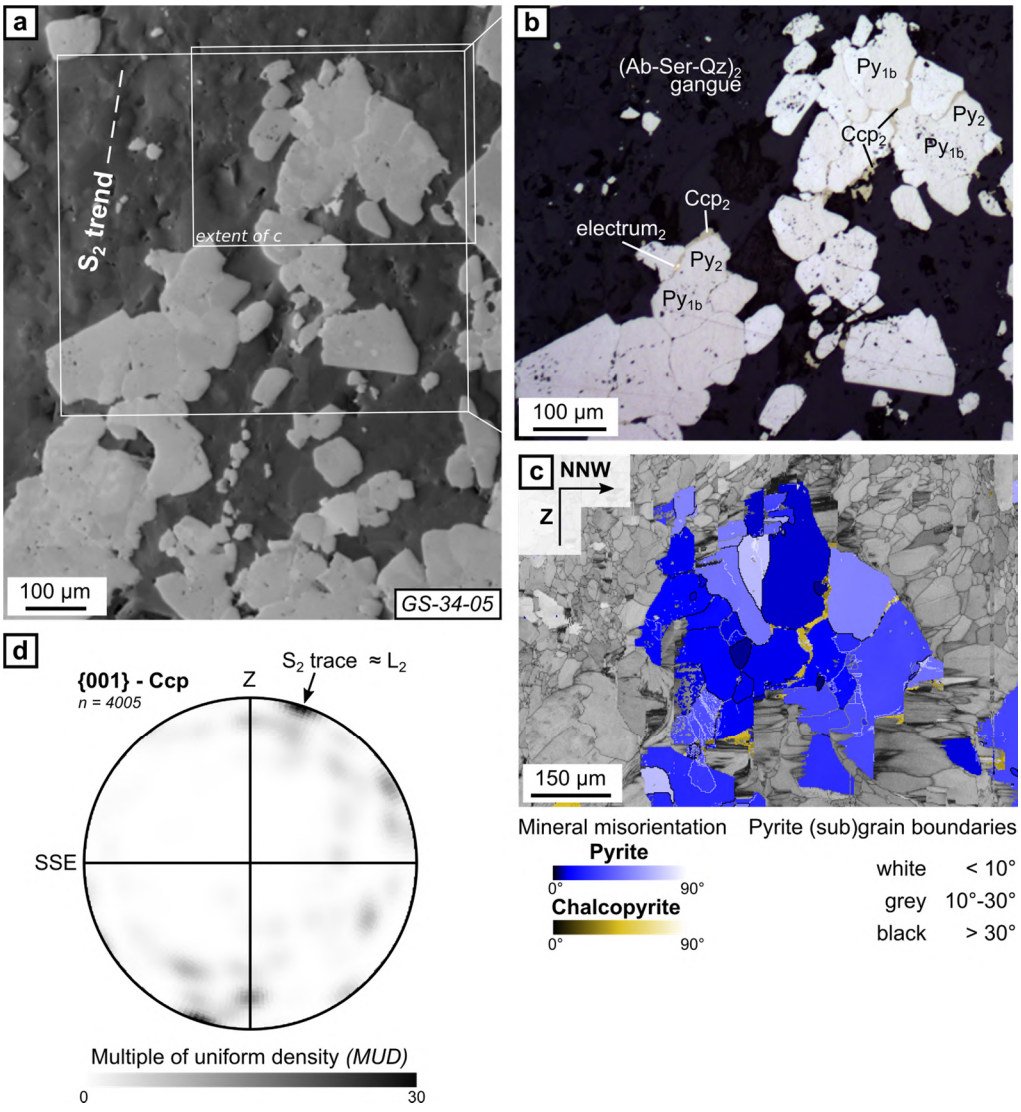


Figure 4-7: Electron back-scattered diffraction (EBSD) analysis of $Py_{1b/2}$ facies in quartz-pyrite-dominated veinlet (sample GS-34-05). Mineral abbreviations are similar to Figure 4-2. **a** Orientation contrast image with (**b**) a zoom on the Py_{1b}-Py_2-(Ccp_2-electrum2) assemblage of interest (reflected light). **c** Orientation deviation image zoomed on pyrite and interstitial chalcopyrite assemblage (extent in **a**; background: orientation contrast image considering all mineral phases). **d** EBSD pole figure representing the {001} axes of interstitial Ccp_2, representing the distribution of the c long axis of chalcopyrite crystals in the tetragonal system. *n* refers to the number of individual electron EBSPs used to construct the pole figure.

5.4. LA-ICP-MS geochemical signature of pyrite generations

LA-ICP-MS data are summarised in Table 4-2 and are sorted by pyrite generations. Only the median and mean values of trace element concentrations and associated standard deviations are shown, with the complete dataset being made available in Supplementary Material 2. We focus below on the concentrations of some trace elements of interest (Au, Ag, Te, Sb, Cu, Pb, As and Co) in each pyrite generation, displayed in

a box and whisker diagram (Fig. 4-8). Comparisons are made using the median value for trace element concentrations, unless otherwise stated, as the mean value may be overestimated due to nugget effect where micro-inclusions have been analysed.

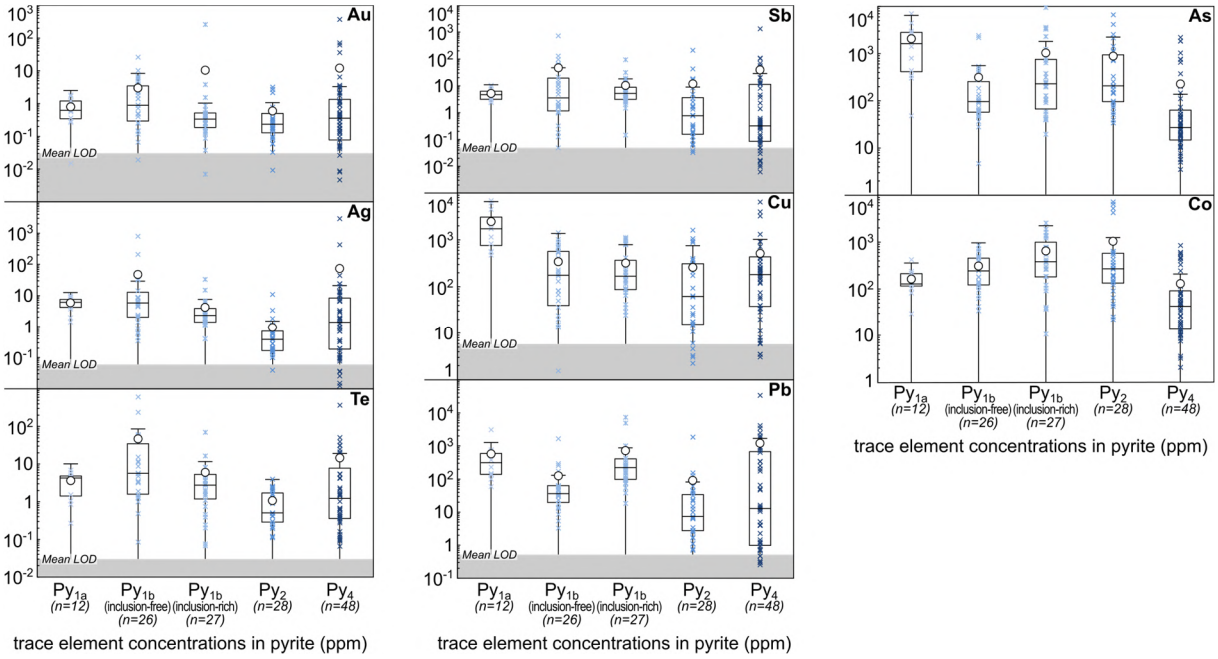


Figure 4-8: Box and whisker plots of some trace element concentrations of the various generations of pyrite from the Galat Sufar South gold deposit, northeastern Sudan. Analyses are grouped by pyrite generations. Py_{1b} free of mineral inclusion is distinguished from altered Py_{1b} grains with evidence of dissolution and with a Py_2 overgrowth rim. The number of analyses for each group of pyrite is given. Data below limit of detection (LOD) have been attributed the LOD/2 value. The median (line in the box), mean (white circle) and first and third quartile (box extent) values are shown as well as 1.5 times the interquartile range value (whiskers).

5.4.1. Py_{1a} and Py_{1b} generations

Py_{1a} and Py_{1b} generations display the highest Au, Ag and Te concentrations (up to 26.0, 793 and 238 ppm, respectively; Fig. 4-8). They can be distinguished by their Cu, Pb and As concentrations which are higher for Py_{1a} than Py_{1b} (1740 *vs* 176 ppm, 304 *vs* 35.4 ppm and 1617 *vs* 95.9 ppm, respectively; Fig. 4-8). This is likely related to the increased amount of accessory sulphide minerals (chalcopyrite, galena, sphalerite, sulfosalt) in quartz-carbonate veinlets from D_{1aGSS} to D_{1bGSS} deformation stages (Fig. 4-2; Perret et al., 2020). D_{1aGSS}- and D_{1bGSS}-gold occurs as nano-inclusions or as structurally bound in pyrite lattice, as no gold micro-inclusion has been observed (subsection 5.1.) and no Au was measured for the corresponding ablation spots.

5.4.2. Py_2 generation

At the grain scale, LA-ICP-MS elemental maps were made for a composite $Py_{1b/2}$ grain, previously investigated by EBSD (GS-22-08; Fig. 4-6). They highlight the relative depletion in Au, Ag and Te where Py_{1b} grains show evidence of dissolution, enclose numerous mineral inclusions and with a Py_2 overgrowth rim which is also depleted in these elements (Fig. 4-9). This trend is confirmed by the overall spot dataset (Fig. 4-8). Outliers with high Au concentrations (up to 260 ppm) may represent a nugget effect related to gold micro-inclusions (Fig. 4-4f) or gold associated with sulphide mineral inclusions in altered Py_{1b} cores such as chalcopyrite (Fig. 4-9). Ag and Te also appear to be preferentially incorporated in these mineral inclusions (Fig. 4-9). Sb, Cu and Pb show a different behavior as Py_{1b} grains are slightly enriched where the core of the pyrite grain is altered (Figs. 4-8, 4-9). The formation of Sb- and Cu-bearing mineral inclusions in altered cores is clearly visible in both petrographic analyses (Fig. 4-4e and f) and elemental maps (Fig. 4-9), and can be related to some outliers datapoints in Figure 4-8 (*e.g.,* galena inclusions corresponding to samples showing Pb concentrations up to 7436 ppm). Similarly, where Py_{1b} grains are aggregated and annealed with interstitial chalcopyrite in a gold-bearing veinlet with dominant quartz and pyrite, metals are preferentially concentrated along pyrite subgrain boundaries and gold inclusions are formed in interstitial chalcopyrite (GS-34-05; Figs. 4-7b, 4-10). The remobilisation of Cu remains however limited as the Cu concentration is invariant whereas Au concentration decreases where Py_{1b} shows evidence of dissolution (Fig. 4-8). On first hand, Py_2 overgrowths are free of mineral inclusions and exhibit lower concentrations of Sb, Cu and Pb regarding mineral inclusion-free Py_{1b} type (0.78 *vs* 3.60 ppm, 62.4 *vs* 176 ppm and 88.5 *vs* 122 ppm, respectively), similarly to Au, Ag and Te behavior (Figs. 4-8, 4-9). On second hand, As and Co exhibit higher concentrations in Py_2 (207 and 270 ppm, respectively) than the portion of Py_{1b} free of mineral inclusions (95.9 and 245 ppm,

respectively) (Fig. 4-8). Primary As and oscillatory zoning of Co in Py_{1b} grain are preserved despite its heavily altered aspect and the presence of a Py_2 rim (Fig. 4-9).

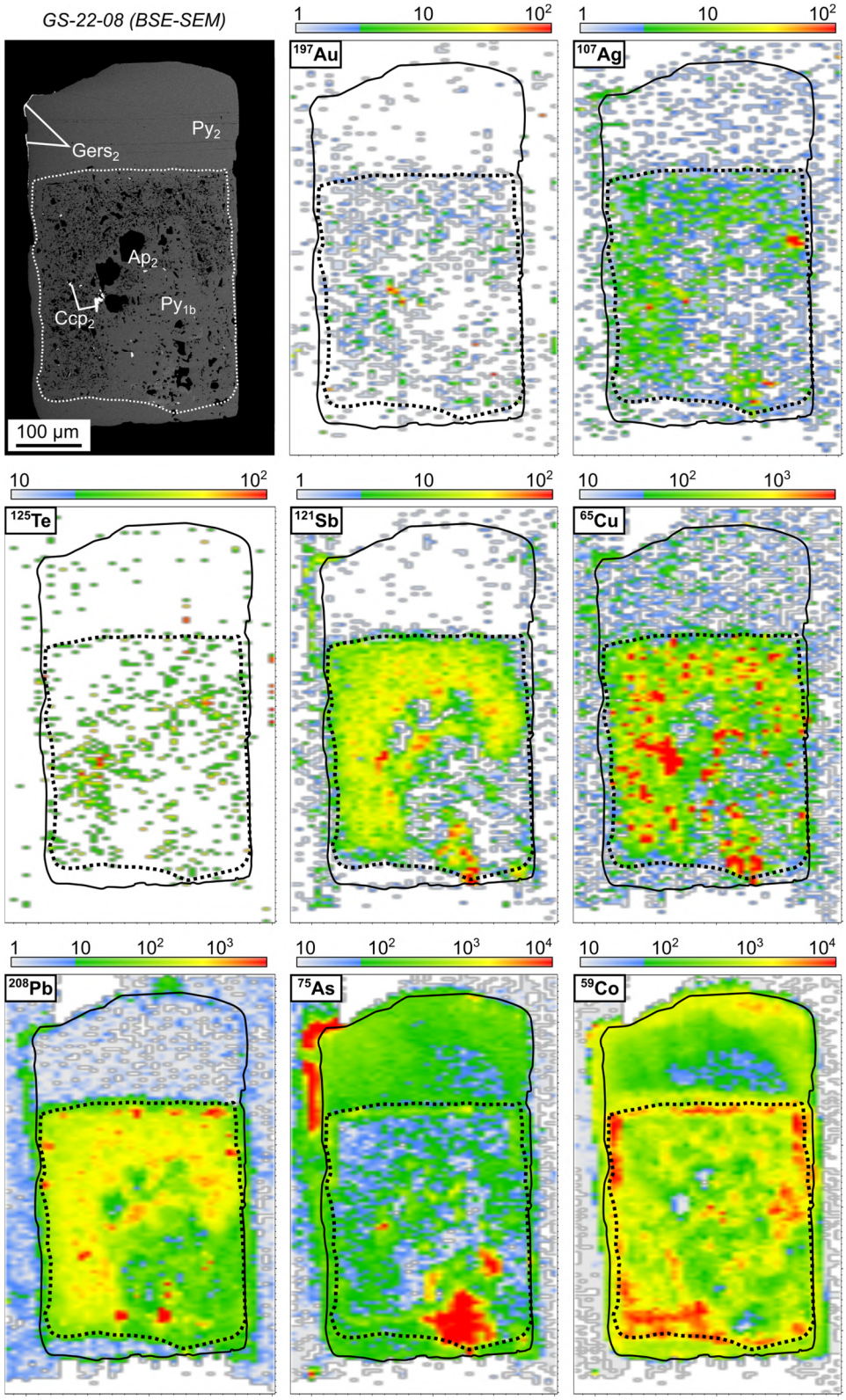


Figure 4-9: LA-ICP-MS trace element maps (Au, Ag, Te, Sb, Cu, Pb, As, Co) of a Py_{1b} altered core enclosing numerous mineral inclusions and with a Py_2 overgrowth (sample GS-22-08). The trace element concentration is semi-quantified (ppm) and illustrated by a color log-scale. Mineral abbreviations are similar to Figure 4-2.

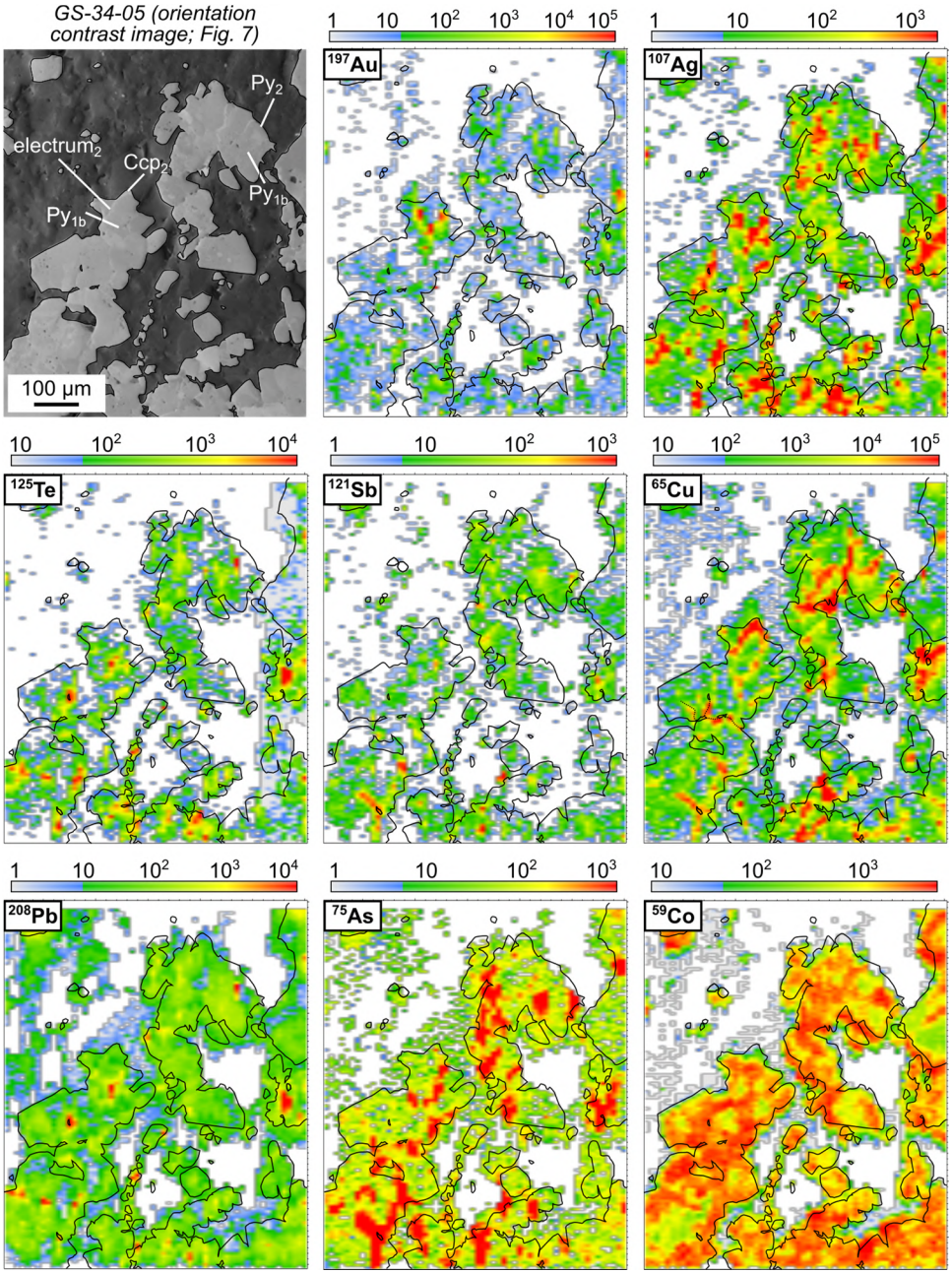


Figure 4-10: LA-ICP-MS trace element maps (Au, Ag, Te, Sb, Cu, Pb, As, Co) of a composite Py_{1b}-Py_2-Ccp_2-electrum$_2$ assemblage within a gold-bearing quartz-pyrite-(carbonate) veinlet (sample GS-34-05). The trace element concentration is semi-quantified (ppm) and illustrated by a color log-scale. Mineral abbreviations are similar to Figure 4-2.

These data strongly suggest that Py_{1b} destabilisation, alteration and recrystallisation by annealing and Py_2 overgrowing are responsible for an overall release of Au-Ag-Te-(Sb-Cu-Pb). According to our observations, these elements seem to start migrating just before the *in situ* crystallisation of electrum-chalcopyrite-sulfosalt-(galena-arsenopyrite) minerals as inclusions in altered pyrite cores and interstitial sulphide assemblage forming along pyrite subgrain boundaries. This is in agreement with the

previously published model for gold mobility, based on macroscopic to microscopic scale petrological-structural observations (Perret et al., 2020). This model suggests that the (D_{1aGSS})-D_{1bGSS} lattice-bound gold input event is followed by metal remobilisation and liberation of the main, free gold mineralisation during the D_{2GSS} deformation stage (Perret et al., 2020).

5.4.3. Py_4 generation

The Au, Ag, Te, Sb, Cu and Pb concentrations in Py_4 grains span a range of values that is similar to that measured for Py_{1a} to Py_2 generations, albeit with higher variability, illustrated by higher standard deviations (Fig. 4-8; Table 4-2). Outlier values for Au and As concentrations may be linked to the presence of gold and sulfosalt micro-inclusions within pyrite grains (Figs. 4-4j and k, 4-8).

Unfortunately, rare studies focused on metal partitioning in hydrothermal systems and calculated partition coefficients for vapor-liquid fractionation (*e.g.,* Pokrovski et al., 2008). Partition coefficients for metals between sulphide minerals remain unknown, but some studies attempted to interpret partitioning trends among coexisting base-metal-bearing sulphide minerals (*e.g.,* Bortnikov et al., 2000; George et al., 2016, 2018), which leads to a *"predictive understanding of the fundamental crystal-structural controls on element partitioning into specific minerals"* (Cook et al., 2016). These studies investigated hydrothermal polymetallic deposits ranging from VMS, skarn, exhalative or porphyry-epithermal deposits formed in various thermodynamic conditions and coexisting sulphide minerals which differ from the ones characterised at the GSS gold deposit. Results are nevertheless consistent and we can approximate that Au preferentially gets enriched into pyrite, Cu into chalcopyrite, Co into sphalerite, Pb-Te-Ag-Bi into galena, As in both galena and sphalerite considering the D_{4GSS} sulphide mineral assemblage, apart from sulfosalts.

The strong dispersion of the metal budget trapped by D_{4GSS}-related sulphide assemblage could therefore depend both on the composition of the *in situ* metallic stock it is sourced from, the partial remobilisation and partial or quantitative recrystallisation together with trace element partitioning between neoformed sulphide minerals. This would support the hypothesis stating that the D_{4GSS} gold event results from the remobilisation of former gold mineralisation at the GSS gold deposit, previously suggested from petrological-structural observations (Perret et al., 2020).

Elements	Si	S	V	Cr	Mn	Fe	Co	Ni	Cu	Zn	Ga	As	Se	Mo	Ag	Cd	In	Sn	Sb	Te	W	Au	Tl	Pb	Bi
Mean LOD	330	1000	0.21	1.3	0.44	58.0	0.19	4.3	5.8	1.24	0.06	1.04	4.5	0.19	0.06	0.16	0.02	0.26	0.05	0.40	0.06	0.03	0.01	0.50	0.02
	Py_{1a} *(n=12)*																								
Median	2463	545876	9.8	3.50	89.0	444134	129	109	1740	76.5	0.38	1617	8.2	0.93	6.2	0.58	0.02	0.18	4.7	4.3	0.18	0.62	0.08	304	0.33
Mean*	6691	542209	13.8	41.2	3675	440852	163	183	2453	1020	0.75	2042	10.5	1.9	5.8	4.7	0.03	0.38	5.2	3.6	0.48	0.79	0.13	568	0.47
SD*	8936	29562	17.1	102	11830	26123	100	207	2207	2362	1.2	2043	7.6	2.0	2.7	10.6	0.02	0.57	2.6	2.1	0.53	0.58	0.13	828	0.40
	Mineral inclusion-free Py_{1b} *(n=26)*																								
Median	637	542072	0.62	1.4	2.0	450294	245	348	176	9.8	0.04	95.9	7.3	0.11	5.9	0.08	0.02	0.16	3.6	5.6	0.15	0.89	0.04	35.4	0.61
Mean*	2958	542755	10.7	7.9	54.9	451890	309	378	344	101	0.47	313	12.3	0.36	48.0	0.98	0.02	0.19	47.1	46.0	3.5	3.0	1.4	122	1.0
SD*	6682	22017	33.4	19.7	218	22921	234	208	385	201	1.7	602	11.1	0.85	157	2.0	0.02	0.15	142	125	7.5	5.4	4.6	322	1.2
	Mineral inclusion-rich, altered Py_{1b} *(n=27)*																								
Median	3495	505019	8.1	13.8	148	479351	384	153	169	28.2	0.42	228	5.1	0.08	2.3	0.06	0.02	0.25	5.3	2.8	0.29	0.34	0.13	217	2.17
Mean*	4287	509377	22.5	29.6	311	477029	652	268	323	261	0.68	1032	6.4	0.42	4.2	0.77	0.02	0.64	10.5	5.9	4.8	10.4	0.86	709	1894
SD*	3109	33991	23.9	46.0	384	34204	662	355	354	711	0.61	2008	5.1	0.82	6.5	2.4	0.01	0.95	17.8	13.3	10.7	49.9	3.7	1635	9804
	Py_{2} *(n=28)*																								
Median	1095	542543	1.0	1.2	4.2	452346	270	418	62.4	5.0	0.09	207	7.0	0.16	0.38	0.08	0.01	0.17	0.78	0.50	0.16	0.24	0.02	7.1	0.25
Mean*	5766	533899 (	8.3	4.1	553	456691	1045	535	259	112	0.44	877	9.0	0.35	0.94	0.20	0.03	0.23	11.8	1.1	0.59	0.59	0.08	88.5	40.8
SD*	9144	34942	24.8	8.1	2560	32973	2003	510	397	269	1.2	1456	6.4	0.54	2.1	0.35	0.05	0.20	39.5	1.0	1.0	0.90	0.13	347	204
	Py_{4} *(n=48)*																								
Median	265	531593	0.21	0.54	1.8	450057	42.7	70.3	184	9.1	0.04	27.1	27.9	0.17	1.4	0.11	0.01	0.18	0.33	1.21	0.04	0.36	0.02	12.5	0.25
Mean*	6315	532650	7.5	0.92	38.0	456228	131	378	514	67.3	0.45	225	24.7	1.9	73.6	0.69	0.03	2.6	39.5	14.3	34.5	12.0	0.54	1192	107
SD*	18283	27277	38.5	0.87	126	24883	203	926	1142	200	1.2	504	18.7	5.1	417	2.4	0.07	13.2	193	53.2	203	55.1	1.6	4936	729

Concentrations are in ppm.

** Arithmetic means and standard deviations (SD) are calculated considering the LOD/2 value for <LOD values.*

Table 4-2: Summary of the LA-ICP-MS trace element concentrations (in ppm) of the various pyrite generations from the Galat Sufar South gold deposit, northeastern Sudan.

6. A holistic ore-forming model

6.1. Structural control on mineralisation

When studying deformed gold deposits, the upscaling from the district-scale structures up to microscopic sub-samples is a challenge, mostly due to the difficulty in switching from 3D field observations and measurements to conventional 2D micro-structural description of thin sections. The access to reconstructed 3D structural information at the microscopic and crystallographic scales *via* HRXCT and EBSD techniques is therefore of special interest for multi-scale structural reconciliation. Linking 3D structural information acquired from the field all the way to the laboratory observations by ways of different methods helps to characterise in a more robust manner the structural control on mineralisation from the tens of km- to the µm-scales (Fig. 4-11).

Documenting structural control on mineralisation at several scales remains rare in ore deposit geology (Cnudde and Boone, 2013; Kyle and Ketcham, 2015). The present study of the GSS gold deposit is a first example of how this multi-scale approach can be used. Indeed, coupling the integrated EBSD and HRXCT results from this study with the petrological-structural study of Perret et al. (2020) confirms that structural control on mineralisation is consistently represented at every scale:

(i) The progressive nature of the ductile D_{1GSS}-D_{2GSS}-(D_{3GSS}) deformation episode is defined up to the crystallographic scale and observed shear sense remains the same at every scale;

(ii) Sulphide-rich ore shoots are oriented along the L_2 lineation from the deposit- to the microscopic scale, which corresponds to the dominant regional fabric. Structural control on mineralisation is therefore the same at every scale and we clearly illustrated that ore shoot geometry is fractal from the km-scale to the µm-scale.

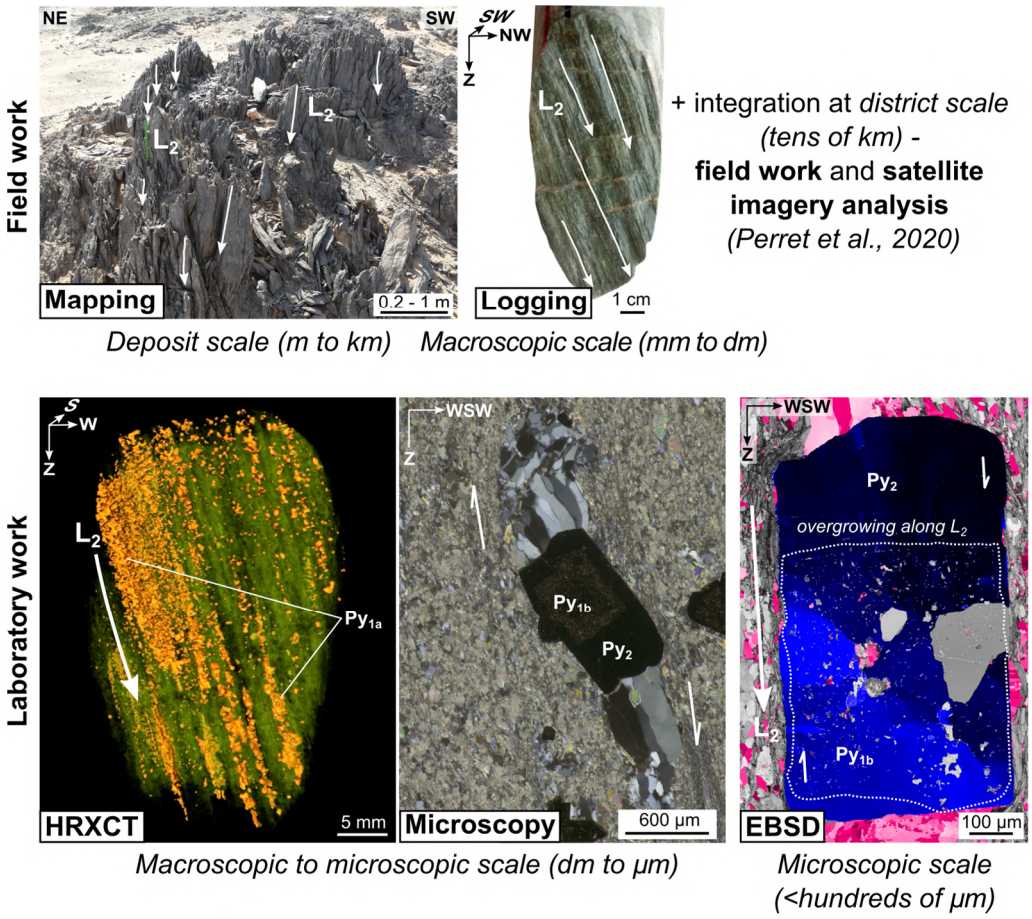


Figure 4-11: Insights from the suggested multi-scale, multi-method approach for the understanding of the structural control defined by L_2 on gold mineralisation at the Galat Sufar South gold deposit, northeastern Sudan. Field and laboratory methods are separated, and their respective scale of investigation is indicated.

These conclusions are crucial for greenfield exploration targeting and near-mine exploration as constraining the mineralisation-related tectonic history allows to discuss when mineralisation occurred through time and to which tectonic event it relates (*e.g.*, Kolb et al., 2003). In the GSS gold deposit, the gold mineralisation occurred during the ~ 750-700 Ma Atmur-Delgo suturing (Schandelmeier et al., 1994b; Perret et al., 2020), as the mineralised structures appear to be structurally-controlled by the L_2 lineation from the district to the crystallographic scales. L_2-related structures are therefore pathfinders to GSS-like gold mineralisation throughout the Atmur-Delgo suture and nearby GSS gold deposit. Under-explored suture zones similar to the Atmur-Delgo suture could also be considered as new exploration targets for vein-type gold deposits at the scale of the Arabian Nubian shield. Additionally, the knowledge of the orebody geometry at the deposit-scale is mandatory for resource estimation and important for choosing the best-

suited exploitation strategy, among other criteria. Finally, at the microscopic scale, an accurate description of ore mineral textures and paragenetic association is highly required to prevent potential ore processing issues.

To go further, constraining structural control on mineralisation could even be extended up to the sub-nanometric, atomic scale. This is possible thanks to the emergence of the atom probe tomography that can image mineral defects, dislocations, *etc…* and better constraint micro-deformation processes (Reddy et al., 2020 and references therein).

6.2. Deformation-induced geochemical ore forming processes

Combining the deposit- to grain-scale structural evolution of the ore-bearing assemblage with *in situ* geochemical investigation allows to better characterise geochemical processes linked to gold (re-)mobilisation and precipitation (Fig. 4-12). For instance, the coupling of HRXCT (or similar 3D neutron tomography) with geochemical investigation techniques such as *in situ* LA-ICP-MS or nanoSIMS carried out on ore minerals brings knowledge about mechanical-geochemical ore formation processes (*e.g., "aseismic refinement"* process for orogenic gold, Voisey et al., 2020). The laboratory-based hyperspectral adaptation of the conventional HRXCT method tested by Egan et al. (2015) even helps reconstructing the internal chemistry of a material, which is of high interest for integrating a textural and geochemical characterisation of ore mineral assemblages. *In situ* geochemical analyses *via* electron microprobe (EMPA; *e.g.,* Wille et al., 2018), LA-ICP-MS (*e.g.,* Reddy and Hough, 2013; Dubosq et al., 2018), synchroton X-ray fluorescence mapping (*e.g.,* Fougerouse et al., 2016) or laser-induced breakdown spectroscopy (LIBS; *e.g.,* Cugerone et al., 2020) have also been coupled with EBSD investigation for the last decade. Dubosq et al. (2018) illustrated how pyrite recrystallisation and fracturing influenced the entrapment of gold along micro-structures at the world-class Detour Lake deposit (Canada). Similarly, Cugerone et al. (2020)

demonstrated that the syn-tectonic dynamic recrystallisation of sphalerite accounts for the release of Ge from the crystal lattice and later Ge minerals recrystallisation.

In the case of the GSS gold deposit, the coupling of LA-ICP-MS elemental maps (Figs. 4-9, 4-10, respectively) matched with EBSD maps (Figs. 4-6, 4-7, respectively) helps to better constraint micro-deformation influence on elemental mobility in sulphide mineral assemblages through time. Besides, the LA-ICP-MS spot analyses assess the mobility of lattice-bound trace elements in pyrite (Fig. 4-8, Table 4-2).

Gold in Py_{1a} and Py_{1b} generations, which show the highest gold enrichment at the GSS gold deposit, is structurally-bound to the pyrite lattice. The (D_{1aGSS})-D_{1bGSS} deformation stages likely correspond to the first gold input to the system, occurring only as refractory gold, as suggested by former petrological-structural observations (Perret et al., 2020).

At the microscopic scale, the high-strain, ductile D_{2GSS} deformation stage is responsible for Py_{1b} destabilisation, alteration and recrystallisation by annealing and Py_2 overgrowing (Perret et al., 2020). *In situ* trace element analyses support a remobilisation of Au-Ag-Te-(Sb-Cu-Pb) from Py_{1b} during this deformation stage. Likely, these elements only migrated over a few µm to cm distance before reprecipitating as electrum-chalcopyrite-sulfosalt-(galena-arsenopyrite) inclusions in altered pyrite cores and as interstitial sulphide assemblage along pyrite subgrain boundaries. LA-ICP-MS data confirm that the D_{2GSS} deformation stage is not related to an additional gold input, but rather to a release of lattice-bound gold together with polymetallic sulphide mineral formation (Perret et al., 2020).

A similar space-limited migration pattern for structurally compatible elements such as Cu, Pb or Zn, whereas other elements, like As, Co or Ni, remain immobile, have been demonstrated in the Naime Pyrite Member and at the Mt. Torrens Pb-Zn-Ag prospect, Kanmantoo Group, South Australia (Dakota Conn et al., 2019). Such trace element

evolution pattern in pyrite is attributed to its recrystallisation under amphibolite facies metamorphism (Dakota Conn et al., 2019). The trace element concentrations in Py_2 thus suggest that D_{2GSS} deformation and mineralisation occurred under amphibolite facies metamorphic conditions at the GSS gold deposit, which correspond to regional peak metamorphism (Ahmed Suliman, 2000). Additional pressure-temperature constraints are however required to clearly state about metamorphic conditions reached in the studied area.

Finally, the large span in trace element concentrations in Py_4 likely characterises partial remobilisation followed by partial or quantitative recrystallisation together with trace element partitioning between neoformed sulphide minerals. It confirms the discrete remobilisation nature of the D_{4GSS} deformation and gold episode, previously inferred from petrological-structural observations (Perret et al., 2020).

The integration of geochemical and micro-structural analytical methods thus appears to be of prime importance when deciphering the deformation, metamorphic and geochemical ore formation-remobilisation processes at the microscopic scale. It may also provide a critical vectoring tools for gold targeting where several barren or ore-related sulphide generations coexist (*e.g.,* Kadel-Harder et al., 2020). Systematically highlighting the relationships between micro-structures and geochemical signatures of ore-related minerals would therefore represent a step forward towards a holistic laboratory approach for the study of deformed ore deposits.

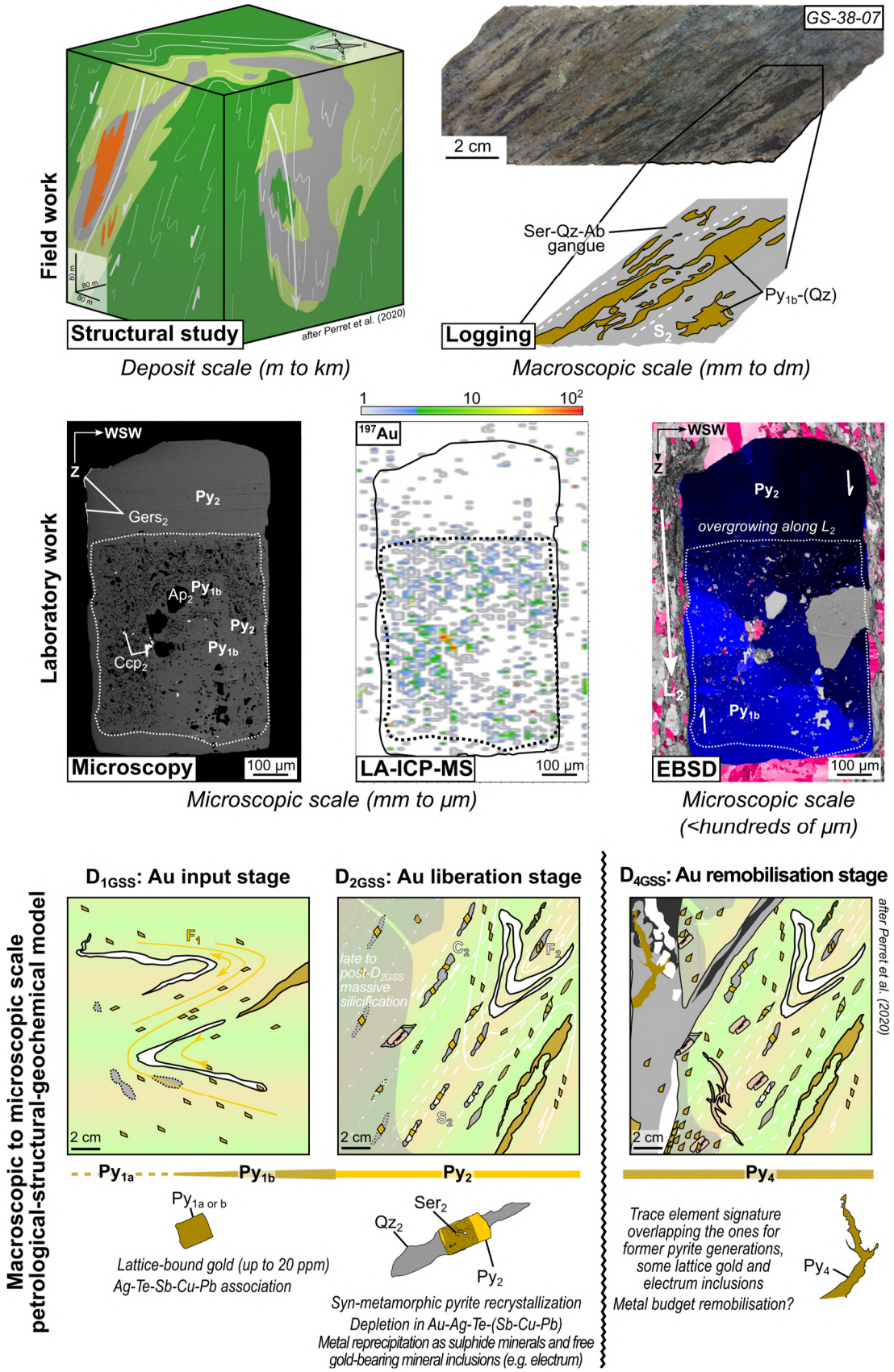


Figure 4-12: Insights from the suggested multi-scale, multi-method approach for the understanding of the geochemical ore-forming processes in relation with deformation at the Galat Sufar South gold deposit, northeastern Sudan. Field and laboratory methods are separated, and their respective scale of investigation is indicated. Mineral abbreviations are similar to Figure 4-2 for the petrological-structural cartoon.

7. Conclusions

Characterising structural control on mineralisation and deformation-induced geochemical processes is critical in ore geology, especially when focusing on deformed ore deposits. The innovative approach advocated here relies on robust preliminary field and microscopy work, oriented sampling and conventional petrological-structural description of mineralisation from the district to the microscopic scales (GIS satellite imagery analysis, field and conventional microscopic observations) and coupling with multiple analytical methods in the laboratory. These are unconventional micro-structural techniques such as high-resolution X-ray computed tomography (HRXCT) and electron back-scattered diffraction (EBSD) in addition to laser ablation inductively-coupled plasma mass spectrometry (LA-ICP-MS) on sulphide minerals.

Through the example of the Galat Sufar South gold deposit, Nubian shield, northeastern Sudan, we illustrate that this combined approach allows for the reconciliation of 3D structural record from the district scale up to the crystallographic scale. We unequivocally demonstrated that the structural control on mineralisation by the L_2 stretching lineation is indeed characterised at every scale, which enable to fully understand the geometry of the deposit and increase our level of confidence in attributing the formation of the GSS gold deposit to hydrothermal fluid flows triggered during Atmur-Delgo suturing. Furthermore, our approach enables to better constrain the micro-textural and -structural evolution of mineralisation-related sulphide mineral assemblages inferred from conventional thin section investigation. The use of *in situ* geochemical methods, such as LA-ICP-MS on ore-related minerals, can help tracking geochemical changes associated with gold mineralising or remobilisation events coeval with deformation and metamorphism. The trace element concentrations in the distinct pyrite generations distinguished at the Galat Sufar South gold deposit provide evidence for syn-deformation and -sulphide recrystallisation metal mobility and gold liberation during the D_{2GSS} deformation stage. There, we clearly demonstrate the relationships between micro-

deformation of sulphide minerals, gold mobility and lower-scale Atmur-Delgo suturing tectonics. The suggested approach therefore improves our understanding of the relationships between deformation, metamorphism, and geochemistry in ore-forming processes.

Our approach is therefore very promising for the study of deformed gold deposits and could be applied to any other sulphide-bearing, structurally-controlled ore deposit type. It leads to conclusive understanding of metallogenic processes but it is also key for mining industry, from greenfield exploration targeting to mining and ore processing.

Acknowledgements

The authors are grateful to the Orca Gold Inc. team and especially to Craig Hartshorne and Emmanuel Abanyin for their welcome on GSS camp and their substantial logistical support. Christophe Nevado (Montpellier University, France) is warmly thanked for thin section specific preparation prior to EBSD analyses. Blandine Gourcerol (BRGM, France) is acknowledged for introducing us with Matthew Leybourne (Queen's University, Canada) who is also thanked for permission to carry out LA-ICP-MS analyses at Queen's Facility for Isotope Research. Marissa Valentino (Queen's University, Canada) is thanked as well for her support with these analyses. This work is part of Julien Perret's PhD project which benefited of a CIFRE funding, reference CIFRE N°2017/1737, attributed by the French National Research and Technology Agency (ANRT).

Supplementary Materials

Supplementary Material 4-1: Video file for the HRXCT-assisted 3D reconstruction of the internal structure of the oriented sample billet GS-34-07. The color scale is the same as that of Figure 4-5. The video file is available from Julien Perret upon request at julien.perret15@laposte.net.

Supplementary Material 4-2: Extensive dataset of LA-ICP-MS trace element concentrations (in ppm) of the various pyrite generations from the Galat Sufar South gold deposit, northeastern Sudan.

ID	Py	Text.	Si	S	V	Cr	Mn	Fe	Co	Ni	Cu	Zn	Ga	As	Se	Mo	Ag	Cd	In	Sn	Sb	Te	W	Au	Tl	Pb	Bi
GS-22-10																											
z1_1	2		3680	498049	0.33	2.0	13.9	495596	139	1390	1063	10.6	0.13	38.7	5.2	1.1	0.10	0.12	0.19	<0.16	0.04	<0.42	0.29	2.7	0.09	2.5	2.6
z1_2	1b	1*	9002	488306	39.5	8.2	118	489215	36.6	9.5	282	846	1.0	102	4.6	0.45	2.3	0.98	0.07	3.8	2.0	5.5	6.5	0.52	0.16	151	1.9
z1_3	2		1212	543009	<0.34	<5.2	4.0	454041	634	160	874	2.2	0.10	57.1	<21.5	<0.26	0.15	<0.37	<0.02	<0.54	0.20	<0.84	0.71	0.18	<0.12	0.71	0.13
z1_4	1b	1*	1164	462782	5.3	<0.92	270	532462	366	23.0	993	53.2	0.32	92.0	<3.7	0.48	4.6	<0.07	<0.004	0.13	7.2	<0.15	0.28	0.12	0.33	835	5.1
z2_1	2		4182	513629	2.4	1.9	903	480409	183	259	93.7	247	0.30	72.1	5.8	0.36	0.14	0.20	0.01	0.32	0.07	<0.24	1.1	0.56	<0.007	2.8	4.1
z2_2	2		447	536948	3.8	<0.96	7.8	461839	197	41.5	312	8.0	<0.02	174	7.0	<0.07	0.19	<0.10	0.02	0.88	0.13	<0.23	<0.14	0.78	0.09	2.7	0.90
z2_3	1b	1*	3446	498653	1.0	<0.81	419	486491	182	87.8	1128	3514	0.22	52.7	4.6	1.1	6.0	3.6	0.04	<0.25	2.7	3.0	1.6	0.34	0.09	4932	19.7
z2_4	1b	1*	7321	469187	1.9	1.1	110	519766	293	19.3	1065	799	0.50	40.3	<2.3	<0.05	6.8	0.16	0.02	0.19	5.3	1.5	0.22	0.13	0.28	1014	34.4
z3_1	2		<482	521266	0.65	<1.3	246	477636	64.3	44.0	64.3	3.3	0.06	327	8.2	<0.40	0.44	<0.16	<0.04	<0.34	0.79	1.5	2.9	<0.02	<0.01	31.9	3.1
z3_2	1b	1*	1988	505019	8.0	<0.94	1032	486252	384	23.9	228	5.7	0.38	3583	5.1	0.62	3.9	0.36	<0.03	0.31	3.8	3.7	13.0	0.45	0.10	126	77.9
z3_3	2		662	527121	1.5	1.0	85.5	469297	122	89.7	15.9	3.8	<0.02	863	11.0	1.6	0.44	<0.11	<0.007	0.13	1.7	2.3	1.0	0.06	<0.008	37.0	3.0
z6_1	2		943	547733	0.80	<1.2	71.2	448240	278	63.9	36.7	1068	0.15	1414	<8.5	0.26	1.1	1.7	<0.05	<0.43	1.8	1.9	0.69	0.08	0.02	43.4	8.4
z6_2	1b	1*	968	489097	<0.32	1.2	29.8	458528	103	11.1	24.5	4.4	<0.02	197	7.0	<0.08	0.39	<0.12	<0.04	<0.30	0.15	1.1	0.08	0.09	0.07	18.3	50948
z6_3	1b	1*	3997	482307	2.0	11.0	128	512334	121	17.8	76.0	17.0	0.59	58.6	<3.0	<0.38	4.6	<0.11	0.02	<0.40	1.5	0.74	0.10	<0.01	0.22	682	4.2
z6_4	2		978	510880	1.2	<0.64	259	482226	157	154	1607	978	0.13	2523	3.4	<0.36	1.8	<0.08	0.01	0.20	8.2	2.3	0.11	0.14	0.31	126	28.0
GS-38-12																											
z1_1	4	4	280	532039	0.14	<0.60	0.90	466533	583	502	5.8	9.6	<0.06	5.8	39.1	<0.05	0.10	<0.07	<0.02	<0.15	0.10	0.30	<0.02	0.05	<0.005	0.47	<0.02
z1_2	4	4	<673	577199	0.37	<2.0	3.0	416064	538	914	144	8.9	0.31	6.9	68.5	<0.17	<0.20	<0.24	<0.02	<0.41	0.43	<0.55	<0.08	0.05	0.48	0.34	5050
z2_1	4	4	<237	531147	0.24	<0.70	<0.29	466935	447	484	907	6.1	<0.02	5.0	44.7	3.3	10.5	<0.08	0.22	0.20	1.4	<0.20	<0.03	0.38	0.02	0.69	0.06
z2_2	4	4	<391	535843	<0.35	<0.77	0.85	463063	473	186	33.7	300	1.6	14.6	49.1	0.45	0.83	0.22	<0.46	<0.20	4.5	0.50	<0.05	0.03	0.12	0.25	0.07
z3_1	4	4	<447	573885	0.45	<1.2	<0.39	419234	848	5739	214	1.8	<0.13	23.4	48.4	<0.10	<0.03	<0.15	<0.01	<0.36	0.08	1.5	<0.05	<0.01	<0.01	0.93	<0.09
z3_2	4	4	<344	555964	<0.18	<0.88	0.46	434872	398	2210	6452	2.2	0.45	19.5	45.5	<0.08	6.5	<0.11	0.03	1.1	0.53	4.2	0.05	0.66	<0.008	13.1	7.0
z3_3	4	4	<237	537662	<0.16	<0.57	0.77	459928	601	1749	6.1	1.3	<0.02	10.0	37.1	<0.06	<0.07	<0.08	0.02	<0.18	0.02	<0.79	<0.03	<0.009	<0.006	0.30	0.07
z4_1	4	4	<342	551091	3.5	<1.3	<0.53	448474	242	98.8	<7.0	3.2	<0.10	3.5	36.1	1.5	0.08	<0.15	<0.07	<0.44	0.61	1.8	<0.05	36.1	<0.01	2.3	0.04
z4_2	4	4	341	527482	0.26	<0.63	<0.29	469978	329	1633	177	2.8	0.04	5.7	46.1	<0.05	0.12	<0.08	<0.02	1.5	0.01	<0.18	<0.03	0.08	<0.005	0.72	0.03
z4_3	4	4	<415	523404	0.23	<0.62	2.1	474876	451	1075	147	2.1	<0.09	10.5	28.2	<0.32	0.32	<0.10	0.01	0.24	<0.09	<0.23	<0.16	0.14	0.02	0.68	0.21
z4_4	4	4	<254	541609	<0.36	<1.1	0.82	457238	113	780	161	6.9	0.04	7.6	71.7	0.11	1.5	<0.12	<0.07	0.16	0.39	<0.26	0.18	0.10	<0.008	3.9	<0.03
GS-36-04																											
z1_1	4	4	<394	529679	<0.19	<1.4	<0.54	465531	21.8	91.6	293	22.0	0.03	52.2	9.3	<0.09	422	0.49	0.03	0.12	20.2	367	<0.04	0.47	0.01	3482	3.8
z1_2	4	4	255	502639	0.14	2.1	8.5	496756	17.2	21.6	255	12.4	0.02	20.9	8.2	0.07	<0.05	0.10	0.02	0.12	0.15	<0.13	<0.02	0.08	0.01	1.1	0.05

Supplementary Material 4-2 ***(continued)***

ID	Py	Text.	Si	S	V	Cr	Mn	Fe	Co	Ni	Cu	Zn	Ga	As	Se	Mo	Ag	Cd	In	Sn	Sb	Te	W	Au	Tl	Pb	Bi
GS-22-10																											
z1_1	2		3680	498049	0.33	2.0	13.9	495596	139	1390	1063	10.6	0.13	38.7	5.2	1.1	0.10	0.12	0.19	<0.16	0.04	<0.42	0.29	2.7	0.09	2.5	2.6
z1_2	1b	1*	9002	488306	39.5	8.2	118	489215	36.6	9.5	282	846	1.0	102	4.6	0.45	2.3	0.98	0.07	3.8	2.0	5.5	6.5	0.52	0.16	151	1.9
z1_3	2		1212	543009	<0.34	<5.2	4.0	454041	634	160	874	2.2	0.10	57.1	<21.5	<0.26	0.15	<0.37	<0.02	<0.54	0.20	<0.84	0.71	0.18	<0.12	0.71	0.13
z1_4	1b	1*	1164	462782	5.3	<0.92	270	532462	366	23.0	993	53.2	0.32	92.0	<3.7	0.48	4.6	<0.07	<0.004	0.13	7.2	<0.15	0.28	0.12	0.33	835	5.1
z2_1	2		4182	513629	2.4	1.9	903	480409	183	259	93.7	247	0.30	72.1	5.8	0.36	0.14	0.20	0.01	0.32	0.07	<0.24	1.1	0.56	<0.007	2.8	4.1
z2_2	2		447	536948	3.8	<0.96	7.8	461839	197	41.5	312	8.0	<0.02	174	7.0	<0.07	0.19	<0.10	0.02	0.88	0.13	<0.23	<0.14	0.78	0.09	2.7	0.90
z2_3	1b	1*	3446	498653	1.0	<0.81	419	486491	182	87.8	1128	3514	0.22	52.7	4.6	1.1	6.0	3.6	0.04	<0.25	2.7	3.0	1.6	0.34	0.09	4932	19.7
z2_4	1b	1*	7321	469187	1.9	1.1	110	519766	293	19.3	1065	799	0.50	40.3	<2.3	<0.05	6.8	0.16	0.02	0.19	5.3	1.5	0.22	0.13	0.28	1014	34.4
z3_1	2		<482	521266	0.65	<1.3	246	477636	64.3	44.0	64.3	3.3	0.06	327	8.2	<0.40	0.44	<0.16	<0.04	<0.34	0.79	1.5	2.9	<0.02	<0.01	31.9	3.1
z3_2	1b	1*	1988	505019	8.0	<0.94	1032	486252	384	23.9	228	5.7	0.38	3583	5.1	0.62	3.9	0.36	<0.03	0.31	3.8	3.7	13.0	0.45	0.10	126	77.9
z3_3	2		662	527121	1.5	1.0	85.5	469297	122	89.7	15.9	3.8	<0.02	863	11.0	1.6	0.44	<0.11	<0.007	0.13	1.7	2.3	1.0	0.06	<0.008	37.0	3.0
z6_1	2		943	547733	0.80	<1.2	71.2	448240	278	63.9	36.7	1068	0.15	1414	<8.5	0.26	1.1	1.7	<0.05	<0.43	1.8	1.9	0.69	0.08	0.02	43.4	8.4
z6_2	1b	1*	968	489097	<0.32	1.2	29.8	458528	103	11.1	24.5	4.4	<0.02	197	7.0	<0.08	0.39	<0.12	<0.04	<0.30	0.15	1.1	0.08	0.09	0.07	18.3	50948
z6_3	1b	1*	3997	482307	2.0	11.0	128	512334	121	17.8	76.0	17.0	0.59	58.6	<3.0	<0.38	4.6	<0.11	0.02	<0.40	1.5	0.74	0.10	<0.01	0.22	682	4.2
z6_4	2		978	510880	1.2	<0.64	259	482226	157	154	1607	978	0.13	2523	3.4	<0.36	1.8	<0.08	0.01	0.20	8.2	2.3	0.11	0.14	0.31	126	28.0
GS-38-12																											
z1_1	4	4	280	532039	0.14	<0.60	0.90	466533	583	502	5.8	9.6	<0.06	5.8	39.1	<0.05	0.10	<0.07	<0.02	<0.15	0.10	0.30	<0.02	0.05	<0.005	0.47	<0.02
z1_2	4	4	<673	577199	0.37	<2.0	3.0	416064	538	914	144	8.9	0.31	6.9	68.5	<0.17	<0.20	<0.24	<0.02	<0.41	0.43	<0.55	<0.08	0.05	0.48	0.34	5050
z2_1	4	4	<237	531147	0.24	<0.70	<0.29	466935	447	484	907	6.1	<0.02	5.0	44.7	3.3	10.5	<0.08	0.22	0.20	1.4	<0.20	<0.03	0.38	0.02	0.69	0.06
z2_2	4	4	<391	535843	<0.35	<0.77	0.85	463063	473	186	33.7	300	1.6	14.6	49.1	0.45	0.83	0.22	<0.46	<0.20	4.5	0.50	<0.05	0.03	0.12	0.25	0.07
z3_1	4	4	<447	573885	0.45	<1.2	<0.39	419234	848	5739	214	1.8	<0.13	23.4	48.4	<0.10	<0.03	<0.15	<0.01	<0.36	0.08	1.5	<0.05	<0.01	<0.01	0.93	<0.09
z3_2	4	4	<344	555964	<0.18	<0.88	0.46	434872	398	2210	6452	2.2	0.45	19.5	45.5	<0.08	6.5	<0.11	0.03	1.1	0.53	4.2	0.05	0.66	<0.008	13.1	7.0
z3_3	4	4	<237	537662	<0.16	<0.57	0.77	459928	601	1749	6.1	1.3	<0.02	10.0	37.1	<0.06	<0.07	<0.08	0.02	<0.18	0.02	<0.79	<0.03	<0.009	<0.006	0.30	0.07
z4_1	4	4	<342	551091	3.5	<1.3	<0.53	448474	242	98.8	<7.0	3.2	<0.10	3.5	36.1	1.5	0.08	<0.15	<0.07	<0.44	0.61	1.8	<0.05	36.1	<0.01	2.3	0.04
z4_2	4	4	341	527482	0.26	<0.63	<0.29	469978	329	1633	177	2.8	0.04	5.7	46.1	<0.05	0.12	<0.08	<0.02	1.5	0.01	<0.18	<0.03	0.08	<0.005	0.72	0.03
z4_3	4	4	<415	523404	0.23	<0.62	2.1	474876	451	1075	147	2.1	<0.09	10.5	28.2	<0.32	0.32	<0.10	0.01	0.24	<0.09	<0.23	<0.16	0.14	0.02	0.68	0.21
z4_4	4	4	<254	541609	<0.36	<1.1	0.82	457238	113	780	161	6.9	0.04	7.6	71.7	0.11	1.5	<0.12	<0.07	0.16	0.39	<0.26	0.18	0.10	<0.008	3.9	<0.03
GS-36-04																											
z1_1	4	4	<394	529679	<0.19	<1.4	<0.54	465531	21.8	91.6	293	22.0	0.03	52.2	9.3	<0.09	422	0.49	0.03	0.12	20.2	367	<0.04	0.47	0.01	3482	3.8
z1_2	4	4	255	502639	0.14	2.1	8.5	496756	17.2	21.6	255	12.4	0.02	20.9	8.2	0.07	<0.05	0.10	0.02	0.12	0.15	<0.13	<0.02	0.08	0.01	1.1	0.05
z1_3	4	4	17819	489816	0.26	<1.3	144	490660	65.0	10.8	194	9.4	1.4	760	7.3	10.1	1.8	0.26	0.02	0.41	13.6	5.3	2.3	0.43	1.1	65.9	0.06
z1_4	4	4	16089	526535	1.3	1.1	39.7	452709	140	32.0	1323	20.9	1.3	648	<7.7	30.6	6.5	<0.12	<0.04	0.86	42.5	15.3	5.9	1.1	4.0	203	0.98

Supplementary Material 4-2 ***(continued)***

ID	Py	Text.	Si	S	V	Cr	Mn	Fe	Co	Ni	Cu	Zn	Ga	As	Se	Mo	Ag	Cd	In	Sn	Sb	Te	W	Au	Tl	Pb	Bi
z2_2	4	4	72482	526985	<0.70	<4.1	20.1	397370	26.8	<18.8	546	64.8	2.2	1842	<8.7	4.3	7.8	0.65	<0.03	<0.60	56.3	24.7	0.27	1.2	8.5	336	0.63
z2_3	4	4	96646	462665	<0.63	<3.6	<1.3	440389	19.2	<16.8	<22.2	4.6	<0.08	146	<7.9	1.9	6.9	<0.43	<0.03	0.65	11.3	5.5	<0.14	0.27	0.57	46.6	0.45
z2_4	4	4	33706	481366	0.17	<1.8	0.86	483519	32.3	<5.5	61.4	3.1	<0.16	373	9.3	2.1	19.7	<0.15	<0.01	0.38	12.3	19.4	0.08	0.34	0.74	872	1.0
z3_1	4	6	197	509955	0.38	4.5	0.89	488946	2.0	357	471	9.5	0.08	28.2	7.6	<0.04	0.32	0.13	0.02	0.55	0.29	0.61	0.04	0.05	0.27	12.0	0.12
z3_2	4	6	347	549858	<0.25	<0.96	1.7	449094	25.8	19.1	226	5.3	0.07	35.0	11.5	0.36	<0.17	<0.10	<0.03	<0.23	0.10	0.35	0.16	374	0.04	0.72	0.05
z3_3	4	6	258	510184	0.15	<0.81	2.5	488034	3.5	162	28.8	23.6	<0.01	32.2	7.0	0.14	1.7	0.13	<0.04	<0.20	2.3	1.6	0.05	0.27	0.03	1255	0.22
z3_4	4	6	<332	517113	<0.22	1.5	2.9	480532	13.3	53.2	190	14.9	<0.08	44.9	6.9	0.12	3.3	0.32	0.02	<0.27	20.0	4.3	<0.03	0.91	0.04	1995	0.25
z4_1	4	6	364	550306	<0.33	<1.1	3.7	448858	12.7	153	249	7.4	0.04	33.8	11.0	<0.46	0.70	0.13	<0.03	<0.27	<0.07	<0.27	0.23	0.05	<0.008	<21.1	<0.05
z4_2	4	6	250	528697	0.21	<0.58	1.8	470904	3.2	40.7	20.0	45.7	<0.01	13.0	6.8	0.26	0.68	0.53	<0.02	<0.14	0.31	0.36	<0.02	0.18	0.03	14.5	0.03
GS-55-02																											
z1_1	1b	1*	1300	503180	12.4	13.8	94.7	492358	720	330	41.7	29.8	0.23	43.3	<2.9	<0.04	1.2	<0.06	<0.004	0.74	3.5	<0.14	0.31	0.04	0.13	245	1.2
z1_2	1b	1*	5925	462924	57.3	34.6	1491	527382	261	146	176	43.0	1.8	40.7	2.9	0.08	3.5	<0.05	0.02	0.59	9.7	1.8	1.4	0.33	0.30	632	0.71
z1_3	1b	1*	3966	502766	6.7	25.5	104	489323	2554	477	142	12.6	0.34	377	15.5	<0.04	1.4	<0.06	0.01	0.15	3.0	2.8	0.07	0.32	0.08	72.6	1.6
z2_1	2		6389	530434	<0.21	<0.56	0.48	454658	7132	379	4.6	5.3	0.02	891	23.1	<0.04	0.18	<0.07	<0.004	<0.19	17.1	0.30	0.29	0.25	0.02	3.4	0.27
z2_2	1b	1*	1721	515656	7.0	8.5	91.4	479351	1217	748	116	12.0	0.19	315	7.5	<0.04	2.4	0.15	<0.02	0.37	19.1	2.0	0.04	0.24	0.08	236	4.7
z2_3	2		9133	445258	41.8	31.5	13586	520609	5206	1096	274	156	<0.57	4133	24.7	<0.43	1.1	<0.64	<0.04	<1.5	208	2.4	<0.98	0.55	0.59	153	2.7
z2_4	1b	1*	13080	477532	82.4	30.6	246	498294	415	225	858	19.5	0.71	19.4	5.1	0.17	2.9	<0.07	<0.02	3.0	5.2	0.46	0.29	0.19	0.10	264	0.27
z3_1	1b	1*	1306	490151	8.1	8.9	148	504942	785	1428	65.3	71.4	0.17	714	12.5	<0.12	1.1	<0.18	0.01	0.24	31.6	2.8	<0.01	0.27	0.21	53.6	1.7
z3_2	1b	1*	3814	491427	20.4	21.8	228	502234	687	219	203	82.6	0.79	795	10.0	<0.03	2.3	0.18	0.01	0.41	4.5	2.9	0.06	0.41	0.07	164	2.2
z3_3	1b	1*	5171	462369	43.3	28.9	201	517084	545	1221	169	19.4	0.67	128	22.5	1.4	3.5	<0.04	0.01	2.7	13.6	6.3	15.6	0.52	0.17	427	5.2
z3_4	2		518	486802	1.8	1.8	40.6	509339	365	1686	27.0	3.8	0.15	97.8	20.6	<0.02	0.27	<0.03	<0.002	0.10	0.31	0.19	<0.01	0.06	0.01	6.4	1082
z3_5	2		403	476831	1.4	1.7	45.9	515845	4205	559	954	3.0	0.07	1092	18.9	<0.09	0.62	<0.03	<0.002	<0.12	16.5	1.6	<0.01	0.20	0.01	15.3	1.3
z3_6	2		22026	469507	9.9	5.7	174	498488	6376	817	18.0	313	2.1	2145	19.7	<0.38	0.99	<0.06	<0.003	0.14	42.9	2.6	<0.02	2.1	0.08	21.4	3.0
z4_1	1b	1*	3495	519689	16.9	16.6	292	474677	753	286	210	27.0	0.70	39.3	13.8	<0.06	1.4	<0.08	0.01	0.25	2.4	<0.79	<0.03	0.15	0.03	183	0.26
z4_2	1b	1*	1525	521409	7.2	22.7	122	475464	268	187	29.2	12.8	0.42	633	3.4	<0.44	0.40	<0.07	<0.004	0.33	2.7	0.20	<0.02	0.19	0.05	109	0.47
GS-22-06																											
z1_1	1a	2	3585	555236	12.0	91.9	123	426539	120	83.7	6159	2666	0.46	4422	9.3	4.6	7.2	17.0	<0.05	0.41	9.4	4.0	1.4	1.8	0.29	772	0.36
z1_2	1a	2	7172	545436	12.6	4.8	54.7	441633	81.2	113	1736	60.4	1.0	2991	<3.8	6.5	8.6	0.95	0.05	0.17	7.5	5.9	1.3	0.57	0.09	546	0.92
z1_3	1a	2	905	562014	0.52	<1.5	12.7	429209	120	85.6	472	25.0	<0.03	6977	7.9	0.17	3.7	<0.17	<0.009	<0.35	5.3	3.6	<0.05	1.2	0.02	148	0.25
z1_4	1a	2	14140	587872	<0.30	5.8	225	386427	236	775	1743	8135	<0.05	340	<14.5	<0.17	1.9	34.9	<0.06	<0.57	3.3	1.1	<0.08	<0.03	<0.02	59.1	0.24
z2_1	1a	2	970	541919	6.7	1.7	106	447797	104	124	6845	148	0.41	1398	12.1	3.6	7.2	0.99	0.04	0.46	10.3	1.5	0.44	0.27	0.19	542	0.32
z2_2	1a	2	<361	524651	7.6	2.4	72.4	473523	122	112	551	11.4	0.07	794	6.3	1.0	4.4	<0.11	0.04	0.18	2.4	0.85	0.14	0.64	0.04	99.1	0.09
z2_3	1a	1	482	509261	0.25	<0.77	11.2	487605	29.3	76.1	2312	10.1	<0.06	48.2	3.6	0.77	9.9	<0.09	0.01	<0.25	2.4	4.8	0.06	0.36	0.04	137	0.85

Supplementary Material 4-2 ***(continued)***

ID	Py	Text.	Si	S	V	Cr	Mn	Fe	Co	Ni	Cu	Zn	Ga	As	Se	Mo	Ag	Cd	In	Sn	Sb	Te	W	Au	Tl	Pb	Bi
z2_4	1a	1	29350	474111	33.9	<1.5	41202	451534	213	66.6	2596	92.6	4.3	303	<8.4	0.70	1.4	0.58	0.09	2.2	2.9	<0.53	1.2	1.7	0.43	135	0.23
z2_5	1a	2	1341	539855	3.5	4.6	56.3	450475	157	107	4469	53.6	0.35	2744	8.6	2.2	6.8	0.24	<0.008	<0.29	4.7	4.5	0.10	1.2	0.19	688	0.33
z3_1	1a	1	16139	546316	15.5	25.0	269	432230	136	100	1150	28.8	0.50	436	19.3	0.41	5.7	0.68	<0.04	<0.16	4.7	4.7	0.06	0.29	0.12	3079	1.5
z4_1	1a	1	4952	571632	59.2	355	1905	416613	214	147	829	571	1.7	2218	27.2	1.4	9.0	<0.22	0.02		5.9	4.8	0.85	0.60	0.06	377	0.41
z4_2	1a	1	1081	548208	13.7	<0.72	64.1	446635	420	403	569	432	0.22	1837	18.7	0.81	4.3	0.59	0.02	<0.27	3.5	6.8	0.21	0.79	0.03	231	0.22
GS-36-05																											
z1_1	4	1	11910	490420	260	2.4	73.1	414355	64.1	9.7	480	75.1	2.4	1031	5.9	15.7	13.9	2.1	0.32	89.1	107	31.0	1391	3.6	6.4	341	0.79
z1_2	4	5	335	479603	1.3	<0.40	82.4	517107	11.5	68.2	546	102	0.39	199	4.1	0.49	23.9	1.7	0.03	0.18	102	31.8	0.62	3.0	0.26	1762	1.3
z1_3	4	5	388	501208	3.1	0.60	307	497735	7.5	23.2	75.2	4.9	0.13	60.2	3.2	0.13	0.94	<0.06	<0.004	0.20	3.7	2.1	0.04	0.49	0.06	174	0.10
z1_4	4	5	1942	502236	9.6	0.95	812	492524	8.4	39.5	146	47.9	0.87	110	<3.9	<0.44	13.5	0.31	0.02	0.78	45.1	20.8	0.44	1.8	0.15	2012	1.2
z1_5	4	5	259	522701	1.3	2.1	125	475183	17.5	<1.6	119	43.3	<0.01	748	4.8	0.09	12.3	0.20	<0.004	0.15	32.8	17.6	0.08	2.0	0.21	727	0.79
z1_6	4	5	<192	528035	0.51	<0.93	33.5	470950	15.2	2.4	193	6.4	0.03	73.5	6.2	0.47	13.3	<0.09	<0.005	<0.20	8.1	15.6	0.04	2.2	0.16	642	0.55
z1_7	4	5	1185	507158	0.87	<0.73	76.7	449087	9.8	2.8	3949	1084	0.28	1827	20.1	0.11	44.1	15.3	<0.03		1340	50.3	0.12	61.9	0.22	34069	12.1
z1_8	4	1	33641	506921	66.8	<1.4	48.4	437795	50.7	10.6	235	68.0	7.8	2189	<5.2	6.9	23.6	1.6	0.15	22.6	68.0	39.2	252	3.3	2.1	4148	1.3
z1_9	4	5	<369	550189	0.16	<0.87	1.8	449439	10.4	28.3	39.4	2.8	<0.02	10.9	7.0	0.45	1.2	<0.11	0.03	0.17	0.49	1.4	0.55	0.43	0.02	252	0.16
GS-22-07																											
z1_1	4	1	2471	555467	<0.13	<0.84	<0.37	441804	13.7	132	6.9	2.5	<0.06	46.8	43.9	0.18	2.0	<0.13	<0.007	0.28	0.10	<0.79	0.04	0.05	<0.02	4.1	1.7
z1_2	4	1	<504	561778	<0.11	<1.4	<0.49	437996	19.1	155	<6.2	<0.83	<0.03	18.5	32.3	<0.09	<0.02	<0.15	<0.10	<0.30	0.03	<0.32	<0.04	<0.02	<0.008	0.30	0.11
z1_3	4	1	<434	556387	<0.19	<0.88	<0.32	443371	9.8	140	<7.0	1.4	0.03	29.8	49.3	4.8	0.19	0.20	<0.008	<0.36	<0.02	0.42	<0.04	0.05	<0.008	1.2	0.06
z1_4	4	1	263	521424	<0.22	<0.78	0.64	476731	10.0	103	126	2.4	<0.09	44.7	27.0	0.11	10.2	<0.12	0.01	0.18	0.27	14.5	<0.03	1.1	<0.007	1236	5.7
z2_1	4	4	366	565225	0.23	2.0	4.4	430375	48.8	316	717	12.2	<0.04	18.2	29.4	<0.06	2869	<0.10	0.11	0.32	<0.03	<0.21	0.06	6.5	0.01	5.0	0.60
z2_2	4	4	569	546720	0.38	3.0	6.3	449272	49.4	82.3	3227	7.0	0.06	14.9	31.6	0.68	0.16	0.12	0.01	0.20	0.07	1.0	0.30	0.89	0.08	0.96	0.06
z2_3	4	4	<250	555891	<0.15	<0.92	1.7	443379	56.2	192	400	15.0	<0.02	26.1	35.3	<0.08	0.12	0.29	0.02	<0.18	0.09	0.59	<0.03	0.17	0.03	0.47	<0.03
z2_4	4	4	320	560748	0.21	2.5	<0.46	436793	80.1	65.8	928	73.4	<0.02	13.0	34.6	3.1	1.9	0.25	0.01	0.23	0.35	1.6	<0.03	0.52	0.01	928	5.1
z2_6	4	4	<192	563473	<0.10	<0.96	4.6	435906	44.9	37.6	462	10.9	<0.02	19.4	35.3	<0.05	1.3	0.22	0.01	0.13	<0.01	<0.19	0.11	2.2	<0.005	1.2	0.10
z3_1	4	4	283	557532	0.17	<0.94	0.45	441937	35.6	29.4	55.8	5.0	<0.08	18.2	27.4	0.28	<0.07	<0.11	0.01	<0.20	0.26	0.45	<0.03	70.8	0.02	1.5	0.34
z3_2	4	4	<406	556384	<0.13	<0.95	0.86	440435	57.5	66.6	424	4.8	<0.02	51.9	45.9	<0.42	3.0	0.18	0.01	<0.25	<0.10	2.3	<0.03	0.22	0.02	2509	14.5
z3_3	4	4	1016	547981	0.94	<0.94	2.1	450676	40.5	154	40.1	4.7	0.15	17.0	28.7	<0.29	0.36	<0.12	<0.006	<0.24	0.13	0.66	0.05	0.15	0.01	16.2	0.75
z3_4	4	4	<225	561529	<0.25	<0.75	0.31	437732	84.1	72.5	342	150	0.03	41.7	40.4	<0.06	2.9	<0.10	<0.005	<0.14	<0.18	0.40	<0.03	0.21	<0.006	0.75	0.26
z3_5	4	4	5569	521072	4.7	<1.1	7.5	473008	48.5	34.3	8.0	33.6	1.2	24.7	29.8	<0.06	0.98	<0.11	<0.02	0.53	0.22	1.6	0.54	0.12	0.11	50.4	0.48
z3_6	4	4	<534	574005	<0.22	<1.8	<0.60	424876	76.5	64.7	34.7	882	<0.13	19.3	28.7	0.67	0.20	6.2	<0.04	0.07	<0.02	0.68	<0.05	<0.08	<0.01	4.0	0.55
GS-38-08																											
z1_1	1b	3	496	536278	<0.10	<0.67	0.33	462539	402	196	15.4	5.4	<0.01	49.7	<4.2	<0.21	0.62	<0.08	<0.004	0.19	0.18	<0.17	0.09	<0.04	<0.005	12.7	0.12

Supplementary Material 4-2 ***(continued)***

ID	Py	Text.	Si	S	V	Cr	Mn	Fe	Co	Ni	Cu	Zn	Ga	As	Se	Mo	Ag	Cd	In	Sn	Sb	Te	W	Au	Tl	Pb	Bi
z1_2	1b	3	<465	560205	<0.20	<1.4	1.3	439054	140	473	67.8	2.4	<0.03	44.3	7.5	<0.47	0.43	<0.16	0.05	<0.13	0.05	0.99	<0.16	0.07	0.02	3.3	0.06
z1_3	1b	3	1791	544267	<0.16	<1.3	179	452727	62.3	510	49.8	56.7	<0.03	56.7	7.1	<0.09	4.6	0.33	<0.03	<0.33	20.9	5.7	<0.04	0.26	<0.08	258	1.8
z1_4	1b	3	<318	516828	0.13	<0.92	<0.29	482429	242	436	<3.1	3.5	<0.08	36.4	7.8	<0.28	1.4	<0.11	0.01	<0.10	0.32	1.3	0.04	0.47	<0.06	5.4	0.25
z1_5	1b	3	659	499364	0.93	1.0	43.4	499364	71.6	28.9	81.1	2.4	<0.06	281	<1.9	<0.05	5.0	<0.09	<0.005	<0.14	57.9	1.9	<0.02	0.25	2.7	30.7	0.09
z1_6	1b	3	28081	532539	<0.15	<0.95	<0.66	438266	94.3	320	13.7	532	<0.03	64.5	<13.0	<0.47	8.1	5.2	<0.04	<0.38	1.6	8.7	<0.05	0.90	0.02	62.2	0.78
z1_7	1b	3	<353	523476	0.16	<0.92	0.52	475713	42.0	536	13.3	3.1	<0.02	60.6	9.6	<0.33	41.1	<0.14	<0.03	<0.33	1.5	55.4	<0.04	6.8	<0.007	36.6	0.61
z2_1	1b	1	1527	550328	18.5	7.6	0.77	434737	712	305	131	3.6	0.03	2181	4.0	3.9	2.4	0.14	0.01	0.55	57.4	3.3	32.7	0.88	1.1	45.1	0.11
z2_2	2		12410	544672	26.2	7.3	4.0	441254	579	400	15.0	24.8	1.3	207	8.6	0.27	0.68	<0.10	0.01	0.30	2.5	1.2	4.3	0.03	0.20	12.5	0.15
z2_4	2		16348	554161	1.1	<1.4	1.5	428551	317	490	17.5	10.0	0.32	80.4	3.1	<0.09	0.37	<0.16	0.01	<0.31	3.3	0.50	<0.04	0.17	0.16	7.4	0.05
z2_5	2		41298	547775	126	32.6	11.2	409300	321	437	24.5	45.6	6.0	33.9	<9.7	<0.83	0.61	<0.29	<0.02	0.55	0.76	0.99	2.6	0.16	0.27	6.7	0.33
z2_6	1b	1*	1416	597368	2.1	<2.8	<0.84	397095	90.9	79.4	88.6	1116	0.13	2302	<13.8	<0.17	14.8	12.4	0.02	<0.40	93.2	70.2	<0.08	3.8	19.3	218	4.2
z2_7	2		<704	608066	<0.26	<2.3	<0.72	391219	193	467	<6.6	2.3	<0.04	51.0	<11.2	<0.15	0.17	<0.25	<0.01	<0.35	0.12	<0.51	<0.06	0.18	<0.01	0.76	<0.06
z3_1	1b	3	<476	577748	<0.27	<1.4	<0.42	421394	143	487	36.2	3.5	<0.10	139	5.2	<0.09	2.0	<0.16	0.09	0.22	1.1	4.8	<0.04	0.72	0.02	34.1	0.43
z3_10	1b	3	2070	552498	6.5	1.2	3.3	443770	459	197	24.2	757	0.23	95.0	<6.5	<0.06	14.2	5.6	0.01	0.28	10.5	5.7	0.04	0.49	0.19	60.4	0.66
z3_2	1b	3	864	567769	7.8	2.1	2.2	430039	33.9	344	227	30.0	0.28	61.5	5.6	<0.05	0.34	<0.10	<0.04	0.21	0.97	1.3	2.6	2.2	0.01	13.8	0.24
z3_3	1b	3	431	556544	0.51	0.86	0.65	441426	249	235	530	6.5	<0.02	431	<5.4	<0.07	8.9	<0.12	<0.02	<0.22	66.3	11.1	0.07	1.8	3.3	43.9	0.39
z3_4	1b	3	<246	537394	<0.13	<0.65	2.1	460808	302	354	909	84.4	<0.01	96.7	8.6	0.35	2.1	1.2	0.03	0.16	15.6	3.2	0.21	0.15	<0.004	14.3	0.28
z3_5	1b	3	<261	578466	<0.15	1.6	0.47	419143	109	490	711	376	<0.02	482	6.7	0.11	5.6	6.7	<0.03	0.16	128	3.5	<0.03	0.40	0.09	62.9	0.97
z3_6	1b	3	<279	572158	0.74	1.1	1.2	426861	131	217	82.9	5.0	0.03	391	5.0	0.10	6.2	<0.11	0.05	<0.17	95.2	1.5	<0.03	0.49	3.3	32.1	0.18
z3_7	1b	3	<225	571654	0.21	<0.68	<0.21	427533	330	238	20.1	6.9	<0.02	106	<16.9	0.14	0.58	<0.10	<0.005	<0.25	4.8	1.5	0.39	2.4	0.11	23.3	0.71
z3_8	1b	3	1168	529067	9.9	6.0	1108	463270	181	158	779	497	0.15	2404	<4.3	<0.21	31.6	3.9	0.05	0.13	725	12.0	1.2	1.4	23.2	293	2.2
z3_9	1b	3	8472	562465	6.5	4.7	6.6	426216	456	291	183	44.5	0.43	118	7.1	<0.08	4.4	<0.53	<0.007	<0.24	12.3	5.5	0.78	0.12	0.31	1659	4.7
GS-34-05																											
z1_1	1b	2	320	529787	0.19	2.7	1.9	468622	120	668	414	11.1	0.07	4.7	31.1	0.38	0.88	<0.09	0.04	<0.32	0.12	0.48	0.08	1.4	0.17	8.5	0.16
z1_2	1b	2	406	531283	0.37	3.0	15.1	465634	177	1083	1015	35.9	0.04	183	17.5	<0.05	46.7	<0.58	0.03	<0.24	1.9	60.2	0.53	4.8	0.02	22.6	0.62
z1_3	1b	2	616	527955	7.3	5.2	3.4	466316	384	491	697	8.6	0.11	27.8	40.2	0.29	8.7	0.11	0.01	<0.20	2.4	48.2	9.2	3.8	0.05	55.4	2.7
z3_1	1b	2	2042	499204	3.7	3.0	0.92	496142	503	351	1429	13.3	<0.51	88.8	25.6	<0.09	6.8	<0.11	<0.01	<0.20	0.95	15.3	2.1	0.14	0.04	17.7	0.17
z3_2	1b	2	1246	520319	19.5	55.9	30.5	477100	492	166	169	6.6	0.81	99.1	30.9	<0.07	8.6	<0.08	<0.008	<0.15	6.3	55.1	0.35	5.6	0.14	173	1.0
z6_1	1b	2	1356	548146	7.2	5.7	11.4	447862	705	509	558	6.7	0.14	46.8	25.1	<0.11	34.2	<0.14	<0.04	0.24	1.7	41.0	14.5	6.2	<0.01	29.7	1.3
z6_2	1b	2	21320	546010	172	88.7	9.9	427708	636	476	572	125	8.8	533	26.7	0.42	793	0.53	0.08	0.68	8.1	611	13.7	26.0	0.30	49.4	3.7
z6_3	1b	2	2738	539878	15.6	9.4	3.2	454461	856	265	209	11.2	0.67	70.1	23.3	2.4	209	0.45	0.04	<0.92	2.4	238	12.8	10.3	0.03	119	2.3
GS-22-08																											
z1_1	2		15890	542077	7.7	4.9	3.5	440501	518	754	6.0	15.3	0.61	152	6.6	<0.09	0.10	0.21	<0.01	<0.28	0.18	0.50	0.20	0.22	0.03	6.7	0.21

Supplementary Material 4-2 ***(continued)***

ID	Py	Text.	Si	S	V	Cr	Mn	Fe	Co	Ni	Cu	Zn	Ga	As	Se	Mo	Ag	Cd	In	Sn	Sb	Te	W	Au	Tl	Pb	Bi
z1_2	1b	1*	6609	513629	50.7	137	589	474346	1326	166	815	64.8	1.7	248	10.8	0.16	2.7	0.78	0.04	<0.55	7.1	8.2	1.7	0.86	0.21	372	8.0
z1_3	2		376	536646	<0.15	<2.0	<0.45	461620	263	875	60.4	1.8	<0.03	143	9.7	<0.10	0.21	<0.14	<0.01	<0.25	0.06	1.1	<0.05	0.36	<0.01	1.7	0.23
z1_4	1b	1*	7906	510677	59.3	118	665	474385	1624	153	415	29.4	1.7	238	5.3	<0.07	1.6	<0.08	<0.03	0.46	8.3	4.3	11.6	0.39	0.35	269	2.2
z1_5	2		414	548642	<0.27	1.2	2.4	448269	628	1462	312	3.8	<0.03	252	7.1	<0.09	0.16	<0.12	<0.01	<0.57	0.09	0.49	<0.04	0.09	0.04	1.7	0.04
z1_6	1b	1*	7508	524839	45.1	191	414	461769	1877	271	788	39.0	1.8	228	4.9	<0.06	1.8	<0.07	0.01	<0.30	8.5	16.3	2.3	0.47	0.21	311	3.5
z5_1	2		288	532330	0.14	<0.71	0.67	465189	144	1623	208	4.8	<0.02	203	7.4	0.10	0.28	<0.06	<0.05	<0.12	0.17	0.30	0.18	0.34	0.05	1.1	0.14
z5_2	1b	1*	5198	530599	30.3	35.7	1213	454799	1343	240	128	28.2	1.3	1224	7.1	<0.14	1.2	<0.17	0.02	<0.45	4.4	1.6	14.0	260	0.13	91.0	0.83
z5_3	2		1810	545926	<0.26	<1.0	0.87	450651	576	511	295	3.2	<0.03	207	6.2	<0.77	0.55	<0.11	<0.04	<0.18	0.35	0.41	0.13	0.49	<0.008	9.9	0.62
z5_4	1b	1*	2244	510603	34.5	48.9	14.2	437780	1380	568	85.5	18.5	0.25	204	7.8	1.2	1.9	<0.08	<0.03	1.1	12.0	8.1	52.5	0.44	0.05	77.1	2.2
z5_5	2		322	555035	0.16	<0.93	2.0	443351	425	745	3.0	2.7	0.08	91.7	7.4	<0.07	0.12	<0.08	0.06	<0.18	<0.07	<0.22	0.05	0.26	0.06	1.1	0.03
z5_6	1b	1*	9107	530100	60.7	13.8	350	457707	186	122	91.9	21.8	1.9	108	<2.9	<0.06	1.5	<0.08	0.03	0.22	6.3	5.1	4.5	0.25	0.16	98.9	0.81
GS-38-05																											
z2_1	2		2458	565909	<0.45	<1.3	4.0	430441	25.0	56.6	371	2.7	0.25	705	<9.1	0.13	0.39	0.69	<0.05	<0.28	1.6	0.42	<0.21	0.31	<0.04	23.7	0.07
z2_2	1b	2*	1522	554636	1.2	3.8	17.8	433754	37.7	86.0	320	8.2	0.08	9493	<4.3	<0.07	3.8	0.60	0.03	0.50	5.4	3.8	<0.40	9.5	<0.05	93.2	0.15
z2_3	2		772	566914	1.9	3.1	2.3	432099	22.1	23.0	<4.5	<4.6	0.06	144	10.5	<1.1	0.04	<0.16	0.04	<0.39	0.28	<0.43	<0.06	0.10	<0.01	6.2	0.01
z2_4	1b	2*	2661	571612	<0.20	<2.5	<0.46	422345	10.5	25.5	35.9	<5.3	<0.05	3263	3.7	<1.3	1.4	<0.19	<0.02	<0.45	3.3	<0.49	<0.07	0.64	0.10	37.7	0.04
z8_1	1b	2*	2393	566653	4.8	13.8	4.4	419648	40.2	59.0	137	137	0.41	3333	<4.1	4.0	33.3	0.74	<0.04	<0.26	17.3	6.2	3.4	1.5	0.22	7436	0.51
z8_2	2		9027	557829	1.9	6.1	4.4	431681	90.3	145	10.8	3.6	<0.17	1134	<8.6	2.4	0.75	<0.16	<0.06	<0.70	1.3	0.89	0.39	0.30	0.01	60.2	0.06
z8_3	2		8510	586036	0.98	3.9	13.9	396493	47.4	158	174	90.9	0.09	6576	2.1	0.86	10.8	<0.56	<0.05	<0.38	18.4	4.0	0.69	3.2	0.09	1847	0.13
z8_4	2		362	549685	0.06	<0.91	0.40	448507	42.3	88.3	400	106	0.03	748	1.4	0.10	3.3	0.80	0.23	0.29	4.8	2.1	<0.03	2.7	<0.005	44.5	0.19

Concentrations are in ppm.

*Pyrite-bearing structures and pyrite textures are: 1 = disseminated; 2 = dismembered veinlet; 3 = pyrite-dominated veinlet; 4 = polymetallic breccia; 5 = pyrite stringer; 6 = quartz-dominated breccia; * = altered.*

Chapitre V – Pyrite as a micro-texural and geochemical tracer of ore-forming processes at the Central Zone orogenic gold deposit, Gabgaba district, NE Sudan

Célestine Berthier[1], Julien Perret[1,2,*], Aurélien Eglinger[2], Anne-Sylvie André-Mayer[2], Julien Feneyrol[1], Alexandre Voinot[3,4], Yoram Teitler[2], Aomar Ennaciri[3], Rémi Bosc[1]

Article en préparation pour soumission à *Economic Geology*.

[1] GeoRessources, Université de Lorraine, CNRS, 54000 Nancy, France

[2] Arethuse Geology EURL, BP 80017, Latitude Arbois, 1060 rue René Descartes, 13290 Les Milles, France

[3] Department of Geological Sciences and Geological Engineering, Queen's University, K7L 3N6 Kingston, Canada

[4] MacDonald Institute, Canadian Particle Astrophysics Research Centre, Stirling Hall, Department of Physics, Engineering Physics & Astronomy, Queen's University, 64 Bader lane, Kingston, ON, Canada

[4] Managem, BP5199, Twin Center, Tour A, Boulevard Zerktouni, Casablanca, Maroc

Résumé

L'étude des processus minéralisateurs à l'origine des gîtes aurifères contrôlés structuralement est difficile car elle nécessite d'intégrer des données structurales, texturales et géochimiques obtenues à grande échelle dans le cadre structural régional. Dans le cas du gisement aurifère de Central Zone appartenant au district de Gabgaba (bouclier arabo-nubien néoprotérozoïque), seule l'évolution tectonique de la partie centrale de la suture de Keraf l'hébergeant est connue. Nous proposons donc d'étudier conjointement (i) l'expression de la déformation aux échelles macroscopique et miscroscopique, (ii) les textures des veines minéralisées et des générations de pyrite associées et (iii) leur concentrations en élements traces *via* LA-ICP-MS afin de mieux contraindre les processus minéralisateurs en jeu dans ce gisement d'or orogénique.

La minéralisation aurifère de Central Zone est synchrone de la mise en place de la zone de cisaillement de Keraf se superposant à la suture éponyme. Elle est exprimée sous forme de veines de type *crack-seal* à quartz-ankerite-(albite) et or libre hébergées par des granitoïdes. De l'or invisible est contenu dans le réseau cristallin de la pyrite également enrichie en As, Ni et Co, formée dans le halo d'altération proximal de ces veines, riche en séricite, albite et ankérite. Ces signatures sont typiques de l'or orogénique. Enfin, les textures des veines minéralisées ainsi que la zonation oscillatoire texturale et chimique présentée par la pyrite aurifère suggèrent que la mise en place des veines se fait en réponse à des chutes de pression épisodiques, brutales et répétées du fluide minéralisateur, engendrant le phénomène de *fluid boiling*. Ces processus sont typiques du mécanisme de faille-valve qui est largement décrit dans les modèles de formation de l'or orogénique.

Mots-clés

Gisement de Central Zone ; District aurifère de Gabgaba ; or orogénique ; *fluid boiling* ; mécanisme de faille-valve.

Abstract

Studying ore-forming processes in structurally-controlled deposits is challenging as it requires to consider collectively numerous large-scale structural, textural and geochemical information that need to be consistently interpreted in the regional deformation setting. Except the regional tectonic evolution, all these data lack to the understanding of ore-forming processes involved at the Neoproterozoic Central Zone gold deposit, located in the Gabgaba gold district, central Keraf suture, Nubian shield. To fill this gap in knowledge, we carried out a coupled investigation of (i) macroscopic- and microscopic-scale expression of regional deformation, (ii) textures of mineralized veins and pyrite generations and (iii) LA-ICP-MS trace element concentrations of pyrite.

Central Zone mineralization is associated with Keraf strike-slip shearing, subsequently to Keraf suturing. It is expressed by visible gold-bearing quartz-ankerite-(albite) crack-seal veins hosted by granitoids. Some structurally lattice-bound gold occurs in proximal As-Au-Ni-Co-enriched pyrite associated with sericite-albite-ankerite alteration, typical of orogenic gold. Vein textures and proximal pyrite oscillatory zoning and geochemical signature indicate that vein infilling occurred as a response to sudden pressure drops and boiling of the mineralizing fluid. We therefore interpret the Central Zone deposit as a typical orogenic gold deposit, with evidence for earthquake-induced fault-valve processes such as crack-seal veining and fluid boiling.

Keywords

Central Zone deposit; Gabgaba gold district; Orogenic gold; Fluid boiling; Fault-valve mechanism.

1. Introduction

Orogenic gold deposits typically form at 10-15 km-depth under amphibolite-greenschist facies conditions, via deformation-induced fluid circulation preferentially driven along ductile-brittle transcurrent structures deeply rooted into the lithosphere, at Archean to Phanerozoic convergent tectonic margins (*e.g.*, Kerrich and Wyman, 1990; Sawkins, 1990; Goldfarb et al., 2001; Groves et al., 2003; Weinberg et al., 2004; Goldfarb et al., 2005; Bierlein et al., 2006a; Tomkins and Grundy, 2009; Eglinger et al., 2017; Groves et al., 2019). The broadly accepted fault-valve model accounts for orogenic gold-bearing quartz-carbonate veining along permeable conduits such as faults, shear zones and fold noses, with gold deposition relating to seismic-aseismic fluid pressurization-pressure drop cycles (*e.g.*, Sibson et al., 1988; Sibson, 1990; Ridley, 1993; Wilkinson and Johnston, 1996; Sibson and Scott, 1998; Cox, 1999; Cox et al., 2001; Robert and Poulsen, 2001; Sibson, 2001; Micklethwaite and Cox, 2004; Weatherley and Henley, 2013; Peterson and Mavrogenes, 2014; Cox, 2016).

Relationships between district-scale deformation and gold-bearing fluid flow events are specific to every single deposit, with different expressions of structural control on mineralization (*e.g.*, Boullier and Robert, 1992; Sibson and Scott, 1998; Thébaud et al., 2018; Perret et al., 2020). Gold-forming processes at the microscopic scale may then differ from one deposit to another and no generic rule can be generalized. In the last decades, numerous studies have therefore zoomed at the microscopic scale to address gold transport and deposition mechanisms in relation to deformation by considering both textural and chemical characteristics of sulfide minerals, which are ubiquitous in structurally-controlled gold deposits (*e.g.*, Tomkins and Mavrogenes, 2001; Li et al., 2014; Velásquez et al., 2014; Fougerouse et al., 2017; Velásquez et al., 2018; Dubosq et al.,

2018; Gaboury, 2019; Gourcerol et al., 2020; Voisey et al., 2020; Petrella et al., 2020; Perret et al., under review[1]).

Sulfide minerals are widely documented as important contributors for gold endowment in orogenic gold deposits (*e.g.*, Boiron et al., 1989; Cathelineau et al., 1989; Cook and Chryssoulis, 1990; Large et al., 2009; Velásquez et al., 2014; Deditius et al., 2014; Fougerouse et al., 2016a; Wu et al., 2019a). They are common gold bearers, notably of invisible gold, *i.e.*, lattice-bound gold and submicroscopic inclusions (Cook and Chryssoulis, 1990), or as visible gold, *i.e.*, nano- to micro-inclusions. Their crystalline deformation, in a lower scale tectono-metamorphic setting, is known to be associated with elemental mobility leading to metal remobilization and potential liberation or endowment (*e.g.*, Fougerouse et al., 2016a; Dubosq et al., 2018; Wu et al., 2019a). When focusing on pyrite, the most documented gold-bearing sulfide mineral, many a publication has reported frequent coupling of Au with other metals and metalloids, *e.g.*, Ni, Co or As, in the pyrite-lattice and textural changes indicative of mineral dissolution/precipitation conditions, possibly associated with deformation-driven hydrothermal fluid events (*e.g.*, Reich et al., 2005; Large et al., 2007; Deditius et al., 2009; Velásquez et al., 2014; Deditius et al., 2014; Keith et al., 2018; Román et al., 2019; Keith et al., 2020; Kadel-Harder et al., 2020). Influence of deformation on the ore history of a pyrite-bearing structurally-controlled deposit can therefore be unraveled at the microscopic scale by the coupled study of the textural evolution of pyrite and its gold and trace element signatures.

In this study, we follow such approach to better understand ore-forming processes leading to the formation of the Central Zone gold deposit, Gabgaba gold district (Fig. 5-1; combined measured and indicated resources of 438 kozt Au @1.90 g/t Au with a 0.33 g/t Au cut-off as of May 2013; Managem, 2014). This work largely relies on the central

[1] **Chapter IV**

Keraf suture deformation history and relative timing of the Central Zone mineralization previously constrained at the district and deposit scales (Perret et al., under review[2]). In agreement with the established framework, we aim at discriminating (i) the petrological-structural evolution of the Central Zone gold deposit and related mineral textures, (ii) pyrite generations and their related geochemical signatures. These new data will ultimately lead to a better understanding of ore shoot- to microscopic-scale gold endowment processes and their relation to district-scale deformation events.

2. Geological setting

2.1. Regional geology

The Arabian-Nubian shield (ANS) is the northernmost part of the Neoproterozoic East African-Antarctic orogen (Kröner, 1993; Stern, 1994; Jacobs et al., 1998; Kusky et al., 2003; Li et al., 2008; Seton et al., 2012; Fritz et al., 2013; Domeier and Torsvik, 2014; Merdith et al., 2017; Grenholm, 2019). The Red Sea opening during Miocene divided the shield into the western Nubian shield, from Sinai to northern Kenya, and the eastern Arabian shield, forming the western part of the Arabian peninsula (Fig. 5-1a; Vail, 1983). The ANS results from a *ca.* 850-550 Ma *"Supercontinent Cycle"* leading to the consumption of the Mozambique ocean and formation of the Gondwana supercontinent (Stern and Johnson, 2010; Johnson et al., 2011). The final set-up of the ANS is mostly composed of juvenile magmatic arcs, volcanosedimentary series and ophiolite assemblages preserved from the Mozambique ocean, back-arc and suprasubduction zones (*e.g.*, Abdelrahman, 1993; Zimmer et al., 1995; Dilek and Ahmed, 2003; Stern et al., 2004; Blades et al., 2019; Sehsah and Eldosouky, 2020). These various rock units formed litho-tectonic blocks, *i.e.*, terranes, that were amalgamated and collided onto the Archean to Paleoproterozoic gneiss-dominated Saharan meta-craton, which is part of West

[2] **Chapter III**

Gondwana (Fig. 5-1b; *e.g.*, Burke and Sengör, 1986; Johnson et al., 2011; Fritz et al., 2013 and references therein). Late to post-collisional plutons intruded these rock units (Fig. 5-1b). Suture zones between terranes and lithospheric-scale shear zones dominate the structural framework of the Nubian shield, as exemplified by the north-striking Keraf suture-shear zone which hosts the Gabgaba gold district this study focuses on (Fig. 5-1b, c).

The extent of the ~500 km-long, ~70 km-wide, north-striking ophiolite-decorated Keraf suture is limited to Egypt and Sudan. It resulted from arc-continent suturing between Neoproterozoic juvenile arcs related to the ANS eastwards and the Saharan meta-craton westwards (Fig. 5-1b; Vearncombe, 1983; Burke and Sengör, 1986; Frisch and Pohl, 1986; Almond and Ahmed, 1987; Berhe, 1990; Abdelsalam and Dawoud, 1991; Ries et al., 1992; Mosley, 1993; Abdelrahman, 1993; Abdelsalam et al., 1995; Abdelsalam and Stern, 1996b; Abdelsalam et al., 1998; Ahmed Suliman, 2000; Fritz et al., 2013). The Gabgaba gold district is located in the central section of the Keraf suture and its lithological framework is dominated by meta-volcanosediments, arc-related and late to post-collisional intrusive rocks from the *"Keraf Pre-Tectonic Assemblage"* gathering all rocks specific to the Keraf area and affected by Keraf tectonics (Fig. 5-1b, c; Ahmed Suliman, 2000).

Two main deformation stages dominate the Keraf structural framework and occurred during a prolonged, northwest-orientated oblique convergence between *ca.* 750-580 Ma (Abdelsalam et al., 1998; Perret et al., under review). Firstly, the ductile D_{1a} deformation stage which refers to Keraf thrusting during arc-continent collision between the Gabgaba-Gebeit terrane and the Saharan meta-craton (Fig. 5-1b). Earlier deformation related to magmatic and tectonic accretion during Keraf arc activity likely occurred but it is not considered as not clearly visible at the district scale probably due to an intense superimposition by the D_{1a} deformation stage. D_{1a} is characterized by the regional penetrative cleavage S_{1a} affecting every pre- to syn-Keraf suture lithologies and

structures (Fig. 5-1c). Secondly, the ductile-brittle D_{1b} deformation stage is a north-northwest-orientated sinistral strike-slip shearing, with a weak non-coaxial component, expressed by the late collisional Keraf shear zone overprinting the Keraf suture. The resulting C_{1b} shear zones are visible at every scale, and more or less rotated inherited structures nearby (Fig. 5-1c). Second-order structures to the Keraf shear zone have formed during this deformation stage, *e.g.*, the several km-wide *"West Corridor"* which cuts across the Gabgaba gold district and hosts the Central Zone and UTM deposits (Figs. 1c, 2; Gaboury et al., 2020). Finally, a late brittle D_2 extensional deformation is expressed by normal-slip reactivation of C_{1b} shear zones, with a very limited spatial extent not investigated in our study.

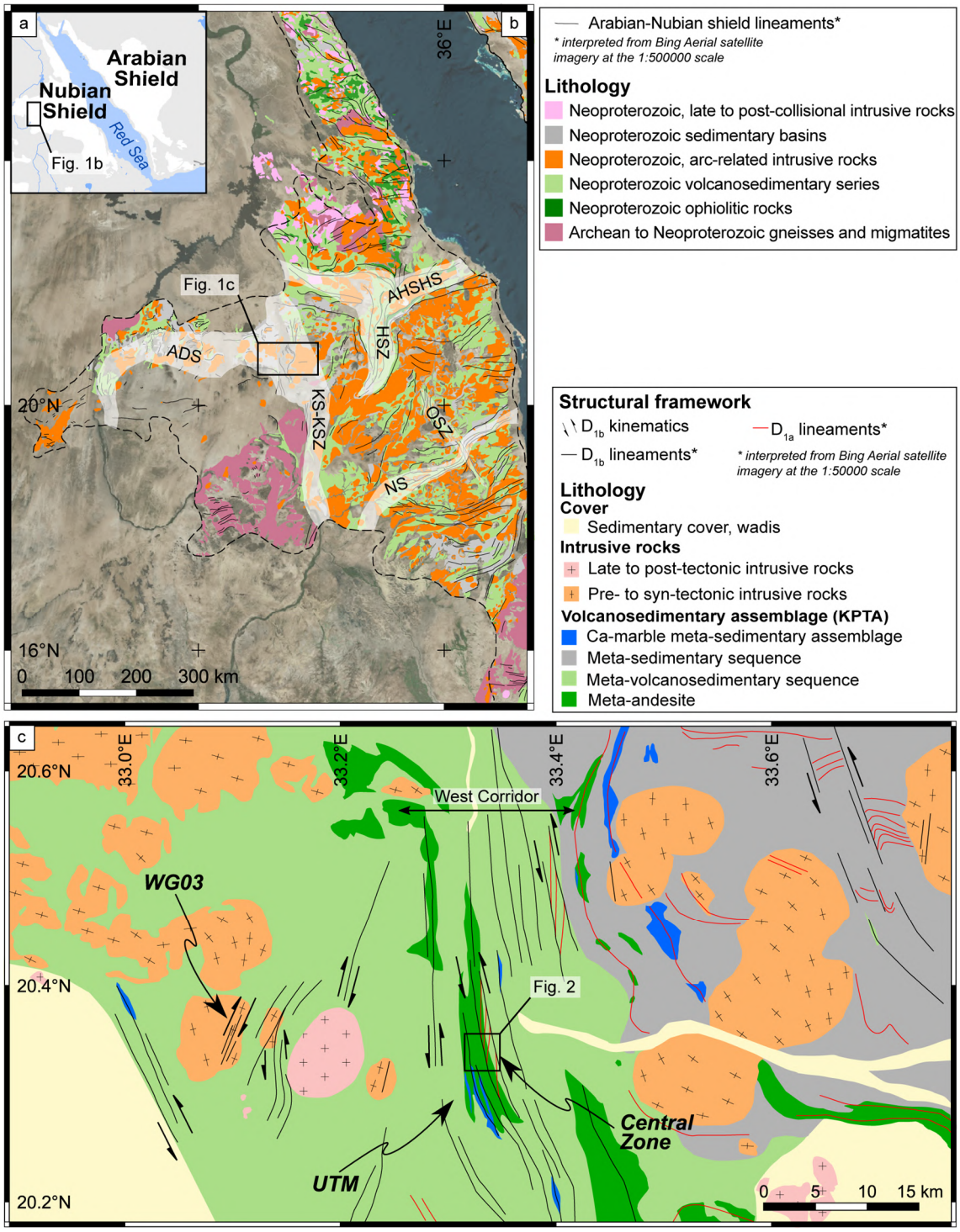


Figure 5-1: Geological setting of the Gabgaba gold district in the framework of the Sudanese Nubian shield, modified after Perret et al. (under review). **a** Location of the Arabian-Nubian shield and extent of b. **b** Geological map of the western Nubian shield. Lithological units are harmonized from the Egyptian, Sudanese and Eritrean geological maps (Egyptian Geological Survey and Mining Authority, 1981; Geological Research Authority of the Sudan, 1988; Tadesse et al., 2000). The main structural belts are indicated, whether sutures and/or shear zones, after Johnson et al. (2011). Abbreviations are ADS = Atmur-Delgo suture; KS-KSZ = Keraf suture-Keraf shear zone; AHSHS = Allaqi-Heiani Sol Hamed suture; HSZ = Hamisana shear zone; NS = Nakasib suture; OSZ = Oko shear zone. Background is from Google satellite imagery. Geographic coordinates are reported as WGS84. **c** Geological map of the Gabgaba gold district in the central part of the Keraf suture. The location of Central Zone, WG03 and UTM deposits is indicated, as well as the "West Corridor" second-order structure to the Keraf shear zone, named by Gaboury et al. (2020). "KPTA" stands for Keraf Pre-Tectonic Assemblage. Geographic coordinates are reported as WGS84.

2.2. Local geology

The Central Zone gold deposit lies in the central part of the Block 15 exploration license, granted to Manub - a subsidiary of the Moroccan mining group Managem Ltd. - in 2008. It forms together with the WG03 and UTM deposits (combined measured and indicated resources of 1.659 Mozt Au @1.56 g/t Au with a 0.43 g/t Au cut-off and 308 kozt Au @1.85 g/t Au with a 0.35 g/t Au cut-off as of May 2013, respectively; Managem, 2014), the Gabgaba gold district (Fig. 5-1c).

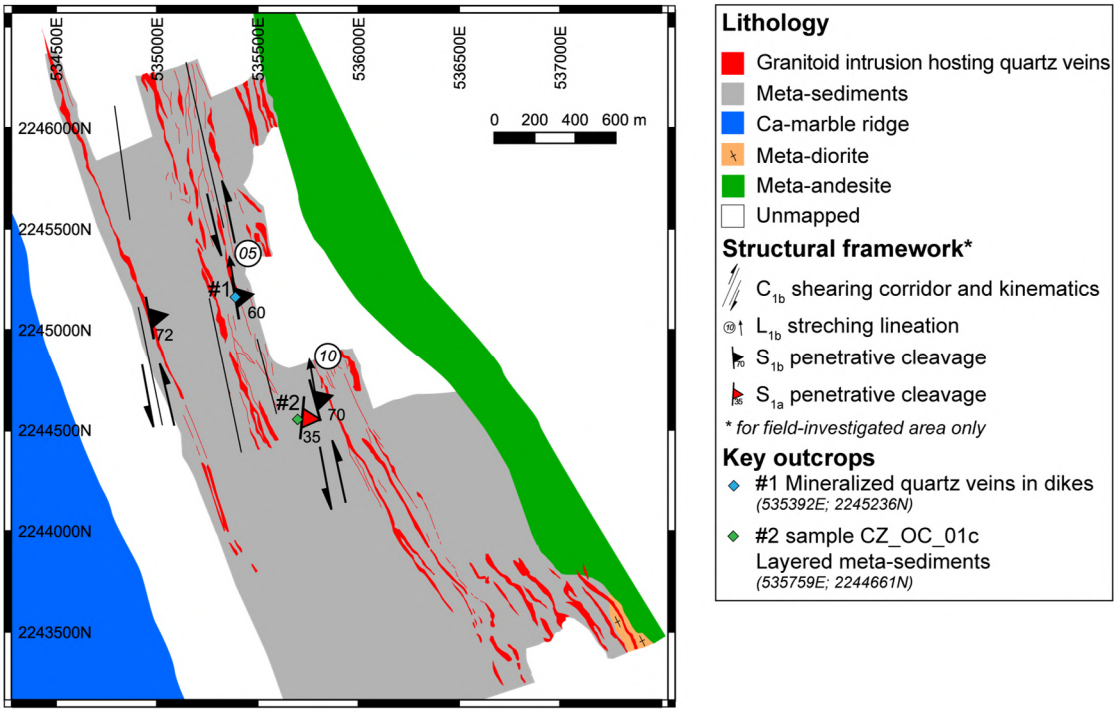


Figure 5-2: Lithological-structural framework of the Central Zone deposit (Perret et al., under review). Location of key outcrops are indicated as well as their coordinates. Sampled drill hole location is confidential. Geographic coordinates are reported as WGS84 / UTM zone 36N.

The Central Zone deposit is hosted in the sediment-dominated part of the meta-volcanosedimentary sequence of the *"Keraf Pre-Tectonic Assemblage"* (Ahmed Suliman, 2000), mainly composed of greenschist facies meta-turbidites with alternating silty to sandy layers, interlayered with marble ridges. These lithological units are interpreted as metamorphosed remnants of a carbonate-platform formed in a passive margin setting (Stern et al., 1993; Schandelmeier et al., 1994b; Stern, 1994; Abdelsalam et al., 1995; Johnson et al., 2011; Abdelrahman et al., 2017). Granitoid intrusions form a north-

northwest-trending network enclosed in surrounding meta-sediments (Fig. 5-2). Perret et al. (under review) interpreted them as predating Keraf thrusting but the debate remains open as Gaboury et al. (2020) suggested that they were intruded along thrusts and reverse faults.

2.3. Mineralized structures and pyrite generations at the deposit to macroscopic scales

Perret et al. (under review) have already undertaken a macroscopic-scale study of the ore-bearing veins at the Central Zone gold deposit, with main observations as following. Granitoids host two sets of mineralized cm- to several dm-wide, interconnected, flat to gently east- or west-dipping veins (Fig. 5-3a, b). The vein infilling consists of a carbonate-(albite) assemblage, with a comb texture, often enclosing inner massive quartz (Fig. 5-3c, d) where lies most of the gold budget as visible gold (Fig. 5-3e). Relying on the syntaxial texture of ankerite and albite crystals and vein orientation, Perret et al. (under review) demonstrated that Central Zone gold-bearing veins are purely dilational and can be classified as extension veins in the orogenic gold structural model (reviewed by Sibson, 2020a). Gold veining likely formed as a response to the late collisional progressive D_{1b} Keraf strike-slip shearing at the Central Zone deposit. Evidence for (i) gold mineralization occurring as quartz-ankerite-albite extension veins, (ii) syn-greenschist facies retrograde metamorphism and late-collisional shearing timing and (iii) syn-mineralization proximal to distal pyritization, among other alterations, led to classify Central Zone as an orogenic gold deposit (Perret et al., under review). This interpretation is in line with the metamorphic nature of mineralizing fluids and metallogenic model proposed by Gaboury et al. (2020).

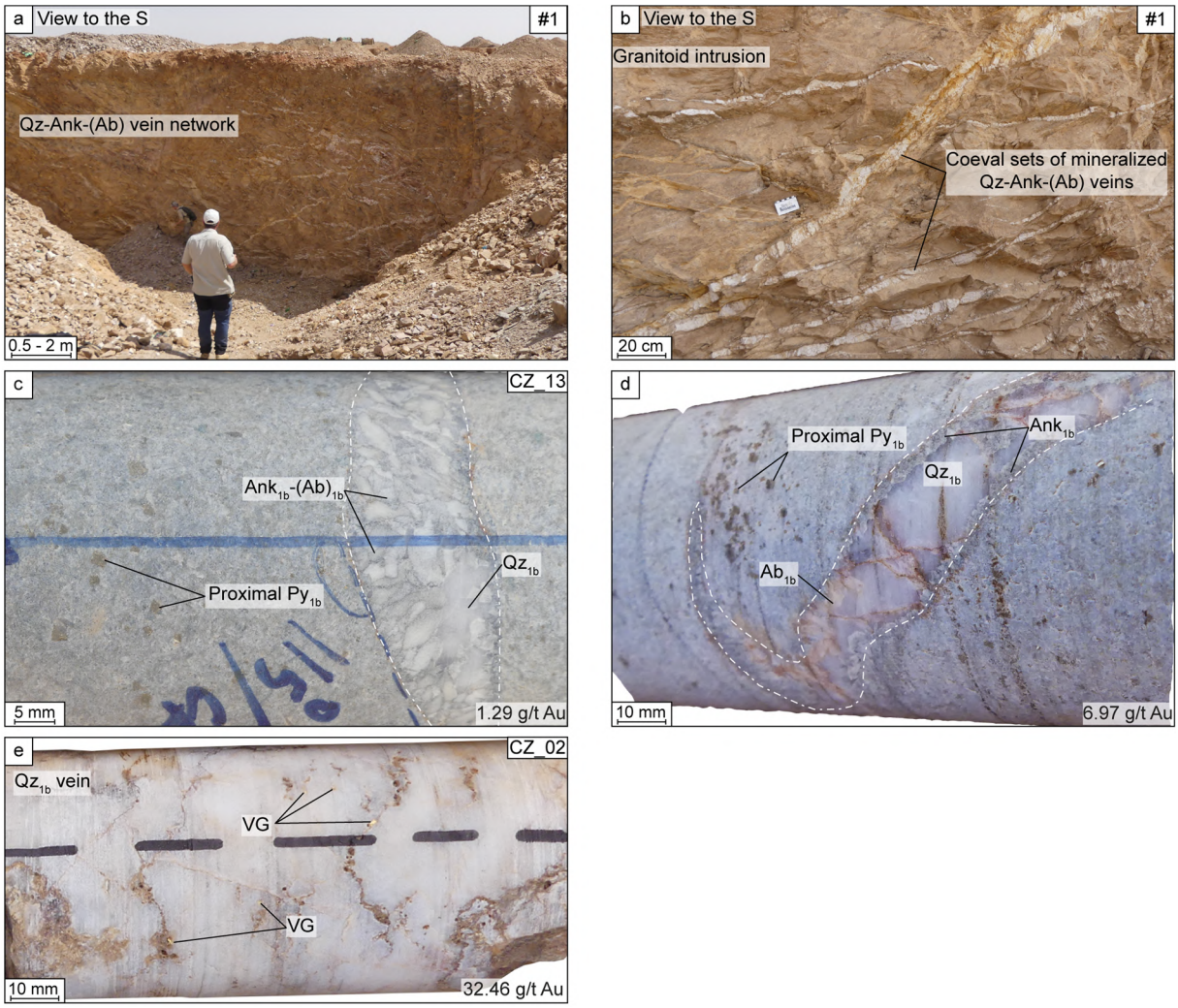


Figure 5-3: Field and macroscopic observations of the main structural and textural features of the mineralized veins at the Central Zone deposit. Mineral abbreviations are Ab = albite; Ank = ankerite; Py = pyrite; Qz = quartz; VG = visible gold. **a** and **b** The mineralization is hosted by D_{1b}-related, gently east- or west-dipping, conjugated gold-bearing quartz-ankerite-(albite) extension veins crosscutting a granitoid intrusion. See Figure 5-2 for location (#1). **c** Ankerite-(albite-quartz) vein with proximal pyritization and comb texture cutting across a granitoid intrusion. **d** Ankerite-(albite) vein infilled by massive quartz in its core part. **e** D_{1b}-related massive quartz vein enclosing visible gold grains. Fire assay gold grades are given for drillhole samples (Table 5-1).

In what follows, we bring additional macroscopic-scale observations on pyrite generations at the Central Zone gold deposit. We discriminate three types of pyrite, with distinct alteration patterns, mineral assemblages, textures and structural characteristics (Fig. 5-4). The first facies corresponds to pyrite grains which have grown in the meta-sediments along the S_{1a} main penetrative cleavage (Fig. 5-4a). They all display a complex texture with fractured cores and shinier and less altered recrystallized-like rims (Fig. 5-4b). In dm-wide C_{1b} shear zones, these pyrite grains may rotate along the C_{1b}/S_{1b} shear band cleavage and display asymmetric quartz-ankerite strain fringes (Fig. 5-4b). Pyrite

rims are mostly elongated along the S_{1a} penetrative cleavage, despite evidence for minor rotation of pyrite grains where C_{1b} shear zones are visible (Fig. 5-4b). The second pyrite facies is hosted by granitoids, and forms small clusters of few µm-wide grains in an altered ankerite-albite-(sericite-quartz) gangue (Fig. 5-4c). Finally, where D_{1b}-related quartz-ankerite-(albite) veins cut across granitoids, a few cm-wide albite-quartz-(sericite-ankerite) alteration halo is visible and contains cm-wide euhedral to subhedral aggregated pyrite grains (Fig. 5-4d). The D_{1b}-related pyrite stock rapidly decreases away from the veins, accompanied by decreasing grain sizes (Fig. 5-4d). The similarity in texture but increase in size from pyrite visible in barren granitoid to pyrite nearby mineralized veins suggests that D_{1b}-related pyrite overgrows D_{1a}-related pyrite in the proximal alteration halo of veins (Fig. 5-4c, d). Where rare quartz-ankerite-(albite) veins cut across meta-sediments, D_{1b}-related pyrite also overgrows the early meta-sediment-hosted pyrite facies (Fig. 5-4a).

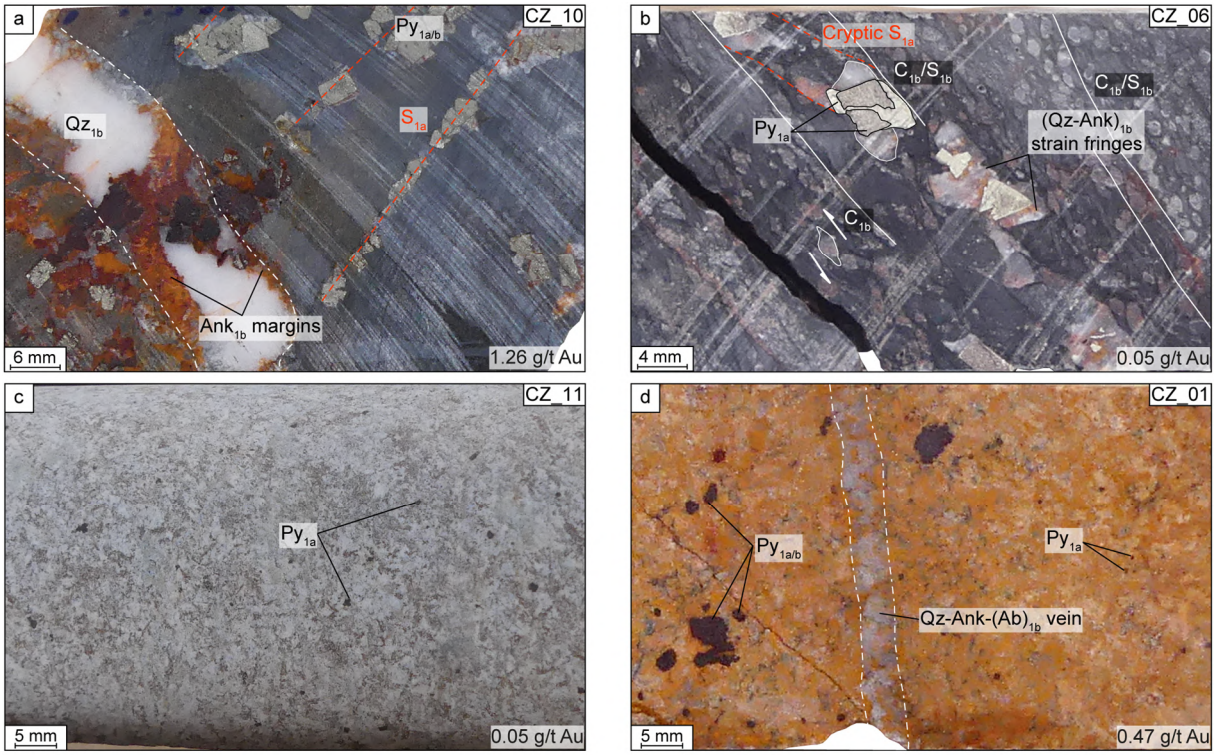


Figure 5-4: Macroscopic observations on drill core of the different pyrite generations at the Central Zone deposit. Mineral abbreviations are Ab = albite; Ank = ankerite; Py = pyrite; Qz = quartz. **a** Pyrite grains are aligned along the S_{1a} penetrative cleavage in surrounding meta-sediments. A gold-bearing D_{1b}-related quartz-ankerite vein cuts across meta-sediments. **b** Pyrite cores overgrown by shinier rims form coarse euhedral pyrite grains which are disseminated in meta-sediments along the S_{1a} main penetrative cleavage and are strongly affected by C_{1b} sinistral strike-slip shear bands. **c** Few µm-wide pyrite clusters scattered in altered granitoids. **d** Pyrite aggregates formed in the D_{1b}-related

alteration halo of the quartz-ankerite-(albite) veins. Their size increases towards vein margins. Fire assay gold grades are given for drillhole samples (Table 5-1).

The highest gold grades generally relate to >10 cm-wide quartz-dominated veins (up to 32.46 g/t Au; Fig. 5-3e; Table 5-1) and up to ten cm-wide alteration halos. Ankerite-dominated veins tend to be less enriched in gold (*e.g.*, 1.29 *vs* 6.97 g/t Au in ankerite- *vs* quartz-dominated veins of similar width; Fig. 5-3c, d). Where no vein crosscuts the host rocks, whether the meta-sediments or the granitoids, grades average < 0.05 g/t Au (Fig. 5-4b). The mineralization thus mostly, if not exclusively, relates to the quartz-ankerite-(albite) veining event. Nonetheless, if visible gold scattered in quartz veins forms most of the metallic budget of the deposit (Fig. 5-3e), the amount of gold trapped in pyrite has not yet been investigated.

3. Sampling and analytical methods

3.1. Sampling

Sampling for an integrated petrographic, structural and geochemical study of the Central Zone gold deposit was carried out on both barren samples, *i.e.* gold grades < 0.05 g/t, and gold-bearing samples (n=16) from the ore-hosting granitoids and surrounding meta-sediments. All of them were collected on non-oriented diamond drill cores, to the exception of the CZ_OC_01c outcrop sample. Studied samples and the analytical work carried out for each of them are listed in Table 5-1.

3.2. Optical and scanning electron microscopy

The deciphering of the relative timing of the main silicate and sulfide minerals regarding regional D_{1a} and D_{1b} deformation stages expressed by macro- and micro-structures was conducted in macroscopy and microscopy under either natural, transmitted or reflected light. We better characterized micro-textures, internal zoning

and mineral inclusions in pyrite using a scanning electron microscope in back-scattered electron mode at the GeoRessources laboratory (Université de Lorraine, Nancy, France).

3.3. Laser-ablation inductively-coupled plasma mass-spectroscopy analysis of the trace element concentrations of pyrite

LA-ICP-MS data on the different pyrite generations separated at the Central Zone gold deposit were collected at Queen's Facility for Isotope Research (Queen's University, Ontario, Canada) using a ThermoScientific X Series 2® quadrupole ICP-MS coupled to a NewWave/ESI 193-nm ArF Excimer laser system. Samples for which laser ablation analyses were carried out are listed in Table 5-1. The isotopes measured were ^{29}Si, ^{34}S, ^{51}V, ^{52}Cr, ^{55}Mn, ^{57}Fe, ^{59}Co, ^{60}Ni, ^{65}Cu, ^{66}Zn, ^{71}Ga, ^{75}As, ^{77}Se, ^{95}Mo, ^{107}Ag, ^{111}Cd, ^{115}In, ^{118}Sn, ^{121}Sb, ^{125}Te, ^{182}W, ^{197}Au, ^{205}Tl, ^{208}Pb and ^{209}Bi, with a dwell time of 10 ms. Spot analyses were performed to closely match the observed micro-textures in pyrite grains with their specific trace element signatures. Care was taken in selecting spot positions to minimize the ablation of any visible mineral inclusion. Prior to each analysis, the background signal, or gas blank, was measured for a duration of 25 s. The beam diameter was set to 50 µm for all samples and reference materials, with a pulse frequency of 10 Hz. The gas fluence was about 8.0 J/cm^2.

LA-ICP-MS data were reduced with Iolite 3.65 (Paton et al., 2011). Spot analyses comprise blocks of 30 spots on samples bracketed by a series of 3 spots on each of the 6 certified reference materials. The reference standards were USGS GSE-1G (Jochum et al., 2005), MASS-1 (Wilson et al., 2002), as well as FeS-4, FeS-5, PTC-1b and CCU-1e sulfide reference materials from Université du Québec à Chicoutimi, Canada (CCRM, CANMET). FeS-5 was used for trace element quantification in pyrite spot analyses and correction for variations in ablation efficiency. Limits of detection (LOD) were calculated following the Howell's method (see references in Howell and Blakey, 2013).

Sample ID	Gold grade (g/t)	Lithology	Pyrite generation	Results presented in this study	
				Petrography (Figs. 5-3 to 5-10)	*LA-ICP-MS (Figs. 5-11 to 5-14; Table 5-2; Sup. Mat. 5-1)*
CZ_01*	0.47	Granitoid dike + Qz-Ank vein	$Py_{1a/b}$	x	
CZ_02*	32.5	Qz vein	-	x	
CZ_03	0.31	Meta-sediments + Qz-Ank vein	$Py_{1a/b}$	x	
CZ_04*	0.05	Meta-sediments	Py_{1a}	x	x
CZ_05	0.05	Meta-sediments	Py_{1a}	x	
CZ_06*	0.05	Meta-sediments	Py_{1a}	x	
CZ_07	0.05	Meta-sediments	Py_{1a}	x	
CZ_08	0.05	Granitoid dike	$Py_{1a/b}$	x	
CZ_09*	0.05	Meta-sediments	Py_{1a}	x	x
CZ_10*	1.3	Meta-sediments + Qz-Ank vein	$Py_{1a/b}$	x	x
CZ_11*	0.05	Granitoid dike	$Py_{1a/b}$	x	
CZ_12*	0.35	Granitoid dike + Qz-Ank-Ab vein	$Py_{1a/b}$	x	x
CZ_13*	1.0	Granitoid dike + Ank-Ab vein	$Py_{1a/b}$	x	x
CZ_14*	0.05	Meta-sediments	Py_{1a}	x	
CZ_15	0.05	Meta-sediments	Py_{1a}	x	
CZ_OC_01c*	-	Meta-sediments	-	x	

** Samples illustrated in Figures 5-3 to 5-10 of this study.*
Samples are named after the ID of the diamond drill hole they have been sampled from.
Fire assay results of the corresponding 1 m-large drill core interval were provided by Manub Mining Company Ltd.
Mineral abbreviations are Ab = albite; Ank = ankerite; Qz = quartz.

Table 5-1: List of the studied samples. Their gold grade, lithology and the pyrite generation(s) they may host are indicated as well as analytical work carried out for each of them. Mineral abbreviations are Qz = quartz, Ank = ankerite, Ab = albite.

4. Results

4.1. Deformation, alteration and mineralization at the microscopic scale

The kinematics of micro-structures could not be defined on drill core samples as drill holes where not oriented. Thus, matching 3D field observations of structures and orientation measurements with their microscopic 2D expression in thin section was uncertain. We chose to correlate between micro-structures and the district-scale deformation history knowing that (i) the D_{1a} stage corresponds to the development of the main S_{1a} penetrative cleavage and (ii) D_{1b} stage led to the formation of C_{1b} strike-slip shear zones and the development of a C_{1b}/S_{1b} shear band cleavage in shear lenses. Please note that the characterization of the ductile and ductile-brittle nature of D_{1a} and D_{1b}

stages, respectively, relies on the observations at the macroscopic scale from Perret et al. (under review). As the definition of such terms is scale-sensitive (Snoke et al., 1998), they may not necessarily fits with microscopic scale observations presented below.

4.1.1. Main ductile D_{1a} deformation stage

At the microscopic scale, the S_{1a} cleavage is the main penetrative fabric and is north-northwest-striking (Fig. 5-5). The orientation of the S_0 primary bedding, highlighted in meta-sediments by clay-rich beds alternating with silty to sandy layers, is strongly to completely rotated along S_{1a} planes (Fig. 5-5). In the meta-sediments, D_{1a} is coeval with intense pervasive sericitization and carbonation in clay-rich layers, resulting in a sericite-ankerite-rich mineral gangue, alternating with quartz-ankerite-rich bands (Fig. 5-5). The preferential orientation of sericite and rutile grains in the mineral gangue characterizes the S_{1a} penetrative cleavage (Figs. 5-5, 5-6a), locally affected by C_{1b} shear bands (Fig. 5-5). In the granitoids, an intense hydrothermal alteration entirely overprinted the protolith mineralogy. The alteration pattern consists of a strong pervasive carbonation, albitization and sericitization, together with a weak silicification (Fig. 5-6b). A strong pyritization is associated to D_{1a} deformation stage in both meta-sediments and granitoids (Figs. 5-4a and b, 5-6b).

In the meta-sediments, D_{1a}-related pseudo-rounded ankerite porphyroblasts and anhedral pyrite grains trapped the S_{1a} penetrative cleavage orientation, characterized by the preferred orientation of sublinear to curved rutile-(quartz) inclusion trails (Fig. 5-6a, c). The S_{1a} expressed in the gangue partially anastomoses these D_{1a}-related porphyroblasts and pyrite grains, indicative of their coeval development (Fig. 5-6a). The curving of mineral inclusion trails, *i.e.*, the rotation of the S_{1a} cleavage in the porphyroblasts and pyrite grains, reveals the existence of a non-coaxial horizontal D_{1a} shear component, with no possible interpretation of the shear sense orientation from observations on non-oriented thin sections (Fig. 5-6a; Passchier and Trouw, 2005). In most meta-sedimentary samples, D_{1a}-related pyrite grains are formed of cores around

which a second set of pyrite overgrew, labelled $Py_{1a\text{-}core}$ and $Py_{1a\text{-}rim}$, respectively (Fig. 5-7).

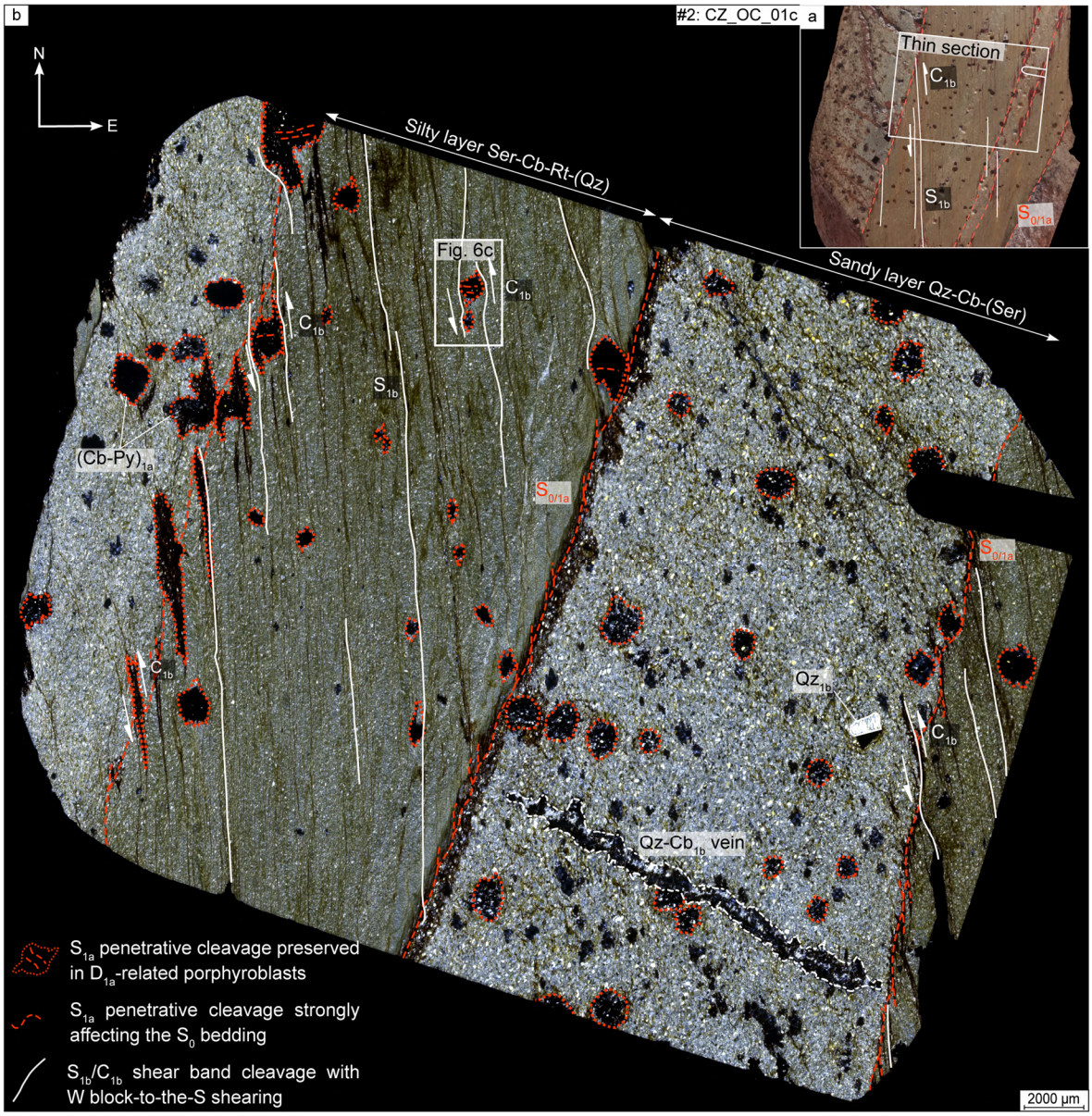


Figure 5-5: a Macroscopic and **b** microscopic (cross-polarized, transmitted light) observations of the oriented metasedimentary sample collected on outcrop. See Figure 5-2 for location (#2). Silty to sandy and clay-rich layers alternate along the composite $S_{0/1a}$ penetrative cleavage. C_{1b} shear bands affects the clay-rich layers. Mineral abbreviations are Cb = carbonate; Py = pyrite; Qz = quartz; Rt= rutile; Ser = sericite.

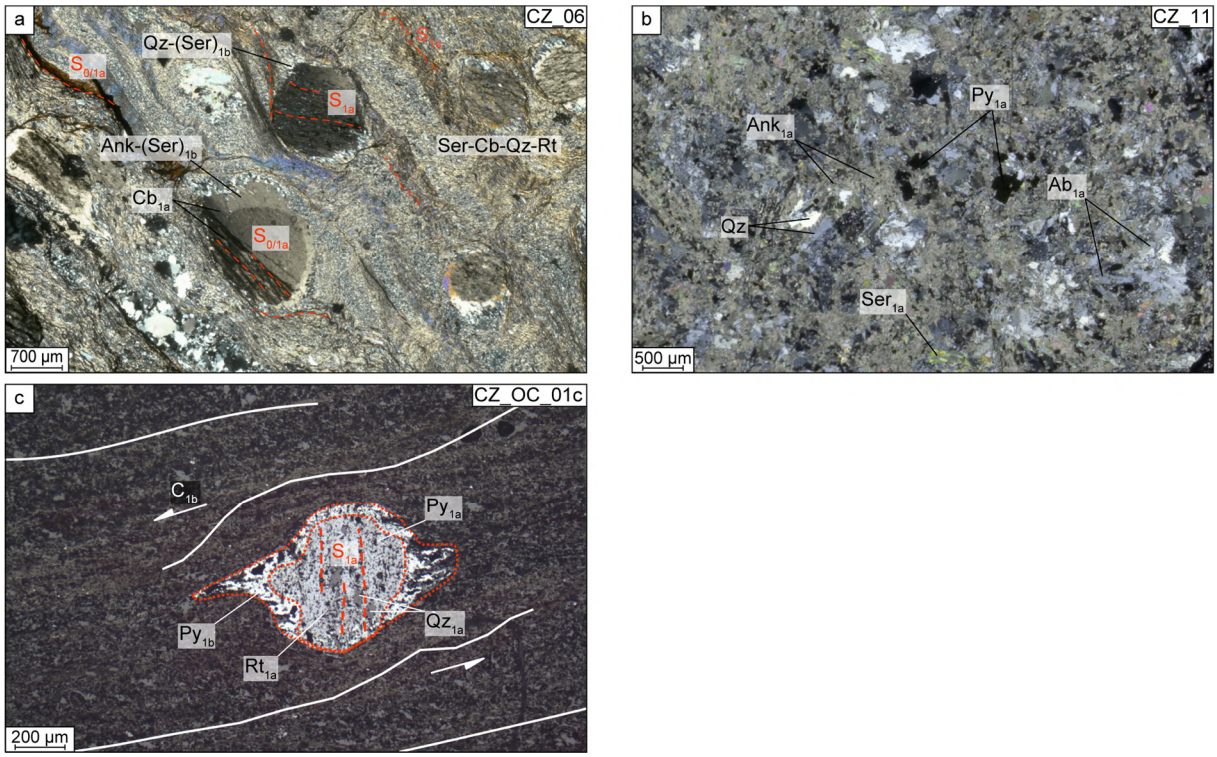


Figure 5-6: Main petrological-structural features of the D_{1a} main deformation stage. Mineral abbreviations are the same as in Figure 5-5. **a** In meta-sediments, D_{1a}-related carbonate-rich porphyroblasts host gangue mineral inclusion trails highlighting the S_{1a} cleavage. D_{1b}-related quartz-ankerite-sericite strain fringes are developed around these objects (cross-polarized, transmitted light). **b** Ankerite-albite-(sericite-pyrite) assemblage forms a pervasive alteration in granitoids (cross-polarized, transmitted light). **c** In meta-sediments, D_{1b}-related pyrite mantled σ-type porphyroclasts host inclusion trails highlighting the S_{1a} cleavage and their asymmetry relates to D_{1b} strike-slip shearing (reflected light).

4.1.2. Ductile-brittle D_{1b} deformation stage

The D_{1b} ductile-brittle deformation stage is well expressed in the meta-sediments. Although D_{1a} is the main ductile deformation and D_{1b} strain intensity may not be very high, the change in competency between clay-rich and silty layers in meta-turbidites is responsible for cleavage refraction. It resulted in C_{1b}/S_{1b} being the main penetrative cleavage within clay-rich layers, while no inner fabric is expressed in the silty to sandy layers (Fig. 5-5). C_{1b}-type shear bands also cut across lithological contacts transposed along the S_{1b} penetrative cleavage (Fig. 5-5). C_{1b}-type shear band asymmetry is a reliable shear sense indicator for the unique oriented thin section at our disposal (Fig. 5-5; Passchier and Trouw, 2005). Other shear sense indicators, of varying reliability, are visible in most samples such as the development of pyrite σ-type mantled porphyroclasts

and quartz-dominated asymmetrical strain shadows around ankerite clasts or Py_{1a} grains (Figs. 5-6a and c, 5-7).

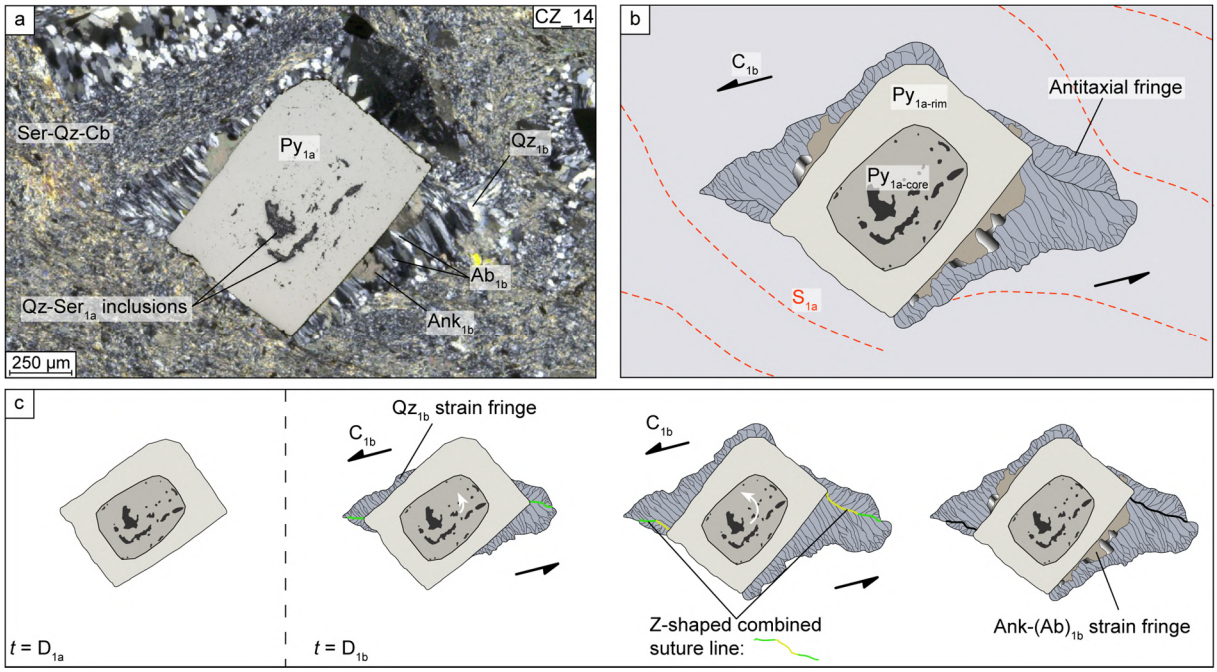


Figure 5-7: Interpretative sketch of the progressive formation of asymmetric strain fringes around a pyrite grain. Mineral abbreviations are Ab = albite; Ank = ankerite; Py = pyrite; Qz = quartz; Ser = sericite. **a** Photomicrograph and **b** drawing of a composite micro-photograph taken under reflected and cross-polarized transmitted light, showing a Py_{1a} grain surrounded by antitaxial strain fringes filled with quartz, ankerite and albite. Partial dissolution is visible within the Py_{1a} core. **c** Reconstruction of the fringe-growth stages during the D_{1b}-related sinistral strike-slip shearing and compression, by following face-controlled non-deforming fibers. The Z shape of the neoformed suture line is highlighted in green and yellow.

In contrast, the D_{1b} deformation stage is poorly expressed in the granitoids. If evidence for strike-slip shearing were observed at the contacts between granitoids and meta-sediments at the deposit scale (Perret et al., under review), the inner part of the intrusions remains undeformed at the microscopic scale. At the macroscopic scale, the gold-mineralized veins are considered to have formed during the late D_{1b} deformation stage in relation to the late collisional D_{1b} Keraf strike-slip shearing at the Central Zone deposit (Perret et al., under review). The elongate blocky crystal texture of the comb ankerite-(albite) is characteristic of syntaxial veins (Figs. 5-3c and d, 5-8a and b; Bons et al., 2012). If quartz veins display a massive texture at the macroscopic scale, the texture is rather blocky at the microscopic scale (Figs. 5-3c and d, 5-8b and c). Micro-crystalline anhedral quartz grains present distinctive interpenetrated grain boundaries,

attesting of bulging and subgrain rotation dynamic recrystallization (BLG and SGR, respectively; Fig. 5-8c), characteristic of the jigsaw, or mosaic, texture (Dong et al., 1995; Stipp et al., 2002; Passchier and Trouw, 2005). All visible gold grains observed are enclosed within such quartz infilling at the Central Zone deposit (Fig. 5-8c). The presence of highly altered granitoid fragments within the veins suggests the existence of multiple, at least two, crack-seal extension vein opening and infilling events along the same vein (Fig. 5-8b; Passchier and Trouw, 2005; Bons et al., 2012). The host rock demonstrates strong alteration at the immediate selvages of the gold-bearing veins, the main alteration pattern consisting of strong albitization, sericitization and pyritization (Fig. 5-8d).

Two generations of strain fringes developed around D_{1a}-related pyrite with a progressive shift from (i) asymmetrical quartz-dominated strain fringes to (ii) symmetrical ankerite-(albite) inward infilling. The earliest likely formed during the D_{1b} strike-slip shearing, whereas the ankerite-dominated strain fringes postdate the shearing, attested by ankerite fringes locally truncating the C_{1b}/S_{1b} shear band cleavage (Figs. 5-6a, 5-7a-b, 5-8e). The change from asymmetrical quartz-dominated to symmetrical ankerite-(albite) strain fringes may thus portray the progressive change from ductile-brittle D_{1b} strike-slip shearing to late brittle D_{1b} veining comprising an ankerite-(albite) infilling event (see section 2.3).

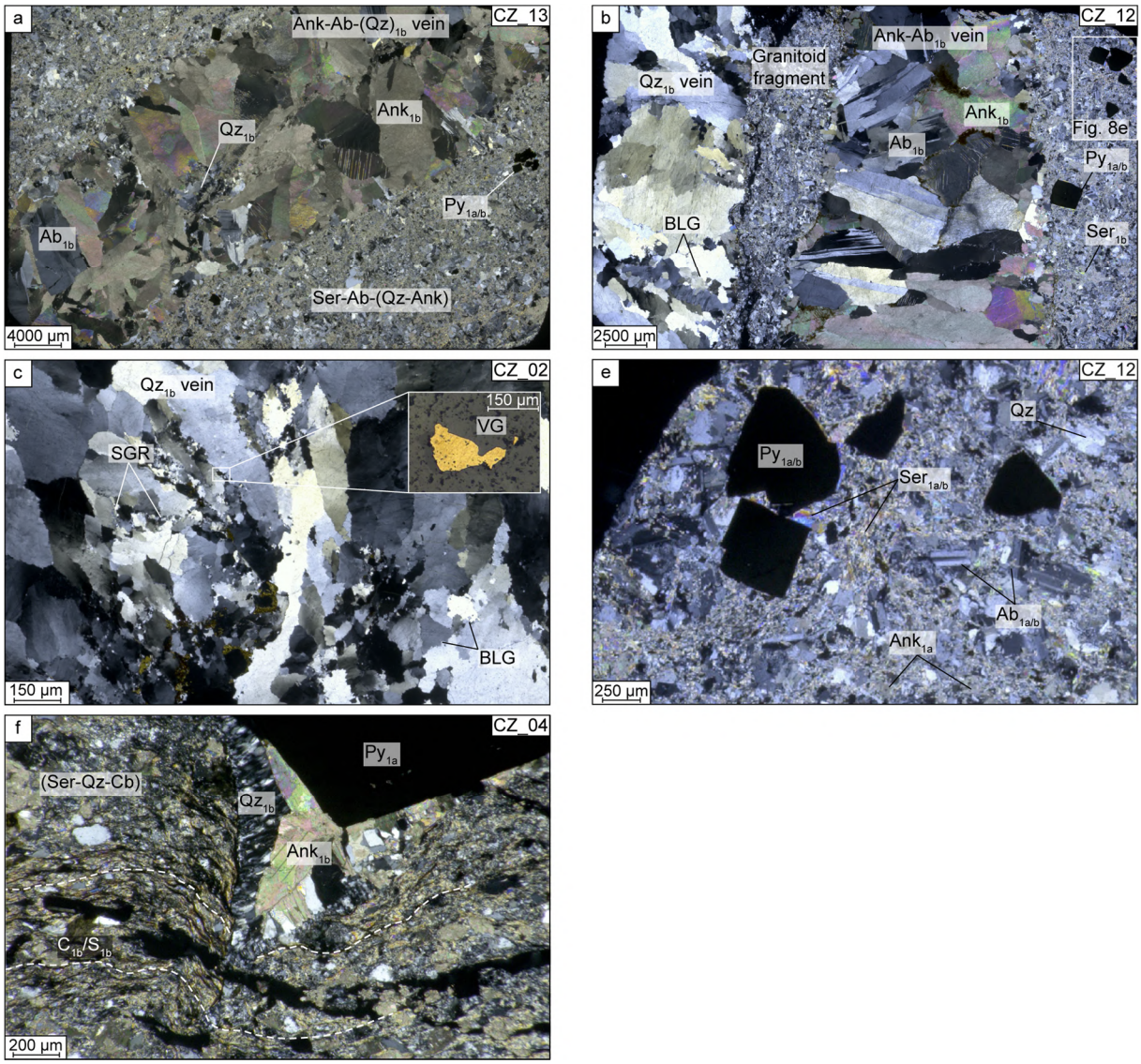


Figure 5-8: Main petrological-structural features of the D_{1b} deformation stage at the microscopic scale. Mineral abbreviations are Ab = albite; Ank = ankerite; Py = pyrite; Qz = quartz; Ser = sericite; VG = visible gold. **a** An ankerite-(albite-quartz) vein with a comb texture cuts across strongly sericitized and carbonated granitoids. Py_{1b} aggregates are visible at the vein margins (cross-polarized, transmitted light). **b** Blocky quartz infills the inner part of fractured ankerite-(albite) vein with comb texture. An altered granitoid fragment is trapped in the core part of the vein as well Py_{1b} are visible at the vein margins (cross-polarized, transmitted light). Bulging recrystallization (BLG) affects quartz. **c** A free gold grain is enclosed in a quartz vein with jigsaw texture (cross-polarized, transmitted light and inset under reflected light). Bulging and subgrain rotation recrystallization, BLG and SGR, respectively, affect quartz. **d** An albite-pyrite-(sericite-ankerite) assemblage forms the proximal alteration halo around quartz-ankerite-(albite) veins (cross-polarized, transmitted light). See inset in Figure 5-8b for location. **e** Focus on progressive D_{1b}-related quartz- to ankerite-dominated strain fringes with antitaxial growth of crystals perpendicular to the pyrite boundaries. The ankerite fringe locally truncates the C_{1b}/S_{1b} shear band cleavage (cross-polarized, transmitted light).

4.2. Micro-textures of pyrite

The two sets of pyrite distinguished at the macroscopic scale are affected by distinct micro-structures, show various micro-textures, and host different mineral inclusions. Their microscopic characteristics are described below.

Py_{1a} grains are abundant in both meta-sediments and granitoids. In the meta-sediments, they are zoned (Figs. 5-4a, 5-7). Py_{1a} cores occur as up to 1 cm-wide subhedral, altered grains disseminated grains along the S_{1a} main penetrative cleavage, with evidence for partial dissolution (Figs. 5-7a-b, 5-9a-c). Mineral inclusion-free Py_{1a} rims commonly overgrow Py_{1a} cores with a large amount of rutile inclusions trapped at the contact between cores and rims (Figs. 5-7a-b, 5-9a-c, 5-10b). Some Py_{1a} cores are fractured and fragments were later sealed together by Py_{1a} rims (Fig. 5-9a, c). Where Py_{1a} rims overgrew Py_{1a} cores, carbonate-quartz-chalcopyrite-sphalerite-pyrrhotite-arsenopyrite-(monazite) inclusions are abundant in the cores (Fig. 5-10a, b). Well-expressed quartz-(sericite) asymmetrical and ankerite-(sericite) symmetrical strain fringes developed around Py_{1a} grains in meta-sediments (Figs. 5-7a, 5-8e). In the granitoids, Py_{1a} form inclusion-rich clusters of a few tens of µm subhedral pyrite (Fig. 5-6b).

The D_{1b}-related pyrite does not occur beyond the alteration halo of quartz-ankerite-(albite) veins, and forms Py_{1b} rhythmic overgrowths over inclusion-rich Py_{1a} core, resulting into up to 2 cm-wide euhedral grains (Fig. 5-8d). The Py_{1a} cores are locally micro-fractured, infilled with chalcopyrite (Fig. 5-9e), and enclose albite, quartz and chalcopyrite inclusions (Fig. 5-9d, e, f). Py_{1b} rims have sharp boundaries with Py_{1a} cores alike the abrupt transitions between light and dark Py_{1b} oscillatory rims visible in back-scattered electron imagery (Fig. 5-9d, i). The highest the quartz width in veins, the higher the number of Py_{1b} rim oscillations is, *e.g.*, at least three Py_{1b} rim oscillations near a 60 cm-wide quartz vein (Fig. 5-9e, f) whereas a single oscillation is observed nearby 10-15 cm-wide quartz veins (Fig. 5-9h, i).

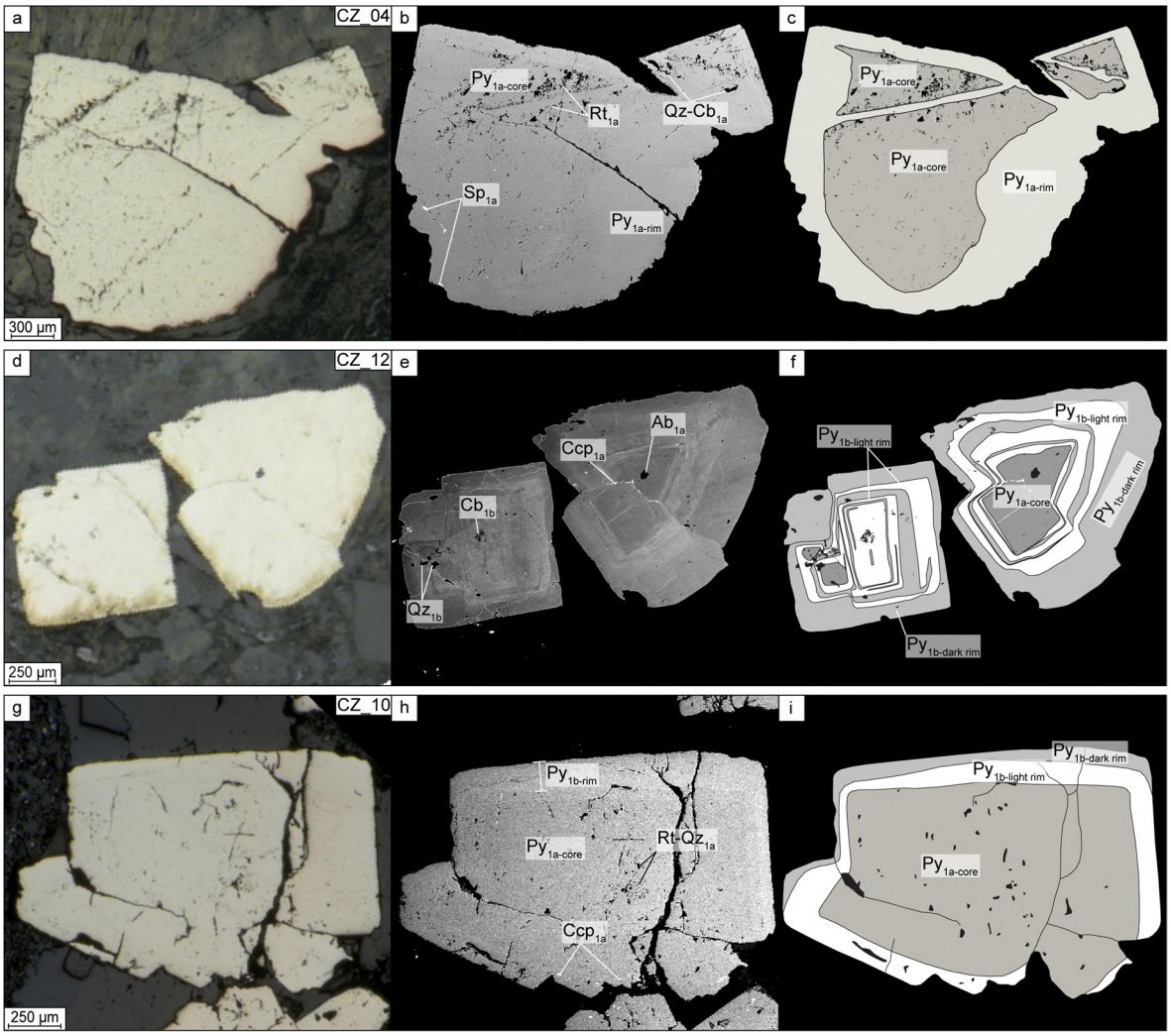


Figure 5-9: Micro-textures of the main pyrite generations unraveled at the Central Zone gold deposit. Photomicrographs are taken under reflected light (**a**, **d**, **g**) or in back-scattered electron scanning microscopy (BSE-SEM; **b**, **e**, **h**) and interpretation sketches are drawn for each of the three photographs (**c**, **f**, **i**). **a** to **c** Py_{1a} core and rim in meta-sediments. **d** to **f** Py_{1a} core and Py_{1b} rims in granitoids. **g** to **i** Py_{1a} core and Py_{1b} rims in meta-sediments. Mineral abbreviations are Ab = albite; Cb = carbonate; Ccp = chalcopyrite; Py = pyrite; Qz = quartz; Rt = rutile; Sp = sphalerite.

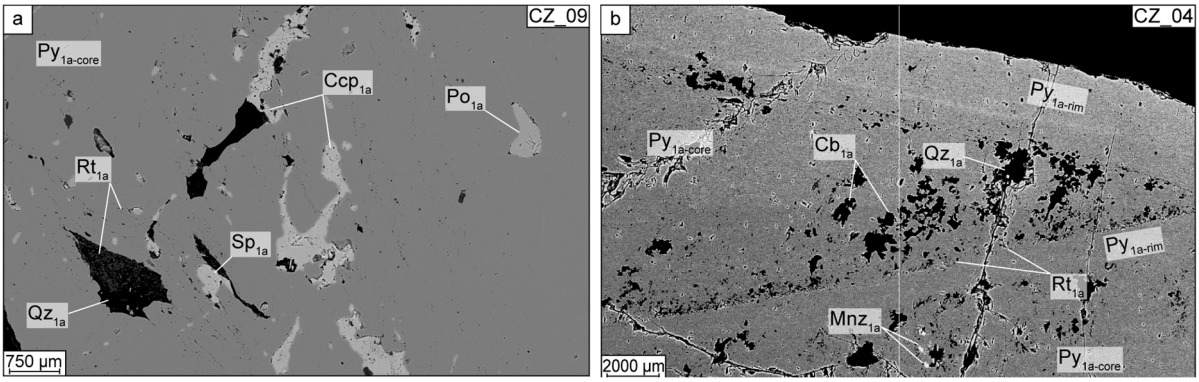


Figure 5-10: Mineral inclusions in the Py_{1a} generation. **a** Chalcopyrite-sphalerite-pyrrhotite inclusions within Py_{1a} cores where surrounded by a mineral inclusion-free Py_{1a} rim (not visible on the photograph extent) (BSE-SEM). **b** Two Py_{1a} rims seal Py_{1a} core fragments into a single, composite grain. The contact between Py_{1a} cores and Py_{1a} rims is sharp and underlined by rutile inclusions (BSE-SEM). Mineral abbreviations are Cb = carbonate; Ccp = chalcopyrite; Mnz = monazite; Po = pyrrhotite; Py = pyrite; Qz = quartz; Rt = rutile; Sp = sphalerite.

4.3. Trace element concentrations of pyrite

LA-ICP-MS concentrations of minor and trace elements in pyrite grains have been measured in five samples, representative of all meta-sediment- and granitoid-hosted pyrite generations of the Central Zone deposit. A wide range of minor and trace elements were detected by LA-ICP-MS, of which As, Ni, Co, Pb, Cu, Zn, Te, Ag and Au are represented in typical time-resolved LA-ICP-MS outputs for each set of pyrite to better understand how metals and metalloids are incorporated within pyrite (Fig. 5-11).

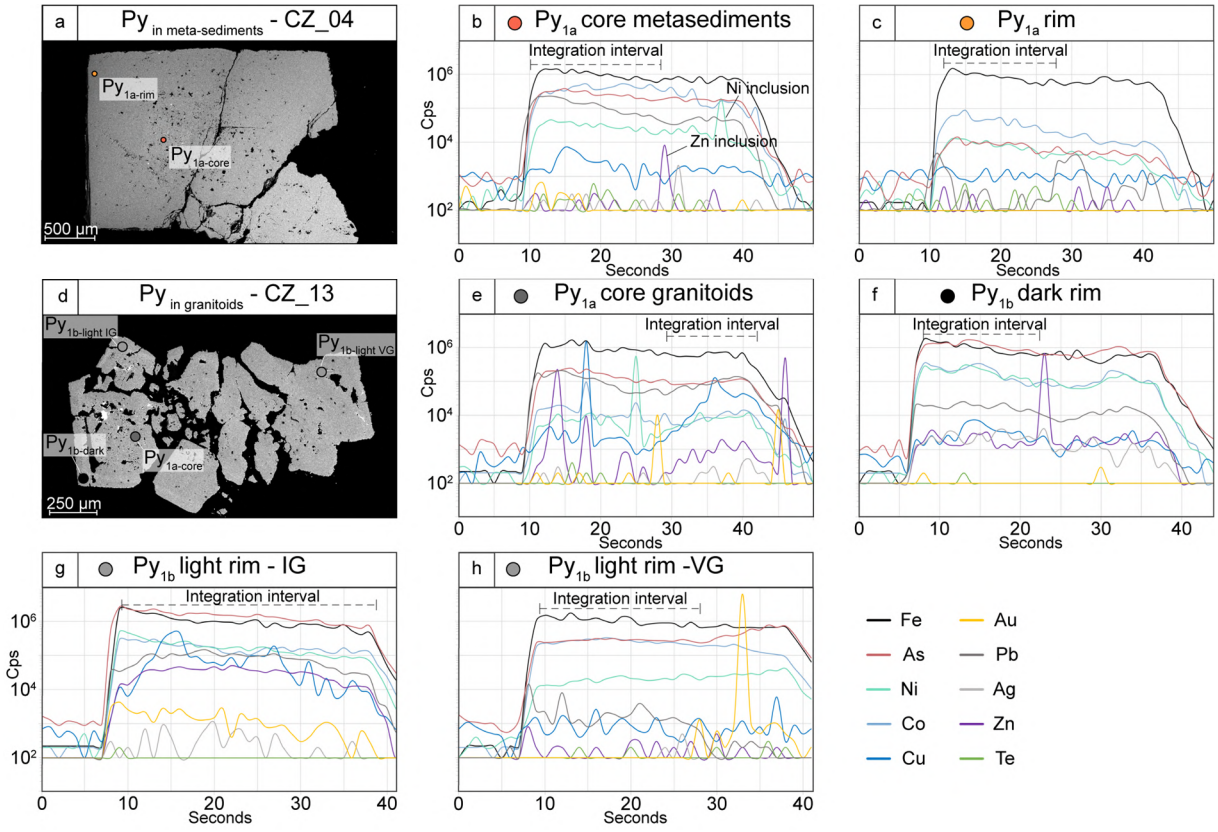


Figure 5-11: Representative time-resolved LA-ICP-MS outputs for Py_{1a} grains: **a** location of the 50 µm-large ablation spots; **b** Py_{1a} core and **c** rim. Representative time-resolved LA-ICP-MS outputs for Py_{1b} grains: **d** location of the 50 µm-large ablation spots; **e** core, **f** dark rim and **g, h** light rim**.** Two outputs are proposed for the latter generation, with gold occurring as structurally-bound in the pyrite lattice or as micro-inclusions, *i.e.*, invisible or visible gold - IG or VG, respectively.

Fairly flat patterns of elements, correlated with the Fe reference pattern for pyrite, suggest that the given elements are structurally-bound into the pyrite lattice (*e.g.*, As, Ni, Co and Pb; Fig. 5-11b). Spikes in an elemental pattern indicate that the given element is concentrated in a mineral micro-inclusion enclosed in the pyrite volume that has been

ablated (*e.g.* Zn and Ni; Fig. 5-11b). We delimited integration intervals during data processing with great care to avoid the integration of any sulfide or metal alloy mineral inclusion and only measure the lattice-bound trace element composition in pyrite (Fig. 5-11b, c, e-h). The medians, means and standard deviations for trace element concentrations are summarized in Table 5-2 for the distinct pyrite facies. Geochemical data were distinguished for Py_{1a} cores, in meta-sediments and granitoids, Py_{1a} rims, as well as for Py_{1b} light and dark rims. Note that the trace element signature of Py_{1a} cores in the granitoids was solely measured in the alteration halo of veins, *i.e.*, only where overgrown by Py_{1b} rims. The number of datapoints where gold is present, whether as free gold micro-inclusions, *i.e.*, visible gold (VG), or structurally-bound in the pyrite lattice or occurring as nano-inclusions, *i.e.* invisible gold (IG), is indicated. We considered a 0.8 ppm threshold on gold concentration in pyrite to count invisible gold-bearing datapoints. The extended trace element dataset is provided in Supplementary Material 5-1.

Further comparisons of elemental concentrations in the different pyrite generations are made between median values. Both Fe and S concentrations are consistent across all pyrite generations, with a S/Fe ratio ranging from 1.27 to 1.31 (Table 5-2). Relying on the As/Ag *vs* Sb/Bi diagram from Augustin and Gaboury (2018), we discriminate an hydrothermal origin for each pyrite generation at the Central Zone gold deposit (Fig. 5-12a). The highest concentrations of invisible gold in pyrite positively correlate with the highest As, Ni and Co concentrations (Figs. 5-12b-c, 5-13). No datapoint plots above the solubility line in the Au *vs* As diagram from Reich et al. (2005) (Fig. 5-12b), attesting the removal of all gold micro-inclusions in the integration of LA-ICP-MS outputs as specified above. Au and Te demonstrate a decoupled behavior as Py_{1b} light rims are enriched in Au and depleted in Te whereas Py_{1a} grains and Py_{1b} dark rims tend to follow an Au-low Te-rich trend (Fig 5-12d).

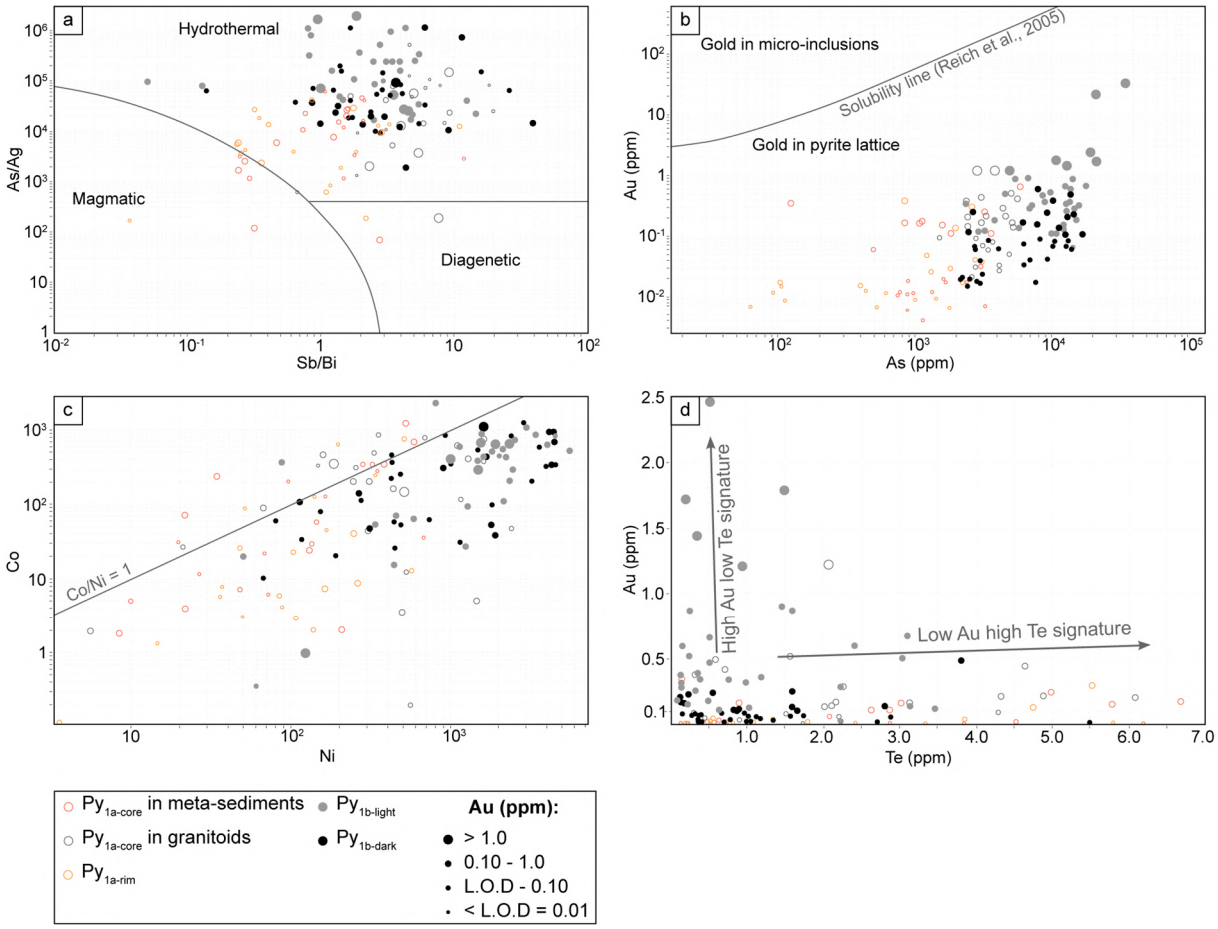


Figure 5-12: Binary diagrams discriminating the different pyrite generations from the Central Zone deposit. **a** As/Ag *vs* Sb/Bi, modified after Augustin and Gaboury (2019). **b** Au (ppm) *vs* As (ppm), modified after Reich et al. (2005). **c** Co (ppm) *vs* Ni (ppm) and **d** Au (ppm) *vs* Te (ppm) diagrams. Spot size represents gold concentration in pyrite.

In meta-sediments, Py_{1a} cores are fairly enriched in As, Ni, Co, Pb in the pyrite lattice, with respect to the Py_{1a} rims which are depleted in all of these elements, with often a difference of an order of magnitude in signal intensity (*e.g.*, around 10^5 *vs* 10^4 As counts per second in $Py_{1a\text{-}core}$ and $Py_{1a\text{-}rim}$, respectively; Fig. 5-11b, c). More generally, when considering box and whisker plots (Fig. 5-13), Py_{1a} rims are depleted in almost all trace elements (*e.g.*, 35.7 ppm Co in Py_{1a} core *vs* 8.8 ppm Co in Py_{1a} rims; Fig. 5-13; Table 5-2). Furthermore, Py_{1a} rims do not systematically show significant concentrations of Pb and Co and they enclose very rare Pb-Zn-Te-rich micro-inclusions. Small spikes in the Au signal, accompanied by small spikes in the Te and Pb signals, attest of the presence of very rare micro-inclusions of gold alloys in Py_{1a} cores (4 out of 23 datapoints with VG; Table 5-2) and even scarcer in Py_{1a} rims (1 out of 21 datapoints with VG; Table 5-2).

If all Py_{1a} cores display rather similar signatures for most trace elements, they are significantly enriched in As, Au and Ni in the vein alteration halo in granitoids (3603 ppm As, 0.16 ppm Au, 472 ppm Ni; Table 5-2), with respect to Py_{1a} cores in the meta-sediments (1148 ppm As, 0.02 ppm Au, 132 ppm Ni; Table 5-2). LA-ICP-MS outputs are in agreement with micro-textural observations made above. Where surrounded by Py_{1b} rims, Py_{1a} cores in granitoids indeed show numerous spikes in Ni, Co, Zn, Cu, Ag and Au due to the presence of sulfide mineral inclusions, whereas mineral inclusion-poor Py_{1b} rims mostly display rare micro-inclusions, *e.g.*, Zn and Cu (Fig. 5-11e, h). Both free gold micro-inclusions and invisible gold are visible in Py_{1a} cores (5 and 1 out of 24 datapoints with VG and IG, respectively; Table 5-2).

As, Ni, Co, Cu and Zn are mostly incorporated in the lattice of Py_{1b} rims. Py_{1b} light rims notably differ from dark rims by the presence of Au, whether as invisible gold in the lattice (9 out of 35 datapoints with IG; Fig. 5-11g; Table 5-2), often accompanied by Ag, or as micro-inclusions of native gold (6 out of 35 datapoints; Fig. 5-11h; Table 5-2). Only one of the Py_{1b} dark rims datapoints shows Au signal above background signal, as visible gold (Table 5-2). As a result, the mean concentration of Au in Py_{1b} light rims is an order of magnitude above that of Py_{1a} cores in granitoids, whereas Py_{1b} dark rims contain about twice less invisible gold than these cores (0.39, 0.16 and 0.07 ppm Au in $Py_{1b\text{-}light}$, $Py_{1a\text{-}core}$ and $Py_{1b\text{-}dark}$, respectively; Fig. 5-13; Table 5-2). Py_{1b} light rims are systematically gold-enriched regarding Py_{1b} dark rims, whether they overgrew Py_{1a} cores in meta-sediments or in granitoids (Fig. 5-14a, b and c, d; respectively). The As concentration also majorly differs between Py_{1b} dark and light rims, the first being depleted with respect to the second (respectively 7 784 ppm *vs* 10 250 ppm As; Table 5-2).

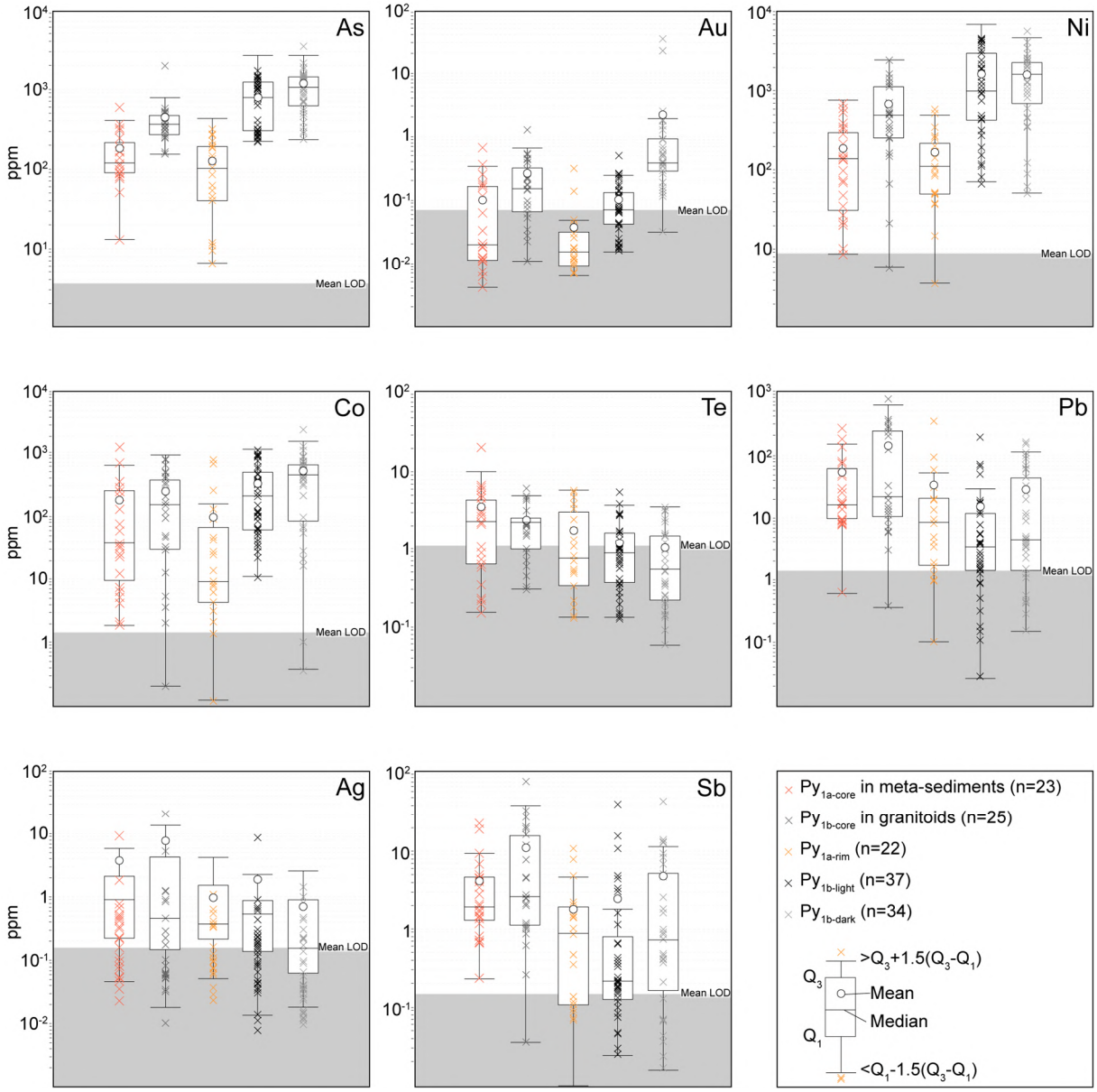


Figure 5-13: Box and whisker plots of As, Au, Ni, Co, Te, Pb, Ag and Sb concentrations in pyrite generations from the Central Zone deposit. Data below limit of detection (LOD) have been attributed the LOD/2 value. The median (line in the box), mean (white circle) and first and third quartile (box extent) values are shown as well as 1.5 times the interquartile range value (whiskers).

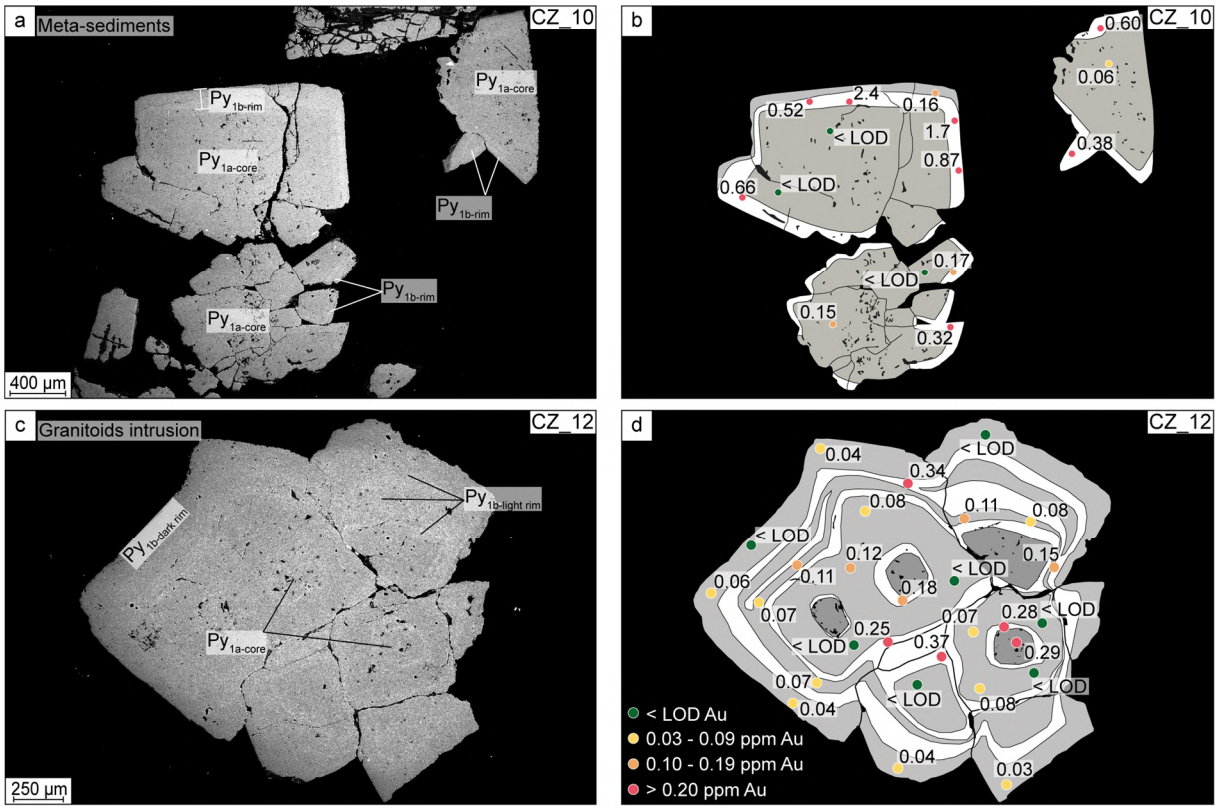


Figure 5-14: Gold concentration in different pyrite grains depending on the textural position of the LA-ICP-MS 50 µm-large ablation spots. **a** (BSE-SEM) and **b** (interpretation sketch) Py_{1a} core-rim grain. **c** (BSE-SEM) and **d** (interpretation sketch) Py_{1b} core and dark and light Py_{1b} rims.

	Si	S	V	Cr	Mn	Fe	Co	Ni	Cu	Zn	Ga	As	Se	Mo	Ag	Cd	In	Sn	Sb	Te	W	Au	Tl	Pb	Bi	S/Fe
Mean LOD	596	5679	0.36	3.2	0.83	1542	1.5	8.9	11.3	2.8	0.14	37.8	6.9	0.39	0.17	0.67	0.04	0.64	0.16	1.1	0.14	0.06	0.04	1.7	0.16	1.3
$Py_{1a\text{-}core}$ in meta-sediments *(n=23, VG=4, IG=0)*																										
Median	455	571186	1.2	3.3	0.51	422036	35.7	132	6.5	3.0	0.13	1148	19.0	0.11	0.23	0.17	0.01	0.24	1.9	2.2	0.67	0.02	0.01	16.9	2.5	1.4
Mean*	1117	557072	6.4	9.7	8.6	436269	178	190	456	6.7	0.17	1727	21.9	5.3	0.72	1.0	0.05	0.58	4.1	3.2	2.4	0.10	0.03	49.0	4.5	1.3
SD*	2467	35143	8.5	14.6	18.6	34527	285	200	2109	13.4	0.19	1330	13.6	16.5	1.9	1.3	0.14	0.89	5.5	4.3	5.1	0.15	0.06	66.5	4.9	0.17
$Py_{1a\text{-}rim}$ in meta-sediments *(n=21, VG=1, IG=0)*																										
Median	494	575943	0.28	1.8	0.46	423171	8.8	107	4.1	2.3	0.22	1021	12.4	0.10	0.11	0.11	0.03	0.23	0.84	0.72	0.37	0.01	0.01	83.0	0.51	1.4
Mean*	1475	577367	1.4	3.7	3.7	419381	99.0	161	20.5	4.7	0.28	1178	14.7	0.54	0.25	0.55	0.06	0.30	1.7	1.6	0.51	0.04	0.03	32.4	3.8	1.4
SD*	2859	17246	2.3	4.5	14.4	19317	211	155	68.6	6.5	0.38	976	7.7	1.3	0.27	0.89	0.07	0.20	2.7	1.9	0.70	0.07	0.05	78.9	7.4	0.1
$Py_{1a\text{-}core}$ in granitoids *(n=24, VG=5, IG=1)*																										
Median	783	551199	1.9	1.3	1.3	436048	156	472	10.6	2.5	0.08	3603	37.1	0.12	0.14	0.15	0.01	0.45	2.5	2.0	0.17	0.16	0.02	21.1	0.38	1.4
Mean*	4861	540883	13.2	6.4	23.0	447890	236	675	76.3	61.5	0.96	4279	36.4	0.19	1.4	0.28	0.15	0.96	10.0	2.2	1.6	0.23	0.20	130	1.7	1.3
SD*	11712	51549	36.8	11.2	61.7	49390	246	629	173	225	2.9	3457	10.0	0.21	4.2	0.29	0.67	1.51	17.0	1.6	3.2	0.26	0.44	190	2.5	0.22
Py_{1b} rims *(n=73, VG=7, IG=9)*																										
Median	484	568263	0.40	2.5	0.57	414854	321	1300	7.3	2.5	0.06	9285	20.5	0.12	0.12	0.15	0.01	0.26	0.40	0.70	0.08	0.15	0.01	4.0	0.20	1.4
Mean*	3034	554479	7.8	15.9	61.1	429962	398	1626	35.8	39.7	0.70	9438	25.4	0.36	0.31	0.36	0.04	0.41	3.6	1.1	6.4	1.1	0.10	21.4	0.77	1.3
SD*	11581	46850	22.4	41.0	282	42747	396	1403	93.5	125	2.4	5883	16.0	0.69	1.0	0.74	0.09	0.55	8.7	1.1	20.2	4.6	0.52	40.3	1.5	0.22
$Py_{1b\text{-}dark\ rim}$ *(n=38, VG=1, IG=0)*																										
Median	518	584752	0.37	2.6	0.58	406761	215	972	7.9	2.6	0.05	7784	19.2	0.12	0.16	0.16	0.01	0.28	0.21	0.85	0.08	0.07	0.01	3.2	0.16	1.5
Mean*	3111	570161	6.0	11.7	78.7	416503	321	1651	36.8	43.1	0.59	7875	23.8	0.46	0.42	0.31	0.05	0.35	2.3	1.1	3.5	0.10	0.14	14.6	0.48	1.4
SD*	11750	40974	18.9	37.1	359	35715	316	1587	102	146	2.3	4581	13.7	0.90	1.4	0.54	0.11	0.30	6.8	1.1	13.6	0.09	0.70	34.8	0.76	0.20
$Py_{1b\text{-}light\ rim}$ *(n=35, VG=6, IG=9)*																										
Median	420	539912	0.40	1.9	0.53	433018	426	1590	5.6	2.5	0.08	10250	21.0	0.11	0.06	0.12	0.01	0.24	0.72	0.51	0.08	0.39	0.01	4.6	0.39	1.2
Mean*	2950	537452	9.7	20.5	41.9	444575	482	1599	34.7	35.9	0.82	11135	27.2	0.25	0.20	0.41	0.04	0.48	4.9	1.0	9.6	2.1	0.06	28.8	1.1	1.2
SD*	11565	47411	25.9	44.9	166	45379	457	1195	84.3	98.6	2.6	6689	18.2	0.33	0.31	0.92	0.08	0.73	10.2	1.0	25.2	6.5	0.18	44.9	1.9	0.22

*Concentrations are in ppm. VG and IG indicate the number of datapoints with visible and invisible gold, i.e., micro-inclusions or > 0.8 ppm Au in pyrite lattice, ablated among the overall n analyses for a given pyrite generation. * Arithmetic means and standard deviations (SD) are calculated considering the LOD/2 value for <LOD values.*

Table 5-2: L Summary of the LA-ICP-MS trace element concentrations (in ppm) of the various pyrite generations from the Central Zone gold deposit.

5. Petrological-structural model of the Central Zone gold deposit

The relationships between deformation, structures, alteration and mineralization unraveled from the macroscopic to the microscopic scales at the Central Zone are summarized in the proposed paragenetic sequence (Fig. 5-15). The suggested petrological-structural model for the Central Zone gold deposit emphasizes the existence of successive deformation-(mineralization) events associated with distinct pyrite generations (Fig. 5-16). If the study of the relative chronology of structural markers and petrological features at the macroscopic to microscopic scales showed consistency with the model proposed at the deposit scale (Perret et al., under review), it also provided new insights on the history of deformation and better constrained the ore-forming processes at the Central Zone gold deposit.

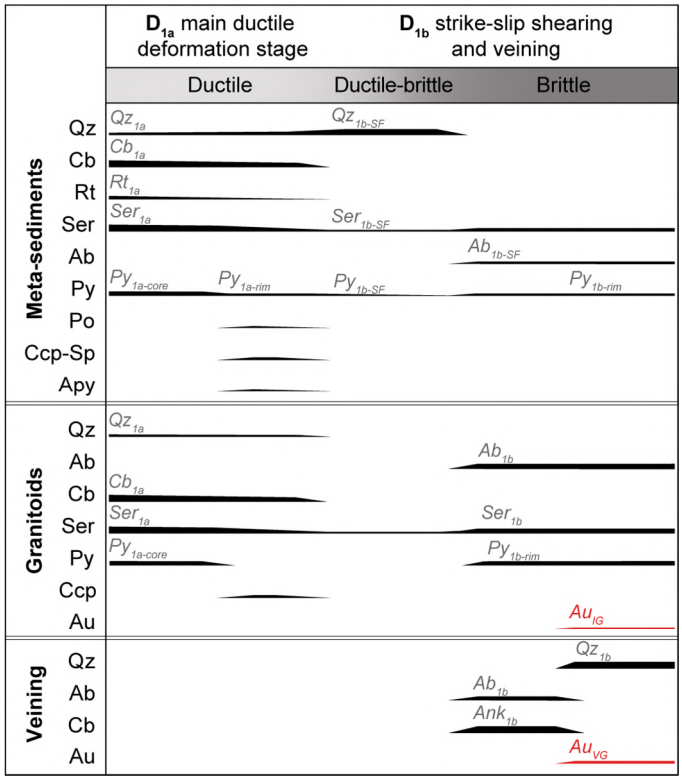


Figure 5-15: Mineral paragenesis recorded at the Central Zone gold deposit. Mineral abbreviations are: Ab=albite; Ank=ankerite; Apy=arsenopyrite; Cb=carbonate; Ccp=chalcopyrite; Sp=sphalerite; Po=pyrrhotite; Py=pyrite; Qz=quartz; Rt=rutile; Ser=sericite. "SF" refers to strain fringe infilling and IG and VG refer the presence of invisible or visible gold, respectively.

The S_{1a} penetrative cleavage transposes the primary bedding in meta-sediments (Figs. 5, 5-16a$_1$). The S_{1a} apparent orientation in thin section is consistent with the gently east-dipping north-northeast-striking penetrative cleavage at the district scale (Fig. 5-16a$_1$; Perret et al., under review). D_{1a} corresponds to the major deformation stage affecting the Central Zone deposit area, and illustrates the north-west oblique convergence associated to the formation of the Keraf suture (Abdelsalam et al., 1995; Abdelsalam et al., 1998; Perret et al., under review).

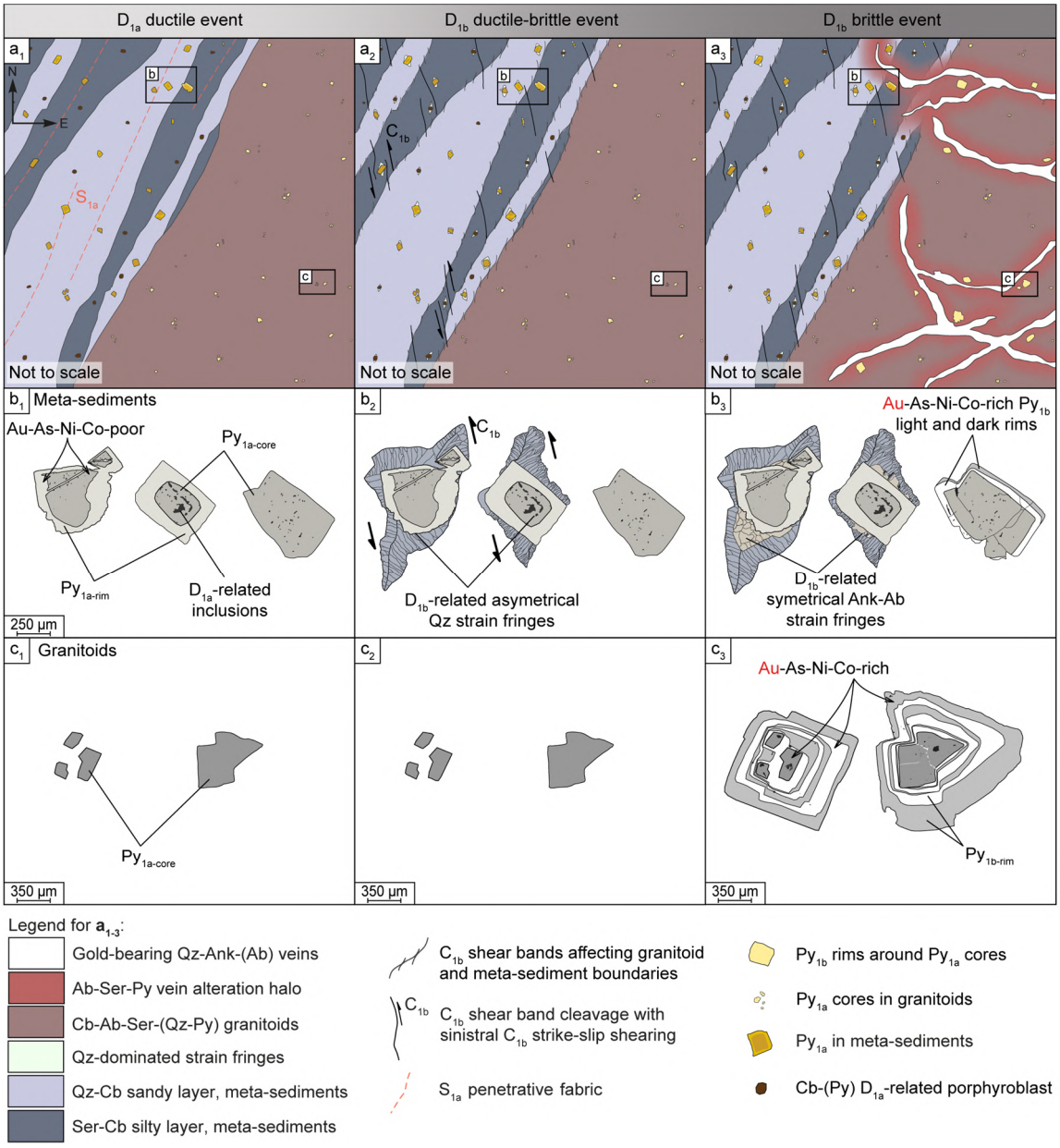


Figure 5-16: Suggested petrological-structural model for the Central Zone gold deposit, from D_{1a} to D_{1b} deformation stages. **a$_1$** to **a$_3$** Macroscopic-scale relationships between deformation, alteration, magmatism and mineralization in both meta-sediments and granitoid intrusions. **b$_1$** to **b$_3$** Focus on the textural-geochemical evolution of pyrite grains in meta-sediments. **c$_1$** to **c$_3$** Focus on the textural-geochemical evolution of pyrite grains in ore-hosting granitoids.

Asymmetrical quartz strain fringes, mantled σ-type porphyroclasts and presence of C_{1b} shear bands crosscutting the S_{1a} penetrative cleavage record the non-coaxial ductile D_{1b} strike-slip shearing at the macroscopic and microscopic scales (Fig. 5-16a_2, b_2). Where visible, the geometry of strain fringes around Py_{1a} grains indicates antitaxial non-deforming face-controlled growth of the quartz-(sericite) assemblage as outlined in Figure 5-7c (Urai et al., 1991; Koehn et al., 2003; Passchier and Trouw, 2005; Bons et al., 2012). These structures grew independently of the relative motion of both fringe and object due to the C_{1b} simple shearing. As a result, the fringe crystals show no deformation and curved sutures are clearly visible, attached to the corner between two pyrite faces and separating two strain fringe populations of different orientation (Fig. 5-7c). If displacement-controlled strain fringes track the displacement path of the pyrite and enable to reconstruct the object movement, face-controlled fringes are no such indicators (Passchier and Trouw, 2005; Bons et al., 2012). However, the shape of the sutures around them is a reliable shear band indicator: as combined sutures define a Z shape, the apparent shear sense is therefore sinistral (Fig. 5-7c). Non-coaxial shearing at the Central Zone deposit exclusively relates to D_{1b} deformation stage. Thus, despite observations were mostly made on non-oriented thin sections, these asymmetrical strain fringes are likely associated with D_{1b} left-lateral strike-slip shearing. The north-northwest-striking orientation of the related shearing planes and left-lateral kinematics inferred from textural and geometrical study of D_{1b}-related shear bands, strain fringes and object rotation or transposition, visible on the oriented thin section observed in this study, confirm these micro-structures express the regional D_{1b} sinistral strike-slip shearing (Figs. 5, 5-16a_2-b_2).

The syn-D_{1b} ore-bearing quartz-ankerite-(albite) veins are purely dilational, syntaxial extension veins, preferentially crosscutting granitoids as confirmed from macroscopic and microscopic observations (Figs. 5-3c-d, 5-7d-e, 5-16a_3; Bons et al., 2012 and references therein). The progressive shift from asymmetrical quartz-dominated to

symmetric ankerite-dominated strain fringes demonstrates the progressive change from strike-slip shearing to carbonation and early veining during D_{1b} deformation (Figs. 5-6a, 5-7, 5-16b_3). We therefore illustrate the prolonged nature of the D_{1b} deformation stage, similarly to what Perret et al. (under review) proposed at the district scale.

The Central Zone deposit is a typical orogenic gold deposit, hosted in meta-sediments metamorphosed at the amphibolite facies early in the orogenic cycle. The gold budget is concentrated in gold-bearing quartz-ankerite-(albite) veins, formed late in the history of the deposit, at the transition from ductile to brittle regimes, all of which are widely documented as typical features of orogenic gold deposits (Fig. 5-16; Gaboury, 2019; Sillitoe, 2020).

6. Discussion

The petrological-structural model detailed in the previous section illustrates the spatial continuity from district- to deposit-scale deformation to micro-structures, which is crucial to interpret the timing of structurally-controlled gold mineralization in terms of tectonic setting (*e.g.*, Combes et al., in press; Perret et al., submitted). The mineralization at the Central Zone gold deposit therefore formed during the late D_{1b} veining stage, in a prolonged northwest-orientated compressive event associated with the development of a Keraf district-scale shear zone, namely the "*West Corridor*" hosting the deposit (Gaboury et al., 2020; Perret et al. under review). The present section attempts to bring further insights into the ore deposition mechanisms involved at the ore shoot and ore mineral scales in the latter tectonic setting, relying on the coupled interpretation of (i) vein and pyrite textures (section 6.1) and (ii) trace element evolution in pyrite generations (section 6.2).

6.1. Constraints on structurally-driven mineralizing fluid flow mechanisms

6.1.1. Constraints from vein textures

The geometry and texture of veins, their paragenetic relationships and related wall-rock alteration patterns, in particular the presence of various sulfide minerals, constrain the thermodynamic and tectonic conditions under which the gold-bearing veins formed in orogenic gold deposits (*e.g.*, Johnston Jr, 1940; McCuaig and Kerrich, 1998; Goldfarb et al., 2001; Goldfarb and Groves, 2015; Velásquez et al., 2018). At the Central Zone deposit, the change from ankerite-(albite) syntaxial growth over the vein walls to jigsaw quartz at their core, characterizes multiple crack-seal events during D_{1b} veining (Figs. 5-3c-e, 5-6b, 5-8d; Ramsay, 1980; Dong et al., 1995; Passchier and Trouw, 2005; Bons et al., 2012). In other words, the presence of early ankerite-(albite) veins in granitoids favored their reactivation and reopening during subsequent fluid flow pulses and the cascading growth of mineralized veins.

On one hand, ankerite-(albite) combs in veins are a primary texture indicating they formed by infilling of opened fractures by overpressured fluids (Dong et al., 1995; Hilgers et al., 2003). Provided that these fluids are either of hydrothermal-metamorphic or magmatic origin, as usually described for orogenic gold, isothermal boiling with a loss of CO_2, or fluid heating by the host rock are the most plausible mechanisms accounting for carbonate precipitation prior to quartz in vein systems (Dong et al., 1995 and references therein; Parry, 1998). Therefore, veining at Central Zone most likely resulted from repeated cycles of fluid decompression as is also suggested by the crack-seal texture described in the previous paragraph.

On the other hand, jigsaw quartz is a secondary vein texture and is interpreted as resulting from the recrystallization of amorphous silica (Dong et al., 1995; Camprubí and Albinson, 2007). If silica had crystallized under supra-lithostatic pressure, quartz would occur as elongated crystals with a comb texture, rather than as an amorphous silica gel (Sibson et al., 1988; Dong et al., 1995; Sibson and Scott, 1998). The large amount of

jigsaw quartz in mineralized extension veins therefore points towards a vein infilling yielding in response to wall stresses and rapid drop of pressure (Dong et al., 1995; Sibson and Scott, 1998; Henley and Hughes, 2000; Camprubí and Albinson, 2007; Moncada et al., 2012). The jigsaw quartz-dominated veins are the gold-richest at the Central Zone deposit. This observation is in line with the model for high-grade gold-bearing veins formation from Petrella et al. (2020), in which the mineralized veins formed from amorphous silica, as well as with vastly documented gold-bearing jigsaw quartz veins in numerous hydrothermal gold deposits (*e.g.*, Camprubí and Albinson, 2007; Moncada et al., 2012; Velásquez et al., 2018).

6.1.2. Constraints from pyrite textures

Pyrite formed as an alteration marker to veining in ore-hosting granitoids and is characterized by oscillatory zoning, with alternating light and dark rims overgrowing inherited pyrite cores (Fig. 5-9e, f). The thicker the veins are, the greater the pyrite stock in proximal alteration is. Indeed, a single Py_{1b} light and dark rim oscillation formed around Py_{1a} cores at the selvages of veins with minor inner quartz infilling (Fig. 5-9i) whereas pyrite grains nearby wide quartz-dominated veins display a developed zoning pattern (Figs. 5-9f, 5-12d). Py_{1b} light and dark rims abruptly transition between one another (Fig. 5-9f), indicating that they formed as a response to cascading changes in physical-chemical conditions of the mineralizing fluid, *i.e.*, boiling or fluid mixing, rather than from a prolonged and progressive growth, *i.e.*, conductive cooling (Deditius et al., 2009; Keith et al., 2020).

The oscillatory zoning and abrupt changes between dark and light Py_{1b} rims remind of the sharp, cyclic compositional zoning in pyrite observed in the structurally-controlled El Callao and Porgera gold deposits, Venezuela and Papua New Guinea, respectively (Velásquez et al., 2014; Peterson and Mavrogenes, 2014, respectively). Authors attributed such geochemical textures to fluid boiling, triggered by sudden drops of pressure. Such pressure drops could relate to the succession of opening and sealing events already

characterized by vein textures in the previous subsection. The boiling hypothesis, involving fluid immiscibility and phase separation, is further supported by the presence of jigsaw texture and ankerite as precursor of quartz veins, coeval to Py_{1b} rims, associated with boiling mechanism in literature (*e.g.*, Dong et al., 1995; Parry, 1998; Moncada et al., 2012; Román et al., 2019; Petrella et al., 2020). Another option would be to relate oscillatory zoning in Py_{1b} rims to mixing of fluids with distinct compositions (Deditius et al., 2009; Velásquez et al., 2014; Peterson and Mavrogenes, 2014; Hazarika et al., 2017). Yet, Gaboury et al. (2020) reported the existence of a single fluid trapped in fluid inclusions in quartz veins at the Central Zone gold deposit, lessening the credibility of the latter hypothesis. Therefore, vein and pyrite textures consistently demonstrate that gold mineralization at the Central Zone deposit is related to veining in granitoids with vein infilling triggered by sudden drops of mineralizing fluid pressure.

6.2. From deposit-scale footprints to microscopic-scale fingerprints

6.2.1. From bulk rock alteration pattern…

The alteration affecting the ore-hosting granitoids shifted from the D_{1a}-related pervasive carbonate-quartz-sericite alteration to proximal sericitization, albitization and pyritization surrounding D_{1b}-related veins (Figs. 5-6a-b, 5-8d, 5-15, 5-16). The transition from regional carbonation, silicification and sericitization to the important input of alkali-rich silicate minerals, *e.g.*, sericite and albite, and sulfide minerals, *e.g.*, pyrite, in close vicinity of mineralized veins is a classical feature of orogenic gold deposits (Ord et al., 2012; Gaboury, 2019). In the next subsection, we zoom on the geochemical record of pyrite to track metal mobility related to alteration and gold mineralization at the Central Zone deposit.

6.2.2. … to pyrite geochemical signatures

Given a single pyrite core or rim generation, the trace element signature remains rather homogenous. Conversely, zoned grains display a strong change in trace element concentrations from one zonation to another (with the example of Au; Fig. 5-12). Such texture indicates that the preferential incorporation of a batch of elements within a pyrite zonation is likely controlled by physical-chemical conditions at crystallization time rather than crystal-chemical properties of pyrite (Deditius et al., 2009; Román et al., 2019; Keith et al., 2020). Furthermore, all pyrite generations at the Central Zone orogenic gold deposit bear a hydrothermal/metamorphic signature in the As/Ag *vs* Sb/Bi elemental diagram (Fig. 5-12a). Pyrite zoning at the Central Zone gold deposit therefore illustrates changes in fluid physical-chemical conditions during its deformation-assisted hydrothermal history.

(i) Syn-metamorphic pyrite recrystallization and elemental mobility

In meta-sediments, there is a depletion in most metals (Co, Cu, Pb, Au, Ag) and metalloids (As, Sb, Bi) in the mineral inclusion-free Py_{1a} rims with respect to mineral inclusion-rich Py_{1a} cores showing evidence of dissolution (Fig. 5-13; Table 5-2). Several gold deposits metamorphosed at the amphibolite facies display similar pyrite textures, interpreted as syn-metamorphic partial remobilization and recrystallization as mineral inclusion-poor pyrite overgrowths with lower metallic trace element contents (Kampmann et al., 2018; Dakota Conn et al., 2019). Such syn-metamorphic elemental mobility in pyrite is in agreement with D_{1a} deformation stage relating to Keraf suturing under amphibolite facies-peak metamorphic conditions (Ahmed Suliman, 2000; Perret et al., under review). The relative depletion in metals and metalloids in Py_{1a} rims regarding Py_{1a} cores may also result from the preferential incorporation of these elements in co-precipitating chalcopyrite-sphalerite-arsenopyrite-pyrrhotite inclusions enclosed in Py_{1a} cores (Fig. 5-15; Genna and Gaboury, 2015). The absence of these Py_{1a} metamorphic rims within the granitoids may be due to local strain partitioning with D_{1a} to D_{1b}

deformation mostly affecting the less competent surrounding meta-sediments. This is concordant with the exclusive development of strain fringes around Py_{1a} in the meta-sediments.

In granitoids, Py_{1a} cores overgrown by Py_{1b} rims display significantly higher Au-As-Ni concentrations than Py_{1a} cores in meta-sediments (Fig. 5-13). They also show dissolution textures, are rich in metal and metalloid mineral inclusions and enclose frequent gold alloy micro-inclusions (Figs. 5-10a, 5-11; Table 5-2). We can attribute the change of trace element signature between Py_{1a} cores in meta-sediments and granitoids to alteration-metamorphic processes. In that scenario, two processes may be involved: (i) metamorphic metal remobilization (*e.g.*, Velásquez et al., 2014; Wu et al., 2019a; Perret et al., 2020) and (ii) entrapment of gold-rich micro-inclusions in granitoid-hosted pyrite cores buffered by the mineralizing fluid flow event leading to ore veining nearby. The gold budget in Py_{1a} cores would therefore exclusively relate to D_{1b} ore-veining rather than the pervasive D_{1a} hydrothermal event, in agreement with observations made at lower scales. Another would be to attribute the difference of composition between Py_{1a} cores in granitoids and meta-sediments to distinct host rock-fluid interactions when they crystallized. Further analysis of the trace element concentrations of Py_{1a} cores without Py_{1b} overgrowth in granitoids is mandatory to clearly state about the inherited and/or syn-tectonic origin of this geochemical difference.

(ii) Pyrite as a proxy for mineralizing thermodynamic conditions

There is an abrupt change in trace element concentrations in pyrite from D_{1a} to D_{1b} deformation stages. Py_{1b} is indeed significantly enriched in As-Au-Ni-Co, with respect to Py_{1a}, to the exception of Py_{1a} cores in the alteration halo of the veins affecting the granitoids as discussed above (Figs. 5-13, 5-14a, c; Table 5-2). If Ni-Co behavior in pyrite has long been linked to the ore environment deposition, reflecting magmatic, hydrothermal or sedimentary processes (*e.g.*, Price, 1972; Bajwah et al., 1987; Cook, 1996; Li et al., 2014; Geng et al., 2018), recent publications have questioned the reliability

of such indicator and suggested that the Ni-Co distribution in pyrite generations rather relates to variations in temperature, pH, salinity of the precipitating fluid and potential mixing between fluids (*e.g.*, Liu et al., 2011; Genna and Gaboury, 2015; Dakota Conn et al., 2019; Large and Maslennikov, 2020). The important shift from Ni-Co-poor Py_{1a} to Ni-Co-rich Py_{1b} generations at the Central Zone gold deposit (Fig. 5-13; Table 5-2) could therefore result from significant cooling of a unique mineralizing fluid from peak amphibolite facies metamorphism D_{1a} to retrograde greenschist facies metamorphism D_{1b} deformation stages. This is in agreement with Ni-Co enrichment ratios at 250-300°C (*e.g.*, Liu et al., 2011; Large and Maslennikov, 2020) and the deformation history portrayed at the district scale (Perret et al., under review). Such decrease in temperature would also account for the significant increase in concentrations of Au and As from Py_{1a} to Py_{1b} (2.6 enrichment factor for As in granitoids; Table 5-2). Velásquez et al. (2014) suggested that a decrease in fluid temperature, from 350 to 300 °C, could result in a decrease in Au-As solubility, and an As enrichment in pyrite by a factor of 2 to 5, in the same range of order as observed at Central Zone. Finally, as variations in Ni and Co concentrations between Py_{1b} light and dark rims are not significant, it is suggested that temperature conditions remain fairly stable during the overall D_{1b} deformation-mineralization stage (Fig. 5-13; Table 5-2).

Another option would be to attribute changes in trace element composition of Py_{1a} towards Py_{1b} to a change of fluid nature and/or composition from D_{1a} to D_{1b}. Yet, there is no drastic change in mineral assemblages from D_{1a} to D_{1b} stages that could support this hypothesis.

(iii) Evidence for fluid boiling

The negative correlation between Au and Te in Py_{1b} rims is similar to the Au-Te concentric zoning in pyrite at the epithermal Cripple Creek district (*e.g.*, Keith et al., 2020). In moderately reduced conditions and temperatures between 200 to 300 °C, boiling partitions Te in the vapor phase, while Au easily precipitates from the liquid phase

(Grundler et al., 2013 and references therein; Keith et al., 2020). These conditions may have led to temporal-spatial zoning between relatively Au-rich, Te-poor light rims and Au-poor, Te-rich dark rims at the Central Zone gold deposit. The coupling of As-Au, discussed above, is another indicator for fluid boiling (Velásquez et al., 2014; Peterson and Mavrogenes, 2014).

Furthermore, the fluid study carried out by Gaboury et al. (2020) in the Gabgaba gold district, central Keraf suture, demonstrated that mineralizing fluids have both liquid and vapor phases. The two phase liquid-vapor inclusions are characteristic of phase separation which may have been favored, or even triggered by drops of pressure and fluid boiling (*e.g.*, Coulibaly et al., 2008; Velásquez et al., 2014), two processes that likely occurred at the Central Zone deposit as discussed above.

6.3. Towards a fault-valve system?

The D_{1b} deformation stage is characterized by episodic vein opening-sealing cycles, with sudden pressure drops, attested by the crack-seal texture of quartz-ankerite-(albite) veins, jigsaw quartz and the oscillatory zoning of Py_{1b} light and dark rims. Besides, vein and pyrite textures and trace element signatures in pyrite collectively suggest the existence of fluid boiling under relatively constant temperature as the primary mechanism for scavenging gold in the pyrite structure and quartz-dominated veins. Relying on very similar observations, Velasquez et al. (2018) and Peterson and Mavrogenes (2014) both proposed earthquake-induced fault-valve processes as the sole mechanism accounting for all these ore-forming processes. The fault-valve model is widely documented when it comes to orogenic gold (*e.g.*, Sibson, 1990; Ridley, 1993; Sibson and Scott, 1998; Cox et al., 2001; Robert and Poulsen, 2001; Sibson, 2001; Micklethwaite and Cox, 2004; Faleiros et al., 2007; Weatherley and Henley, 2013; Cox, 2016; Sibson, 2020a; Sibson, 2020b). Dual-driven fault-valve hydrothermal flow implies that fluid circulation is fractioned in several sequential events, triggered by micro-seisms. In compressional or

transpressional regime, the episodic seismogenic fault failure happens once the fluid pressure reaches supralithostatic values, due to shear compressional stress (Sibson and Scott, 1998). Pressure drops instantly along the fluid pathway, where hydrothermal deposition of quartz-ankerite-(albite) seals the fractures. Minerals are assumed to crystallize syn-fracturing, preventing a drop of fluid pressure under hydrostatic values.

The Figure 5-17 illustrates the model we propose for multi-episodic crack-seal veining at the Central Zone deposit, relying on interpretations discussed in the previous sections. It consists of cascading seismogenically-induced vein failure events, leading to successive, discrete drops of fluid pressure under lithostatic values, sealing of reopened veins and fluid boiling.

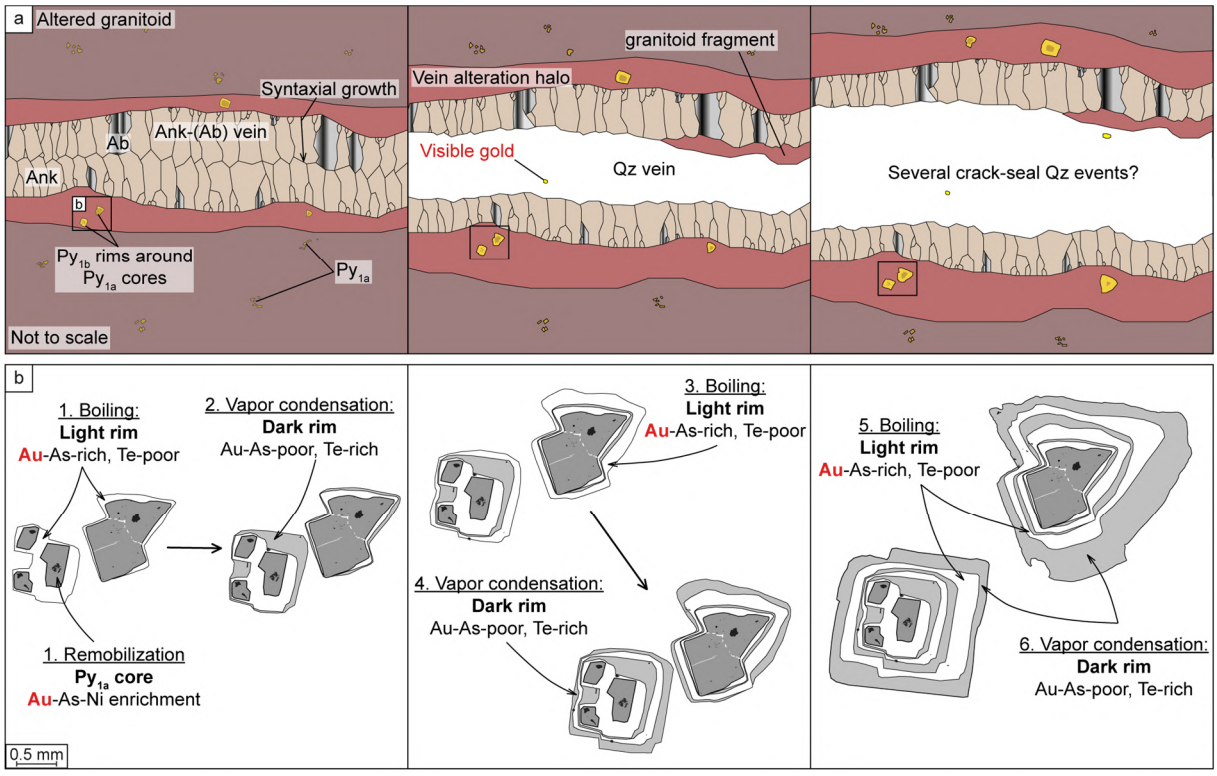


Figure 5-17: Inferred fault-valve mechanism during the D_{1b} deformation stage for the formation of mineralized quartz-ankerite-(albite) veins and their alteration halos in granitoids. **a** The initial fracturing leads to ankerite-(albite) syntaxial infilling and limited alteration with the formation of a set of Py_{1b} light and dark rims. Then, one or cascading crack-seal events affected preferentially the preexisting vein and led to inner quartz infilling coeval with visible gold entrapment in veins and the development of new Py_{1b} rims in the limited alteration halo. **b** Py_{1a} cores are overgrown by a set Py_{1b} light and dark rims related to each crack-seal event. Oscillatory zoning discriminates relatively Au-As-poor and Te-rich dark rims from Au-As-rich, Te-poor light rims.

Firslty, overpressured fluids first fractured the host rocks, sealed with an elongate-blocky ankerite-(albite) infilling. The drop of fluid pressure led to fluid boiling and an Au-As-enriched light rim formed around Py_{1a} cores in the alteration halo of the veins (Velasquez et al., 2014). Secondly, sealing of the opened space induced a decrease in permeability and therefore allowed fluid re-pressurization. As a result, boiling ceased and vapor condensation favored the incorporation of Te in the Au-As-depleted dark rim (Keith et al., 2020). Then, repetitive seismogenically-induced vein failure events led to host rock fracturing, preferentially along mechanically weakened zones (Micklethwaite et al., 2015; Sibson, 2020b), *e.g.*, along early ankerite-(albite) veins crosscutting the ore-hosting granitoids (Fig. 5-17). A new fluid pressure drop resulted in fluid boiling, amorphous silica and gold deposition in the quartz-rich core part of complex veins and new Au-As-enriched light overgrowths were formed around pyrite grains in the alteration halo (Fig. 5-17). After each boiling event, vapor condensation led to Au-As-depleted dark rims deposition around pyrite grains. Finally, this cycle may have repeated itself several times in a limited amount of time (*e.g.*, 1-16 cascading earthquake-aftershock sequences could account for the formation of a 5 Mozt Au goldfield in less than 10^4 years; Micklethwaite et al., 2016), leading to very complex vein and pyrite macro- to micro-textures.

However, we did not observe laminated fault-fill quartz veins at the Central Zone deposit, a commonly documented feature in fault-valve orogenic gold systems (*e.g.*, Cox, 1999; Cox and Ruming, 2004; Cox, 2016; Velásquez et al., 2018). Nevertheless, Gaboury et al. (2020) did observe such fault-fill veins along reverse shear zones reactivating contacts between surrounding meta-sediments and granitoids near the Central Zone deposit, meaning they likely exist. Extension veins may nevertheless be predominant at the Central Zone gold deposit due to the low non-coaxial component for D_{1b} shearing, implying that displacement and space opening along shear planes are limited (Perret et al., under review). However, if the fault-valve model is appealing to account for several

gold mineralization-related features characterized at the Central Zone deposit, further micro-structural and geochemical study of fluid inclusions in gold-bearing quartz veins is mandatory to check modalities of gold transport (*e.g.*, colloids with silica gel; Petrella et al., 2020), destabilization and precipitation as free gold or within pyrite (*e.g.*, Velásquez et al., 2014) and the record of multiple crack-seal events, fluid immiscibility and pressure drops from microthermobarometric measurements (*e.g.*, Velásquez et al., 2018).

7. Conclusions

The Central Zone deposit recorded a two-stage deformation history at the macroscopic and microscopic scales. The S_{1a} main penetrative cleavage characterizes the ductile D_{1a} stage at the microscopic scale, related to the Keraf suturing. Evidence for strike-slip shearing at the microscopic scale likely relate to the ductile-brittle D_{1b} Keraf sinistral shearing and the formation of the "*West Corridor*" in the Gabgaba gold district. Two pyrite generations formed throughout the deformation history, displaying distinct micro-textures and -structures, some of them being genetically and spatially related to mineralized features. Gold is primarily confined as visible gold in a complex network of interconnected crack-seal quartz-ankerite-(albite) extension veins mostly hosted in granitoids and formed during the late brittle D_{1b} stage. Some gold was also incorporated in the D_{1b}-related pyrite lattice in proximal vein alteration halos. Vein typology and host-rock alteration patterns - with characteristic sericite, ankerite, albite, pyrite - are typical of orogenic gold deposits. The integration of vein textures, trace element signatures and textures of the different pyrite generations provides insights into the physical and chemical ore-forming processes. We suggest that gold endowment at the Central Zone deposit is likely controlled by a decrease in temperature from D_{1a} to D_{1b} deformation stages, associated with an enrichment in As-Au-Ni-Co in Py_{1b} grains, with respect to Py_{1a} generation. Quartz-ankerite-(albite) vein textures, oscillatory zoning between As-Au-rich, Te-poor, light Py_{1b} rims and Te-rich, As-Au-poor dark Py_{1b} rims and constant Ni-Co concentrations in Py_{1b} are strong arguments for fluid boiling and vapor condensation happening under relatively constant temperature.

We finally interpret crack-seal vein textures and fluid boiling as the result of fault-valve mechanism. Multiple fluid re-pressurization - drop in pressure cycles may have induced phase separation in the hydrothermal fluid and, consequently, provided favorable conditions for (i) initial ankerite-(albite) veining event, followed by (ii) infilling of quartz enclosing gold grains in reopened veins, and the precipitation of Au-As in proximal pyrite.

Acknowledgements

The authors are grateful to the Manub and Managem team and especially to Attaiaa Hachem, Hassan Ait Benmouh, Mohamed Niyazi and El Alami Boukkari for their welcome on Gabgaba mining camp and their substantial logistical support. Blandine Gourcerol (BRGM, France) is acknowledged for introducing us with Matthew Leybourne (Queen's University, Canada), who is thanked for permission to carry out LA-ICP-MS analyses at Queen's Facility for Isotope Research. Marissa Valentino (Queen's University, Canada) is also thanked for her support with these analyses. This work relies on the Master research thesis of Célestine Berthier carried out at the Université de Lorraine, Nancy, France, and funded by Arethuse Geology EURL. Early comments on the master thesis manuscript from Alexandre Tarantola and Michel Cathelineau (GeoRessources laboratory, Université de Lorraine, Nancy, France) were greatly appreciated. This work is part of Julien Perret's PhD project which benefited of a CIFRE funding, reference CIFRE N°2017/1737, attributed by the French National Research and Technology Agency (ANRT).

Supplementary Materials

Supplementary Material 5-1: Extensive dataset of LA-ICP-MS trace element concentrations (in ppm) of the various pyrite generations from the Central Zone gold deposit, northeastern Sudan.

ID	Py	Si	S	V	Cr	Mn	Fe	Co	Ni	Cu	Zn	Ga	As	Se	Mo	Ag	Cd	In	Sn	Sb	Te	W	Au	Tl	Pb	Bi
CZ_04																										
z1_1	r*	760	565694	<0.17	<2.0	<0.55	432142	651	200	<4.8	2.2	0.56	534	6.5	<0.23	<0.08	0.26	<0.007	0.65	<0.14	<0.26	<0.12	<0.01	<0.05	4.1	0.02
z1_2	r*	1903	564052	8.3	10.7	66.7	432070	40.4	247	<10.4	<4.2	1.6	842	12.4	6.1	<0.06	<0.28	0.16	<0.64	2.0	3.3	0.79	<0.75	<0.02	20.3	1.1
z1_3	r*	<1200	566162	0.56	<3.0	<1.3	433446	127	141	<13.0	<3.0	<1.7	106	9.9	<0.18	<0.25	<0.28	<0.02	<0.45	<0.18	5.8	<0.09	<0.03	<0.02	1.7	<0.16
z1_4	r*	658	556363	1.6	18.8	<1.0	441934	45.0	168	<8.2	3.2	0.41	442	13.4	1.9	<0.22	1.7	<0.06	<0.76	7.5	2.4	<1.0	<0.02	<0.02	96.0	4.1
z1_5	c*	1755	544424	18.0	63.3	82.4	445329	688	592	80.0	16.6	0.74	3629	11.7	64.5	0.48	3.5	<0.01	0.54	9.0	2.9	5.1	0.11	<0.01	78.8	7.2
z1_6	c*	<876	553066	15.6	22.7	<0.90	438190	1220	526	20.6	1.9	<0.33	3269	14.3	49.7	0.34	4.3	0.02	0.66	18.2	5.0	6.5	<0.50	<0.01	182	6.4
z1_7	c*	<429	570430	0.67	<3.7	2.8	429267	4.0	22.0	8.5	5.0	<0.12	125	9.2	2.0	1.8	<0.15	0.03	0.26	6.5	<0.30	<1.6	0.35	<0.01	80.9	2.4
z1_8	r*	420	572278	5.9	<2.7	<0.58	425881	7.9	37.4	<6.9	<1.9	<0.50	115	11.2	<0.10	0.06	<0.17	<0.10	0.93	0.84	<1.4	0.87	<0.02	<0.01	9.6	0.59
z1_9	c*	12254	558093	17.3	4.4	27.7	401584	129	164	<4.4	5.0	0.18	781	9.1	<0.91	<1.3	<0.24	<0.01	3.6	4.0	6.2	23.9	<0.02	<0.41	46.0	2.7
z1_10	r*	643	542025	<0.12	<2.2	0.64	457211	5.9	36.3	<4.7	2.5	0.05	63.6	10.0	<0.08	<0.75	<0.14	0.01	0.40	<0.02	<0.27	<1.1	<0.01	<0.04	0.97	0.26
z2_1	r*	<837	550522	<0.38	<3.5	<0.82	449323	1.3	14.7	20.2	10.9	<0.86	92.6	6.9	<0.53	<0.05	<0.23	<0.15	<0.55	0.34	<1.6	<0.07	<0.02	<0.01	5.0	0.54
z2_2	r*	<797	576564	<0.34	<6.4	<0.92	423223	26.2	48.3	<14.0	3.1	<0.49	105	9.7	<0.20	<1.1	<0.32	0.21	<0.52	1.0	1.1	<0.1	<0.03	<0.08	13.6	0.46
z2_3	r*	<747	571532	<0.34	<3.3	<1.7	427931	23.1	103	<7.3	<2.6	<0.05	399	9.0	<0.19	<1.3	<4.5	<0.02	0.12	0.11	<3.6	<1.4	<0.03	<0.37	1.9	0.10
z2_4	c*	<888	574655	5.9	9.7	2.6	422037	5.0	10.0	<18.7	3.0	<1.1	1690	8.7	<0.22	<0.07	<0.34	<0.09	<0.34	0.64	<0.69	2.8	<0.03	<0.02	9.7	0.31
z2_5	c*	<775	577612	8.4	7.3	<1.5	418009	57.5	146	<10.2	<3.0	<0.06	2417	<10.2	<0.21	<0.32	<7.0	0.15	<0.47	1.3	0.73	1.4	<0.03	<0.02	18.4	0.96
z3_1	r*	<704	575943	3.3	6.9	<0.86	422120	3.1	50.1	<10.4	3.6	<0.04	618	11.9	<0.13	0.06	<0.21	<0.23	<0.32	1.5	<0.44	0.75	<0.02	<0.01	8.3	0.51
z3_2	c*	<1013	571186	7.2	6.8	<0.84	423783	345	284	<10.0	5.3	<0.04	3053	10.4	<0.16	0.11	<2.8	<0.01	0.55	0.78	0.63	1.0	0.03	<0.06	9.3	0.49
z3_3	c*	737	577651	17.4	13.7	1.4	416283	22.1	68.8	18.7	2.8	<0.04	754	9.8	1.1	0.22	<2.7	<0.01	0.83	2.7	2.2	2.5	<0.02	0.07	28.8	1.5
z3_4	r*	573	574303	0.91	<2.4	<0.49	423171	249	340	<10.1	<3.8	<0.13	1021	10.9	<0.10	<0.16	<0.17	<0.01	0.57	0.46	0.51	0.13	<0.02	0.12	3.4	0.17
z3_6	r*	<988	578225	<0.31	<5.3	<0.99	419357	3.0	107	<13.2	<3.0	<0.06	2233	5.2	<0.21	<0.33	<4.9	<0.09	<0.56	0.13	<0.67	0.37	<0.03	<0.02	1.7	0.33
CZ_09																										
z1_1	r*	9609	580163	0.86	<3.2	0.92	407195	13.0	572	<6.0	22.3	0.22	1850	28.2	1.0	0.34	<0.17	0.02	<0.36	1.3	<1.0	<0.65	0.03	<0.01	19.6	5.8
z1_2	r*	1028	572295	<0.15	<3.9	0.62	425021	6.0	85.0	<5.2	2.3	0.04	1331	28.7	<0.65	0.36	<0.18	<0.09	<0.55	2.2	0.48	<0.86	0.02	<0.01	31.8	8.5
z1_3	c*	391	572994	<0.13	<3.4	<0.61	425480	7.2	48.0	4.3	1.9	<0.44	892	22.1	<0.10	0.76	<0.16	<0.04	0.17	1.6	0.57	1.0	0.02	<0.01	16.5	5.6
z1_4	r*	570	591055	<0.14	<2.3	<0.61	406830	4.2	88.8	<7.9	<3.1	<0.13	1426	13.5	<0.11	<0.15	<0.18	<0.26	<0.38	0.11	<0.36	<0.06	<0.02	0.07	1.3	0.31
z1_5	c*	<652	600583	0.38	<5.3	<1.0	397463	6.2	72.7	32.6	2.9	<0.38	1348	14.8	<0.15	0.43	<0.24	<0.05	<0.49	1.4	<0.46	0.35	<0.02	0.19	16.9	5.6
z1_6	c*	<716	584846	0.85	<5.4	<0.86	412973	2.0	210	103	2.2	<0.04	849	21.7	0.26	0.51	<0.21	<0.01	<1.0	1.4	<1.8	<0.07	0.17	<0.01	16.4	6.0

Supplementary Material 5-1 ***(continued)***

ID	Py	Si	S	V	Cr	Mn	Fe	Co	Ni	Cu	Zn	Ga	As	Se	Mo	Ag	Cd	In	Sn	Sb	Te	W	Au	Tl	Pb	Bi
z1_7	r*	10393	599774	4.5	10.6	1.5	383154	7.4	167	319	24.2	<0.56	2655	18.7	<0.16	1.1	<0.25	0.24	<0.39	10.5	5.5	3.3	0.30	<0.02	362	29.4
z1_8	r*	<895	591190	1.3	<6.4	<0.73	405426	8.8	263	14.5	<7.9	<0.61	1996	19.3	<0.18	0.34	0.47	<0.02	<0.41	4.6	4.7	0.52	0.13	<0.02	59.3	19.3
z1_9	r*	<746	608862	<0.77	<5.7	<0.78	387569	2.1	139	<11.1	2.3	<0.04	2751	22.6	<0.16	0.10	<5.6	<0.07	<0.43	1.7	<7.7	1.0	0.04	<0.02	19.8	5.5
z1_10	c*	783	593660	0.78	3.3	<0.79	402729	240	34.4	19.7	4.2	0.06	1137	12.0	<0.10	0.45	<3.0	<0.01	<0.27	4.8	6.7	0.13	0.18	<0.01	50.0	17.7
z1_11	c*	1184	570986	3.2	4.3	23.4	420727	73.8	21.9	18.6	5.0	0.19	5928	55.6	<0.09	0.23	<2.6	<0.008	0.28	22.2	20.3	0.31	0.66	0.02	272	14.2
z2_1	c*	701	569859	1.2	2.6	31.2	416923	24.4	132	10131	66.2	0.18	1092	34.7	<0.08	9.4	<0.13	0.67	3.1	4.4	3.0	0.33	0.16	0.01	137	14.0
z2_2	c*	549	580160	0.18	<2.5	<0.38	418191	32.0	19.9	<5.1	2.3	0.17	885	28.7	<0.08	<0.11	0.81	<0.007	<0.39	0.70	1.1	<0.04	<0.01	<0.03	8.1	0.34
z2_3	c*	1866	575565	3.6	22.5	10.3	419766	1.8	8.5	10.4	4.3	0.52	1856	19.0	0.74	0.32	<3.2	0.02	<0.40	3.3	<5.3	0.35	0.11	0.01	73.4	6.9
z2_4	r*	464	588713	<0.18	<2.4	<0.37	408855	89.0	52.2	<5.5	2.9	<0.02	1808	12.5	<0.34	0.43	<0.13	<0.03	<0.40	<0.17	<0.26	0.19	<0.01	<0.23	1.0	0.31
z3_1	r*	<562	597060	<0.56	<4.3	<0.94	401703	<0.23	<7.1	<7.2	<4.2	<0.16	1221	14.8	<0.57	<0.20	<0.22	<0.01	<0.34	<0.13	0.55	<0.07	<0.09	<0.01	<0.21	<0.01
z3_2	r*	<438	601928	<0.45	<3.4	<0.74	393445	764	516	<5.7	<3.3	0.31	3133	33.4	<0.46	<0.15	<0.17	<0.01	<0.27	1.4	1.3	0.08	<0.07	<0.01	20.0	1.6
z3_3	c*	<696	578622	0.92	<2.8	<0.94	419928	204	97.5	<8.1	4.6	<0.17	975	23.3	<0.13	<0.05	<4.5	<0.01	<0.48	0.67	<5.7	<0.07	<0.02	<0.01	9.0	0.32
z3_4	c*	<598	572801	0.08	<4.6	<0.75	426242	11.8	26.6	<5.0	2.0	<0.17	887	26.4	<2.7	<0.62	<0.22	<0.01	<0.49	<0.46	<0.44	1.0	<0.02	<0.08	0.62	0.02
CZ_10																										
z1_1	lr	624	453812	23.8	18.0	0.77	520662	559	2128	25.7	3.1	0.15	12727	10.4	<0.11	0.31	<0.06	<0.004	0.26	4.9	<1.0	36.0	0.66	0.01	32.1	3.4
z1_2	c*	455	466729	13.8	11.2	<0.22	525691	276	347	4.2	2.6	0.29	1148	43.3	<0.13	0.10	0.28	<0.005	0.20	2.0	3.8	0.67	<0.01	<0.004	8.3	1.4
z1_3	c*	642	502552	0.19	<1.4	1.4	494417	343	325	<4.4	4.0	<0.06	1636	47.0	<0.08	0.07	<0.14	<0.008	0.11	1.9	4.5	<0.03	<0.04	<0.02	13.6	2.5
z1_4	lr	<132	441535	0.19	<0.61	1.2	548112	69.5	462	2.9	1.8	<0.03	9795	12.0	0.15	0.04	0.66	0.04	<0.04	0.96	<0.49	0.06	0.52	1.1	4.3	0.39
z1_5	lr	206	463809	<0.07	<0.50	0.47	515343	407	989	6.8	4.0	0.08	19222	8.9	<0.03	<0.02	<0.05	<0.003	<0.12	0.07	<0.41	<0.01	2.4	<0.009	<1.1	0.07
z1_6	dr	<333	513881	0.14	<1.3	<0.35	477882	48.5	311	3.6	<1.5	<0.02	7857	16.1	<0.24	<0.02	<0.14	<0.008	<0.21	<0.09	<0.39	<0.04	0.16	<0.008	<0.06	<0.01
z1_7	lr	338	514483	<0.18	<1.7	<0.46	461481	707	1590	<2.7	1.6	<0.06	21383	14.0	<0.08	<0.02	<0.15	<0.02	<0.26	<0.13	<0.39	<0.04	1.7	<0.008	<0.87	<0.07
z1_8	lr	579	513732	<0.23	<2.2	<0.59	470075	321	905	<3.4	<1.1	<0.08	14356	13.8	<0.11	0.30	<0.19	<0.03	<0.34	1.6	<0.51	0.08	0.87	<0.01	8.8	1.2
z1_9	dr	243	483987	<0.11	<1.1	<0.38	508262	311	910	2.2	1.3	<0.14	6221	27.3	<0.42	0.27	<0.11	<0.02	<0.15	3.2	<0.30	0.08	0.17	<0.006	17.6	2.5
z1_10	c*	<308	509394	0.19	<1.7	<0.34	486480	35.7	687	<2.9	1.7	<0.02	3270	15.2	<0.24	0.05	<0.14	<0.008	<0.33	1.1	<0.39	0.33	<0.01	<0.02	7.7	1.1
z1_11	c*	529	496649	31.8	35.6	8.8	484137	346	386	6.5	7.5	0.13	1598	31.8	<0.25	0.08	<0.15	<0.03	0.71	4.2	5.8	5.9	0.15	<0.009	25.6	2.7
z1_12	lr	458	478370	38.3	51.1	<0.26	495643	510	1832	24.8	1.9	0.19	7239	21.0	<0.24	0.44	<0.13	<0.02	1.1	12.6	0.98	105	0.32	<0.007	45.1	5.0
z1_13	lr	399	490175	0.13	<1.2	<0.23	493307	893	1590	<2.4	1.6	<0.04	13625	9.9	<0.06	<0.07	<0.09	<0.006	<0.20	0.07	<0.26	<0.02	0.38	<0.005	<0.56	0.03
z1_14	c*	378	510143	0.42	0.92	<0.25	488566	29.8	136	6.2	1.8	<0.01	499	30.1	<0.05	0.05	0.13	<0.005	<0.19	1.7	2.1	<0.02	0.06	<0.005	16.3	2.3
z1_15	lr	333	524740	14.3	10.7	<0.35	453068	426	1630	3.7	2.0	<0.07	13822	14.2	<0.07	0.14	<0.12	<0.007	<0.20	1.8	<0.32	30.0	0.60	<0.007	10.8	1.0
CZ_12																										
z1_1	c	5462	350408	19.8	<2.5	259	622276	31.2	362	199	1075	0.14	19574	28.4	0.89	0.83	0.21	<0.008	<0.31	16.2	<1.2	1.7	0.50	<0.05	273	0.58
z1_2	c	233	583027	<0.21	<2.1	<0.40	413501	0.20	565	<4.2	1.8	<0.02	2628	35.4	<0.30	0.29	<0.12	<0.007	<0.26	0.26	1.0	0.17	0.02	<0.04	3.0	0.14
z1_3	c	914	558370	2.3	<1.5	4.0	435912	5.1	1462	192	9.1	<0.28	2403	26.3	0.33	1.2	<0.12	0.02	0.42	7.7	0.33	0.06	0.38	<0.007	292	3.3

Supplementary Material 5-1 ***(continued)***

ID	Py	Si	S	V	Cr	Mn	Fe	Co	Ni	Cu	Zn	Ga	As	Se	Mo	Ag	Cd	In	Sn	Sb	Te	W	Au	Tl	Pb	Bi
z1_4	lr	928	522168	5.5	<0.77	61.2	464150	53.5	1805	41.5	400	0.13	10250	12.0	0.46	1.0	0.37	0.13	0.21	8.9	<0.71	1.0	0.39	<0.005	98.6	1.0
z1_5	lr	<507	559712	1.5	<1.4	166	403099	295	1513	26.1	128	<0.21	34971	20.2	<0.08	1.4	0.88	0.01	<0.28	2.5	<0.26	0.10	33.3	<0.008	24.9	0.55
z1_6	dr	<741	586380	1.6	<2.4	19.4	399907	40.0	1921	30.6	153	<0.16	11458	12.4	<0.13	0.61	<0.21	0.06	<0.48	3.0	<5.6	0.30	0.14	<0.01	70.8	1.0
z1_7	dr	282	542189	0.17	<0.83	<0.39	447237	99.8	1851	<2.8	2.5	<0.06	8325	8.7	<0.05	<0.02	<0.08	<0.02	<0.17	0.05	<1.9	<0.02	0.09	<0.005	0.11	<0.06
z1_8	lr	178	522446	0.14	<1.2	<0.16	453552	637	1952	4.7	1.6	<0.04	21185	17.1	<0.04	0.31	<0.06	<0.003	<0.12	0.07	<0.11	0.20	21.9	<0.03	0.48	0.07
z1_9	c	<275	573489	0.19	<1.7	0.92	421169	164	444	12.4	4.3	<0.22	4628	45.3	<0.06	0.88	<0.10	<0.006	0.03	2.5	4.3	<0.03	0.21	0.01	33.0	0.72
z1_10	c	<562	572783	9.8	29.9	1.4	416485	315	257	11.7	3.2	<0.20	3173	40.1	<0.08	5.1	0.78	<0.008	0.49	2.4	1.7	1.6	0.07	<0.008	786	3.7
z1_11	dr	<434	572254	0.19	<1.6	<0.43	418816	31.6	1158	<5.4	7.0	<0.02	7710	15.2	<0.08	0.09	<1.5	0.03	<0.28	0.21	<0.27	<0.04	0.02	<0.009	3.7	0.06
z1_12	lr	<436	564557	<0.21	<1.7	<0.44	423417	744	2566	<3.3	1.6	<0.02	8665	45.8	<0.07	<0.02	<0.51	<0.007	<0.16	0.02	<1.0	<0.04	0.47	<0.008	0.44	0.03
z1_13	c	325	595152	1.3	10.2	<0.48	398122	44.7	307	<6.5	2.3	0.03	5677	41.8	0.56	<0.20	<1.1	<0.01	<0.16	1.1	<1.4	2.9	0.42	<0.01	11.2	0.22
z1_14	lr	<390	567008	0.08	<2.0	<0.57	412888	875	3415	<4.4	2.7	<0.10	15792	12.8	<0.37	<0.03	<0.13	<0.03	<0.18	0.41	<0.28	<0.04	0.32	<0.009	2.2	0.50
z1_15	lr	<367	565125	<0.36	<2.1	<0.35	417399	426	2261	<7.5	2.5	<0.02	14773	7.3	<0.50	<0.03	<0.14	<0.008	<0.28	<0.08	<0.29	<0.05	0.29	<0.009	0.16	0.01
z2_1	dr	<993	580215	32.6	35.5	<0.75	397213	265	485	<12.5	<6.0	0.10	6313	<12.1	<0.87	<0.38	<0.31	<0.08	1.5	4.7	<2.7	80.9	0.03	<0.09	17.3	0.79
z2_2	dr	<877	595904	<0.31	<5.0	<0.67	392904	871	926	<11.0	<5.2	<0.05	9351	13.9	<0.75	<0.34	<0.28	<0.07	<0.85	<0.37	<2.4	0.10	0.04	<0.08	1.9	<0.09
z2_3	dr	<2485	578346	8.8	<7.5	2191	415686	226	434	<38.4	63.5	<0.79	3027	<21.0	3.7	<0.16	<6.6	0.22	<1.6	<0.47	<1.6	<0.25	<0.08	<0.05	11.3	0.37
z2_4	dr	<1117	595327	<0.80	<4.8	<1.5	392343	544	1499	<10.6	2.9	<0.49	10272	12.0	<0.23	<0.41	1.0	<0.02	<0.59	<0.29	<0.74	<0.12	0.07	<0.02	<0.63	0.04
z2_5	dr	<773	589516	0.59	<5.4	<0.67	404801	354	1018	<15.7	2.3	<0.05	4114	18.2	<0.18	<0.06	<0.29	<0.07	<0.29	0.42	1.1	3.5	<0.12	<0.02	2.2	0.15
z2_6	dr	<1081	598955	<0.37	<9.0	<1.1	381283	839	4510	<17.1	<2.8	0.11	14369	31.0	<0.90	<0.30	<0.33	<0.02	0.22	0.64	1.7	<0.61	0.07	<0.02	7.7	0.22
z2_7	dr	<1400	609095	2.8	<5.2	<1.2	386379	461	432	<21.9	<4.0	<0.08	3138	38.1	<0.29	<0.10	<0.46	<0.03	0.39	0.64	1.0	0.19	<0.05	<0.03	12.3	0.22
z2_8	dr	<1332	584274	0.32	<5.4	<1.1	401121	112	2180	77.2	<3.6	<0.06	12230	<16.7	0.39	<0.32	<1.5	<0.02	<0.80	<0.23	<3.2	<0.12	0.13	<0.02	1.5	0.89
z2_9	dr	<1159	609739	<0.46	<5.2	<1.4	387184	59.4	441	<10.8	2.0	<0.07	2530	38.4	<0.24	<0.37	<0.40	<0.02	<0.41	<0.26	1.1	<0.12	<0.04	<0.02	1.8	0.02
z2_10	dr	<472	567065	<0.16	<2.6	<0.68	428863	53.7	490	<10.2	1.7	<0.03	3477	43.0	<0.12	<0.18	<0.20	<0.01	<0.60	<0.16	0.67	<0.06	0.08	<0.01	0.15	<0.10
z2_11	dr	<860	586632	<0.93	<5.0	<0.82	410504	116	275	<13.9	<2.5	<0.22	2427	37.3	<0.79	<0.26	<0.29	<0.02	<0.29	0.32	<11.0	<0.09	<0.03	<0.02	5.4	0.19
z2_12	lr	<637	579512	<0.39	<4.0	0.23	410083	27.2	1252	117	3.1	<0.04	8989	12.5	<1.2	<0.19	<0.21	<0.01	<0.49	0.04	1.2	<0.07	0.37	0.02	1.5	0.71
z2_13	dr	<772	573407	0.26	<5.6	<1.4	423625	109	113	<16.6	2.3	<0.06	2693	45.4	<1.0	<0.45	<0.35	<0.12	<0.56	0.39	<3.2	<0.11	0.25	<0.02	4.0	0.10
z2_14	dr	<1329	590097	<0.60	<7.3	<2.1	406908	144	269	25.9	2.9	<0.07	2488	40.5	<0.26	<0.37	<0.42	<0.02	<0.57	4.3	0.89	<0.13	0.12	<0.03	16.9	2.1
z2_15	dr	<1157	605008	<0.28	<6.9	<1.5	391131	372	434	<11.3	2.7	<0.25	3018	33.8	<0.21	<0.60	<0.34	<0.16	<0.44	<0.05	0.70	<0.11	<0.03	<0.02	0.50	<0.02
z2_16	c	9499	573322	57.1	<3.7	83.7	411616	205	250	17.5	2.7	5.7	4444	28.9	<0.12	0.06	0.38	0.08	0.36	19.2	2.3	0.18	0.29	<0.01	236	5.5
z2_17	lr	3522	579454	5.2	<3.7	28.7	408010	385	1489	<10.9	<3.5	2.0	6951	35.2	<0.17	<0.06	<0.28	0.02	<0.78	6.5	2.2	<0.09	0.28	0.10	87.7	2.1
z2_18	lr	2597	572671	4.7	4.3	8.9	411878	610	1126	<10.5	3.1	<0.33	5776	46.0	0.17	<0.05	<1.5	<0.07	<0.80	4.6	3.1	3.0	0.14	<0.02	63.1	1.2
z2_19	dr	<702	595205	0.22	<3.5	<0.74	401733	81.0	155	<11.8	2.5	0.06	2760	40.7	<0.92	<0.23	<0.26	<0.07	<0.58	0.16	1.6	<0.08	0.07	<0.02	2.7	0.07
z2_20	dr	<993	591008	<0.69	<3.8	<1.7	406614	34.4	118	<8.4	<2.4	<0.07	2175	47.0	<1.0	<0.47	<0.38	<0.02	<0.77	0.13	2.7	<0.12	<0.04	<0.03	1.4	<0.09
z2_21	dr	<1067	592886	<0.55	<8.0	<1.3	399963	64.2	737	<11.1	<14.7	<0.07	6305	39.1	<1.1	<0.08	<0.41	<0.02	<0.42	<0.35	<0.82	<0.13	0.08	<0.03	1.9	<0.02

Supplementary Material 5-1 ***(continued)***

ID	Py	Si	S	V	Cr	Mn	Fe	Co	Ni	Cu	Zn	Ga	As	Se	Mo	Ag	Cd	In	Sn	Sb	Te	W	Au	Tl	Pb	Bi
z2_22	dr	<1268	620384	<1.1	<8.2	<0.94	377301	10.4	67.7	<19.4	<4.5	<0.07	2237	<9.5	<0.25	<0.09	<0.40	<0.02	<0.55	<0.06	<0.82	<0.13	<0.04	<0.03	<0.36	<0.02
z2_23	dr	<1007	585229	<0.83	<6.5	<0.75	399738	1078	2991	<15.8	<3.6	<0.06	10942	19.0	<0.20	<0.07	<0.33	<0.02	<0.43	0.18	0.82	0.16	0.11	<0.02	0.88	0.03
z2_24	dr	1022	614780	<0.60	<4.9	<1.2	376710	25.6	451	<16.8	3.4	<0.06	7002	<14.0	1.6	<0.07	<1.5	<0.02	<0.62	0.13	<0.71	<0.11	0.04	<0.02	1.6	0.09
z2_25	lr	<1205	596714	<0.80	<6.4	<1.2	387657	295	2464	<26.3	2.9	<0.07	12834	26.0	0.87	<0.08	<0.37	<0.24	<1.0	0.44	<0.76	<0.12	0.34	<0.02	4.7	0.54
z2_26	lr	<1343	625397	3.7	<7.0	<1.0	362362	93.8	1300	23.9	<9.6	<0.50	9970	12.9	<1.8	<0.13	<0.63	<0.04	<0.66	<0.40	<1.3	23.9	0.11	<0.04	1.2	0.17
z2_27	dr	686	604903	<0.83	<3.6	<0.76	376664	321	4075	<15.4	<1.8	<0.24	13302	40.3	<0.87	0.09	<0.32	<0.02	<0.32	0.63	<0.64	<0.1	0.08	<0.02	5.6	0.45
z2_28	lr	365	573857	<0.58	<2.6	<0.53	410940	457	2030	<10.7	2.3	<0.17	12316	10.7	<0.61	<0.05	<0.23	<0.01	<0.23	<0.03	<0.45	0.16	0.15	<0.01	0.43	<0.01
z2_29	lr	5171	609448	18.8	<5.2	56.9	381115	20.5	50.5	<26.9	3.5	2.6	3845	30.7	<1.3	<0.45	<0.49	0.04	<0.49	12.4	<0.99	<0.16	0.18	<0.03	154	2.7
z2_30	dr	<858	597854	<0.47	<3.8	<1.3	399071	20.8	193	<19.6	2.9	<0.27	2846	8.7	<0.96	<0.32	<0.36	<0.02	<0.36	0.15	<0.72	<0.11	<0.04	<0.02	2.7	0.09
z3_1	dr	1719	568263	1.3	<3.2	30.6	412355	845	2419	21.3	217	<0.17	14032	13.0	<0.17	0.23	<0.28	<0.08	<0.83	10.3	<2.0	1.9	0.06	<0.02	65.6	0.41
z3_2	lr	<967	592007	<0.46	<4.9	<1.1	404588	<0.71	61.0	<22.3	2.6	<0.07	3287	51.9	0.27	<0.08	<7.0	<0.02	<1.2	<0.25	1.0	<0.12	0.12	<0.02	1.1	<0.10
z3_3	lr	<968	590478	<0.64	<3.3	<1.1	398395	1.0	124	<8.7	<2.8	<0.06	10885	98.2	<0.21	0.21	<0.34	<0.02	<0.53	0.40	<3.0	0.18	1.8	<0.18	4.0	0.12
z3_4	dr	71273	471085	110	222	118	439354	439	1684	481	859	13.7	12692	<43.9	<8.5	0.88	<0.88	0.58	<2.0	39.3	<1.8	13.9	0.10	0.40	198	1.0
z3_5	c	1744	596479	3.1	<7.2	<2.4	396123	12.4	535	8.1	8.7	0.09	4909	56.7	<0.28	<0.90	<2.1	<0.03	<0.66	0.61	<0.90	0.32	0.05	<1.1	9.3	0.20
CZ_13																										
z1_1	c	652	488907	0.47	<2.8	1.5	505204	115	1164	<5.4	1.0	<0.03	3748	46.6	0.30	<0.10	<0.22	<0.04	<0.42	1.2	1.5	0.17	0.08	0.06	7.2	0.19
z1_2	dr	1827	503015	2.8	<2.9	<0.54	482934	1255	2872	67.3	<0.88	0.35	7992	18.1	<0.14	0.22	0.59	<0.04	<0.44	0.47	2.4	<0.06	0.60	<0.01	3.6	0.55
z1_3	c	3113	472706	6.2	2.4	14.5	521968	328	150	9.4	2.7	1.1	1614	17.8	<0.13	1.2	<0.21	<0.01	0.69	4.5	<3.5	<0.05	<0.02	0.05	22.8	2.4
z1_4	dr	2940	505545	14.2	<2.5	34.8	487235	350	188	14.7	2.3	3.2	2858	42.7	<0.11	0.22	<0.18	0.06	0.60	9.7	1.0	0.23	1.2	0.02	71.8	2.4
z1_5	c	1580	553719	3.1	5.5	<0.91	436184	629	1111	44.4	2.0	<0.05	5198	36.6	<0.61	0.22	<0.37	0.07	<2.4	2.7	3.1	0.22	0.17	<0.02	<24.8	<0.57
z1_6	c	<486	507176	<0.35	<2.2	<0.84	490148	2.0	5.6	8.9	2.3	<0.10	2445	43.2	<0.15	0.17	<0.24	<0.01	<0.69	11.8	6.1	<0.06	0.21	0.05	123	2.0
z1_7	c	<535	544061	<0.26	<2.7	2.7	451404	91.5	67.7	832	<2.6	0.11	3089	48.9	<0.40	0.83	<0.25	<0.06	<5.7	32.5	4.6	<0.34	0.44	<0.08	350	6.1
z1_8	dr	<520	524420	<0.20	<2.7	<0.50	467820	1097	1616	8.1	<58.9	<0.03	4990	41.6	<0.15	<0.11	<0.24	<0.01	<0.53	0.72	0.94	0.44	<2.4	<0.01	4.6	0.20
z1_9	c	14224	556178	30.1	49.8	<0.84	414854	728	4437	22.8	4.3	3.6	9285	32.7	<0.24	0.70	<0.41	<0.07	<0.56	1.1	<1.1	<0.30	<0.49	<0.07	<22.8	1.1
z2_1	dr	<139	474792	1.6	3.9	222	506444	345	4305	13.5	17.1	<0.01	13801	24.1	<0.05	0.44	<0.08	0.03	<0.11	1.6	3.8	0.19	0.49	<0.01	19.1	1.2
z2_2	lr	209	483924	0.82	4.0	<2.8	495486	633	4019	3.0	2.3	0.66	15250	36.3	0.11	<0.03	<0.07	<0.004	0.21	0.88	<0.18	2.3	0.19	<0.004	3.4	0.26
z2_3	dr	<355	481553	7.4	6.1	371	495595	942	4460	78.5	32.2	<0.07	16850	19.0	<0.10	8.7	0.30	<0.64	<0.18	15.0	1.7	1.5	0.11	4.3	50.6	3.5
z2_4	dr	719	530739	39.9	144	977	430135	656	2341	349	359	1.5	13038	20.5	0.54	0.47	4.4	0.41	2.8	42.1	<0.69	101	1.4	<0.01	163	10.1
z2_5	lr	2625	458161	12.3	140	57.7	530231	2291	813	16.5	10.3	0.83	4602	32.4	<0.04	0.22	<0.06	<0.004	0.26	8.1	3.0	0.55	0.50	0.09	70.0	1.7
z2_6	c	34473	510984	2.6	<1.6	14.0	448990	148	517	170	310	1.2	3861	20.3	<0.29	20.6	0.62	3.3	0.73	77.4	2.1	14.7	1.2	1.4	371	10.1
z2_7	c	2012	523989	1.5	<2.2	<0.66	469719	48.7	2433	<150	<35.6	0.27	1525	16.8	<0.13	<0.12	<0.56	<0.01	4.5	20.1	<0.60	5.1	0.09	0.22	199	1.0
z2_8	lr	<493	573374	<0.20	<1.7	2.8	410993	209	2374	<5.4	2.4	<0.15	13013	30.7	<0.58	<0.11	<0.25	<0.04	<0.38	0.45	<0.65	0.15	0.26	0.05	<5.5	0.13
z2_9	dr	<414	561067	<0.18	<1.9	<0.53	434615	27.6	21.3	<6.0	4.1	<0.03	4187	40.4	<0.53	<0.10	<0.22	<0.05	<0.45	4.5	<1.8	<0.05	<0.07	<0.01	32.9	0.24

Supplementary Material 5-1 ***(continued)***

ID	Py	Si	S	V	Cr	Mn	Fe	Co	Ni	Cu	Zn	Ga	As	Se	Mo	Ag	Cd	In	Sn	Sb	Te	W	Au	Tl	Pb	Bi
z2_10	dr	7360	551970	16.6	8.2	71.9	433018	368	88.1	32.5	4.1	3.4	6761	45.4	<0.33	0.17	<0.14	<0.03	1.0	13.6	1.5	<0.03	0.91	0.08	112	1.1
z2_11	c	<466	545101	0.10	<2.6	<3.7	449735	407	1300	75.9	<1.7	<0.03	3338	33.6	<0.14	<0.16	<0.24	<0.01	<2.2	1.0	4.9	<0.06	0.22	1.6	<11.9	0.33
z2_12	c	48771	548679	176	42.5	161	397961	205	310	<237	16.8	13.4	2456	29.5	<0.93	<0.34	<0.51	<0.03	<1.0	26.9	2.1	3.2	0.14	0.61	295	3.2
z2_13	dr	341	539185	1.2	<1.2	<0.36	457040	61.2	82.1	437	1.7	<0.08	2796	44.6	<0.24	<0.09	<0.13	<0.008	0.61	0.21	2.9	0.06	0.06	<0.02	2.4	<0.34
z2_14	c	<314	574048	0.61	<1.9	1.1	422155	486	337	24.1	<3.5	0.06	2786	46.1	<0.32	<0.12	<0.19	<0.04	<12.6	0.86	4.3	0.15	0.09	<0.01	<11.5	0.18
z2_15	c	253	539912	0.24	<1.1	<0.32	455780	860	354	5.6	<2.0	<0.02	2785	42.5	<0.18	<0.07	0.15	<0.03	<6.9	0.36	2.2	<0.03	0.03	<0.006	<6.6	0.05
z2_16	c	3309	538653	19.0	1.6	1.8	443975	469	161	5.1	1.0	0.08	5065	37.4	<0.08	0.03	<0.13	0.01	0.70	2.1	1.6	4.4	0.51	<0.24	13.8	0.23
z2_17	dr	68814	489180	146	89.6	12.8	416168	535	5585	371	263	15.1	17888	28.3	<0.38	0.80	<0.66	0.17	<2.7	43.1	3.1	30.8	0.68	0.25	60.2	<6.0
z2_18	dr	326	534948	<0.69	<1.3	8.3	450410	204	3257	15.9	215	<0.13	10602	11.2	<0.07	0.17	<0.12	<0.007	0.90	<0.15	<0.31	0.23	0.08	<0.02	<7.6	<1.0
z3_1	dr	1631	526788	1.6	5.0	0.61	453735	593	3726	3.4	1.9	0.11	13231	19.4	<0.15	0.66	0.15	0.01	0.66	0.35	<0.25	1.6	0.21	<0.005	4.0	<0.30
z3_2	dr	577	568515	<0.28	<1.9	<0.45	411285	915	4104	<5.1	<1.7	0.06	14568	33.8	<0.10	<0.03	<0.18	<0.04	<0.25	0.10	<0.47	0.12	0.23	0.03	<1.8	<0.03
z3_3	lr	1011	531227	1.4	173	11.1	463833	15.7	446	7.3	3.8	0.30	2924	39.6	<0.08	0.09	<0.14	<0.008	<0.24	1.6	3.5	0.81	0.12	<0.008	19.9	0.29
z3_4	lr	420	545063	0.57	42.9	2.8	451648	54.0	343	3.3	1.8	0.16	2374	30.9	1.5	<0.02	<0.12	<0.007	0.69	0.82	0.75	<0.09	0.34	0.01	11.8	0.16
z3_5	lr	328	578632	<0.09	1.9	<0.41	414868	64.8	596	<5.1	<2.1	<0.07	5459	42.7	<0.09	<0.07	<0.16	<0.22	<1.2	0.41	1.6	<0.04	0.87	<0.009	5.1	0.11
z3_6	c	1013	533524	2.4	28.8	0.91	460003	787	695	4.8	1.1	0.23	3457	37.4	<0.08	<0.06	<0.41	<0.008	<0.18	2.0	2.2	<0.03	0.06	<0.008	19.3	0.30
z3_7	c	1246	555261	10.0	13.8	1.5	434350	379	1628	7.3	3.4	<0.06	4157	35.7	<0.09	<0.07	<0.43	<0.009	0.93	2.0	2.2	2.0	0.03	<0.008	15.4	0.43
z3_8	c	613	536144	<0.32	<1.5	<0.32	455547	762	1621	<2.7	1.6	<0.02	5256	36.8	<0.21	<0.02	<1.8	<0.007	0.14	1.1	<4.0	<0.03	0.14	<0.007	15.6	0.23
z3_9	c	<342	584153	<0.15	<1.8	<0.46	412209	3.5	501	<5.6	<1.7	<0.08	3086	44.1	<0.11	<0.13	<0.19	<0.03	<0.97	<0.07	2.2	<0.05	0.17	<0.01	<0.76	<0.04
z3_10	dr	13376	554909	17.5	51.1	17.6	413830	334	4535	<5.7	5.4	2.5	12822	<15.7	<0.11	0.19	<0.21	0.05	<1.0	0.20	<0.54	1.2	0.07	<0.01	4.0	0.23

Concentrations are in ppm.

Pyrite generations and textures are: c = Py_{1a} core in meta-sediments; r* = Py_{1a} rim in meta-sediments; c = Py_{1a} core in granitoids; dr = Py_{1b} dark rim; lr = Py_{1b} light rim.*

PARTIE IV – Données complémentaires et discussion générale

Préambule

En accord avec l'approche par système métallogénique suivie pour étudier l'or panafricain dans la partie occidentale du bouclier nubien, les parties précédentes de ce manuscrit ont successivement abordé : (i) l'évolution géodynamique et les processus de croissance crustale en jeu le long de la zone de suture de Keraf (**Partie I**) ; (ii) la chronologie relative des événements aurifères à l'origine des gisements de Galat Sufar South, WG03, Central Zone et UTM vis-à-vis de la déformation régionale associée à la mise en place des zones de suture d'Atmur-Delgo et de Keraf (**Partie II**) ; et (iii) les mécanismes couplant micro-déformation et minéralisation à travers les exemples des gisements de Galat Sufar South et Central Zone (**Partie III**). La dimension temporelle d'un système métallogénique ne peut cependant se réduire à des éléments de chronologie relative, certes nécessaires, mais insuffisants à la compréhension des processus d'évolution lithosphérique, de fertilisation crustale, puis de mobilisation des métaux avant leur concentration sous forme d'occurrences minéralisées. Le recours à des méthodes de chronologie absolue est donc primordial afin de mieux tracer ces mécanismes couplant géodynamique, tectonique et minéralisation au cours du temps (Stein, 2014).

Dans un premier temps (**Chapitre VI**), nous présenterons les premières contraintes temporelles absolues sur les événements de déformation-minéralisation principaux à l'origine des gisements de Galat Sufar South et WG03, obtenues par datation U-Pb sur apatite hydrothermale synchrone de la minéralisation. Des données géochimiques et isotopiques U-Pb et Hf sur zircon magmatique ainsi que des contraintes de pression-température établies par calcul de multi-équilibres chlorite-phengite-quartz-eau seront également présentées afin d'intégrer la minéralisation aurifère de Galat Sufar South à l'évolution lithosphérique de la suture d'Atmur-Delgo, en lien direct avec les conclusions tirées pour la suture de Keraf dans la **Partie I**.

Enfin, le **Chapitre VII** fera office de discussion générale. Nous proposerons une synthèse du système métallogénique aurifère panafricain exprimé le long de la zone de suture de Keraf, et de son extension, la zone de suture d'Atmur-Delgo, selon les trois piliers de ce concept (*e.g.*, McCuaig et al., 2010 ; Huston et al., 2012 ; McCuaig et Hronsky, 2014 ; Wyman et al., 2016; Occhipinti et al., 2020) : (i) la différentiation crustale permettant la fertilisation de la croûte en or, (ii) l'architecture lithosphérique à crustale et l'évolution tectonique régionale permettant la mobilisation des fluides minéralisateurs et (iii) les mécanismes de précipitation et de concentration de la minéralisation. Nous discuterons ensuite la validité de ce modèle à l'échelle du bouclier arabo-nubien et des clés d'exploration aurifère qui en découlent. Enfin, les compléments de recherche qui pourraient faire suite à ces travaux de thèse seront présentés.

Chapitre VI – Complementary data: timing of gold mineralization along the Neoproterozoic Atmur-Delgo and Keraf sutures, western Nubian shield

Avec la contribution de :

Aurélien Eglinger[1], Anne-Sylvie André-Mayer[1], Hugo Ceinturet[1], Yoram Teitler[1], Patrick Carr[1], Jérôme Ganne[2], Marc Poujol[3], Julien Feneyrol[4], Armin Zeh[5], Rémi Bosc[4]

[1] GeoRessources, Université de Lorraine, CNRS, 54000 Nancy, France

[2] IRD, UR234, GET, Université Toulouse III, 14 Avenue Edouard Belin, 31400 Toulouse, France

[3] Géosciences Rennes, UMR CNRS 6118, OSUR, Université Rennes 1, 35042 Rennes Cedex, France

[4] Arethuse Geology EURL, BP 80017, Latitude Arbois, 1060 rue René Descartes, 13290 Les Milles, France

[5] KIT-Karlsruhe Institute of Technology, Campus South, Institute for Applied Geosciences, Mineralogy and Petrology, 76131 Karlsruhe, Germany

Résumé

L'apport de contraintes géochronologiques absolues concernant les événements minéralisateurs est un des fondamentaux de l'approche du système métallogénique puisqu'il permet d'intégrer contexte géodynamique, croissance crustale, mobilité et concentration des métaux au cours du temps. Ces données manquent encore à la parfaite connaissance du système métallogénique de l'or panafricain exprimé le long des zones de suture d'Atmur-Delgo et de Keraf, abordé dans les parties précédentes de ce manuscrit. Nous proposons donc de contraindre par datation U-Pb sur apatite hydrothermale associée à la minéralisation les événements aurifères exprimés par les gisements de Galat Sufar South et WG03.

Le gisement de Galat Sufar South, hébergé par une séquence volcanosédimentaire affectée par des plis en fourreau, a été formé à 737,9±15,6 Ma. Des données complémentaires (i) géochronologiques U-Pb sur zircon provenant d'un intrusif d'arc et (ii) thermodynamiques par calcul de multi-équilibres chlorite-phengite-quartz-eau dans les tufs porteurs de la minéralisation ont également été obtenues. Elles suggèrent que cet événement aurifère est associé à la phase d'accrétion tectonique et au métamorphisme au faciès amphibolite inférieur associés à l'évolution d'un l'arc insulaire le long de la suture d'Atmur-Delgo. Galat Sufar South est à ce jour le gisement aurifère exprimé sous forme de veine le plus ancien du bouclier nubien. Dans la partie centrale de la suture de Keraf, l'épisode d'or orogénique à l'origine du gisement de WG03 est daté entre *ca.* 600-550 Ma. Ces données indiquent que l'activation et/ou réactivation des structures d'ordre multiple héritées de la suture de Keraf en décrochements ductiles-fragiles à fragiles s'exprime de façon (i) répétée et (ii) localisée (iii) jusqu'à 550 Ma au moins.

Mots-clés

Bouclier nubien ; Galat Sufar South ; WG03 ; Datation U-Pb sur apatite; Chronologie des événements aurifères ; Accrétion tectonique ; Collision arc-continent.

Abstract

Bringing geochronological constraints is critical in the mineral system approach, as it enables a better integration between geodynamical evolution, crustal growth processes and metal mobility and concentration modalities. These data are however lacking so far in the characterization of the Pan-African gold mineral system along the Atmur-Delgo and Keraf sutures, western Nubian shield. We therefore aimed at bringing absolute timing data that constrain the deformation-mineralization events forming the Galat Sufar South and WG03 deposits *via* U-Pb dating of hydrothermal apatite coeval to gold mineralization in the studied area.

The formation of the Galat Sufar South gold deposit, hosted in an arc-related volcanosedimentary sequence affected by sheath folding, was dated at 737.9±15.6 Ma. Additional U-Pb dating of magmatic zircon from a subvolcanic intrusive and chlorite-phengite-quartz-water multi-equilibria calculations in ore-hosting volcanosediments suggest the gold event occurred during tectonic accretion and amphibolite-facies metamorphism related to the evolution of an island arc along the Atmur-Delgo suture. The GSS deposit is the oldest lode gold occurrence documented throughout the Nubian shield to date. Moving to the central Keraf suture, the main orogenic gold event contributing to the formation of the WG03 deposit occurred at *ca.* 600-550 Ma, making it the youngest orogenic gold occurrence reported for the Arabian-Nubian shield to date. As the formation of the WG03 deposit relates to ductile-brittle Keraf strike-slip shearing, its age thus constrains the timing of late Keraf arc-continent-collision. These complementary data suggest that the late collisional, episodic ductile-brittle to brittle activation and/or reactivation of the Keraf-related multiple-order shears is repeated, localized and spanned until *ca.* 550 Ma at least.

Keywords

Nubian shield; Galat Sufar South; WG03; U-Pb dating of apatite; Gold event timing; Tectonic accretion; Arc-continent collision.

1. Introduction

In the previous parts of the manuscript, we have followed the mineral system approach to characterize the Pan-African gold mineralization events recorded throughout the complex Atmur-Delgo-Keraf suture system (Fig. 6-1). We successively unraveled (i) the geodynamical evolution of the central Keraf suture and how it fits into the formation of the Gondwana supercontinent (**Part I**), (ii) the relative timing of mineralizing events accounting for the formation of the Galat Sufar South (GSS), WG03, Central Zone and UTM gold deposits, Gabgaba district, and their relationships to the regional deformation history (**Part II**) and (iii) the ore forming processes involved for the GSS and Central Zone deposits (**Part III**). However, if we have provided relative timing constraints on the age of gold events, absolute geochronological constraints are missing so far. The only exception is the WG03 deposit where we can legitimately approximate that the earliest gold event considered to be magmatic(-hydrothermal)-related (Perret et al., under review; **Chapter III**) formed at *ca.* 810 Ma, which is the U-Pb zircon crystallization age of the ore-hosting quartz-diorite intrusion (**Chapter I**). Yet, integrating time as a fourth dimension in addition to the three spatial dimensions in the study of mineral systems is critical to better understand the lithospheric evolution, crustal growth and ore-forming processes relationships (Stein, 2014; Champion and Huston, 2016). Besides, the recent gains in robustness and precision of geochronological methods and the development of analytical devices enabling *in situ* micro-sampling and isotopic composition measurement have favored the collection of geochronological data for mineral systems (Stein, 2014). *In situ* dating indeed prevents from misinterpretation of the obtained isotopic age as micro-structures, textures of the dated mineral phase and its isotopic composition are considered all together.

The most suitable radiogenic systems for gold mineralization dating are Re-Os on mineralization-related ore-bearing sulfide minerals (Arne et al., 2001; Lawley et al., 2013; André-Mayer et al., 2014; Stein, 2014; Yakubchuk et al., 2014; Zoheir et al., 2015; Le

Mignot et al., 2017; Zhang et al., 2017), U-Pb, and Pb-Pb at a lesser extent, on titanite (*e.g.,* Lawley et al., 2014), rutile (*e.g.,* Feng et al., 2020) or apatite genetically associated with mineralization (*e.g.,* Norcross et al., 2000; Yu et al., 2020). These systems indeed present isotopic similar closure temperature ranges (review by Bernet et al., 2019) which are consistent with lower amphibolite to upper greenschist facies ore-forming conditions valid for most of vein-type gold deposits, such as orogenic gold (*e.g.,* Groves et al., 2003; Tomkins and Grundy, 2009). Lower temperature thermogeochronometers, *e.g.*, K-Ar or Ar-Ar on biotite and sericite, apatite fission-track or (U-Th)/He dating, may be used to provide constraints on the cessation of deformation and related hydrothermal flows potentially associated with gold mineralization (*e.g.,* Yang et al., 2014; Liu et al., 2017; Zoheir et al., 2019d). Except from Re-Os dating of sulfide mineral which may provide a direct age on mineralization in case if there is some invisible gold in the system, the main challenge is that gold mineralization can only be constrained by indirect dating on hydrothermal accessory minerals. A robust petrological-structural preliminary study is therefore mandatory to clearly define what are the datable accessory minerals coexisting and coeval with gold mineralization.

In this chapter, we characterize apatite as an accessory mineral coeval to gold mineralization and present additional geochronological data for the GSS (Perret et al., 2020; **Chapter II**) and WG03 deposits (for the main *en échelon* quartz-veining related mineralization; Perret et al., under review; **Chapter III**). Apatite may also occur as a magmatic mineral. It is the case in ore-hosting granitoid intrusions of the Central Zone deposit and dating of this magmatic apatite provide further insights into the timing of these plutonic rocks, which remains uncertain (Perret et al., under review; **Chapter III**). Besides, we bring complementary whole rock geochemical data and coupled U-Pb and Hf isotope analyses for igneous rocks from the GSS area as well as pressure-temperature constraints on GSS gold mineralization to better characterize the related geodynamical setting during the Atmur-Delgo suturing, that is not addressed in details in **Chapter I**.

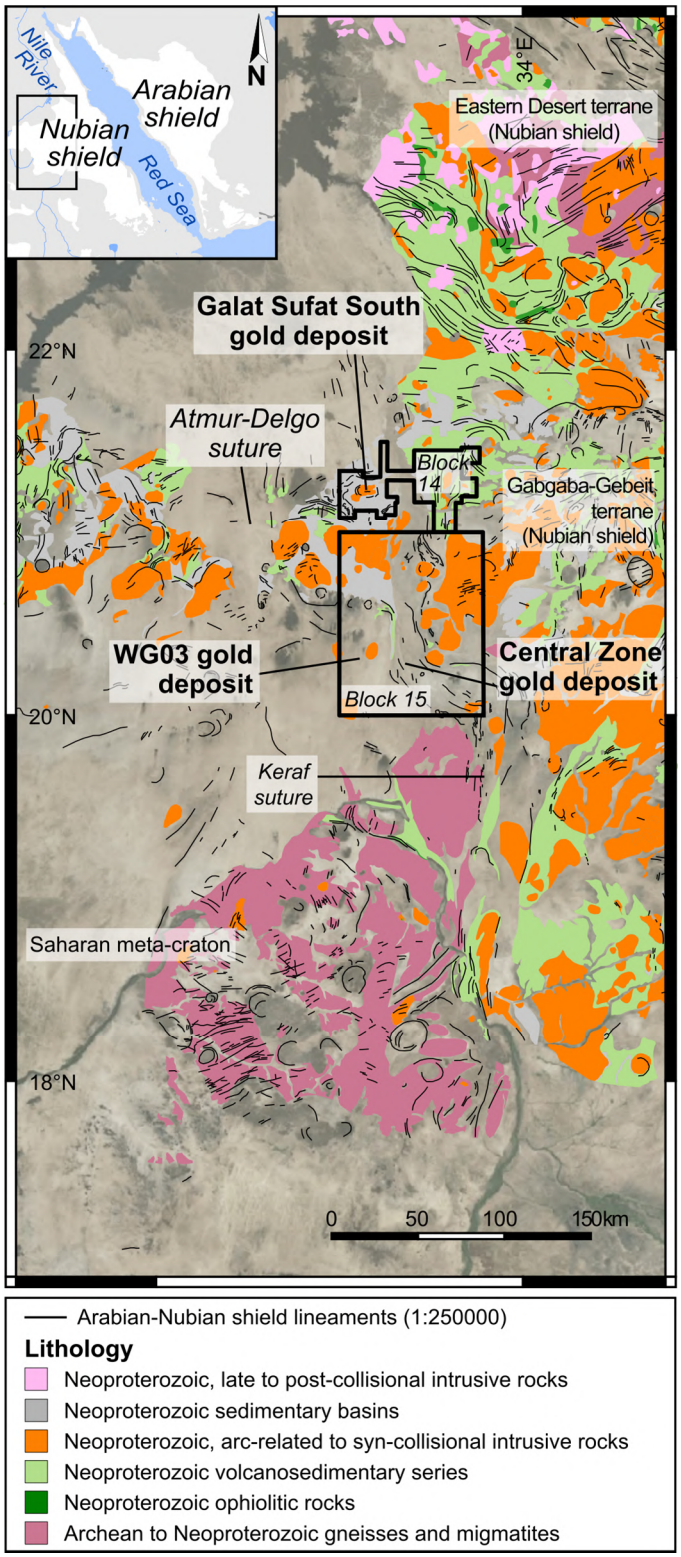


Figure 6-1: Location of the Galat Sufar South, WG03 and Central Zone deposits within the Atmur-Delgo and Keraf sutures, western Nubian shield. Lithological units are drawn from Egypt, Sudan and Eritrea national geological maps (Egyptian Geological Survey and Mining Authority, 1981; Geological Research Authority of the Sudan, 1988; Tadesse et al., 2000) after legend homogenization. Background with no lithological information is Google Satellite imagery from which lineaments have been drawn at 1:250000 scale. Geographic coordinates are reported as WGS 84.

2. Geological setting

The reader is referred to **Part II** for the detailed description of geological settings and district-scale deformation events occurring in the GSS area and across the Gabgaba gold district. As a reminder, the high-strain ductile D_{2GSS} deformation stage is expressed by the main penetrative L_2 stretching lineation and S_2 penetrative fabric throughout the GSS area **(Chapter II)**. These structures, contemporaneous to gold mineralization and controlling the ore-shoot geometry at every scale **(Chapter IV)**, likely result from sheath folding during the regional-scale $D_{1/2ADS}$ Atmur-Delgo suturing, *i.e.*, intra-oceanic subduction and arc-continent collision **(Chapter II)**. Besides, the progressive ductile to ductile-brittle D_1 deformation phase dominates the tectonic setting of the central Keraf suture **(Chapter III)**. We interpreted the D_{1a} deformation stage, expressed by the main regional penetrative cleavage as resulting from thrusting during Keraf arc-Saharan meta-craton collision. However, it is very likely that deformation initiated as early as tectonic accretion and arc-back-arc stacking during Keraf intra-oceanic subduction, but it is weakly to not recorded due to strong superimposition of later deformation. Then, the syn-D_{1b} sinistral Keraf shear zone overprinted the Keraf suture in a prolonged northwest-orientated compressive regime. The main gold mineralization formed at the WG03 and Central Zone deposits, Gabgaba district, at this period **(Chapter III)**.

3. Sampling and analytical techniques

3.1. Sampling philosophy

Sample location and the analytical work carried out for each of them are given in Table 6-1. On first hand, we will present geochemical and isotopic data from Atmur-Delgo arc-related volcanic and pyroclastic rocks collected either on outcrop or diamond drill core in the GSS area. On second hand, we will describe mineral assemblages of interest related to gold-mineralized structures and/or host rocks in drill core samples

from the GSS, WG03 and Central Zone gold deposits. For more clarity, the "meta-" prefix will not precede the name of deformed and metamorphosed rocks in what follows.

Thin sections and one-inch epoxy laser mounts have been prepared. Optical microscopy and additional analyses using a scanning electron microscope in back-scattered electron mode (BSE-SEM) were carried out for petrographic investigation at the GeoRessources laboratory (Université de Lorraine-CNRS, Nancy, France).

				Results presented in this study			
Sample ID	**Easting (°)**	**Northing (°)**	**Description****	*Petrography (Figs. 6-2 to 6-9)*	*Whole-rock geochemistry (Fig. 6-10; Table 6-2)*	*U-Pb and Hf isotopes (Figs. 6-11, 6-12; Tables 6-3, 6-4)*	*Multi-eq. calculation (Figs. 6-13, 6-15; Tables 6-5, 6-6)*
GSS gold deposit (syn-Atmur-Delgo arc)							
GS-OC-01	33.16528	21.24736	Trachyte	x	x	xx	
GS-22-08*	33.16686	20.2845	Ash tuff	x			
GS-24-01*	33.16839	21.22183	Ash tuff	x	x		
GS-34-01*	33.16737	21.22116	Ash tuff	x	x		
GS-34-03*	33.16737	21.22116	Ash tuff	x	x		
GS-34-04*	33.16737	21.22116	Ash tuff	x	x		
GS-34-05*	33.16737	21.22116	Ash tuff	x	x		
GS-34-10*	33.16737	21.22116	Ash tuff	x	x		
GS-34-13*	33.16737	21.22116	Ash tuff	x	x		
GS-34-14*	33.16737	21.22116	Trachyandesite	x	x		
GS-36-07*	33.16682	21.22114	Trachyte	x	x		
GS-36-08*	33.16682	21.22114	Trachyandesite	x	x		
GS-38-17*	33.16582	21.22093	Tephrite	x	x		
GS-38-18*	33.16582	21.22093	Ash tuff	x	x		
GS-38-19*	33.16582	21.22093	Ash tuff	x			
GS-55-02*	33.16735	21.22051	Ash tuff	x		xxx	x
GS-55-03*	33.16735	21.22051	Ash tuff	x	x		
GS-55-04*	33.16735	21.22051	Ash tuff	x		xxx	x
WG03 gold deposit							
WG03-05*	33.1405	20.3578		x			
WG03-11*	33.4512	20.5002	Quartz-diorite cut across by mineralized veins	x		xxx	
WG03-12*	33.4698	20.4969		x		xxx	
Central Zone deposit							
CZ11*	33.1838	20.3233	Altered granitoid	x			
CZ12*	33.1838	20.3233	Granitoid dike cut across by mineralized veins	x		xxx	

Table 6-1: List of studied samples. Geographic coordinates are reported as WGS 84. Analytical work carried out for each sample is detailed.

3.2. Analytical techniques

3.2.1. Micro-X-ray fluorescence mapping

In addition to microscopy work, complementary micro-X-ray fluorescence (XRF) elemental maps were acquired for thin sections from the WG03 and Central Zone deposits using the M4 TORNADO analyzer (GeoRessources, Université de Lorraine-CNRS, Nancy, France) with beam conditions of 50 kV, 300 µA, 30 µm-spatial resolution and 10 ms/pixel-dwell time. Micro-XRF maps were processed to obtain quantitative mineral maps using the open source MARCIA Python routine (Meyer and Cauzid, 2020). Basically, MARCIA enables mineral classification by defining masks that are linear combination of elemental intensities in spectra, as illustrated in Supplementary Material 6-1.

3.2.2. Whole-rock geochemistry

Whole-rock major and trace element compositions of sixteen samples were respectively determined by inductively-coupled plasma optical emission spectrometry and mass spectrometry, using a Thermo Fischer ICap 6500 and a Thermo Fischer IcapQ spectrometers, respectively, at the Service d'Analyse des Roches et des Minéraux (SARM, CRPG-CNRS, Vandœuvre-lès-Nancy, France). Sample preparation, analytical conditions and limits of detection are detailed in Carignan et al. (2001). Relative analytical uncertainties are close to 2% for major elements, and between 5% and 20% for trace elements depending on their concentration. The whole-rock S concentration of studied samples has been measured using a CS-analyzer with a limit of detection of 0.01 wt. % approximately.

3.2.3. Separation, U-Pb dating and Hf isotope analysis of zircon

One Atmur-Delgo arc-related trachyte from the Galat Sufar South area was selected for U-Pb dating and Hf isotope analyses on zircon (Table 6-1). Zircon separation was performed at the Centre de Recherches Pétrographiques et Géochimiques (CRPG-CNRS,

Vandœuvre-lès-Nancy, France). The sample was crushed using a jaw and then a roll crusher. Zircon grains were extracted from the 75-125 and 125-250 µm size fractions using a Frantz magnetic separator and di-iodomethane heavy liquid separation with a density of 3.32 g/cm^3. Selected zircon grains of various shape and size were handpicked in ethanol using a binocular microscope. The most representative crystals were mounted into epoxy resin blocks and then ground and polished to expose their center parts. They were then imaged using back-scattered and secondary electron scanning microscopy (BSE- and SE-SEM) at the Karlsruhe Institute of Technology (Germany).

Zircon grains were first analyzed for U-Pb and later for Hf isotopes by laser ablation-inductively coupled plasma-sector fieldmass spectrometry (LA-ICP-SF-MS). U-Pb dating was performed with a Resonetics M50 193 nm Excimer laser system coupled to a Thermo-Scientific ELEMENT 2 at Goethe University (Frankfurt, Germany). Hf isotopes were analyzed with a Resonetics M50 193 nm Excimer laser system coupled to a Thermo-Scientific NEPTUNE at Goethe University (Frankfurt, Germany). Instruments and processing parameters are described by Gerdes and Zeh (2009) with modifications in Zeh and Gerdes (2012). Laser spots of 40-50 µm diameter for Hf isotope analyses were placed on-top of U-Pb laser spots of 25-33 µm-diameter. εHf_i values are calculated back to $^{206}Pb/^{238}U$ single zircon concordant ages for magmatic zircon grains. Zircon standards used in the bracketing procedure are GJ-1 (Jackson et al., 2004), Plešovice (Sláma et al., 2008) and BB (Santos et al., 2017) for U-Pb dating and GJ-1 (Morel et al., 2008) and Temora 2 (Woodhead et al., 2004; Xu et al., 2004; Woodhead and Hergt, 2005; Wu et al., 2006) for Hf isotopes.

3.2.4. Cathodoluminescence imagery and U-Pb dating of apatite

Five samples, two from GSS, three from WG03 and two from Central Zone gold deposits, were selected for U-Pb dating on apatite (Table 6-1). Apatite grains were imaged by cathodoluminescence using a TESCAN VEGA3 LM scanning electron microscope equipped with a Gatan ChromaCL2UV system at the GeoRessources

laboratory (Fig. 6-2; Université de Lorraine-CNRS, Nancy, France). Analyzed apatite grains from GSS deposit range from up to 500 µm-long subhedral with a sharp zoning between a rounded core and darker rims. Conversely, apatite is weakly zoned and more globular-shaped at the WG03 gold deposit. At the Central Zone deposit, apatite is coarse-grained, euhedral with no limited zoning but it is finer-grained, anhedral with predominant bright cores and relatively thin darker rims where mineralized veins cut across the host granitoid.

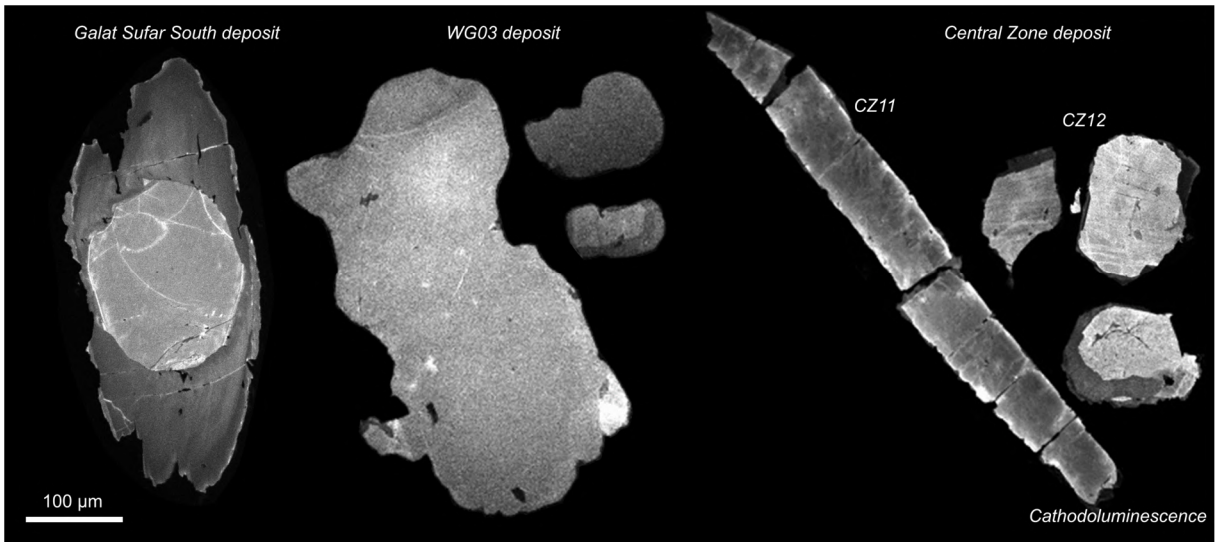


Figure 6-2: Cathodoluminescence photographs representative of dated apatite grains recovered from the Galat Sufar South, WG03 and Central Zone deposits.

U-Pb dating on apatite from the Galat Sufar South gold deposit was conducted at Géosciences Rennes (Université de Rennes-CNRS, France) by *in situ* laser ablation-inductively coupled plasma-mass spectrometry (LA-ICP-MS) using a ESI NWR193UC excimer laser coupled to a quadripole Agilent 7700x ICP-MS equipped with a dual pumping system to enhance sensitivity (Paquette et al., 2014). Prior to each analysis, the background signal, or gas blank, was measured for a duration of 20 s. The beam diameter was set to 40 µm, with a pulse frequency of 5 Hz and a fluence of 5.3 J/cm^2. After a 60 s-long integration time with the laser firing, there is a 10 s delay to wash out the previous sample prior to beginning a new analysis.

U-Pb dating on apatite from the WG03 and Central Zone gold deposits was conducted at the GeoRessources laboratory (Université de Lorraine-CNRS, Nancy, France) using a ESI NWR 193 nm excimer laser coupled to a Nu Atomm LA-ICP-SF-MS. Prior to each analysis, the background signal, or gas blank, was measured for a duration of 20 s. The beam diameter was set to 20 and 50 µm for thin sections and epoxy mounts, respectively, with a pulse frequency of 5 Hz and a fluence of 5 J/cm^2. After a 25 or 40 s-long integration time with the laser firing for thin sections and epoxy mounts, respectively, there is a 20 s delay to wash out the previous sample prior to beginning a new analysis.

The LA-ICP-MS data were reduced with Iolite 3.65 (Paton et al., 2011). For analyses carried out at Géosciences Rennes, apatite standards used in the bracketing procedure are Madagascar (473.5 Ma; Thomson et al., 2012; Cochrane et al., 2014), used as the primary apatite reference material, Durango (31.4 Ma; McDowell et al., 2005) and McClure (523.5 Ma; Schoene and Bowring, 2006). Data were corrected for U–Pb fractionation, common Pb and for mass bias using the Madagascar apatite standard (Chew et al., 2014; Cochrane et al., 2014) following the procedure detailed in Pochon et al. (2016). The Durango and McClure apatite standards measurements were treated as unknown and used to control the reproducibility and accuracy of the corrections. The Durango and McClure standards provided ^{207}Pb-corrected ages of 32.5 ± 0.6 Ma (MSWD = 0.19; probability = 1.00) and 532 ± 6.0 Ma (MSWD = 0.58; probability = 0.91). For the second analytical session carried out at GeoRessources, apatite standards used are McClure and Madagascar. The FC1 apatite reference material is also used, approximating its age is the same as the 1099 Myr-old FC1 zircon (Paces and Miller Jr, 1993; Iwano et al., 2019). In addition, the NIST612 and 614 glass reference materials (Hollocher and Ruiz, 1995) were added in the bracketing procedure during analyses on thin section and epoxy-mounts, respectively, for calibration of U, Th and Pb concentrations. The correction of data followed the same procedure as for the first

analytical session, using either McClure or Madagascar as the primary apatite reference material. The Madagascar or McClure and FC1 standards, treated as unknown, respectively provided ^{207}Pb-corrected ages of 472.1 ± 6.1 Ma (MSWD = 0.33; probability = 1.00), 524.3 ± 2.8 Ma (MSWD = 3.7; probability = 0.00 due to 6 over 30 measurements with a questionable reliability) and 1061.6 ± 7.0 Ma (MSWD = 3.1; probability = 0.001). The reliability of the FC1 apatite standard is questionable as the age of the apatite is considered to be the same as the age of the magmatic zircon but it is not supported by robust isotopic evidence.

3.2.5. Chlorite-phengite-quartz-water multi-equilibria calculations

We observed textural and inferred geochemical equilibria between chlorite - a well-known geothermometer (*e.g.,* Cathelineau and Nieva, 1985; Cathelineau, 1988; Hillier and Velde, 1991; Inoue et al., 2009; Bourdelle et al., 2013; Lanari et al., 2014) -, phengite - a geobarometer (*e.g.,* Massonne and Schreyer, 1987; Parra et al., 2002; Dubacq et al., 2010) - and quartz in the D_{2GSS}-related mineral assemblage at the GSS deposit (see section 4.1.1). This enables to carry out multi-equilibria calculations (*e.g.,* Vidal and Parra, 2000).

As detailed by Ganne et al. (2012), the strength of the multi-equilibrium approach is to resolve pressures and temperatures (*P*-*T*) at thermodynamic equilibrium for high variance mineral paragenesis. Based on the Gibbs phase rule, considering an equilibrium between classical geothermobarometers which have multiple end-members theoretically enables to find a single *P*-*T* couple for crystallization conditions instead of a less constrained *P*-*T* field when using conventional thermobarometry. Multi-equilibria calculations were performed with Matlab© and using the latest thermodynamic model for phengite (Dubacq et al., 2010), which takes into account the *T*-dependent interlayer water content of dioctahedral mica. *P*-*T* estimates for the chlorite, phengite, quartz and water parageneses were calculated using the thermodynamic data of five chlorite and six phengite end-members following the multi-equilibria calculation of Ganne et al. (2012).

These end-members are Fe-amesite (Fe-Am: $Fe_4^{VI}Al_2^{VI}Si_2^{IV}Al_2^{IV}O_{10}(OH)_8$), Mg-amesite (Mg-Am: $Mg_4^{VI}Al_2^{VI}Si_2^{IV}Al_2^{IV}O_{10}(OH)_8$), clinochlore (Clin: $Mg_5^{VI}Al^{VI}Si_3^{IV}Al^{IV}O_{10}(OH)_8$), daphnite (Daph: $Fe_5^{VI}Al^{VI}Si_3^{IV}Al^{IV}O_{10}(OH)_8$) and sudoite (Sud: $\square^{VI}(Fe,Mg)_2^{VI}Al_3^{VI}Si_3^{IV}Al^{IV}O_{10}(OH)_8$) for chlorite, and muscovite (Ms: $K^{XII}Al_2^{VI}Si_3^{IV}Al^{IV}O_{10}(OH)_2$), pyrophyllite (Prl: $\square^{XII}Al_2^{VI}Si_4^{IV}O_{10}(OH)_2$), hydrated pyrophyllite (Prl.H_2O: $\square^{XII}Al_2^{VI}Si_4^{IV}O_{10}(OH)_2 . H_2O$), Fe-celadonite (Fe-Cel: $K^{XII}Fe^{VI}Al^{VI}Si_4^{IV}O_{10}(OH)_2$), Mg-celadonite (Mg-Cel: $K^{XII}Mg^{VI}Al^{VI}Si_4\ O_{10}(OH)_2$) and phlogopite (Phl: $K^{XII}Mg_3^{VI}Si_3\ Al^{IV}O_{10}(OH)_2$) for phengite. With these end-members, 359 equilibria can be written for the chlorite-phengite-quartz-water assemblage. Among them, seven are independent. The P and T of equilibrium between chlorite, phengite and quartz (Qz), as well as the Fe^{3+} content in chlorite and phengite and the water content of phengite, were calculated in order to minimize the sum of the Gibbs free energy of the following seven independent reactions:

(i) Sud + 15 Qz + 10 Fe-Cel + 2 Mg-Am ↔ 4 Prl + 10 Mg-Cel + 2 Daph

(ii) 6 Mg-Cel + 7 Qz + 4 Fe-Am + 4 H_2O ↔ 6 Fe-Cel + 3 Sud + 2 Daph

(iii) 5 Mg-Am + 4 Daph ↔ 5 Fe-Am + 4 Clin

(iv) 14 Qz + 5 Fe-Am + 3 Mg-Am + 8 H_2O ↔ 4 Daph + 6 Sud

(v) 2 Sud + 4 Qz + 4 Daph + 4 Ms → 2 Prl.H_2O + 4 Mg-Cel + 5 Fe-Am

(vi) 1 Prl + 1 H_2O →1 Prl.H_2O

(vii) 11 Qz + 2 Ms + 1 Phl + 2 H_2O → 3 Mg-Cel + 2 Prl

Equilibrium is considered to be achieved when the Gibbs free energy $\sqrt{(\Sigma\Delta G^2/n_r)}$ is below 2400 J, where n_r is the number of equilibria reactions considered (Vidal et al., 2006). $\sqrt{(\Sigma\Delta G^2/n_r)}$ is simplified into $\sqrt{\Sigma\Delta G^2}$ below. Calculated P-T equilibrium couples with Gibbs free energy $\sqrt{\sum\Delta G^2} > 2400$ J are therefore filtered. The pressure and temperature 2σ standard deviations of calculated equilibrium are estimated to ±0.8 kbar and ±10°C (Ganne et al., 2012).

Electron microprobe analyses (EMPA) of coexisting chlorite and phengite were carried out at the GeoRessources laboratory (Université de Lorraine-CNRS, Nancy, France) using a CAMECA SX100 electron probe micro-analyzer (EPMA). Operating conditions were set at 12 nA-emission current, 15 kV-acceleration voltage and 1 µm-beam diameter. The concentrations of Si, Ti, Al, Fe, Mn, Mg, Ca, Na and K were measured. Structural formulae were calculated on a 14-anhydrous-oxygen basis for chlorite and on an 11-oxygen basis for phengite.

4. Results

4.1. Petrographic description of studied samples

4.1.1. Galat Sufar South gold deposit

Samples from the GSS gold deposit area are part of the ore-bearing volcanosedimentary sequence dominating the regional lithological framework (Perret et al., 2020). Andesitic rocks are fine-grained and enclose chlorite patches and plagioclase-quartz porphyroclasts wrapped in the pervasively altered and foliated chlorite-white mica-dominated mineral gangue (Fig. 6-3a, b). Pyroclastic rocks are completely formed of <2 mm-wide ash, thus being ash tuffs (Fisher and Schmincke, 2012). They enclose coarse quartz-plagioclase ash grains wrapped by the S_2 penetrative fabric (Fig. 6-3c, d). Finally, more felsic trachytic intrusive body is dismembered within this rock assemblage and deformed by the S_2 and L_2 fabrics at the outcrop scale (Fig. 6-3e). It displays a subvolcanic porphyritic texture with coarse euhedral plagioclase feldspar grains embedded in a microlithic plagioclase feldspar-quartz-dominated mineral gangue slightly affected by carbonation and sericitization and deformed along the S_2 main fabric (Fig. 6-3e, f).

At the microscopic scale, chlorite, phengite and quartz form most of the silicate mineral assemblage related to the main mineralization-related D_{2GSS} deformation stage in the ore-bearing tuffaceous horizon (see the mineral paragenesis interpreted by Perret et

al. (2020). They are in textural equilibrium (i) in the mineral gangue and (ii) between quartz-chlorite strain fringes around pyrite grains and the phengite-dominated matrix in which pyrite grains are embedded (Fig. 6-4a-d). Besides, syn-D_{2GSS} apatite forms up to 500 µm-long subhedral grains intergrown and stretched in the phengite-chlorite mineral gangue affected by the S_2 fabric in these pyroclastics (Fig. 6-4d, e). Scarcer grains are found as mineral inclusions in altered Py_1 cores where they are overgrown by a mineral inclusion-free Py_2 rim (Fig. 6-4f).

Figure 6-3 (p. 394): Macroscopic and microscopic features of lithologies mapped nearby the Galat Sufar South gold deposit and considered in this study. Mineral abbreviations are Qz = quartz; Cb = carbonate; white mica = generic term for non-discriminated sericite and phengite; Chl = chlorite; Pl = plagioclase feldspar; Fe-Ti ox. = Fe-Ti oxides. **a** (natural light) and **b** (plane-polarized, transmitted light) Schistose chlorite-sericite-dominated trachyte with chlorite and plagioclase-quartz porphyroclasts stretched along the S_2 penetrative fabric. **c** (natural light) and **d** (cross-polarized, transmitted light) Schistose ash tuff with a quartz-white mica-chlorite-rich mineral gangue enclosing coarse quartz-plagioclase ash grains wrapped by the S_2 penetrative fabric. **e** (natural light) and **f** (cross-polarized, transmitted light) Pre- to syn-Atmur-Delgo trachyte affected by the S_2 and L_2 fabrics at the outcrop scale (inset) and showing a subvolcanic porphyritic texture with coarse euhedral plagioclase feldspar grains embedded in a microlithic plagioclase feldspar-quartz-dominated mineral gangue.

Figure 6-4 (p. 395): Syn-gold mineralization D_{2GSS}-chlorite-phengite-apatite-pyrite mineral assemblage in ash tuffs at the Galat Sufar gold deposit. Mineral abbreviations are Ap = apatite; Ccp = chalcopyrite; Chl = chlorite; Gers = gersdorffite; Phg = phengite; Py = pyrite; Qz = quartz. Index refers to the mineral generation inherited from protolith (index "0") or occurring during subsequent D_{1GSS} to D_{4GSS} deformation events (index "1" to "4"), in agreement with the petrological-structural model of Perret et al. (2020). **a** Hydrothermal chlorite and phengite bands alternate and are intimately intergrown along the S_2 main fabric (plane-polarized, transmitted light). **b** D_{2GSS}-related quartz-chlorite asymmetrical strain fringes formed around $Py_{1/2}$ grains embedded in the phengite-dominated schistose mineral gangue (cross-polarized, transmitted light). **c** There is evidence for a textural equilibrium between D_2-related intergrown chlorite and phengite from the mineral gangue. The position of EMPA dataspots for coexisting chlorite and phengite is indicated (back-scattered electron mode, scanning electron microscopy, BSE-SEM). **d** Chlorite and phengite are spatially associated (<200 µm-distant) at the contact between D_{2GSS}-related chlorite-rich strain fringe and phengite-dominated altered mineral gangue. The position of EMPA dataspots for coexisting chlorite and sericite is indicated. Up to 200 µm-wide anhedral to subhedral apatite is intergrown with phengite and preferentially grown along the S_2 penetrative fabric (BSE-SEM). **e** Apatite mostly occurs as fine-grained elongated crystals intergrown with phengite in the schistose mineral gangue which is weakly overprinted by late carbonation and pyritization (BSE-SEM). **f** Apatite also occurs as <40 to 80 µm-wide euhedral mineral inclusions coexisting with chalcopyrite at the core of a zoned $Py_{1/2}$ pyrite grain (BSE-SEM).

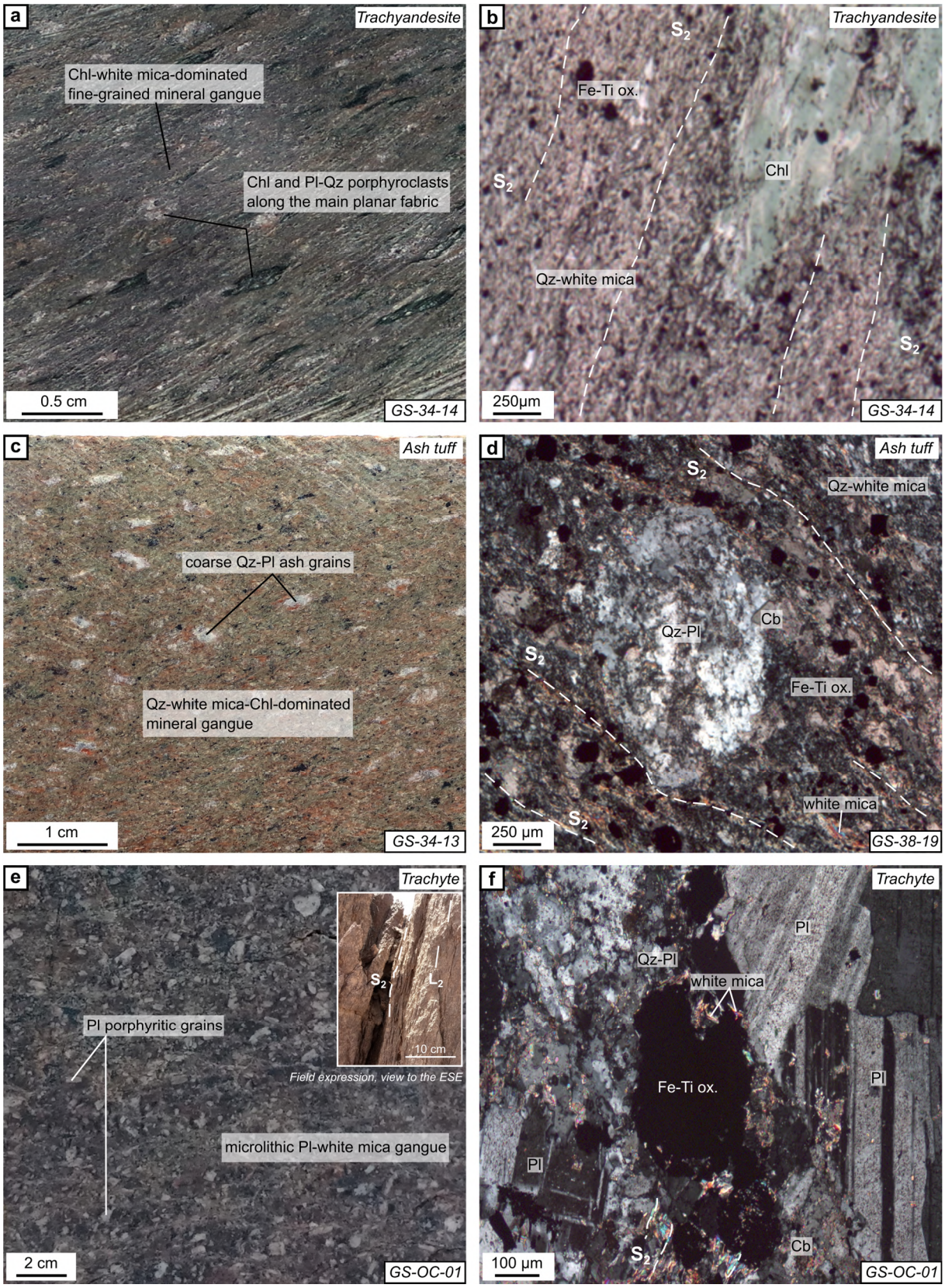


Figure 6-3: Macroscopic and microscopic features of lithologies mapped nearby the Galat Sufar South gold deposit and considered in this study. See detailed caption on p. 393.

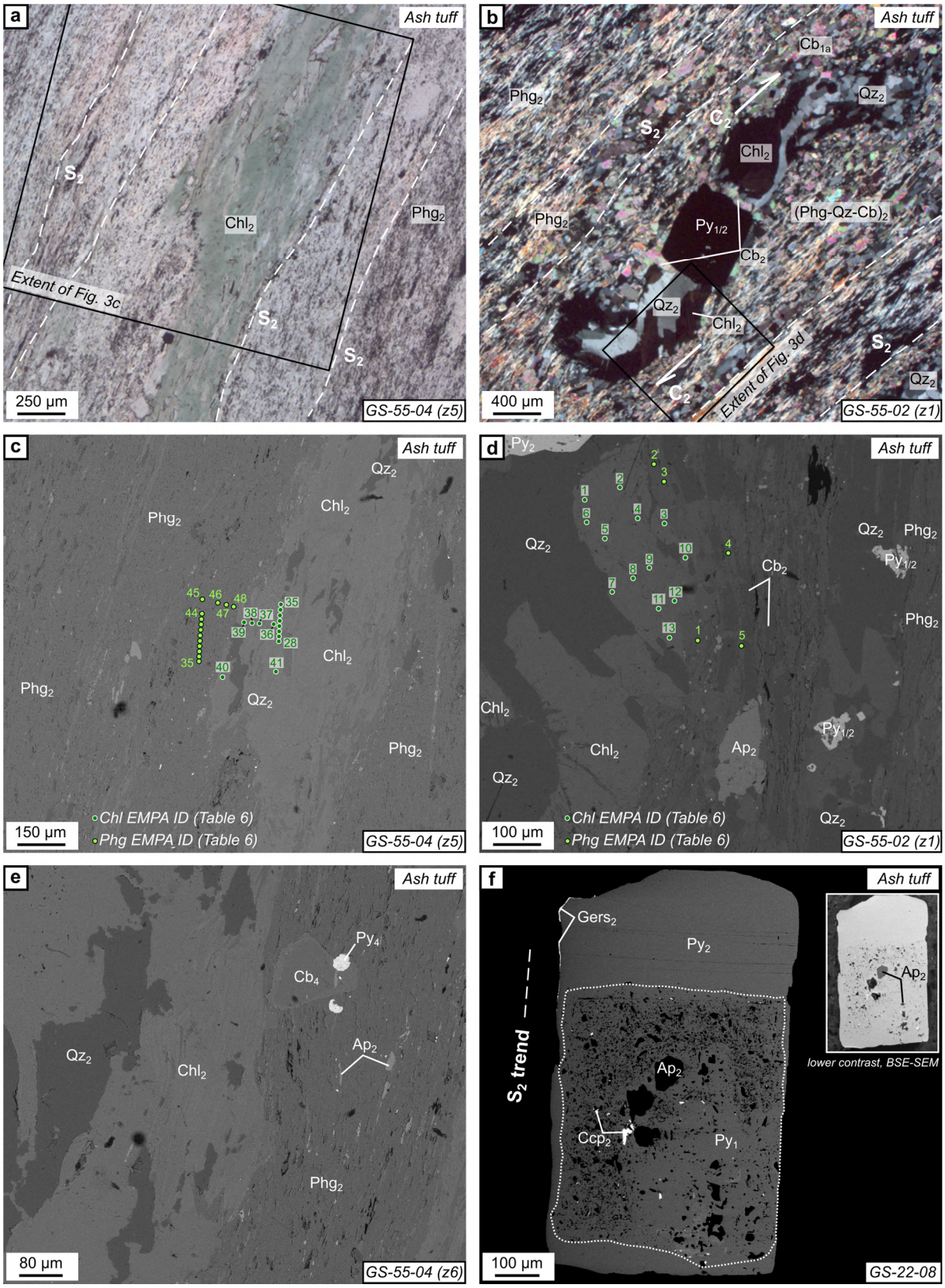


Figure 6-4: Syn-gold mineralization D_{2GSS}-chlorite-phengite-apatite-pyrite mineral assemblage in ash tuffs at the Galat Sufar gold deposit. See detailed caption on p. 393.

4.1.2. WG03 gold deposit

Samples from the WG03 gold deposit are quartz-diorite cut across by mineralized quartz-dominated *en échelon* veins accounting for most of the gold mineralization (Figs. 6-5a, 6-6a, 6-7a; **Chapter III**; Perret et al., under review). The mineral gangue of the quartz-diorite is metamorphosed in the amphibolite facies and dominated by amphibole, plagioclase, and biotite with disseminated pyrrhotite-chalcopyrite-magnetite patches and rare ilmenite (Figs. 6-5b-d, 6-6b-d, 6-7b-d). Greenschist facies retrograde metamorphism is expressed by pyrite replacement of pyrrhotite, chlorite and epidote-titanite patches cut across by the mineralized veins (Figs. 6-5d, 6-6d, 6-7d). Apatite occurs mostly as up to 500 µm-long globular grains in proximal alteration to these veins (Figs. 6-2, 6-5d, 6-6d, 6-7d).

4.1.3. Central Zone gold deposit

The CZ11 sample from the Central Zone gold deposit is a granitoid intrusive affected by pervasive albitization and sericitization, mostly, with coarse-grained, acicular, euhedral apatite grains enclosed within the mineral gangue (Fig. 6-8a-d). Where cut across by a dilational mineralized carbonate-albite-quartz veins (Fig. 6-9a; Perret et al., under review), a fragment of the ore-hosting granitoid is trapped between the carbonate-albite edge of the vein with comb texture and the massive quartz inner infilling, suggesting a crack-seal formation mechanism (Fig. 6-9a-c; **Chapter V**). There is evidence for intense pervasive carbonation, albitization, sericitization and moderate pyritization that almost completely overprint the original mineral assemblage of the granitoid (Fig. 6-9b-d). Apatite occurs as up to 100 µm-wide anhedral to fractured weakly zoned grains widespread in the granitoid mineral gangue deformed by the mineralized vein (Fig. 6-9d).

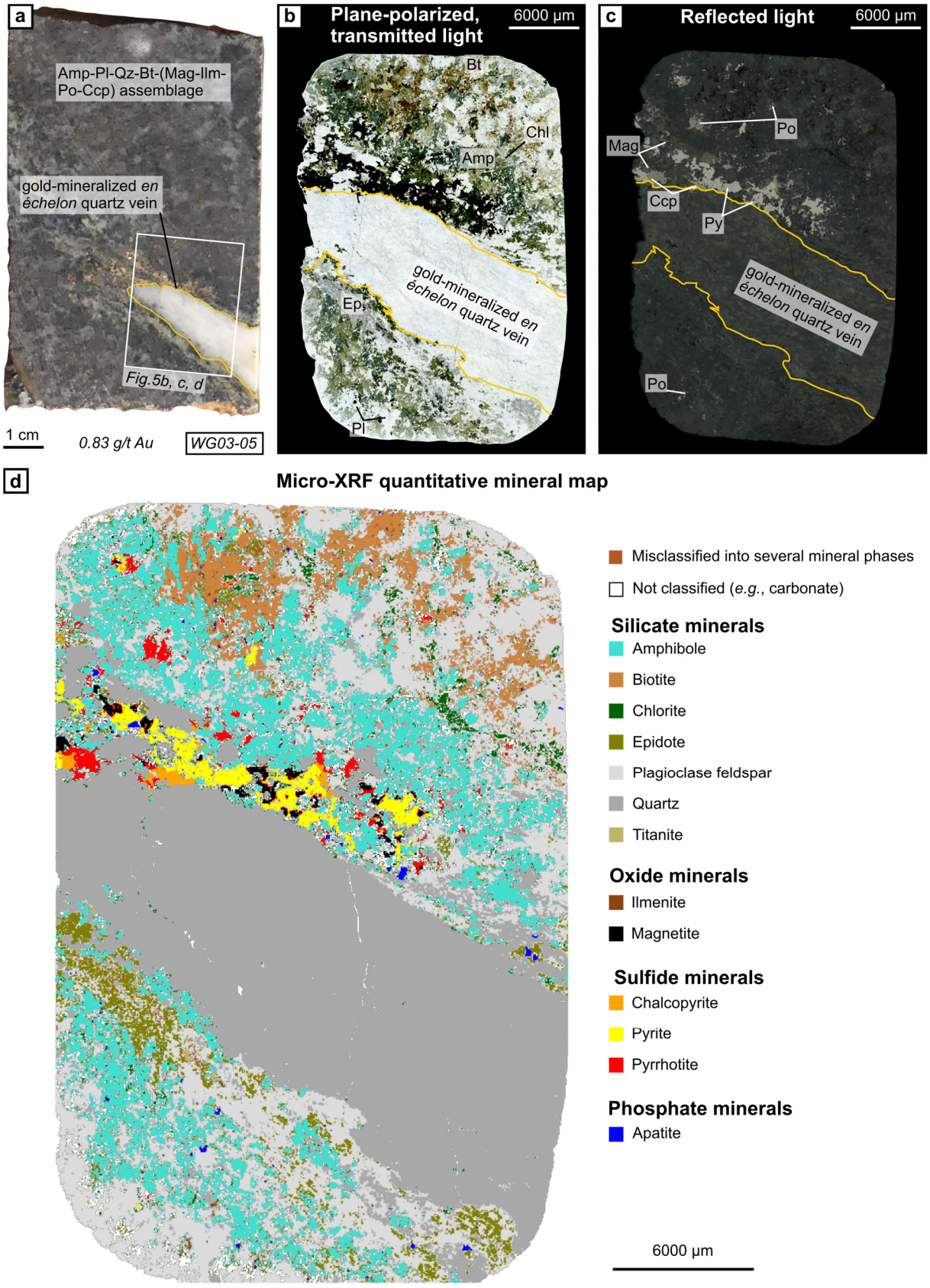


Figure 6-5: Syn-gold mineralization hydrothermal apatite at the WG03 deposit, Gabgaba gold district (WG03-05). See detailed caption on p. 402.

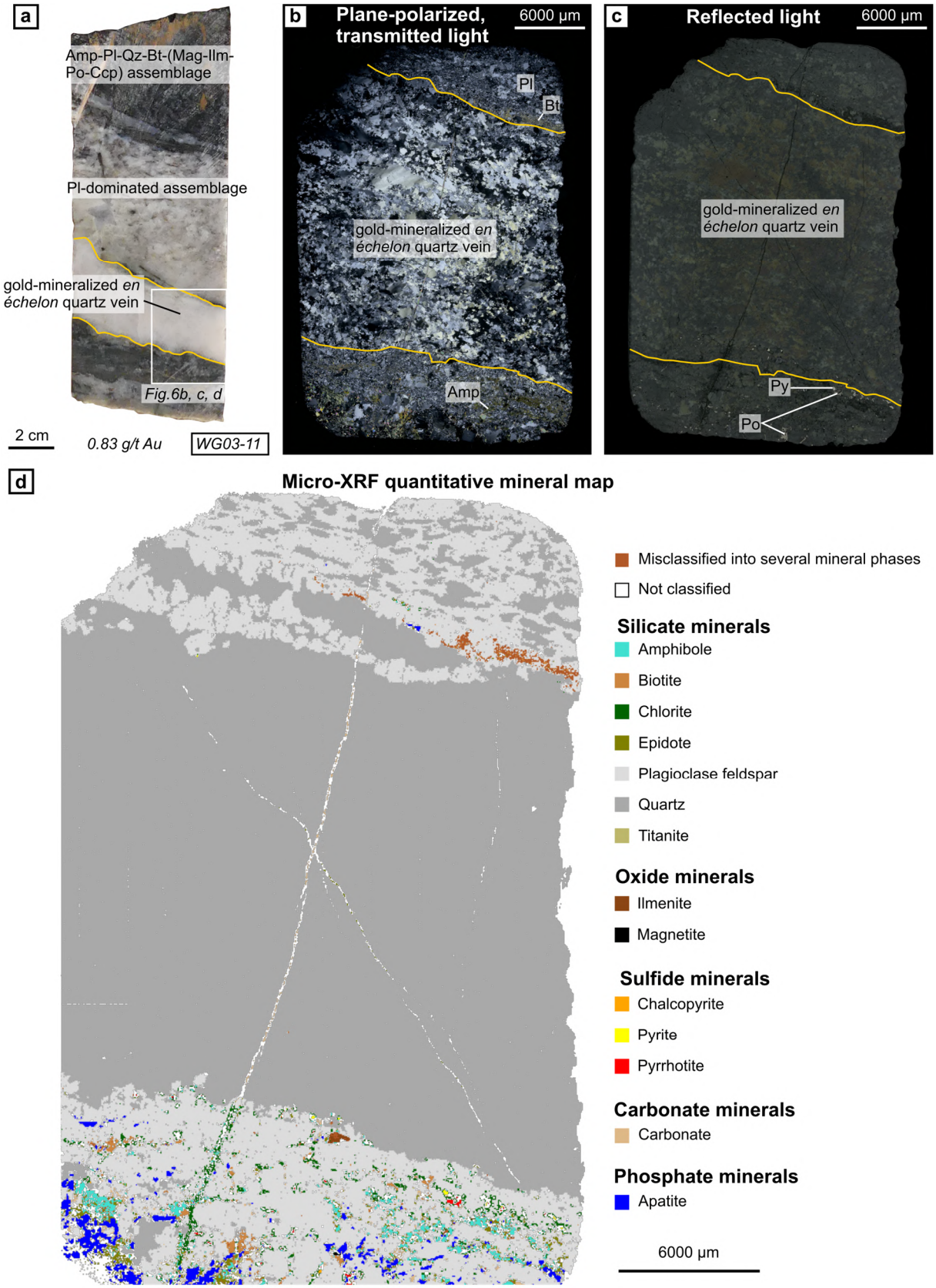


Figure 6-6: Syn-gold mineralization hydrothermal apatite at the WG03 deposit, Gabgaba gold district (WG03-11). Same legend as for Figure 6-5, in addition to the presence of carbonate (Cb) as a proximal marker of mineralized veins. Please note that chlorite is misindexed as infilling mineral of late cracks cutting across mineralized veins.

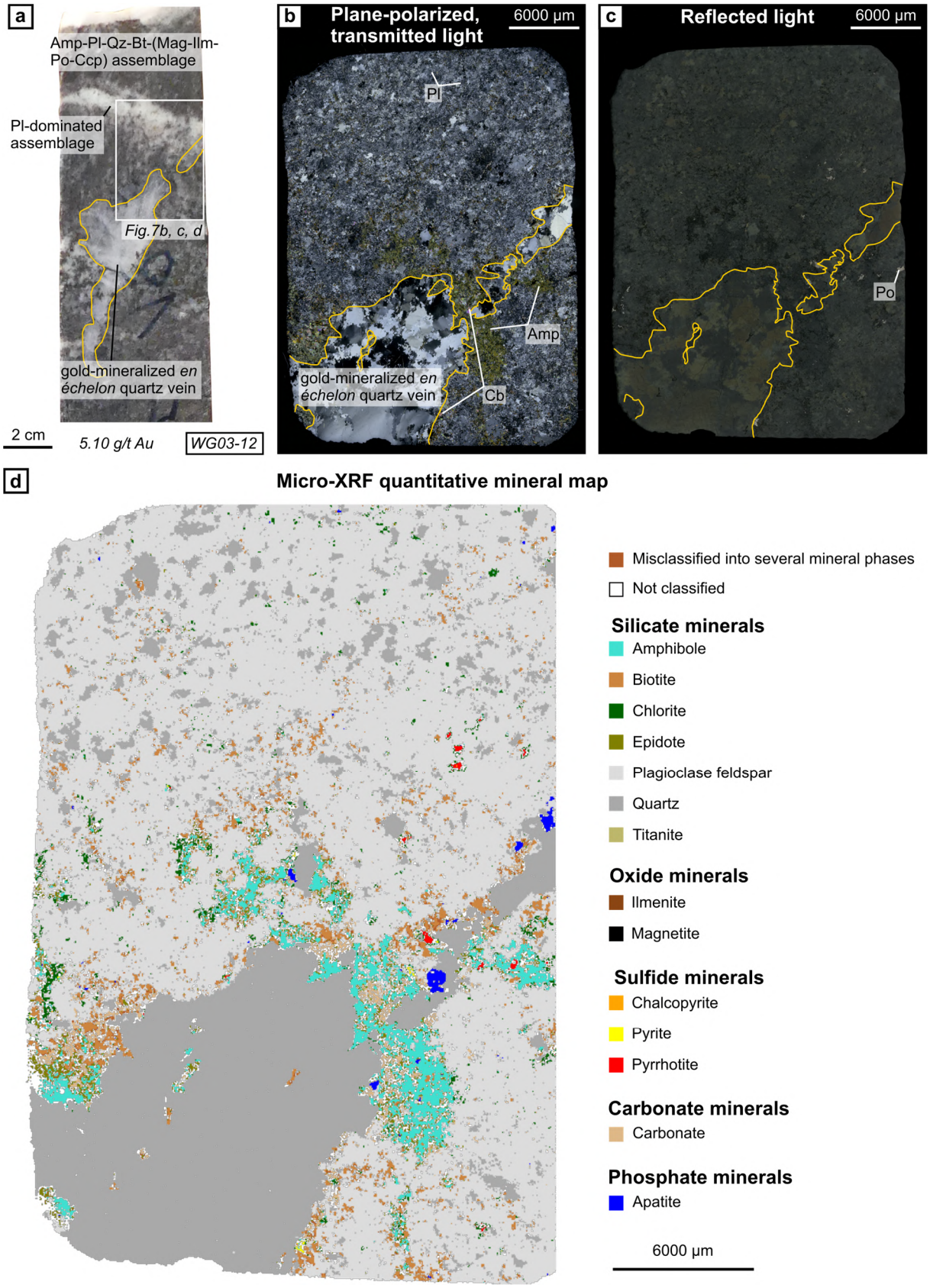


Figure 6-7: Syn-gold mineralization hydrothermal apatite at the WG03 deposit, Gabgaba gold district (WG03-12). Same legend as for Figure 6-5, in addition to the presence of carbonate (Cb) as a proximal marker of mineralized veins.

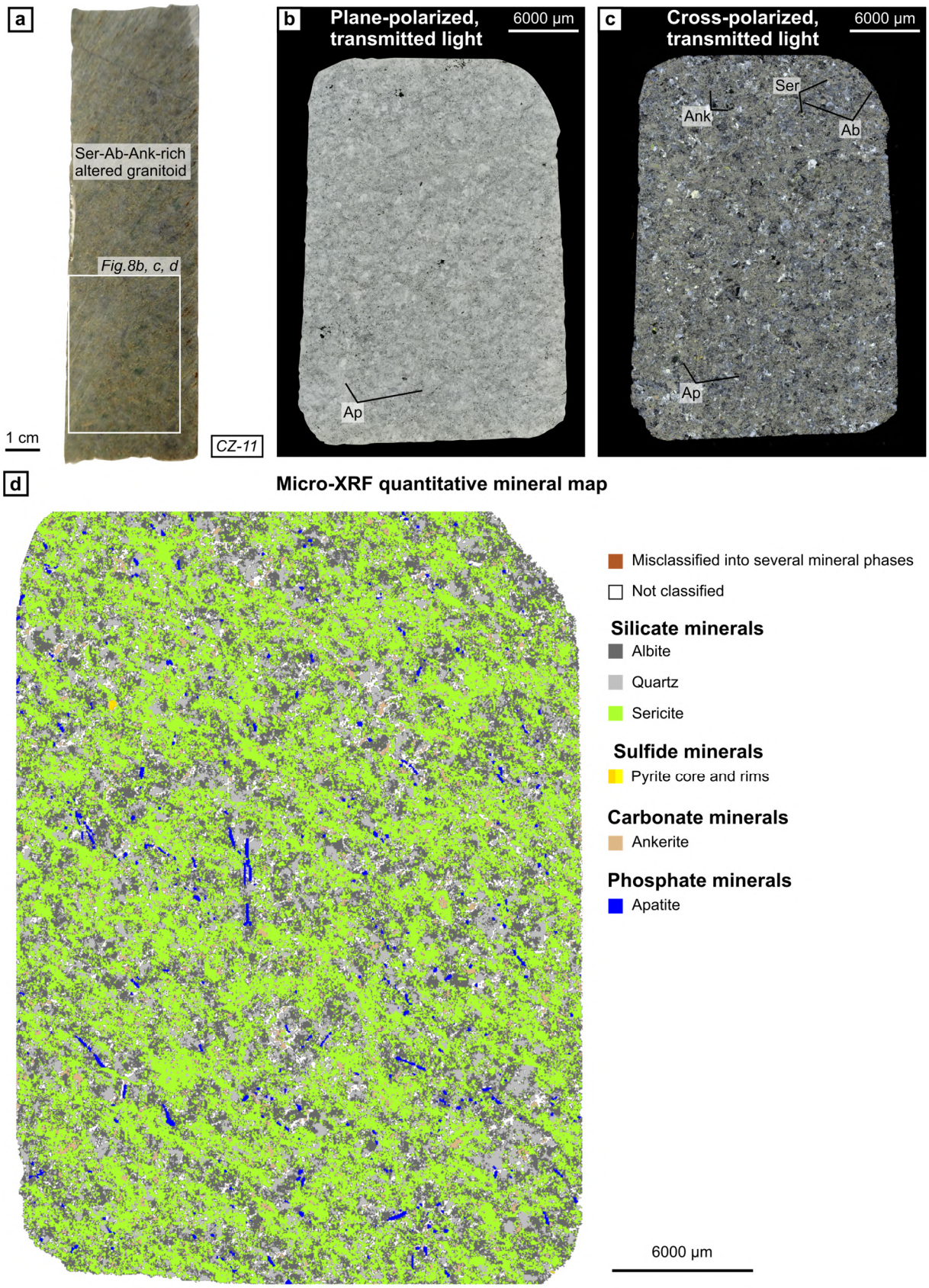


Figure 6-8: Magmatic apatite in ore-hosting granitoid at the Central zone deposit, Gabgaba gold district (CZ11). See detailed caption on p. 402.

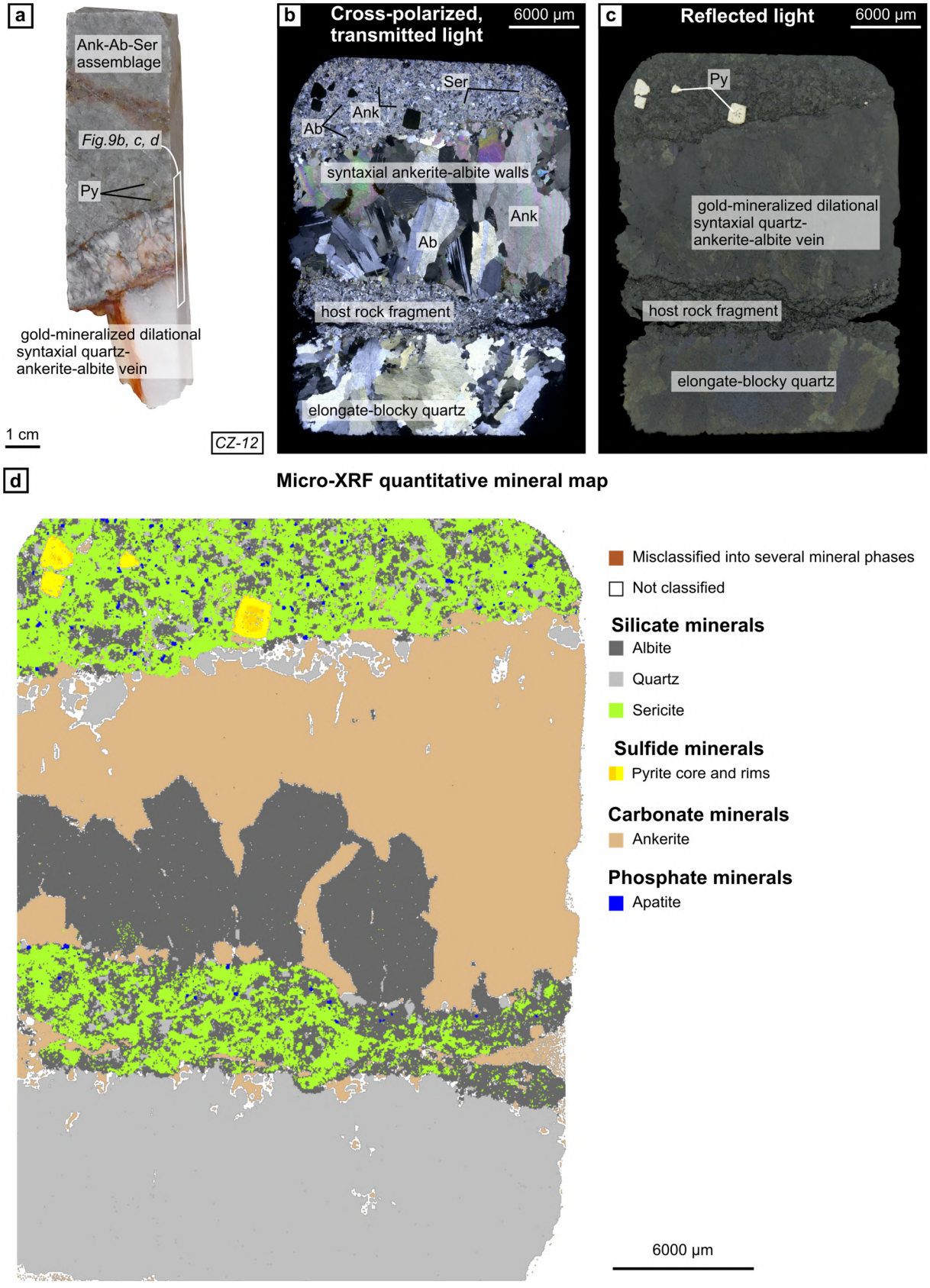


Figure 6-9: Magmatic apatite in ore-hosting granitoid at the Central zone deposit, Gabgaba gold district (CZ12). See detailed caption on p. 402.

Figure 6-5 (p. 397): Syn-gold mineralization hydrothermal apatite at the WG03 deposit, Gabgaba gold district (WG03-05). Mineral abbreviations are Amp = amphibole; Bt = biotite; Ccp = chalcopyrite; Chl = chlorite; Ep = epidote: Ilm = ilmenite; Mag = magnetite; Pl = plagioclase feldspar; Py = pyrite; Po = pyrrhotite; Qz = quartz; **a** Photograph of the drill core sample from which the thin section illustrated by **b** (plane-polarized, transmitted light), **c** (reflected light) and **d** (micro-XRF quantitative mineral map) has been made. The sample is characterized by a quartz-dominated vein that cuts across the WG03 deposit-hosting quartz-diorite. The vein cuts across the amphibole-plagioclase-biotite-pyrrhotite-(chalcopyrite-magnetite-ilmenite) preexisting mineral gangue. A proximal alteration halo of pyrite, apatite, epidote and titanite surrounds the vein and overprints the mineral gangue assemblage.

Figure 6-8 (p. 400): Magmatic apatite in ore-hosting granitoid at the Central zone deposit, Gabgaba gold district (CZ11). Mineral abbreviations are Ab = albite; Ank = ankerite; Ap = apatite; Ser = sericite. **a** Photograph of the drill core sample from which the thin section illustrated by **b** (cross-polarized, transmitted light), **c** (reflected light) and **d** (micro-XRF quantitative mineral map) has been made. The sample is characterized by a purely dilational syntaxial carbonate-albite-quartz mineralized vein that cuts across the Central Zone mineralization-hosting granitoids. The granitoid mineral gangue is affected by intense pervasive carbonation, albitization and sericitization and weak pyritization. Apatite forms as a proximal alteration marker of the mineralized vein.

Figure 6-9 (p. 401): Magmatic apatite in ore-hosting granitoid at the Central zone deposit, Gabgaba gold district (CZ12). Mineral abbreviations are Ab = albite; Ank = ankerite; Py = pyrite; Ser = sericite. **a** Photograph of the drill core sample from which the thin section illustrated by **b** (cross-polarized, transmitted light), **c** (reflected light) and **d** (micro-XRF quantitative mineral map) has been made. The sample is characterized by a purely dilational syntaxial carbonate-albite-quartz mineralized vein that cuts across the Central Zone mineralization-hosting granitoid. The mineral gangue is affected by intense pervasive carbonation, albitization, sericitization and pyritization. Apatite forms fractured grains widespread in the granitoid host rock and fragments.

4.2. Whole-rock geochemistry

The major element compositions classify syn-Atmur-Delgo suture volcanic and subvolcanic rocks of the GSS area as mostly intermediate, metaluminous, I-type trachyandesite to trachyte with a single basic tephrite sample (Table 6-2; Fig. 6-10a, b). Despite the procedure detailed in Le Maitre et al. (2005) compels from using the Total Alkali-Silica and A/NK *vs* A/CNK diagrams to classify volcanoclastic rocks, it appears that ash tuffs of the GSS area have compositions similar to (sub)volcanic rocks, confirming they are all from a single volcanosedimentary pile. Both subvolcanic, volcanic and volcanoclastic rocks consistently display chondrite-normalized rare earth element (REE) patterns with a steeper decreasing slope for light REE than for heavy REE (Fig.

6-10c-e). The Eu anomaly is negative and weak to null for all samples. The wider diversity in both major elements and REE behavior for volcanoclastic rocks regarding volcanic rocks likely results from some mixing with sediments that may not necessary derive from igneous rocks crystallized from the same magmatic pulse(s).

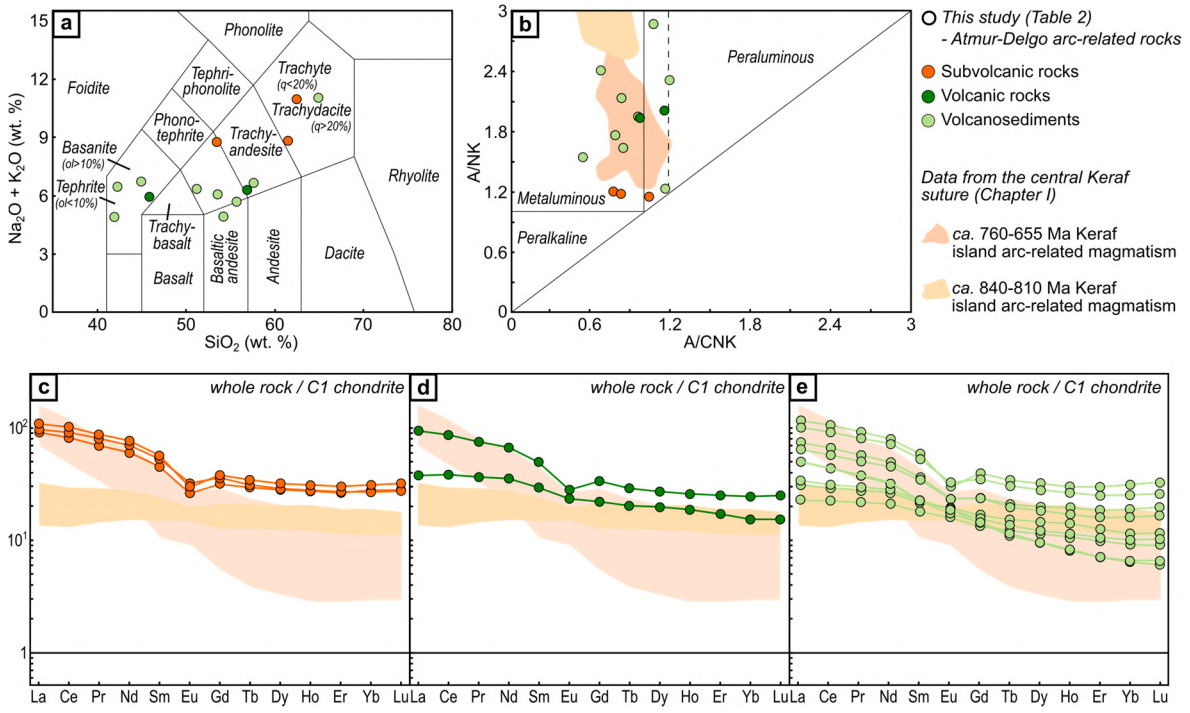


Figure 6-10: Whole-rock major and trace element composition of Galat Sufar South igneous and pyroclastic rocks. Whole rock compositional data for island arc magmatism in the central Keraf suture are plotted (**Chapter I**). **a** Total Alkali-Silica classification diagram for (sub)volcanic rocks (Le Bas et al., 1992). ol and q refer to the modal proportion of olivine and quartz, respectively. **b** A/CNK vs A/NK crossplot for all samples (Shand, 1943). C1 chondrite-normalized rare earth trace element diagram (Sun and McDonough, 1989) for (**c**) subvolcanic rocks, (**d**) volcanic rocks and (**e**) volcanosediments. Whole-rock compositions of samples from this study are compiled in Table 6-2.

ID	*Atmur-Delgo arc-related (sub)volcanic rocks*					*Atmur-Delgo arc-related volcanoclastic rocks*								
	GS-OC-1	GS-36-07	GS-36-08	GS-34-14	GS-38-17	GS-24-01	GS-34-01	GS-34-03	GS-34-04	GS-34-05	GS-34-10	GS-34-13	GS-38-18	GS-55-03
Major elements (wt. %)														
SiO_2	61.5	62.5	53.4	56.9	45.9	41.9	54.3	53.6	51.2	42.3	65.0	57.7	44.9	55.7
Al_2O_3	15.0	15.2	15.7	15.4	16.2	13.6	15.4	14.6	14.9	13.5	14.7	14.0	15.5	16.2
Fe_2O_3	5.2	5.9	7.8	7.5	10.0	9.3	5.5	5.9	8.4	8.2	4.0	6.0	9.7	5.8
MnO	0.13	0.12	0.54	0.17	0.18	0.18	0.18	0.20	0.19	0.32	0.02	0.20	0.27	0.24
MgO	0.28	0.49	2.1	3.1	3.7	5.4	2.7	2.3	3.0	5.0	0.19	2.0	3.5	2.2
CaO	3.9	0.84	3.2	3.1	4.6	8.0	5.0	5.6	4.4	8.9	0.42	4.5	6.2	3.5
Na_2O	5.2	2.3	7.0	1.6	3.5	0.58	0.07	3.1	1.4	3.1	0.12	2.5	0.05	1.6
K_2O	3.6	8.7	1.8	4.7	2.4	4.3	4.8	3.0	4.9	3.3	10.9	4.1	6.6	4.1
TiO_2	0.57	0.80	0.81	0.81	1.1	0.76	0.71	0.71	0.81	0.72	0.69	0.72	0.90	0.75
P_2O_5	0.18	0.30	0.35	0.33	0.24	0.19	0.17	0.21	0.20	0.15	0.25	0.31	0.18	0.18
S	0.04	0.02	4.0	<0.01	0.48	<0.01	0.08	1.3	2.8	2.1	2.8	<0.01	0.04	0.06
L.O.I.	3.8	2.0	6.7	5.5	10.7	14.7	10.0	10.0	9.4	14.3	2.8	6.9	11.1	8.4
Minor and trace elements (ppm)														
Au*	0.02	0.05	0.30	<0.01	<0.01	0.02	0.06	0.20	1.1	6.5	0.14	0.16	0.27	<0.01
As	14.8	6.6	8.1	7.1	10.0	6.1	7.6	31.1	106	55.9	91.5	10.5	17.8	6.1
Ba	436	1107	367	421	108	182	436	418	268	188	433	318	246	573
Be	1.6	1.3	1.2	2.5	1.0	0.67	1.3	0.80	1.9	0.90	1.3	1.7	1.0	1.2
Cd	0.09	0.08	0.63	0.21	0.06	0.10	0.29	0.25	0.42	0.44	0.42	0.22	0.07	0.30
Co	6.2	3.0	14.1	15.3	30.7	30.2	14.3	13.0	32.0	30.7	3.0	14.5	27.4	13.3
Cr	6.9	8.4	41.7	102	150	87.6	50.9	31.4	101	93.9	6.9	45.7	56.0	55.7
Cs	0.45	0.58	0.49	1.5	0.71	1.3	0.90	0.35	0.80	0.55	0.42	1.1	1.4	1.0
Cu	<2.0	7.2	154	7.2	11.0	<2.0	37.2	39.4	88.5	140	190	3.7	7.8	22.0
Ga	18.9	20.9	16.8	19.4	19.4	15.5	19.1	17.8	21.5	15.1	21.8	17.8	18.4	19.6
Ge	1.3	1.6	1.3	1.9	1.3	1.3	1.2	1.1	1.6	1.1	1.8	1.9	1.8	1.1
Hf	9.0	9.9	7.6	7.3	3.0	1.8	3.1	5.6	5.1	1.7	10.4	7.2	2.1	3.2
In	0.04	0.04	<0.03	0.06	0.06	0.05	0.04	<0.03	0.07	<0.03	0.07	0.05	0.05	0.04
Nb	7.2	8.2	6.8	6.1	2.0	1.5	1.9	4.4	4.1	1.2	8.6	6.1	1.7	2.0

Table 6-2 ***(continued)***

ID	*Atmur-Delgo arc-related (sub)volcanic rocks*					*Atmur-Delgo arc-related volcanoclastic rocks*								
	GS-OC-1	GS-36-07	GS-36-08	GS-34-14	GS-38-17	GS-24-01	GS-34-01	GS-34-03	GS-34-04	GS-34-05	GS-34-10	GS-34-13	GS-38-18	GS-55-03
Minor and trace elements (ppm)														
Ni	3.5	3.8	21.5	24.4	24.9	26.6	19.5	13.7	35.6	30.0	<2.0	13.5	21.5	19.9
Pb	8.0	12.4	43.9	3.4	3.5	3.4	8.5	8.5	131	12.2	16.6	5.1	2.6	5.5
Rb	89.6	111	34.4	107	55.5	87.5	115	51.3	101	67.7	141	95.2	148	108
Sb	0.61	4.5	4.6	4.7	5.9	8.4	4.8	4.7	9.1	6.9	49.8	4.0	4.4	3.4
Sc	10.8	13.2	15.6	19.1	35.9	25.7	10.1	11.0	24.2	26.1	11.4	14.9	28.0	10.8
Sn	2.0	3.4	2.4	2.6	1.7	0.84	1.1	2.8	2.6	1.2	4.4	2.0	1.0	1.2
Sr	85.2	79.1	59.5	91.0	64.7	184	141	154	205	222	67.9	76.6	68.9	108
Ta	0.54	0.62	0.51	0.47	0.16	0.11	0.18	0.35	0.32	0.10	0.67	0.45	0.13	0.18
Th	5.0	5.9	4.6	4.3	1.1	0.87	1.9	3.4	2.9	0.73	6.3	4.2	1.0	1.9
U	2.7	2.8	1.7	2.4	0.59	0.48	0.83	1.7	1.7	0.42	3.3	2.1	0.50	0.81
V	57.8	73.5	49.9	91.4	327	228	109	83.7	201	193	47.2	66.3	249	118
W	0.9	19.1	10.4	6.8	12.5	4.5	2.3	11.5	22.6	29.0	12.8	6.9	6.7	1.1
Y	40.2	43.7	39.5	36.8	26.3	15.9	11.9	24.7	27.2	15.3	42.5	39.0	19.5	11.4
Zn	51.9	76.2	215	195	76.1	66.9	148	111	171	153	68.4	123	80.6	291
Zr	334	364	271	262	99.6	60.6	108	203	171	54.9	371	268	71.2	109
La	21.3	25.8	23.0	22.1	8.9	7.5	11.8	17.5	15.1	5.4	27.8	24.2	8.0	11.9
Ce	49.4	62.3	55.1	52.6	23.2	18.1	26.4	40.9	35.2	13.9	65.8	56.7	19.0	27.1
Pr	6.3	8.1	7.4	6.9	3.4	2.6	3.5	5.3	4.7	2.0	8.6	7.5	2.7	3.5
Nd	26.9	34.4	32.1	30.2	16.1	12.2	14.6	22.6	20.6	9.6	36.5	33.0	12.9	15.0
Sm	6.6	8.2	7.8	7.3	4.3	3.2	3.3	5.3	5.0	2.7	8.7	7.8	3.3	3.3
Eu	1.5	1.6	1.8	1.6	1.3	1.0	1.0	1.3	1.3	0.90	1.7	1.8	1.1	1.0
Gd	6.3	7.5	7.1	6.6	4.3	3.0	2.8	4.7	4.7	2.7	7.8	7.0	3.3	2.8
Tb	1.1	1.2	1.1	1.0	0.73	0.48	0.42	0.72	0.76	0.44	1.2	1.1	0.55	0.4
Dy	6.9	7.8	7.0	6.6	4.8	3.0	2.4	4.5	4.9	2.8	7.9	6.9	3.6	2.3
Ho	1.5	1.7	1.5	1.4	1.0	0.62	0.45	0.93	1.1	0.60	1.7	1.5	0.8	0.44

Table 6-2 ***(continued)***

ID	*Atmur-Delgo arc-related (sub)volcanic rocks*					*Atmur-Delgo arc-related volcanoclastic rocks*								
	GS-OC-1	GS-36-07	GS-36-08	GS-34-14	GS-38-17	GS-24-01	GS-34-01	GS-34-03	GS-34-04	GS-34-05	GS-34-10	GS-34-13	GS-38-18	GS-55-03
Minor and trace elements (ppm)														
Er	4.2	4.8	4.2	4.0	2.7	1.6	1.1	2.6	3.0	1.6	4.8	4.0	2.0	1.1
Tm	0.66	0.75	0.66	0.61	0.40	0.25	0.16	0.40	0.48	0.24	0.76	0.62	0.30	0.16
Yb	4.4	5.0	4.2	4.0	2.4	1.6	1.0	2.6	3.0	1.5	5.1	4.1	1.8	1.0
Lu	0.69	0.79	0.67	0.62	0.37	0.25	0.16	0.41	0.49	0.23	0.81	0.65	0.28	0.15
Total	99.4	99.1	99.4	99.2	98.6	98.9	98.7	99.2	98.7	99.8	99.0	99.0	99.0	98.7

L.O.I. = loss on ignition.

Total is given in wt.%.

** For drill core samples, the gold content refers to unpublished fire assay results provided by Orca Gold Inc. Au concentration in GS-OC-01 dacite is from ALS fire assays.*

Table 6-2: Results of major and trace elements of whole-rock analyses for samples from the Galat Sufar South gold deposit.

4.3. U-Pb ages and Hf compositions of zircon

U-Pb and Hf isotope laser spot emplacements on BSE-SEM images of dated zircon grains are provided in Supplementary Material 6-2. Results and raw data processing details for U-Pb and Hf isotopic composition of zircon are given in Tables 6-3 and 6-4, respectively. U-Pb and Hf isotopic compositions of zircon standards used in this study are the ones of the first analytical session in Supplementary Materials 1-2 and 1-3 of **Chapter I**, respectively.

Recovered zircon grains range from weakly to strongly prismatic grains with a pyramidal shape, are strongly fractured and show no to weak oscillatory magmatic zoning with patchy recrystallization patterns. The most significantly zoned zircon grains are composed of a subrounded core serving as a substrate for later zircon autocryst overgrowing and may be considered as antecrysts, relying on nomenclature and characteristic features described by Miller et al. (2007). U content is low (all analyses < 312 ppm U except two datapoints with 384 and 529 ppm U) and Th/U ratios are typically magmatic, varying between 0.34 and 0.99. Thirty measurements were made on the same number of zircon grains. One analysis (U21) has been filtered as its degree of concordance is way below the 95-105 % range considered for concordant datapoints. $^{206}Pb/^{238}U$ single zircon ages span continuously over *ca.* 750-695 Ma. There is no textural, nor geochemical and analytical reason that would lead us not to attribute such a spread in $^{206}Pb/^{238}U$ concordant to the crystallization history of the GS-OC-01 trachyte. We interpret the youngest zircon grain as an autocryst which $^{206}Pb/^{238}U$ single age of 695.4±16.0 Ma (Fig. 6-11a) is the crystallization age of subvolcanic intrusive whereas older zircon grains are antecrysts recording cascading magmatic pulses between *ca.* 750-695 Ma. Further cathodoluminescence imagery is however required to better investigate zircon internal zoning to confirm the latter hypothesis and the antecryst-autocryst nomenclature.

Dated zircon grains have rather consistent εHf_i values averaging +10.6±1.7 (n=10; Fig. 6-11b). Accordingly, the two-stage model age range is tight from 0.93 to 1.03 Ga (Table 6-4).

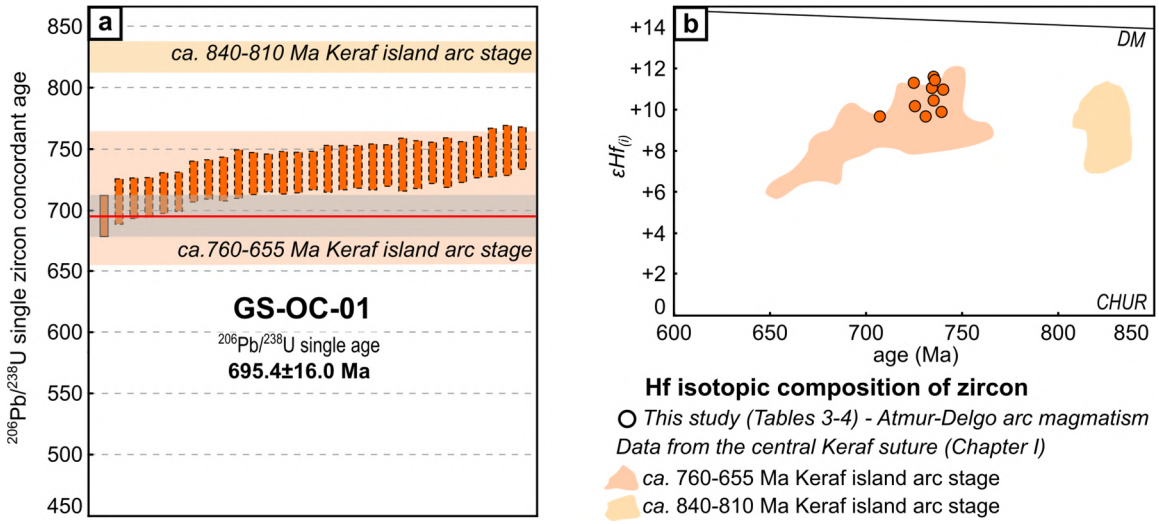


Figure 6-11: U-Pb dating and Hf isotope composition of zircon from the syn-Atmur Delgo suture GS-OC-01 trachyandesite, Galat Sufar South gold deposit. Isotopic data for island arc magmatism in the central Keraf suture are plotted (**Chapter I**). **a** Plot of $^{206}Pb/^{238}U$ single zircon ages arranged in descending order. Data out of the 95-105% range of degree of concordance have been filtered prior to plotting. The data bars with plain-line contour is considered for $^{206}Pb/^{238}U$ crystallization age calculation. The plot is produced using Isoplot program (Ludwig, 2007). **b** $^{206}Pb/^{238}U$ concordant age of single zircon vs initial zircon epsilon hafnium composition $\varepsilon Hf_{(i)}$ crossplot. The depleted mantle (DM) evolution is from Blichert-Toft and Puchtel (2010). The accompanying BSE-SEM images illustrating zircon morphologies and dataspot location are provided in Supplementary Material 6-2. U-Pb and Hf isotopic compositions of zircon from this study are compiled in Tables 6-3 and 6-4, respectively.

4.4. U-Pb ages of apatite

U-Pb laser spot emplacements on cathodoluminescence images of dated apatite grains from Galat Sufar South, WG03 and Central Zone gold deposits grains are provided in Supplementary Material 6-3. U-Pb isotopic compositions of dated apatite grains are given in Table 6-5.

4.4.1. Galat Sufar South gold deposit

There is a sharp zoning in apatite from the GSS gold deposit between a rounded bright core and a large subhedral darker rim forming most of the grain, overgrown by a late and thin brighter apatite liseré (Fig. 6-2; Supplementary Material 6-3). Apatite rims are almost not radiogenic (<1.1 ppm U except for two datapoints with 2.5 and 2.7 ppm

U) whereas cores are slightly U-enriched (~1.5-6.5 ppm U) but U/Th ratio is almost systematically <1 (Table 6-5). After filtering of the original dataset, seventy-six measurements remain on thirty apatite grains from GS-55-02 (n=19 for nine grains) and GS-55-04 (n=57 for twenty-one grains) samples. Despite their low radiogenic content, plotting U-Pb isotopic compositions of GSS apatite cores and rims in a Tera-Wasserburg diagram enables to draw a *Discordia* defining a lower intercept of 737.9±15.6 Ma (n=76, MSWD=1.2, Fig. 6-12a). This age is similar to the lower intercept age obtained if considering only GS-55-04 analyses (*ca.* 758-728 Ma) as most of the apatite core measurements are from this sample (Table 6-5). The 737.9±15.6 Ma date is considered as a reliable hydrothermal crystallization age as the initial $^{207}Pb/^{206}Pb$ value obtained is ~0.88, which is close to the expected common Pb ratio at this age following the Pb evolution model of Stacey and Kramers (1975).

4.4.2. WG03 gold deposit

Apatite occurs at the WG03 deposit at the selvages of mineralized quartz-dominated veins as mostly rounded grains of various size, more or less aggregated, with no clear evidence for zoning in spite of the presence of lighter rims around amalgamated grains (Figs. 6-2, 6-5, 6-6, 6-7; Supplementary Material 6-3). U concentration in apatite ranges between ~0.8-6.0 ppm with only three measurements above 15 ppm and U/Th ratios averaging 20, with values up to 104 (Table 6-5). Sixty-seven and twenty-four measurements have been made on forty-eight and thirteen apatite grains from WG03-11 and WG03-12 samples, respectively. The U-Pb isotopic compositions of apatite from WG03-11 provides a *Discordia* lower intercept in a Tera-Wasserburg diagram of 553.7±3.3 Ma (n=67, MSWD=2.1, Fig. 6-12b). For sample WG03-12, we obtained an intercept at 584.1±15.1 Ma (n=24, MSWD=1.4, Fig. 6-12c). These dates are interpreted as the hydrothermal crystallization ages of apatite occurring as a proximal alteration marker of mineralized veins at the WG03 gold deposit, as the *Discordia* upper intercepts provide reliable ~0.86-0.87 initial $^{207}Pb/^{206}Pb$ values (Fig. 6-12b, c).

ID	$^{207}Pb^{a}$	U^{b}	Pb^{b}	$\frac{Th^{b}}{U}$	$^{206}Pbc^{c}$	$\frac{^{206}Pb^{d}}{^{238}U}$	±2σ	$\frac{^{207}Pb^{d}}{^{235}U}$	±2σ	$\frac{^{207}Pb^{d}}{^{206}Pb}$	±2σ	ρ[e]	$\frac{^{206}Pb}{^{238}U}$	±2σ	$\frac{^{207}Pb}{^{235}U}$	±2σ	$\frac{^{207}Pb}{^{206}Pb}$	±2σ	conc.[f]
U-Pb	(cps)	(ppm)	(ppm)	U	(%)		(%)		(%)		(%)			(Ma)		(Ma)		(Ma)	(%)
GS-OC-01 *(syn-Atmur-Delgo arc)*																			
U08	11536	73	9	0.46	b.d.	0.11390	2.4	0.9946	3.2	0.06333	2.03	0.77	695	16	701	16	719	43	97
U09	59435	384	54	0.99	b.d.	0.12150	2.2	1.07	3.8	0.06384	3.145	0.57	739	15	739	20	736	67	100
U10	13560	93	11	0.36	b.d.	0.12000	2.3	1.049	2.8	0.06337	1.52	0.84	731	16	728	15	721	32	101
U11	31435	197	26	0.68	b.d.	0.12080	2.5	1.066	3.2	0.06404	2.108	0.76	735	17	737	17	743	45	99
U12	23212	149	19	0.61	b.d.	0.12080	2.5	1.055	3.1	0.06331	1.775	0.82	735	18	731	16	719	38	102
U13	41902	268	35	0.73	b.d.	0.12080	2.3	1.057	3.3	0.06345	2.394	0.70	735	16	732	18	723	51	102
U14	9036	60	7	0.41	b.d.	0.12060	2.6	1.047	3.0	0.06299	1.593	0.85	734	18	728	16	708	34	104
U15	17268	108	13	0.49	b.d.	0.12140	2.3	1.058	2.9	0.06318	1.814	0.78	739	16	733	15	714	39	103
U16	31664	205	26	0.51	b.d.	0.11910	2.4	1.056	3.1	0.06434	1.967	0.78	725	17	732	17	753	42	96
U17	18132	122	14	0.34	b.d.	0.11590	2.6	1.002	2.9	0.06268	1.221	0.91	707	18	705	15	698	26	101
U18	12717	80	10	0.48	b.d.	0.11910	2.2	1.041	3.1	0.06343	2.145	0.71	725	15	725	16	723	46	100
U19	17236	110	13	0.42	b.d.	0.11880	2.3	1.037	2.9	0.06335	1.757	0.79	723	16	723	15	720	37	100
U20	14274	84	10	0.39	b.d.	0.12030	2.1	1.081	2.7	0.06513	1.726	0.77	733	15	744	14	778	36	94
U22	35419	231	30	0.65	b.d.	0.11990	2.3	1.059	2.6	0.06406	1.273	0.87	730	16	734	14	744	27	98
U23	32224	204	26	0.67	b.d.	0.12000	2.2	1.064	2.6	0.0643	1.356	0.86	731	16	736	14	752	29	97
U24	22538	146	19	0.58	b.d.	0.12140	2.7	1.065	2.9	0.0636	1.071	0.93	739	19	736	16	728	23	101
U25	35714	231	28	0.41	b.d.	0.11640	2.3	1.014	2.7	0.0632	1.363	0.86	710	16	711	14	715	29	99
U26	15274	103	13	0.40	b.d.	0.12120	2.9	1.058	3.8	0.06332	2.476	0.77	737	21	733	20	719	53	103
U27	25691	159	21	0.60	b.d.	0.12320	2.8	1.083	3.0	0.06378	1.159	0.92	749	19	745	16	734	25	102
U28	13634	85	11	0.41	b.d.	0.12350	2.3	1.085	3.5	0.0637	2.569	0.67	751	16	746	18	732	54	103
U29	27084	173	22	0.50	b.d.	0.12220	2.2	1.073	2.5	0.06365	1.034	0.91	743	16	740	13	730	22	102
U30	39446	247	30	0.54	b.d.	0.11710	2.3	1.033	2.4	0.06397	0.7165	0.95	714	15	721	12	741	15	96
U37	24263	155	19	0.45	b.d.	0.11980	2.7	1.049	2.9	0.06346	1.018	0.94	730	19	728	15	724	22	101
U38	20786	128	16	0.40	b.d.	0.12110	2.3	1.073	2.8	0.06427	1.648	0.81	737	16	740	15	751	35	98
U39	18523	117	15	0.62	b.d.	0.11730	2.2	1.023	2.5	0.06322	1.192	0.88	715	15	715	13	716	25	100
U40	18412	114	15	0.56	b.d.	0.12120	2.7	1.066	3.0	0.06378	1.412	0.88	737	19	737	16	734	30	100
U41	49867	312	41	0.72	b.d.	0.12000	2.1	1.06	2.3	0.06405	1.086	0.89	731	14	734	12	743	23	98
U42	74480	529	67	0.78	0.94	0.11650	2.2	1.016	2.7	0.06323	1.527	0.83	711	15	712	14	716	32	99
U43	22135	139	18	0.47	b.d.	0.12290	2.7	1.072	2.9	0.06328	1.207	0.91	747	19	740	15	718	26	104
U21	*81334*	*814*	*44*	*0.83*	*b.d.*	*0.04209*	*3.5*	*0.3473*	*5.4*	*0.05984*	*4.063*	*0.65*	*266*	*9*	*303*	*14*	*598*	*88*	*44*

In italics: excluded for crystallization age calculation (out of the 95-105% degree of concordance range, inherited zircon grains, later tectono-metamorphic event-related Pb-loss or Th/U<0.2).

In bold: datapoints considered for crystallization age calculation.

Spot size = 33µm.

$^{206}Pb/^{238}U$ error is the quadratic additions of the within run precision (2 S.E.) and the external reproducibility (2 S.D.) of the reference zircon. $^{207}Pb/^{206}Pb$ error propagation (^{207}Pb signal dependent) following Gerdes and Zeh (2009). $^{207}Pb/^{235}U$ error is the quadratic addition of the $^{207}Pb/^{206}Pb$ and $^{206}Pb/^{238}U$ uncertainty.

[a] *Within run background-corrected mean ^{207}Pb signal in cps (counts per second).*

[b] *U and Pb content and Th/U ratio were calculated relative to GJ-1 reference zircon.*

[c] *Percentage of the common Pb on the ^{206}Pb. b.d. = below detection limit.*

[d] *Corrected for background, within-run Pb/U fractionation (in case of $^{206}Pb/^{238}U$) and common Pb using Stacey and Kramers (1975) model Pb composition and subsequently normalized to GJ-1 (ID-TIMS value/measured value); $^{207}Pb/^{235}U$ calculated using $^{207}Pb/^{206}Pb/(^{238}U/^{206}Pb*1/137.88)$.*

[e] *ρ is the $^{206}Pb/^{238}U$ / $^{207}Pb/^{235}U$ error correlation coefficient.*

[f] *Degree of concordance (%) = $^{206}Pb/^{238}U$ age / $^{207}Pb/^{206}Pb$ age.100.*

Table 6-3: U-Pb isotopic compositions of zircon grains recovered from GS-OC-01 trachyandesite used in this study. BSE- and SE-SEM images illustrating zircon morphologies and dataspots are provided in Supplementary Material 6-2.

ID Lu-Hf	$^{176}Yb/^{177}Hf$ [a]	±2σ	$^{176}Lu/^{177}Hf$ [a]	±2σ	$^{178}Hf/^{177}Hf$	Sig_{Hf} [b] (V)	$^{176}Hf/^{177}Hf$	±2σ [c]	$^{176}Hf/^{177}Hf_{(i)}$ [d]	age [f] (Ma)	±2σ	conc. [g]	$\varepsilon Hf_{(i)}$ [d]	±2σ [c]	T_{DM2} (Ga)
GS-OC-01 *(syn-Atmur-Delgo arc)*															
U09	0.0791	7	0.00236	3	1.46725	7	0.282658	34	0.282626	739	15	100	10.9	1.2	0.97
U10	0.0209	6	0.00064	1	1.46724	10	0.282603	29	0.282595	731	16	101	9.6	1.0	1.03
U11	0.0907	8	0.00266	1	1.46725	10	0.282685	30	0.282648	735	17	99	11.6	1.1	0.93
U12	0.0505	41	0.00148	11	1.46719	10	0.282636	30	0.282616	735	18	102	10.5	1.1	0.99
U13	0.0925	15	0.00268	5	1.46725	10	0.282681	30	0.282644	735	16	102	11.4	1.1	0.94
U14	0.0255	4	0.00079	1	1.46729	10	0.282646	28	0.282635	734	18	104	11.1	1.0	0.96
U15	0.0286	13	0.00090	4	1.46728	10	0.282608	29	0.282596	739	16	103	9.8	1.0	1.03
U16	0.0473	4	0.00148	1	1.46727	10	0.282664	29	0.282644	725	17	96	11.2	1.0	0.94
U17	0.0381	9	0.00119	3	1.46722	10	0.282626	31	0.282610	707	18	101	9.6	1.1	1.00
U18	0.0344	15	0.00106	5	1.46726	10	0.282627	28	0.282612	725	15	100	10.1	1.0	1.00

Corresponding U-Pb dataspot IDs are indicated.

[a] $^{176}Yb/^{177}Hf=(^{176}Yb/^{173}Yb)_{true}.(^{173}Yb/^{177}Hf)_{measured}.(M^{173}(Yb)/M^{177}(Hf))b(Hf)$, $b(Hf)=ln(^{179}Hf/^{177}Hf_{true} / {}^{179}Hf/^{177}Hf_{measured})/ln(M^{179}(Hf)/M^{177}(Hf))$, M=mass of respective isotope. The Lu/Hf were calculated in a similar way by using the Lu/Hf and b(Yb). Quoted uncertainties (absolute) relate to the last quoted figure. The effect of the inter-element fractionation on the Lu/Hf was estimated to be about 6% or less based on analyses of the GJ-1 and Temora zircons.

[b] Mean Hf signal in volt.

[c] Uncertainties are quadratic additions of the within-run precision and the daily reproducibility of the zircon GJ-1. Uncertainties for GJ-1 is 2 S.D. (2 standard deviation).

[d] Initial $^{176}Hf/^{177}Hf$ and $\varepsilon Hf_{(i)}$ calculated using the age (Ma), and the CHUR parameters:
$^{176}Lu/^{177}Hf = 0.0336$, and $^{176}Hf/^{177}Hf = 0.282785$ (Bouvier et al., 2008).

[e] Two stage-model age in billion years using the measured $^{176}Lu/^{177}Lu$, the estimated age (Ma), a value of 0.01113 for the average continental crust (second stage), and a depleted mantle $^{176}Lu/^{177}Hf$ and $^{176}Hf/^{177}Hf$ of 0.03933 and 0.283294 (Blichert-Toft and Puchtel, 2010).

[f] $^{206}Pb/^{238}U$ age.

[g] Degree of concordance (%) = $^{206}Pb/^{238}U$ age / $^{207}Pb/^{206}Pb$ age.100.

Table 6-4: Lu-Hf isotopic compositions of zircon grains recovered from GS-OC-01 trachyandesite used in this study. BSE- and SE-SEM images illustrating zircon morphologies and dataspots are provided in Supplementary Material 6-2.

4.4.3. Central Zone gold deposit

Apatite from the Central Zone gold deposits occurs as euhedral grains disseminated in the gangue of the ore-hosting granitoids. These grains are fragmented where the host rock is deformed by crosscutting mineralized veins. They are composed of a predominant core with thin darker rims (Figs. 6-2, 6-7, 6-8; Supplementary Material 6-3). Except for a single datapoint, the U concentration in apatite is systematically >4.0 ppm and reaches up to 24.1 ppm, with <1 Th/U ratios (Table 6-5). Two batches of seven and sixteen measurements on four and eleven grains have been made for sample CZ12. Despite there is no clear evidence for change in apatite morphology, texture and radiogenic content, the two batches lead to different *Discordia* upper intercepts of 663.9±17.8 Ma (n=7, MSWD=3.9) and 791.5±19.4 Ma (n=16, MSWD=1.8) with initial $^{207}Pb/^{206}Pb$ values of

0.89 and 0.86, respectively (Fig. 6-12d). The interpretation of these dates remains unclear and is discussed further in section 5.4.

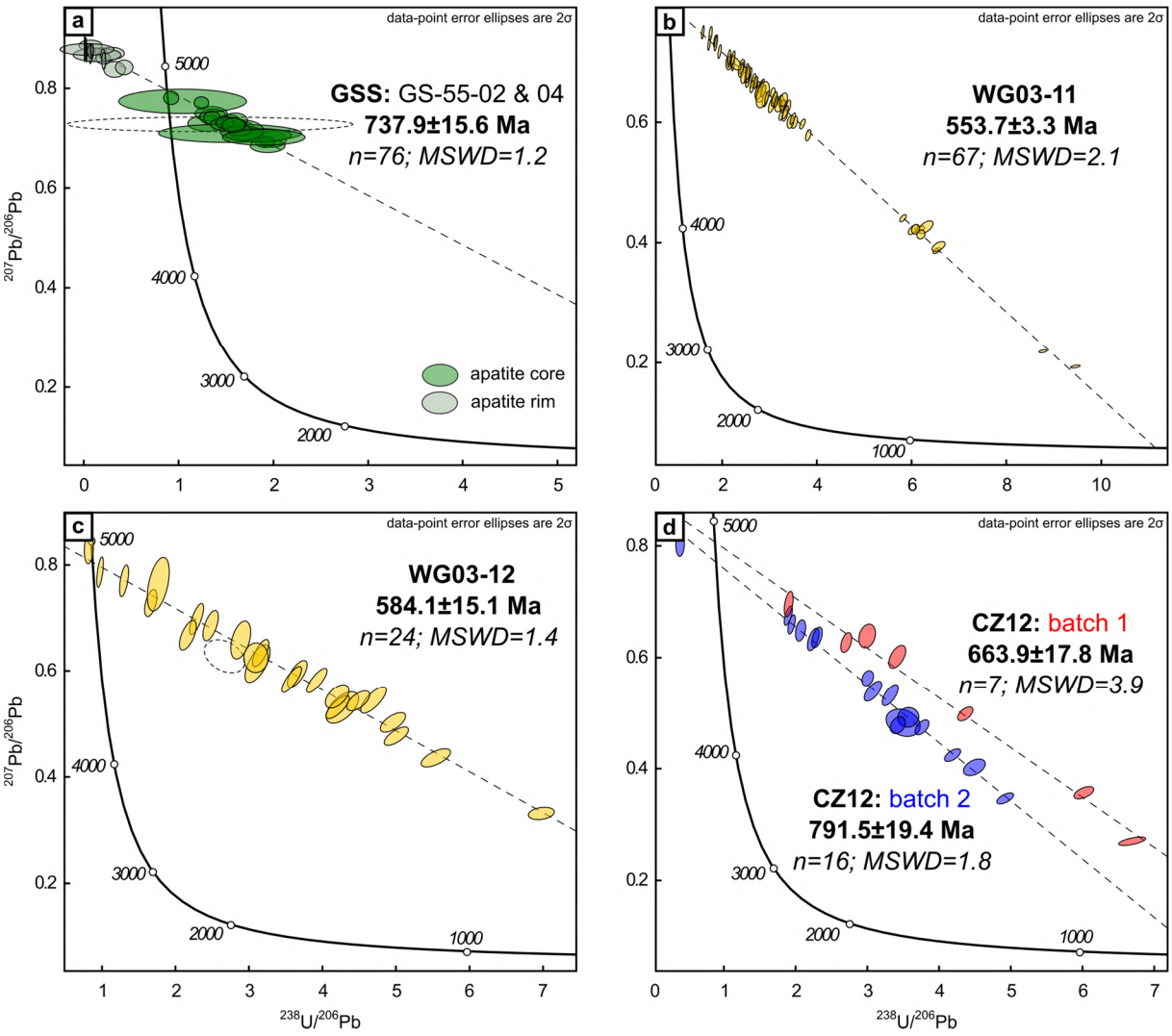


Figure 6-12: Tera-Wasserburg diagrams for U-Pb dating of apatite grains from the (**a**) Galat Sufar South, (**b** and **c**) WG03 and (**d**) Central Zone gold deposits. Error ellipses are 2σ. The plots are produced using Isoplot program (Ludwig, 2007). The accompanying cathodoluminescence images illustrating apatite morphologies and dataspot location are provided in Supplementary Material 6-3. U-Pb isotopic compositions of apatite from this study are compiled in Table 6-5.

ID U-Pb		U (ppm)	U/ Th	^{238}U/ ^{206}Pb	±2σ	^{207}Pb/ ^{206}Pb	±2σ
GS-55-02 (Galat Sufar South gold deposit)							
z7-1	B_1	0.08	0.17	0.015	0.002	0.880	0.014
z7-2	A_1	0.37	0.10	0.200	0.036	0.869	0.010
z7-2	B_3	0.03	0.15	0.005	0.001	0.876	0.009
z8-1	A_2	0.50	0.21	0.208	0.012	0.862	0.010
z8-1	A_3	0.46	0.21	0.214	0.017	0.864	0.012
z8-1	B_1	0.30	0.22	0.065	0.010	0.864	0.012
z8-1	B_2	2.5	1.5	0.323	0.094	0.838	0.013
z8-1	B_3	0.17	0.15	0.028	0.003	0.876	0.013
z8-1	B_4	0.11	0.25	0.011	0.002	0.882	0.008
z8-1	B_5	0.09	0.18	0.010	0.002	0.882	0.011
z8-2	B_1	0.04	0.12	0.008	0.001	0.882	0.013
z11-1	B_1	0.07	0.29	0.015	0.002	0.878	0.017
z11-1	B_2	0.10	0.06	0.024	0.002	0.885	0.013
z15-1	B_1	0.32	0.45	0.040	0.005	0.876	0.007
z19-2	B_1	0.30	0.19	0.067	0.100	0.886	0.009
z19-2	B_2	0.05	0.10	0.003	0.000	0.867	0.011
z19-2	B_3	0.03	0.08	0.003	0.000	0.887	0.010
z19-3	A_1	0.60	0.26	0.286	0.114	0.870	0.010
z19-3	B_1	0.47	0.21	0.203	0.062	0.860	0.009
GS-55-04 (Galat Sufar South gold deposit)							
z3-1	**A_1**	3.1	0.57	1.299	0.167	0.730	0.013
z3-1	B_1	0.02	0.55	0.004	0.001	0.884	0.013
z3-1	B_2	0.48	0.74	0.097	0.024	0.868	0.011
z5-1	**A_1**	2.8	0.55	1.563	0.100	0.730	0.010
z5-1	B_1	0.42	0.81	0.137	0.206	0.867	0.011
z6-1	**A_1**	3.2	0.60	1.992	0.119	0.698	0.013
z6-1	B_1	0.02	0.10	0.006	0.000	0.891	0.009
z6-1	B_2	0.29	0.71	0.079	0.005	0.868	0.010
z6-1	B_3	0.12	0.79	0.031	0.233	0.878	0.010
z6-2	**A_2**	3.1	0.44	1.646	0.119	0.722	0.010
z6-2	B_2	0.08	0.39	0.023	0.004	0.878	0.011
z6-2	B_3	2.7	0.31	0.920	0.065	0.781	0.011
z7_1	**A_1**	3.4	0.55	1.905	0.076	0.693	0.009
z7-1	**A_2**	3.1	0.54	1.805	0.062	0.706	0.010
z7-1	B_1	0.02	0.60	0.003	0.000	0.889	0.010
z7-1	B_2	0.21	1.1	0.049	0.018	0.879	0.008
z7-1	B_3	0.04	0.23	0.006	0.001	0.887	0.008
z7-2	**A_1**	3.6	0.56	1.531	0.098	0.734	0.011
z7-2	B_2	0.02	0.29	0.005	0.001	0.890	0.010
z7-2	B_3	0.03	0.26	0.007	0.001	0.887	0.009
z9-1	***A_1***	*3.3*	*0.62*	*1.328*	*1.235*	*0.728*	*0.012*
z9-1	**A_2**	3.8	0.64	1.541	0.617	0.710	0.015
z9-1	B_1	0.02	0.33	0.004	0.000	0.884	0.009
z9-1	B_2	0.03	0.26	0.006	0.001	0.885	0.011
z9-1	B_3	0.02	0.32	0.006	0.001	0.886	0.011
z9-1	B_4	0.02	0.62	0.005	0.001	0.894	0.008
z9-2	**A_1**	3.5	0.59	1.937	0.064	0.693	0.009
z9-2	B_1	0.27	0.90	0.066	0.009	0.878	0.010
z9-2	B_2	0.08	0.03	0.026	0.005	0.872	0.016
z11-1	**A_1**	4.2	0.65	1.938	0.150	0.685	0.011
z11-1	**A_2**	3.6	0.63	1.718	0.148	0.710	0.011
z12-3	**A_2**	2.3	0.51	1.350	0.071	0.741	0.011
z12-3	B_1	0.02	0.03	0.009	0.002	0.890	0.026
z12-3	B_2	0.02	0.07	0.007	0.001	0.873	0.010
z13-1	**A_1**	2.8	0.56	1.522	0.155	0.728	0.011
z13-1	B_1	0.02	0.41	0.005	0.001	0.894	0.010
z13-1	B_2	0.02	0.26	0.004	0.000	0.869	0.011
z14-1	**A_1**	3.7	0.61	1.239	0.063	0.771	0.010
z14-1	**A_2**	3.8	0.61	1.486	0.077	0.732	0.010
z14-1	B_1	0.14	0.74	0.018	0.003	0.886	0.012
z14-1	B_3	0.86	0.51	0.208	0.016	0.855	0.014
z14-2	**A_1**	3.9	0.57	1.580	0.100	0.726	0.012
z14-2	B_1	1.1	0.55	0.424	0.075	0.842	0.012
z16-1	**A_1**	3.5	0.57	1.898	0.356	0.702	0.013
z16-1	B_1	0.31	0.57	0.085	0.012	0.878	0.009
CZ12 (Central Zone gold deposit)							
batch1	33	7.6	0.57	2.705	0.062	0.627	0.015
batch1	34	16.0	0.66	6.020	0.113	0.357	0.009
batch1	35	24.1	0.60	6.694	0.154	0.270	0.006
batch1	36	12.5	0.64	4.366	0.087	0.498	0.010
batch1	37	5.5	0.54	1.903	0.050	0.696	0.019
batch1	38	8.3	0.45	3.417	0.096	0.602	0.017
batch1	39	10.8	0.57	2.997	0.095	0.639	0.017
batch2	129	5.7	0.46	3.078	0.100	0.539	0.015
batch2	130	8.9	0.67	3.570	0.121	0.492	0.015
batch2	131	4.5	0.38	2.245	0.067	0.633	0.016
batch2	132	7.2	0.59	4.493	0.124	0.402	0.012
batch2	133	4.6	0.50	1.943	0.042	0.660	0.014
batch2	134	4.5	0.53	2.298	0.060	0.636	0.015
batch2	135	4.0	0.51	1.897	0.047	0.676	0.014
batch2	136	7.6	0.63	3.426	0.087	0.478	0.012
batch2	137	10.4	0.65	4.189	0.092	0.424	0.009
batch2	138	4.3	0.48	2.068	0.058	0.649	0.016
batch2	139	8.4	0.61	3.500	0.195	0.482	0.020
batch2	141	6.8	0.65	3.004	0.066	0.563	0.011
batch2	140	7.8	0.67	3.762	0.080	0.474	0.011
batch2	142	10.7	0.62	4.923	0.096	0.347	0.008
batch2	143	4.7	0.53	3.319	0.092	0.532	0.016
batch2	144	1.5	0.25	0.387	0.049	0.803	0.018
WG03-11 (WG03 gold deposit)							
	1	2.7	15.7	2.412	0.056	0.692	0.010
	2	2.7	16.6	3.072	0.039	0.649	0.007
	3	2.3	24.2	2.417	0.030	0.690	0.008
	5	2.0	15.1	2.524	0.032	0.686	0.009
	6	1.9	19.1	2.516	0.036	0.676	0.009
	7	2.1	17.2	2.596	0.028	0.681	0.008
	8	2.3	28.0	2.769	0.031	0.657	0.009
	9	2.3	23.4	2.678	0.047	0.666	0.008
	10	2.4	16.9	2.788	0.071	0.646	0.010
	11	1.8	26.2	2.400	0.046	0.685	0.009
	12	2.6	21.2	2.879	0.041	0.653	0.007
	13	1.6	2.6	1.854	0.026	0.734	0.008
	14	2.8	31.9	3.401	0.038	0.627	0.008

Table 6-5 ***(continued)***

ID U-Pb		U (ppm)	U/ Th	$^{238}U/^{206}Pb$	±2σ	$^{207}Pb/^{206}Pb$	±2σ
z11-1	B_1	0.02	0.22	0.004	0.001	0.881	0.008
z11-1	B_2	0.61	0.93	0.200	0.019	0.868	0.009
z11-1	B_3	0.21	0.13	0.068	0.027	0.874	0.010
z11-1	B_4	0.04	0.51	0.007	0.001	0.881	0.010
z11-1	B_5	0.02	0.44	0.005	0.001	0.880	0.010
z11-2	**A_1**	3.3	0.52	1.342	0.141	0.749	0.012
z11-2	**A_2**	4.0	0.59	1.845	0.283	0.706	0.011
z11-2	B_1	0.40	1.1	0.086	0.008	0.872	0.010
z12-1	**A_1**	3.4	0.44	1.664	0.188	0.716	0.017
z12-2	**A_1**	3.0	0.55	1.645	0.103	0.716	0.009
z12-2	**A_2**	3.6	0.66	1.362	0.115	0.743	0.013
z12-2	**A_3**	2.9	0.62	1.597	0.105	0.736	0.012
z12-3	**A_1**	1.5	0.45	1.041	0.552	0.774	0.020
	29	1.7	27.2	2.663	0.047	0.669	0.010
	30	1.6	17.0	2.219	0.028	0.702	0.008
	31	1.9	28.0	2.707	0.040	0.666	0.008
	32	2.0	21.3	2.817	0.038	0.659	0.008
	33	1.8	38.5	2.906	0.047	0.638	0.010
	34	1.7	47.9	2.849	0.034	0.662	0.008
	35	1.0	10.6	1.948	0.029	0.717	0.009
	36	1.9	42.7	3.192	0.068	0.627	0.008
	37	2.1	54.4	3.276	0.041	0.629	0.008
	38	1.2	37.3	2.766	0.058	0.649	0.010
	40	0.82	47.5	2.860	0.115	0.646	0.018
	41	1.9	38.4	2.270	0.108	0.698	0.009
	42	1.7	18.9	3.102	0.050	0.638	0.010
	43	2.4	20.8	3.445	0.059	0.601	0.009
	44	1.3	31.9	2.140	0.049	0.698	0.009
	45	0.94	30.4	1.595	0.023	0.749	0.009
	46	0.95	40.9	1.728	0.024	0.731	0.010
	47	0.77	34.3	1.870	0.030	0.732	0.011
	48	1.3	52.3	2.158	0.029	0.702	0.009
	49	1.1	45.6	2.149	0.029	0.708	0.010
	50	0.85	35.2	2.462	0.054	0.678	0.011
	51	1.1	47.5	2.233	0.035	0.706	0.010
	52	1.3	60.1	2.547	0.036	0.677	0.009
	53	1.3	59.1	2.547	0.037	0.682	0.009
	55	0.86	104	1.759	0.028	0.747	0.010
	56	1.3	24.3	3.336	0.051	0.617	0.009
	57	1.3	36.5	2.630	0.034	0.659	0.008
	58	1.9	38.3	3.493	0.047	0.606	0.008
	59	1.7	16.0	3.301	0.065	0.638	0.009
	60	1.7	19.8	2.947	0.037	0.641	0.009
	61	2.0	9.9	3.142	0.038	0.634	0.008
	62	5.7	5.5	6.167	0.085	0.423	0.004
	63	4.7	4.8	6.031	0.084	0.422	0.007
	64	5.5	4.4	6.299	0.126	0.426	0.009
	16	2.7	35.8	3.109	0.046	0.635	0.007
	17	2.7	31.1	3.255	0.043	0.612	0.007
	18	1.8	21.5	2.236	0.025	0.695	0.008
	19	2.5	22.9	3.241	0.044	0.635	0.008
	20	1.8	22.3	3.051	0.060	0.629	0.011
	21	2.8	25.7	3.820	0.047	0.579	0.008
	22	2.6	21.8	3.323	0.048	0.611	0.008
	23	2.3	23.1	2.869	0.043	0.652	0.008
	24	2.8	23.4	3.697	0.049	0.597	0.007
	25	1.7	19.1	2.544	0.039	0.670	0.010
	26	2.3	17.5	3.115	0.038	0.640	0.008
	27	2.6	20.6	3.525	0.057	0.600	0.008
	28	2.5	27.2	3.295	0.044	0.627	0.008
	65	4.7	5.6	6.196	0.070	0.414	0.006
	66	5.6	5.5	6.531	0.065	0.387	0.004
	67	4.3	5.6	5.818	0.056	0.441	0.005
	68	5.0	5.7	6.569	0.112	0.394	0.007
	69	18.4	8.1	8.773	0.070	0.219	0.002
	70	3.9	5.3	6.086	0.069	0.423	0.007
	71	16.9	2.9	9.455	0.085	0.193	0.002
WG03-12 (WG03 gold deposit)							
	1	6.1	26.0	5.003	0.135	0.477	0.014
	8	3.3	20.8	3.117	0.140	0.614	0.029
	9	1.9	12.9	1.300	0.050	0.770	0.024
	10	15.8	21.3	6.975	0.144	0.331	0.009
	11	1.2	12.9	0.975	0.036	0.786	0.023
	12	3.7	16.0	3.656	0.110	0.595	0.021
	13	2.4	24.4	1.664	0.068	0.728	0.021
	14	3.8	18.9	3.159	0.091	0.634	0.021
	15	*3.1*	*21.0*	*2.668*	*0.225*	*0.628*	*0.025*
	16	3.8	35.6	3.095	0.136	0.625	0.023
	17	2.3	21.2	2.478	0.085	0.686	0.023
	18	3.6	26.4	4.270	0.180	0.531	0.024
	19	7.1	23.9	5.541	0.164	0.436	0.014
	20	4.7	21.9	4.206	0.130	0.531	0.018
	21	4.6	22.3	4.693	0.142	0.545	0.020
	22	3.9	28.8	3.922	0.114	0.582	0.019
	23	1.7	18.0	2.287	0.078	0.698	0.024
	24	3.2	28.6	3.580	0.110	0.584	0.020
	25	1.8	3.9	1.766	0.122	0.764	0.041
	26	4.5	23.5	4.198	0.131	0.552	0.018
	27	2.1	28.7	2.887	0.111	0.659	0.029
	28	4.9	20.9	4.485	0.128	0.543	0.015
	29	6.1	22.6	4.957	0.140	0.503	0.015
	30	2.2	32.3	2.169	0.094	0.668	0.023
	32	1.1	1.4	0.823	0.051	0.831	0.024

In italics: excluded for crystallization age calculation.
In bold: apatite cores in samples from the Galat Sufar South gold deposit.

Table 6-5: U-Pb isotopic compositions of apatite grains used in this study. Cathodoluminescence images illustrating apatite morphologies and dataspots are provided in Supplementary Material 6-3.

4.5. Chlorite-phengite-quartz-water multi-equilibria calculations

The major element compositions of syn-D_{2GSS} coexisting chlorite and phengite from the GSS gold deposit (Fig. 6-4c, d) are given in Table 6-6. Approximately half of chlorite compositions plot outside of the amesite-sudoite-(clinochore-daphnite) ternary diagram (Fig. 6-13a) and involve other substitutions than those corresponding to elemental exchanges between the end-members considered in this study (see subsection 3.2.5). Nevertheless, chlorite compositions are mostly comprised between the clinochore-daphnite and (Fe, Mg)-amesite end-members. Phengite compositions are mostly muscovite- and celadonite-enriched although some datapoints show an up to 20% contribution of pyrophyllite where celadonite proportion is below 10% (Fig. 6-13b). Both chlorite and phengite compositions suggest the predominance of the Tschermak substitution ($Al^{VI}Al^{IV} \leftrightarrow (Fe^{2+},Mg)^{VI}Si^{IV}$) with little contribution of the pyrophyllitic substitution ($K^{XII}Al^{IV} \leftrightarrow \square^{XII}Si^{IV}$ where $\square^{XII}$ represents a vacancy in the A1 site of a white mica) for phengite.

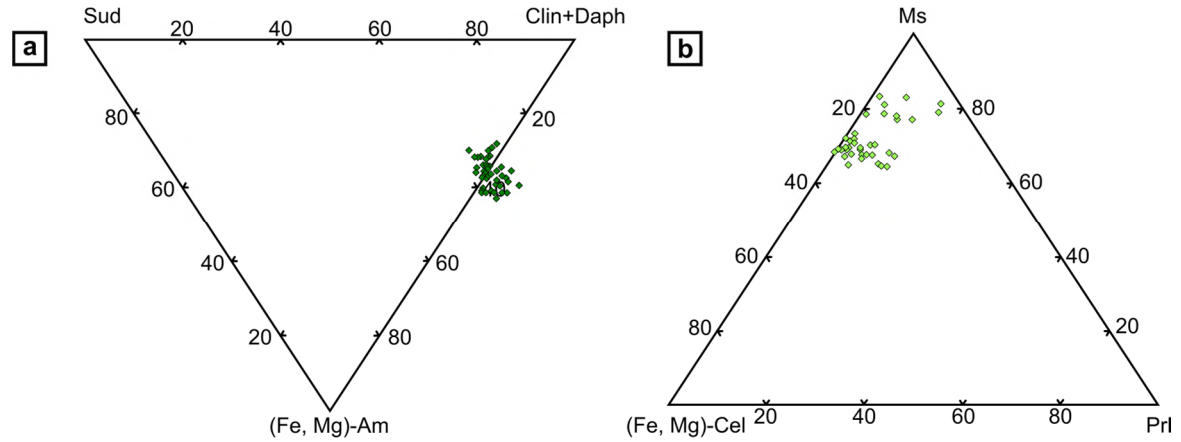


Figure 6-13: Plot of the phyllosilicate compositions from the samples GS-55-02 and GS-55-04 in **am**esite-(**clin**ochlore + **daph**nite)-**sud**oite (**a**, chlorite, n=41) and **cel**adonite-**mu**scovite-**py**ro**phyll**ite (**b**, phengite, n=45) end-member ternaries. Each point represents the chlorite or phengite composition obtained from conventional EMPA spot analysis. The analyses were first filtered before multi-equilibria calculation on the basis of the compositional criteria detailed in Vidal and Parra (2000). Chlorite and phengite compositions from this study are compiled in Table 6-6.

Prior to multi-equilibria calculations, data were filtered on the basis of the compositional criteria detailed in Vidal and Parra (2000). 18 out of 41 chlorite analyses and 1 out of 45 phengite analyses were removed from the original dataset and are not

considered further (in italics in Table 6-6). Chlorite-phengite-quartz-water multi-equilibria calculated from coexisting chlorite and white mica compositions considered below are listed in Supplementary Material 6-4. We distinguish between redundant, non-redundant and local *P-T* equilibria. Redundant and non-redundant equilibria are calculated considering a chlorite-phengite compositional couple for EMPA dataspots that do not necessary correspond to the same sample or to the same zone within a single samples. If several *P-T* thermodynamic equilibria are calculated from a given phengite composition and distinct chlorite compositions, they are classified as redundant except the one associated to the lower free Gibbs energy, *i.e.,* the non-redundant equilibrium. Local *P-T* equilibria are considered if calculated from chlorite and phengite coexisting at the microscopic scale within a given sample.

When plotting all calculated *P-T* equilibria, there are two distinct populations at ~260-360°C and ~400-500°C (Fig. 6-14). >450°C equilibria are considered as unlikely as they mostly correspond to unrealistic compositions. For instance, there are < 60 % water molecules between tetrahedron-octahedron-tetrahedron sheets of phengite against 70-100% in classical chlorite-di-octahedral mica reactions and #Fe^{3+} values mostly <12 % for chlorite differing from the ~15-25 % range of values calculated at lower temperatures (*e.g.,* Ganne et al., 2012; Supplementary Material 6-4). In order to reach a theoretical thermodynamic equilibrium, the calculation is indeed optimized by filling the mica sites with water and/or Fe^{3+}, leading to unrealistic and badly constrained equilibria as suggested by their relatively high Gibbs free energy (Fig. 6-14). These high-*T* equilibria are therefore not considered further. The two remaining, most stable *P-T* equilibrium fields, where almost all non-redundant and local equilibria plots, are therefore constrained at ~300-350°C – 1-4 kbar and ~400-440°C – 4.5-8 kbar (Fig. 6-14).

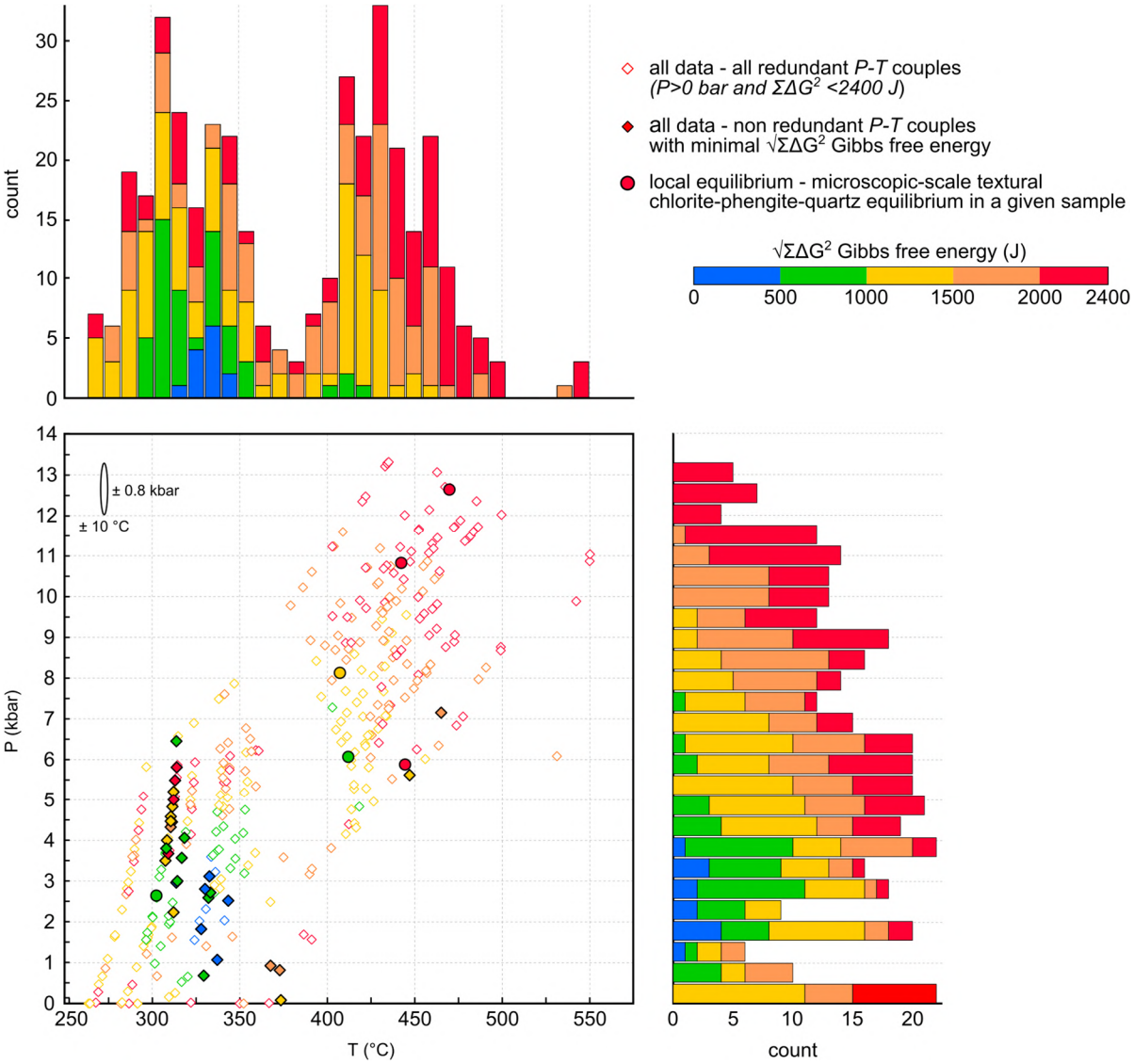


Figure 6-14: Pressure-temperature equilibrium conditions resulting from chlorite-phengite-quartz-water multi-equilibria calculation for the syn-gold mineralization D_{2GSS} deformation stage at the Galat Sufar South deposit. Phengite and chlorite compositions used for this calculation are compiled in Table 6-6 and illustrated in Figure 6-13. All the pressure-temperature conditions calculated from this dataset are compiled in Supplementary Material 6-4.

The lower *P-T* field of stability of the chlorite-phengite-quartz assemblage is predominant and corresponds to the most stable calculated thermodynamic equilibria with $\sqrt{\sum}\Delta G^2 < 500$ J. It refers to the typical greenschist facies metamorphic conditions (Yardley, 1989). The statistical robustness of the less-recorded higher *P-T* field of stability has been tested by plotting the $\sqrt{\Sigma}\Delta G^2$ Gibbs free energy running mean over 21 points against pressure (left) or temperature (right) sorted by increasing values (Fig. 6-15). These plots illustrate the existence of two stability gaps, *i.e.*, *P* and *T* ranges associated with relatively low $\sqrt{\Sigma}\Delta G^2$ values regarding calculated multi-equilibria with

close P and T values, centered on ~2.6 kbar-330°C and ~7.2 kbar-420 °C. The syn-D_{2GSS} chlorite-phengite-quartz assemblage therefore records ~7.2 kbar-420 °C stability conditions interpreted as lower amphibolite facies crystallization conditions (Yardley, 1989), whereas the ~2.6 kbar-330°C conditions more likely refer to resetting of the chlorite-phengite-quartz compositions during greenschist-facies retrograde metamorphism.

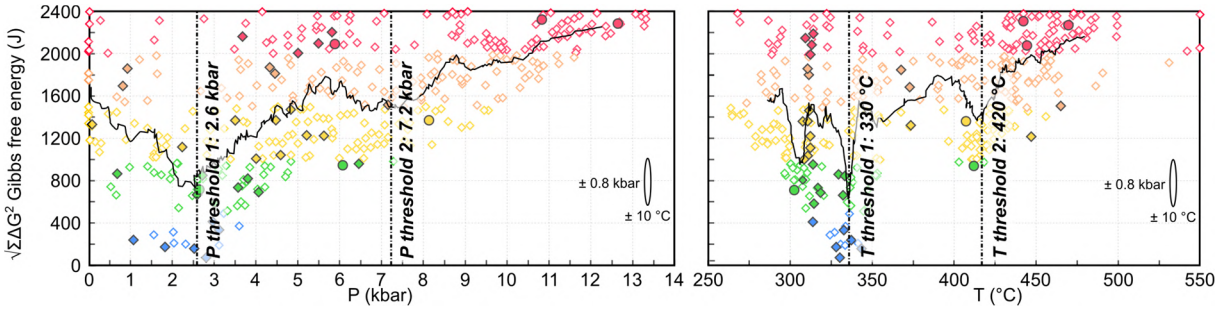


Figure 6-15: Statistical processing of pressure-temperature conditions estimated from chlorite-phengite-quartz-water multi-equilbria calculations for the syn-gold mineralization D_{2GSS} deformation stage at the Galat Sufar South deposit. P (left) and T (right) are sorted by increasing values and plotted against $\sqrt{\Sigma\Delta G^2}$ Gibbs free energy. The black line gives the Gibbs free energy running mean over 21 points.

EMPA ID	Texture	SiO_2	Al_2O_3	FeO	MnO	MgO	CaO	Na_2O	K_2O	TiO_2	Total
Chlorite											
GS-55-02											
1	Strain fringe	25.1	21.2	24.4	0.32	15.5	0.01	<L.O.D.	0.01	0.02	86.6
2	Strain fringe	25.0	21.7	23.0	0.45	16.6	0.03	<L.O.D.	<L.O.D.	0.05	86.7
3	Strain fringe	25.2	21.2	23.5	0.35	16.2	0.08	0.03	0.02	0.04	86.7
4	Strain fringe	25.6	21.3	23.6	0.36	16.7	0.02	0.07	0.01	0.04	87.7
5	*Strain fringe*	*25.0*	*21.4*	*23.5*	*0.36*	*16.8*	*0.05*	*0.04*	*0.02*	*0.04*	*87.1*
6	*Strain fringe*	*24.9*	*21.4*	*23.4*	*0.38*	*16.7*	*0.02*	*0.04*	*<L.O.D.*	*0.05*	*86.9*
7	*Strain fringe*	*25.0*	*21.0*	*23.6*	*0.32*	*16.7*	*0.02*	*0.07*	*0.02*	*0.03*	*86.8*
8	*Strain fringe*	*25.1*	*21.4*	*24.2*	*0.36*	*16.5*	*0.01*	*0.01*	*<L.O.D.*	*0.04*	*87.6*
9	*Strain fringe*	*25.2*	*21.1*	*22.9*	*0.38*	*16.9*	*0.02*	*0.14*	*0.01*	*0.05*	*86.6*
10	*Strain fringe*	*25.2*	*21.1*	*22.7*	*0.30*	*16.0*	*0.13*	*0.08*	*0.01*	*0.05*	*85.4*
11	Strain fringe	25.2	21.4	24.2	0.29	16.5	0.05	<L.O.D.	0.02	0.05	87.8
12	*Strain fringe*	*25.1*	*21.6*	*24.0*	*0.39*	*16.0*	*0.03*	*0.09*	*<L.O.D.*	*0.06*	*87.2*
13	Strain fringe	25.1	21.9	23.2	0.42	16.6	0.04	0.02	0.01	0.05	87.3
14	*Strain fringe*	*24.7*	*21.4*	*22.9*	*0.39*	*16.5*	*0.04*	*0.02*	*0.01*	*0.04*	*85.9*
15	*Strain fringe*	*25.0*	*21.5*	*23.4*	*0.30*	*16.8*	*0.02*	*0.07*	*0.02*	*0.02*	*87.1*
16	Strain fringe	25.2	21.4	23.0	0.26	15.9	0.01	0.08	<L.O.D.	0.03	85.9
17	Strain fringe	25.0	21.2	24.6	0.24	15.4	0.05	0.01	<L.O.D.	0.02	86.6
GS-55-04											
18	*Strain fringe*	*25.3*	*20.6*	*25.0*	*0.57*	*15.7*	*<L.O.D.*	*0.04*	*<L.O.D.*	*0.03*	*87.2*
19	Strain fringe	25.2	19.9	25.5	0.55	13.7	0.09	0.09	0.02	0.02	85.1
20	*Strain fringe*	*25.2*	*21.0*	*23.2*	*0.53*	*17.7*	*<L.O.D.*	*0.04*	*<L.O.D.*	*0.05*	*87.7*
21	Strain fringe	25.8	20.7	22.8	0.72	16.7	0.02	0.01	<L.O.D.	0.03	86.7
22	*Strain fringe*	*25.2*	*19.8*	*25.5*	*0.42*	*15.7*	*0.05*	*0.06*	*0.02*	*0.04*	*86.8*
23	Gangue – S_2	24.3	19.8	25.4	0.53	13.7	0.07	0.03	<L.O.D.	0.01	83.8
24	Gangue – S_2	25.3	20.3	27.1	0.46	14.3	0.08	0.08	0.02	0.02	87.6
25	Gangue – S_2	25.4	20.3	22.8	0.64	17.4	0.04	0.02	<L.O.D.	0.03	86.7
26	Gangue – S_2	25.4	20.7	23.2	0.73	17.3	0.01	0.03	<L.O.D.	0.03	87.3
27	Gangue – S_2	25.0	20.2	24.4	0.62	15.5	0.10	0.07	0.02	0.02	85.9
28	*Gangue – S_2*	*25.3*	*20.2*	*25.6*	*0.55*	*15.8*	*0.05*	*0.06*	*<L.O.D.*	*0.01*	*87.6*
29	Gangue – S_2	25.3	21.0	24.4	0.61	15.5	0.01	<L.O.D.	0.02	0.05	86.8
30	Gangue – S_2	25.4	20.3	23.4	0.59	16.9	0.02	0.04	0.01	0.05	86.6
31	Gangue – S_2	25.3	19.9	25.7	0.43	15.1	0.05	0.11	0.02	<L.O.D.	86.6
32	Gangue – S_2	25.7	20.5	23.9	0.57	15.7	0.02	0.03	0.01	0.05	86.6
33	*Gangue – S_2*	*24.2*	*19.2*	*24.7*	*0.57*	*15.6*	*<L.O.D.*	*0.04*	*0.02*	*0.03*	*84.3*
34	Gangue – S_2	25.6	20.1	26.0	0.44	14.4	<L.O.D.	0.02	0.02	0.01	86.5
35	Gangue – S_2	25.6	20.2	26.6	0.53	14.1	0.03	0.04	0.29	<L.O.D.	87.3
36	Gangue – S_2	25.7	19.9	25.1	0.52	14.7	0.07	0.04	0.04	0.02	86.1
37	Gangue – S_2	25.1	20.8	24.1	0.53	15.7	<L.O.D.	<L.O.D.	0.02	0.01	86.3
38	*Gangue – S_2*	*25.3*	*20.9*	*23.7*	*0.62*	*16.5*	*0.06*	*<L.O.D.*	*0.02*	*0.05*	*87.2*
39	Gangue – S_2	25.2	19.9	24.8	0.51	14.7	0.02	0.04	0.03	0.06	85.2
40	*Gangue – S_2*	*24.9*	*20.5*	*22.5*	*0.69*	*17.3*	*<L.O.D.*	*0.02*	*0.03*	*0.06*	*86.1*
41	*Gangue – S_2*	*25.6*	*20.6*	*26.9*	*0.47*	*12.9*	*0.09*	*0.05*	*0.01*	*<L.O.D.*	*86.7*
Phengite											
GS-55-02											
1	Gangue – S_2	46.9	31.1	4.2	0.06	1.6	0.07	0.28	9.8	0.36	94.3
2	Gangue – S_2	46.8	31.3	4.0	0.03	1.5	0.04	0.35	10.1	0.29	94.3
3	Gangue – S_2	46.6	30.6	4.0	<L.O.D.	1.9	0.01	0.23	10.2	0.16	93.7
4	Gangue – S_2	45.3	31.3	4.0	0.01	1.4	<L.O.D.	0.40	10.5	0.31	93.3
5	Gangue – S_2	45.7	30.6	3.5	0.05	1.5	0.07	0.29	10.2	0.37	92.4
6	Gangue – S_2	46.5	32.8	2.2	<L.O.D.	1.5	<L.O.D.	0.16	9.7	0.05	93.0
7	Gangue – S_2	46.9	32.6	2.3	<L.O.D.	1.4	0.07	0.20	9.5	0.06	93.1

Table 6-6 ***(continued)***

EMPA ID	Texture	SiO_2	Al_2O_3	FeO	MnO	MgO	CaO	Na_2O	K_2O	TiO_2	Total
Phengite											
GS-55-02											
8	Gangue – S_2	44.8	31.6	2.4	0.02	1.3	0.02	0.22	10.0	0.10	90.5
9	Gangue – S_2	45.2	31.2	2.6	0.02	1.3	0.03	0.28	10.3	0.14	91.0
10	Gangue – S_2	44.6	29.6	3.5	<L.O.D.	1.5	0.13	0.25	10.2	0.24	89.9
GS-55-04											
11	Gangue – S_2	47.5	28.4	5.0	<L.O.D.	2.3	<L.O.D.	0.13	10.1	0.40	93.6
12	Gangue – S_2	46.6	28.3	5.3	0.07	2.1	<L.O.D.	0.23	10.7	0.55	93.8
13	Gangue – S_2	46.8	28.2	5.2	0.07	2.2	<L.O.D.	0.20	10.7	0.54	93.9
14	Gangue – S_2	47.8	27.7	4.8	0.05	2.5	0.01	0.07	10.2	0.26	93.4
15	Gangue – S_2	47.2	27.7	5.6	<L.O.D.	2.2	<L.O.D.	0.09	10.9	0.41	94.0
17	Gangue – S_2	46.8	27.2	5.4	0.05	2.3	<L.O.D.	0.14	10.3	0.38	92.7
18	Gangue – S_2	53.6	23.9	3.8	0.05	1.6	0.09	2.7	5.9	0.25	92.0
20	Gangue – S_2	47.4	27.3	5.8	<L.O.D.	2.2	0.02	0.15	9.9	0.51	93.2
21	Gangue – S_2	47.3	27.9	5.6	0.05	2.4	0.01	0.10	9.9	0.42	93.6
22	Gangue – S_2	46.6	28.1	5.2	<L.O.D.	2.2	<L.O.D.	0.17	10.3	0.62	93.2
23	Gangue – S_2	50.2	29.3	4.9	0.04	2.2	0.20	0.12	10.0	0.38	97.5
25	Gangue – S_2	46.4	27.8	5.3	0.04	2.3	0.02	0.17	10.7	0.41	93.2
26	Gangue – S_2	46.6	27.5	5.4	0.06	2.3	0.02	0.14	10.5	0.42	92.9
27	Gangue – S_2	46.5	27.6	5.0	0.02	2.2	<L.O.D.	0.15	10.7	0.50	92.7
28	Gangue – S_2	48.0	27.4	5.1	0.01	2.5	0.03	0.22	10.5	0.26	94.0
29	Gangue – S_2	47.6	27.7	4.7	0.02	2.4	0.02	0.14	10.8	0.35	93.7
30	Gangue – S_2	46.8	27.5	5.0	0.02	2.4	0.19	0.07	10.0	0.31	92.3
31	Gangue – S_2	46.4	27.1	5.4	<L.O.D.	2.4	0.07	0.18	10.1	0.51	92.2
32	Gangue – S_2	47.3	28.6	4.6	0.05	2.2	0.01	0.14	10.5	0.36	93.8
33	Gangue – S_2	47.1	27.7	5.1	<L.O.D.	2.3	0.04	0.14	10.3	0.35	93.0
34	Gangue – S_2	47.6	27.7	5.2	0.04	2.6	0.01	0.11	10.8	0.22	94.3
35	Gangue – S_2	46.3	27.2	5.8	0.03	2.2	<L.O.D.	0.14	10.8	0.44	92.9
36	Gangue – S_2	46.7	27.3	4.8	<L.O.D.	2.3	<L.O.D.	0.18	11.0	0.46	92.8
37	Gangue – S_2	47.3	27.3	5.1	0.04	2.4	0.04	0.19	11.0	0.43	93.7
38	Gangue – S_2	46.7	27.7	5.6	0.02	2.2	<L.O.D.	0.19	11.2	0.52	94.2
39	Gangue – S_2	45.7	27.2	5.8	0.04	2.6	0.01	0.18	10.7	0.36	92.6
40	Gangue – S_2	46.8	27.5	4.7	0.05	2.5	<L.O.D.	0.10	11.0	0.32	92.9
41	Gangue – S_2	47.2	27.5	5.3	<L.O.D.	2.4	<L.O.D.	0.17	11.1	0.39	93.9
42	Gangue – S_2	45.6	27.3	6.1	0.03	2.7	0.02	0.14	10.7	0.40	92.9
43	*Gangue – S_2*	*46.3*	*26.9*	*4.9*	*0.06*	*2.6*	*<L.O.D.*	*0.07*	*11.2*	*0.27*	*92.3*
44	Gangue – S_2	47.4	27.6	4.8	0.04	2.4	<L.O.D.	0.11	11.1	0.35	93.9
45	Gangue – S_2	47.4	28.4	4.4	0.06	2.3	<L.O.D.	0.07	10.8	0.36	93.8
46	Gangue – S_2	47.5	28.2	4.8	0.02	2.2	<L.O.D.	0.19	11.0	0.36	94.3
47	Gangue – S_2	46.8	27.1	5.1	<L.O.D.	2.2	<L.O.D.	0.16	11.1	0.40	92.8
48	Gangue – S_2	47.1	27.5	4.9	0.09	2.4	0.04	0.18	11.0	0.44	93.6

Data are expressed as oxide wt. %. Limit of detection (L.O.D.) is in the range of order of 1000 oxide ppm for every oxide.
In italics: phengite and chlorite dataspots that do not fulfill the compositional criteria of Vidal and Parra (2000).

Table 6-6: Electron microprobe analyses of white mica-phengite (n=45) and chlorite (n=41) from samples GS-55-02 and -04 collected from the Galat Sufar South gold deposit.

5. Discussion

5.1. How does the Galat Sufar South magmatic event fit into the regional lithospheric evolution?

The (sub)volcanic andesite to trachyte series and pyroclastic rocks of the GSS area define a metaluminous volcanoclastic sequence with a calc-alkaline signature (Figs. 6-3, 6-10; Tables 6-1, 6-2). Their major and trace element signatures suggest their formation relates to magmatic arc volcanism. Providing their position along the Atmur-Delgo suture (Fig. 6-1; *e.g.,* Schandelmeier et al., 1994b) and U-Pb ages on zircon, we infer they record a part of the Atmur-Delgo arc magmatic activity, at least expressed by a flare-up recorded between *ca.* 760-700 Ma by zircon antecrysts and autocrysts (Figs. 6-11a, 6-16; Supplementary Material 6-2). The Hf isotopic composition of *ca.* 750-695 Myr-old zircon antecrysts from the syn-tectonic subvolcanic trachyte demonstrates that the Atmur-Delgo arc rocks are juvenile with melt extraction from the mantle occurring between *ca.* 1.03-0.93 Ga (Fig. 6-16; Table 6-4). Conversely, crustal reworking of ancient crust of the Saharan meta-craton is recorded in the western Delgo suture (Fig. 6-16; Harms et al., 1994), similarly to what is suggested along a continental arc parallel to the Keraf suture southwards (**Chapter I**).

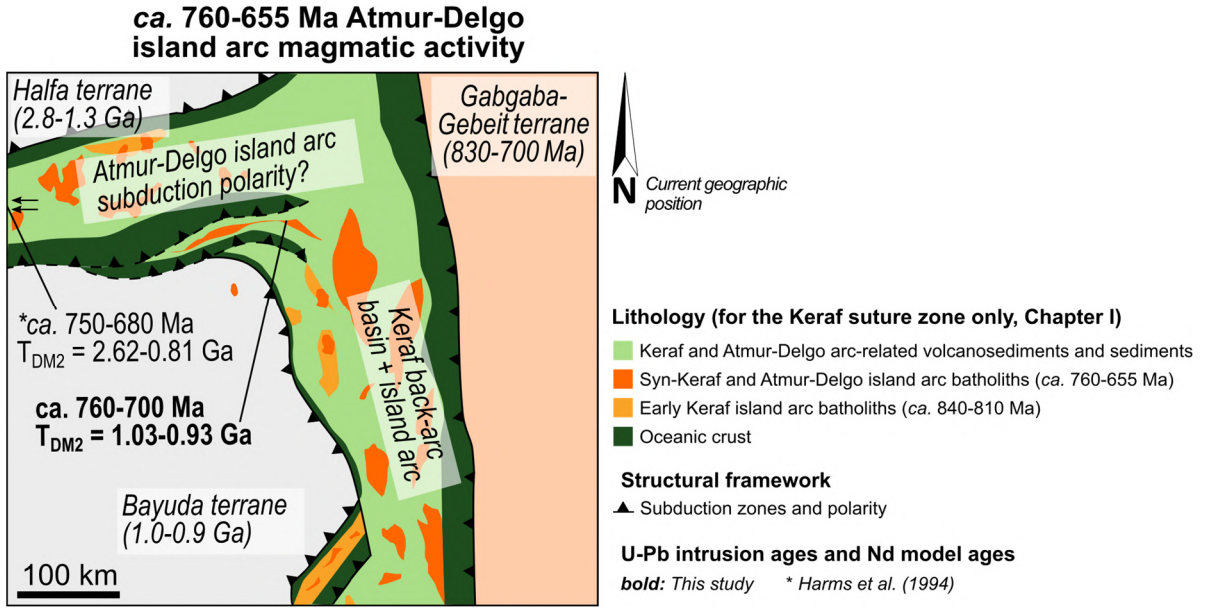


Figure 6-16: Map view of the possible regional-scale oceanic subduction scenario recorded along the Atmur-Delgo suture (modified after **Chapter I**). Isotopic data from literature summarized in this figure and discussed in the text are from Harms et al. (1994) for the western Delgo suture.

In addition to similar U-Pb ages and Hf isotopic compositions (Fig. 6-11; **Chapter I**), the *ca.* 760-695 Ma island arc volcanic rocks of the GSS area have chondrite-normalized LREE abundances somehow comparable to *ca.* 760-655 Ma Keraf island arc granitoids (Fig. 6-10c-e; **Chapter I**). We could therefore suggest the same geodynamical setting, *i.e.,* ocean-ocean subduction and island arc magmatism, for the Keraf basin and the Atmur-Delgo oceanic re-entrant at *ca.* 760-655 Ma, in agreement with coeval Atmur-Delgo and Keraf suturing documented in literature (**Chapter I**; Denkler et al., 1993, 1994; Harms et al., 1994; Schandelmeier et al., 1994b; Abdelsalam et al., 1998). However, (sub)volcanic and pyroclastic rocks from the GSS area have higher HREE contents which are close to the ones measured for *ca.* 840-810 Ma early Keraf island arc igneous rocks. We interpreted the relative HREE depletion of *ca.* 760-655 Ma cumulates in the central Keraf suture due to melt production and fractionation at pressure conditions high enough to ensure garnet stability, in agreement with arc maturation lasting since 50 Myr at least (**Chapter I**). Despite a very limited sampling in the GSS area, there is no evidence for >800 Ma island arc magmatism, which is besides not documented elsewhere along the Atmur-Delgo suture neither. We may suggest that island arc magmatism initiated earlier in the Keraf oceanic basin than in the Atmur-Delgo aulacogen re-entrant, which has therefore recorded a less mature intra-oceanic subduction setting at *ca.* 760-655 Ma. These data enable to reappraise the D_{1a} Atmur-Delgo subduction timing that was so far thought to occur prior to 750 Ma with arc-continent collision at ~700 Ma (Schandelmeier et al., 1994b; Abdelsalam et al., 1998).

5.2. Pressure-temperature-timing constraints on Galat Sufar South gold mineralization and related geodynamical setting

As suggested by its preferential paragenetic association with chlorite, sericite and pyrite coeval to the gold mineralizing D_{2GSS} deformation stage, we infer that apatite likely records the main gold event forming the GSS deposit (Fig. 6-4d-f). Apatite is interpreted

to be hydrothermal, and the rounded and fractured aspect of the cores may suggest it results from progressive crystallization during the D_{1GSS}-D_{2GSS} deformation episode, coeval with D_{1ADS} Atmur-Delgo intra-oceanic subduction and island arc magmatic activity (Perret et al., 2020). Rims have likely recrystallized from dissolution/precipitation processes affecting the cores as they show similar radiogenic elemental concentrations. The obtained 737.9±15.6 Ma age is therefore interpreted as the age of D_{1GSS}-D_{2GSS} deformation and concomitant gold mineralization at the GSS deposit. These geochronological considerations confirm the conclusions from Perret et al. (2020) stating that the GSS deposit cannot be considered as typical of orogenic gold genetically associated to late orogenic Keraf strike-slip shearing. Despite the spatial relationship between the GSS deposit and the Keraf shear zone at its junction with the Atmur-Delgo suture (Johnson et al., 2017), the GSS gold event irrevocably relates to the early Atmur-Delgo suturing, prior to arc-continent collision.

P-T multi-equilibria conditions constrain the D_{2GSS} deformation stage and concomitant gold mineralization ~7.2 kbar-420 °C for the GSS gold deposit. These conditions reflect upper greenschist to lower amphibolite facies metamorphism, which is the peak metamorphism facies reached at the regional and Arabian-Nubian shield scale (Ahmed Suliman, 2000; Johnson et al., 2011; Fritz et al., 2013; Abanyin et al., 2015). Such *P-T* conditions support our hypothesis stating that the trace element evolution pattern in pyrite observed at the GSS deposit is indicative of syn-gold mineralization pyrite recrystallization under amphibolite facies metamorphism (**Chapter IV**; Dakota Conn et al., 2019). Besides, these metamorphic conditions are important enough to observe sheath folds (*e.g.,* Muir, 2002; Tomkins et al., 2004) and non-coaxial ductile flow of pyroclastic deposits (*e.g.,* Calderón et al., 2005), as observed for the ore-bearing volcanosedimentary horizon at the GSS gold deposit (**Chapter II**; Perret et al., 2020). Our data suggest that the GSS gold deposit is coeval with tectonic accretion and the formation of the volcanosedimentary assemblage-dominated wedge in an accretionary-

type subduction setting (review by Guillot et al., 2009). The *P-T* conditions recorded and the regional lithological framework (**Chapter II**; Perret et al., 2020) indeed match those of exhumed high pressure rocks in accretionary wedges formed in an intra-oceanic subduction context (*e.g.,* Indus suture, Pakistan or Sapi-Shergol mélange zone, India; Anczkiewicz et al., 2000; Mahéo et al., 2006). We can approximate a 21 km-depth of formation for the GSS deposit and exhumation of ore-hosting medium-grade metamorphic rocks, by considering a 0.3 kbar/km lithostatic pressure gradient. The sedimentary prism must therefore have been narrow enough at depth to prevent from exhumation of higher pressure rocks which are further recycled in the mantle: the pro-wedge and plug uplift model of Guillot et al. (2009) likely suits the geometry of the Atmur-Delgo fore-arc at *ca.* 750-720 Ma, when the GSS deposit formed.

The geodynamical setting of the GSS gold deposit suggests that mineralizing fluids may be derived from prograde to peak metamorphism in the fore-arc and the suturing area hosts gold deposits. The main insight is that we propose a different timing than the typical late tectonic mobilization of mineralizing fluids along major crustal shear zones invoked by Kerrich et al. (2005) in such settings. Most of lode gold deposits and occurrences previously studied in the Arabian-Nubian shield are indeed typical of orogenic gold *sensu stricto* or intrusion-related gold, formed in a *ca.* 650-600 Ma late orogenic context (*e.g.,* Doebrich et al., 2004; Zoheir et al., 2015, 2018b, 2019d, 2019e; Harbi et al., 2018; Abd El Monsef, 2019), under retrograde greenschist facies metamorphic conditions according to the minimal *P-T* conditions calculated from fluid inclusions in quartz (*e.g.,* Helmy et al., 2004; Zoheir and Moritz, 2014; Helmy and Zoheir, 2015; Abd El Monsef et al., 2018, 2020; Zoheir et al., 2019c). At the GSS deposit, the record of ~2.6 kbar-330°C retrograde greenschist facies metamorphism likely relates to ductile-brittle D_{3GSS} deformation stage or later brittle D_{4GSS} deformation phase, associated with late ore remobilization, unraveled at the deposit scale (Perret et al., 2020).

These new *P-T* and geochronological data make the GSS deposit (i) the oldest lode gold occurrence documented throughout the Nubian shield and (ii) the only one to occur at peak regional metamorphism conditions, recorded to date, in an intra-oceanic subduction setting to date. The relationships of the GSS gold mineralization with magmatic and tectonic accretion prior to arc-continent collision is therefore roughly valid at the Nubian shield scale, despite the diachronism of geodynamical events across the Arabian-Nubian shield (Johnson et al., 2011; Fritz et al., 2013). The potential for syn-tectonic accretion lode gold deposit formation in the Neoproterozoic Arabian-Nubian shield must therefore not be underestimated.

5.3. Timing of orogenic gold at the Gabgaba district recorded by the WG03 deposit

Due to its preferential location at the margins of mineralized veins, apatite is considered as a proximal marker coeval to gold mineralization at the WG03 deposit (Figs. 6-5, 6-6, 6-7; Table 6-5). Obtained ages therefore constrain veining at 584.1±15.1 Ma and 553.7±3.3 Ma (Fig. 6-12b, c). The formation of gold-bearing veins at the WG03 and Central Zone gold deposits is attributed to typical orogenic gold formation during late collisional Keraf strike-slip shearing affecting the central Keraf suture (**Chapter III**). However, an undeformed monzogranite pluton, interpreted as post-collisional and located just a few km east to the WG03 deposit, was dated at *ca.* 620 Ma (**Chapter I**). The only way to interpret collectively these data is to suggest that Keraf strike-slip shearing is responsible for localized deformation along multiple-order shear zones, which may have been reactivated at multiple times (*e.g.,* the West Corridor in the central Gabgaba district which is a second-order structure to the Keraf shear zone; **Chapter III**). The shift from (i) distributed ductile deformation during Keraf thrusting, at the climax of arc-continent collision and leading to the emplacement of the regional main penetrative fabric (**Chapter III**), to (ii) late collisional ductile-brittle to brittle Keraf strike-slip shearing with strain partitioning is typical of the tectonic evolution of crustal- to

lithospheric-scale shear zones (*e.g.,* Ramsay and Graham, 1970; Mancktelow and Pennacchioni, 2005; Mehl et al., 2005; Meyer et al., 2019). In addition of bringing the youngest ages for orogenic gold in the Arabian-Nubian shield to date (see references cited above), U-Pb dating of veining-related hydrothermal apatite therefore illustrates the episodic tectonic activity linked to late collisional Keraf strike-slip shearing at the dusk of Neoproterozoic.

5.4. Additional constraints on Keraf island arc magmatic activity

According to its euhedral shape and widespread position in the Central Zone ore-bearing granitoid, apatite is interpreted as magmatic (Figs. 6-8, 6-9; Table 6-5). Where the granitoid is deformed by veins, anhedral apatite likely resulted from fracturing of magmatic grains, as suggested by their similar internal textures (Fig. 6-2). U-Pb dating of apatite leads to consider two distinct ages of a 791.5±19.4 Ma and 663.9±17.8 Ma. There is however no textural, geochemical nor analytical reason that could account for such a difference in ages obtained for the two analytical batches. We therefore have to question ourselves about the significance of these ages and their reliability and a misprocessing of raw data cannot be excluded. In addition to checking and reprocessing of these data, we plan to perform further U-Pb dating on magmatic apatite from sample CZ11 in the weeks to come to address this uncertainty. If we consider one of these two ages as a reliable date of intrusion for granitoids in the Central Zone area, this magmatic event would fall in the range of a Keraf island arc magmatic flare-up expressed throughout the central Zone (**Chapter I**)**.** Unfortunately, the granitoid samples are intensively altered and their whole rock composition cannot be consistently compared to the ones of the batholiths dated in **Chapter I** to confirm this assumption

Despite uncertainties about the obtained dates, they nevertheless suggest that the ore-hosting granitoid intrusion occurred at least ~65 Myr earlier than the gold event forming the Central Zone deposit, provided it is coeval to the WG03 deposit (**Chapter**

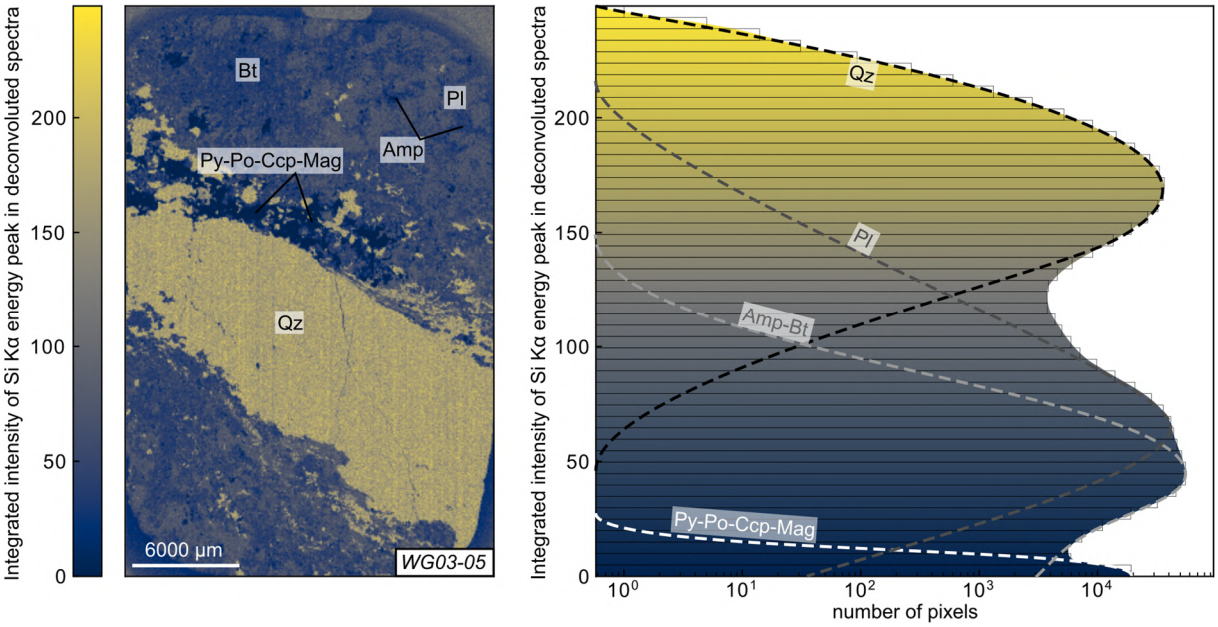
III). This information is crucial to the understanding of the Central Zone deposit history as it was uncertain whether the granitoid intrusions predated or were concomitant to Keraf strike-slip shearing. Indeed, the influence of Keraf deformation on granitoids is hardly visible due to its preferential expression in surrounding sediments in answer to a strong enhanced rheological contrast (**Chapter III**). Pending confirmation, U-Pb dating of magmatic apatite at the Central Zone deposit finally support a pre-Keraf deformation timing for the magmatic intrusion of ore-hosting granitoids, in agreement with the suggested deposit-scale petrological-structural-ore history (**Chapter V)**.

6. Conclusions

U-Pb dating of hydrothermal and magmatic apatite from the Galat Sufar South, WG03 and Central Zone gold deposits provide additional constraints on the Pan-African gold mineral system of the western Nubian shield. The Galat Sufar South gold deposit formed at 737.9±15.6 Ma under ~7.2 kbar-420 °C amphibolite facies metamorphism conditions. The formation of the Galat Sufar South deposit is coeval with intra-oceanic subduction and prolonged island arc volcanism dated at *ca.* 760-700 Ma (U-Pb dating on zircon from subvolcanic trachyte), during the Atmur-Delgo intra-oceanic subduction, coexisting with the Keraf island arc southeastwards. In agreement with the nature of host rocks at the Galat Sufar South deposit and deformation style previously documented, these data support a gold mineralization event occurring during the tectonic accretion of the sedimentary wedge in the fore-arc of the Atmur-Delgo arc complex. These new *P-T* and geochronological data make the GSS deposit (i) the oldest lode gold occurrence documented throughout the Nubian shield and (ii) the only one to occur at peak regional metamorphism conditions in an intra-oceanic subduction setting to date. Moving to the central Keraf suture, we bring additional temporal constraints on the late collisional orogenic gold event contributing to the formation of the WG03 deposit and expressed by *en échelon* quartz veins. These structures relate to the ductile-brittle Keraf strike-slip shearing and formed episodically at *ca.* 600-550 Ma according to U-Pb dating of proximal hydrothermal apatite. The Central Zone gold deposit formed over the same period by dilational veining affecting granitoids intruded at least 65 Myr earlier, pending confirmation of U-Pb ages of magmatic apatite. Ages for the main gold mineralization and host rocks at the WG03 and Central Zone deposits, respectively, are consistent with the petrological-structural models suggested in previous chapters of this manuscript. Ages reported for orogenic gold deposits in this study are the youngest at the Arabian-Nubian shield scale up to date. Besides, they illustrate the localized, episodic and polyphase nature of Keraf strike-slip shearing lasting at least until *ca.* 550 Ma.

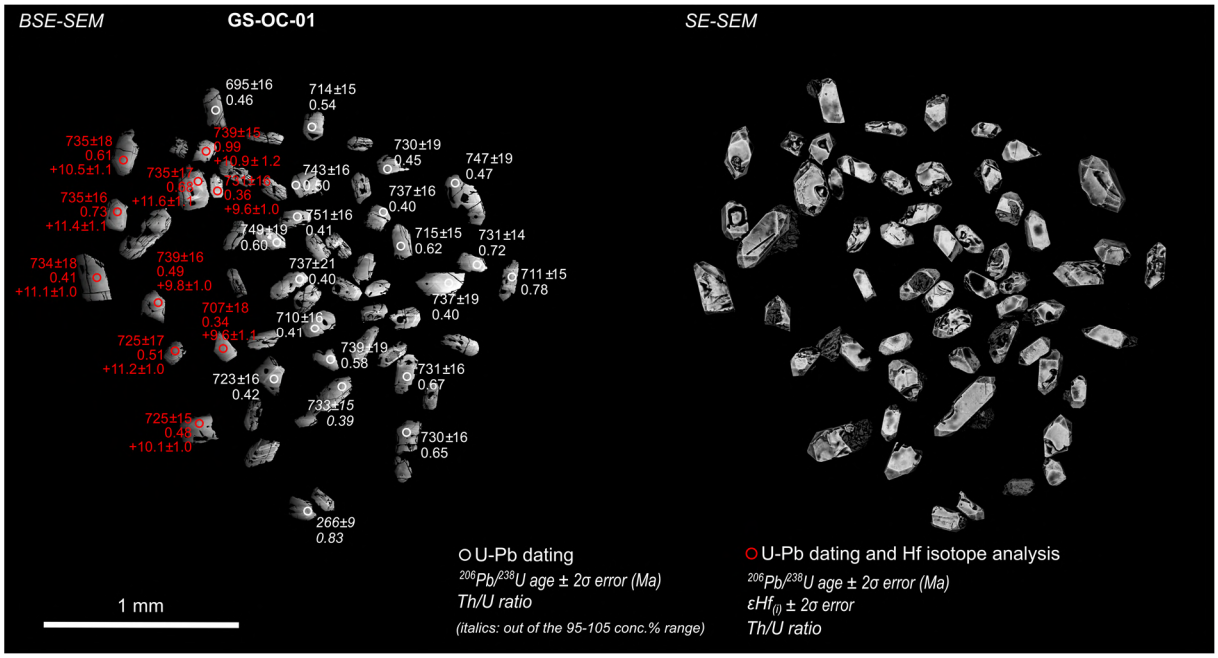
Supplementary Materials

Supplementary Material 6-1: Processing of micro-XRF elemental maps using the open-source MARCIA Python routine to get a quantitative mineral map: example of setting of thresholds in Si intensity in spectra for thin section WG03-05.

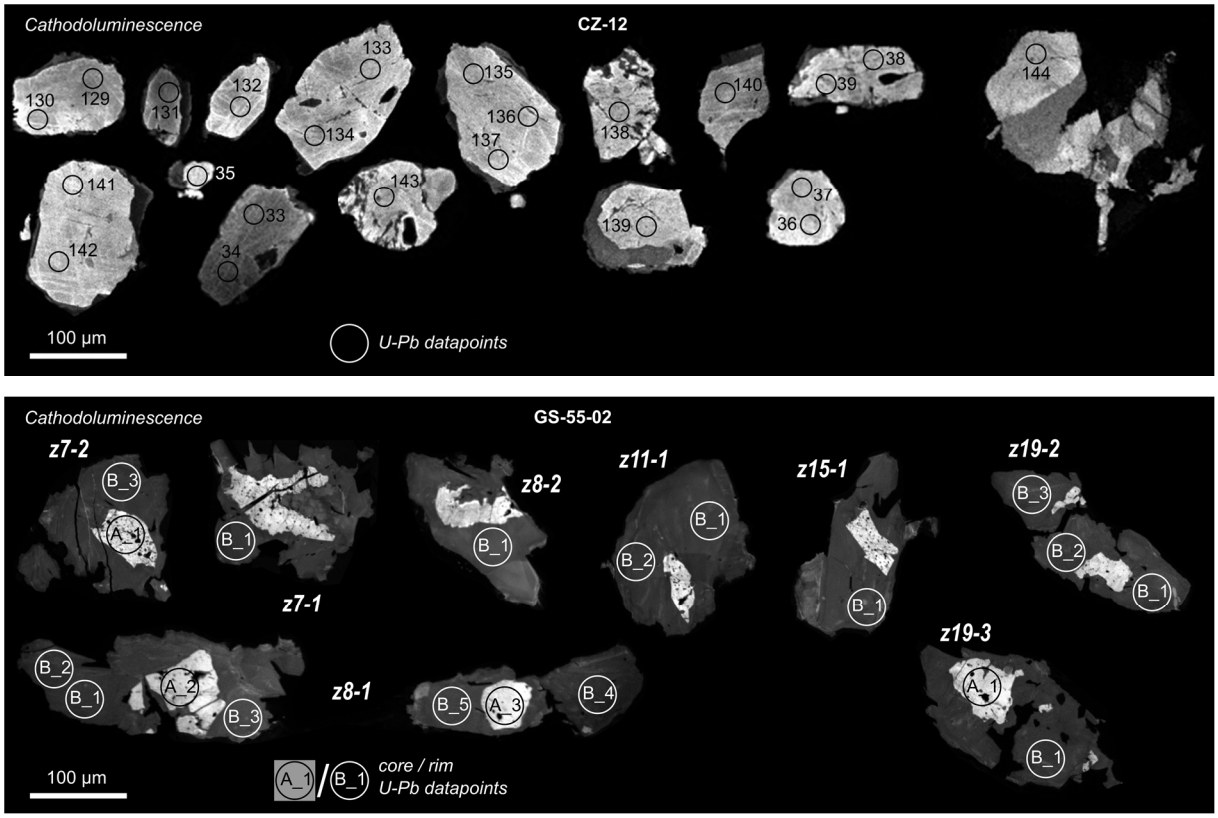


The raw elemental maps have been deconvoluted following a pseudo-Voigt function using the PyMca toolkit (Solé et al., 2007). The comparison between the histogram of Si intensity in spectra and the associated map enables to approximate the range of Si intensity associated to each mineral phase described. Thresholds can be therefore fixed for mineral indexing. The histogram is dominated by the signature of the predominant Si-bearing minerals in this example, *i.e.*, quartz, plagioclase feldspar, amphibole and biotite, hiding the signature of minor epidote or titanite. Besides, Si intensity ranges may largely overlap for different minerals (*e.g.,* plagioclase and amphibole-biotite). Mineral classification therefore requires to define masks from a linear combination of elemental intensities in spectra to better discriminate between mineral species that share similar intensity pattern for a given element. Mineral abbreviations are Amp = amphibole; Bt = biotite; Ccp = chalcopyrite; Mag = magnetite; Pl = plagioclase feldspar; Po = pyrrhotite; Py = pyrite; Qz = quartz.

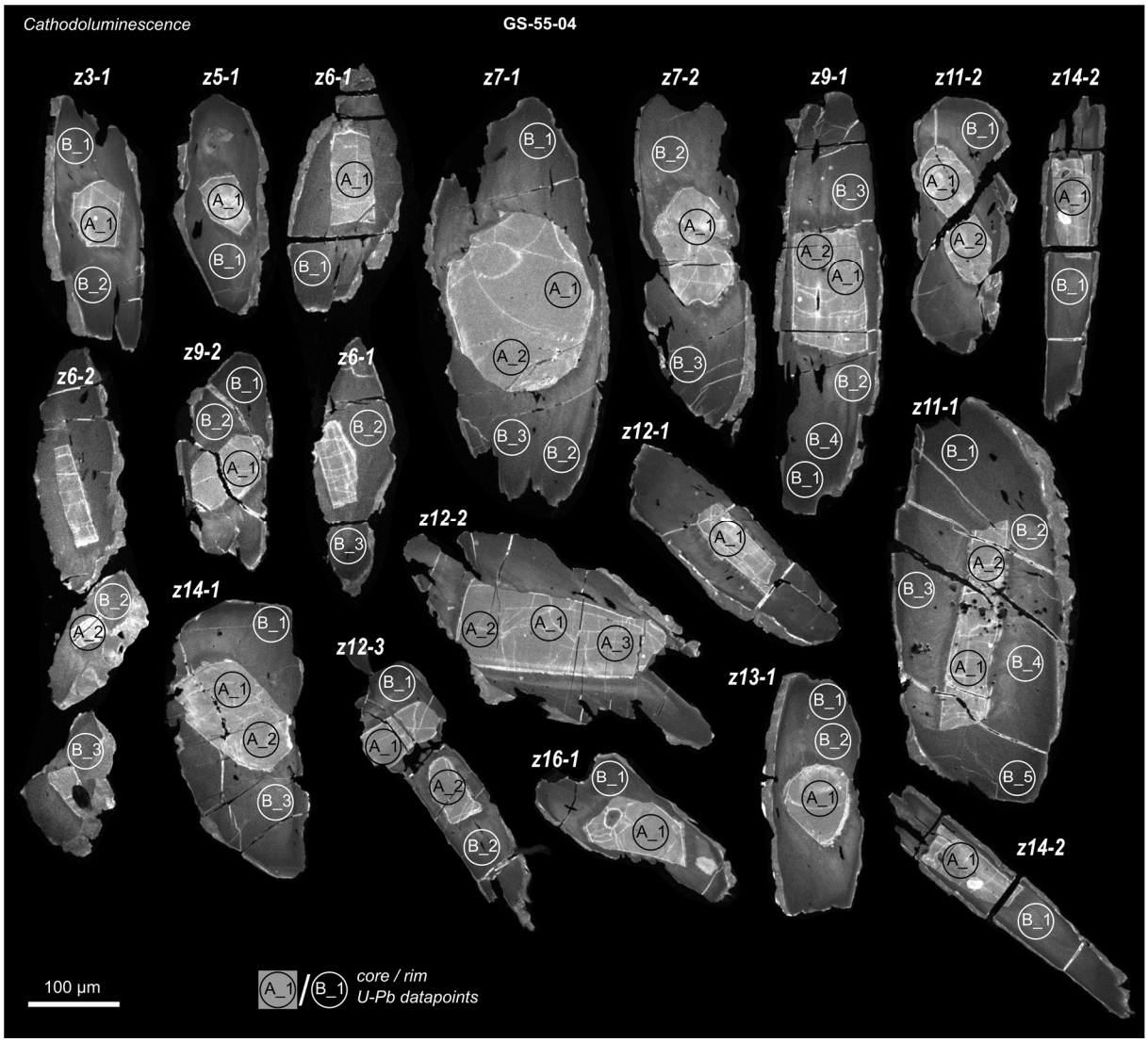
Supplementary Material 6-2: Scanning electron microscopy images illustrating zircon morphologies of GS-OC-01 trachyandesite and U-Pb and Hf zircon isotope dataspot location in back-scattered electron mode (BSE-SEM).



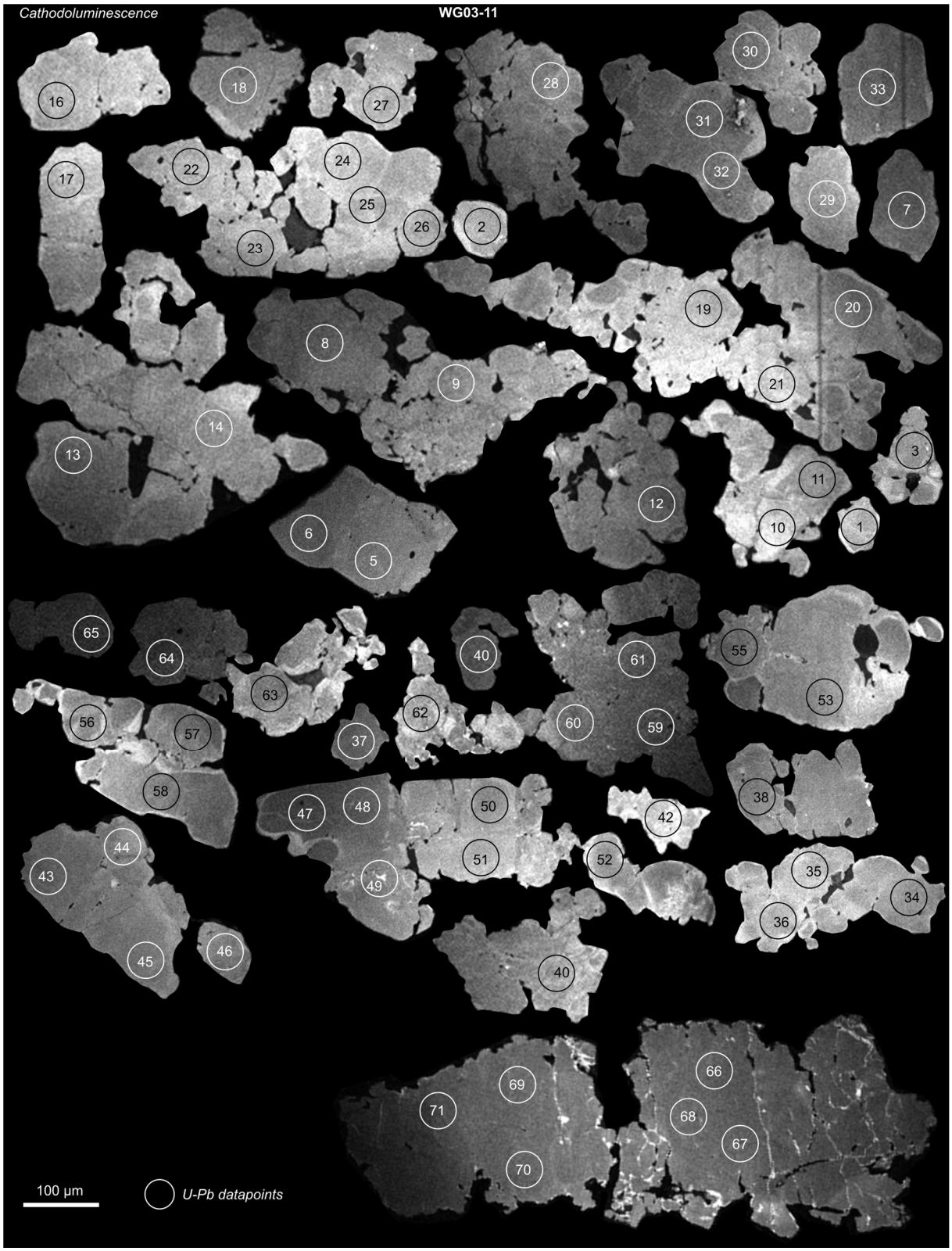
Supplementary Material 6-3: Cathodoluminescence microphotographs of dated apatite grains with U-Pb dataspot location.



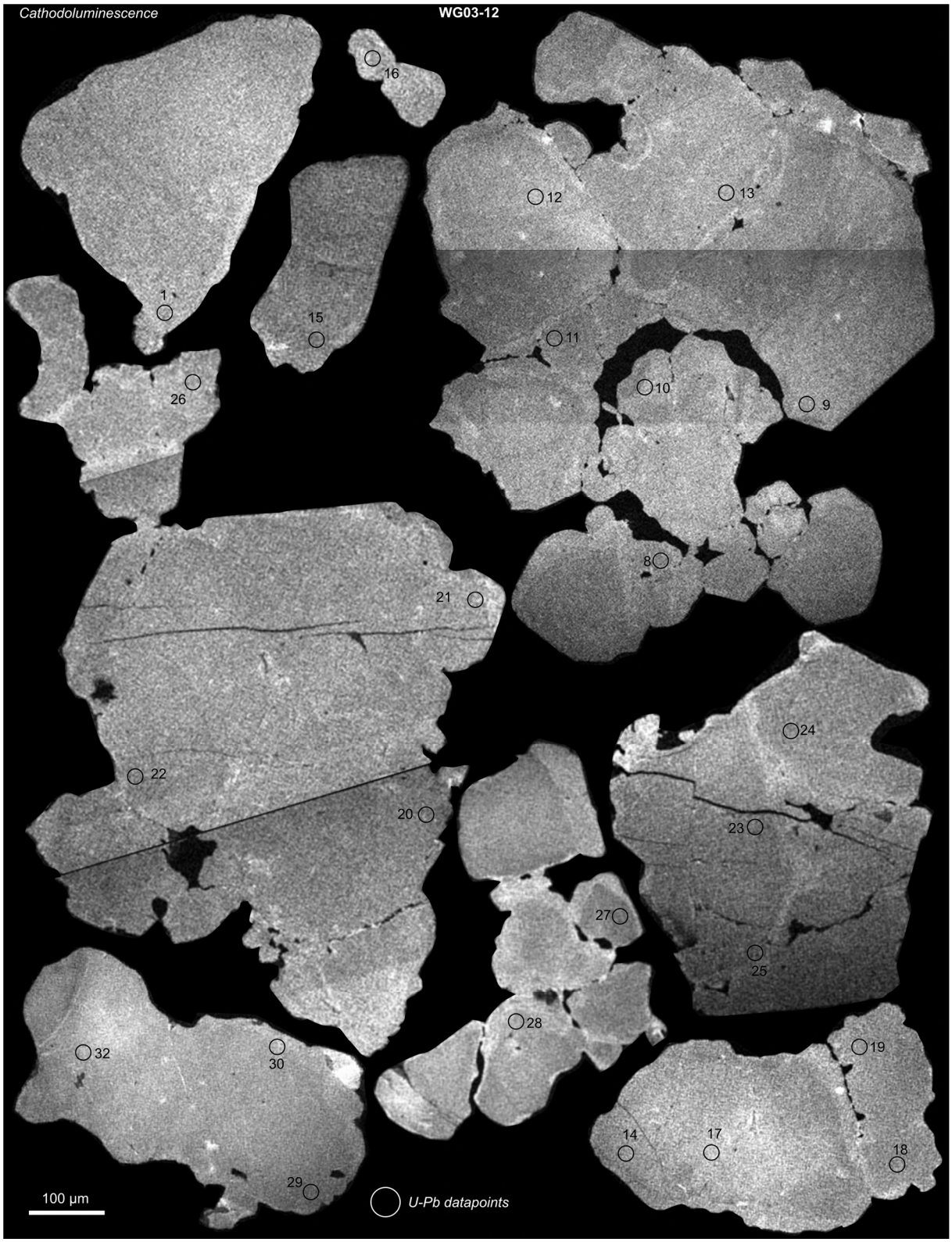
Supplementary Material 6-3 ***(continued)***



Supplementary Material 6-3 ***(continued)***



Supplementary Material 6-3 ***(continued)***



Supplementary Material 6-4: Chlorite-phengite-quartz-water multi-equilibria calculated from coexisting chlorite and white mica compositions.

Eq.	**Chl**	**Phg**	#Fe^{3+}		$H_{v,\ Phg}$	P	T	$\sqrt{\Sigma\Delta G^2}$	Eq.	**Chl**	**Phg**	#Fe^{3}		$H_{v,\ Phg}$	P	T	$\sqrt{\Sigma\Delta G^2}$
Type	**ID**	**ID**	Chl	Phg	(%)	(kbar)	(°C)	(J)	Type	**ID**	**ID**	Chl	Phg	(%)	(kbar)	(°C)	(J)
2	39	44	0.22	0.98	90.3	2.8	330	73	1	34	46	0.23	0.90	92.1	1.0	302	927
2	32	12	0.20	0.96	89.4	2.5	343	158	1	35	22	0.20	1.00	89.6	4.4	341	929
2	35	46	0.20	0.91	90.4	1.8	328	174	1	34	12	0.23	0.96	91.9	1.4	305	934
1	35	44	0.20	0.99	90.1	3.1	333	190	1	34	45	0.23	1.00	91.0	4.2	319	940
1	35	12	0.20	0.98	90.2	2.3	331	201	1	19	22	0.23	1.00	91.9	3.3	305	941
1	32	46	0.20	0.90	89.6	2.0	341	210	1	21	13	0.17	0.95	74.6	6.1	412	945
2	32	3	0.19	0.24	89.8	1.1	337	240	3	21	14	0.17	0.95	74.6	6.1	412	945
1	39	46	0.21	0.90	90.7	1.6	324	288	2	36	23	0.27	1.00	91.3	6.5	314	960
1	39	12	0.21	0.96	90.5	2.0	327	314	1	19	13	0.23	1.00	92.2	2.1	300	961
2	39	13	0.21	1.00	90.1	3.1	333	335	1	36	13	0.26	1.00	92.2	2.1	300	965
1	39	15	0.22	1.00	90.0	3.6	334	371	1	21	12	0.16	0.85	72.8	4.8	418	981
2	34	15	0.23	1.00	91.3	3.0	314	413	1	21	22	0.18	1.00	77.3	7.3	403	982
1	35	13	0.20	1.00	89.9	3.2	336	490	1	32	35	0.18	1.00	88.0	3.4	355	1004
1	32	44	0.21	0.99	89.3	3.3	345	515	1	21	3	0.16	0.00	75.0	4.2	411	1008
1	34	44	0.23	0.98	91.6	2.2	309	543	2	36	29	0.25	1.00	91.7	4.0	308	1008
1	32	13	0.20	1.00	89.2	3.6	348	562	1	23	13	0.14	1.00	74.8	6.6	411	1012
1	35	15	0.20	1.00	89.8	3.7	337	567	1	21	25	0.16	1.00	74.1	6.0	414	1013
2	34	27	0.23	1.00	91.3	3.0	314	587	1	32	32	0.20	1.00	88.4	5.2	353	1019
1	39	27	0.21	1.00	90.0	3.6	335	601	1	36	35	0.25	1.00	92.4	1.6	297	1022
1	34	13	0.23	1.00	91.5	2.5	312	658	1	36	25	0.26	1.00	92.5	1.5	297	1023
1	35	3	0.19	0.27	90.9	0.7	320	664	1	23	12	0.13	0.91	73.6	5.3	415	1036
2	39	25	0.20	1.00	90.1	2.6	332	666	1	23	3	0.13	0.00	73.6	4.4	416	1040
2	34	32	0.23	1.00	91.0	4.1	318	691	2	36	11	0.26	1.00	91.5	4.6	311	1042
3	19	15	0.23	1.00	92.0	2.7	302	716	1	35	35	0.18	1.00	89.7	2.8	339	1042
1	19	15	0.23	1.00	92.0	2.7	302	716	1	35	32	0.20	1.00	89.6	4.8	341	1043
1	36	15	0.26	1.00	92.0	2.6	303	718	1	19	25	0.22	1.00	92.5	1.6	297	1054
1	32	15	0.21	1.00	89.2	4.0	347	720	1	19	35	0.22	1.00	92.4	1.7	298	1067
2	34	22	0.23	1.00	91.1	3.6	317	735	1	35	1	0.20	0.00	91.4	0.3	313	1070
1	39	22	0.21	1.00	89.9	4.2	337	739	1	23	25	0.13	1.00	71.8	6.4	421	1098
1	39	3	0.20	0.20	91.1	0.5	317	742	1	21	35	0.16	1.00	73.5	6.2	416	1100
1	36	32	0.26	1.00	91.7	3.7	308	749	1	19	23	0.24	1.00	91.3	6.6	315	1103
1	35	27	0.20	1.00	89.8	3.8	338	792	1	21	27	0.18	1.00	76.7	6.7	405	1114
1	36	27	0.26	1.00	92.1	2.6	302	809	2	34	40	0.22	1.00	91.4	2.2	312	1118
1	19	32	0.23	1.00	91.7	3.7	308	810	1	19	29	0.22	1.00	91.6	4.1	309	1124
1	19	27	0.23	1.00	92.0	2.7	303	815	1	41	15	0.22	1.00	94.3	1.6	279	1132
1	34	25	0.22	1.00	91.6	2.0	310	816	1	36	40	0.25	1.00	92.2	1.9	300	1132
1	35	25	0.19	1.00	89.9	2.7	336	817	1	23	22	0.14	1.00	75.1	7.7	410	1132
2	36	45	0.26	1.00	91.7	3.8	308	820	1	31	22	0.18	1.00	72.4	8.2	420	1140
1	39	32	0.22	1.00	89.8	4.7	337	836	1	34	23	0.24	1.00	90.7	6.9	324	1143
1	32	25	0.18	1.00	88.4	3.2	353	849	1	31	13	0.17	1.00	72.1	7.1	420	1149
2	39	35	0.20	1.00	90.1	2.7	333	850	1	34	11	0.23	1.00	90.8	5.0	322	1152
1	19	44	0.23	0.98	92.5	1.7	297	855	1	19	11	0.23	1.00	91.5	4.6	311	1152
1	32	27	0.20	1.00	88.6	4.2	352	857	1	36	46	0.26	0.89	93.5	0.3	286	1154
2	32	1	0.20	0.00	90.3	0.7	329	865	1	21	15	0.17	0.97	75.8	6.4	408	1159
1	36	44	0.26	0.98	92.5	1.6	297	876	1	41	45	0.22	1.00	93.5	3.0	286	1163
1	32	22	0.20	1.00	88.3	4.8	353	877	1	39	1	0.22	0.00	91.6	0.2	310	1166
1	34	35	0.22	1.00	91.5	2.0	310	880	1	34	29	0.22	1.00	90.9	4.5	320	1167
1	36	22	0.26	1.00	91.9	3.1	304	907	1	21	46	0.16	0.83	73.3	4.3	416	1168
1	19	45	0.23	1.00	91.7	3.9	308	926	1	41	32	0.22	1.00	93.6	2.8	286	1172

Supplementary Material 6-4 ***(continued)***

Eq.	Chl	Phg	#Fe^{3+}		$H_{v,\ Phg}$	P	T	$\sqrt{\Sigma\Delta G^2}$	Eq.	Chl	Phg	#Fe^{3}		$H_{v,\ Phg}$	P	T	$\sqrt{\Sigma\Delta G^2}$
Type	ID	ID	Chl	Phg	(%)	(kbar)	(°C)	(J)	Type	ID	ID	Chl	Phg	(%)	(kbar)	(°C)	(J)
1	21	32	0.19	1.00	78.9	7.5	397	1180	1	41	35	0.22	1.00	95.0	0.7	272	1447
1	19	46	0.23	0.88	93.9	0.0	283	1182	1	32	39	0.15	1.00	85.2	2.5	368	1455
1	19	12	0.23	0.95	93.1	0.9	291	1186	1	35	40	0.18	1.00	89.7	3.1	339	1457
1	21	44	0.16	0.94	73.7	5.4	415	1190	1	24	27	0.15	1.00	68.4	8.3	433	1458
1	23	35	0.12	1.00	71.0	6.6	424	1201	1	32	23	0.23	1.00	89.2	7.9	347	1463
1	41	23	0.22	1.00	92.5	5.8	297	1203	1	16	22	0.11	1.00	64.8	9.6	445	1464
1	19	40	0.22	1.00	92.2	1.9	300	1207	1	10	32	0.13	1.00	68.9	9.5	431	1465
1	23	27	0.14	1.00	74.9	7.2	411	1210	2	36	21	0.25	1.00	91.5	4.8	312	1472
1	23	46	0.13	0.87	74.1	4.8	414	1222	1	41	20	0.22	1.00	92.9	4.4	293	1472
2	21	39	0.13	1.00	64.2	5.6	447	1224	1	35	45	0.19	1.00	89.4	5.1	343	1473
1	41	27	0.22	1.00	94.3	1.7	279	1227	1	23	40	0.12	1.00	68.3	7.1	433	1473
2	36	20	0.26	1.00	91.4	5.2	312	1228	1	39	29	0.21	1.00	89.7	5.1	339	1476
1	23	15	0.14	0.99	75.9	6.9	408	1237	1	21	11	0.19	1.00	79.6	8.4	394	1479
1	39	45	0.21	1.00	89.8	4.9	338	1238	1	19	26	0.22	1.00	91.7	3.5	308	1480
1	23	44	0.13	0.96	74.1	5.9	414	1249	1	31	46	0.17	0.88	71.6	5.3	422	1495
1	31	25	0.17	1.00	69.5	6.8	429	1252	1	41	44	0.20	0.97	95.7	0.0	264	1496
1	39	40	0.20	1.00	89.9	2.9	336	1279	1	19	33	0.22	1.00	91.5	4.5	311	1498
1	31	27	0.17	1.00	72.1	7.6	420	1283	1	24	15	0.16	1.00	70.3	8.1	426	1499
1	31	12	0.17	0.93	71.1	5.8	424	1288	1	24	25	0.14	1.00	65.0	7.5	444	1501
1	41	22	0.22	1.00	93.9	2.3	283	1292	1	34	26	0.22	1.00	91.0	3.9	320	1504
1	41	29	0.22	1.00	93.4	3.2	288	1292	1	24	32	0.15	1.00	69.9	9.3	428	1513
1	36	12	0.27	1.00	92.7	1.4	295	1296	2	21	42	0.12	1.00	58.8	7.2	465	1516
1	24	22	0.15	1.00	68.4	8.9	433	1303	1	24	12	0.16	0.99	70.6	6.6	425	1518
1	21	10	0.16	0.02	84.0	0.1	373	1316	1	41	40	0.21	1.00	94.8	0.9	273	1544
1	10	22	0.13	1.00	67.2	9.1	437	1320	1	34	33	0.22	1.00	90.8	4.9	322	1555
1	31	35	0.16	1.00	68.1	7.1	434	1326	1	39	39	0.18	1.00	90.2	1.4	331	1557
2	23	10	0.12	0.00	83.9	0.1	374	1332	1	10	13	0.13	1.00	66.9	8.0	438	1559
1	31	15	0.18	0.99	73.2	7.4	417	1336	1	10	27	0.13	1.00	67.0	8.5	437	1573
1	34	3	0.24	0.35	93.0	0.0	292	1341	1	21	23	0.22	1.00	82.7	9.8	379	1575
1	41	13	0.22	1.00	94.7	1.1	275	1342	1	23	1	0.15	0.00	80.1	3.3	391	1582
1	21	40	0.15	1.00	71.3	6.6	423	1345	1	16	32	0.12	1.00	66.5	9.9	439	1582
1	24	13	0.15	1.00	68.6	7.7	432	1345	1	21	45	0.18	1.00	77.4	8.0	403	1586
1	41	11	0.22	1.00	93.2	3.8	290	1347	1	31	40	0.16	1.00	67.8	7.3	435	1587
1	31	3	0.16	0.00	70.3	5.0	426	1354	1	34	39	0.20	1.00	92.0	0.7	303	1591
1	19	20	0.23	1.00	91.4	5.2	313	1356	1	41	33	0.21	1.00	93.3	3.6	289	1600
1	31	32	0.18	1.00	73.6	8.6	415	1359	1	19	21	0.22	1.00	91.4	4.9	312	1601
1	32	40	0.17	1.00	87.1	3.7	359	1361	1	35	11	0.19	1.00	89.4	5.8	344	1605
1	39	23	0.23	1.00	89.8	7.5	338	1361	1	39	20	0.22	1.00	89.7	6.3	339	1609
2	36	26	0.25	1.00	91.7	3.5	308	1369	1	35	23	0.22	1.00	89.6	7.6	341	1613
3	23	32	0.14	1.00	76.1	8.1	407	1370	1	31	39	0.14	1.00	59.3	6.4	464	1640
1	23	32	0.14	1.00	76.1	8.1	407	1370	1	24	44	0.16	0.98	70.9	7.1	425	1641
2	36	33	0.25	1.00	91.5	4.5	311	1371	1	34	21	0.22	1.00	90.7	5.2	323	1646
1	39	11	0.21	1.00	89.7	5.7	339	1386	1	41	26	0.21	1.00	93.6	2.7	285	1647
1	34	20	0.23	1.00	90.7	5.6	323	1388	1	10	15	0.13	1.00	68.9	8.3	431	1647
1	32	45	0.20	1.00	88.1	5.5	354	1400	1	32	29	0.21	1.00	88.3	5.7	353	1647
1	23	39	0.10	1.00	61.5	6.0	456	1415	1	24	35	0.15	1.00	67.7	7.4	435	1651
1	41	46	0.23	0.93	95.6	0.0	265	1418	1	24	3	0.14	0.00	67.2	5.5	437	1672
1	32	11	0.20	1.00	88.2	6.2	354	1427	1	21	1	0.19	0.00	80.4	3.2	390	1675
1	41	25	0.22	1.00	95.2	0.5	270	1432	1	10	11	0.13	1.00	69.7	10.3	428	1679
1	31	44	0.17	0.97	71.7	6.3	422	1438	1	36	17	0.25	1.00	91.5	4.4	311	1681
1	41	12	0.23	0.98	95.7	0.0	264	1443	1	32	20	0.20	1.00	88.2	6.8	354	1685

Supplementary Material 6-4 ***(continued)***

Eq.	Chl	Phg	#Fe^{3+}		$H_{v,\ Phg}$	P	T	$\sqrt{\Sigma\Delta G^2}$	Eq.	Chl	Phg	#Fe^{3}		$H_{v,\ Phg}$	P	T	$\sqrt{\Sigma\Delta G^2}$
Type	ID	ID	Chl	Phg	(%)	(kbar)	(°C)	(J)	Type	ID	ID	Chl	Phg	(%)	(kbar)	(°C)	(J)
2	21	5	0.19	0.00	84.1	0.8	373	1695	1	10	26	0.11	1.00	61.9	10.1	455	1936
1	41	21	0.21	1.00	93.1	4.0	291	1700	1	23	26	0.12	1.00	68.7	8.9	432	1937
1	35	29	0.20	1.00	89.5	5.3	342	1700	1	16	45	0.11	1.00	65.5	10.2	443	1940
1	31	11	0.18	1.00	74.0	9.5	414	1702	1	32	42	0.14	1.00	83.6	3.6	375	1942
1	23	42	0.09	1.00	52.5	8.0	486	1706	1	21	33	0.18	1.00	76.8	8.7	405	1944
1	21	20	0.20	1.00	80.3	8.9	390	1712	1	36	42	0.23	1.00	92.5	1.2	297	1944
1	10	25	0.12	1.00	63.5	7.8	449	1734	1	10	40	0.11	1.00	60.6	8.3	459	1945
1	16	27	0.11	1.00	64.7	8.9	445	1738	1	10	29	0.13	1.00	67.6	10.0	436	1945
1	24	46	0.16	0.91	70.8	6.1	425	1746	1	23	29	0.14	1.00	74.6	8.7	412	1947
1	19	3	0.25	0.60	93.9	0.0	282	1749	1	35	26	0.19	1.00	89.4	4.8	344	1958
1	23	5	0.15	0.05	88.5	0.0	352	1751	1	16	25	0.10	1.00	61.3	8.1	457	1964
1	16	13	0.11	1.00	64.6	8.4	446	1751	1	16	23	0.15	1.00	75.5	11.6	409	1965
1	39	26	0.20	1.00	89.6	4.6	340	1753	1	34	42	0.20	1.00	91.5	1.6	311	1982
1	31	45	0.18	1.00	72.6	8.9	419	1758	1	23	23	0.17	1.00	81.2	10.2	386	1982
1	32	26	0.18	1.00	87.0	5.3	359	1760	1	16	20	0.12	1.00	69.2	11.2	430	1982
1	16	11	0.12	1.00	67.4	10.7	436	1764	1	31	20	0.19	1.00	76.0	9.8	407	1983
1	23	11	0.14	1.00	76.4	9.0	406	1769	1	31	29	0.16	1.00	69.1	9.7	431	1987
1	29	22	0.13	1.00	59.9	10.4	461	1769	1	16	35	0.10	1.00	60.7	8.3	459	1995
1	10	35	0.11	1.00	62.9	7.9	451	1772	1	19	31	0.21	1.00	91.5	4.4	311	2002
1	23	45	0.14	1.00	75.0	8.5	411	1778	1	19	39	0.24	1.00	93.3	0.5	289	2005
1	24	40	0.13	1.00	61.4	8.2	456	1802	2	36	28	0.24	1.00	91.4	5.0	312	2005
1	27	22	0.16	1.00	59.3	10.5	464	1802	1	29	11	0.13	1.00	62.7	11.6	452	2009
1	16	15	0.12	1.00	66.7	8.7	439	1804	1	21	2	0.20	0.09	89.0	0.0	350	2020
1	35	39	0.15	1.00	89.3	1.6	346	1810	1	24	10	0.16	0.03	85.4	0.0	367	2032
1	34	1	0.25	0.00	93.0	0.0	292	1811	1	24	26	0.14	1.00	62.7	10.0	452	2037
2	19	17	0.21	1.00	91.5	4.5	311	1812	1	21	29	0.09	0.36	36.1	9.9	542	2037
1	36	3	0.28	0.66	93.9	0.0	282	1815	1	16	29	0.11	1.00	65.2	10.4	444	2040
1	39	33	0.21	1.00	89.6	5.6	340	1825	1	27	11	0.16	1.00	62.6	11.7	452	2042
1	35	20	0.20	1.00	89.4	6.4	343	1826	1	16	12	0.12	1.00	67.5	7.3	436	2042
1	31	42	0.13	1.00	51.2	8.3	491	1829	1	41	31	0.20	1.00	93.2	3.5	290	2043
1	10	45	0.13	1.00	68.0	9.8	434	1831	1	35	33	0.20	1.00	89.4	5.8	344	2045
1	10	12	0.14	1.00	69.4	7.0	430	1850	1	16	26	0.10	1.00	59.1	10.6	464	2051
1	41	17	0.21	1.00	93.2	3.6	290	1850	1	29	27	0.13	1.00	60.3	9.7	460	2058
1	29	32	0.13	1.00	61.9	10.8	455	1854	1	24	29	0.15	1.00	68.4	9.9	433	2059
2	23	2	0.15	0.00	85.2	0.9	368	1859	1	23	20	0.15	1.00	77.3	9.5	403	2061
1	24	11	0.15	1.00	69.4	10.3	429	1867	1	24	39	0.12	1.00	56.2	6.8	474	2062
1	39	21	0.21	1.00	89.6	5.9	341	1869	1	10	21	0.13	1.00	68.1	10.8	434	2062
1	32	33	0.19	1.00	87.6	6.2	357	1870	1	21	26	0.08	0.28	33.8	10.9	550	2066
2	36	31	0.24	1.00	91.5	4.3	311	1871	1	34	31	0.21	1.00	90.7	4.8	323	2075
1	31	26	0.16	1.00	67.7	9.1	435	1879	1	16	44	0.13	0.99	69.0	7.8	431	2082
1	27	32	0.16	1.00	61.2	10.9	457	1886	1	35	21	0.20	1.00	89.4	6.1	345	2084
1	32	21	0.20	1.00	87.7	6.5	356	1891	3	1	3	0.12	0.00	65.0	5.9	444	2091
1	34	17	0.22	1.00	90.8	4.8	322	1894	1	10	3	0.12	0.00	65.0	5.9	444	2091
1	10	23	0.16	1.00	77.1	11.2	404	1904	1	27	27	0.16	1.00	59.5	9.8	463	2091
1	31	1	0.19	0.00	77.5	3.8	402	1906	2	36	30	0.25	1.00	91.4	5.5	313	2097
1	10	44	0.14	0.99	69.6	7.3	429	1907	1	29	13	0.13	1.00	60.8	9.1	458	2098
1	10	20	0.14	1.00	71.4	10.7	423	1911	1	10	33	0.12	1.00	66.9	10.6	438	2101
1	24	45	0.15	1.00	68.8	9.6	432	1917	1	29	15	0.14	1.00	62.5	9.5	453	2103
1	31	23	0.21	1.00	80.1	10.6	391	1928	1	10	46	0.14	0.92	69.4	6.4	429	2103
1	35	42	0.05	0.00	39.3	6.1	531	1928	1	41	28	0.21	1.00	93.0	4.3	292	2104
1	21	21	0.18	1.00	78.5	8.8	399	1932	1	31	21	0.17	1.00	72.7	9.9	419	2113

Supplementary Material 6-4 ***(continued)***

Eq.	Chl	Phg	#Fe^{3+}		$H_{v,\ Phg}$	P	T	$\sqrt{\Sigma\Delta G^2}$	Eq.	Chl	Phg	#Fe^{3}		$H_{v,\ Phg}$	P	T	$\sqrt{\Sigma\Delta G^2}$
Type	ID	ID	Chl	Phg	(%)	(kbar)	(°C)	(J)	Type	ID	ID	Chl	Phg	(%)	(kbar)	(°C)	(J)
1	36	39	0.21	0.96	93.5	0.0	287	2114	1	30	11	0.19	1.00	58.2	12.7	467	2279
1	27	15	0.17	1.00	61.7	9.6	455	2137	1	18	11	0.16	1.00	57.4	12.6	470	2284
1	24	20	0.16	1.00	71.7	10.7	422	2138	1	19	34	0.21	1.00	91.6	3.8	310	2287
1	16	21	0.11	1.00	65.8	11.2	442	2141	1	22	11	0.19	1.00	57.3	12.7	470	2300
1	19	28	0.21	1.00	91.4	5.1	313	2149	1	16	46	0.13	0.93	68.8	6.9	432	2306
1	16	40	0.10	1.00	58.0	8.8	468	2160	1	32	31	0.18	1.00	86.7	6.2	361	2309
1	22	22	0.18	1.00	54.2	11.4	481	2161	1	27	29	0.16	1.00	59.5	11.4	463	2313
2	36	34	0.24	1.00	91.6	3.7	309	2162	1	41	42	0.20	1.00	95.2	0.3	269	2313
1	29	23	0.16	1.00	72.2	12.4	420	2167	1	31	2	0.19	0.00	81.1	1.7	387	2313
1	24	23	0.18	1.00	77.4	11.2	403	2173	3	24	33	0.14	1.00	65.6	10.8	442	2322
1	41	30	0.21	1.00	92.8	4.8	294	2174	1	24	33	0.14	1.00	65.6	10.8	442	2322
1	24	42	0.11	1.00	48.7	8.7	499	2175	1	37	23	0.16	1.00	67.8	13.3	435	2326
1	37	22	0.14	1.00	54.8	11.4	479	2183	1	41	34	0.19	1.00	93.5	2.8	287	2329
1	16	33	0.11	1.00	63.9	11.1	448	2186	1	29	26	0.11	1.00	53.3	11.6	483	2331
1	32	17	0.19	1.00	87.0	6.2	359	2188	1	18	23	0.19	1.00	68.4	13.2	433	2352
1	23	21	0.14	1.00	74.8	9.5	411	2191	1	19	14	0.22	1.00	91.3	5.9	314	2355
1	27	23	0.19	1.00	71.7	12.5	422	2192	1	39	31	0.20	1.00	89.5	5.5	342	2355
1	18	32	0.16	1.00	56.5	11.7	473	2197	1	29	44	0.15	1.00	66.4	8.6	440	2356
1	37	32	0.14	1.00	56.7	11.7	472	2202	1	27	26	0.14	1.00	52.5	11.7	486	2357
2	36	14	0.24	1.00	91.3	5.8	314	2203	1	34	30	0.22	1.00	90.6	5.9	324	2359
1	29	20	0.14	1.00	65.0	12.0	444	2203	1	16	3	0.11	0.00	63.0	6.3	451	2363
1	29	45	0.13	1.00	60.9	11.1	458	2203	1	10	17	0.11	1.00	64.1	10.9	447	2366
1	21	17	0.17	1.00	75.1	8.9	410	2215	1	10	42	0.08	1.00	48.7	8.8	499	2368
1	39	17	0.20	1.00	89.6	5.4	341	2226	1	29	12	0.14	1.00	62.7	8.1	452	2373
1	30	22	0.18	1.00	53.8	11.5	482	2230	1	30	20	0.19	1.00	59.5	13.1	463	2374
1	27	45	0.16	1.00	60.1	11.2	461	2234	1	29	25	0.12	1.00	56.6	8.9	472	2374
1	30	32	0.19	1.00	55.5	11.9	476	2234	1	22	23	0.21	1.00	68.0	13.3	434	2380
1	41	14	0.21	1.00	92.7	5.1	295	2237	1	10	39	0.10	1.00	55.1	7.1	478	2381
1	19	30	0.22	1.00	91.3	5.6	314	2247	1	29	21	0.13	1.00	60.8	12.1	458	2382
1	22	32	0.18	1.00	52.8	12.4	485	2259	1	21	34	0.08	0.40	33.8	11.0	550	2385
1	30	23	0.22	1.00	68.0	13.3	434	2260	1	27	44	0.18	1.00	65.6	8.7	442	2394
1	34	28	0.22	1.00	90.7	5.4	324	2262	1	34	34	0.21	1.00	90.8	4.2	322	2396
1	21	31	0.16	1.00	74.1	8.9	414	2274	1	41	39	0.22	1.00	95.3	0.0	268	2396
1	24	21	0.15	1.00	68.6	10.7	432	2277	1	29	35	0.12	1.00	56.5	9.1	473	2397

Calculated multi-equilibria with $P < 0$ bar and $\sqrt{\Sigma\Delta G^2} > 2400$ J are filtered (see details in text). The remaining ones are ordered by increasing $\sqrt{\Sigma\Delta G^2}$ (J). Chlorite-white mica composition couples are identified by their respective EMPA ID.

$\#Fe^{3+} = \#Fe^{3+} / (\#Fe^{3+} + \#Fe^{2+})$. $H_{v,\ Phg}$ is the proportion (%) of water molecules between tetrahedron-octahedron-tetrahedron sheets of phengite. Equilibrium types are: 1 – redundant multi-equilibrium calculated from all data; 2 – non redundant multi-equilibrium calculated from all data. They correspond to the chlorite-phengite couple leading to the most stable equilibrium for a given phengite EMPA composition; 3 – multi-equilibrium calculated from chlorite-phengite couple that coexist at the microscopic scale within a given sample.

Chapitre VII – General discussion

1. Deciphering of the Pan-African gold mineral system along the Keraf suture

As a reminder, this PhD project was designed to characterize the Pan-African gold mineral system of the Neoproterozoic Arabian-Nubian shield, through the example of the Keraf suture and its interference zone with the Atmur-Delgo suture. The successive parts composing the present manuscript describe critical elements required to characterize the backbones of a mineral system (*e.g.*, McCuaig et al., 2010; Huston et al., 2012; McCuaig and Hronsky, 2014 ; Wyman et al., 2016; Occhipinti et al., 2020): (i) a geodynamical setting favorable to crustal gold fertilization during crustal differentiation (**Chapter I**); (ii) a whole-lithospheric structural architecture coupled to transient geodynamics acting as a throttle for metal, fluid and ligand mobilization (**Chapters II-III**) and (iii) the existence and/or formation of structural traps and/or geomechanical and/or geochemical gradients permitting ore deposition, which are highly depending on the regional lithological-structural framework (**Chapters IV-V**). We also bring additional pressure-temperature-absolute timing constraints on mineralization events (**Chapters I, VI**). In what follows, we therefore integrate what we have learned to constrain the gold mineral system recorded along the studied area in the Galat Sufar South, WG03, Central Zone and UTM deposits, as summarized in Figure 7-1. A last subsection will address the question of ore preservation since their formation in Neoproterozoic times.

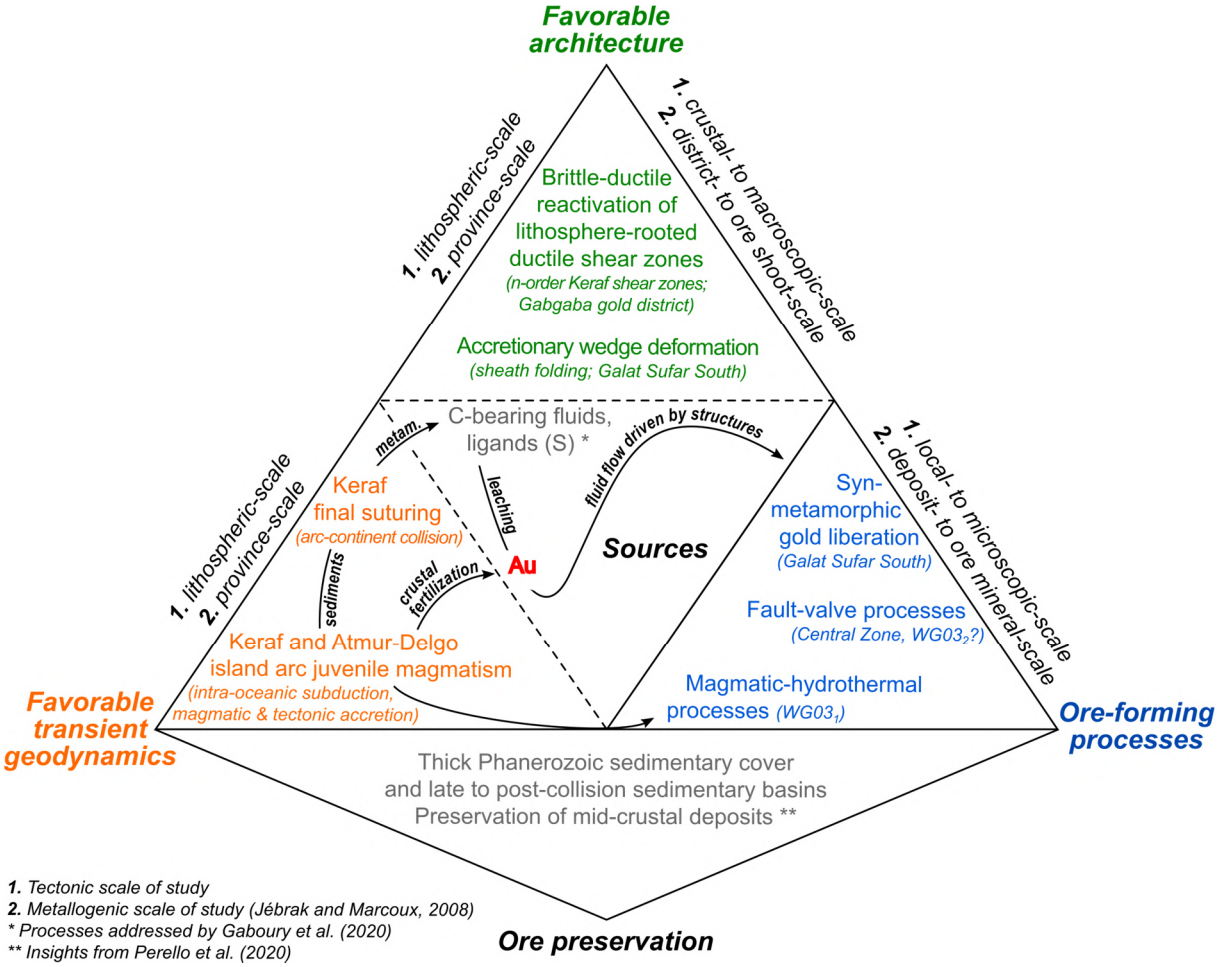


Figure 7-1: Gold mineral system diamond illustrating critical factors for ore genesis along the Atmur-Delgo and Keraf sutures, western Neoproterozoic Nubian shield. This Figure is inspired from Occhipinti et al. (2020) who used this diamond shape to represent mineral systems.

1.1. Geodynamical setting favorable for crustal growth and gold fertilization

1.1.1. Juvenile magmatism and gold fertilization at intra-oceanic subduction sites

The enrichment in gold, among other lithophile and chalcophile metals, of primitive melts formed in arc-back-arc settings depends on several factors such as (i) the rate of saturation in sulfur (*e.g.,* Keays and Lightfoot, 2010), (ii) the oxygen fugacity (*e.g.,* Jugo et al., 2005; Mungall et al., 2006; Jugo, 2009) and (iii) the partial melting and fractional crystallization rates (Hamlyn et al., 1985; Keays, 1995). Subduction-derived fluids are known to directly or indirectly favor crustal gold fertilization and Cu-(Au) porphyry ore formation (Hedenquist and Lowenstern, 1994; Mungall, 2002; Wilkinson, 2013; Richards, 2015), but their influence is not necessary to form gold-enriched arc-back arc crust (*e.g.,* modern-day Lau back-arc basin, Tonga-Kermadec arc complex; Jenner et al., 2012).

These studies illustrate how critical magmatic processes in arc settings are to secular crustal gold endowment through time. What matters the most is the duration of arc activity and the relative contribution of gold-enriched melts to the arc building (*e.g.,* Sawkins, 1990; Saunders and Tarney, 1991; Bierlein et al., 2009; Cawood et al., 2009; Pitcairn, 2011; Hronsky et al., 2012). A complementary gold endowment may occur in a metasomatized island arc mantle wedge where re-fertilized by slab-derived fluids and melts (*e.g.,* Kepezhinskas et al., 2002). In the case of continental arcs, the delamination of the likely gold-enriched arc root and recycling of arc-derived sediments during ongoing subduction and later arc-continent subduction may also lead to the formation of a gold-enriched metasomatized sub-continental lithospheric mantle; its melting triggered during late orogenic slab delamination may remobilize once more the original arc-related gold budget and form late collisional gold deposits (*e.g.,* Eglinger et al., 2017).

The Arabian-Nubian shield constitutes both the largest track of Neoproterozoic crust and the main Neoproterozoic gold province worldwide (Johnson, 2014; Johnson et al., 2017). It is considered as the Neoproterozoic equivalent of the Paleoproterozoic Birrimian orogen in the West African craton as they share (i) a similar lithological-

tectonic architecture resulting from geodynamical events that lasted approximately the same duration, (ii) an overall juvenile crustal signature and record (iii) comparable range of metamorphic conditions and (iv) subduction- and collision-related magmatic events with similar duration and geochemical signature (Grenholm, 2019). Through the example of the central Keraf suture, we demonstrated that the western boundary of the Arabian-Nubian shield mostly resulted from a ~185 Myr-long-lasting island arc in a maturing arc-back-arc system favorable for crustal gold endowment, accounting for the juvenile and fertile nature of the central Keraf suture (**Chapter I**).

1.1.2. Towards an estimation of gold fertilization along the central Keraf suture

As the studied Keraf and Atmur-Delgo suture areas are known for hosting gold deposits (Gaboury et al., 2020; Perret et al., 2020, under review), this section attempts to quantify the gold fertilization of the central Keraf suture crust during the geodynamical scenario detailed in **Chapter I**. As a reminder, we suggested that the Keraf island arc evolved from (i) juvenile magmatism between *ca.* 840-810 Ma to (ii) protracted juvenile magmatism mixed with older arc crust reworking between *ca.* 760-655 Ma. We therefore attempt to estimate the gold budget that migrated from the mantle to the crust during the long-lived Keraf arc juvenile magmatic activity in what follows. Prior to carrying out our calculation, we need to fix several parameters.

(i) Duration of the arc activity

As we did not estimate the respective contribution of juvenile magmatism and arc crustal reworking during the *ca.* 760-655 Ma Keraf arc activity, we will only consider the crustal gold fertilization related to the *ca.* 840-810 Ma Keraf island arc magmatic activity. We therefore considered a steady arc activity over 30 Myr, which is consistent with the duration of continuous crust formation reported for the Mesozoic Kohistan arc, Pakistan, for instance (*e.g.,* Jagoutz et al., 2009). Considering such a long-lasting continuous magmatic arc activity remains however questionable as the <0.5-10 Myr incremental

growth of individual batholiths during ~10-60 Myr-long flare-ups, *i.e.,* periods of high magma addition rate to arcs, separated by lulls, *i.e.,* periods of low magma addition rate, is widely documented in both modern-day and paleo-arc systems, in both oceanic and continental settings (Jicha et al., 2006; Miller et al., 2007, 2011; Paterson et al., 2011; De Silva et al., 2015; Paterson and Ducea, 2015; Olierook et al., 2020). It is worth noticing that such an arc tempo is mostly recognized for continental arcs and expressed in a fractal way in space and time from the arc-segment to the caldera-forming eruptions (De Silva et al., 2015; Paterson and Ducea, 2015). From the geochronological data presented in **Chapter 1**, there is no evidence for such an episodic magmatic activity of the Keraf island arc, except if considering a *ca.* 810-760 Ma lull separating the *ca.* 840-810 Ma and *ca.* 760-655 Ma flare-ups.

(ii) Arc crust production rate

We demonstrated in **Chapter I** that the Neoproterozoic Keraf arc magmatic evolution involved processes similar to what is described for Mesozoic arcs such as the Kohistan-Ladakh arc. We can therefore consider magma production and arc crust formation rates published for such arc systems (*e.g.,* Jagoutz and Schmidt, 2013; Jagoutz and Kelemen, 2015; Jicha and Jagoutz, 2015). Addition to the arc crust volume is typically one third of the total magma that was produced. Despite magma production rate is up to 220-290 $km^3.km^{-1}.Myr^{-1}$ in the Kohistan-Ladakh arc, we will rather consider a more conservative ~150 $km^3.km^{-1}.Myr^{-1}$ magma production rate accounting for ~50 $km^3.km^{-1}.Myr^{-1}$ arc crust formation. Such a rate is indeed widely reported for *ca.* 80-30 Ma and modern-day intra-oceanic paleo-arcs (Jicha and Jagoutz, 2015), and slightly lower than the ~60-180 $km^3.km^{-1}.Myr^{-1}$ rates reported for the rapidly growing modern-day Aleutian, Izu-Bonin, Mariana and Tonga-Kermadec island arcs (Cosca et al., 1998; Dimalanta et al., 2002; Arculus, 2004; Jicha et al., 2006).

(iii) Along-strike length of the arc system and density of the arc crust

The north-northwest-orientated central Keraf suture is ~50 km-long (Fig. 1-2). To simplify things, we approximate the *ca.* 840-810 Ma Keraf island arc formed the same amount of arc crust along strike, despite it certainly leads to overestimate the total volume added to the arc crust. We fix the arc crust density at 3.22, which is value reached by mafic cumulates in the deep Kohistan arc root (Jagoutz and Kelemen, 2015). Considering a unique density value for the entire arc system is however a disputable shortcut as this value decreases down to ~2.60 in felsic plutonics of the upper arc (Jagoutz and Kelemen, 2015).

(iv) Gold concentration of the newly crystallized juvenile arc rocks

Fire assay data indicate an 11 ppb gold concentration for the bulk of the early Keraf island arc-related WG03-OC-03b quartz-diorite (Table 1-2; **Chapter I**). This concentration is way higher than the clarke of gold (1.3 ppb; Rudnick and Gao, 2003). It is in the same range of order as gold contents from magmatic rocks formed in arc-back arc systems (compilation by Pitcairn, 2011), which is consistent with our geodynamical interpretation (Fig. 1-9). We consider a constant gold concentration for the entire arc crust despite an obvious lack of representativeness, as it is very unlikely that all igneous arc rocks show the same gold concentration as this mid-crustal cumulate. Approximations made in the two last paragraphs could be addressed by carrying out a careful sampling of the entire Keraf arc section to (i) estimate the relative volumetric proportion of the different lithologies, (ii) measure their respective density and gold concentrations and (iii) implement these data in our calculation of crustal gold fertilization.

(v) Approximate amount of gold accumulated by the Keraf arc

Relying on parameters with values fixed above, we therefore approximate that ~2.7 Mt of gold were extracted from the mantle to the crust during the early Keraf island arc activity. Of course, this number does not mean anything in itself due to numerous

approximations made to simplify calculations and no consideration of crustal recycling by removing of the delaminated arc root. It is nevertheless critical to mention that this amount of gold is five ranges of order above the ~75 t cumulated gold resources that form the Gabgaba gold district in the central Keraf suture (Managem, 2014). The development of the Keraf island arc at *ca.* 840-810 Ma is therefore important enough in terms of mantle-derived material added to the crust, *i.e.,* crustal growth, to account for a huge gold fertilization of the central Keraf suture crust. During subsequent Keraf crustal deformation, gold can be leached from these crustal rocks where it is likely disseminated and diluted. It is then transported and concentrated to ultimately form gold deposits (Gaboury et al., 2020; Perret et al., under review). The central Keraf suture therefore exemplifies the importance of juvenile island arc crustal growth for gold fertilization during Neoproterozoic.

The deposition of Keraf arc-related volcanoclastics interbedded with sediments derived from the erosion of the Keraf island arc likely resulted in the formation of a gold-enriched sedimentary cover within the Keraf back-arc basin (Fig. 1-9). Turbidites of the central Keraf suture are therefore a potential gold source, in addition to a reservoir for sulfur acting as a ligand (Fig. 7-1), as suggested by Gaboury et al. (2020). Such scenario presents the advantage of reconciliating classical models which oppose mafic rock (*e.g.,* Powell et al., 1991; Phillips and Powell, 2009, 2010; Wilson et al., 2013; Pitcairn et al., 2015; Augustin and Gaboury, 2017) and sedimentary (*e.g.,* Large et al., 2007, 2011; Tomkins, 2010; Gaboury, 2013) sources for orogenic gold and are still widely discussed (*e.g.,* Tomkins, 2013).

During the geodynamical evolution of the central Keraf suture, gold, ligands and fluids were therefore available whatever the nature of the remobilized metallic reservoir and processes involved in gold liberation and transport: all the ingredients of what could be called the *gold deposit-recipe* were gathered. The next step towards forming gold deposits requires to *mix* all these features together, using the proper *utensils*, *i.e.,*

favorable transient geodynamics and tectonic processes triggering hydrothermal fluid flow events, gold leaching and further concentration into gold-bearing structures in restricted host-rock volumes.

1.2. Favorable lithospheric architecture and tectonic triggers for gold mineralization

Relying on relative and absolute timing constraints on deformation, magmatism and gold events along the Keraf and Atmur-Delgo sutures, we attempted to illustrate their spatial and temporal relationships in cross-section and as a timechart (Figs. 7-2 and 7-3, respectively). These Figures highlight the transient geodynamics favorable for gold mobilization and the formation of the studied Galat Sufar South, WG03, Central Zone and UTM deposits.

1.2.1. Syn-magmatic accretion $WG03_1$ gold event

The earliest $WG03_1$ gold event described in this study is responsible for uneconomic disseminated mineralization at the WG03 gold deposit, Gabgaba district (Figs. 7-2, 7-3). It is expressed by mineralized plagioclase-amphibole-biotite-(pyrrhotite-chalcopyrite-magnetite) magmatic-hydrothermal features intergrown with the bulk of the amphibole-dominated mineral gangue of the WG03 deposit-hosting quartz-diorite (**Chapter III**). We therefore infer that the $WG03_1$ gold event occurred when this batholith formed, during the *ca.* 840-810 Ma Keraf island arc flare-up (**Chapter I**). In addition to favoring the overall crustal gold fertilization, the early evolution of the Keraf arc complex thus led to gold concentration, at some extent.

The relationship between arc magmatism at convergent margins and gold mineralization is well documented through Earth history, where there is a gold endowment in magmas and/or exsolved aqueous fluids migrating along subduction-induced structures (Binns and Scott, 1993; Müller and Groves, 1993; Sillitoe, 1997, 2000;

Ulrich et al., 1999; Müller et al., 2001; Mungall, 2002; Sun et al., 2004; Richards, 2015). Gold-bearing epithermal and porphyry mineralization types range in that class of deposits. However, the $WG03_1$ gold event cannot be classified as such as it does not display the typical alteration and structural patterns of these deposits (synthetized in White and Hedenquist, 1995; Hedenquist et al., 2000; Sillitoe, 2000; Taylor, 2007; Richards, 2013).

Despite its association to a magmatic intrusion, the $WG03_1$ gold event cannot be classified as intrusion-related neither, as the WG03 deposit-hosting quartz-diorite batholith formed in an island arc setting rather than during post-collisional extension (Sillitoe, 1991; Thompson et al., 1999; Hart, 2005, 2007). At the end of this study, this island arc magmatism-related gold event therefore remains quite enigmatic and further work will be carried out to better understand the magmatic-hydrothermal ore-forming processes involved (see section 3.2).

1.2.2. Syn-tectonic accretion Galat Sufar South gold event

In the framework of this PhD project, we designed a multi-scale and –method approach, conducted from the field to the laboratory, which demonstrated that the Galat Sufar gold deposit is characterized by a strong structural control on gold mineralization from the district to the ore-mineral scale (**Chapters II, IV**). Multi-scale structural evidence collectively imply that the Galat Sufar South gold deposit formed during Atmur-Delgo arc-continent suturing. Additional pressure-temperature and geochronological constraints imply that it more specifically relates to tectonic accretion of the volcano-sedimentary wedge between *ca.* 753-723 Ma, under amphibolite facies metamorphic conditions (Figs. 7-2, 7-3; **Chapter VI**), in agreement with the regional-scale deformation style (**Chapter II)** and syn-metamorphic elemental remobilization recorded by pyrite (**Chapter IV)**.

The migration of deformation-assisted mineralizing fluids is therefore triggered by the compressional regime and the development of intra-oceanic subduction-related crustal structures in a fore-arc setting. It is also worth noticing that geochronological constraints on the gold mineralization makes the Galat Sufar South deposit the oldest vein-type gold deposit documented throughout the Arabian-Nubian shield. It can be compared to early Eoeburnean gold deposits, like $Wassa_1$ gold event in Ghana, in terms of geodynamical setting (Perrouty et al., 2015; reviews by Thébaud et al., 2020 and Masurel et al., in press). In absence of geochronological constraints to the contrary, such a vein-type gold occurrence hosted in a deformed and metamorphosed volcanosedimentary pile is usually interpreted as resulting from late collisional reactivation of early tectonic structures within complex lithospheric-scale shear zones (*e.g.,* Kerrich et al., 2005). The Galat Sufar South gold mineralization is no exception to the rule as it used to be described as orogenic gold related to late collisional Keraf strike-slip shearing, in spite of the lack of a detailed study (Johnson et al., 2017). The atypical Galat Sufar South deposit is therefore the perfect case study to illustrate that the spatial relationship between a deposit and a lithospheric-scale structure does not necessary imply they are genetically related. It also illustrates how valuable the proposed multi-scale and -method approach is for the understanding of ore-forming processes, without relying at all costs on classical ore deposit classifications.

1.2.3. Late arc-continent collision $WG03_2$ and Central Zone gold event

The major $WG03_2$-Central Zone gold event (Figs. 7-2, 7-3) broadly relates to *en échelon* dilational ore veining as a response to the late arc-continent collision at the very end of Keraf suturing, leading to the formation of the ductile-brittle Keraf shear zone (**Chapter III**). Relying on deposit- to ore shoot-scale observations, we demonstrated that the Central Zone deposit can be considered as typical of orogenic gold formed in a late compressional regime along second-order shear zones with typical structural, fluid, alteration and metamorphic footprints. WG03 and Central Zone deposits cannot be

considered as intrusion-related due to the relative timing of host intrusions. This point was already addressed for WG03 (see subsection 1.2.1). Regarding the Central Zone deposit, we relied on rare evidence for shearing and >650 Ma U-Pb ages of magmatic apatite (pending confirmation) to infer that the intrusion of ore-hosting granitoids must have occurred during Keraf island arc magmatic activity, prior to late collisional Keraf strike-slip shearing (**Chapters III, VI**). WG03 and Central Zone can nevertheless be classified as intrusion-hosted deposits (Hart and Goldfarb, 2005).

These deposits express a strong structural and rheological control, as (i) they are located along second-order structures where deformation is localized and related to the Keraf shear zone deeply rooted into the lithosphere and (ii) the strong rheological contrast between surrounding volcanosediments and plutonic batholiths is responsible for preferential veining in quartz-diorite and granitoids at WG03 and Central Zone deposits, respectively (**Chapter III**). Dating of hydrothermal apatite spatially and genetically related to ore veining at the WG03 deposit indicates that it occurred episodically over *ca.* 600-550 Ma (Fig. 2-3; **Chapter VI**). We interpreted veining as resulting from Keraf strike-slip shearing (**Chapter III**) and we dated an undeformed post-collisional monzogranite pluton at *ca.* 620 Ma nearby the WG03 deposit (**Chapter I**). We infer that these data reflect the record of episodic and localized deformation along Keraf multiple-order shear zones, which may have been reactivated at multiple times (**Chapter VI**). More globally speaking, the Gabgaba gold district therefore illustrates the typical shift from distributed ductile deformation to localized ductile-brittle deformation with strain partitioning during the tectonic evolution of crustal- to lithospheric-scale shear zones.

Finally, we attributed the formation of the UTM gold deposit to ore veining during late brittle extension and normal faulting along reactivated Keraf multiple-order shear zones (**Chapter III**). However, deformation in an extensional regime is hardly interpretable at the province scale as spatially limited to the UTM area and the genetic

link between ore veins and normal faults is not clearly established. Due to its numerous similarities with the Central Zone deposit in terms of alteration patterns and structures, the UTM deposit may also be attributed to gold mineralizing fluid flows during Keraf strike-slip shearing (Gaboury et al., 2020). Yet, both options are not mutually exclusive, as we demonstrated in the previous paragraph that Keraf strike-slip shearing is discrete and polyphase, in time and space, and may have locally resulted in normal-slip reactivation of inherited shear zones.

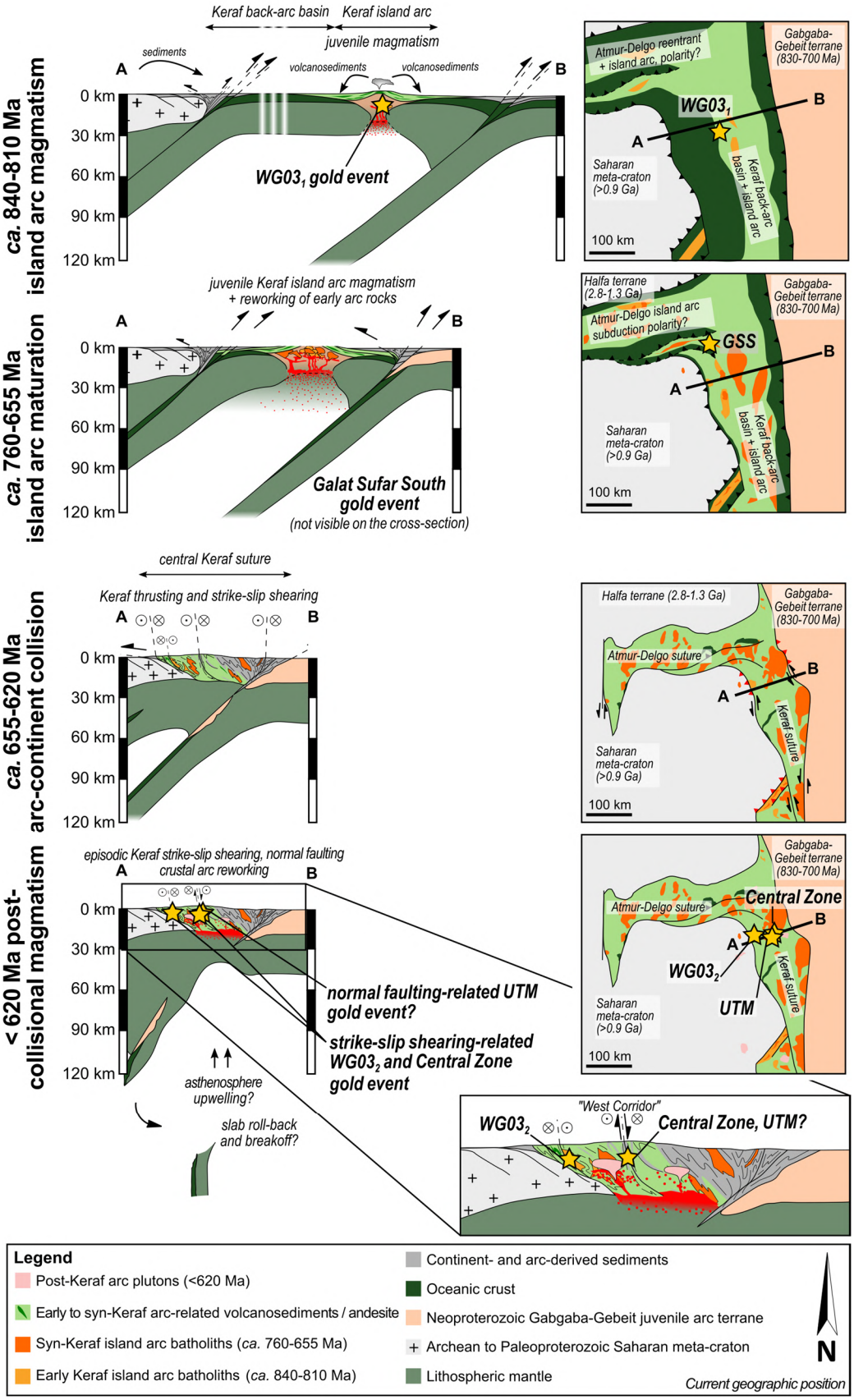


Figure 7-2: Geodynamical sketch in a lithospheric cross-section across the central Keraf suture with representation of the successive gold events occurring during Keraf suturing, with associated schematic map views. The Galat Sufar South gold event occurred along the Atmur-Delgo suture and is therefore not represented on the cross-sections, although the Keraf and Atmur-Delgo sutures likely share a similar geodynamical evolution.

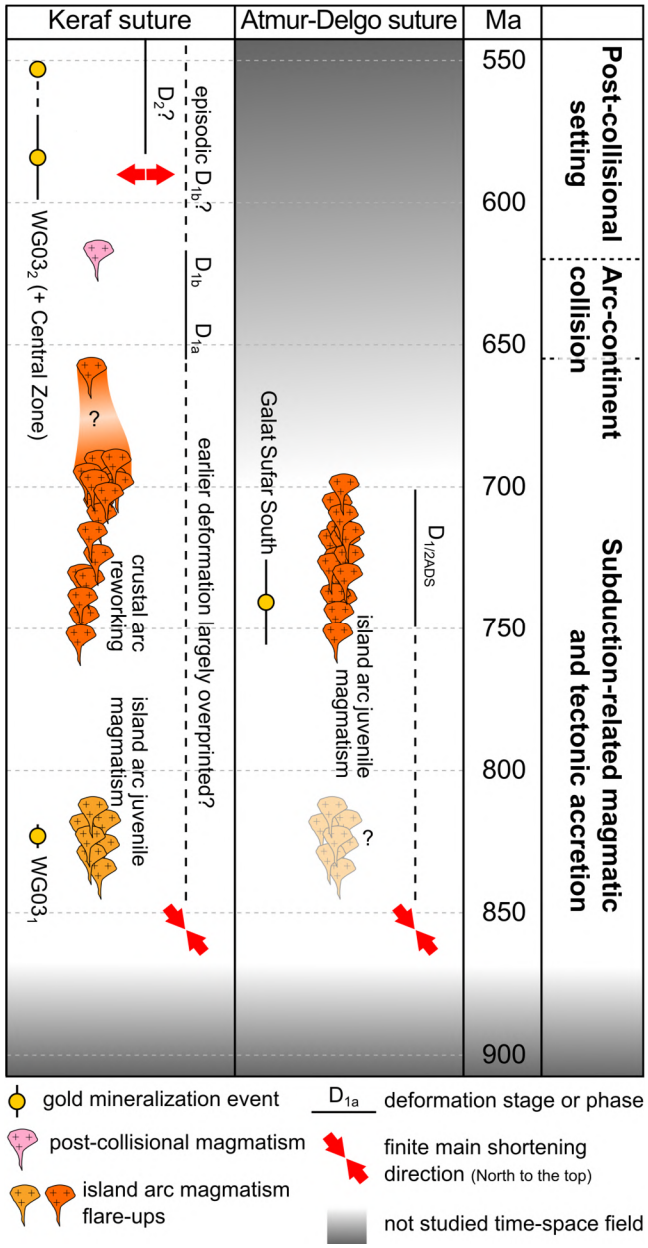


Figure 7-3: Timechart summarizing the gold mineralization, magmatic and tectonic events unraveled across the Neoproterozoic Keraf and Atmur-Delgo sutures during this study.

1.3. Ore deposition mechanisms

1.3.1. Syn-metamorphic metal remobilization from gold-bearing pyrite

The example of the Galat Sufar South deposit illustrates gold release and concentration to form an economic ore from syn- loweramphibolite facies metamorphic remobilization of the metallic budget contained within earlier pyrite generations (**Chapter IV**). A similar space-limited migration pattern for pyrite-structurally compatible elements such as Cu, Pb or Zn, is attributed to pyrite recrystallization under amphibolite facies metamorphism at the Mt. Torrens Pb-Zn-Ag prospect, Kanmantoo Group, South Australia (Dakota Conn et al., 2019). Besides, ore refining resulting from similar syn-metamorphic recrystallization of sulfide minerals is widely documented, notably for volcanogenic massive sulfide (VMS) deposits, and involves either mechanical (*e.g.,* Zaw 1991; Zaw and Large 1996; Castroviejo et al. 2011; Pierre et al. 2016) or hydrothermal processes (*e.g.*, Soltani Dehnavi et al. 2018). Similar mechanisms favor ore upgrading in orogenic gold deposits as well (Fougerouse et al., 2016a; Dubosq et al., 2018; Wu et al., 2019a; Gourcerol et al., 2020). These examples illustrate how important the knowledge of thermodynamic conditions related to gold mineralization is to interpret the coupled metamorphism- and deformation-induced elemental mobility leading to metal concentration are the formation of a deposit.

1.3.2. Fault-valve system and gold mineralization in dilational quartz veins

Macroscopic to microscopic structures of ore-bearing dilational veins and textural-geochemical patterns of the distinct pyrite generations unraveled at the Central Zone gold deposit indicate that the main ore-forming processes involve crack-seal mechanisms and boiling (**Chapter V**). We therefore interpret the Central Zone deposit as a typical orogenic gold deposit with evidence for fault-valve-related gold deposition. The fault-valve mechanism is induced by episodic pressure fluctuations in cascading seismic-aseismic cycles and is widely considered in the orogenic gold model (*e.g.*, Sibson, 1990; Ridley, 1993; Sibson and Scott, 1998; Cox et al., 2001; Robert and Poulsen, 2001; Sibson,

2001; Micklethwaite and Cox, 2004; Faleiros et al., 2007; Weatherley and Henley, 2013; Peterson and Mavrogenes, 2014; Cox, 2016; Sibson, 2020a, 2020b). We may be quite confident that the fault-valve mechanism is also involved in ore formation at the WG03 gold deposit, regarding timing and structural similarities between $WG03_2$ and Central Zone ore events (see subsection 1.2.3). In addition to the record of structural control on mineralization from the district- to the microscopic scale, these two deposits therefore recorded the rhythmic and discrete nature of Keraf strike-slip shearing and related gold mineralization at several time scales: (i) over several tens of Myr with ages of mineralized veins spanning between *ca.* 600-550 Ma (**Chapter VI**) and (ii) over tens to a few thousands years, corresponding to the duration of seismic-aseismic cycles leading to the incremental growth of mineralized veins during a single Keraf shear zone (re)activation episode (Micklethwaite et al., 2015). This study therefore demonstrates that structurally-controlled deposits record deformation processes at several scales of time and space, which makes of them precious witnesses of the regional-scale tectonic evolution. The Gabgaba gold district case study illustrates well the bivalence of the mineral system approach in that sense, as it provides knowledge about both (i) the metallogenic processes leading to ore deposition and (ii) what is the tectonic and geodynamical setting favorable for these processes to take place.

1.4. Ore preservation

The record of ore deposits through the Earth history is incomplete due to: (i) crustal recycling at subduction sites; (ii) syn-tectonic and/or –metamorphic remobilization of preexisting ore deposits and (iii) exhumation, which is the balance between burial, uplift and erosion processes, including supergene weathering, erosion and sedimentation, and leads to the exposition of primary deposits at the subsurface (Kesler and Wilkinson, 2006; Cawood and Hawkesworth, 2015). Thus, ore deposits formed at shallow depth and early during an orogenic cycle have less chances to be preserved than deposits formed deeply

in late to post-collisional settings, and the probability of preservation decreases for deposits that have undergone at least one entire supercontinent cycle (Groves et al., 2005a; Cawood and Hawkesworth, 2015). This is notably illustrated by the weak record of Precambrian porphyry-type and epithermal deposits (Groves et al., 2005a; Kerrich et al., 2005). As the Arabian-Nubian shield is described as a collage of island arc-derived litho-tectonic blocks, the record of pre-collision ore history was preserved during subsequent stages of the Gondwana supercontinent cycle. We now have to focus on the influence of Gondwana-related post-collisional and Phanerozoic geodynamical processes on the exhumation of the Arabian-Nubian shield.

Orogenic gold formed under ductile-brittle deformation, exemplified by the Central Zone and WG03 gold deposits in the studied area, is known to form at mid-crustal depths (~10-15 km; *e.g.,* Kerrich and Wyman, 1990; Groves et al., 1998 among others). Besides, we can estimate a ~20 km-depth of formation for the Galat Sufar South gold deposit, prior to potential partial exhumation within the ore-hosting accretionary wedge (*e.g.,* Guillot et al., 2009), relying on estimated pressure conditions (**Chapter VI**). The preservation of these gold deposits implies that the cumulated exhumation of the western Nubian shield did not exceed ~10-20 km since Neoproterozoic times. Actually, exhumation is even less important at the Arabian-Nubian shield scale as porphyry Cu-(Au) and epithermal gold deposits crop out (*e.g.,* Bierlein et al., 2016, 2020; El-shafei et al., 2020; Perelló et al., 2020). Several explanations may account for such a low exhumation rate. Firstly, lithospheric processes leading to surface uplift, such as lithospheric mantle delamination in a post-collisional setting, are weakly documented throughout the Arabian-Nubian shield, except for the Eastern Desert of Egypt where crustal levels deeper than the average crop out (Avigad and Gvirtzman, 2009; Eliwa et al., 2014; Khalil et al., 2015; Eyal et al., 2018; Megerssa et al., 2020). Secondly, Perelló et al. (2020) suggested that the entire Arabian-Nubian shield was buried beneath a thick post-amalgamation volcanosedimentary basinal cover derived from erosion of collided arc

rocks, itself thickened by stacking of collision-related thrust sheets. Finally, later Phanerozoic sedimentary strata were unconformably deposited over the Neoproterozoic basement from which they derive (*e.g.,* Avigad et al., 2003; Kolodner et al., 2009; Morag et al., 2011), preserving it from erosion for a few additional hundreds millions of years. The Arabian-Nubian shield indeed formed a stable craton relatively weakly affected by the Pangea assembly (*e.g.,* Kohn et al., 1992; Schandelmeier and Reynolds, 1997; Bojar et al., 2002), and modern-day tectono-magmatic events affecting the shield are associated with the early stages of the ongoing orogenic cycle (*i.e.,* Red Sea opening in Miocene; *e.g.,* Kohn and Eyal, 1981; Martinez and Cochran, 1988; Bohannon et al., 1989; Omar et al., 1989; Ghebreab, 1998). All these reasons explain why Neoproterozoic magmatic, tectonic and mineralization features are so well preserved, making the Arabian-Nubian shield an extraordinary window into the Gondwana supercontinent cycle.

2. Downscaling of the Keraf gold mineral system at the Arabian-Nubian shield scale

In the framework of this PhD project, the study conducted along the Keraf and Atmur-Delgo sutures should set an example prior to downscaling the Pan-African gold mineral system to the Arabian-Nubian shield extent. For more convenience, we decided to keep our comments to the primary gold deposits of the Nubian shield. Despite it lacks mineral exploration with respect to the neighbor Arabian shield, the Nubian shield represents an emerging gold province in itself, *i.e.,* with >1.4 t of gold discovered over the last decade and an increasing artisanal mining activity, especially in Sudan and Eritrea (Barrie et al., 2016; Johnson et al., 2017; Chevrillon-Guibert et al., 2019). Gold deposits of the Nubian shield formed from magmatic and/or tectonic accretion to syn-arc-arc or arc-continent collision periods of the Gondwana supercontinent cycle (Fig. 7-4; Elsamani et al., 2001; Botros, 2002, 2004; Bierlein et al., 2016; Johnson et al., 2017; El Aref et al., 2020). Our focus is to highlight (i) the similarities and differences between

them and those studied in the present manuscript in terms of ore types and geodynamical contexts and (ii) the potential genetic relationships between the successive deposit types formed through the geodynamical evolution of the Nubian shield.

2.1. Gold deposits coeval to magmatic and/or tectonic accretion

The presence of gold-rich VMS is largely manifested in the Red Sea Hills region, northeastern Sudan, and in Eritrea (Fig. 7-4). The Sudanese Ariab mining district, located along the Nakasib suture in the northern part of the Haya terrane, hosts more than twenty gold deposits, including thirteen VMS deposits mined since 1991 (> 62.2 t Au mined by 2012; Barrie et al., 2016). They are part of a lithostratigraphic column presenting a geochemical evolution from tholeiitic to calc-alkaline volcanism (Cottard et al., 1986; Abu Fatima, 2006), suggesting a transitional arc regime from primitive oceanic island arc to mature calc-alkaline island arc (Abu Fatima, 2006). Through the example of the well-documented Ariab district, the formation of gold-rich VMS deposits appears to relate to island arc complex magmatic activity throughout the Nubian shield, with no evidence of earlier occurrences formed at mid-ocean ridges. This is not surprising as back-arc settings are favorable for the emplacement of gold-enriched VMS deposits (Hannington et al., 1999; Dubé et al., 2007; Mercier-Langevin et al., 2011). The ages considered for VMS mineralization from Egypt to Ethiopia range between *ca.* 892-688 Ma, which illustrates the diachronism of the set-up of arc systems at the shield scale (Fig. 7-4). No VMS-like gold occurrence has been investigated during this study. It is however worth noticing that the Tanashieb prospect represents a highly altered VMS-related gossan and the unusual Wadi Doum base metal-gold deposit may present some characteristics of this type of deposit, both being located a few tens of km east to the Galat Sufar South gold deposit in Block 14 exploration license (Bowen, 2016).

Arc-related porphyry and epithermal gold-bearing deposits are also recognized throughout the Arabian-Nubian shield (Fig. 7-4; *e.g.,* Bierlein et al., 2016, 2020; El-Shafei

et al., 2020; Perelló et al., 2020). Except from the post-collisional Um Mongul prospect (Abd El-Rahman et al., 2017), these deposits also reflect arc activity between *ca.* 885-810 Ma. It corresponds to $WG03_1$ gold event coeval to the first Keraf island arc flare-up unraveled in **Chapter I** (Figs. 7-2 to 7-4). However, the tectonic accretion-related Galat Sufar South deposit is the only deposit of the Nubian shield associated with the *ca.* 760-655 Ma flare-up recorded by both the Atmur-Delgo and Keraf magmatic arcs (Figs. 7-2 to 7-4; **Chapter VI**). Apart from well-characterized porphyry Cu-Au deposits, this deposit is the oldest gold-bearing vein-type deposit of the Nubian shield to date. The case study of the Galat Sufar South deposit therefore questions the classification of numerous unstudied lode gold and gold-bearing vein occurrences into orogenic gold throughout the Nubian shield, relying mostly on their spatial relationship to major shear zones (Fig. 7-4; Johnson et al., 2017).

The presence of gold-rich VMS is largely manifested in the Red Sea Hills region, northeastern Sudan, and in Eritrea (Fig. 7-4). The Sudanese Ariab mining district, located along the Nakasib suture in the northern part of the Haya terrane, hosts more than twenty gold deposits, including thirteen VMS deposits mined since 1991 (> 62.2 t Au mined by 2012; Barrie et al., 2016). They are part of a lithostratigraphic column presenting a geochemical evolution from tholeiitic to calc-alkaline volcanism (Cottard et al., 1986; Abu Fatima, 2006), suggesting a transitional arc regime from primitive oceanic island arc to mature calc-alkaline island arc (Abu Fatima, 2006). Through the example of the well-documented Ariab district, the formation of gold-rich VMS deposits appears to relate to island arc complex magmatic activity throughout the Nubian shield, with no evidence of earlier occurrences formed at mid-ocean ridges. This is not surprising as back-arc settings are favorable for the emplacement of gold-enriched VMS deposits (Hannington et al., 1999; Dubé et al., 2007; Mercier-Langevin et al., 2011). The ages considered for VMS mineralization from Egypt to Ethiopia range between *ca.* 892-688 Ma, which illustrates the diachronism of the set-up of arc systems at the shield scale

(Fig. 7-4). No VMS-like gold occurrence has been investigated during this study. It is however worth noticing that the Tanashieb prospect represents a highly altered VMS-related gossan and the unusual Wadi Doum base metal-gold deposit may present some characteristics of this type of deposit, both being located a few tens of km east to the Galat Sufar South gold deposit in Block 14 exploration license (Bowen, 2016).

Arc-related porphyry and epithermal gold-bearing deposits are also recognized throughout the Arabian-Nubian shield (Fig. 7-4; *e.g.,* Bierlein et al., 2016, 2020; El-Shafei et al., 2020; Perelló et al., 2020). Except from the post-collisional Um Mongul prospect (Abd El-Rahman et al., 2017), these deposits also reflect arc activity between *ca.* 885-810 Ma. It corresponds to $WG03_1$ gold event coeval to the first Keraf island arc flare-up unraveled in **Chapter I** (Figs. 7-2 to 7-4). However, the tectonic accretion-related Galat Sufar South deposit is the only deposit of the Nubian shield associated with the *ca.* 760-655 Ma flare-up recorded by both the Atmur-Delgo and Keraf magmatic arcs (Figs. 7-2 to 7-4; **Chapter VI**). Apart from well-characterized porphyry Cu-Au deposits, this deposit is the oldest gold-bearing vein-type deposit of the Nubian shield to date. The case study of the Galat Sufar South deposit therefore questions the classification of numerous unstudied lode gold and gold-bearing vein occurrences into orogenic gold throughout the Nubian shield, relying mostly on their spatial relationship to major shear zones (Fig. 7-4; Johnson et al., 2017).

Figure 7-4 (p.462): Pressure-temperature-timing constraints on gold mineralization throughout the Nubian shield. Lithological units are harmonized from the Egyptian, Sudanese, Eritrean, Ethiopian and Saudi geological maps (Egyptian Geological Survey and Mining Authority, 1981; Geological Research Authority of the Sudan, 1988; USGS, 1998; Tadesse et al., 2000; AMEC, 2004). Gold occurrences are from the Arethuse Geology GIS compilation database. Plotted pressure-temperature-timing constraints on gold occurrences are from **Chapters I** and **VI** of the present manuscript and literature (Stern et al., 1991; Billay et al., 1997; Deksissa and Koeberl, 2004; Doebrich et al., 2004; Helmy et al., 2004; Barrie et al., 2007; Zoheir et al., 2008; Zoheir, 2008; Harbi et al., 2014; Zoheir and Moritz, 2014; Zoheir et al., 2015; Bierlein et al., 2016; Abd El-Rahman et al., 2017; Boskabadi et al., 2017; Abd El Monsef et al., 2018; Harbi et al., 2018; Zhao et al., 2019; Zoheir et al., 2019c, 2019d, 2019e; Bierlein et al., 2020; El Aref et al., 2020; Perelló et al., 2020). Background is from Google satellite imagery. Geographic coordinates are reported as WGS84.

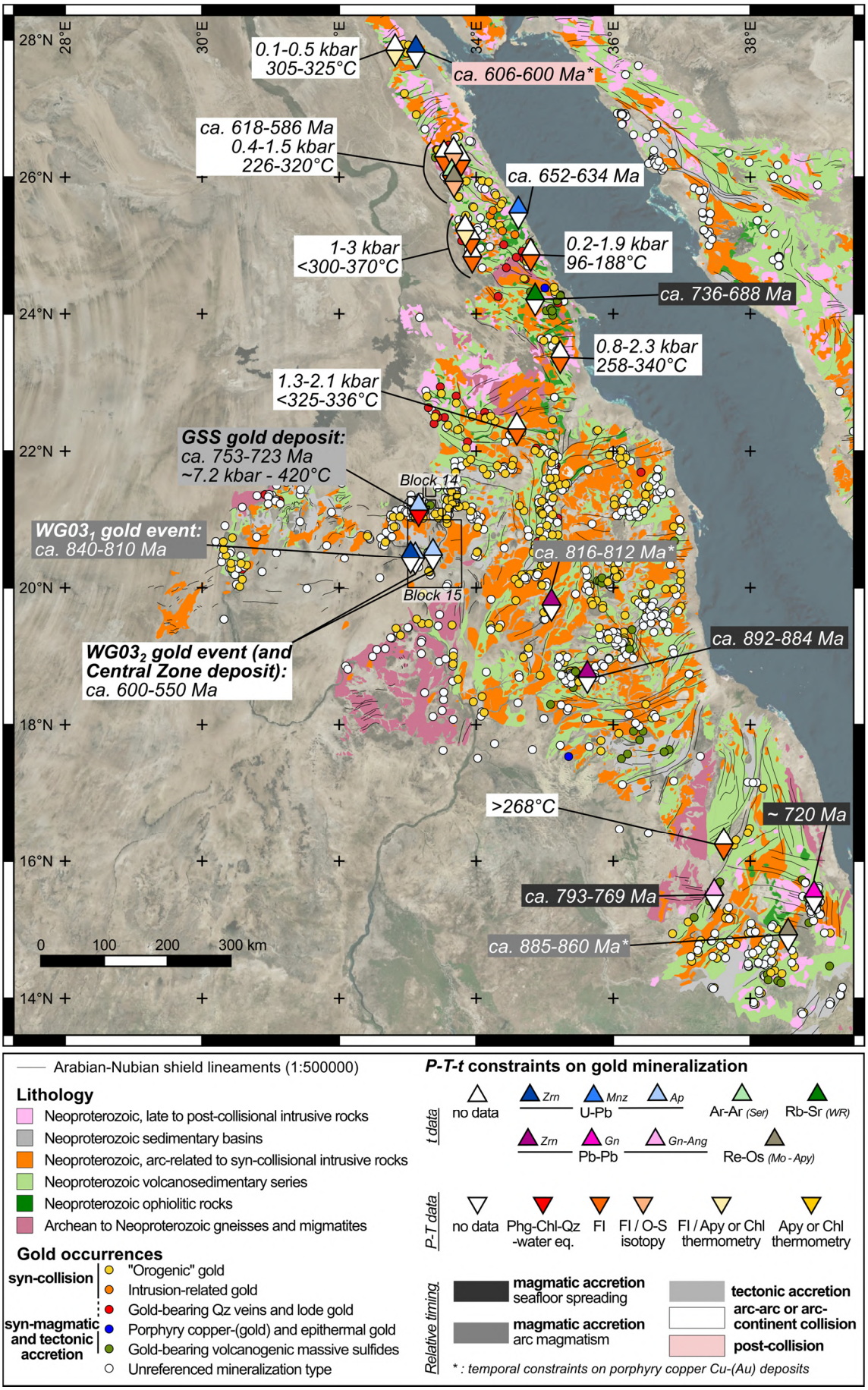


Figure 7-4: Pressure-temperature-timing constraints on gold mineralization throughout the Nubian shield.

2.2. Syn- to late collisional orogenic gold deposits

Typical orogenic gold mineralization is widespread in the Nubian shield, and especially well-described in the Eastern Desert of Egypt where exploration is much more developed than southwards (Fig. 7-4; reviews by Zoheir et al., 2019a; El Aref et al., 2020). These deposits formed in *ca.* 650-586 late collisional setting under pressure-temperature conditions typical of greenschist facies retrograde metamorphism (Fig. 7-4). The $WG03_2$ and Central Zone gold event described in this study is typical of orogenic gold as well is recorded as early as *ca.* 550 Ma, making it the youngest orogenic gold deposit of the Nubian shield to date (Figs. 7-2 to 7-4; **Chapter VI**). The large span of orogenic gold ages relates to (i) diachronism of late collisional events throughout the shield and (ii) the episodic, rhythmic reactivation of late collisional shear zones over several tens millions of years, as exemplified by the WG03 gold deposit (**Chapter VI**).

A lot of gold occurrences are only described as gold-bearing quartz veins and lode gold throughout the Nubian shield (Fig. 7-4). If they used to be abusively interpreted as orogenic gold because of their spatial association with crustal shear zones (Johnson et al., 2017), the Galat Sufar South case study demonstrates that we should rather be cautious prior to classifying these occurrences as they may relate to very different geodynamical settings.

2.3. Polyphase gold mineralization: ore remobilization and/or superimposition

The syngenetic or epigenetic nature of gold mineralization in gold-rich VMS deposits is widely discussed, especially for the world-class deposits of Canada (review by Dubé et al., 2007). It is still very controversial for VMS in the Nubian shield as well. In Block 14, the genetic relationships between the Tanashieb VMS, Wadi Doum VMS-like and Galat Sufar South vein-type gold deposits remain very uncertain (Bowen, 2016). In Egypt, Botros (2003) suggested a syngenetic gold enrichment for gold-rich VMS.

Conversely, Abu Fatima (2006) rather supported a late tectonic timing for gold mineralization in the Ariab mining district, with overprinting of earlier VMS mineralization by orogenic gold which presence is illustrated by the Kamoeb deposit (Abu Fatima, 2006). Yet, Perret et al. (2017) relied on textural and geochemical characteristics of the distinct generations of sulfide minerals to demonstrate that ore refining mostly resulted from syn-tectonic mechanical remobilization, with no additional gold input after the massive sulfide deposition at the Hadayamet VMS deposit, Ariab district. At the opposite, these early gold-rich VMS deposits can be seen as potential gold sources for later mineralization as they provide a rather important amount of gold concentrated in a reduced volume at subsurface. They are besides formed in a geodynamical setting that evolved towards collision with formation and reactivation of lithospheric to crustal structures along which fluids may be driven and leach the gold budget of early VMS.

Besides, the record of both a Keraf island arc-related $WG03_1$ gold event and a late collisional $WG03_2$ intrusion-hosted orogenic gold episode within a single deposit raises to wonder whether late orogenic gold resulted from (i) a new gold input from the district-scale fertile crustal reservoir, (ii) the deposit-scale remobilization of early disseminated gold mineralization in the WG03-hosting batholith, (iii) or a combination of both. In the same sense, an overprinting between intrusion-related and orogenic gold is also questioned in the Central Eastern Desert by Abd El Monsef et al. (2020). The overlap of magmatic accretion-related to collision-related gold events is also widely recognized throughout world-class gold provinces such as the Archean Yilgarn craton (*e.g.,* Duuring et al., 2007) and Abitibi subprovince (*e.g.,* Boullier and Robert, 1992; Dubé and Gosselin, 2007; Dubé et al., 2007; Dubé and Mercier-Langevin, 2015) and the Paleoproterozoic West African craton (Thébaud et al., 2020; Masurel et al., in press). It illustrates how complex the record of gold events record could be, with the succession of several

geodynamical settings favorable to mobilization and remobilization of gold from a primary crustal reservoir within a single orogenic cycle.

3. Perspectives

3.1. Towards a better understanding of geodynamical processes...

3.1.1. ... at the Atmur-Delgo suture scale

If the geodynamical evolution of the Keraf suture is addressed in details in **Chapter I**, it is not the case for the Atmur-Delgo suture. The comparisons made with the geodynamical history proposed for the Keraf suture only rely on literature and a few additional geochemical, geochronological and isotopic constraints presented in **Chapter VI**. Besides, we pointed out in **Chapter I** that the proposed geometry for the combined Keraf-Atmur-Delgo intra-oceanic system is problematic due to the north-verging polarity considered by previous studies for the Atmur-Delgo subduction. Our understanding of the geodynamical evolution of the Atmur-Delgo suture and its lithospheric-scale geometry remains thus uncertain at the end of this PhD project (Fig. 7-3). Yet, we provided robust thermodynamic and geochronological constraints on the formation of the Galat Sufar South gold deposit, which likely formed under peak amphibolite facies metamorphism conditions during tectonic accretion of the sedimentary wedge at the Atmur-Delgo intra-oceanic subduction site (**Chapter VI**). Carrying out a geological cross-section across the accretionary wedge, the magmatic arc and the ophiolites Atmur-Delgo suture, following the sampling and analytical strategy applied to the central Keraf suture (**Chapters I, III**), appears therefore critical to (i) fill the gap in knowledge about its geodynamical evolution and (ii) draw incremental cross-sections of the Atmur-Delgo suture fitting with information brought by Galat Sufar South (*e.g.,* Fig. 7-2 for the Keraf suture).

3.1.2. ... at the Keraf suture scale

The structural study and sampling of igneous rocks carried out across the central Keraf suture enabled the deciphering of its geodynamical evolution (**Chapter I**). However, there is a lack of representativeness of the magmatic rocks collected regarding the complexity of the Keraf island arc magmatic record, which compels us from building the detailed section of the Keraf arc complex. Carrying out a careful and more detailed sampling of the entire Keraf arc section could help to better estimate the relative proportion and nature of lithologies in presence, with insights into a more detailed record of the arc magmatic activity through time. Besides, as evoked in subsection 1.1.2, such sampling combined to systematic measurement of rock density and gold concentration could provide a more accurate estimation of gold crustal fertilization during the maturation of the Keraf island arc, despite the deep arc root does likely not crop out and could therefore not be characterized.

3.1.3. ... at the Arabian-Nubian shield scale

In order to downscale the insights from our study, which focused on the Keraf and Atmur-Delgo sutures, an extensive geochronological (U-Pb, Pb-Pb, K-Ar, Ar-Ar, Re-Os, Rb-Sr isotopic systems applied to mineral phases or bulk rock) and isotopic (Hf, Nd and Sr) database has been built and gathers all the constraints on magmatic, tectonic and mineralization events reported throughout the Arabian-Nubian shield (almost 2900 data rows). The Supplementary Material 1-4 is extracted from this database and all publications and reports which have been compiled are referenced at the end of this manuscript.

As illustrated by **Chapter I**, this database has been useful to consider collectively our new data with previous ones published for the studied area. This data compilation will be useful if any future research project was designed to unravel the tectono-magmatic evolution of another place of the Arabian-Nubian shield, following a similar approach as

the present study. Besides, the careful report of geographic coordinates is of huge importance if we ever try to use the database for the paleo-reconstruction of the evolution of arc complexes. Implementing a modelling approach could be interesting in that sense, using tools such as the GPlates software (Boyden et al., 2011; Müller et al., 2018). This would indeed be a great step forward in the understanding of the complex assembly of the Arabian-Nubian shield with east-west/north-south diachronism of suturing (**Introduction chapter**), with promising perspectives towards a renewal of province-scale mineral exploration (see section 3.3.).

3.2. Towards a better understanding of magmatic-hydrothermal gold-forming processes during island arc magmatism

Despite the main mineralizing event contributing to gold endowment at the WG03 deposit is well characterized in terms of structural and timing relationships to Keraf strike-slip shearing (**Chapters III, VI**), the early arc magmatic accretion-related gold event is not clearly described nor interpreted in **Chapter III**. As it is expressed by plagioclase-dominated magmatic-hydrothermal features, with no sharp boundaries with the surrounding ore-hosting quartz-diorite, we suggested this gold event occurred at *ca.* 840-810 Ma relying on the U-Pb zircon age of the intrusion (see subsection 1.2.1.; Figs. 7-2, 7-3). Yet, there is certainly much more to learn about this gold event and how it relates with intense crustal growth and gold fertilization (**Chapter I**; see section 1.1.), as suggested by the coexistence of chalcopyrite, pyrrhotite and magnetite that can be very insightful into understanding magmatic processes in arc settings (Sun et al., 2004; Chen et al., 2020).

To bring further knowledge about this gold event, a MSc thesis work is currently carried out by Hugo Ceinturet (Université de Lorraine, Nancy, France), supervised by Julien Perret, Aurélien Eglinger and Anne-Sylvie André-Mayer. It aims at better describing the textural and geochemical changes relative to the progressive shift from the

amphibole-dominated host-quartz-diorite towards the plagioclase-enriched mineralized magmatic-hydrothermal features, with a particular focus on sulfide-oxide mineral assemblages and changes in dominant silicate compositions.

4. Shifting from the gold mineral system to exploration targeting

If the contribution of the mineral system approach to the understanding of modalities of formation of ore deposits are undeniable, their translation into effective exploration strategies is not optimal (McCuaig et al., 2010), although more and more documented (Hronsky et al., 2012; Joly et al., 2012; McCuaig and Hronsky, 2014; Groves et al., 2019, 2020). There has been an increasing use of geographic information system (GIS)-assisted modelling for exploration targeting for the two last decades. It mostly relies on the use of geochemical and/or geophysical data and remote sensing, especially in desert areas, to trace alteration and mineralization footprints as well as major structural pathways and traps (Kusky and Ramadan, 2002; Sprague et al., 2006; Ramadan and Abdel Fattah, 2010; Kreuzer et al., 2014; Ibrahim et al., 2016; Reimann et al., 2016; Salem et al., 2016; Haldar, 2018; Yousefi et al., 2019; Gaillard et al., 2020; Kreuzer et al., 2020), with attempts for quantifying the spatial prospectivity (*e.g.,* Niiranen et al., 2019).

However, the use of such methods is limited to places where extended geological, geochemical and geophysical are available. Besides, it applies to the exploration of one or a few deposit types, as alteration patterns and lithological-structural frameworks vary from one to another. These methods also rely on classical ore deposit classification schemes, in which every deposit is sorted according to strictly-defined boxes. As exemplified by the Galat Sufar South gold deposit in this study (see subsection 1.2.2, such an approach does not reflect the incredible diversity in ore deposit types, whereas they may share similar geodynamical settings, tectonic triggers and ore-forming

processes. The latter statement is well illustrated by one of the most-known structurally controlled deposit worldwide, the Porgera deposit, Papua New Guinea: it displays characteristics of porphyry, epithermal and orogenic gold which is quite confusing, but it serves as the typical case study for earthquake-induced fault-valve processes (Peterson and Mavrogenes, 2014).

In agreement with our support of focusing on geodynamical and tectonic processes to better understand why, when and where mineralization formed, we therefore adopt the *"practical regional-scale targeting methodology"* of Hronsky et al. (2012). In order to target exploration for a commodity such as gold, they consider the combination of *"a fertile upper-mantle source region, a favorable transient remobilization event, and favorable lithospheric-scale plumbing structure"* into a unified model. The guiding philosophy for this approach relies on the fact that once a gold enriched reservoir is available, it can be accessed later in a wide range of tectono-magmatic settings (Hronsky et al., 2012), accounting for multiple ore remobilization possibilities as well (see section 2.3). It therefore represents a convenient alternative to distinct building mineral systems for each of the gold-bearing deposit types recognized throughout a metallogenic province (*e.g.,* VMS, porphyry Cu-(Au), from syn-tectonic accretion lode gold to late collisional orogenic gold for primary gold deposits reported in the Nubian shield; Fig. 7-4). In what follows, we apply this concept to the Arabian-Nubian shield.

As exemplified by the Keraf and Atmur-Delgo suture case studies, it appears that juvenile magmatism during island arc magmatic activity in the early evolution of the Arabian-Nubian shield implies a widespread crustal gold fertilization. The crustal endowment of gold is therefore a prerequisite fulfilled for almost the entire Arabian-Nubian shield, except from the reworked Khida crustal block (**Introduction chapter**). Spotting the reworked paleo-oceanic arc-back-arc systems is however of interest as they may host gold-bearing VMS, porphyry Cu-(Au) and accretionary wedge-hosted lode gold deposits (*e.g.,* the Hassai camp, the Jebel Ohier and the Galat Sufar South gold deposits,

respectively; Fig. 7-4). These arc complexes are particularly well-documented along arc-arc and arc-continent suture zones. Through the example of the Keraf suture, we demonstrated that the complex, progressive and then polyphaser-protracted tectonic record along these zones led to their superimposition by crustal- to shear zones rooted into the lithosphere. This tectonic evolution is coeval with transient remobilization of gold along neoformed and reactivated multiple-order structures, resulting in the formation of the Gabgaba gold district (WG03, Central Zone deposit) or numerous orogenic gold deposits in the Eastern Desert of Egypt (Fig. 7-4). All parts of the Arabian-Nubian shield where (i) juvenile magmatism during intra-oceanic subduction and (ii) complex, polyphase subsequent ductile-brittle to brittle deformation during arc-arc or arc-continent collision are likely to host gold deposits considering this unified model. In that sense, implementing geochronological and isotopic database similar to the one built during this project into the existing GIS-assisted techniques for computing mineral exploration targets looks very promising. It may definitely represent a step forward for mineral exploration, with a strong collaborative work between academic research and exploration industry, as exemplified by the West African Exploration Initiative ongoing since 2006.

RÉFÉRENCES

A

Abanyin, E., Abdel Salam, B., Ackah, E., Appiah, M., Mohamedy, M., Mills, S., Stuart, H., 2015. The discovery and geology of the Galat Sufar south deposit, Republic of the Sudan. Presented at the NewGenGold 2015, Perth, Western Australia, 115–130.

Abd El Monsef, M., Slobodník, M., Salem, I.A., 2018. Hydrothermal evolution of granitoid-hosted gold mineralization in gidami area: An example for orogenic-gold deposits in Egypt. Journal of African Earth Sciences 146, 132–149.

Abd El Monsef, M., 2019. Ore Controls and Metallogenesis of Au-Ag Deposits at Atalla Mine, Central Eastern Desert of Egypt. Acta Geologica Sinica - English Edition.

Abd El Monsef, M., Slobodník, M., Salem, I.A., 2020. Characteristics and nature of gold-bearing fluids in Fatira area, North Eastern Desert of Egypt: possible transition from intrusion-related to orogenic deposits. Arabian Journal of Geosciences 13.

Abd El-Naby, H., Frisch, W., Siebel, W., 2008. Tectono-metamorphic evolution of the Wadi Hafafit Culmination (central Eastern Desert, Egypt). Implication for Neoproterozoic core complex exhumation in NE Africa. Geologica Acta: An International Earth Science Journal 6, 293–312.

Abd El-Rahman, Y., Seifert, T., Gutzmer, J., Said, A., Hofmann, M., Gärtner, A., Linnemann, U., 2017. The South Um Mongul Cu-Mo-Au prospect in the Eastern Desert of Egypt: From a mid-Cryogenian continental arc to Ediacaran post-collisional appinite-high Ba-Sr monzogranite. Ore Geology Reviews 80, 250–266.

Abdeen, M.M., Abdelghaffar, A.A., 2011. Syn- and post-accretionary structures in the Neoproterozoic Central Allaqi-Heiani suture zone, Southeastern Egypt. Precambrian Research 185, 95–108.

Abdel-Rahman, A.-F.M., Doig, R., 1987. The Rb-Sr geochronological evolution of the Ras Gharib segment of the northern Nubian Shield. Journal of the Geological Society 144, 577–586.

Abdel-Rahman, A.-F.M., 2020. Petrogenesis of a rare Ediacaran tonalite–trondhjemite–granodiorite suite, Egypt, and implications for Neoproterozoic Gondwana assembly. Geological Magazine 1–22.

Abdelrahman, E.M.A, 1993. Geochemical and geotectonic controls of the metallogenic evolution of selected ophiolite complexes from the Sudan. Reimer.

Abdelrahman, E.M.A, Matheis, G., Schandelmeier, H., Karfis, M.A., Gadir, I.A., El Khedir, M., 2017. Evolution of the Keraf back-arc basin: Constraints on the Nubian Shield margin. Geoscientific Research in Northeast Africa. CRC Press, 93–98.

Abdelsalam, M.G., Dawoud, A.S., 1991. The Kabus ophiolitic melange, Sudan, and its bearing on the western boundary of the Nubian Shield. Journal of the Geological Society 148, 83–92.

Abdelsalam, M.G., Stern, R.J., 1993. Structure of the late Proterozoic Nakasib suture, Sudan. Journal of the Geological Society 150, 1065–1074.

Abdelsalam, M.G., 1994. The Oko Shear Zone, Sudan: post-accretionary deformation in the Arabian-Nubian Shield. Journal of the Geological Society 151, 767–776.

Abdelsalam, M.G., Stern, R.J., Schandelmeier, H., Sultan, M., 1995. Deformational History of the Neoproterozoic Keraf Zone in NE Sudan, Revealed by Shuttle Imaging Radar. The Journal of Geology 103, 475–491.

Abdelsalam, M.G., Stern, R.J., 1996a. Mapping Precambrian structures in the Sahara Desert with SIR-C/X-SAR radar: The Neoproterozoic Keraf Suture, NE Sudan. Journal of Geophysical Research: Planets 101, 23063–23076.

Abdelsalam, M.G., Stern, R.J., 1996b. Sutures and shear zones in the Arabian-Nubian Shield. Journal of African Earth Sciences 23, 289–310.

Abdelsalam, M.G., Stern, R.J., Copeland, P., Elfaki, E.M., Elhur, B., Ibrahim, F.M., 1998. The Neoproterozoic Keraf Suture in Ne Sudan: Sinistral Transpression Along the Eastern Margin of West Gondwana. The Journal of Geology 106, 133–148.

Abdelsalam, M.G., Abdel-Rahman, E.-S.M., El-Faki, E.-F.M., Al-Hur, B., El-Bashier, F.-R.M., Stern, R.J., Thurmond, A.K., 2003. Neoproterozoic deformation in the northeastern part of the Saharan Metacraton, northern Sudan. Precambrian Research 123, 203–221.

Abdelsalam, M.G., 2010. Quantifying 3D post-accretionary tectonic strain in the Arabian–Nubian Shield: Superimposition of the Oko Shear Zone on the Nakasib Suture, Red Sea Hills, Sudan. Journal of African Earth Sciences 56, 167–178.

Abdelsalam, M.G., Stern, R.J., 2017. Timing of events along the Nakasib suture and the Oko shear zone, Sudan. Geoscientific Research in Northeast Africa. CRC Press, 99–103.

Abu El-Enen, M.M., Whitehouse, M.J., 2013. The Feiran–Solaf metamorphic complex, Sinai, Egypt: Geochronological and geochemical constraints on its evolution. Precambrian Research 239, 106–125.

Abu El-Enen, M.M., Abu-Alam, T.S., Whitehouse, M.J., Ali, K.A., Okrusch, M., 2016. P–T path and timing of crustal thickening during amalgamation of East and West Gondwana: A case study from the Hafafit Metamorphic Complex, Eastern Desert of Egypt. Lithos 263, 213–238.

Abu Fatima, M., 2006. Metallogenic genesis and geotectonic evolution of the polymetallic massive sulphides and the associated gold deposits at Ariab-Arbaat Belt, Red Sea Hills, NE Sudan. PhD thesis. Université Henri Poincaré (Nancy 1).

Adam, M.M.A., Lv, X., Abdel Rahman, A.A., Stern, R.J., Abdalrhman, A.A.A., Ullah, Z., 2020. In-situ sulfur isotope and trace element compositions of pyrite from the Neoproterozoic Haweit gold deposit, NE Sudan: Implications for the origin and source of the sulfur. Ore Geology Reviews 120, 103405.

Ahmed Suliman, E.T.B., 2000. Keraf shear zone, NE Sudan: geodynamic characteristics of the Nile Craton - Nubian Shield boundary. Technischen Universität Berlin.

Alexander, C., Litosh, S., Alway, B., Wiebe, J., Li, S., Saha, D., Scott-Gray, N., Gay, F., Goenka, S., 2019. GFMS GOLD SURVEY 2019. Refinitiv.

Ali, B.H., Wilde, S.A., Gabr, M.M.A., 2009. Granitoid evolution in Sinai, Egypt, based on precise SHRIMP U–Pb zircon geochronology. Gondwana Research 15, 38–48.

Ali, B.H., 2015. SHRIMP U–Pb zircon geochronology: evidence for emplacement time of some granitoids north Eastern Desert, Egypt. Arabian Journal of Geosciences 8, 5465–5474.

Ali, K.A., Stern, R.J., Manton, W.I., Kimura, J.-I., Khamees, H.A., 2009. Geochemistry, Nd isotopes and U–Pb SHRIMP zircon dating of Neoproterozoic volcanic rocks from the Central Eastern Desert of Egypt: New insights into the ∼750Ma crust-forming event. Precambrian Research 171, 1–22.

Ali, K.A., Azer, M.K., Gahlan, H.A., Wilde, S.A., Samuel, M.D., Stern, R.J., 2010a. Age constraints on the formation and emplacement of Neoproterozoic ophiolites along the Allaqi–Heiani Suture, South Eastern Desert of Egypt. Gondwana Research 18, 583–595.

Ali, K.A., Stern, R.J., Manton, W.I., Kimura, J.-I., Whitehouse, M.J., Mukherjee, S.K., Johnson, P.R., Griffin, W.R., 2010b. Geochemical, U–Pb zircon, and Nd isotope investigations of the Neoproterozoic Ghawjah Metavolcanic rocks, Northwestern Saudi Arabia. Lithos 120, 379–392.

Ali, K.A., Wilde, S.A., Stern, R.J., Moghazi, A.-K.M., Ameen, S.M.M., 2013. Hf isotopic composition of single zircons from Neoproterozoic arc volcanics and post-collision granites, Eastern Desert of Egypt: Implications for crustal growth and recycling in the Arabian-Nubian Shield. Precambrian Research 239, 42–55.

Ali, K.A., Kröner, A., Hegner, E., Wong, J., Li, S.-Q., Gahlan, H.A., Abu El Ela, F.F., 2015. U–Pb zircon geochronology and Hf–Nd isotopic systematics of Wadi Beitan granitoid gneisses, South Eastern Desert, Egypt. Gondwana Research 27, 811–824.

Ali, K.A., Zoheir, B.A., Stern, R.J., Andresen, A., Whitehouse, M.J., Bishara, W.W., 2016. Lu–Hf and O isotopic compositions on single zircons from the North Eastern Desert of Egypt, Arabian–Nubian Shield: Implications for crustal evolution. Gondwana Research 32, 181–192.

Allan, J.F., 1992. Geochemistry of igneous rocks from Legs 127 and 128, Sea of Japan. Proc. ODP Sci. Res. 905–929.

Allen, A., Tadesse, G., 2003. Geological setting and tectonic subdivision of the Neoproterozoic orogenic belt of Tuludimtu, western Ethiopia. Journal of African Earth Sciences 36, 329–343.

Allibone, A., Teasdale, J., Cameron, G., Etheridge, M., Uttley, P., Soboh, A., Appiah-Kubi, J., Adanu, A., Arthur, R., Mamphey, J., 2002. Timing and structural controls on gold mineralization at the Bogoso gold mine, Ghana, West Africa. Economic Geology 97, 949–969.

Allibone, A., Blakemore, H., Gane, J., Moore, J., MacKenzie, D., Craw, D., 2018. Contrasting Structural Styles of Orogenic Gold Deposits, Reefton Goldfield, New Zealand. Economic Geology 113(7), 1479–1497.

Almond, D.C., Ahmed, F., 1987. Ductile shear zones in the northern Red Sea Hills, Sudan and their implication for crustal collision. Geological Journal 22, 175–184.

Almond, D.C., Darbyshire, D.P.F., Ahmed, F., 1989. Age limits for major shearing episodes in the Nubian Shield of NE Sudan. Journal of African Earth Sciences (and the Middle East) 9, 489–496.

Alonso-Perez, R., Müntener, O., Ulmer, P., 2009. Igneous garnet and amphibole fractionation in the roots of island arcs: experimental constraints on andesitic liquids. Contributions to Mineralogy and Petrology 157, 541–558.

Al-Saleh, A.M., Boyle, A.P., 2001. Neoproterozoic ensialic back-arc spreading in the eastern Arabian shield: geochemical evidence from the Halaban Ophiolite. Journal of African Earth Sciences 33, 1–15.

Alsop, G.I., Holdsworth, R.E., 2004. The geometry and topology of natural sheath folds: a new tool for structural analysis. Journal of Structural Geology 26, 1561–1589.

Alsop, G.I., Holdsworth, R.E., 2006. Sheath folds as discriminators of bulk strain type. Journal of Structural Geology 28, 1588–1606.

Alsop, G.I., Holdsworth, R.E., McCaffrey, K.J.W., 2007. Scale invariant sheath folds in salt, sediments and shear zones. Journal of Structural Geology 29, 1585–1604.

AMEC, 2004. General Geology Map of Eritrea, scale 1:3500000, Nevsun Bisha Technical Report.

Anczkiewicz, R., Burg, J.P., Villa, I.M., Meier, M., 2000. Late Cretaceous blueschist metamorphism in the Indus suture zone, Shangla region, Pakistan Himalaya. Tectonophysics 324, 111–134.

Andersson, U.B., Ghebreab, W., Teklay, M., 2006. Crustal evolution and metamorphism in east-central Eritrea, south-east Arabian-Nubian Shield. Journal of African Earth Sciences 44, 45–65.

André-Mayer, A.S., Ramiandrisoa, N., Vanderhaeghe, O., Reisberg, L., Rabeandrasana, S., Zimmermann, C., 2014. Re–Os geochronological constraints on the Dabolava mesothermal gold occurence, Madagascar: Implications for the Ikalamavony sub-domain deposition age. Journal of African Earth Sciences 94, 119–127.

Andresen, A., El-Rus, M.A.A., Myhre, P.I., Boghdady, G.Y., Corfu, F., 2009. U–Pb TIMS age constraints on the evolution of the Neoproterozoic Meatiq Gneiss Dome, Eastern Desert, Egypt. International Journal of Earth Sciences 98, 481–497.

Andresen, A., Augland, L.E., Boghdady, G.Y., Lundmark, A.M., Elnady, O.M., Hassan, M.A., El-Rus, M.A., 2010. Structural constraints on the evolution of the Meatiq gneiss dome (Egypt), east-African orogen. Journal of African Earth Sciences 57, 413–422.

Anhaeusser, C.R., Fritze, K., Fyfe, W.S., Gill, R.C.O., 1975. Gold in "primitive" Archaean volcanics. Chemical Geology 16, 129–135.

Anhaeusser, C.R., 2014. Archaean greenstone belts and associated granitic rocks–a review. Journal of African Earth Sciences 100, 684–732.

Arculus, R.J., 2004. Evolution of arc magmas and their volatiles. In: Sparks, R.S.J., Hawkesworth, C.J. (Eds.), Geophysical Monograph Series. American Geophysical Union, Washington, D. C., 95–108.

Arne, D.C., Bierlin, F.P., Morgan, J.W., Stein, H.J., 2001. Re-Os dating of sulfides associated with gold

mineralization in central Victoria, Australia. Economic Geology 96, 1455–1459.

Ashley, P.M., Craw, D., 2004. Structural controls on hydrothermal alteration and gold?antimony mineralisation in the Hillgrove area, NSW, Australia. Mineralium Deposita 39, 223–239.

Augland, L.E., Andresen, A., Boghdady, G.Y., 2012. U–Pb ID-TIMS dating of igneous and metaigneous rocks from the El-Sibai area: time constraints on the tectonic evolution of the Central Eastern Desert, Egypt. International Journal of Earth Sciences 101, 25–37.

Augustin, J., Gaboury, D., Crevier, M., 2016. The world-class Wona-Kona gold deposit, Burkina Faso. Ore Geology Reviews 78, 667–672.

Augustin, J., Gaboury, D., 2017. Paleoproterozoic plume-related basaltic rocks in the Mana gold district in western Burkina Faso, West Africa: Implications for exploration and the source of gold in orogenic deposits. Journal of African Earth Sciences 129, 17–30.

Augustin, J., Gaboury, D., Crevier, M., 2017. Structural and gold mineralizing evolution of the world-class orogenic Mana district, Burkina Faso: Multiple mineralizing events over 150 million years. Ore Geology Reviews 91, 981–1012.

Augustin, J., Gaboury, D., 2018. Multi-stage and multi-sourced fluid and gold in the formation of orogenic gold deposits in the world-class Mana district of Burkina Faso - Revealed by LA-ICP-MS analysis of pyrites and arsenopyrites. Ore Geology Reviews 104, 495–521.

Avigad, D., Kolodner, K., McWilliams, M., Persing, H., Weissbrod, T., 2003. Origin of northern Gondwana Cambrian sandstone revealed by detrital zircon SHRIMP dating. Geology 31, 227–230.

Avigad, D., Gvirtzman, Z., 2009. Late Neoproterozoic rise and fall of the northern Arabian–Nubian shield: The role of lithospheric mantle delamination and subsequent thermal subsidence. Tectonophysics 477, 217–228.

Avigad, D., Weissbrod, T., Gerdes, A., Zlatkin, O., Ireland, T.R., Morag, N., 2015. The detrital zircon U–Pb–Hf fingerprint of the northern Arabian–Nubian Shield as reflected by a Late Ediacaran arkosic wedge (Zenifim Formation; subsurface Israel). Precambrian Research 266, 1–11.

Ayalew, T., Bell, K., Moore, J.M., Parrish, R.R., 1990. U-Pb and Rb-Sr geochronology of the Western Ethiopian Shield. Geological Society of America Bulletin 102, 1309–1316.

Ayer, J.A., Thurston, P.C., Lafrance, B., 2008. A special issue devoted to base metal and gold metallogeny at regional, camp, and deposit scales in the Abitibi greenstone belt: Preface. Economic Geology 103, 1091–1096.

Azer, M.K., Stern, R.J., 2007. Neoproterozoic (835–720 Ma) serpentinites in the Eastern Desert, Egypt: fragments of forearc mantle. The Journal of Geology 115, 457–472.

Azer, M.K., Stern, R.J., Kimura, J.-I., 2010. Origin of a late Neoproterozoic (605 ± 13 Ma) intrusive carbonate–albitite complex in Southern Sinai, Egypt. International Journal of Earth Sciences 99, 245–267.

B

Bajwah, Z.U., Seccombe, P.K., Offler, R., 1987. Trace element distribution, Co: Ni ratios and genesis of the Big Cadia iron-copper deposit, New South Wales, Australia. Mineralium Deposita 22, 292–300.

Bailo, T., Schandelmeier, H., Franz, G., Sun, C.-H., Stern, R.J., 2003. Plutonic and metamorphic rocks from the Keraf Suture (NE Sudan): a glimpse of Neoproterozoic tectonic evolution on the NE margin of W. Gondwana. Precambrian Research 123, 67–80.

Baratoux, L., Metelka, V., Naba, S., Ouiya, P., Siebenaller, L., Jessell, M.W., Naré, A., Salvi, S., Béziat, D., Franceschi, G., 2015. Tectonic evolution of the Gaoua region, Burkina Faso: Implications for mineralization. Journal of African Earth Sciences 112, 419–439.

Barley, M.E., Groves, D.I., 1992. Supercontinent cycles and the distribution of metal deposits through time. Geology 20, 291–294.

Barnes, S.-J., Naldrett, A.J., Gorton, M.P., 1985. The origin of the fractionation of platinum-group elements in terrestrial magmas. Chemical Geology 53, 303–323.

Barnes, H.L., 1997. Geochemistry of hydrothermal ore deposits. John Wiley & Sons.

Barnicoat, A.C., 2007. Mineral systems and exploration science: linking fundamental controls on ore deposition with the exploration process. Digging Deeper. Proceedings of the Ninth Biennial SGA Meeting, Dublin. 1407–1411.

Barou, F., Maurice, C., Feppon, J.-M., Driver, J., 2009. Sub-grain boundary mobilities during recovery of binary Al–Mn alloys. International Journal of Materials Research 100, 516–521.

Barrie, C.D., Boyle, A.P., Cook, N.J., Prior, D.J., 2010a. Pyrite deformation textures in the massive sulfide ore deposits of the Norwegian Caledonides. Tectonophysics 483, 269–286.

Barrie, C.D., Cook, N.J., Boyle, A.P., 2010b. Textural variation in the pyrite-rich ore deposits of the Røros district, Trondheim Region, Norway: implications for pyrite deformation mechanisms. Mineralium Deposita 45, 51–68.

Barrie, C.T., Nielsen, F.W., Aussant, C.H., 2007. The Bisha volcanic-associated massive sulfide deposit, western Nakfa Terrane, Eritrea. Economic Geology 102, 717–738.

Barrie, C.T., Abdalla, M.A.F., Hamer, R.D., 2016. Volcanogenic Massive Sulphide–Oxide Gold Deposits of the Nubian Shield in Northeast Africa. In: Bouabdellah, M., Slack, J.F. (Eds.), Mineral Deposits of North Africa. Springer International Publishing, Cham, 417–435.

Barth, A.P., Tani, K., Meffre, S., Wooden, J.L., Coble, M.A., Arculus, R.J., Ishizuka, O., Shukle, J.T., 2017. Generation of silicic melts in the early Izu-Bonin Arc recorded by detrital zircons in proximal arc volcaniclastic rocks from the Philippine Sea. Geochemistry, Geophysics, Geosystems 18, 3576–3591.

Bateman, R., Hagemann, S., 2004. Gold mineralisation throughout about 45 Ma of Archaean orogenesis: protracted flux of gold in the Golden Mile, Yilgarn craton, Western Australia. Mineralium Deposita 39, 536–559.

Bayliss, P., 1968. The crystal structure of disordered gersdorffite. American Mineralogist: Journal of Earth and Planetary Materials 53, 290–293.

Bayliss, P., 1977. Crystal structure refinement of a weakly anisotropic pyrite. American Mineralogist 62, 1168–1172.

Bea, F., Abu-Anbar, M., Montero, P., Peres, P., Talavera, C., 2009. The ~844Ma Moneiga quartz-diorites of the Sinai, Egypt: Evidence for Andean-type arc or rift-related magmatism in the Arabian-Nubian Shield? Precambrian Research 175, 161–168.Beaudoin, G., Pitre, D., 2005. Stable isotope geochemistry of the Archean Val-d 'Or (Canada) orogenic gold vein field. Mineralium Deposita 40, 59–75.

Beaudoin, G., Chiaradia, M., 2016. Fluid mixing in orogenic gold deposits: Evidence from the HO-Sr isotope composition of the Val-d'Or vein field (Abitibi, Canada). Chemical Geology 437, 7–18.

Bedeaux, P., Pilote, P., Daigneault, R., Rafini, S., 2017. Synthesis of the structural evolution and associated gold mineralization of the Cadillac Fault, Abitibi, Canada. Ore Geology Reviews 82, 49–69.

Be'eri-Shlevin, Y., Katzir, Y., Whitehouse, M., 2009a. Post-collisional tectonomagmatic evolution in the northern Arabian–Nubian Shield: time constraints from ion-probe U–Pb dating of zircon. Journal of the Geological Society 166, 71–85.

Be'eri-Shlevin, Y., Katzir, Y., Valley, J.W., 2009b. Crustal evolution and recycling in a juvenile continent: Oxygen isotope ratio of zircon in the northern Arabian Nubian Shield. Lithos 107, 169–184.

Be'eri-Shlevin, Y., Katzir, Y., Whitehouse, M.J., Kleinhanns, I.C., 2009c. Contribution of pre Pan-African crust to formation of the Arabian Nubian Shield: New secondary ionization mass spectrometry U-Pb and O studies of zircon. Geology 37, 899–902.

Be'eri-Shlevin, Y., Katzir, Y., Blichert-Toft, J., Kleinhanns, I.C., Whitehouse, M.J., 2010. Nd–Sr–Hf–O isotope provinciality in the northernmost Arabian–Nubian Shield: implications for crustal evolution. Contributions to Mineralogy and Petrology 160, 181–201.

Be'eri-Shlevin, Y., Samuel, M.D., Azer, M.K., Rämö, O.T., Whitehouse, M.J., Moussa, H.E., 2011. The Ediacaran Ferani and Rutig volcano-sedimentary successions of the northernmost Arabian-Nubian Shield (ANS): New insights from zircon U–Pb geochronology, geochemistry and O–Nd isotope ratios. Precambrian Research 188, 21–44.

Be'eri-Shlevin, Y., Eyal, M., Eyal, Y., Whitehouse, M.J., Litvinovsky, B., 2012. The Sa'al volcano-sedimentary complex (Sinai, Egypt): A latest Mesoproterozoic volcanic arc in the northern Arabian Nubian Shield. Geology 40, 403–406.

Berhe, S.M., 1990. Ophiolites in Northeast and East Africa: implications for Proterozoic crustal growth. Journal of the Geological Society 147, 41–57.

Belissont, R., Boiron, M.-C., Luais, B., Cathelineau, M., 2014. LA-ICP-MS analyses of minor and trace elements and bulk Ge isotopes in zoned Ge-rich sphalerites from the Noailhac – Saint-Salvy deposit (France): Insights into incorporation mechanisms and ore deposition processes. Geochimica et Cosmochimica Acta 126, 518–540.

Belousov, I., Large, R.R., Meffre, S., Danyushevsky, L.V., Steadman, J., Beardsmore, T., 2016. Pyrite compositions from VHMS and orogenic Au deposits in the Yilgarn Craton, Western Australia: Implications for gold and copper exploration. Ore Geology Reviews 79, 474–499.

Bennett, J.D., Mosley, P.N., 1987. Tiered-tectonics and evolution, Eastern Desert and Sinai, Egypt. Colloquium on African Geology. 14. 79–82.

Berhe, S.M., 1990. Ophiolites in Northeast and East Africa: implications for Proterozoic crustal growth. Journal of the Geological Society 147, 41–57.

Bernau, R., Darbyshire, D.P.F., Franz, G., Harms, U., Huth, A., Mansour, N., Pasteels, P., Schandelmeier, H., 1987. Petrology, geochemistry and structural development of the Bir Safsaf-Aswan uplift, Southern Egypt. Journal of African Earth Sciences (1983) 6, 79–90.

Bernet, M., Piraquive, A., Urueña, C., López-Isaza, J.A., Bermúdez, M.A., Zuluaga, C., Amaya, S., Villamizar, N., 2019. Multidisciplinary petro-geo-thermochronological approach to ore deposit exploration. Ore Geology Reviews 112, 103017.

Beyth, M., Stern, R.J., Matthews, A., 1997. Significance of high-grade metasediments from the Neoproterozoic basement of Eritrea. Precambrian Research 86, 45–58.

Bielski, M., Jäger, E., Steinitz, G., 1979. The geochronology of Iqna granite (Wadi Kid pluton), southern Sinai. Contributions to Mineralogy and Petrology 70, 159–165.

Bierlein, F.P., Gray, D.R., Foster, D.A., 2002. Metallogenic relationships to tectonic evolution – the Lachlan Orogen, Australia. Earth and Planetary Science Letters 202, 1–13.

Bierlein, F.P., McKnight, S., 2005. Possible intrusion-related gold systems in the western Lachlan Orogen, southeast Australia. Economic Geology 100, 385–398.

Bierlein, F.P., Groves, D.I., Goldfarb, R.J., Dubé, B., 2006a. Lithospheric controls on the formation of provinces hosting giant orogenic gold deposits. Mineralium Deposita 40, 874–886.

Bierlein, F.P., Murphy, F.C., Weinberg, R.F., Lees, T., 2006b. Distribution of orogenic gold deposits in relation to fault zones and gravity gradients: targeting tools applied to the Eastern Goldfields, Yilgarn Craton, Western Australia. Mineralium Deposita 41, 107–126.

Bierlein, F.P., Pisarevsky, S., 2008. Plume-related oceanic plateaus as a potential source of gold mineralization. Economic Geology 103, 425–430.

Bierlein, F.P., Groves, D.I., Cawood, P.A., 2009. Metallogeny of accretionary orogens — The connection between lithospheric processes and metal endowment. Ore Geology Reviews 36, 282–292.

Bierlein, F.P., McKeag, S., Reynolds, N., Bargmann, C.J., Bullen, W., Murphy, F.C., Al-Athbah, H., Brauhart, C., Potma, W., Meffre, S., McKnight, S., 2016. The Jebel Ohier deposit—a newly discovered porphyry copper–gold system in the Neoproterozoic Arabian–Nubian Shield, Red Sea Hills, NE Sudan. Mineralium Deposita 51, 713–724.

Bierlein, F.P., Potma, W., Cernuschi, F., Brauhart, C., Robinson, J., Bargmann, C.J., Bullen, W., Henriquez, J.F., Davies, I., Kennedy, A., 2020. New Insights into the Evolution and Age of the Neoproterozoic Jebel Ohier

Porphyry Copper Deposit, Red Sea Hills, Northeastern Sudan. Economic Geology 115, 1–31.

Bilibilin, Y.A., 1955. Metallogenic provinces and metallogenic epochs, Translation 1968. ed. Queen's College Press, Flushing, New York.

Billay, A.Y., Kisters, A.F.M., Meyer, F.M., Schneider, J., 1997. The geology of the Lega Dembi gold deposit, southern Ethiopia: implications for Pan-African gold exploration. Mineralium Deposita 32, 491–504.

Binns, R.A., Scott, S.D., 1993. Actively forming polymetallic sulfide deposits associated with felsic volcanic rocks in the eastern Manus back-arc basin, Papua New Guinea. Economic Geology 88, 2226–2236.

Bissig, T., Cooke, D.R., 2014. Introduction to the special issue devoted to alkalic porphyry Cu-Au and epithermal Au deposits. Economic Geology 109, 819–825.

Blades, M.L., Collins, A.S., Foden, J., Payne, J.L., Xu, X., Alemu, T., Woldetinsae, G., Clark, C., Taylor, R.J.M., 2015. Age and hafnium isotopic evolution of the Didesa and Kemashi Domains, western Ethiopia. Precambrian Research 270, 267–284.

Blades, M.L., Foden, J., Collins, A.S., Alemu, T., Woldetinsae, G., 2019. The origin of the ultramafic rocks of the Tulu Dimtu Belt, western Ethiopia – do they represent remnants of the Mozambique Ocean? Geological Magazine 156, 62–82.

Blasband, B., Brooijmans, P., Dirks, P., Visser, W., White, S., 1997. A Pan-African core complex in the Sinai, Egypt. Geologie En Mijnbouw 76, 247–266.

Blasband, B., White, S., Brooijmans, P., De Boorder, H., Visser, W., 2000. Late Proterozoic extensional collapse in the Arabian-Nubian Shield. Journal of the Geological Society 157, 615–628.

Blenkinsop, T.G., Doyle, M.G., 2014. Structural controls on gold mineralization on the margin of the Yilgarn craton, Albany–Fraser orogen: The Tropicana deposit, Western Australia. Journal of Structural Geology 67, 189–204.

Blenkinsop, T.G., Tripp, G., Vearncombe, J.R., 2014. Preface and Introduction – Structural Geology and Resources. Journal of Structural Geology 67, 187–188.

Blenkinsop, T.G., Oliver, N.H.S., Dirks, P.G.H.M., Nugus, M., Tripp, G., Sanislav, I.V., 2020a. Structural Geology Applied to the Evaluation of Hydrothermal Gold Deposits. Reviews in Economic Geology 21, 1–23.

Blenkinsop, T.G., Rowland, J.V., Baker, T., 2020b. Mechanical Regimes of Hydrothermal Gold Mineralization. Reviews in Economic Geology 21, 205–214.

Blewett, R.S., Czarnota, K., Henson, P.A., 2010. Structural-event framework for the eastern Yilgarn Craton, Western Australia, and its implications for orogenic gold. Precambrian Research 183, 203–229.

Blichert-Toft, J., Puchtel, I.S., 2010. Depleted mantle sources through time: evidence from Lu–Hf and Sm–Nd isotope systematics of Archean komatiites. Earth and Planetary Science Letters 297, 598–606.

Block, S., Ganne, J., Baratoux, L., Zeh, A., Parra-Avila, L.A., Jessell, M., Ailleres, L., Siebenaller, L., 2015. Petrological and geochronological constraints on lower crust exhumation during Paleoproterozoic (Eburnean) orogeny, NW Ghana, West African Craton. Journal of Metamorphic Geology 33, 463–494.

Block, S., Jessell, M., Aillères, L., Baratoux, L., Bruguier, O., Zeh, A., Bosch, D., Caby, R., Mensah, E., 2016. Lower crust exhumation during Paleoproterozoic (Eburnean) orogeny, NW Ghana, West African Craton: Interplay of coeval contractional deformation and extensional gravitational collapse. Precambrian Research 274, 82–109.

Bohannon, R.G., Naeser, C.W., Schmidt, D.L., Zimmermann, R.A., 1989. The timing of uplift, volcanism, and rifting peripheral to the Red Sea: a case for passive rifting? Journal of Geophysical Research: Solid Earth 94, 1683–1701.

Boiron, M.-C., Cathelineau, M., Trescases, J.-J., 1989. Conditions of gold-bearing arsenopyrite crystallization in the Villeranges Basin, Marche-Combrailles shear zone, France; a mineralogical and fluid inclusion study. Economic Geology 84, 1340–1362.

Bojar, A.-V., Fritz, H., Kargl, S., Unzog, W., 2002. Phanerozoic tectonothermal history of the Arabian–Nubian shield in the Eastern Desert of Egypt: evidence from fission track and paleostress data. Journal of African Earth Sciences 34, 191–202.

Boniface, N., 2019. An overview of the Ediacaran-Cambrian orogenic events at the southern margins of the Tanzania Craton: Implication for the final assembly of Gondwana. Journal of African Earth Sciences 150, 123–130.

Bonin, B., Janoušek, V., Moyen, J.-F., 2019. Chemical variation, modal composition and classification of granitoids. Geological Society, London, Special Publications SP491-2019–138.

Bonnet, J., Mosser-Ruck, R., Caumon, M.-C., Rouer, O., Andre-Mayer, A.-S., Cauzid, J., Peiffert, C., 2016. Trace Element Distribution (Cu, Ga, Ge, Cd, and Fe) in Sphalerite From the Tennessee MVT Deposits, USA, By Combined EMPA, LA-ICP-MS, Raman Spectroscopy, and Crystallography. The Canadian Mineralogist 54, 1261–1284.

Bons, P.D., Elburg, M.A., Gomez-Rivas, E., 2012. A review of the formation of tectonic veins and their microstructures. Journal of Structural Geology 43, 33–62.

Bortnikov, N.S., Cabri, L., Vikent ev, I.V., McMahon, G., Bogdanov, Y.A., 2000. Invisible gold in sulfides from recent submarine hydrothermal mounds. DOKLADY EARTH SCIENCES C/C OF DOKLADY-AKADEMIIA NAUK. INTERPERIODICA PUBLISHING, 863–866.

Bosc, R., Tamlyn, N., Kachrillo, J.J., 2012. The Hassai mine project - VMS resources update. Red Sea State, Sudan. Technical report. La Mancha Resources Inc.

Bosch, D., Garrido, C.J., Bruguier, O., Dhuime, B., Bodinier, J.-L., Padròn-Navarta, J.A., Galland, B., 2011. Building an island-arc crustal section: Time constraints from a LA-ICP-MS zircon study. Earth and Planetary Science Letters 309, 268–279.

Boskabadi, A., Pitcairn, I.K., Broman, C., Boyce, A., Teagle, D.A.H., Cooper, M.J., Azer, M.K., Stern, R.J., Mohamed, F.H., Majka, J., 2017. Carbonate alteration of ophiolitic rocks in the Arabian–Nubian Shield of Egypt: sources and compositions of the carbonating fluid and implications for the formation of Au deposits. International Geology Review 59, 391–419.

Botros, N.S., 2002. Metallogeny of gold in relation to the evolution of the Nubian Shield in Egypt. Ore Geology Reviews 19, 137–164.

Botros, N.S., 2003. On the relationship between auriferous talc deposits hosted in volcanic rocks and massive sulphide deposits in Egypt. Ore Geology Reviews 23, 223–257.

Botros, N.S., 2004. A new classifiaction of the gold deposits of Egypt. Ore Geology Reviews 25, 1–37.

Bouilhol, P., Schaltegger, U., Chiaradia, M., Ovtcharova, M., Stracke, A., Burg, J.-P., Dawood, H., 2011. Timing of juvenile arc crust formation and evolution in the Sapat Complex (Kohistan–Pakistan). Chemical Geology 280, 243–256.

Bouilhol, P., Jagoutz, O., Hanchar, J.M., Dudas, F.O., 2013. Dating the India–Eurasia collision through arc magmatic records. Earth and Planetary Science Letters 366, 163–175.

Bouilhol, P., Schmidt, M.W., Burg, J.-P., 2015. Magma Transfer and Evolution in Channels within the Arc Crust: the Pyroxenitic Feeder Pipes of Sapat (Kohistan, Pakistan). Journal of Petrology 56, 1309–1342.

Boullier, A.-M., Robert, F., 1992. Palaeoseismic events recorded in Archaean gold-quartz vein networks, Val d'Or, Abitibi, Quebec, Canada. Journal of Structural Geology 14, 161–179.

Bourdelle, F., Parra, T., Chopin, C., Beyssac, O., 2013. A new chlorite geothermometer for diagenetic to low-grade metamorphic conditions. Contributions to Mineralogy and Petrology 165, 723–735.

Bouvier, A., Vervoort, J.D., Patchett, P.J., 2008. The Lu–Hf and Sm–Nd isotopic composition of CHUR: constraints from unequilibrated chondrites and implications for the bulk composition of terrestrial planets. Earth and Planetary Science Letters 273, 48–57.

Bowen, J., 2016. Base Metal Associations in Orogenic Gold Deposits, Block 14, Northern Sudan. MSc thesis. University of Leicester.

Boyden, J.A., Müller, R.D., Gurnis, M., Torsvik, T.H., Clark, J.A., Turner, M., Ivey-Law, H., Watson, R.J., Cannon, J.S., 2011. Next-generation plate-tectonic reconstructions using GPlates.

Boyle, A.P., Nelson, E., Hitzman, M., Churchill, J., Lopez-Pedrosa, M., Freitag, K., 2004. The use of electron backscatter diffraction and orientation contrast imaging as tools for sulphide textural studies: example from the Greens Creek deposit (Alaska). Mineralium Deposita 39, 103–113.

Bregar, M., Bauernhofer, A., Pelz, K., Kloetzli, U., Fritz, H., Neumayr, P., 2002. A late Neoproterozoic magmatic core complex in the Eastern Desert of Egypt: emplacement of granitoids in a wrench-tectonic setting. Precambrian Research 118, 59–82.

Breitkreuz, C., Eliwa, H., Khalaf, I., Gameel, K.E., Bühler, B., Sergeev, S., Larionov, A., Murata, M., 2010. Neoproterozoic SHRIMP U–Pb zircon ages of silica-rich Dokhan Volcanics in the North Eastern Desert, Egypt. Precambrian Research 182, 163–174.

BRGM, 2018. Point de vue français sur la criticité des métaux | BRGM [WWW Document], BRGM. URL https://www.brgm.fr/projet/point-vue-francais-sur-criticite-metaux (accessed 4.1.20).

Brito Neves, B.B. de, Campos Neto, M. da C., Fuck, R.A., 1999. From Rodinia to Western Gondwana: an approach to the Brasiliano-Pan African Cycle and orogenic collage. Episodes-Newsmagazine of the International Union of Geological Sciences 22, 155–166.

Brown, D., Ryan, P.D., Afonso, J.C., Boutelier, D., Burg, J.P., Byrne, T., Calvert, A., Cook, F., DeBari, S., Dewey, J.F., Gerya, T.V., Harris, R., Herrington, R., Konstantinovskaya, E., Reston, T., Zagorevski, A., 2011. Arc–Continent Collision: The Making of an Orogen. Arc-Continent Collision, Frontiers in Earth Sciences. Springer Berlin Heidelberg, Berlin, Heidelberg, 477–493.

Brown, M., Johnson, T., Gardiner, N.J., 2020. Plate Tectonics and the Archean Earth. Annual Review of Earth and Planetary Sciences 48, 291–320.

Brügmann, G.E., Arndt, N.T., Hofmann, A.W., Tobschall, H.J., 1987. Noble metal abundances in komatiite suites from Alexo, Ontario and Gorgona Island, Colombia. Geochimica et Cosmochimica Acta 51, 2159–2169.

Bühler, B., Breitkreuz, C., Pfänder, J.A., Hofmann, M., Becker, S., Linnemann, U., Eliwa, H.A., 2014. New insights into the accretion of the Arabian-Nubian Shield: Depositional setting, composition and geochronology of a Mid-Cryogenian arc succession (North Eastern Desert, Egypt). Precambrian Research 243, 149–167.

Burg, J.-P., Bouilhol, P., 2019. Timeline of the South Tibet – Himalayan belt: the geochronological record of subduction, collision, and underthrusting from zircon and monazite U–Pb ages. Canadian Journal of Earth Sciences 56, 1318–1332.

Burke, K., Sengör, C., 1986. Tectonic escape in the evolution of the continental crust. In: Barazangi, M., Brown, L. (Eds.), Geodynamics Series. American Geophysical Union, Washington, D. C., 41–53.

Butler, I.B., Nesbitt, R.W., 1999. Trace element distributions in the chalcopyrite wall of a black smoker chimney: insights from laser ablation inductively coupled plasma mass spectrometry (LA–ICP–MS). Earth and Planetary Science Letters 167, 335–345.

C

Cagnard, F., 2005. Compression des lithosphères continentales" chaudes". Application à la tectonique précambrienne.

Calderón, M., Galaz, G., Tascón, G., Ramírez, C., Luca, R., Massonne, H.J., Brandelik, A., Hervé, F., 2005. Metamorphic PT constraints for non-coaxial ductile flow of Jurassic pyroclastic deposits: key evidence for the closure of the Rocas Verdes basin in southern Chile. International Symposium on Andean Geodynamics. 138–141.

Calvert, A.J., 2011. The Seismic Structure of Island Arc Crust. Arc-Continent Collision, Frontiers in Earth Sciences. Springer Berlin Heidelberg, Berlin, Heidelberg, 87–119.

Camprubí, A., Albinson, T., 2007. Epithermal deposits in México—Update of current knowledge, and an empirical reclassification. Geology of Mexico: Celebrating the Centenary of the Geological Society of Mexico 422, 377.

Carignan, J., Hild, P., Mevelle, G., Morel, J., Yeghicheyan, D., 2001. Routine analyses of trace elements in geological samples using flow injection and low pressure on-line liquid chromatography coupled to ICP-MS: A study of geochemical reference materials BR, DR-N, UB-N, AN-G and GH. Geostandards Newsletter 25, 187–198.

Carr, M.J., Feigenson, M.D., Bennett, E.A., 1990. Incompatible element and isotopic evidence for tectonic control of source mixing and melt extraction along the Central American arc. Contributions to Mineralogy and Petrology 105, 369–380.

Carreras, J., Druguet, E., 2019. Complex fold patterns developed by progressive deformation. Journal of Structural Geology 125, 195–201.

Castroviejo, R., Quesada, C., Soler, M., 2011. Post-depositional tectonic modification of VMS deposits in Iberia and its economic significance. Mineralium Deposita 46, 615–637.

Cathelineau, M., Nieva, D., 1985. A chlorite solid solution geothermometer the Los Azufres (Mexico) geothermal system. Contributions to Mineralogy and Petrology 91, 235–244.

Cathelineau, M., 1988. Cation site occupancy in chlorites and illites as a function of temperature. Clay Minerals 23, 471–485.

Cathelineau, M., Boiron, M.C., Holliger, P., Marion, P., Denis, M., 1989. Gold in arsenopyrites: crystal chemistry, location and state, physical and chemical conditions of deposition. Economic Geology Monograph 6, 328–341.

Cawood, P.A., Fryer, B.J., 1994. Noble metal abundances in backarc basin basalts (Lau Basin, southwest Pacific). Proceedings of the Ocean Drilling Program. Scientific Results. 595–602.

Cawood, P.A., Kröner, A., Collins, W.J., Kusky, T.M., Mooney, W.D., Windley, B.F., 2009. Accretionary orogens through Earth history. Geological Society, London, Special Publications 318, 1–36.

Cawood, P.A., Hawkesworth, C.J., Dhuime, B., 2013. The continental record and the generation of continental crust. Geological Society of America Bulletin 125, 14–32.

Cawood, P.A., Hawkesworth, C.J., 2015. Temporal relations between mineral deposits and global tectonic cycles. Geological Society, London, Special Publications 393, 9–21.

Champion, D.C., Huston, D.L., 2016. Radiogenic isotopes, ore deposits and metallogenic terranes: Novel approaches based on regional isotopic maps and the mineral systems concept. Ore Geology Reviews 76, 229–256.

Chappell, B.W., Wyborn, D., 2004. Cumulate and cumulative granites and associated rocks. Resource Geology 54, 227–240.

Chauvet, A., 2019a. Editorial for Special Issue "Structural Control of Mineral Deposits: Theory and Reality." Minerals 9, 171.

Chauvet, A., 2019b. Structural Control of Ore Deposits: The Role of Pre-Existing Structures on the Formation of Mineralised Vein Systems. Minerals 9, 56.

Chen, K., Tang, M., Lee, C.-T.A., Wang, Z., Zou, Z., Hu, Z., Liu, Y., 2020. Sulfide-bearing cumulates in deep continental arcs: The missing copper reservoir. Earth and Planetary Science Letters 531, 115971.

Chetty, T., 2017. Orogens. Proterozoic Orogens of India. Elsevier, 1–34.

Chevrillon-Guibert, R., Gagnol, L., Magrin, G., 2019. Les ruées vers l'or au Sahara et au nord du Sahel. Ferment de crise ou stabilisateur ? Hérodote N° 172, 193.

Chew, D.M., Petrus, J.A., Kamber, B.S., 2014. U–Pb LA–ICPMS dating using accessory mineral standards with variable common Pb. Chemical Geology 363, 185–199.

Chouinard, A., Paquette, J., Williams-Jones, A.E., 2005. Crystallographic controls on trace-element incorporation in auriferous pyrite from the Pascua epithermal high-sulfidation deposit, Chile Argentina. The Canadian Mineralogist 43, 951–963.

Cnudde, V., Boone, M.N., 2013. High-resolution X-ray computed tomography in geosciences: A review of the current technology and applications. Earth-Science Reviews 123, 1–17.

Cobbold, P.R., Quinquis, H., 1980. Development of sheath folds in shear regimes. Journal of Structural Geology 2, 119–126.

Cochrane, R., Spikings, R.A., Chew, D., Wotzlaw, J.-F., Chiaradia, M., Tyrrell, S., Schaltegger, U., Van der Lelij, R., 2014. High temperature (> 350 C) thermochronology and mechanisms of Pb loss in apatite. Geochimica et Cosmochimica Acta 127, 39–56.

Collins, A.S., Windley, B.F., 2002. The tectonic evolution of central and northern Madagascar and its place in the final assembly of Gondwana. The Journal of Geology 110, 325–339.

Collins, A.S., Pisarevsky, S.A., 2005. Amalgamating eastern Gondwana: the evolution of the Circum-Indian Orogens. Earth-Science Reviews 71, 229–270.

Combes, V., Eglinger, A., André-Mayer, A.-S., Teitler, Y., Heuret, A., Gibert, P., Béziat, D., in press. Polyphase gold mineralisation at the Yaou deposit, French Guiana. In: Torvela, T., Chapman, R.J., Lambert-Smith, J. (Eds.), Geological Society, London, Special Publications.

Condie, K.C., 1998. Episodic continental growth and supercontinents: a mantle avalanche connection? Earth and Planetary Science Letters 163, 97–108.

Condie, K.C., 2000. Episodic continental growth models: afterthoughts and extensions. Tectonophysics 322, 153–162.

Condie, K.C., 2007. Accretionary orogens in space and time. Geological Society of America Memoirs. Geological Society of America, 145–158.

Condie, K.C., Belousova, E., Griffin, W.L., Sircombe, K.N., 2009. Granitoid events in space and time: Constraints from igneous and detrital zircon age spectra. Gondwana Research 15, 228–242.

Condie, K.C., 2015. Earth as an evolving planetary system. Academic Press.

Cook, N.J., Chryssoulis, S.L., 1990. Concentrations of invisible gold in the common sulfides. The Canadian Mineralogist 28, 1–16.

Cook, N.J., 1996. Mineralogy of the sulphide deposits at Sulitjelma, northern Norway. Ore Geology Reviews 11, 303–338.

Cook, N.J., Ciobanu, C.L., Meria, D., Silcock, D., Wade, B., 2013. Arsenopyrite-pyrite association in an orogenic gold ore: Tracing mineralization history from textures and trace elements. Economic Geology 108, 1273–1283.

Cook, N.J., Ciobanu, C., George, L., Zhu, Z.-Y., Wade, B., Ehrig, K., 2016. Trace Element Analysis of Minerals in Magmatic-Hydrothermal Ores by Laser Ablation Inductively-Coupled Plasma Mass Spectrometry: Approaches and Opportunities. Minerals 6, 111.

Cosca, M., Arculus, R., Pearce, J., Mitchell, J., 1998. 40Ar/39Ar and K-Ar geochronological age constraints for the inception and early evolution of the Izu-Bonin - Mariana arc system. The Island Arc 7, 579–595.

Cottard, F., Braux, C., Cortial, P., Deschamps, Y., El Samani, Y., Hotitn, A.M., Omar Younis, M., 1986. Les amas sulfurés polymétalliques et les minéralisations aurifères du district dAriab (Red Sea Hills, Sudan). Historique de la découverte, cadre géologique et principaux caractères des gisements. Chron. Rech. Min 19–40.

Coulibaly, Y., Boiron, M. C., Cathelineau, M., and Kouamelan, A. N., 2008, Fluid immiscibility and gold deposition in the Birimian quartz veins of the Angovia deposit (Yaouré, Ivory Coast): Journal of African Earth Sciences, v. 50, p. 234–254.

Couzinié, S., Ménot, R.-P., Doumnang, J.-C., Paquette, J.-L., Rochette, P., Quesnel, Y., Deschamps, P., Ménot, G., 2020. Crystalline inliers near Lake Iro (SE Chad): Post-collisional Ediacaran A2-type granitic magmatism at the southern margin of the Saharan Metacraton. Journal of African Earth Sciences 172, 103960.

Cowan, E.J., 2020. Deposit-scale structural architecture of the Sigma-Lamaque gold deposit, Canada—insights from a newly proposed 3D method for assessing structural controls from drill hole data. Mineralium Deposita 55, 217–240.

Cox, G.M., Lewis, C.J., Collins, A.S., Halverson, G.P., Jourdan, F., Foden, J., Nettle, D., Kattan, F., 2012. Ediacaran terrane accretion within the Arabian–Nubian Shield. Gondwana Research 21, 341–352.

Cox, S.F., 1999. Deformational controls on the dynamics of fluid flow in mesothermal gold systems. Geological Society, London Special Publications 155, 123–140.

Cox, S.F., Knackstedt, M.A., Braun, J., 2001. Principles of structural control on permeability and fluid flow in hydrothermal systems. Society of Economic Geologists Reviews 14, 1–24.

Cox, S.F., Ruming, K., 2004. The St Ives mesothermal gold system, Western Australia—a case of golden aftershocks? Journal of Structural Geology 26, 1109–1125.

Cox, S.F., 2016. Injection-Driven Swarm Seismicity and Permeability Enhancement: Implications for the Dynamics of Hydrothermal Ore Systems in High Fluid-Flux, Overpressured Faulting Regimes—An Invited Paper. Economic Geology 111, 559–587.

Crocket, J.H., 1993. Distribution of gold in the Earth's crust. In: Foster, R.P. (Ed.), Gold Metallogeny and Exploration. Springer Netherlands, Dordrecht, 1–36.

Cugerone, A., Cenki-Tok, B., Oliot, E., Muñoz, M., Barou, F., Motto-Ros, V., Le Goff, E., 2020. Redistribution of germanium during dynamic recrystallization of sphalerite. Geology 48, 236–241.

D

Daigneault, R., Mueller, W.U., Chown, E.H., 2002. Oblique Archean subduction: accretion and exhumation of an oceanic arc during dextral transpression, Southern Volcanic Zone, Abitibi Subprovince Canada. Precambrian Research 115, 261–290.

Dakota Conn, C., Spry, P.G., Layton-Matthews, D., Voinot, A., Koenig, A., 2019. The effects of amphibolite facies metamorphism on the trace element composition of pyrite and pyrrhotite in the Cambrian Nairne Pyrite Member, Kanmantoo Group, South Australia. Ore Geology Reviews 114, 103128.

da Silva Schmitt, R., Trouw, R.A., Van Schmus, W.R., Pimentel, M.M., 2004. Late amalgamation in the central part of West Gondwana: new geochronological data and the characterization of a Cambrian collisional orogeny in the Ribeira Belt (SE Brazil). Precambrian Research 133, 29–61.

Dawoud, A.S., 1980. Structural and metamorphic evolution of the area southwest of Abu Hamed, Nile Province, Sudan. Unpublished Ph. D Thesis, University of Khartoum.

DeBari, S.M., Greene, A.R., 2011. Vertical Stratification of Composition, Density, and Inferred Magmatic Processes in Exposed Arc Crustal Sections. Arc-Continent Collision, Frontiers in Earth Sciences. Springer Berlin Heidelberg, Berlin, Heidelberg, 121–144.

De Silva, S.L., Riggs, N.R., Barth, A.P., 2015. Quickening the pulse: fractal tempos in continental arc magmatism. Elements 11, 113–118.

de Wall, H., Greiling, R.O., Fouad Sadek, M., 2001. Post-collisional shortening in the late Pan-African Hamisana high strain zone, SE Egypt: field and magnetic fabric evidence. Precambrian Research 107, 179–194.

Deditius, A.P., Utsunomiya, S., Ewing, R.C., Chryssoulis, S.L., Venter, D., Kesler, S.E., 2009. Decoupled geochemical behavior of As and Cu in hydrothermal systems. Geology 37, 707–710.

Deditius, A.P., Reich, M., Kesler, S.E., Utsunomiya, S., Chryssoulis, S.L., Walshe, J., Ewing, R.C., 2014. The coupled geochemistry of Au and As in pyrite from hydrothermal ore deposits. Geochimica et Cosmochimica Acta 140, 644–670.

Deksissa, D.J., Koeberl, C., 2004. Geochemistry, alteration, and genesis of gold mineralization in the Okote area, southern Ethiopia. GEOCHEMICAL JOURNAL 38, 307–331.

Denkler, T., Franz, G., Schandelmeier, H., Darbyshire, D.P.F., Harms, U., Pilot, J., 1993. Evolution of the south-western part of the Atmur-Delgo suture. Geoscientific Research in Northeast Africa. Balkema, Rotterdam Brookfield 87–89.

Denkler, T., Franz, G., Schandelmeier, H., 1994. Tectonometamorphic evolution of the Neoproterozoic Delgo suture zone, northern Sudan. Geologische Rundschau 83, 578–590.

Dewey, J.F., 1969. Evolution of the Appalachian/Caledonian orogen. Nature 222, 124–129.

Dhawan, N., Safarzadeh, M.S., Miller, J.D., Moats, M.S., Rajamani, R.K., Lin, C.-L., 2012. Recent advances in the

application of X-ray computed tomography in the analysis of heap leaching systems. Minerals Engineering 35, 75–86.

Dilek, Y., Ahmed, Z., 2003, Proterozoic ophiolites of the Arabian Shield and their significance in Precambrian tectonics: Geological Society, London, Special Publications, v. 218, p. 685–700.

Dimalanta, C., Taira, A., Yumul Jr, G.P., Tokuyama, H., Mochizuki, K., 2002. New rates of western Pacific island arc magmatism from seismic and gravity data. Earth and Planetary Science Letters 202, 105–115.

DiPietro, J.A., 2012. Landscape evolution in the United States: an introduction to the geography, geology, and natural history. Newnes.

Doebrich, J.L., Zahony, S.G., Leavitt, J.D., Portacio, J.S., Siddiqui, A.A., Wooden, J.L., Fleck, R.J., Stein, H.J., 2004. Ad Duwayhi, Saudi Arabia: Geology and Geochronology of a Neoproterozoic Intrusion-Related Gold System in the Arabian Shield. Economic Geology 99, 713–741.

Doebrich, J.L., Al-Jehani, A.M., Siddiqui, A.A., Hayes, T.S., Wooden, J.L., Johnson, P.R., 2007. Geology and metallogeny of the Ar Rayn terrane, eastern Arabian shield: Evolution of a Neoproterozoic continental-margin arc during assembly of Gondwana within the East African orogen. Precambrian Research 158, 17–50.

Domeier, M., Torsvik, T.H., 2014. Plate tectonics in the late Paleozoic. Geoscience Frontiers 5, 303–350.

Dong, G., Morrison, G., Jaireth, S., 1995. Quartz textures in epithermal veins, Queensland; classification, origin and implication. Economic Geology 90, 1841–1856.

Dubacq, B., Vidal, O., De Andrade, V., 2010. Dehydration of dioctahedral aluminous phyllosilicates: thermodynamic modelling and implications for thermobarometric estimates. Contributions to Mineralogy and Petrology 159, 159–174.

Dubé, B., Gosselin, P., 2007. Greenstone-hosted quartz-carbonate vein deposits. Mineral Deposits of Canada - A Synthesis of Major Deposit-Types, District Metallogeny, the Evolution of Geological Provinces, and Exploration Methods, Special Publications. Goodfellow W.D., 49–73.

Dubé, B., Gosselin, P., Mercier-Langevin, P., Hannington, M.D., Galley, A., 2007. Gold-rich volcanogenic massive sulphide deposits. Mineral Deposits of Canada: A Synthesis of Major Deposit-Types, District Metallogeny, the Evolution of Geological Provinces, and Exploration Methods, Special Publication. Goodfellow W.D., 75–94.

Dubé, B., Mercier-Langevin, P., 2015. Targeted Geoscience Initiative 4: Contributions to the understanding of Precambrian lode gold deposits and implications for exploration. No. 7852.

Dubosq, R., Lawley, C.J.M., Rogowitz, A., Schneider, D.A., Jackson, S., 2018. Pyrite deformation and connections to gold mobility: Insight from micro-structural analysis and trace element mapping. Lithos 310–311, 86–104.

Duckworth, G., 2018. Feasibility study - NI 43-101 Technical report - Block 14 gold project. Lycopodium Minerals Pty Ltd.

Duuring, P., Cassidy, K.F., Hagemann, S.G., 2007. Granitoid-associated orogenic, intrusion-related, and porphyry style metal deposits in the Archean Yilgarn Craton, Western Australia. Ore Geology Reviews 32, 157–186.

Duyverman, H.J., Harris, N.B.W., Hawkesworth, C.J., 1982. Crustal accretion in the Pan African: Nd and Sr isotope evidence from the Arabian Shield. Earth and Planetary Science Letters 59, 315–326.

E

Egan, C.K., Jacques, S.D.M., Wilson, M.D., Veale, M.C., Seller, P., Beale, A.M., Pattrick, R.A.D., Withers, P.J., Cernik, R.J., 2015. 3D chemical imaging in the laboratory by hyperspectral X-ray computed tomography. Scientific Reports 5(9), 1–9.

Eglinger, A., 2013. Cycle de l'uranium et évolution tectono-métamorphique de la ceinture orogénique Pan-Africaine du Lufilien (Zambie). Université de Lorraine.

Eglinger, A., Vanderhaeghe, O., André-Mayer, A.-S., Goncalves, P., Zeh, A., Durand, C., Deloule, E., 2016. Tectono-metamorphic evolution of the internal zone of the Pan-African Lufilian orogenic belt (Zambia): Implications for crustal reworking and syn-orogenic uranium mineralizations. Lithos 240, 167–188.

Eglinger, A., Thébaud, N., Zeh, A., Davis, J., Miller, J., Parra-Avila, L.A., Loucks, R., McCuaig, C., Belousova, E., 2017. New insights into the crustal growth of the Paleoproterozoic margin of the Archean Kéména-Man domain, West African craton (Guinea): Implications for gold mineral system. Precambrian Research 292, 258–289.

Eglinger, A., André-Mayer, A.-S., Combes, V., Teitler, Y., Heuret, A., 2020. Les gisements d'or de la Guyane française. Géologues 206, 36–40.

Egyptian Geological Survey and Mining Authority, 1981. Geologic Map of Egypt, scale 1:2000000, Ministry of Industry and Mineral Resources - Egyptian Geological Survey and Mining Authority.

El Aref, M., Abd El-Rahman, Y., Zoheir, B., Surour, A., Helmy, H.M., Abdelnasser, A., Ahmed, A.H., El-Ahmadi Ibrahim, M., 2020. Mineral Resources in Egypt (I): Metallic Ores. In: Hamimi, Z., El-Barkooky, A., Martínez Frías, J., Fritz, H., Abd El-Rahman, Y. (Eds.), The Geology of Egypt. Springer International Publishing, Cham, 521–587.

El Kazzaz, Y.A., 2012. Shear zones-related gold-bearing quartz veins in Shinai area, South eastern desert, Egypt. Egyptian Journal of Geology 56, 67–89.

Elisha, B., Katzir, Y., Kylander-Clark, A., 2017. Ediacaran (~620 Ma) high-grade regional metamorphism in the northern Arabian Nubian Shield: U-Th-Pb monazite ages of the Elat schist. Precambrian Research 295, 172–186.

Elisha, B., Katzir, Y., Kylander-Clark, A.R.C., Golan, T., Coble, M.A., 2019. The timing of migmatization in the northern Arabian–Nubian Shield: Evidence for a juvenile sedimentary component in collision-related batholiths. Journal of Metamorphic Geology 37, 591–610.

Eliwa, H.A., Abu El-Enen, M.M., Khalaf, I.M., Itaya, T., Murata, M., 2008. Metamorphic evolution of Neoproterozoic metapelites and gneisses in the Sinai, Egypt: Insights from petrology, mineral chemistry and

K–Ar age dating. Journal of African Earth Sciences 51, 107–122.

Eliwa, H.A., El-Bialy, M.Z., Murata, M., 2014. Edicaran post-collisional volcanism in the Arabian-Nubian Shield: The high-K calc-alkaline Dokhan Volcanics of Gabal Samr El-Qaa (592 ± 5 Ma), North Eastern Desert, Egypt. Precambrian Research 246, 180–207.

El Kazzaz, Y.A., 2012. Shear zones-related gold-bearing quartz veins in Shinai area, South eastern desert, Egypt. Egyptian Journal of Geology 56, 67–89.

El-Naby, H.A., Frisch, W., 2006. Geochemical constraints from the Hafafit Metamorphic Complex (HMC): evidence of Neoproterozoic back-arc basin development in the central Eastern Desert of Egypt. Journal of African Earth Sciences 45, 173–186.

Elsamani, Y., Almuslem, A.A., Tokhi, M.E., 2001. Geology and Geotectonic Classification of Pan-African Gold Mineralizations in the Red Sea Hills, Sudan. International Geology Review 43, 1117–1128.

El-Shafei, S.A., Abdel-Maksoud, K.M., Helmy, H.M., Ahmed, A.H., 2020. Geology, mineralogy and genesis of the world-class Mahd Adh Dhahab epithermal Au-(Ag)-telluride deposit, Kingdom of Saudi Arabia. Journal of Asian Earth Sciences 201, 104510.

El-Sayed, M.M., Obeid, M.A., Furnes, H., Moghazi, A.M., 2004. Late Neoproterozoic volcanism in the southern Eastern Desert, Egypt: petrological, structural and geochemical constraints on the tectonic-magmatic evolution of the Allaqi Dokhan volcanic suite. Neues Jahrbuch Für Mineralogie - Abhandlungen 180, 261–286.

Etheridge, M.A., Wall, V.J., Cox, S.F., Vernon, R.H., 1984. High fluid pressures during regional metamorphism and deformation: implications for mass transport and deformation mechanisms. Journal of Geophysical Research: Solid Earth 89, 4344–4358.

Evans, K.A., Phillips, G.N., Powell, R., 2006. Rock-Buffering of Auriferous Fluids in Altered Rocks Associated with the Golden Mile-Style Mineralization, Kalgoorlie Gold Field, Western Australia. Economic Geology 101, 805–817.

Evuk, D., 2013. Geodynamic evolution of the central-eastern Bayuda Desert Basement, Sudan. PhD Thesis. Berlin, Germany.

Evuk, D., Franz, G., Frei, D., Lucassen, F., 2014. The Neoproterozoic evolution of the central-eastern Bayuda Desert (Sudan). Precambrian Research 240, 108–125.

Evuk, D., Lucassen, F., Franz, G., 2017. Lead isotope evolution across the Neoproterozoic boundary between craton and juvenile crust, Bayuda Desert, Sudan. Journal of African Earth Sciences 135, 72–81.

Eyal, M., Be'eri-Shlevin, Y., Eyal, Y., Whitehouse, M.J., Litvinovsky, B., 2014. Three successive Proterozoic island arcs in the Northern Arabian–Nubian Shield: Evidence from SIMS U–Pb dating of zircon. Gondwana Research 25, 338–357.

Eyal, Y., Eyal, M., Litvinovsky, B., Jahn, B., Calvo, R., Golan, T., 2018. The evolution of the Neoproterozoic Elat Metamorphic Complex, northernmost Arabian-Nubian Shield: Island arc to syncollisional stage and post-collisional magmatism. Precambrian Research.

F

Faleiros, F.M., da Cruz Campanha, G.A., da Silveira Bello, R.M., Fuzikawa, K., 2007. Fault–valve action and vein development during strike–slip faulting: An example from the Ribeira Shear Zone, Southeastern Brazil. Tectonophysics 438, 1–32.

Farahat, E.S., Mohamed, H.A., Ahmed, A.F., El Mahallawi, M.M., 2007. Origin of I-and A-type granitoids from the Eastern Desert of Egypt: implications for crustal growth in the northern Arabian–Nubian Shield. Journal of African Earth Sciences 49, 43–58.

Farahat, E.S., Zaki, R., Hauzenberger, C., Sami, M., 2011. Neoproterozoic calc-alkaline peraluminous granitoids of the Deleihimmi pluton, Central Eastern Desert, Egypt: implications for transition from late- to post-collisional tectonomagmatic evolution in the northern Arabian-Nubian Shield. Geological Journal 46, 544–560.

Fawzy, K.M., 2017. Ore Mineralogical and Geochemical Studies on El-Daghbag-I Gold Deposit, Central Eastern Desert, Egypt. Open Journal of Geology 07, 395–419.

Feneyrol, J., 2012. Pétrologie, géochimie et genèse des gisements de tsavorite associés aux gneiss et roches calco-silicatées graphiteux de Lemshuku et Namalulu, Tanzanie. Université de Lorraine.

Feng, H., Shen, P., Zhu, R., Ma, G., Li, C., Li, J., 2020. SIMS U-Pb dating of vein-hosted hydrothermal rutile and carbon isotope of fluids in the Wulong lode gold deposit, NE China: Linking gold mineralization with craton destruction. Ore Geology Reviews 127, 103838.

Feybesse, J.-L., Billa, M., Guerrot, C., Duguey, E., Lescuyer, J.-L., Milesi, J.-P., Bouchot, V., 2006. The paleoproterozoic Ghanaian province: Geodynamic model and ore controls, including regional stress modeling. Precambrian Research 149, 149–196.

Finch, E.G., Tomkins, A.G., 2017. Pyrite-Pyrrhotite Stability in a Metamorphic Aureole: Implications for Orogenic Gold Genesis. Economic Geology 112, 661–674.

Finger, F., Dörr, W., Gerdes, A., Gharib, M., Dawoud, M., 2008. U-Pb zircon ages and geochemical data for the Monumental Granite and other granitoid rocks from Aswan, Egypt: implications for the geological evolution of the western margin of the Arabian Nubian Shield. Mineralogy and Petrology 93, 153–183.

Fisher, R.V., Schmincke, H.-U., 2012. Pyroclastic rocks. Springer Science & Business Media.

Fleck, R.J., Greenwood, W.R., Hadley, D.G., Anderson, R.E., Schmidt, D.L., 1978. Age and evolution of the southern part of the Arabian Shield. Precambrian Research 6, A21–A22.

Fleck, R.J., Hadley, D.G., 1985. Ages and strontium initial ratios of plutonic rocks in a transect of the Arabian Shield. Ministry of Petroleum and Mineral Resources.

Flowerdew, M.J., Whitehouse, M.J., Stoeser, D.B., 2013. The Nabitah fault zone, Saudi Arabia: a Pan-African suture separating juvenile oceanic arcs. Precambrian Research 239, 95–105.

Fontaine, A., Eglinger, A., Ada, K., André-Mayer, A.-S., Reisberg, L., Siebenaller, L., Le Mignot, E., Ganne, J., Poujol, M., 2017. Geology of the world-class Kiaka

polyphase gold deposit, West African Craton, Burkina Faso. Journal of African Earth Sciences 126, 96–122.

Fontaine, A., Dubé, B., Malo, M., Turcotte, J., Doucet, D., 2018. Geology of the Cheechoo gold property, Eeyou Istchee Baie-James, Superior Province, northern Quebec. No. 8403.

Fossen, H., 2016. Structural geology. Cambridge University Press.

Fossen, H., Cavalcante, G.C.G., Pinheiro, R.V.L., Archanjo, C.J., 2019. Deformation – Progressive or multiphase? Journal of Structural Geology 125, 82–99.

Fougerouse, D., Micklethwaite, S., Tomkins, A.G., Mei, Y., Kilburn, M., Guagliardo, P., Fisher, L.A., Halfpenny, A., Gee, M., Paterson, D., Howard, D.L., 2016a. Gold remobilisation and formation of high grade ore shoots driven by dissolution-reprecipitation replacement and Ni substitution into auriferous arsenopyrite. Geochimica et Cosmochimica Acta 178, 143–159.

Fougerouse, D., Reddy, S.M., Saxey, D.W., Rickard, W.D., Van Riessen, A., Micklethwaite, S., 2016b. Nanoscale gold clusters in arsenopyrite controlled by growth rate not concentration: Evidence from atom probe microscopy. American Mineralogist 101, 1916–1919.

Fougerouse, D., Micklethwaite, S., Ulrich, S., Miller, J., Godel, B., Adams, D.T., McCuaig, T.C., 2017. Evidence for Two Stages of Mineralization in West Africa's Largest Gold Deposit: Obuasi, Ghana. Economic Geology 112, 3–22.

Frenzel, M., Hirsch, T., Gutzmer, J., 2016. Gallium, germanium, indium, and other trace and minor elements in sphalerite as a function of deposit type — A meta-analysis. Ore Geology Reviews 76, 52–78.

Frisch, W., Pohl, W., 1986. Petrochemistry of some mafic and ultramafic rocks from the Mozambique Belt, SE Kenya. Mitteilungen Der Osterreichischen Geologischen Gesellschaft 78, 97–114.

Frimmel, H.E., 2008. Earth's continental crustal gold endowment. Earth and Planetary Science Letters 267, 45–55.

Frimmel, H.E., 2018. Episodic concentration of gold to ore grade through Earth's history. Earth-Science Reviews 180, 148–158.

Frisch, W., Pohl, W., 1986. Petrochemistry of some mafic and ultramafic rocks from the Mozambique Belt, SE Kenya. Mitteilungen Der Osterreichischen Geologischen Gesellschaft 78, 97–114.

Fritz, H., Dallmeyer, D.R., Wallbrecher, E., Loizenbauer, J., Hoinkes, G., Neumayr, P., Khudeir, A.A., 2002. Neoproterozoic tectonothermal evolution of the Central Eastern Desert, Egypt: a slow velocity tectonic process of core complex exhumation. Journal of African Earth Sciences 34, 137–155.

Fritz, H., Wallbrecher, E., Khudeir, A.A., Abu el Ela, F., Dallmeyer, D.R., 1996. Formation of Neoproterozoic metamorphic complex during oblique convergence (Eastern Desert, Egypt). Journal of African Earth Sciences 23, 311–329.

Fritz, H., Abdelsalam, M., Ali, K.A., Bingen, B., Collins, A.S., Fowler, A.R., Ghebreab, W., Hauzenberger, C.A., Johnson, P.R., Kusky, T.M., Macey, P., Muhongo, S., Stern, R.J., Viola, G., 2013. Orogen styles in the East African Orogen: A review of the Neoproterozoic to Cambrian tectonic evolution. Journal of African Earth Sciences 86, 65–106.

Fryer, B.J., Greenough, J.D., 1992. Evidence for mantle heterogeneity from platinum-group-element abundances in Indian Ocean basalts. Canadian Journal of Earth Sciences 29, 2329–2340.

G

Gaboury, D., Carrier, A., Crevier, M., Pelletier, C., Sketchley, D.A., 2001. Predictive distribution of fault-fill and extensional veins: example from the Sigma gold mine, Abitibi Subprovince, Canada. Economic Geology 96, 1397–1405.

Gaboury, D., 2013. Does gold in orogenic deposits come from pyrite in deeply buried carbon-rich sediments?: Insight from volatiles in fluid inclusions. Geology 41, 1207–1210.

Gaboury, D., 2019. Parameters for the formation of orogenic gold deposits. Applied Earth Science 128, 124–133.

Gaboury, D., Oré Sanchez, C., 2020. Electrochemical gold precipitation to explain extensive vertical and lateral mineralization in the world-class Poderosa-Pataz district, Peru. Terra Nova 32, 97–107.

Gaboury, D., Nabil, H., Ennaciri, A., Maacha, L., 2020. Structural setting and fluid composition of gold mineralization along the central segment of the Keraf suture, Neoproterozoic Nubian Shield, Sudan: implications for the source of gold. International Geology Review, 1-27.

Gaillard, N., Williams-Jones, A.E., Clark, J.R., Salvi, S., Perrouty, S., Linnen, R.L., Olivo, G.R., 2020. The use of lithogeochemistry in delineating hydrothermal fluid pathways and vectoring towards gold mineralization in the Malartic district, Québec. Ore Geology Reviews 120, 103351.

Galkin, S.V., Efimov, A.A., Krivoshchekov, S.N., Savitskiy, Y.V., Cherepanov, S.S., 2015. X-ray tomography in petrophysical studies of core samples from oil and gas fields. Russian Geology and Geophysics 56, 782–792.

Gamal El Dien, H., Arai, S., Doucet, L.-S., Li, Z.-X., Kil, Y., Fougerouse, D., Reddy, S.M., Saxey, D.W., Hamdy, M., 2019. Cr-spinel records metasomatism not petrogenesis of mantle rocks. Nature Communications 10, 5103.

Ganne, J., De Andrade, V., Weinberg, R.F., Vidal, O., Dubacq, B., Kagambega, N., Naba, S., Baratoux, L., Jessell, M., Allibon, J., 2012. Modern-style plate subduction preserved in the Palaeoproterozoic West African craton. Nature Geoscience 5, 60–65.

Ganne, J., Feng, X., 2017. Primary magmas and mantle temperatures through time: A NOT SO HOT MANTLE ABOUT 2.5 GYR AGO. Geochemistry, Geophysics, Geosystems 18, 872–888.

Gao, F., Du, Yangsong, Pang, Z., Du, Yilun, Xin, F., Xie, J., 2019. LA-ICP-MS Trace-Element Analysis of Pyrite from the Huanxiangwa Gold Deposit, Xiong'ershan District, China: Implications for Ore Genesis. Minerals 9, 157.

Gapais, D., Cagnard, F., Gueydan, F., Barbey, P., Ballevre, M., 2009. Mountain building and exhumation processes through time: inferences from nature and models. Terra Nova 21, 188–194.

Geisler, T., Rashwan, A.A., Rahn, M.K.W., Poller, U., Zwingmann, H., Pidgeon, R.T., Schleicher, H., Tomaschek, F., 2003. Low-temperature hydrothermal alteration of natural metamict zircons from the Eastern Desert, Egypt. Mineralogical Magazine 67, 485–508.

Geng, H., Gu, X., Zhang, Y., 2018. Characteristics of genetic mineralogy of pyrite and quartz and their indicating significance in the Gaosongshan Gold Deposit, Heilongjiang Province, NE China. Earth Sciences Research Journal 22, 301–318.

Genna, A., Guerrot, C., Deschamps, Y., Nehlig, P., Shanti, M., 1999. Les formations Ablah d'Arabie Saoudite (datation et implication géologique). Comptes Rendus de l'Académie Des Sciences-Series IIA-Earth and Planetary Science 329, 661–667.

Genna, D., Gaboury, D., 2015. Deciphering the Hydrothermal Evolution of a VMS System by LA-ICP-MS Using Trace Elements in Pyrite: An Example from the Bracemac-McLeod Deposits, Abitibi, Canada, and Implications for Exploration. Economic Geology 110, 2087–2108.

Geological Research Authority of the Sudan, 1988. Geological Map of the Sudan, scale 1:1000000, Robertson Research.

George, L.L., Cook, N.J., Ciobanu, C.L., 2016. Partitioning of trace elements in co-crystallized sphalerite–galena–chalcopyrite hydrothermal ores. Ore Geology Reviews 77, 97–116.

George, L.L., Cook, N.J., Crowe, B.B.P., Ciobanu, C.L., 2018. Trace elements in hydrothermal chalcopyrite. Mineralogical Magazine 82, 59–88.

Geoscience Analyst (2.60) Software, 2018. Mira Geoscience Limited consulted on. https://mirageoscience.com/mining-industry-software/geoscience-analyst/#GAioGas.

Gerdes, A., Zeh, A., 2009. Zircon formation versus zircon alteration—new insights from combined U–Pb and Lu–Hf in-situ LA-ICP-MS analyses, and consequences for the interpretation of Archean zircon from the Central Zone of the Limpopo Belt. Chemical Geology 261, 230–243.

Gerya, T.V., 2011. Intra-oceanic Subduction Zones. Arc-Continent Collision, Frontiers in Earth Sciences. Springer Berlin Heidelberg, Berlin, Heidelberg, 23–51.

Ghanem, H., McAleer, R.J., Jarrar, G.H., Al Hseinat, M., Whitehouse, M., 2020. 40Ar/39Ar and U-Pb SIMS zircon ages of Ediacaran dikes from the Arabian-Nubian Shield of south Jordan. Precambrian Research 343, 105714.

Ghebreab, W., 1998. Tectonics of the Red Sea region reassessed. Earth-Science Reviews 45, 1–44.

Ghebreab, W., Talbot, C.J., Page, L., 2005. Time constraints on exhumation of the East African Orogen from field observations and 40Ar/39Ar cooling ages of low-angle mylonites in Eritrea, NE Africa. Precambrian Research 139, 20–41.

Gilbert, G.K., 1890. Lake Bonneville. United States Geological Survey.

Gill, S.B., Piercey, S.J., Layton-Matthews, D., 2016. Mineralogy and Metal Zoning of the Cambrian Zn-Pb-Cu-Ag-Au Lemarchant Volcanogenic Massive Sulfide (VMS) Deposit, Newfoundland. The Canadian Mineralogist 54, 1307–1344.

Godel, B., Barnes, S.J., Barnes, S.-J., Maier, W.D., 2010. Platinum ore in three dimensions: Insights from high-resolution X-ray computed tomography. Geology 38(12), 1127-1130.

Godel, B., 2013. High-Resolution X-Ray Computed Tomography and Its Application to Ore Deposits: From Data Acquisition to Quantitative Three-Dimensional Measurements with Case Studies from Ni-Cu-PGE Deposits. Economic Geology 108, 2005–2019.

Godel, B.M., Barnes, S.J., Barnes, S.-J., 2013. Deposition Mechanisms of Magmatic Sulphide Liquids: Evidence from High-Resolution X-Ray Computed Tomography and Trace Element Chemistry of Komatiite-hosted Disseminated Sulphides. Journal of Petrology 54, 1455–1481.

Goldfarb, R.J., Groves, D.I., Gardoll, S., 2001. Orogenic gold and geologic time: a global synthesis. Ore Geology Reviews 18, 1–75.

Goldfarb, R.J., Baker, T., Dubé, B., Groves, D.I., Hart, C.J.R., Gosselin, P., 2005. Distribution, character and genesis of gold deposits in metamorphic terranes. Economic Geology 100th Anniversary Volume, 407–450.

Goldfarb, R.J., Bradley, D., Leach, D.L., 2010. Secular Variation in Economic Geology. Economic Geology 105, 459–465.

Goldfarb, R.J., Groves, D.I., 2015. Orogenic gold: Common or evolving fluid and metal sources through time. Lithos 233, 2–26.

Goldfarb, R.J., André-Mayer, A.-S., Jowitt, S.M., Mudd, G.M., 2017. West Africa: The World's Premier Paleoproterozoic Gold Province. Economic Geology 112, 123–143.

Goldstein, S.L., O'Nions, R.K., Hamilton, P.J., 1984. A Sm-Nd isotopic study of atmospheric dusts and particulates from major river systems. Earth and Planetary Science Letters 70, 221–236.

Goswami, S., Mamtani, M.A., Rana, V., 2018. Quartz CPO and kinematic analysis in deformed rocks devoid of visible stretching lineations: An integrated AMS and EBSD investigation. Journal of Structural Geology 115, 270–283.

Gourcerol, B., Kontak, D.J., Thurston, P.C., Petrus, J.A., 2018a. Results of LA-ICP-MS sulfide mapping from Algoma-type BIF gold systems with implications for the nature of mineralizing fluids, metal sources, and deposit models. Mineralium Deposita 53, 871–894.

Gourcerol, B., Kontak, D.J., Thurston, P.C., Petrus, J.A., 2018b. Application of LA-ICP-MS sulfide analysis and methodology for deciphering elemental paragenesis and associations in addition to multi-stage processes in metamorphic gold settings. The Canadian Mineralogist 56, 39–64.

Gourcerol, B., Kontak, D.J., Petrus, J.A., Thurston, P.C., 2020. Application of LA ICP-MS analysis of arsenopyrite to gold metallogeny of the Meguma Terrane, Nova Scotia, Canada. Gondwana Research 81, 265–290.

Gray, D.R., Foster, D.A., Meert, J.G., Goscombe, B.D., Armstrong, R., Trouw, R.A.J., Passchier, C.W., 2008. A Damara orogen perspective on the assembly of southwestern Gondwana. Geological Society, London, Special Publications 294, 257–278.

Greiling, R.O., Kroner, A., El-Ramly, M.F., Rashwan, A.A., 1988. Structural relationships between in the Southern and Central parts of the Eastern Desert of Egypt: details

of a fold and thrust belt. The Pan-African Belt of Northeast Africa and Adjacent Areas: Tectonic Evolution and Economic Aspects of a Late Proterozoic Oregon. 121–145.

Gregory, D.D., Cracknell, M.J., Large, R.R., McGoldrick, P., Kuhn, S., Maslennikov, V.V., Baker, M.J., Fox, N., Belousov, I., Figueroa, M.C., Steadman, J.A., Fabris, A.J., Lyons, T.W., 2019. Distinguishing Ore Deposit Type and Barren Sedimentary Pyrite Using Laser Ablation-Inductively Coupled Plasma-Mass Spectrometry Trace Element Data and Statistical Analysis of Large Data Sets. Economic Geology 114, 771–786.

Grenholm, M., 2019. The global tectonic context of the ca. 2.27-1.96 Ga Birimian Orogen – Insights from comparative studies, with implications for supercontinent cycles. Earth-Science Reviews 193, 260–298.

Griffin, W.L., Begg, G.C., O'Reilly, S.Y., 2013. Continental-root control on the genesis of magmatic ore deposits. Nature Geoscience 6, 905–910.

Groves, D.I., 1993. The crustal continuum model for late-Archaean lode-gold deposits of the Yilgarn Block, Western Australia. Mineralium Deposita 28, 366–374.

Groves, D.I., Goldfarb, R.J., Gebre-Mariam, M., Hagemann, S.G., Robert, F., 1998. Orogenic gold deposits: a proposed classification in the context of their crustal distribution and relationship to other gold deposit types. Ore Geology Reviews 13, 7–27.

Groves, D.I., Goldfarb, R.J., Robert, F., Hart, C.J., 2003. Gold deposits in metamorphic belts: overview of current understanding, outstanding problems, future research, and exploration significance. Economic Geology 98, 1–29.

Groves, D.I., Condie, K.C., Goldfarb, R.J., Hronsky, J.M., Vielreicher, R.M., 2005a. 100th Anniversary Special Paper: secular changes in global tectonic processes and their influence on the temporal distribution of gold-bearing mineral deposits. Economic Geology 100, 203–224.

Groves, D.I., Vielreicher, R.M., Goldfarb, R.J., Condie, K.C., 2005b. Controls on the heterogeneous distribution of mineral deposits through time. Geological Society, London, Special Publications 248, 71–101.

Groves, D.I., Bierlein, F.P., 2007. Geodynamic settings of mineral deposit systems. Journal of the Geological Society 164, 19–30.

Groves, D.I., Santosh, M., Goldfarb, R.J., Zhang, L., 2018. Structural geometry of orogenic gold deposits: Implications for exploration of world-class and giant deposits. Geoscience Frontiers 9, 1163–1177.

Groves, D.I., Santosh, M., Deng, J., Wang, Q., Yang, L., Zhang, L., 2019. A holistic model for the origin of orogenic gold deposits and its implications for exploration. Mineralium Deposita 55, 275–292.

Grundler, P.V., Brugger, J., Etschmann, B.E., Helm, L., Liu, W., Spry, P.G., Tian, Y., Testemale, D., Pring, A., 2013. Speciation of aqueous tellurium(IV) in hydrothermal solutions and vapors, and the role of oxidized tellurium species in Te transport and gold deposition. Geochimica et Cosmochimica Acta 120, 298–325.

Guillot, S., Hattori, K., Agard, P., Schwartz, S., Vidal, O., 2009. Exhumation Processes in Oceanic and Continental Subduction Contexts: A Review. In: Lallemand, S., Funiciello, F. (Eds.), Subduction Zone Geodynamics. Springer Berlin Heidelberg, Berlin, Heidelberg, 175–205.

H

Haldar, S.K., 2020. Introduction to mineralogy and petrology. Elsevier.

Halfpenny, A., Hough, R., Nugus, M., 2013. Crystallography of Natural and Synthetic Gold Alloy Microstructures. Materials Science Forum 753, 477–480.

Hamlyn, P.R., Keays, R.R., Cameron, W.E., Crawford, A.J., Waldron, H.M., 1985. Precious metals in magnesian low-Ti lavas: implications for metallogenesis and sulfur saturation in primary magmas. Geochimica et Cosmochimica Acta 49, 1797–1811.

Hanna, R.D., Ketcham, R.A., 2017. X-ray computed tomography of planetary materials: A primer and review of recent studies. Geochemistry 77, 547–572.

Hannington, M.D., Poulsen, K.H., Thomsen, J.F., Sillitoe, R.H., 1999. Volcanogenic gold in the massive sulfide environment. In: Barrie, C.T., Hannington, M.D. (Eds.), Volcanic-Associated Massive Sulfide Deposits: Processes and Examples in Modern and Ancient Settings, Reviews in Economic Geology. 325–356.

Harbi, H.M., Surour, A.A., Davidson, G.J., 2014. Genesis of Neoproterozoic Au-bearing volcanogenic sulfides and quartz veins in the Ar Rjum goldfield, Saudi Arabia. Ore Geology Reviews 58, 110–125.

Harbi, H.M., Ali, K.A., McNaughton, N.J., Andresen, A., 2018. U-Pb zircon and 40Ar/39Ar geochronology of sericite from hydrothermal alteration zones: new constraints for the timing of Ediacaran gold mineralization in the Sukhaybarat area, western Afif terrane, Saudi Arabia. Mineralium Deposita 53, 459–476.

Hargrove, U.S., Stern, R.J., Kimura, J.-I., Manton, W.I., Johnson, P.R., 2006. How juvenile is the Arabian–Nubian Shield? Evidence from Nd isotopes and pre-Neoproterozoic inherited zircon in the Bi'r Umq suture zone, Saudi Arabia. Earth and Planetary Science Letters 252, 308–326.

Harms, U., Schandelmeier, H., Darbyshire, D.P.F., 1990. Pan-African reworked early/middle Proterozoic crust in NE Africa west of the Nile: Sr and Nd isotope evidence. Journal of the Geological Society 147, 859–872.

Harms, U., Darbyshire, D.P.F., Denkler, T., Hengst, M., Schandelmeier, H., 1994. Evolution of the Neoproterozoic Delgo suture zone and crustal growth in northern Sudan: geochemical and radiogenic isotope constraints. Geologische Rundschau 83, 591–603.

Hart, C.J.R., 2005. Classifying, distinguishing and exploring for intrusion-related gold systems. The Gangue 87, 4–9.

Hart, C.J.R., Goldfarb, R.J., 2005. Distinguishing intrusion-related from orogenic gold systems. New Zealand Minerals Conference Proceedings. 125–133.

Hart, C.J.R., 2007. Reduced intrusion-related gold systems. Mineral Deposits of Canada: A Synthesis of Major Deposit Types, District Metallogeny, the Evolution of Geological Provinces, and Exploration Methods:

Geological Association of Canada, Mineral Deposits Division, Special Publication 5, 95–112.

Hassaan, M.M., El-Sawy, E.K., 2009. Tectonic environments and distribution of gold deposits in the Pan African Nubian Shield, Egypt. Australian Journal of Basic and Applied Sciences 3, 797–809.

Hazarika, P., Mishra, B., Chinnasamy, S.S., Bernhardt, H.-J., 2013. Multi-stage growth and invisible gold distribution in pyrite from the Kundarkocha sediment-hosted gold deposit, eastern India. Ore Geology Reviews 55, 134–145.

Heard, H.C., 1960. Chapter 7: Transition from Brittle Fracture to Ductile Flow in Solenhofen Limestone as a Function of Temperature, Confining Pressure, and Interstitial Fluid Pressure. Geological Society of America Memoirs. Geological Society of America, 193–226.

Hedenquist, J.W., Lowenstern, J.B., 1994. The role of magmas in the formation of hydrothermal ore deposits. Nature 370, 519–527.

Hedenquist, J.W., Arribas, A., Gonzalez-Urien, E., 2000. Exploration for epithermal gold deposits. Reviews in Economic Geology 13, 45–77.

Hegner, E., Pallister, J.S., 1989. Pb, Sr, and Nd isotopic characteristics of Tertiary Red Sea rift volcanics from the central Saudi Arabian Coastal Plain. Journal of Geophysical Research 94, 7749.

Helgeson, H.C., Garrels, R.M., 1968. Hydrothermal transport and deposition of gold. Economic Geology 63, 622–635.

Helmy, Hassan, M., Kaindl, R., Fritz, H., Loizenbauer, J., 2004. The Sukari Gold Mine, Eastern Desert, Egypt: structural setting, mineralogy and fluid inclusion study. Mineralium Deposita 39, 495–511.

Helmy, H., Zoheir, B., 2015. Metal and fluid sources in a potential world-class gold deposit: El-Sid mine, Egypt. International Journal of Earth Sciences 104, 645–661.

Henley, R.W., Hughes, G.O., 2000. Underground fumaroles:" Excess heat" effects in vein formation. Economic Geology 95, 453–466.

Hilgers, C., Dilg-Gruschinski, K., Urai, J.L., 2003. Microstructures grown experimentally from advectivesupersaturated solution and their implication for natural vein systems. Journal of Geochemical Exploration 78–79, 221–225.

Hillier, S., Velde, B., 1991. Octahedral occupancy and the chemical composition of diagenetic (low-temperature) chlorites. Clay Minerals 26, 149–168.

Hodgson, C.J., 1989. The structure of shear-related, vein-type gold deposits: a review. Ore Geology Reviews 4, 231–273.

Hofstra, A.H., John, D.A., Theodore, T.G., 2003. A special issue devoted to gold deposits in Northern Nevada: Part 2. Carlin-type deposits. Economic Geology 98, 1063–1067.

Hollocher, K., Ruiz, J., 1995. Major and trace element determinations on NIST glass standard reference materials 611, 612, 614 and 1834 by inductively coupled plasma-mass spectrometry. Geostandards Newsletter 19, 27–34.

Hough, R.M., Noble, R.R.P., Reich, M., 2011. Natural gold nanoparticles. Ore Geology Reviews 42, 55–61.

Howell, E.R., Blakey, R.C., 2013. Sedimentological constraints on the evolution of the Cordilleran arc: New insights from the Sonsela Member, Upper Triassic Chinle Formation, Petrified Forest National Park (Arizona, USA). Geological Society of America Bulletin 125, 1349–1368.

Hronsky, J.M.A., Groves, D.I., Loucks, R.R., Begg, G.C., 2012. A unified model for gold mineralisation in accretionary orogens and implications for regional-scale exploration targeting methods. Mineralium Deposita 47, 339–358.

Hronsky, J.M.A., 2020. Deposit-scale structural controls on orogenic gold deposits: an integrated, physical process–based hypothesis and practical targeting implications. Mineralium Deposita 55, 197–216.

Huston, D.L., Sie, S.H., Suter, G.F., Cooke, D.R., Both, R.A., 1995. Trace elements in sulfide minerals from eastern Australian volcanic-hosted massive sulfide deposits; Part I, Proton microprobe analyses of pyrite, chalcopyrite, and sphalerite, and Part II, Selenium levels in pyrite; comparison with delta 34 S values and implications for the source of sulfur in volcanogenic hydrothermal systems. Economic Geology 90, 1167–1196.

Huston, D.L., Blewett, R.S., Champion, D.C., 2012. Australia through time: a summary of its tectonic and metallogenic evolution. Episodes 35, 23–43.

I, J

Ibrahim, W.S., Watanabe, K., Yonezu, K., 2016. Structural and litho-tectonic controls on Neoproterozoic base metal sulfide and gold mineralization in North Hamisana shear zone, South Eastern Desert, Egypt: The integrated field, structural, Landsat 7 ETM + and ASTER data approach. Ore Geology Reviews 79, 62–77.

Inoue, A., Meunier, A., Patrier-Mas, P., Rigault, C., Beaufort, D., Vieillard, P., 2009. Application of Chemical Geothermometry to Low-Temperature Trioctahedral Chlorites. Clays and Clay Minerals 57, 371–382.

Iwano, H., Danhara, T., Yuguchi, T., Hirata, T., Ogasawara, M., 2019. Duluth Complex apatites: Age reference material for LA–ICP–MS-based fission-track dating. Terra Nova 31, 247–256.

Jackson, S.E., Pearson, N.J., Griffin, W.L., Belousova, E.A., 2004. The application of laser ablation-inductively coupled plasma-mass spectrometry to in situ U–Pb zircon geochronology. Chemical Geology 211, 47–69.

Jacobs, J., Fanning, C. M., Henjes-Kunst, F., Olesch, M., and Paech, H., 1998, Continuation of the Mozambique Belt Into East Antarctica: Grenville-Age Metamorphism and Polyphase Pan-African High-Grade Events in Central Dronning Maud Land: The Journal of Geology, v. 106, p. 385–406.

Jacobs, Joachim, Fanning, C.M., Bauer, W., 2003. Timing of Grenville-age vs. Pan-African medium-to high grade metamorphism in western Dronning Maud Land (East Antarctica) and significance for correlations in Rodinia and Gondwana. Precambrian Research 125, 1–20.

Jacobsen, S.B., Wasserburg, G.J., 1980. Sm-Nd isotopic evolution of chondrites. Earth and Planetary Science Letters 50, 139–155.

Jagoutz, O.E., Burg, J.-P., Hussain, S., Dawood, H., Pettke, T., Iizuka, T., Maruyama, S., 2009. Construction of the granitoid crust of an island arc part I: geochronological

and geochemical constraints from the plutonic Kohistan (NW Pakistan). Contributions to Mineralogy and Petrology 158, 739–755.

Jagoutz, O., Schmidt, M.W., 2013. The composition of the foundered complement to the continental crust and a re-evaluation of fluxes in arcs. Earth and Planetary Science Letters 371–372, 177–190.

Jagoutz, O., Kelemen, P.B., 2015. Role of Arc Processes in the Formation of Continental Crust. Annual Review of Earth and Planetary Sciences 43, 363–404.

Janoušek, V., Rogers, G., Bowes, D.R., 1995. Sr-Nd isotopic constraints on the petrogenesis of the Central Bohemian Pluton, Czech Republic. Geologische Rundschau 84, 520–534.

Jarrar, G.H., Theye, T., Yaseen, N., Whitehouse, M., Pease, V., Passchier, C., 2013. Geochemistry and P–T–t evolution of the Abu-Barqa Metamorphic Suite, SW Jordan, and implications for the tectonics of the northern Arabian–Nubian Shield. Precambrian Research 239, 56–78.

Jébrak, M., Marcoux, E., 2008. Géologie des ressources minérales. Ressources Minérales et Faune du Québec.

Jenkin, G.R., Lusty, P.A., McDonald, I., Smith, M.P., Boyce, A.J., Wilkinson, J.J., 2015. Ore deposits in an evolving Earth: an introduction. Geological Society, London, Special Publications 393, 1–8.

Jenner, F.E., Arculus, R.J., Mavrogenes, J.A., Dyriw, N.J., Nebel, O., Hauri, E.H., 2012. Chalcophile element systematics in volcanic glasses from the northwestern Lau Basin. Geochemistry, Geophysics, Geosystems 13.

Jicha, B.R., Scholl, D.W., Singer, B.S., Yogodzinski, G.M., Kay, S.M., 2006. Revised age of Aleutian Island Arc formation implies high rate of magma production. Geology 34, 661.

Jicha, B.R., Jagoutz, O., 2015. Magma Production Rates for Intraoceanic Arcs. Elements 11, 105–111.

Jicha, B.R., Kay, S.M., 2018. Quantifying arc migration and the role of forearc subduction erosion in the central Aleutians. Journal of Volcanology and Geothermal Research 360, 84–99.

Jochum, K.P., Willbold, M., Raczek, I., Stoll, B., Herwig, K., 2005. Chemical Characterisation of the USGS Reference Glasses GSA-1G, GSC-1G, GSD-1G, GSE-1G, BCR-2G, BHVO-2G and BIR-1G Using EPMA, ID-TIMS, ID-ICP-MS and LA-ICP-MS. Geostandards and Geoanalytical Research 29, 285–302.

John, T., Schenk, V., Mezger, K., Tembo, F., 2004. Timing and PT evolution of whiteschist metamorphism in the Lufilian Arc–Zambezi Belt orogen (Zambia): implications for the assembly of Gondwana. The Journal of Geology 112, 71–90.

Johnson, P.R., Kattan, F.H., Wooden, J.L., 2001. Implications of SHRIMP and microstructural data on the age and kinematics of shearing in the Asir Terrane, southern Arabian Shield, Saudi Arabia. Gondwana Research 4, 172–173.

Johnson, P.R., Woldehaimanot, B., 2003. Development of the Arabian-Nubian Shield: perspectives on accretion and deformation in the northern East African Orogen and the assembly of Gondwana. Geological Society, London, Special Publications 206, 289–325.

Johnson, P.R., Abdelsalam, M.G., Stern, R.J., 2003. The Bi'r Umq-Nakasib Suture Zone in the Arabian-Nubian Shield: A Key to Understanding Crustal Growth in the East African Orogen. Gondwana Research 6, 523–530.

Johnson, P.R., Andresen, A., Collins, A.S., Fowler, A.R., Fritz, H., Ghebreab, W., Kusky, T.M., Stern, R.J., 2011. Late Cryogenian–Ediacaran history of the Arabian–Nubian Shield: A review of depositional, plutonic, structural, and tectonic events in the closing stages of the northern East African Orogen. Journal of African Earth Sciences 61, 167–232.

Johnson, P.R., 2013. Geology and mineralization of the Arabian-Nubian Shield (ANS).

Johnson, P.R., Halverson, G., Kusky, T., Stern, R., Pease, V., 2013. Volcanosedimentary Basins in the Arabian-Nubian Shield: Markers of Repeated Exhumation and Denudation in a Neoproterozoic Accretionary Orogen. Geosciences 3, 389–445.

Johnson, P.R., 2014. An expanding Arabian-Nubian Shield geochronologic and isotopic dataset: defining limits and confirming the tectonic setting of a Neoproterozoic accretionary orogen. The Open Geology Journal 8, 3–33.

Johnson, P.R., Zoheir, B.A., Ghebreab, W., Stern, R.J., Barrie, C.T., Hammer, R.D., 2017. Gold-bearing volcanogenic massive sulfides and orogenic-gold deposits in the Nubian Shield. South African Journal of Geology 120, 63–76.

Johnson, T.E., Ayalew, T., Mogessie, A., Kruger, F.J., Poujol, M., 2004. Constraints on the tectonometamorphic evolution of the Western Ethiopian Shield. Precambrian Research 133, 305–327.

Johnston Jr, W.D., 1940. The gold quartz veins of Grass Valley, California. United States Government Printing Office.

Joly, A., Porwal, A., McCuaig, T.C., 2012. Exploration targeting for orogenic gold deposits in the Granites-Tanami Orogen: Mineral system analysis, targeting model and prospectivity analysis. Ore Geology Reviews 48, 349–383.

Jugo, P.J., Luth, R.W., Richards, J.P., 2005. An experimental study of the sulfur content in basaltic melts saturated with immiscible sulfide or sulfate liquids at 1300° C and 1 · 0 GPa. Journal of Petrology 46, 783–798.

Jugo, P.J., 2009. Sulfur content at sulfide saturation in oxidized magmas. Geology 37, 415–418.

K

Kadel-Harder, I.M., Spry, P.G., Layton-Matthews, D., Voinot, A., von der Handt, A., McCombs, A.L., 2020. Paragenetic relationships between low- and high-grade gold mineralization in the Cripple Creek Au-Te deposit, Colorado: Trace element studies of pyrite. Ore Geology Reviews 127, 103847.

Kahl, W.-A., Dilissen, N., Hidas, K., Garrido, C.J., Lopez-Sanchez-Vizcaino, V., Roman-Alpiste, M., 2017. 3-D microstructure of olivine in complex geological materials reconstructed by correlative X-ray-CT and EBSD analyses. Journal of Microscopy 268, 193–207.

Kampmann, T.C., Jansson, N.F., Stephens, M.B., Olin, P.H., Gilbert, S., Wanhainen, C., 2018. Syn-tectonic sulphide remobilization and trace element redistribution at the Falun pyritic Zn-Pb-Cu-(Au-Ag) sulphide deposit, Bergslagen, Sweden. Ore Geology Reviews 96, 48–71.

Karmakar, S., Schenk, V., 2015. Neoproterozoic metamorphic events along the eastern margin of the East Sahara Ghost Craton at Sabaloka and Bayuda, Sudan: Petrology and texturally controlled in-situ monazite dating. Precambrian Research 269, 217–241.

Keay, S., Collins, W.J., McCulloch, M.T., 1997. A three-component Sr-Nd isotopic mixing model for granitoid genesis, Lachlan fold belt, eastern Australia. Geology 25, 307–310.

Keays, R.R., Scott, R.B., 1976. Precious metals in ocean-ridge basalts; implications for basalts as source rocks for gold mineralization. Economic Geology 71, 705–720.

Keays, R.R., 1995. The role of komatiitic and picritic magmatism and S-saturation in the formation of ore deposits. Lithos 34, 1–18.

Keays, R.R., Lightfoot, P.C., 2010. Crustal sulfur is required to form magmatic Ni–Cu sulfide deposits: evidence from chalcophile element signatures of Siberian and Deccan Trap basalts. Mineralium Deposita 45, 241–257.

Keith, M., Häckel, F., Haase, K.M., Schwarz-Schampera, U., Klemd, R., 2016. Trace element systematics of pyrite from submarine hydrothermal vents. Ore Geology Reviews 72, 728–745.

Keith, M., Smith, D.J., Jenkin, G.R.T., Holwell, D.A., Dye, M.D., 2018. A review of Te and Se systematics in hydrothermal pyrite from precious metal deposits: Insights into ore-forming processes. Ore Geology Reviews 96, 269–282.

Keith, M., Smith, D.J., Doyle, K., Holwell, D.A., Jenkin, G.R., Barry, T.L., Becker, J., Rampe, J., 2020. Pyrite chemistry: A new window into Au-Te ore-forming processes in alkaline epithermal districts, Cripple Creek, Colorado. Geochimica et Cosmochimica Acta 274, 172–191.

Kelemen, P.B., Yogodzinski, G.M., Scholl, D.W., 2003. Along-strike variation in the Aleutian island arc: Genesis of high Mg# andesite and implications for continental crust. Inside the Subduction Factory 138, 223–276.

Kendrick, J., Yakymchuk, C., 2020. Garnet fractionation, progressive melt loss and bulk composition variations in anatectic metabasites: Complications for interpreting the geodynamic significance of TTGs. Geoscience Frontiers 11, 745–763.

Kendrick, M.A., Honda, M., Walshe, J., Petersen, K., 2011. Fluid sources and the role of abiogenic-CH_4 in Archean gold mineralization: Constraints from noble gases and halogens. Precambrian Research 189, 313–327.

Kennedy, W.Q., 1964. The structural differenciation of Africa in the Pan-African (+/-500 my) tectonic episode. University of Leeds, Research Institute of African Geology, Annual Report on Scientific Results 48–49.

Kepezhinskas, P., Defant, M.J., Widom, E., 2002. Abundance and distribution of PGE and Au in the island-arc mantle: implications for sub-arc metasomatism. Lithos 60, 113–128.

Kerr, M.J., Hanley, J.J., Kontak, D.J., Morrison, G.G., Petrus, J., Fayek, M., Zajacz, Z., 2018. Evidence of upgrading of gold tenor in an orogenic quartz-carbonate vein system by late magmatic-hydrothermal fluids at the Madrid Deposit, Hope Bay Greenstone Belt, Nunavut, Canada. Geochimica et Cosmochimica Acta 241, 180–218.

Kerrich, R., Wyman, D., 1990. Geodynamic setting of mesothermal gold deposits: An association with accretionary tectonic regimes. Geology 18, 882.

Kerrich, R., Cassidy, K.F., 1994. Temporal relationships of lode gold mineralization to accretion, magmatism, metamorphism and deformation—Archean to present: A review. Ore Geology Reviews 9, 263–310.

Kerrich, R., Goldfarb, R.J., Richards, J.P., 2005. Metallogenic provinces in an evolving geodynamic framework. Economic Geology 100th Anniversary Volume 13, 1097–1136.

Kesler, S.E., Wilkinson, B.H., 2006. The role of exhumation in the temporal distribution of ore deposits. Economic Geology 101, 919–922.

Ketcham, R.A., Carlson, W.D., 2001. Acquisition, optimization and interpretation of X-ray computed tomographic imagery: applications to the geosciences. Computers & Geosciences 27, 381–400.

Ketris, M.P., Yudovich, Y.E., 2009. Estimations of Clarkes for Carbonaceous biolithes: World averages for trace element contents in black shales and coals. International Journal of Coal Geology 78, 135–148.

Khalil, A.E.S., Obeid, M.A., Azer, M.K., 2015. Late Neoproterozoic post-collisional mafic magmatism in the Arabian–Nubian Shield: A case study from Wadi El-Mahash gabbroic intrusion in southeast Sinai, Egypt. Journal of African Earth Sciences 105, 29–46.

Khalil, K.I., Moghazi, A.M., El Makky, A.M., 2016. Nature and Geodynamic Setting of Late Neoproterozoic Vein-Type Gold Mineralization in the Eastern Desert of Egypt: Mineralogical and Geochemical Constraints. In: Bouabdellah, M., Slack, J.F. (Eds.), Mineral Deposits of North Africa. Springer International Publishing, Cham,

Kiyokawa, S., Suzuki, T., Horie, K., Takehara, M., El-Dokouny, H.A., Dawoud, M., Abuelhasan, M.M., 2020. Tectonic and sedimentary history of the neoproterozoic metavolcanic–volcaniclastic rocks of the El-Dabbah Group, Central Eastern Desert, Egypt. Journal of African Earth Sciences 165, 103807.

Klemenic, P.M., 1985. New geochronological data on volcanic rocks from northeast Sudan and their implication for crustal evolution. Precambrian Research 30, 263–276.

Klemm, D., Klemm, R., Murr, A., 2001. Gold of the Pharaohs – 6000 years of gold mining in Egypt and Nubia. Journal of African Earth Sciences 33, 643–659.

Klemm, R., Klemm, D., 2013a. Value of Gold in Ancient Egypt. Gold and Gold Mining in Ancient Egypt and Nubia, Natural Science in Archaeology. Springer Berlin Heidelberg, Berlin, Heidelberg, 21–27.

Klemm, R., Klemm, D., 2013b. Archaeological Chronology of Gold Mining in Ancient Egypt and Nubian Sudan. Gold and Gold Mining in Ancient Egypt and Nubia, Natural Science in Archaeology. Springer Berlin Heidelberg, Berlin, Heidelberg, 1–20.

Klemm, R., Klemm, D., 2013c. Sequential and Spatial Distribution of Gold Mining Sites in the Egyptian and Nubian Eastern Deserts. Gold and Gold Mining in

Ancient Egypt and Nubia, Natural Science in Archaeology. Springer Berlin Heidelberg, Berlin, Heidelberg, 601–621.

Klemm, R., Klemm, D., 2013d. Gold Production Sites and Gold Mining in Nubia/Sudan. Gold and Gold Mining in Ancient Egypt and Nubia, Natural Science in Archaeology. Springer Berlin Heidelberg, Berlin, Heidelberg, 341–599.

Klemm, R., Klemm, D., 2013e. Gold Production Sites and Gold Mining in Ancient Egypt. Gold and Gold Mining in Ancient Egypt and Nubia, Natural Science in Archaeology. Springer Berlin Heidelberg, Berlin, Heidelberg, 51–339.

Koehn, D., Bons, P.D., Passchier, C.W., 2003. Development of antitaxial strain fringes during non-coaxial deformation: an experimental study. Journal of Structural Geology 25, 263–275.

Kohn, B.P., Eyal, M., 1981. History of uplift of the crystalline basement of Sinai and its relation to opening of the Red Sea as revealed by fission track dating of apatites. Earth and Planetary Science Letters 52, 129–141.

Kohn, B.P., Eyal, M., Feinstein, S., 1992. A major Late Devonian-Early Carboniferous (Hercynian) Thermotectonic event at the NW Margin of the Arabian-Nubian Shield: Evidence from zircon fission track dating. Tectonics 11, 1018–1027.

Kolb, J., Kisters, A.F.M., Meyer, F.M., Siemes, H., 2003. Polyphase deformation of mylonites from the Renco gold mine (Zimbabwe): identi®ed by crystallographic preferred orientation of quartz. Journal of Structural Geology 10.

Kolodner, K., Avigad, D.O.V., Ireland, T.R., Garfunkel, Z.V.I., 2009. Origin of Lower Cretaceous ('Nubian') sandstones of North-east Africa and Arabia from detrital zircon U-Pb SHRIMP dating. Sedimentology 56, 2010–2023.

Kontak, D., Hanley, J.J., Gourcerol, B., Petrus, J., Malcom, K., Kerr, M., Kelly, C., Letourneau, M., Mcdivitt, J., Neyedley, K., 2018. Protracted and complex fluid histories the norm in orogenic-type gold deposits as revealed by LA ICP-MS sulfide mapping.

Kouzmanov, K., Pokrovski, G.S., 2012. Hydrothermal controls on metal distribution in porphyry Cu (-Mo-Au) systems. Society of Economic Geologist, Special Publication 16, 573–618.

Krauskopf, K.B., 1951. The solubility of gold. Economic Geology 46, 858–870.

Kreuzer, O.P., Miller, A.V.M., Peters, K.J., Payne, C., Wildman, C., Partington, G., Puccioni, E., McMahon, M.E., Etheridge, M.A., 2014. Comparing prospectivity modelling results and past exploration data: A case study of porphyry Cu–Au mineral systems in the Macquarie Arc, Lachlan Fold Belt, New South Wales. Ore Geology Reviews.

Kreuzer, O.P., Yousefi, M., Nykänen, V., 2020. Introduction to the special issue on spatial modelling and analysis of ore-forming processes in mineral exploration targeting. Ore Geology Reviews 119, 103391.

Kröner, A., 1982. Rb-Sr geochronology and tectonic evolution of the Pan-African Damara belt of Namibia, southwestern Africa. American Journal of Science 282, 1471–1507.

Kröner, A., 1984. Late Precambrian plate tectonics and orogeny: a need to redefine the term Pan-African. Géologie Africaine. 23–28.

Kröner, A., Grieling, R., Reischmann, T., Hussein, I.M., Stern, R.J., Dürr, S., Krüger, J., Zimmer, M., 1987. Pan-African crustal evolution in the Nubian segment of northeast Africa. In: Kröner, A. (Ed.), Geodynamics Series. American Geophysical Union, Washington, D. C., 235–257.

Kröner, A., Eyal, M., Eyal, Y., 1990. Early Pan-African evolution of the basement around Elat, Israel,and the Sinai Peninsula revealed by single-zircon evaporation dating, and implications for crustal accretion rates. Geology 18, 545.

Kröner, A., Linnebacher, P., Stern, R.J., Reischmann, T., Manton, W., Hussein, I.M., 1991. Evolution of Pan-African island arc assemblages in the southern Red Sea Hills, Sudan, and in southwestern Arabia as exemplified by geochemistry and geochronology. Precambrian Research 53, 99–118.

Kröner, A., Pallister, J.S., Fleck, R.J., 1992a. Age of initial oceanic magmatism in the Late Proterozoic Arabian Shield. Geology 20, 803.

Kröner, A., Todt, W., Hussein, I., Mansour, M., Rashwan, A., 1992b. Dating of late Proterozoic ophiolites in Egypt and the Sudan using the single grain zircon evaporation technique. Precambrian Research 59, 15–32.

Kröner, A., 1993. The Pan African belt of northeastern and eastern Africa, Madagascar, southern India, Sri Lanka and East Antarctica: Terrane amalgamation during formation of the Gondwana supercontinent. In: Thorweihe, U., Schandelmeier, H. (Eds.), Geoscientific Research in Northeast Africa. CRC Press, 3–9.

Kröner, A., Krüger, J., Rashwan, A. el-A.A., 1994. Age and tectonic setting of granitoid gneisses in the Eastern Desert of Egypt and south-west Sinai. Geologische Rundschau 83, 502–513.

Kröner, A., Sassi, F.P., 1996. Evolution of the northern Somali basement: new constraints from zircon ages. Journal of African Earth Sciences 22, 1–15.

Kröner, A., Rojas-Agramonte, Y., Kehelpannala, K.V.W., Zack, T., Hegner, E., Geng, H.Y., Wong, J., Barth, M., 2013. Age, Nd–Hf isotopes, and geochemistry of the Vijayan Complex of eastern and southern Sri Lanka: a Grenville-age magmatic arc of unknown derivation. Precambrian Research 234, 288–321.

Kusky, T.M., Ramadan, T.M., 2002. Structural controls on Neoproterozoic mineralization in the South Eastern Desert, Egypt: an integrated field, Landsat TM, and SIR-C/X SAR approach. Journal of African Earth Sciences 35, 107–121.

Kusky, T.M., Abdelsalam, M., Tucker, R.D., Stern, R.J., 2003. Evolution of the East African and related orogens, and the assembly of Gondwana. Precambrian Research 123, 81–85.

Küster, D., Hengst, M., Pilot, J., 1993. Evolution of Pan-African granitoid magmatism along the southwestern Nakasib suture zone, Red Sea Hills, Sudan. Geoscientific Research in Northeast Africa. Balkema, Rotterdam 111–115.

Küster, D., Liégeois, J.-P., 2001. Sr, Nd isotopes and geochemistry of the Bayuda Desert high-grade

metamorphic basement (Sudan): an early Pan-African oceanic convergent margin, not the edge of the East Saharan ghost craton? Precambrian Research 109, 1–23.

Küster, D., Liégeois, J.-P., Matukov, D., Sergeev, S., Lucassen, F., 2008. Zircon geochronology and Sr, Nd, Pb isotope geochemistry of granitoids from Bayuda Desert and Sabaloka (Sudan): Evidence for a Bayudian event (920–900 Ma) preceding the Pan-African orogenic cycle (860–590 Ma) at the eastern boundary of the Saharan Metacraton. Precambrian Research 164, 16–39.

Kuzmichev, A.B., Larionov, A.N., 2013. Neoproterozoic island arcs in East Sayan: duration of magmatism (*from* U–Pb *zircon dating of volcanic clastics*). Russian Geology and Geophysics 54, 34–43.

Kyle, J.R., Ketcham, R.A., 2003. In Situ Distribution of Gold in Ores Using High-Resolution X-Ray Ccomputed Tomography. Economic Geology 98, 1697–1701.

Kyle, J.R., Ketcham, R.A., 2015. Application of high resolution X-ray computed tomography to mineral deposit origin, evaluation, and processing. Ore Geology Reviews 65, 821–839.

L

Labbé, J.-F., 2019a. Quelques rappels sur l'or et son historique. BRGM.

Labbé, J.-F., 2019b. Aperçu global du marché de l'or dans le monde | Minéralinfo [WWW Document], MinéralInfo. URL http://www.mineralinfo.fr/ecomine/apercu-global-marche-lor-monde (accessed 4.1.20).

Lanari, P., Wagner, T., Vidal, O., 2014. A thermodynamic model for di-trioctahedral chlorite from experimental and natural data in the system MgO–FeO–Al_2O_3–SiO_2–H_2O: applications to P–T sections and geothermometry. Contributions to Mineralogy and Petrology 167.

Large, R.R., Maslennikov, V.V., Robert, F., Danyushevsky, L.V., Chang, Z., 2007. Multistage Sedimentary and Metamorphic Origin of Pyrite and Gold in the Giant Sukhoi Log Deposit, Lena Gold Province, Russia. Economic Geology 102, 1233–1267.

Large, R.R., Danyushevsky, L., Hollit, C., Maslennikov, V., Meffre, S., Gilbert, S., Bull, S., Scott, R., Emsbo, P., Thomas, H., Singh, B., Foster, J., 2009. Gold and Trace Element Zonation in Pyrite Using a Laser Imaging Technique: Implications for the Timing of Gold in Orogenic and Carlin-Style Sediment-Hosted Deposits. Economic Geology 104, 635–668.

Large, R.R., Bull, S.W., Maslennikov, V.V., 2011. A Carbonaceous Sedimentary Source-Rock Model for Carlin-Type and Orogenic Gold Deposits. Economic Geology 106, 331–358.

Large, R., Thomas, H., Craw, D., Henne, A., Henderson, S., 2012. Diagenetic pyrite as a source for metals in orogenic gold deposits, Otago Schist, New Zealand. New Zealand Journal of Geology and Geophysics 55, 137–149.

Large, R.R., Maslennikov, V.V., 2020. Invisible Gold Paragenesis and Geochemistry in Pyrite from Orogenic and Sediment-Hosted Gold Deposits. Minerals 10, 339.

Launay, L., 1913. Traité de métallogénie : gîtes minéraux et métallifères, Ch. Béranger. ed.

Laurent, O., Björnsen, J., Wotzlaw, J.-F., Bretscher, S., Silva, M.P., Moyen, J.-F., Ulmer, P., Bachmann, O., 2020. Earth's earliest granitoids are crystal-rich magma reservoirs tapped by silicic eruptions. Nature Geoscience 13, 163–169.

Lawley, C., Selby, D., Imber, J., 2013. Re-Os Molybdenite, Pyrite, and Chalcopyrite Geochronology, Lupa Goldfield, Southwestern Tanzania: Tracing Metallogenic Time Scales at Midcrustal Shear Zones Hosting Orogenic Au Deposits. Economic Geology 108, 1591–1613.

Le Bas, M.J., Le Maitre, R.W., Woolley, A.R., 1992. The construction of the Total Alkali-Silica chemical classification of volcanic rocks. Mineralogy and Petrology 46, 1–22.

Le Maitre, R.W., Streckeisen, A., Zanettin, B., Le Bas, M.J., Bonin, B., Bateman, P., 2005. Igneous rocks: a classification and glossary of terms: recommendations of the International Union of Geological Sciences Subcommission on the Systematics of Igneous Rocks. Cambridge University Press.

Le Mignot, E., Reisberg, L., André-Mayer, A.-S., Bourassa, Y., Fontaine, A., Miller, J., 2017. Re-Os Geochronological Evidence for Multiple Paleoproterozoic Gold Events at the Scale of the West African Craton. Economic Geology 112, 145–168.

Lescuyer, J.-L., Deschamps, Y., Guerrot, C., Osman, A.A., 2004. Lower Neoproterozoic age of the Ariab volcanogenic massive sulphide mineralisation, Red Sea Hills, NE Sudan. Presented at the 20th Colloquium of African Geology, BRGM, Orléans, France.

Li, N., Deng, J., Yang, L.-Q., Goldfarb, R.J., Zhang, C., Marsh, E., Lei, S.-B., Koenig, A., Lowers, H., 2014. Paragenesis and geochemistry of ore minerals in the epizonal gold deposits of the Yangshan gold belt, West Qinling, China. Mineralium Deposita 49, 427–449.

Li, W., Cook, N.J., Xie, G.-Q., Mao, J.-W., Ciobanu, C.L., Li, J.-W., Zhang, Z.-Y., 2019. Textures and trace element signatures of pyrite and arsenopyrite from the Gutaishan Au–Sb deposit, South China. Mineralium Deposita 54, 591–610.

Li, Z.X., Bogdanova, S.V., Collins, A.S., Davidson, A., De Waele, B., Ernst, R.E., Fitzsimons, I.C.W., Fuck, R.A., Gladkochub, D.P., Jacobs, J., Karlstrom, K.E., Lu, S., Natapov, L.M., Pease, V., Pisarevsky, S.A., Thrane, K., Vernikovsky, V., 2008. Assembly, configuration, and break-up history of Rodinia: A synthesis. Precambrian Research 160, 179–210.

Liu, W., Borg, S.J., Testemale, D., Etschmann, B., Hazemann, J.-L., Brugger, J., 2011. Speciation and thermodynamic properties for cobalt chloride complexes in hydrothermal fluids at 35–440°C and 600bar: An in-situ XAS study. Geochimica et Cosmochimica Acta 75, 1227–1248.

Liégeois, J.-P., Stern, R.J., 2010. Sr–Nd isotopes and geochemistry of granite-gneiss complexes from the Meatiq and Hafafit domes, Eastern Desert, Egypt: No evidence for pre-Neoproterozoic crust. Journal of African Earth Sciences 57, 31–40.

Liégeois, J.-P., Abdelsalam, M.G., Ennih, N., Ouabadi, A., 2013. Metacraton: Nature, genesis and behavior. Gondwana Research 23, 220–237.

Liew, T.C., Hofmann, A.W., 1988. Precambrian crustal components, plutonic associations, plate environment of the Hercynian Fold Belt of central Europe: indications from a Nd and Sr isotopic study. Contributions to Mineralogy and Petrology 98, 129–138.

Lindgren, W., 1909. Metallogenetic epochs. Economic Geology 4, 409–420.

Liu, X., Fan, H.-R., Evans, N.J., Yang, K.-F., Danišík, M., McInnes, B.I.A., Qin, K.-Z., Yu, X.-F., 2017. Exhumation history of the Sanshandao Au deposit, Jiaodong: constraints from structural analysis and (U-Th)/He thermochronology. Scientific Reports 7.

Loizenbauer, J., Wallbrecher, E., Fritz, H., Neumayr, P., Khudeir, A.A., Kloetzli, U., 2001. Structural geology, single zircon ages and fluid inclusion studies of the Meatiq metamorphic core complex: Implications for Neoproterozoic tectonics in the Eastern Desert of Egypt. Precambrian Research 110, 357–383.

Lorand, J.P., Bodinier, J.L., Dupuy, C., Dostal, J., 1989. Abundance and distribution of gold in the orogenic-type spinel peridotites from Ariege (Northeastern Pyrenees, France). Geochimica et Cosmochimica Acta 53, 3085–3090.

Loucks, R.R., Mavrogenes, J.A., 1999. Gold solubility in supercritical hydrothermal brines measured in synthetic fluid inclusions. Science 284, 2159–2163.

Luais, B., Telouk, P., Albaréde, F., 1997. Precise and accurate neodymium isotopic measurements by plasma-source mass spectrometry. Geochimica et Cosmochimica Acta 61, 4847–4854.

Ludwig, K.R., 2007. Isoplot/Ex version 3.41b, a geochronological toolkit for Microsoft Excel. Berkeley Geochronological Centre Special Publication.

Lugmair, G.W., Marti, K., 1978. Lunar initial 143Nd/144Nd: differential evolution of the lunar crust and mantle. Earth and Planetary Science Letters 39, 349–357.

Luguet, A., Lorand, J.-P., Seyler, M., 2003. Sulfide petrology and highly siderophile element geochemistry of abyssal peridotites: A coupled study of samples from the Kane Fracture Zone (45 W 23 20N, MARK area, Atlantic Ocean). Geochimica et Cosmochimica Acta 67, 1553–1570.

Lundmark, A.M., Andresen, A., Hassan, M.A., Augland, L.E., Boghdady, G.Y., 2012. Repeated magmatic pulses in the East African Orogen in the Eastern Desert, Egypt: An old idea supported by new evidence. Gondwana Research 22, 227–237.

M

Mahdy, N.M., El Kalioubi, B.A., Wohlgemuth-Ueberwasser, C.C., Shalaby, M.H., El-Afandy, A.H., 2015. Petrogenesis of U- andMo-bearing A2-type granite of the Gattar batholith in the Arabian Nubian Shield, Northeastern Desert, Egypt: Evidence for the favorability of host rocks for the origin of associated ore deposits. Ore Geology Reviews 71, 57–81.

Mahéo, G., Fayoux, X., Guillot, S., Garzanti, E., Capiez, P., Mascle, G., 2006. Relicts of an intra-oceanic arc in the Sapi-Shergol mélange zone (Ladakh, NW Himalaya, India): implications for the closure of the Neo-Tethys Ocean. Journal of Asian Earth Sciences 26, 695–707.

Maier, W.D., Arndt, N.T., Curl, E.A., 2000. Progressive crustal contamination of the Bushveld Complex: evidence from Nd isotopic analyses of the cumulate rocks. Contributions to Mineralogy and Petrology 140, 316–327.

Maier, W.D., Groves, D.I., 2011. Temporal and spatial controls on the formation of magmatic PGE and Ni–Cu deposits. Mineralium Deposita 46, 841–857.

Managem, 2011. Exploration activities in Sudan.

Managem, 2014. Exploration activities in Sudan.

Managem, 2019. Annual Report 2018. Managem.

Mancktelow, N.S., Pennacchioni, G., 2005. The control of precursor brittle fracture and fluid–rock interaction on the development of single and paired ductile shear zones. Journal of Structural Geology 27, 645–661.

Markwitz, V., Hein, K.A.A., Miller, J., 2016. Compilation of West African mineral deposits: Spatial distribution and mineral endowment. Precambrian Research 274, 61–81.

Martinez, F., Cochran, J.R., 1988. Structure and tectonics of the northern Red Sea: catching a continental margin between rifting and drifting. Tectonophysics 150, 1–31.

Maslennikov, V.V., Maslennikova, S.P., Large, R.R., Danyushevsky, L.V., 2009. Study of Trace Element Zonation in Vent Chimneys from the Silurian Yaman-Kasy Volcanic-Hosted Massive Sulfide Deposit (Southern Urals, Russia) Using Laser Ablation-Inductively Coupled Plasma Mass Spectrometry (LA-ICPMS). Economic Geology 104, 1111–1141.

Massonne, H.-J., Schreyer, W., 1987. Phengite geobarometry based on the limiting assemblage with K-feldspar, phlogopite, and quartz. Contributions to Mineralogy and Petrology 96, 212–224.

Masurel, Q., Thébaud, N., Miller, J., Ulrich, S., Hein, K.A.A., Cameron, G., Béziat, D., Bruguier, O., Davis, J.A., 2017. Sadiola Hill: A World-Class Carbonate-Hosted Gold Deposit in Mali, West Africa. Economic Geology 112, 23–47.

Masurel, Q., Thébaud, N., Allibone, A., André-Mayer, A.-S., Hein, K.A.A., Reisberg, L., Bruguier, O., Eglinger, A., Miller, J., 2019. Intrusion-related affinity and orogenic gold overprint at the Paleoproterozoic Bonikro Au–(Mo) deposit (Côte d'Ivoire, West African Craton). Mineralium Deposita, 1–24.

Masurel, Q., Eglinger, A., Thébaud, N., Allibone, A., André-Mayer, A.-S., McFarlane, H., Miller, J., Jessell, M., Aillères, L., Vanderhaeghe, O., Baratoux, L., Perrouty, S., Begg, G., Wane, O., Tshibubudze, A., Parra-Avila, L., Kouamélan, A. Capturing distinct Paleoproterozoic gold events in the southern West African Craton: review and synopsis. In press for publication in Mineralium Deposita.

Mateen, T., Rehman, H.U., Yamamoto, H., 2013. EBSD study of Quartz c-axis orientations in the silicified host rocks of the Kasuga gold deposit, Southwest Japan. Journal of Mineralogical and Petrological Sciences 108, 278–287.

Mathez, E.A., 1976. Sulfur solubility and magmatic sulfides in submarine basalt glass. Journal of Geophysical Research 81, 4269–4276.

Mathu, E.M., Bauernhofer, A.H., Hauzenberger, C.A., Handler, R., Wallbrecher, E., Hoinkes, G., Muhongo, S., 2015. $^{40}Ar/^{39}Ar$ cooling ages of Pan-African structures from the Mozambique belt in SE Kenya: implications for the cooling history.

McCaffrey, K., Lonergan, Lidia, Lonergan, Leonard, Wilkinson, J., 1999. Fractures, fluid flow and mineralization. Geological Society of London.

McCuaig, T.C., Beresford, S., Hronsky, J., 2010. Translating the mineral systems approach into an effective exploration targeting system. Ore Geology Reviews 38, 128–138.

McCuaig, T.C., Hronsky, J.M., 2014. The mineral system concept: the key to exploration targeting. Society of Economic Geologist, Special Publication 18, 153–175.

McDowell, F.W., McIntosh, W.C., Farley, K.A., 2005. A precise 40Ar–39Ar reference age for the Durango apatite (U–Th)/He and fission-track dating standard. Chemical Geology 214, 249–263.

Meert, J.G., van der Voo, R., Ayub, S., 1995. Paleomagnetic investigation of the Neoproterozoic Gagwe lavas and Mbozi complex, Tanzania and the assembly of Gondwana. Precambrian Research 74, 225–244.

Meert, J.G., 2003. A synopsis of events related to the assembly of eastern Gondwana. Tectonophysics 362, 1–40.

Meert, J.G., Lieberman, B.S., 2008. The Neoproterozoic assembly of Gondwana and its relationship to the Ediacaran–Cambrian radiation. Gondwana Research 14, 5–21.

Mees, F., Swennen, R., Geet, M.V., Jacobs, P., 2003. Applications of X-ray computed tomography in the geosciences. Geological Society, London, Special Publications 215, 1–6.

Meffre, S., Large, R.R., Steadman, J.A., Gregory, D.D., Stepanov, A.S., Kamenetsky, V.S., Ehrig, K., Scott, R.J., 2016. Multi-stage enrichment processes for large gold-bearing ore deposits. Ore Geology Reviews 76, 268–279.

Megerssa, L., Verner, K., Buriánek, D., Sláma, J., 2020. Emplacement and thermal effect of post-collisional Chewo Pluton (Arabian-Nubian Shield); implication for late East-African Orogeny. Journal of African Earth Sciences 162, 103695.

Mehl, C., Jolivet, L., Lacombe, O., 2005. From ductile to brittle: evolution and localization of deformation below a crustal detachment (Tinos, Cyclades, Greece). Tectonics 24.

Meinhold, K.D., 1979. The Precambrian basement complex of the Bayuda Desert, northern Sudan.

Meng, Y.-M., Jébrak, M., Sasseville, C., Huang, X.-W., 2020. Geochemical and mineralogical diagnosis on gold ores: A case study from the Cadillac–Larder Lake Fault Zone, Abitibi, Canada. Ore Geology Reviews 103840.

Mercier-Langevin, P., Hannington, M.D., Dubé, B., Bécu, V., 2011. The gold content of volcanogenic massive sulfide deposits. Mineralium Deposita 46, 509–539.

Merdith, A.S., Collins, A.S., Williams, S.E., Pisarevsky, S., Foden, J.D., Archibald, D.B., Blades, M.L., Alessio, B.L., Armistead, S., Plavsa, D., Clark, C., Müller, R.D., 2017. A full-plate global reconstruction of the Neoproterozoic. Gondwana Research 50, 84–134.

Merdith, A.S., Williams, S.E., Brune, S., Collins, A.S., Müller, R.D., 2019. Rift and plate boundary evolution across two supercontinent cycles. Global and Planetary Change 173, 1–14.

Merkulova, M., Mathon, O., Glatzel, P., Rovezzi, M., Batanova, V., Marion, P., Boiron, M.-C., Manceau, A., 2019. Revealing the Chemical Form of "Invisible" Gold in Natural Arsenian Pyrite and Arsenopyrite with High Energy-Resolution X-ray Absorption Spectroscopy. ACS Earth and Space Chemistry 3, 1905–1914.

Meyer, C., 1988. Ore Deposits as Guides to Geologic History of the Earth. Annual Review of Earth and Planetary Sciences 16, 147–171.

Meyer, G.G., Brantut, N., Mitchell, T.M., Meredith, P.G., 2019. Fault reactivation and strain partitioning across the brittle-ductile transition. Geology 47, 1127–1130.

Meyer, H., Cauzid, J., 2020. hameye/MARCIA: MARCIA v 0.1.0. Zenodo.

Meyer, S.E., Passchier, C., Abu-Alam, T., Stüwe, K., 2014. A strike-slip core complex from the Najd fault system, Arabian shield. Terra Nova 26, 387–394.

Micklethwaite, S., Cox, S.F., 2004. Fault-segment rupture, aftershock-zone fluid flow, and mineralization. Geology 32, 813.

Micklethwaite, S., Ford, A., Witt, W., Sheldon, H.A., 2015. The where and how of faults, fluids and permeability - insights from fault stepovers, scaling properties and gold mineralisation. Geofluids 15, 240–251.

Micklethwaite, S., Ford, A., Witt, W., Sheldon, H.A., 2016. Transient permeability in fault stepovers and rapid rates of orogenic gold deposit formation. In: Gleeson, T., Ingebritse, S.E. (Eds.), Crustal Permeability. John Wiley & Sons, Ltd, Chichester, UK, 249–259.

Miller, C.F., Furbish, D.J., Walker, B.A., Claiborne, L.L., Koteas, G.C., Bleick, H.A., Miller, J.S., 2011. Growth of plutons by incremental emplacement of sheets in crystal-rich host: Evidence from Miocene intrusions of the Colorado River region, Nevada, USA. Tectonophysics 500, 65–77.

Miller, J.D., Lin, C.L., Garcia, C., Arias, H., 2003. Ultimate recovery in heap leaching operations as established from mineral exposure analysis by X-ray microtomography. International Journal of Mineral Processing 72, 331–340.

Miller, J.M., Wilson, C.J.L., 2004. Structural analysis of faults related to a heterogeneous stress history: reconstruction of a dismembered gold deposit, Stawell, western Lachlan Fold Belt, Australia. Journal of Structural Geology 26, 1231–1256.

Miller, J.S., Matzel, J.E., Miller, C.F., Burgess, S.D., Miller, R.B., 2007. Zircon growth and recycling during the assembly of large, composite arc plutons. Journal of Volcanology and Geothermal Research 167, 282–299.

Miller, M.M., Dixon, T.H., 1992. Late Proterozoic evolution of the northern part of the Hamisana zone, northeast Sudan: constraints on Pan-African accretionary tectonics. Journal of the Geological Society 149, 743–750.

Mitchell, R.H., Keays, R.R., 1981. Abundance and distribution of gold, palladium and iridium in some spinel and garnet lherzolites: implications for the nature and origin of precious metal-rich intergranular components in

the upper mantle. Geochimica et Cosmochimica Acta 45, 2425–2442.

Moeller, P., Kersten, G., 1994. Electrochemical accumulation of visible gold on pyrite and arsenopyrite surfaces. Mineralium Deposita 29, 404–413.

Moghazi, A.-K.M., Ali, K.A., Wilde, S.A., Zhou, Q., Andersen, T., Andresen, A., Abu El-Enen, M.M., Stern, R.J., 2012. Geochemistry, geochronology, and Sr–Nd isotopes of the Late Neoproterozoic Wadi Kid volcano-sedimentary rocks, Southern Sinai, Egypt: Implications for tectonic setting and crustal evolution. Lithos 154, 147–165.

Moghazi, A.-K.M., Iaccheri, L.M., Bakhsh, R.A., Kotov, A.B., Ali, K.A., 2015. Sources of rare-metal-bearing A-type granites from Jabel Sayed complex, Northern Arabian Shield, Saudi Arabia. Journal of Asian Earth Sciences 107, 244–258.

Mole, D.R., Kirkland, C.L., Fiorentini, M.L., Barnes, S.J., Cassidy, K.F., Isaac, C., Belousova, E.A., Hartnady, M., Thebaud, N., 2019. Time-space evolution of an Archean craton: A Hf-isotope window into continent formation. Earth-Science Reviews 196, 102831.

Moncada, D., Mutchler, S., Nieto, A., Reynolds, T.J., Rimstidt, J.D., Bodnar, R.J., 2012. Mineral textures and fluid inclusion petrography of the epithermal Ag–Au deposits at Guanajuato, Mexico: Application to exploration. Journal of Geochemical Exploration 114, 20–35.

Monteiro, R.N., Fyfe, W.S., Chemale, F., 2004. The impact of the linkage between grade distribution and petrofabric on the understanding of structurally controlled mineral deposits: Ouro Fino Gold Mine, Brazil. Journal of Structural Geology 26, 1195–1214.

Morag, N., Avigad, D., Gerdes, A., Belousova, E., Harlavan, Y., 2011. Crustal evolution and recycling in the northern Arabian-Nubian Shield: New perspectives from zircon Lu–Hf and U–Pb systematics. Precambrian Research 186, 101–116.

Morag, N., Avigad, D., Gerdes, A., Harlavan, Y., 2012. 1000–580Ma crustal evolution in the northern Arabian-Nubian Shield revealed by U–Pb–Hf of detrital zircons from late Neoproterozoic sediments (Elat area, Israel). Precambrian Research 208–211, 197–212.

Morel, M.L.A., Nebel, O., Nebel-Jacobsen, Y.J., Miller, J.S., Vroon, P.Z., 2008. Hafnium isotope characterization of the GJ-1 zircon reference material by solution and laser-ablation MC-ICPMS. Chemical Geology 255, 231–235.

Morey, A.A., Tomkins, A.G., Bierlein, F.P., Weinberg, R.F., Davidson, G.J., 2008. Bimodal distribution of gold in pyrite and arsenopyrite: Examples from the Archean Boorara and Bardoc shear systems, Yilgarn craton, Western Australia. Economic Geology 103, 599–614.

Morlot, C., Pignatelli, I., Giuliani, G., Sterpenich, J., Boiron, M.C., Ohnenstetter, D., Andriamamonjy, A., Raoul, J., Chatagner, P.Y., 2016. La tomographie de rayons X et ses applications en géologie: exemples de l'émeraude trapiche et du grenat démantoïde. Revue de Gemmologie AFG 198, 13–18.

Morrissey, L.J., Tomkins, A.G., 2020. Evaporite-bearing orogenic belts produce ligand-rich and diverse metamorphic fluids. Geochimica et Cosmochimica Acta 275, 163–187.

Moussa, E.M.M., Stern, R.J., Manton, W.I., Ali, K.A., 2008. SHRIMP zircon dating and Sm/Nd isotopic investigations of Neoproterozoic granitoids, Eastern Desert, Egypt. Precambrian Research 160, 341–356.

Mosley, P.N., 1993. Geological evolution of the late Proterozoic "Mozambique Belt" of Kenya. Tectonophysics 221, 223–250.

Moyen, J.-F., Laurent, O., Chelle-Michou, C., Couzinié, S., Vanderhaeghe, O., Zeh, A., Villaros, A., Gardien, V., 2017. Collision vs. subduction-related magmatism: Two contrasting ways of granite formation and implications for crustal growth. Lithos 277, 154–177.

Mueller, A.G., 2020. Structural setting of Fimiston- and Oroya-style pyrite-telluride-gold lodes, Paringa South mine, Golden Mile, Kalgoorlie: 1. Shear zone systems, porphyry dykes and deposit-scale alteration zones. Mineralium Deposita 55(4), 665–695.

Mueller, A.G., Hagemann, S.G., McNaughton, N.J., 2020. Neoarchean orogenic, magmatic and hydrothermal events in the Kalgoorlie-Kambalda area, Western Australia: constraints on gold mineralization in the Boulder Lefroy-Golden Mile fault system. Mineralium Deposita 55(4), 633-663.

Muir, T.L., 2002. The Hemlo gold deposit, Ontario, Canada: principal deposit characteristics and constraints on mineralization. Ore Geology Reviews 21, 1–66.

Müller, D., Groves, D.I., 1993. Direct and indirect associations between potassic igneous rocks, shoshonites and gold-copper deposits. Ore Geology Reviews 8, 383–406.

Müller, D., Franz, L., Herzig, P.M., Hunt, S., 2001. Potassic igneous rocks from the vicinity of epithermal gold mineralization, Lihir Island, Papua New Guinea. Lithos 57, 163–186.

Müller, R.D., Cannon, J., Qin, X., Watson, R.J., Gurnis, M., Williams, S., Pfaffelmoser, T., Seton, M., Russell, S.H., Zahirovic, S., 2018. GPlates: building a virtual Earth through deep time. Geochemistry, Geophysics, Geosystems 19, 2243–2261.

Mungall, J.E., 2002. Roasting the mantle: Slab melting and the genesis of major Au and Au-rich Cu deposits. Geology 30, 915–918.

Mungall, J.E., Hanley, J.J., Arndt, N.T., Debecdelievre, A., 2006. Evidence from meimechites and other low-degree mantle melts for redox controls on mantle-crust fractionation of platinum-group elements. Proceedings of the National Academy of Sciences 103, 12695–12700.

Münker, C., Cooper, R., 1999. The Cambrian arc complex of the Takaka Terrane, New Zealand: An integrated stratigraphical, paleontological and geochemical approach. New Zealand Journal of Geology and Geophysics 42, 415–445.

N, O

Neumayr, P., Hoinkes, G., Puhl, J., Mogessie, A., Khudeir, A.A., 1998. The Meatiq dome (Eastern Desert, Egypt) a Precambrian metamorphic core complex: petrological and geological evidence. Journal of Metamorphic Geology 16, 259–279.

Niiranen, T., Nykänen, V., Lahti, I., 2019. Scalability of the mineral prospectivity modelling – An orogenic gold case study from northern Finland. Ore Geology Reviews 109, 11–25.

Norcross, C., Davis, D.W., Spooner, E.T.C., Rust, A., 2000. U-Pb and Pb-Pb age constraints on Paleoproterozoic magmatism, deformation and gold mineralization in the Omai area, Guyana Shield. Precambrian Research 102, 69–86.

Nowell, M.M., Witt, R.A., True, B.W., 2005. EBSD sample preparation: Techniques, tips, and tricks. Microscopy Today 13, 44–49.

Occhipinti, S., Metelka, V., Lindsay, M., Aitken, A., Pirajno, F., Tyler, I., 2020. The evolution from plate margin to intraplate mineral systems in the Capricorn Orogen, links to prospectivity. Ore Geology Reviews 127, 103811.

O'Connor, J.T., 1965. A classification for quartz-rich igneous rocks. Geological Survey Professional Paper 525, 79.

Olierook, H.K.H., Kirkland, C.L., Szilas, K., Hollis, J.A., Gardiner, N.J., Steenfelt, A., Jiang, Q., Yakymchuk, C., Evans, N.J., McDonald, B.J., 2020. Differentiating between inherited and autocrystic zircon in granitoids. Journal of Petrology. Orca Gold Inc., 2017. GSS presentation document. Unpublished presentation document.

Omar, G.I., Steckler, M.S., Buck, W.R., Kohn, B.P., 1989. Fission-track analysis of basement apatites at the western margin of the Gulf of Suez rift, Egypt: evidence for synchroneity of uplift and subsidence. Earth and Planetary Science Letters 94, 316–328.

Orca Gold Inc, 2019. www.orcagold.com. consulted on January, 30th 2019.

Oriolo, S., Oyhantçabal, P., Wemmer, K., Siegesmund, S., 2017. Contemporaneous assembly of Western Gondwana and final Rodinia break-up: Implications for the supercontinent cycle. Geoscience Frontiers 8, 1431–1445.

Osman, A.E.M., 2014. An integrated metallotect and petrographic model for gold mineralization in the Eastern Desert of Egypt; a new prospecting vision. Journal of Egyptian Pure and Applied Sciences 52, 41–54.

P

Paces, J.B., Miller, J.D., 1993. Precise U-Pb ages of Duluth complex and related mafic intrusions, northeastern Minnesota: Geochronological insights to physical, petrogenetic, paleomagnetic, and tectonomagmatic processes associated with the 1.1 Ga midcontinent rift system. Journal of Geophysical Research: Solid Earth 98, 13997–14013.

Pallister, J.S., Stacey, J.S., Fischer, L.B., Premo, W.R., 1988. Precambrian ophiolites of arabia: geologic settings, U Pb geochronology, Pb-isotope characteristics, and implications for continental accretion. Precambrian Research 38, 1–54.Palme, H., O'Neill, H.S.C., 2003. Cosmochemical estimates of mantle composition. TrGeo 2, 568.

Paquette, J.-L., Piro, J.-L., Devidal, J.-L., Bosse, V., Didier, A., Sannac, S., Abdelnour, Y., 2014. Sensitivity enhancement in LA-ICP-MS by N2 addition to carrier gas: application to radiometric dating of U-Th-bearing minerals. Agilent ICP-MS Journal 58, 4–5.

Parra, T., Vidal, O., Agard, P., 2002. A thermodynamic model for Fe–Mg dioctahedral K white micas using data from phase-equilibrium experiments and natural pelitic assemblages. Contributions to Mineralogy and Petrology 143, 706–732.

Parry, W.T., 1998. Fault-fluid compositions from fluid-inclusion observations and solubilities of fracture-sealing minerals. Tectonophysics 290, 1–26.

Paterson, S.R., Okaya, D., Memeti, V., Economos, R., Miller, R.B., 2011. Magma addition and flux calculations of incrementally constructed magma chambers in continental margin arcs: Combined field, geochronologic, and thermal modeling studies. Geosphere 7, 1439–1468.

Paterson, S.R., Ducea, M.N., 2015. Arc magmatic tempos: Gathering the evidence. Elements 11, 91–98.

Paton, C., Hellstrom, J., Paul, B., Woodhead, J., Hergt, J., 2011. Iolite: Freeware for the visualisation and processing of mass spectrometric data. Journal of Analytical Atomic Spectrometry 26, 2508–2518.

Patriat, M., Collot, J., Danyushevsky, L., Fabre, M., Meffre, S., Falloon, T., Rouillard, P., Pelletier, B., Roach, M., Fournier, M., 2015. Propagation of back-arc extension into the arc lithosphere in the southern New Hebrides volcanic arc: PROPAGATION OF BACK-ARC EXTENSION IN ARC. Geochemistry, Geophysics, Geosystems 16, 3142–3159.

Passchier, C.W., Trouw, R.A.J., 2005. Microtectonics, 2nd edition. ed. Springer, Berlin, New-York.

Paterson, S.R., Ducea, M.N., 2015. Arc magmatic tempos: Gathering the evidence. Elements 11, 91–98.

Paton, C., Hellstrom, J., Paul, B., Woodhead, J., Hergt, J., 2011. Iolite: Freeware for the visualisation and processing of mass spectrometric data. Journal of Analytical Atomic Spectrometry 26, 2508–2518.

Perelló, J., Sillitoe, R.H., Brockway, H., García, A., 2020. Metallogenic inception of the Arabian-Nubian Shield: Daero Paulos porphyry copper prospect, Eritrea. Gondwana Research 88, 106–125.

Perret, J., André-Mayer, A.-S., Peiffert, C., Ciancaleoni, L., Bosc, R., Barrie, C.T., 2017. Microstructural features and trace element contents of the sulphide generations in the Hadal Awatib Eat Cu -Au (±Zn -Ag) VMS deposit (Red Sea Hills, NE Sudan)., Proceedings of the 14th SGA Biennial Meeting, 20-23 August 2017, Québec City, Canada 685–688.

Perret, J., Eglinger, A., Feneyrol, J., André-Mayer, A.-S., Bosc, R., Hartshorne, C., Abanyin, E., 2019. The structural control on the gold mineralization at the Galat Sufar South deposit (Block 14, NE Sudan). Proceedings of the 15th SGA Biennial Meeting. Presented at the 15th SGA Biennial Meeting, Society for Geology Applied to Mineral Deposits, Glasgow, Scotland, 631–634.

Perret, J., Eglinger, A., André-Mayer, A.-S., Aillères, L., Feneyrol, J., Hartshorne, C., Abanyin, E., Bosc, R., 2020. Subvertical, linear and progressive deformation related to gold mineralization at the Galat Sufar South deposit, Nubian Shield, NE Sudan. Journal of Structural Geology 135, 104032.

Perrouty, S., Jessell, M.W., Bourassa, Y., Miller, J., Apau, D., Siebenaller, L., Velásquez, G., Baratoux, L., Aillères,

L., Béziat, D., Salvi, S., 2015. The Wassa deposit: A poly-deformed orogenic gold system in southwest Ghana – Implications for regional exploration. Journal of African Earth Sciences 112, 536–547.

Peterson, E.C., Mavrogenes, J.A., 2014. Linking high-grade gold mineralization to earthquake-induced fault-valve processes in the Porgera gold deposit, Papua New Guinea. Geology 42, 383–386.

Petrella, L., Thébaud, N., LaFlamme, C., Miller, J., McFarlane, C., Occhipinti, S., Turner, S., Perazzo, S., 2019. Contemporaneous formation of vein-hosted and stratabound gold mineralization at the world-class Dead Bullock Soak mining camp, Australia. Mineralium Deposita, 1–18.

Petrella, L., Thébaud, N., Fougerouse, D., Evans, K., Quadir, Z., Laflamme, C., 2020. Colloidal gold transport: a key to high-grade gold mineralization? Mineralium Deposita 55(7), 1247–1254.

Petrus, J.A., Chew, D.M., Leybourne, M.I., Kamber, B.S., 2017. A new approach to laser-ablation inductively-coupled-plasma mass-spectrometry (LA-ICP-MS) using the flexible map interrogation tool 'Monocle.' Chemical Geology 463, 76–93.

Phillips, G.N., Evans, K.A., 2004. Role of CO2 in the formation of gold deposits. Nature 429, 860–863.

Phillips, G.N., Powell, R., 2009. Formation of gold deposits: Review and evaluation of the continuum model. Earth-Science Reviews 94, 1–21.

Phillips, G.N., Powell, R., 2010. Formation of gold deposits: a metamorphic devolatilization model. Journal of Metamorphic Geology 28, 689–718.

Piazolo, S., Jessell, M.W., Prior, D.J., Bons, P.D., 2004. The integration of experimental in-situ EBSD observations and numerical simulations: a novel technique of microstructural process analysis. Journal of Microscopy 213, 273–284.

Pin, C., Briot, D., Bassin, C., Poitrasson, F., 1994. Concomitant separation of strontium and samarium-neodymium for isotopic analysis in silicate samples, based on specific extraction chromatography. Analytica Chimica Acta 298, 209–217.

Pin, C., Zalduegui, J.S., 1997. Sequential separation of light rare-earth elements, thorium and uranium by miniaturized extraction chromatography: application to isotopic analyses of silicate rocks. Analytica Chimica Acta 339, 79–89.

Pitcairn, I.K., Teagle, D.A.H., Craw, D., Olivo, G.R., Kerrich, R., Brewer, T.S., 2006. Sources of Metals and Fluids in Orogenic Gold Deposits: Insights from the Otago and Alpine Schists, New Zealand. Economic Geology 101, 1525–1546.

Pitcairn, I.K., Olivo, G.R., Teagle, D.A.H., Craw, D., 2010. Sulfide evolution during prograde metamorphism of the Otago and Alpine schists, New Zealand. The Canadian Mineralogist 48, 1267–1295.

Pitcairn, I.K., 2011. Background concentrations of gold in different rock types. Applied Earth Science 120, 31–38.

Pitcairn, I.K., Craw, D., Teagle, D.A.H., 2014. The gold conveyor belt: Large-scale gold mobility in an active orogen. Ore Geology Reviews 62, 129–142.

Pitcairn, I.K., Craw, D., Teagle, D.A.H., 2015. Metabasalts as sources of metals in orogenic gold deposits. Mineralium Deposita 50, 373–390.

Plyley, B., Kachrillo, J.J., Bennett, M., Bosc, R., Barrie, C.T., 2009. Hadal Awatib East Cu-Au VMS Deposit, Sudan Ressources Estimates. NI 43-101 Technical Report.

Pochon, A., Poujol, M., Gloaguen, E., Branquet, Y., Cagnard, F., Gumiaux, C., Gapais, D., 2016. U-Pb LA-ICP-MS dating of apatite in mafic rocks: Evidence for a major magmatic event at the Devonian-Carboniferous boundary in the Armorican Massif (France). American Mineralogist 101, 2430–2442.

Pokrovski, G.S., Borisova, A.Yu., Harrichoury, J.-C., 2008. The effect of sulfur on vapor–liquid fractionation of metals in hydrothermal systems. Earth and Planetary Science Letters 266, 345–362.

Pokrovski, G.S., Akinfiev, N.N., Borisova, A.Y., Zotov, A.V., Kouzmanov, K., 2014. Gold speciation and transport in geological fluids: insights from experiments and physical-chemical modelling. Geological Society, London, Special Publications 402, 9–70.

Pokrovski, G.S., Dubessy, J., 2015. Stability and abundance of the trisulfur radical ion S3− in hydrothermal fluids. Earth and Planetary Science Letters 411, 298–309.

Pokrovski, G.S., Kokh, M.A., Guillaume, D., Borisova, A.Y., Gisquet, P., Hazemann, J.-L., Lahera, E., Del Net, W., Proux, O., Testemale, D., Haigis, V., Jonchière, R., Seitsonen, A.P., Ferlat, G., Vuilleumier, R., Saitta, A.M., Boiron, M.-C., Dubessy, J., 2015. Sulfur radical species form gold deposits on Earth. Proceedings of the National Academy of Sciences 112, 13484–13489.

Pokrovski, G.S., Kokh, M.A., Proux, O., Hazemann, J.-L., Bazarkina, E.F., Testemale, D., Escoda, C., Boiron, M.-C., Blanchard, M., Aigouy, T., Gouy, S., de Parseval, P., Thibaut, M., 2019. The nature and partitioning of invisible gold in the pyrite-fluid system. Ore Geology Reviews 109, 545–563.

Polat, A., Appel, P.W.U., Fryer, B., Windley, B., Frei, R., Samson, I.M., Huang, H., 2009. Trace element systematics of the Neoarchean Fiskenæsset anorthosite complex and associated meta-volcanic rocks, SW Greenland: Evidence for a magmatic arc origin. Precambrian Research 175, 87–115.

Powell, R., Will, T.M., Phillips, G.N., 1991. Metamorphism in Archaean greenstone belts: calculated fluid compositions and implications for gold mineralization. Journal of Metamorphic Geology 9, 141–150.

Price, B.J., 1972. Minor elements in pyrites from the smithers map area, bc and exploration applications of minor element studies. University of British Columbia.

Prichard, H.M., Barnes, S.J., Godel, B., 2018. A mechanism for chromite growth in ophiolite complexes: evidence from 3D high-resolution X-ray computed tomography images of chromite grains in Harold's Grave chromitite in the Shetland ophiolite. Mineralogical Magazine 82, 457–470.

Prior, D.J., Mariani, E., Wheeler, J., 2009. EBSD in the Earth Sciences: Applications, Common Practice, and Challenges. In: Schwartz, A.J., Kumar, M., Adams, B.L., Field, D.P. (Eds.), Electron Backscatter Diffraction in Materials Science. Springer US, Boston, MA, 345–360.

Q, R

Rabeau, O., Royer, J.-J., Jébrak, M., Cheilletz, A., 2013. Log-uniform distribution of gold deposits along major Archean fault zones. Mineralium Deposita 48, 817–824.

Rahman, E.M.A., Harms, U., Schandelmeier, H., Franz, G., Darbyshire, D.P.F., Horn, P., Müller-Sohnius, D., 1990. A new ophiolite occurrence in NW Sudan ? constraints on Late Proterozoic tectonism. Terra Nova 2, 363–376.

Ramadan, T.M., Abdel Fattah, M.F., 2010. Characterization of gold mineralization in Garin Hawal area, Kebbi State, NW Nigeria, using remote sensing. The Egyptian Journal of Remote Sensing and Space Sciences 13, 153–163.

Ramsay, J.G., 1962. Interference patterns produced by the superposition of folds of similar type. The Journal of Geology 70, 466–481.

Ramsay, J.G., Graham, R.H., 1970. Strain variation in shear belts. Canadian Journal of Earth Sciences 7, 786–813.

Ramsay, J.G., 1980. The crack–seal mechanism of rock deformation. Nature 284, 135–139.

Reber, J.E., Dabrowski, M., Galland, O., Schmid, D.W., 2013. Sheath fold morphology in simple shear. Journal of Structural Geology 53, 15–26.

Reddy, S.M., Hough, R.M., 2013. Microstructural evolution and trace element mobility in Witwatersrand pyrite. Contributions to Mineralogy and Petrology 166, 1269–1284.

Reddy, S.M., Saxey, D.W., Rickard, W.D.A., Fougerouse, D., Montalvo, S.D., Verberne, R., Riessen, A., 2020. Atom Probe Tomography: Development and Application to the Geosciences. Geostandards and Geoanalytical Research 44, 5–50.

Rehman, H.U., Mainprice, D., Barou, F., Yamamoto, H., Okamoto, K., 2016. EBSD-measured crystal preferred orientation of eclogites from the Sanbagawa metamorphic belt, central Shikoku, SW Japan. European Journal of Mineralogy 28, 1155–1168.

Reich, M., Kesler, S.E., Utsunomiya, S., Palenik, C.S., Chryssoulis, S.L., Ewing, R.C., 2005. Solubility of gold in arsenian pyrite. Geochimica et Cosmochimica Acta 69, 2781–2796.

Reich, M., Large, R., Deditius, A.P., 2017. New advances in trace element geochemistry of ore minerals and accessory phases. Ore Geology Reviews 81, 1215–1217.

Reimann, C., Ladenberger, A., Birke, M., de Caritat, P., 2016. Low density geochemical mapping and mineral exploration: application of the mineral system concept. Geochemistry: Exploration, Environment, Analysis 16, 48–61.

Reischmann, Th., Bachtadse, V., Kröner, A., Layer, P., 1992. Geochronology and palaeomagnetism of a late Proterozoic island arc terrane from the Red Sea Hills, northeast Sudan. Earth and Planetary Science Letters 114, 1–15.

Ribeiro, J.M., Ishizuka, O., Lee, C.-T.A., Girard, G., 2020. Evolution and maturation of the nascent Mariana arc. Earth and Planetary Science Letters 530, 115912.

Richard, A., Morlot, C., Créon, L., Beaudoin, N., Balistky, V.S., Pentelei, S., Dyja-Person, V., Giuliani, G., Pignatelli, I., Legros, H., Sterpenich, J., Pironon, J., 2019. Advances in 3D imaging and volumetric reconstruction of fluid and melt inclusions by high resolution X-ray computed tomography. Chemical Geology 508, 3–14.

Richards, J.P., Tosdal, R.M., 2001. Structural controls on ore genesis. Society of Economic Geologists.

Richards, J.P., 2011. Magmatic to hydrothermal metal fluxes in convergent and collided margins. Ore Geology Reviews 40, 1–26.

Richards, J.P., 2013. Giant ore deposits formed by optimal alignments and combinations of geological processes. Nature Geoscience 6, 911.

Richards, J.P., 2015. The oxidation state, and sulfur and Cu contents of arc magmas: implications for metallogeny. Lithos 233, 27–45.

Ridley, J., 1993. The relations between mean rock stress and fluid flow in the crust: With reference to vein- and lode-style gold deposits. Ore Geology Reviews 8, 23–37.

Ries, A.C., Shackleton, R.M., Graham, R.H., Fitches, W.R., 1983. Pan-African structures, ophiolites and mélange in the Eastem Desert of Egypt: a traverse at 26 N. Journal of the Geological Society 140, 75–95.

Ries, A.C., Shackleton, R.M., Dawoud, A.S., 1985. Geochronology, geochemistry and tectonics of the NE Bayuda Desert, N Sudan: Implications for the western margin of the late Proterozoic fold belt of NE Africa. Precambrian Research 30, 43–62.

Ries, A.C., Vearncombe, J.R., Price, R.C., Shackleton, R.M., 1992. Geochronology and geochemistry of the rocks associated with a late Proterozoic ophiolite in West Pokot, NW Kenya. Journal of African Earth Sciences (and the Middle East) 14, 25–35.

Robb, L., 2005. Introduction to ore-forming processes, Blackwell Publishing. ed.

Robert, F., Poulsen, K.H., Dubé, P., 1997. Gold Deposits and Their Geological Classification. Presented at the Fourth Decennial International Conference on Mineral Exploration, Gubins, A.G., Toronto, 209–220.

Robert, F., Poulsen, K.H., 2001. Vein formation and deformation in greenstone gold deposits. Reviews in Economic Geology 14, 111–155.

Robinson, F.A., Foden, J.D., Collins, A.S., Payne, J.L., 2014. Arabian Shield magmatic cycles and their relationship with Gondwana assembly: Insights from zircon U–Pb and Hf isotopes. Earth and Planetary Science Letters 408, 207–225.

Robinson, F. A., Foden, J.D., Collins, A.S., 2015a. Zircon Geochemical and Geochronological Constraints on Contaminated and Enriched Mantle Sources beneath the Arabian Shield, Saudi Arabia. The Journal of Geology 123, 463–489.

Robinson, F.A., Foden, J.D., Collins, A.S., 2015b. Geochemical and isotopic constraints on island arc, synorogenic, post-orogenic and anorogenic granitoids in the Arabian Shield, Saudi Arabia. Lithos 220–223, 97–115.

Roeder, D., Roberts, D.G., Bally, A.W., 2013. Convergent margins and orogenic belts. Regional Geology and Tectonics: Principles of Geologic Analysis A 1, 114–177.

Román, N., Reich, M., Leisen, M., Morata, D., Barra, F., Deditius, A.P., 2019. Geochemical and micro-textural fingerprints of boiling in pyrite. Geochimica et Cosmochimica Acta 246, 60–85.

Rosière, C.A., Siemes, H., Quade, H., Brokmeier, H.-G., Jansen, E.M., 2001. Microstructures, textures and deformation mechanisms in hematite. Journal of Structural Geology 23, 1429–1440.

Rosière, C.A., Garcia, O.L., Siemes, H., Schaeben, H., 2013. Domainal fabrics of hematite in schistose, shear zone-hosted high-grade Fe ores: The product of the interplay between deformation and mineralization. Journal of Structural Geology 55, 150–166.

Rowland, J.V., Rhys, D.A. (Eds.), 2020. Applied Structural Geology Of Ore-Forming Hydrothermal Systems. Reviews in Economic Geology 21, 329.

Rudnick, R.L., Gao, S., 2003. Composition of the continental crust. The Crust 3, 1–64.

Rutter, E.H., 1986. On the nomenclature of mode of failure transitions in rocks. Tectonophysics 122, 381–387.

S

Saeed, A., Zeng, Z., Dilek, Y., Awadelseid, S.F., Abdel Rahman, A.A., Adam, M.M.A., 2020. Geochronology, geochemistry, and Hf–Sr-Nd isotopes of the Hamisana Shear Zone granitoids in northeastern Sudan: Petrogenesis and tectonic evolution of neoproterozoic juvenile crust in the Nubian Shield. Precambrian Research 347, 105857.

Salem, S.M., El Sharkawi, M., El-Alfy, Z., Soliman, N.M., Ahmed, S.E., 2016. Exploration of gold occurrences in alteration zones at Dungash district, Southeastern Desert of Egypt using ASTER data and geochemical analyses. Journal of African Earth Sciences 117, 389–400.

Salvi, S., Velásquez, G., Miller, J.M., Béziat, D., Siebenaller, L., Bourassa, Y., 2016. The Pampe gold deposit (Ghana): Constraints on sulfide evolution during gold mineralization. Ore Geology Reviews 78, 673–686.

Santos, M.M., Lana, C., Scholz, R., Buick, I., Schmitz, M.D., Kamo, S.L., Gerdes, A., Corfu, F., Tapster, S., Lancaster, P., 2017. A new appraisal of Sri Lankan BB zircon as a reference material for LA-ICP-MS U-Pb geochronology and Lu-Hf isotope tracing. Geostandards and Geoanalytical Research 41, 335–358.

Santosh, M., Maruyama, S., Sato, K., 2009. Anatomy of a Cambrian suture in Gondwana: Pacific-type orogeny in southern India? Gondwana Research 16, 321–341.

Saunders, J.E., Pearson, N.J., O'Reilly, S.Y., Griffin, W.L., 2018. Gold in the mantle: A global assessment of abundance and noredistribution processes. Lithos 322, 376–391.

Sawkins, F.J., 1990. Metal Deposits in Relation to Plate Tectonics. Springer Berlin, Berlin.

Sayab, M., Suuronen, J.-P., Hölttä, P., Aerden, D., Lahtinen, R., Kallonen, A.P., 2015. High-resolution X-ray computed microtomography: A holistic approach to metamorphic fabric analyses. Geology 43, 55–58.

Sayab, M., Suuronen, J.-P., Molnár, F., Villanova, J., Kallonen, A., O'Brien, H., Lahtinen, R., Lehtonen, M., 2016. Three-dimensional textural and quantitative analyses of orogenic gold at the nanoscale. Geology 44, 739–742.

Sayab, M., Molnár, F., Aerden, D., Niiranen, T., Kuva, J., Välimaa, J., 2020. A succession of near-orthogonal horizontal tectonic shortenings in the Paleoproterozoic Central Lapland Greenstone Belt of Fennoscandia: constraints from the world-class Suurikuusikko gold deposit. Mineralium Deposita 55, 1605–1624.

Schandelmeier, H., Abdel Rahman, E.M., Wipfler, E., Kuster, D., Utke, A., Matheis, G., 1994a. Late Proterozoic magmatism in the Nakasib suture, Red Sea Hills, Sudan. Journal of the Geological Society 151, 485–497.

Schandelmeier, H., Wipfler, E., Küster, D., Sultan, M., Becker, R., Stern, R.J., Abdelsalam, M.G., 1994b. Atmur-Delgo suture: A Neoproterozoic oceanic basin extending into the interior of northeast Africa. Geology 22(6), 563–566.

Schandelmeier, H., Reynolds, P.O., 1997. Paleogeographic–Paleotectonic Atlas of North–Eastern Africa. Arabia and Adjacent Areas: Rotterdam, Netherlands, Balkema.

Schmidt, G., Witt-Eickschen, G., Palme, H., Seck, H., Spettel, B., Kratz, K.-L., 2003. Highly siderophile elements (PGE, Re and Au) in mantle xenoliths from the West Eifel volcanic field (Germany). Chemical Geology 196, 77–105.

Schmitt, R. da S., Fragoso, R. de A., Collins, A.S., 2018. Suturing Gondwana in the Cambrian: The Orogenic Events of the Final Amalgamation. In: Siegesmund, S., Basei, M.A.S., Oyhantçabal, P., Oriolo, S. (Eds.), Geology of Southwest Gondwana, Regional Geology Reviews. Springer International Publishing, Cham, 411–432.

Schoene, B., Bowring, S.A., 2006. U–Pb systematics of the McClure Mountain syenite: thermochronological constraints on the age of the 40 Ar/39 Ar standard MMhb. Contributions to Mineralogy and Petrology 151, 615.

Schwartz, A.J., Kumar, M., Adams, B.L., Field, D.P. (Eds.), 2009. Electron Backscatter Diffraction in Materials Science. Springer US, Boston, MA.

Schwarzer, R.A., Field, D.P., Adams, B.L., Kumar, M., Schwartz, A.J., 2009. Present state of electron backscatter diffraction and prospective developments. Electron Backscatter Diffraction in Materials Science. Springer, 1–20.

Sehsah, H., Eldosouky, A.M., 2020. Neoproterozoic hybrid forearc – MOR ophiolite belts in the northern Arabian-Nubian Shield: no evidence for back-arc tectonic setting. International Geology Review 1–13.

Seton, M., Müller, R.D., Zahirovic, S., Gaina, C., Torsvik, T., Shephard, G., Talsma, A., Gurnis, M., Turner, M., Maus, S., 2012. Global continental and ocean basin reconstructions since 200 Ma. Earth-Science Reviews 113, 212–270.

Seward, T.M., 1973. Thio complexes of gold and the transport of gold in hydrothermal ore solutions. Geochimica et Cosmochimica Acta 37, 379–399.

Shackleton, R.M., Ries, A.C., Graham, R.H., Fitches, W.R., 1980. Late Precambrian ophiolitic melange in the Eastern Desert of Egypt. Nature 285, 472–474.

Shackleton, R.M., Ries, A.C., 1984. The relation between regionally consistent stretching lineations and plate motions. Journal of Structural Geology 6, 111–117.

Shackleton, R.M., 1986. Precambrian collision tectonics in Africa. Geological Society, London, Special Publications 19, 329–349.

Shalaby, A., Stüwe, K., Makroum, F., Fritz, H., Kebede, T., Klötzli, U., 2005. The Wadi Mubarak belt, Eastern Desert of Egypt: a Neoproterozoic conjugate shear system in the Arabian–Nubian Shield. Precambrian Research 136, 27–50.

Shand, S.J., 1943. Eruptive rocks: their genesis, composition, and classification, with a chapter on meteorites. J. Wiley & sons, Incorporated.

Shang, C.K., Morteani, G., Satir, M., Taubald, H., 2010a. Neoproterozoic continental growth prior to Gondwana assembly: Constraints from zircon–titanite geochronology, geochemistry and petrography of ring complex granitoids, Sudan. Lithos 118, 61–81.

Shang, C.K., Satir, M., Morteani, G., Taubald, H., 2010b. Zircon and titanite age evidence for coeval granitization and migmatization of the early Middle and early Late Proterozoic Saharan Metacraton; example from the central North Sudan basement. Journal of African Earth Sciences 57, 492–524.

Sláma, J., Košler, J., Condon, D.J., Crowley, J.L., Gerdes, A., Hanchar, J.M., Horstwood, M.S., Morris, G.A., Nasdala, L., Norberg, N., 2008. Plešovice zircon—a new natural reference material for U–Pb and Hf isotopic microanalysis. Chemical Geology 249, 1–35.

Sibson, R.H., Robert, F., Poulsen, K.H., 1988. High-angle reverse faults, fluid-pressure cycling, and mesothermal gold-quartz deposits. Geology 16, 551–555.

Sibson, R.H., 1990. Conditions for fault-valve behaviour. Geological Society, London, Special Publications 54, 15–28.

Sibson, R.H., Scott, J., 1998. Stress/fault controls on the containment and release of overpressured fluids: Examples from gold-quartz vein systems in Juneau, Alaska; Victoria, Australia and Otago, New Zealand. Ore Geology Reviews 13, 293–306.

Sibson, R.H., 2001. Seismogenic framework for hydrothermal transport and ore deposition. Rev. Econ. Geol. 14, 25–50.

Sibson, R.H., 2020a. Dual-Driven Fault Failure in the Lower Seismogenic Zone. Bulletin of the Seismological Society of America 110, 850–862.

Sibson, R.H., 2020b. Preparation zones for large crustal earthquakes consequent on fault-valve action. Earth, Planets and Space 72, 1–20.

Siddorn, J.P., 2011. The Giant-Con gold deposite: a once-linked Archean lode-gold system. PhD Thesis. University of Toronto.

Sillitoe, R.H., 1991. Intrusion-related gold deposits. Gold Metallogeny and Exploration. Springer, 165–209.

Sillitoe, R.H., 1997. Characteristics and controls of the largest porphyry copper-gold and epithermal gold deposits in the circum-Pacific region. Australian Journal of Earth Sciences 44, 373–388.

Sillitoe, R.H., Thompson, J.F., 1998. Intrusion–Related Vein Gold Deposits: Types, Tectono-Magmatic Settings and Difficulties of Distinction from Orogenic Gold Deposits. Resource Geology 48, 237–250.

Sillitoe, R.H., 2000. Gold-rich porphyry deposits: descriptive and genetic models and their role in exploration and discovery. Society of Economic Geologists Reviews 13, 315–345.

Sillitoe, R.H., 2008. Special paper: major gold deposits and belts of the North and South American Cordillera: distribution, tectonomagmatic settings, and metallogenic considerations. Economic Geology 103, 663–687.

Sillitoe, R.H., 2020. Gold Deposit Types: an Overview. Geology of the World's Major Gold Deposits and Provinces, Society of Economic Geologists Special Publication. 1–28.

Simard, M., Gaboury, D., Daigneault, R., Mercier-Langevin, P., 2013. Multistage gold mineralization at the Lapa mine, Abitibi Subprovince: insights into auriferous hydrothermal and metasomatic processes in the Cadillac–Larder Lake Fault Zone. Mineralium Deposita 48, 883–905.

Simon, A.C., Ripley, E.M., 2011. The Role of Magmatic Sulfur in the Formation of Ore Deposits. Reviews in Mineralogy and Geochemistry 73, 513–578.

Skirrow, R.G., Davidson, G.J., 2007. A special issue devoted to Proterozoic iron oxide Cu-Au-(U) and gold mineral systems of the Gawler Craton: preface. Economic Geology 102, 1373–1375.

SKUA-GOCAD- Paradigm® 15, 2015. Software consulted on. http://www.pdgm.com.

Snoke, A.W., Tullis, J., Todd, V.R., 1998. The Princeton Atlas of Fault-related Rocks. Princeton University Press.

Solé, V.A., Papillon, E., Cotte, M., Walter, Ph., Susini, J., 2007. A multiplatform code for the analysis of energy-dispersive X-ray fluorescence spectra. Spectrochimica Acta Part B: Atomic Spectroscopy 62, 63–68.

Soltani Dehnavi, A., McFarlane, C.R.M., Lentz, D.R., Walker, J.A., 2018. Assessment of pyrite composition by LA-ICP-MS techniques from massive sulfide deposits of the Bathurst Mining Camp, Canada: From textural and chemical evolution to its application as a vectoring tool for the exploration of VMS deposits. Ore Geology Reviews 92, 656–671.

Spencer, C.J., Hawkesworth, C., Cawood, P.A., Dhuime, B., 2013. Not all supercontinents are created equal: Gondwana-Rodinia case study. Geology 41, 795–798.

Spooner, E.T., Barrie, C.T., 1993. A special issue devoted to Abitibi ore deposits in a modern context; preface. Economic Geology 88, 1307–1322.

Sprague, K., de Kemp, E., Wong, W., McGaughey, J., Perron, G., Barrie, T., 2006. Spatial targeting using queries in a 3-D GIS environment with application to mineral exploration. Computers & Geosciences 32, 396–418.

Stacey, J.S., Kramers, J.D., 1975. Approximation of terrestrial lead isotope evolution by a two-stage model. Earth and Planetary Science Letters 26, 207–221.

Stacey, J.S., Hedge, C.E., 1984. Geochronologic and isotopic evidence for early Proterozoic crust in the eastern Arabian Shield. Geology 12, 310–313.

Stacey, J.S., Agar, R.A., 1985. U-Pb Isotopic evidence for the accretion of a continental microplate in the Zalm region of the Saudi Arabian Shield. Journal of the Geological Society 142, 1189–1203.

Steiger, R.H., Jäger, E., 1977. Subcommission on geochronology: convention on the use of decay constants

in geo-and cosmochronology. Earth and Planetary Science Letters 36, 359–362.

Stein, H.J., 2014. Dating and Tracing the History of Ore Formation. Treatise on Geochemistry. Elsevier, 87–118.

Stern, R.J., Hedge, C.E., 1985. Geochronologic and isotopic constraints on late Precambrian crustal evolution in the Eastern Desert of Egypt. American Journal of Science 285, 97–127.

Stern, R.J., Manton, W.I., 1987. Age of Feiran basement rocks, Sinai: implications for late Precambrian crustal evolution in the northern Arabian-Nubian Shield. Journal of the Geological Society, London 144, 569–575.

Stern, R.J., Kröner, A., Manton, W.I., Reischmann, T., Mansour, M., Hussein, I.M., 1989. Geochronology of the late Precambrian Hamisana shear zone, Red sea Hills, Sudan and Egypt. Journal of the Geological Society 146, 1017–1029.

Stern, R.J., Kröner, A., 1993. Late Precambrian Crustal Evolution in NE Sudan: Isotopic and Geochronologic Constraints. The Journal of Geology 101, 555–574.

Stern, R.J., Abdelsalam, M.G., Schandelmeier, H., Sultan, M., Wickham, S., 1993. Carbonates of the Keraf Zone, NE Sudan; a Neoproterozoic (ca. 750Ma) passive margin on the eastern flank of West Gondwanaland. Geological Society of America Annual Meeting, Abstracts with Programs. A49.

Stern, R.J., 1994. Arc Assembly and Continental Collision in the Neoproterozoic East African Orogen: Implications for the Consolidation of Gondwanaland. Annual Review of Earth and Planetary Sciences 22, 319–351.

Stern, R.J., Kröner, A., Bender, R., Reischmann, T., Dawoud, A.S., 1994. Precambrian basement around Wadi Haifa, Sudan: a new perspective on the evolution of the East Saharan Craton. Geologische Rundschau 83, 564–577.

Stern, R.J., Abdelsalam, M.G., 1998. Formation of juvenile continental crust in the Arabian-Nubian shield: evidence from granitic rocks of the Nakasib suture, NE Sudan. Geologische Rundschau 87, 150–160.

Stern, R. J., Ali, K.A., Liegeois, J.P., Johnson, P.R., Kozdroj, W., Kattan, F.H., 2010a. Distribution and significance of pre-Neoproterozoic zircons in juvenile Neoproterozoic igneous rocks of the Arabian-Nubian Shield. American Journal of Science 310, 791–811.

Stern, R.J., Ali, K., Andresen, A., Wilde, S., Abu-El-Enen, M., Hassan, I., 2010b. Results of geochronological investigations in Sinai undertaken as part of the 2008 JEBEL field trip. JEBEL Project October 2009 Field Excursion to the Midyan Terrane, Kingdom of Saudi Arabia with Reports on Research by Participants in the JEBEL Project. 46–51.

Stern, R.J., Ali, K.A., Abdelsalam, M.G., Wilde, S.A., Zhou, Q., 2012. U–Pb zircon geochronology of the eastern part of the Southern Ethiopian Shield. Precambrian Research 206, 159–167.

Stern, R.J., Ali, K., Asimow, P.D., Azer, M.K., Leybourne, M.I., Mubarak, H.S., Ren, M., Romer, R.L., Whitehouse, M.J., 2020. The Atud Gabbro-Diorite Complex: Glimpse of the Cryogenian Mixing, Assimilation, Storage, and Homogenization Zone beneath the Eastern Desert of Egypt. Journal of the Geological Society *177*(5), 965–980.

Stoeser, D.B., Stacey, J.S., 1988. Evolution, U-Pb geochronology, and isotope geology of the Pan-African Nabitah orogenic belt of the Saudi Arabian Shield. The Pan-African Belt of Northeast Africa and Adjacent Areas. Braunschweig/Wiesbaden, Vieweg and Sohn 227–288.

Stoeser, D.B., Frost, C.D., 2006. Nd, Pb, Sr, and O isotopic characterization of Saudi Arabian Shield terranes. Chemical Geology 226, 163–188.

Streckeisen, A., 1976. To each plutonic rock its proper name. Earth-Science Reviews 12, 1–33.

Sturchio, N., Sultan, M., Sylvester, P., Batiza, R., Hedge, C., 1984. Geology, age, and origin of the Meatiq Dome: implications for the Precambrian stratigraphy and tectonic evolution of the Eastern Desert of Egypt.

Sultan, M., Tuckler, R.D., Gharbawi, R.I., Ragab, A.I., El Alfy, Z., 1993. On the location of the boundary between the Nubian Shield and the old African continent: inferences from U–Pb (zircon) and common Pb data. Geoscientific Research in Northeast Africa 75–77.

Sultan, M., Tucker, R.D., El Alfy, Z., Attia, R., Ragab, A.G., 1994. U-Pb (zircon) ages for the gneissic terrane west of the Nile, southern Egypt. Geologische Rundschau 83, 514–522.

Sun, S.-S., McDonough, W.F., 1989. Chemical and isotopic systematics of oceanic basalts: implications for mantle composition and processes. Geological Society, London, Special Publications 42, 313–345.

Sun, W., Arculus, R.J., Kamenetsky, V.S., Binns, R.A., 2004. Release of gold-bearing fluids in convergent margin magmas prompted by magnetite crystallization. Nature 431, 975–978.

Sung, Y.-H., Brugger, J., Ciobanu, C.L., Pring, A., Skinner, W., Nugus, M., 2009. Invisible gold in arsenian pyrite and arsenopyrite from a multistage Archaean gold deposit: Sunrise Dam, Eastern Goldfields Province, Western Australia. Mineralium Deposita 44, 765–791.

Suuronen, J.-P., Sayab, M., 2018. 3D nanopetrography and chemical imaging of datable zircons by synchrotron multimodal X-ray tomography. Scientific Reports 8, 1–13.

T

Tadesse, T., Suzuki, K., Hoshino, M., 1997. Chemical Th–U total Pb isochron age of zircon from the Mareb Granite in northern Ethiopia. J. Earth Planet. Sci. Negoya Uni 44, 21–27.

Tadesse, S., Milesi, J.-P., Deschamps, Y., 2000. Geology and Mineral Map of Ethiopia, scale 1:2000000.

Takenaka, L.B., Lana, C., Scholz, R., Nalini Jr, H.A., de Abreu, A.T., 2015. Optimization of the in-situ U–Pb age dating method via LA-Quadrupole-ICP-MS with applications to the timing of U–Zr–Mo mineralization in the Poços de Caldas Alkaline Complex, SE Brazil. Journal of South American Earth Sciences 62, 70–79.

Tanaka, T., Togashi, S., Kamioka, H., Amakawa, H., Kagami, H., Hamamoto, T., Yuhara, M., Orihashi, Y., Yoneda, S., Shimizu, H., 2000. JNdi-1: a neodymium

isotopic reference in consistency with LaJolla neodymium. Chemical Geology 168, 279–281.

Tardani, D., Reich, M., Deditius, A.P., Chryssoulis, S., Sánchez-Alfaro, P., Wrage, J., Roberts, M.P., 2017. Copper–arsenic decoupling in an active geothermal system: A link between pyrite and fluid composition. Geochimica et Cosmochimica Acta 204, 179–204.

Tatsumi, Y., Oguri, K., Shimoda, G., 1999. The behaviour of platinum-group elements during magmatic differentiation in Hawaiian tholeiites. Geochemical Journal 33, 237–247.

Tatsumi, Y., Oguri, K., Shimoda, G., Kogiso, T., Barsczus, H.G., 2000. Contrasting behavior of noble-metal elements during magmatic differentiation in basalts from the Cook Islands, Polynesia. Geology 28, 131–134.

Taylor, B.E., 2007. Epithermal gold deposits. Mineral Deposits of Canada: A Synthesis of Major Deposit-Types, District Metallogeny, the Evolution of Geological Provinces, and Exploration Methods: Geological Association of Canada, Mineral Deposits Division, Special Publication 5, 113–139.

Taylor, S.R., McLennan, S.M., 1985. The continental crust: its composition and evolution, Blackwell Scientific. ed. Oxford.

Taylor, S.R., McLennan, S.M., 1995. The geochemical evolution of the continental crust. Reviews of Geophysics 33, 241–265.

Teklay, M., Kröner, A., Mezger, K., Oberhänsli, R., 1998. Geochemistry, Pb/Pb single zircon ages and Nd/Sr isotope composition of Precambrian rocks from southern and eastern Ethiopia: implications for crustal evolution in East Africa. Journal of African Earth Sciences 26, 207–227.

Teklay, M., Kröner, A., Mezger, K., 2001. Geochemistry, geochronology and isotope geology of Nakfa intrusive rocks, northern Eritrea: products of a tectonically thickened Neoproterozoic arc crust. Journal of African Earth Sciences 33, 283–301.

Teklay, M., Kröner, A., Mezger, K., 2002. Enrichment from plume interaction in the generation of Neoproterozoic arc rocks in northern Eritrea: implications for crustal accretion in the southern Arabian–Nubian Shield. Chemical Geology 184, 167–184.

Teklay, M., 2006. Neoproterozoic arc–back–arc system analog to modern arc–back–arc systems: evidence from tholeiite–boninite association, serpentinite mudflows and across-arc geochemical trends in Eritrea, southern Arabian-Nubian shield. Precambrian Research 145, 81–92.

Terashima, S., Yuasa, M., Nohara, M., 1994. Gold content of submarine volcanic rocks from the Izu-Ogasawara (Bonin) arc. Shigen-Chishitsu 44, 241–247.

Thébaud, N., Sugiono, D., LaFlamme, C., Miller, J., Fisher, L., Voute, F., Tessalina, S., Sonntag, I., Fiorentini, M., 2018. Protracted and polyphased gold mineralisation in the Agnew District (Yilgarn Craton, Western Australia). Precambrian Research 310, 291–304.

Thébaud, N., Allibone, A., Masurel, Q., Eglinger, A., Davis, J., André-Mayer, A.-S., Miller, J., Ouedrago, M.F., Jessell, M., 2020. The Paleoproterozoic (Rhyacian) Gold Deposits of West Africa. Society of Economic Geologist, Special Publication 18.

Thompson, J.F.H., Sillitoe, R.H., Baker, T., Lang, J.R., Mortensen, J.K., 1999. Intrusion-related gold deposits associated with tungsten-tin provinces. Mineralium Deposita 34, 323–334.

Thomson, S.N., Gehrels, G.E., Ruiz, J., Buchwaldt, R., 2012. Routine low-damage apatite U-Pb dating using laser ablation–multicollector–ICPMS. Geochemistry, Geophysics, Geosystems 13.

Tikoff, B., Blenkinsop, T., Kruckenberg, S.C., Morgan, S., Newman, J., Wojtal, S., 2013. A perspective on the emergence of modern structural geology: Celebrating the feedbacks between historical-based and process-based approaches. The Web of Geological Sciences: Advances, Impacts, and Interactions. Geological Society of America, 65–119.

Titley, S.R., 1993. Characteristics of porphyry copper occurrence in the American Southwest. Mineral Deposit Modelling: Geologic Association of Canada, Special Paper 40, 433–464.

Tomkins, A.G., Mavrogenes, J.A., 2001. Redistribution of Gold within Arsenopyrite and Lollingite during Pro- and Retrograde Metamorphism: Application to Timing of Mineralization. Economic Geology 96, 525–534.

Tomkins, A.G., Pattison, D.R., Zaleski, E., 2004. The Hemlo gold deposit, Ontario: An example of melting and mobilization of a precious metal-sulfosalt assemblage during amphibolite facies metamorphism and deformation. Economic Geology 99, 1063–1084.

Tomkins, A.G., Grundy, C., 2009. Upper temperature limits of orogenic gold deposit formation: Constraints from the granulite-hosted Griffin's Find deposit, Yilgarn craton. Economic Geology 104, 669–685.

Tomkins, A.G., 2010. Windows of metamorphic sulfur liberation in the crust: Implications for gold deposit genesis. Geochimica et Cosmochimica Acta 74, 3246–3259.

Tomkins, A.G., 2013. On the source of orogenic gold. Geology 41, 1255–1256.

Trench, A., Groves, D.I., 2015. The western Arabian-Nubian Shield; a rapidly emerging gold province. SEG News 101.

Triantafyllou, A., Berger, J., Baele, J.-M., Bruguier, O., Diot, H., Ennih, N., Monnier, C., Plissart, G., Vandycke, S., Watlet, A., 2018. Intra-oceanic arc growth driven by magmatic and tectonic processes recorded in the Neoproterozoic Bougmane arc complex (Anti-Atlas, Morocco). Precambrian Research 304, 39–63.

Tunks, A.J., Selley, D., Rogers, J.R., Brabham, G., 2004. Vein mineralization at the Damang Gold Mine, Ghana: controls on mineralization. Journal of Structural Geology 26, 1257–1273.

Turlin, F., Jébrak, M., De Souza, S., Turcotte, J., 2019. Topological characterization of a polyphased gold-bearing vein network. Journal of Structural Geology 128, 103872.

Turneaure, F.S., 1955. Metallogenic provinces and epochs. Economic Geology 50th Anniversary Volume 39–91.

Twiss, R.J., Moores, E.M., 2007. Structural Geology. © WH Freeman and Company. New York 532.

U, V

Ulrich, T., Günther, D., Heinrich, C.A., 1999. Gold concentrations of magmatic brines and the metal budget of porphyry copper deposits. Nature 399, 676–679.

Upton, P., Craw, D., 2014a. Extension and gold mineralisation in the hanging walls of active convergent continental shear zones. Journal of Structural Geology 64, 135–148.

Upton, P., Craw, D., 2014b. Modelling of structural and lithological controls on mobility of fluids and gold in orogenic belts, New Zealand. Geological Society, London, Special Publications 402, 231–253.

Urai, J.L., Williams, P.F., Van Roermund, H.L.M., 1991. Kinematics of crystal growth in syntectonic fibrous veins. Journal of Structural Geology 13, 823–836.

USGS, 1998. Bedrock geology of the Arabian Peninsula and selected adjacent areas (geo2bg).

Vail, J.R., 1979. Outline of geology and mineralization of the Nubian Shield east of the Nile valley, Sudan In: Tahon, S.A. (ed.). Evolution and mineralization of the Arabian Nubian Shield, 1, 97-107. Pergamon press.

Vail, J.R., 1983. Pan-African crustal accretion in north-east Africa. Journal of African Earth Sciences (1983) 1, 285–294.

Vail, J.R., 1985. Pan-African (late Precambrian) tectonic terrains and the reconstruction of the Arabian-Nubian Shield. Geology 13, 839.

Vail, J.R., 1988. Tectonics and evolution of the Proterozoic basement of NE Africa. The Pan-African Belts of NE Africa and Adjacent Areas. Friedr Vieweg and Sohn 185–226.

van Hinsbergen, D.J.J., Peters, K., Maffione, M., Spakman, W., Guilmette, C., Thieulot, C., Plümper, O., Gürer, D., Brouwer, F.M., Aldanmaz, E., Kaymakcı, N., 2015. Dynamics of intraoceanic subduction initiation: 2. Suprasubduction zone ophiolite formation and metamorphic sole exhumation in context of absolute plate motions: SSZ ophiolites and metamorphic soles. Geochemistry, Geophysics, Geosystems 16, 1771–1785.

van Westrenen, W., Blundy, J.D., Wood, B.J., 2001. High field strength element/rare earth element fractionation during partial melting in the presence of garnet: Implications for identification of mantle heterogeneities: MANTLE HETEROGENEITIES. Geochemistry, Geophysics, Geosystems 2, n/a-n/a.

Vanderhaeghe, O., 2012. The thermal–mechanical evolution of crustal orogenic belts at convergent plate boundaries: A reappraisal of the orogenic cycle. Journal of Geodynamics 56, 124–145.

Vasseur, R., Boivin, S., Lathuilière, B., Lazar, I., Durlet, C., Martindale, R.-C., Bodin, S., Elhmidi, K., 2019. Lower Jurassic corals from Morocco with skeletal structures convergent with those of Paleozoic rugosan corals. Palaeontologia Electronica 22(22.2 48).

Vearncombe, J.R., 1983. A dismembered ophiolite from the Mozambique belt, west Pokot, Kenya. Journal of African Earth Sciences (1983) 1, 133–143.

Velásquez, G., Beziat, D., Salvi, S., Siebenaller, L., Borisova, A.Y., Pokrovski, G.S., De Parseval, P., 2014. Formation and Deformation of Pyrite and Implications for Gold Mineralization in the El Callao District, Venezuela. Economic Geology 109, 457–486.

Velásquez, G., Salvi, S., Siebenaller, L., Béziat, D., Carrizo, D., 2018. Control of Shear-Zone-Induced Pressure Fluctuations on Gold Endowment: The Giant El Callao District, Guiana Shield, Venezuela. Minerals 8, 430.

Vidal, O., De Andrade, V., Lewin, E., Munoz, M., Parra, T., Pascarelli, S., 2006. P-T-deformation-Fe3+/Fe2+ mapping at the thin section scale and comparison with XANES mapping: application to a garnet-bearing metapelite from the Sambagawa metamorphic belt (Japan). Journal of Metamorphic Geology 24, 669–683.

Vidal, O., Parra, T., 2000. Exhumation paths of high-pressure metapelites obtained from local equilibria for chlorite-phengite assemblages. Geological Journal 35, 139–161.

Voisey, C.R., Willis, D., Tomkins, A.G., Wilson, C.J.L., Micklethwaite, S., Salvemini, F., Bougoure, J., Rickard, W.D.A., 2020. Aseismic Refinement of Orogenic Gold Systems. Economic Geology 115, 33–50.

Vonlanthen, P., Kunze, K., Burlini, L., Grobety, B., 2006. Seismic properties of the upper mantle beneath Lanzarote (Canary Islands): model predictions based on texture measurements by EBSD. Tectonophysics 428, 65–85.

Voute, F., Hagemann, S.G., Evans, N.J., Villanes, C., 2019. Sulfur isotopes, trace element, and textural analyses of pyrite, arsenopyrite and base metal sulfides associated with gold mineralization in the Pataz-Parcoy district, Peru: implication for paragenesis, fluid source, and gold deposition mechanisms. Mineralium Deposita 54, 1077–1100.

Vroon, P.Z., Van Bergen, M.J., White, W.M., Varekamp, J.C., 1993. Sr-Nd-Pb isotope systematics of the Banda Arc, Indonesia: Combined subduction and assimilation of continental material. Journal of Geophysical Research: Solid Earth 98, 22349–22366.

Vukmanovic, Z., Barnes, S.J., Reddy, S.M., Godel, B., Fiorentini, M.L., 2013. Morphology and microstructure of chromite crystals in chromitites from the Merensky Reef (Bushveld Complex, South Africa). Contributions to Mineralogy and Petrology 165, 1031–1050.

W

Wallis, D., Parsons, A.J., Hansen, L.N., 2019. Quantifying geometrically necessary dislocations in quartz using HR-EBSD: Application to chessboard subgrain boundaries. Journal of Structural Geology 125, 235–247.

Wang, S.-R., Yang, L.-Q., Wang, J.-G., Wang, E.-J., Xu, Y.-L., 2019. Geostatistical Determination of Ore Shoot Plunge and Structural Control of the Sizhuang World-Class Epizonal Orogenic Gold Deposit, Jiaodong Peninsula, China. Minerals 9, 214.

Wang, Y., Han, X., Petersen, S., Frische, M., Qiu, Z., Li, Huaiming, Li, Honglin, Wu, Z., Cui, R., 2017. Mineralogy and trace element geochemistry of sulfide minerals from the Wocan Hydrothermal Field on the slow-spreading Carlsberg Ridge, Indian Ocean. Ore Geology Reviews 84, 1–19.

Weatherley, D.K., Henley, R.W., 2013. Flash vaporization during earthquakes evidenced by gold deposits. Nature Geoscience 6, 294–298.

Webber, A.P., Roberts, S., Taylor, R., Pitcairn, I., 2010. Enrichment of gold in oceanic crust by the Iceland mantle plume: constraints from the Reykjanes Ridge. Proc. Goldschmidt Conf., Knoxville, TN, USA, June, the University of Tennessee and Oak Ridge National Laboratory.

Webber, A.P., Roberts, S., Taylor, R.N., Pitcairn, I.K., 2013. Golden plumes: Substantial gold enrichment of oceanic crust during ridge-plume interaction. Geology 41, 87–90.

Weinberg, R.F., Hodkiewicz, P.F., Groves, D.I., 2004. What controls gold distribution in Archean terranes? Geology 32, 545–548.

Weinberg, R.F., Van der Borgh, P., Bateman, R.J., Groves, D.I., 2005. Kinematic history of the Boulder-Lefroy shear zone system and controls on associated gold mineralization, Yilgarn Craton, Western Australia. Economic Geology 100, 1407–1426.

White, N.C., Hedenquist, J.W., 1995. Epithermal gold deposits: styles, characteristics and exploration. SEG Newsletter 23, 1;9-13.

White, W.M., 2015. Isotope geochemistry. John Wiley & Sons.

Whitehouse, M.J., Windley, B.F., Ba-Bttat, M.A.O., Fanning, C.M., Rex, D.C., 1998. Crustal evolution and terrane correlation in the eastern Arabian Shield, Yemen: geochronological constraints. Journal of the Geological Society 155, 281–295.

Whitehouse, M.J., Stoeser, D.B., Stacey, J.S., 2001. The Khida Terrane ? Geochronological and Isotopic Evidence for Paleoproterozoic and Archean Crust in the Eastern Arabian Shield of Saudi Arabia. Gondwana Research 4, 200–202.

Wilde, S.A., Youssef, K., 2000. Significance of SHRIMP U-Pb dating of the Imperial Porphyry and associated Dokhan Volcanics, Gebel Dokhan, north Eastern Desert, Egypt. Journal of African Earth Sciences 31, 403–413.

Wilkinson, A.J., Britton, T.B., Jiang, J., Karamched, P.S., 2014. A review of advances and challenges in EBSD strain mapping. IOP Conference Series: Materials Science and Engineering 55, 012020.

Wilkinson, J.J., Johnston, J.D., 1996. Pressure fluctuations, phase separation, and gold precipitation during seismic fracture propagation. Geology 24, 395–398.

Wilkinson, J.J., 2013. Triggers for the formation of porphyry ore deposits in magmatic arcs. Nature Geoscience 6, 917–925.

Wille, G., Lerouge, C., Schmidt, U., 2018. A multimodal microcharacterisation of trace-element zonation and crystallographic orientation in natural cassiterite by combining cathodoluminescence, EBSD, EPMA and contribution of confocal Raman-in-SEM imaging: Multimodal characterization of zonation in cassiterite. Journal of Microscopy 270, 309–317.

Wilson, C.J.L., Schaubs, P.M., Leader, L.D., 2013. Mineral Precipitation in the Quartz Reefs of the Bendigo Gold Deposit, Victoria, Australia. Economic Geology 108, 259–278.

Wilson, S.A., Ridley, W.I., Koenig, A.E., 2002. Development of sulfide calibration standards for the laser ablation inductively-coupled plasma mass spectrometry technique. J. Anal. At. Spectrom. 17, 406–409.

Winderbaum, L., Ciobanu, C.L., Cook, N.J., Paul, M., Metcalfe, A., Gilbert, S., 2012. Multivariate Analysis of an LA-ICP-MS Trace Element Dataset for Pyrite. Mathematical Geosciences 44, 823–842.

Windh, J., 1995. Saddle reef and related gold mineralization, Hill End gold field, Australia; evolution of an auriferous vein system during progressive deformation. Economic Geology 90, 1764–1775.

Windley, B.F., 1992. Proterozoic collisional and accretionary orogens. Developments in Precambrian Geology. Elsevier, 419–446.

Windley, B.F., 1996. The evolving continents. Oceanographic Literature Review 8, 785.

Windley, B.F., Whitehouse, M.J., Ba-Bttat, M.A.O., 1996. Early Precambrian gneiss terranes and Pan-African island arcs in Yemen: Crustal accretion of the eastern Arabian Shield. Geology 24, 131.

Windley, B.F., 2003. Continental growth in the Proterozoic: a global perspective. Geological Society, London, Special Publications 206, 23–33.

Wipfler, E.L., 1996. Transpressive structures in the Neoproterozoic Ariab-Nakasib Belt, northeast Sudan: evidence for suturing by oblique collision. Journal of African Earth Sciences 23, 347–362.

Woldemichael, B.W., Kimura, J.-I., Dunkley, D.J., Tani, K., Ohira, H., 2010. SHRIMP U–Pb zircon geochronology and Sr–Nd isotopic systematic of the Neoproterozoic Ghimbi-Nedjo mafic to intermediate intrusions of Western Ethiopia: a record of passive margin magmatism at 855 Ma? International Journal of Earth Sciences 99, 1773–1790.

Wohlgemuth-Ueberwasser, C.C., Viljoen, F., Petersen, S., Vorster, C., 2015. Distribution and solubility limits of trace elements in hydrothermal black smoker sulfides: An in-situ LA-ICP-MS study. Geochimica et Cosmochimica Acta 159, 16–41.

Wood, B.J., Walter, M.J., Wade, J., 2006. Accretion of the Earth and segregation of its core. Nature 441, 825–833.

Woodhead, J., Hergt, J., Shelley, M., Eggins, S., Kemp, R., 2004. Zircon Hf-isotope analysis with an excimer laser, depth profiling, ablation of complex geometries, and concomitant age estimation. Chemical Geology 209, 121–135.

Woodhead, J.D., Hergt, J.M., 2005. A preliminary appraisal of seven natural zircon reference materials for in situ Hf isotope determination. Geostandards and Geoanalytical Research 29, 183–195.

World Gold Council, 2020. About Gold [WWW Document], World Gold Council. URL https://www.gold.org/about-gold, consulted on January, 4th 2020.

Wright, S.I., Nowell, M.M., Field, D.P., 2011. A review of strain analysis using electron backscatter diffraction. Microscopy and Microanalysis 17, 316–329.

Wright, S.I., Nowell, M.M., Lindeman, S.P., Camus, P.P., De Graef, M., Jackson, M.A., 2015. Introduction and comparison of new EBSD post-processing methodologies. Ultramicroscopy 159, 81–94.

Wu, F.-Y., Yang, Y.-H., Xie, L.-W., Yang, J.-H., Xu, P., 2006. Hf isotopic compositions of the standard zircons

and baddeleyites used in U–Pb geochronology. Chemical Geology 234, 105–126.

Wu, Y.-F., Evans, K., Li, J.-W., Fougerouse, D., Large, R.R., Guagliardo, P., 2019a. Metal remobilization and ore-fluid perturbation during episodic replacement of auriferous pyrite from an epizonal orogenic gold deposit. Geochimica et Cosmochimica Acta 245, 98–117.

Wu, Y.-F., Fougerouse, D., Evans, K., Reddy, S.M., Saxey, D.W., Guagliardo, P., Li, J.-W., 2019b. Gold, arsenic, and copper zoning in pyrite: A record of fluid chemistry and growth kinetics. Geology 47, 641–644.

Wyborn, L.A.I., Heinrich, C.A., Jaques, A.L., 1994. Australian Proterozoic mineral systems: essential ingredients and mappable criteria. The AusIMM Annual Conference. AusIMM Darwin, 109–115.

Wyman, D.A., Cassidy, K.F., Hollings, P., 2016. Orogenic gold and the mineral systems approach: Resolving fact, fiction and fantasy. Ore Geology Reviews 78, 322–335.

X, Y, Z

Xing, Y., Brugger, J., Tomkins, A., Shvarov, Y., 2019. Arsenic evolution as a tool for understanding formation of pyritic gold ores. Geology 47, 335–338.

Xu, P., Wu, F., Xie, L., Yang, Y., 2004. Hf isotopic compositions of the standard zircons for U-Pb dating. Chinese Science Bulletin 49, 1642–1648.

Yakubchuk, A., Stein, H., Wilde, A., 2014. Results of pilot Re–Os dating of sulfides from the Sukhoi Log and Olympiada orogenic gold deposits, Russia. Ore Geology Reviews 59, 21–28.

Yang, L.-Q., Deng, J., Goldfarb, R.J., Zhang, J., Gao, B.-F., Wang, Z.-L., 2014. 40Ar/39Ar geochronological constraints on the formation of the Dayingezhuang gold deposit: New implications for timing and duration of hydrothermal activity in the Jiaodong gold province, China. Gondwana Research 25, 1469–1483.

Yang, L.-Q., Zhao, R., Wang, Q., Liu, X., Carranza, E.J.M., 2018. Fault geometry and fluid-rock reaction: Combined controls on mineralization in the Xinli gold deposit, Jiaodong Peninsula, China. Journal of Structural Geology 111, 14–26.

Yardley, B.W.D., 1989. An introduction to metamorphic petrology.

Yardley, B.W.D., Cleverley, J.S., 2015. The role of metamorphic fluids in the formation of ore deposits. Geological Society, London, Special Publications 393, 117–134.

Ye, L., Cook, N.J., Ciobanu, C.L., Yuping, L., Qian, Z., Tiegeng, L., Wei, G., Yulong, Y., Danyushevskiy, L., 2011. Trace and minor elements in sphalerite from base metal deposits in South China: A LA-ICPMS study. Ore Geology Reviews 39, 188–217.

Yousefi, M., Kreuzer, O.P., Nykänen, V., Hronsky, J.M., 2019. Exploration information systems–A proposal for the future use of GIS in mineral exploration targeting. Ore Geology Reviews 111, 103005.

Yu, H.-C., Qiu, K.-F., Nassif, M.T., Geng, J.-Z., Sai, S.-X., Duo, D.-W., Huang, Y.-Q., Wang, J., 2020. Early orogenic gold mineralization event in the West Qinling related to closure of the Paleo-Tethys Ocean–Constraints from the Ludousou gold deposit, central China. Ore Geology Reviews 117, 103217.

Žák, J., Verner, K., Týcová, P., 2008. Grain-scale processes in actively deforming magma mushes: New insights from electron backscatter diffraction (EBSD) analysis of biotite schlieren in the Jizera granite, Bohemian Massif. Lithos 106, 309–322.

Zaw, K., 1991. The effect of Devonian metamorphism and metasomatism on the mineralogy and geochemistry of the Cambrian VMS deposits in the Rosebery-Hercules district, western Tasmania. University of Tasmania.

Zaw, K., Large, R.R., 1996. Petrology and geochemistry of sphalerite from the Cambrian VHMS deposits in the Rosebery-Hercules district, western Tasmania: Implications for gold mineralisation and Devonian metamorphic-metasomatic processes. Mineralogy and Petrology 57, 97–118.

Zeh, A., Gerdes, A., 2012. U–Pb and Hf isotope record of detrital zircons from gold-bearing sediments of the Pietersburg Greenstone Belt (South Africa)—Is there a common provenance with the Witwatersrand Basin? Precambrian Research 204, 46–56.

Zhao, H.-X., Frimmel, H.E., Jiang, S.-Y., Dai, B.-Z., 2011. LA-ICP-MS trace element analysis of pyrite from the Xiaoqinling gold district, China: Implications for ore genesis. Ore Geology Reviews 43, 142–153.

Zhao, K., Yao, H., Wang, J., Ghebretnsae, G.F., Xiang, W., Xiong, Y.-Q., 2019. Genesis of the Koka Gold Deposit in Northwest Eritrea, NE Africa: Constraints from Fluid Inclusions and C-H-O-S Isotopes. Preprints.

Zimmer, M., Kröner, A., Jochum, K.P., Reischmann, T., Todt, W., 1995. The Gabal Gerf complex: A Precambrian N-MORB ophiolite in the Nubian Shield, NE Africa. Chemical Geology 123, 29–51.

Zoheir, B.A., 2008. Characteristics and genesis of shear zone-related gold mineralization in Egypt: A case study from the Um El Tuyor mine, south Eastern Desert. Ore Geology Reviews 34, 445–470.

Zoheir, B., Moritz, R., 2014. Fluid evolution in the El-Sid gold deposit, Eastern Desert, Egypt. Geological Society, London, Special Publications 402, 147–175.

Zoheir, B.A., Creaser, R.A., Lehmann, B., 2015. Re-Os geochronology of gold mineralization in the Fawakhir area, Eastern Desert, Egypt. International Geology Review 57, 1418–1432.

Zoheir, B.A., Emam, A., El-Amawy, M., Abu-Alam, T., 2018a. Auriferous shear zones in the central Allaqi-Heiani belt: Orogenic gold in post-accretionary structures, SE Egypt. Journal of African Earth Sciences 146, 118–131.

Zoheir, B.A., Deshesh, F., Broman, C., Pitcairn, I., El-Metwally, A., Mashaal, S., 2018b. Granitoid-associated gold mineralization in Egypt: a case study from the Atalla mine. Mineralium Deposita 53, 701–720.

Zoheir, B.A., Johnson, P.R., Goldfarb, R.J., Klemm, D.D., 2019a. Orogenic gold in the Egyptian Eastern Desert: Widespread gold mineralization in the late stages of Neoproterozoic orogeny. Gondwana Research 75, 184–217.

Zoheir, B.A, Emam, A., Soliman, N., Holzheid, A., 2019b. Gold Metallogeny of the Egyptian South Eastern Desert. Springer Berlin Heidelberg, Berlin, Heidelberg, 261–263.

Zoheir, B.A, Steele-MacInnis, M., Garbe-Schönberg, D., 2019c. Orogenic gold formation in an evolving, decompressing hydrothermal system: Genesis of the Samut gold deposit, Eastern Desert, Egypt. Ore Geology Reviews 105, 236–257.

Zoheir, B.A., Feigenson, M., Zi, J.-W., Turrin, B., Deshesh, F., El-Metwally, A., 2019d. Ediacaran (~ 600 Ma) orogenic gold in Egypt: age of the Atalla gold mineralization and its geological significance. International Geology Review 61, 779–794.

Zoheir, B., Goldfarb, R., Holzheid, A., Helmy, H., El Sheikh, A., 2019e. Geochemical and geochronological characteristics of the Um Rus granite intrusion and associated gold deposit, Eastern Desert, Egypt. Geoscience Frontiers.

Zoheir, B.A, Lehmann, B., Emam, A., Radwan, A., Zhang, R., Bain, W.M., Steele-MacInnis, M., Nolte, N., 2020. Extreme fractionation and magmatic–hydrothermal transition in the formation of the Abu Dabbab rare-metal granite, Eastern Desert, Egypt. Lithos 352–353, 105329.

Zoheir, B., Zeh, A., El-Bialy, M., Ragab, A., Deshesh, F., Steele-MacInnis, M., 2021. Hybrid granite magmatism during orogenic collapse in the Eastern Desert of Egypt: Inferences from whole-rock geochemistry and zircon U–Pb–Hf isotopes. Precambrian Research 354, 106044.

Résumé : L'or est un élément sidérophile préférentiellement contenu dans les enveloppes internes de la Terre. La compréhension des mécanismes permettant son transfert vers l'écorce terrestre passe par l'étude de l'évolution géodynamique des segments de croûte dite juvénile, *i.e.,* dérivée de matériel extrait directement du manteau. Le système métallogénique de l'or s'intéresse donc (i) à l'environnement géodynamique favorable à la fertilisation en or de la croûte et (ii) au(x) contexte(s) tectono-métamorphique(s) ayant permis la remobilisation de ce réservoir et sa concentration sous forme d'occurrences minéralisées. Cette démarche est appliquée aux sutures de Keraf et d'Atmur-Delgo au sein du bouclier arabo-nubien, le plus grand segment au monde de croûte juvénile néoprotérozoïque et l'une des principales provinces aurifères panafricaines. Si ces structures sont considérées comme des marqueurs de la formation du supercontinent Gondwana au Soudan et hébergent de nombreux gisements aurifères, leur évolution géodynamique et métallogénique reste méconnue.

Deux pics d'activité magmatique à signatures isotopiques Hf et Nd suprachondritiques enregistrent la formation et la maturation de différents arcs insulaires le long de ces zones de suture entre 840-810 Ma et 760-655 Ma. La longue durée de vie (185 millions d'années) de l'arc insulaire décrit le long de la suture de Keraf et sa nature juvénile prédominante expliqueraient la fertilisation crustale en or à l'échelle régionale. La première phase de croissance crustale, uniquement enregistrée le long de la suture de Keraf, est associée à un événement aurifère mineur, de nature magmato-hydrothermale. La seconde période d'activité magmatique est associée au fonctionnement d'arcs insulaires le long des sutures de Keraf et d'Atmur-Delgo. Le couplage d'observations et de mesures réalisées du terrain au laboratoire illustre la continuité spatiale du contrôle structural des minéralisations postérieures au premier événement aurifère décrit. D'une part, un épisode minéralisateur a lieu vers 755-725 Ma, lors d'un continuum de déformation exprimé par la mise en place de plis en fourreau et de structures minéralisées linéaires. Les roches encaissantes de la minéralisation sont affectées par un métamorphisme au faciès amphibolite inférieur. À l'échelle du district, cet événement aurifère est associé à l'accrétion tectonique dans le prisme sédimentaire en avant de l'arc d'Atmur-Delgo. À l'échelle microscopique, la minéralisation résulte de la remobilisation syn-métamorphique du stock d'or contenu par les sulfures préexistant. D'autre part, plusieurs gisements d'or orogénique sont exprimés sous forme de veines d'extension hébergées par des corps intrusifs, illustrant un fort contrôle rhéologique de la minéralisation. Les veines minéralisées sont formées selon le mécanisme de faille-valve, en réponse à la réactivation épisodique et localisée de décrochements crustaux jusqu'à 550 Ma au sein de la suture de Keraf. Les deux événements minéralisateurs exprimés le long des sutures d'Atmur-Delgo et de Keraf sont respectivement le plus ancien associé à des veines aurifères et le plus jeune d'or orogénique décrits à ce jour au sein du bouclier arabo-nubien.

L'application du système métallogénique permet de définir des clés d'exploration à l'échelle du district qui traduisent des processus magmatiques (*e.g.,* reliques d'arc insulaire) et contextes tectono-métamorphiques (*e.g.,* prisme d'accrétion, décrochements tardi-orogéniques) contrôlant des minéralisations aurifères aux caractéristiques structurales, géochimiques et chronologiques très variables dans la partie occidentale du bouclier arabo-nubien. Cette stratégie diffère singulièrement de l'approche typologique dont l'efficacité se limite à (i) un unique type de minéralisation et à (ii) la prospection à l'échelle du gisement.